Applications of Ferromagnetic and Optical Materials, Storage and Magnetoelectronics

MATERIALS RESEARCH SOCIETY
SYMPOSIUM PROCEEDINGS VOLUME 674

Applications of Ferromagnetic and Optical Materials, Storage and Magnetoelectronics

Symposia held April 16–20, 2001, San Francisco, California, U.S.A.

EDITORS:

Herman J. Borg
Philips Research Laboratories
Eindhoven, The Netherlands

Konrad Bussmann
Naval Research Laboratory
Washington, D.C., U.S.A.

William F. Egelhoff, Jr.
National Institute of Standards and
  Technology
Gaithersburg, Maryland, U.S.A.

Lambertus Hesselink
Stanford University
Stanford, California, U.S.A.

Sara A. Majetich
Carnegie Mellon University
Pittsburgh, Pennsylvania, U.S.A.

Edward S. Murdock
Seagate Technology
Minneapolis, Minnesota, U.S.A.

Bethanie J.H. Stadler
University of Minnesota
Minneapolis, Minnesota, U.S.A.

Manuel Vázquez
Instituto de Ciencia de Materiales de Madrid
Madrid, Spain

Matthias Wuttig
RWTH Aachen
Aachen, Germany

John Q. Xiao
University of Delaware
Newark, Delaware, U.S.A.

|M|R|S|

Materials Research Society
Warrendale, Pennsylvania

Single article reprints from this publication are available through
University Microfilms Inc., 300 North Zeeb Road, Ann Arbor, Michigan 48106

CODEN: MRSPDH

Published by:

Materials Research Society
506 Keystone Drive
Warrendale, PA 15086
Telephone (724) 779-3003
Fax (724) 779-8313
Web site: http://www.mrs.org/

Manufactured in the United States of America

CONTENTS

SYMPOSIUM T

NEW DIRECTIONS IN MATERIALS

*Invited Paper

MICROMAGNETICS TO NANOMAGNETICS— THE NEXT STEP

MATERIALS FOR MAGNETIC DEVICES

SYMPOSIUM U

SOFT MAGNETIC ALLOYS
AND FERRITES

*Invited Paper

MAGNETIC NANOPARTICLES, NANOWIRES AND ARRAYS

MAGNETIC MICRO- AND NANOCOMPOSITES

*Invited Paper

MAGNETOSTRICTION

*Invited Paper

SYMPOSIUM V

*PHASE CHANGE RECORDING
MATERIALS AND MECHANISMS*

*MAGNETO-OPTIC AND HOLOGRAPHIC
RECORDING: MATERIALS, MECHANISMS
AND NEW CONCEPTS*

*Invited Paper

*OPTICAL DATA STORAGE:
MATERIALS AND MECHANISMS*

*Invited Paper

PREFACE

SYMPOSIUM T

Symposium T, "Materials for Magnetic Devices—Magneto-Electronics and Recording," held April 16–19 at the 2001 MRS Spring Meeting in San Francisco, California, highlighted the exciting new area of spintronics and its applications to recording, sensors, and quantum computing. It covered new materials and structures that use the mechanism of spin dependent transport, including giant magnetoresistive (GMR) materials and magnetic tunnel junctions (MTJs). The symposium kicked off with Jim Daughton's (NVE) tutorial on the "Spintronics Revolution" (pun intended!).

One of the key factors that limits the performance of both GMR spin valves and MTJs are pinholes, which are not easily detected. A novel technique was introduced that uses the strong low-temperature dependence of the coupling field on pinholes to separate their effects from effects of magnetostatic coupling, such as the orange-peel effect. Other new directions in materials covered artificial lattices and superlattices, NiO-Co bilayers, and room temperature spin-flip bilayers of $CoFe_2O_4/\alpha\text{-}Fe_2O_3$. Taking the field to the "next step," the talks moved from micromagnetics to nanomagnetics, including fabrication and characterization techniques. Many different materials for magnetic devices were covered in oral and poster sessions. The last session dealt with the elusive topic of spins in semiconductors. The material needed to inject the spin into the semiconductor is the most provocative issue, and speakers argued magnetic semiconductors vs. Heusler alloys, each with its own shortcomings.

General financial support of this symposium was provided by the Materials Research Society (MRS), the Army Research Office (ARO), and the Office of Naval Research (ONR). The editors are indebted to the staff of MRS for the guidance and help that was provided beginning with the symposium proposal and continuing through the symposium execution and the publication of this book. We also thank the invited speakers for their top quality presentations and the session chairs for keeping the sessions lively and timely.

Konrad Bussmann
William F. Egelhoff, Jr.
Edward S. Murdock
Bethanie J.H. Stadler

August 2001

PREFACE

SYMPOSIUM U

Ferromagnetic materials are used in a wide variety of applications, including permanent magnets, transformer cores, electrical generators, and magnetic data storage. In the past decade there have been unprecedented developments in ferromagnetic materials, resulting in much-improved magneto-optical, magneto-resistive, magnetostrictive, permanent and nanocrystalline soft magnetic materials. These materials are often achieved by controlling different length scales in nanostructured materials and composites such as exchange and spin diffusion length, electron mean free path, and structural ordering. This symposium, "Ferromagnetic Materials," held April 17–20 at the 2001 MRS Spring Meeting in San Francisco, California, focused on both fundamental principles and applications of new ferromagnetic materials. The role of disorder in nanostructured materials was a recurrent theme of this symposium. Structural disorder in a variety of nanocrystalline materials (compacted clusters of elemental ferromagnets, mechanically milled GdAl and SmCo alloys, recrystallized melt-spun ribbons) is related to the magnetic properties. The degree of order within ferromagnetic materials is also related to magnetic properties. Here the order could be chemical, as in the cell structure phases of Sm_2Co_{17} alloys for permanent magnets, or charge ordering, as in colossal magnetoresistance compounds. There were also numerous talks on structural ordering in self-assembled materials made from either micron-sized or nanoscale particles, which could be structured with or without magnetic fields. The third major theme of the symposium was the optimization of magnetic materials for various applications through controlling composition and processing. These materials include FeCo composites with improved mechanical properties for high temperature, magnetostrictive materials (NiMnGa and TbFe alloys) for actuators and sensors, and nanocrystalline wires for possible nanomotor applications.

Sara A. Majetich
Manuel Vázquez
John Q. Xiao

August 2001

PREFACE

SYMPOSIUM V

Symposium V, "Optical Data Storage—Materials, Mechanisms, and Emerging Technologies," held April 19 at the 2001 MRS Spring Meeting in San Francisco, California, was attended by 50-75 people. CD and DVD technologies are pervasive throughout society and they are one of the success stories involving optical materials and devices. Technology roadmaps predict storage capacities exceeding 100 GB for CD size removable disks, using blue lasers and optics with high light-collection efficiency for the second half of this decade. Larger storage capacities require commensurately faster data recording and readout rates.

Invited and contributed papers highlighted different pathways by which these future product goals might be achieved. Magneto-optic recording technology will incorporate ingenious apertures that open and close, and amplify signals under light illumination providing small windows through which data can be recorded and readout at rates exceeding 200 Mbit/sec with recording densities over 110 GB per disk. The competitive phase change recording technology is predicted to have transfer rates approaching 120 Mbit/sec with similar capacities. Both technologies have their fiercely competitive proponents and even within the broad class of recording media, competing optical and materials approaches will provide the consumer with a dazzling array of options and acronyms to store movies and high density television multimedia information.

On the scientific front, excellent progress was reported on understanding the materials physics at the nanoscale level, based both on extensive modeling and experimental data. Preliminary results on phase change media responding to femto-second pulses were reported as well as detailed data on the relationship between optical recording properties and materials parameters. And if 100 GB per disk is not sufficient capacity, volumetric storage techniques based on holography and multi-layer phase change media promise additional capacity approaching TB per disk before the end of this decade.

<div align="right">

Herman J. Borg
Lambertus Hesselink
Matthias Wuttig

September 2001

</div>

MATERIALS RESEARCH SOCIETY SYMPOSIUM PROCEEDINGS

MATERIALS RESEARCH SOCIETY SYMPOSIUM PROCEEDINGS

SYMPOSIUM T

New Directions in Materials

Detection of Pinholes in Ultrathin Films by Magnetic Coupling

W. F. Egelhoff, Jr., L. Gan, P. J. Chen, C. J. Powell, R. D. McMichael, and R. A. Fry,
National Institute of Standards and Technology
Gaithersburg, MD 20899

G. Beach, D. Martien, and A. E. Berkowitz
Center for Magnetic Recording Research
University of California at San Diego
La Jolla, CA 92093

Abstract

When two magnetic films are separated by a nonmagnetic film, pinholes in the nonmagnetic film can allow direct contact and, thereby, direct magnetic exchange coupling between the two magnetic films. We have studied this coupling by having one of the magnetic films pinned and leaving the other free to switch at low field. The pinning is accomplished with test structures based on exchange bias and synthetic antiferromagnetic layers. Since the pinning strength increases sharply at low temperatures but orange-peel coupling does not, low-temperature (77 K) measurements appear to identify whether an observed coupling arises primarily from magnetic coupling through pinholes or primarily from orange-peel roughness. Our measurements appear to indicate that the observed coupling arises primarily from magnetic coupling through pinholes for Cu films less than 2.1 nm thick and for Al_2O_3 films less than 0.6 nm thick but primarily from roughness-induced (orange-peel) magnetostatic coupling for larger thicknesses.

Introduction

Pinholes are widely believed to play a key role in limiting the performance of both giant magnetoresistance (GMR) spin valves and magnetic tunnel junctions (MTJs).[1] It is generally believed that as the spacer layer, Cu in the case of spin valves and Al_2O_3 in the case of MTJs, is made thinner the value of the magnetoresistance (MR) increases until pinholes occur. Pinholes couple the two magnetic layers ferromagnetically, making it difficult to achieve antiparallel alignment, and thereby limiting the MR.

Pinholes are not easy to observe. There is some evidence from transmission electron microscopy (TEM) for the existence of pinholes, but in systems such as Co/Cu/Co the low electron-scattering contrast between elements of similar atomic number makes conclusive identification of pinholes difficult.[1] Another problem is that the thickness of the Cu layer is typically much smaller ($\approx$ 2 nm) than the depth of the TEM sample in the beam direction ($\approx$ 20 nm). If the diameter of a pinhole in the Cu film is similar to the thickness of the Cu film, it would be only $\approx$ 10 % of the sample depth thus exacerbating the contrast problem. In systems such as Al_2O_3/Co, there is some evidence that electrochemical deposition of Cu clusters can identify pinholes, although the applied potential may also create pinholes .[1]

Two groups have recently reported the use of magnetic hysteresis loops to study coupling between magnetic films of different coercivity separated by an insulating film.[2] The method appears to have much promise, and the present work is an extension of this concept.

The present work has two aims. One is to develop an improved method for observing the onset of pinholes as the spacer layer is made thinner. The other is to develop an improved method for distinguishing the regime of spacer-layer thickness in which pinhole coupling dominates from the one in which orange-peel coupling dominates.

Experimental

The NiO substrates used in this work were polycrystalline films ≈ 50 nm thick, deposited on 4" Si wafers by reactive magnetron sputtering at the University of California at San Diego. At the National Institute of Standards and Technology (NIST), the wafers were cleaved into ≈ 1 cm^2 squares, cleaned ultrasonically in a detergent solution, rinsed in distilled water, blown dry, and installed in the deposition chamber. After bakeout, the deposition chamber has a base pressure of 3×10^{-8} Pa (2×10^{-10} Torr), of which 90% is H$_2$. The metal films were deposited at room temperature by dc-magnetron sputtering in 0.3 Pa (2 mTorr) Ar at a typical rate of ≈ 0.05 nm/s. Oxide fims are deposited by reactive sputtering, adding 0.01 Pa (10^{-4} Torr) O$_2$ to the Ar.

Magnetoresistance (MR) measurements were made at NIST with a 4-point probe in a direct current mode. The values of the coupling reported have an estimated uncertainty of ± 5 % due to the slight skew in the hysteresis loop of the free Co layer. The calibration of the Hall probe used for measurement of the applied field during MR measurements has an uncertainty of ± 2 % . The measurements at 77 K were performed with the sample immersed in liquid nitrogen. Additional experimental details may be found in Ref. 3.

Results and Discussion

Structures of the type illustrated in Fig. 1 were used to investigate the magnetic coupling between two ferromagnetic layers. The concept behind the structure in Fig. 1 is to have two Co films separated by a non-magnetic spacer layer. The upper Co film is magnetically pinned by the synthetic antiferromagnet Co/Ru/Co and the natural antiferromagnet Ir$_{20}$Mn$_{80}$. The Co film below the non-magnetic spacer layer is free switch at low field whenever the non-magnetic spacer layer is thick enough to prevent magnetic coupling.

The lower parts of the structure constitute a GMR spin valve. GMR measurements are used to observe the hysteresis loop of the free Co layer. The synthetic antiferromagnet Co/Ru/Co and the natural antiferromagnet NiO substrate serve to pin the Co layer that is under the Cu. The Cu layer thickness in the spin valve is chosen to be 4 nm to ensure that the contribution to the coupling is insignificant from the Co layer below the Cu.

The coupling is observed as a shift from zero field in the center of the GMR hysteresis loop of the "free" Co. Figure 2 presents the coupling data for Al$_2$O$_3$ as the non-magnetic spacer layer. With no spacer layer, the two Co films form a single layer 5 nm thick and the hysteresis loop center is shifted ≈ 30 mT (300 Oe) from zero field. At 77 K this shift increases to ≈ 60 mT (600 Oe) as the synthetic antiferromagnet Co/Ru/Co becomes stronger.

10 nm IrMn
2.5 nm Co
0.5 nm Ru
2.5 nm Co
Non-magnetic spacer layer
Free 2.5 nm Co layer
4 nm Cu
2.5 nm Co
0.5 nm Ru
2.5 nm Co
NiO substrate

Figure 1.   An illustration of the type of test structure used in this study.

In Fig. 2 a spacer layer of 0.6 nm Al_2O_3 is sufficient to suppress any significant temperature dependence in the coupling field. Apparently, this is the thickness at which magnetic pinholes cease to be significant. The coupling that is observed for 0.6 nm or more of Al_2O_3 is probably magnetostatic and comes from the orange-peel effect.[4] Only a very slight increase in orange-peel coupling would be expected since the magnetization of Co increases by less than 1 % from 295 K to 77 K.
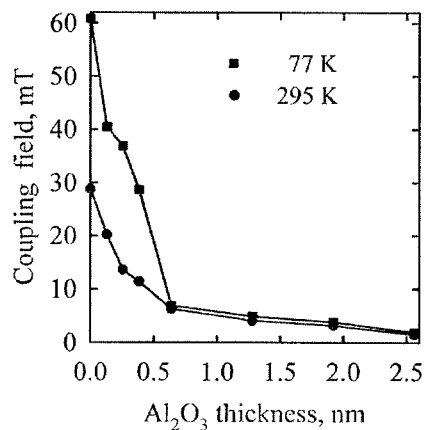
Figure 2. The coupling field observed in the GMR hysteresis loop of the free Co layer when the non-magnetic spacer layer is Al_2O_3, as a function of the spacer layer thickness.

It is significant that the magnetic pinholes appear to close up at an Al_2O_3 thickness of 0.6 nm. In studies of magnetic tunnel junctions, it is generally found that this is the practical limit on how thin the Al_2O_3 barrier can be made. Thinner Al_2O_3 layers yield drastic reductions in tunneling MR. The results of Fig. 2 suggest that, in this thickness regime, magnetic pinholes would make it difficult to achieve the antiparallel magnetic state. Moreover, if as seems likely, the magnetic pinholes represent direct Co-Co contacts, these pinholes may be expected to act as current short circuits as well.
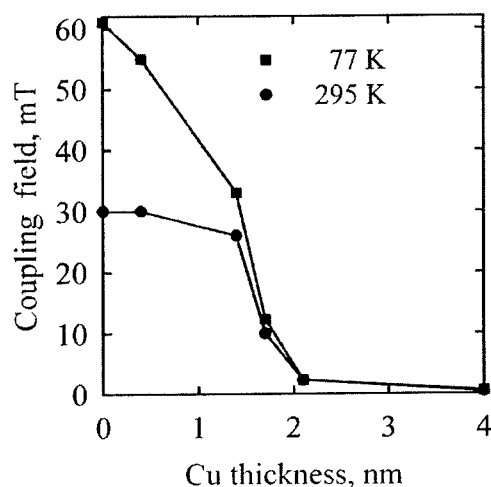
Figure 3.   The coupling field observed in the GMR hysteresis loop of the free Co layer when the non-magnetic spacer layer is Cu, as a function of the spacer layer thickness.

Figure 3 presents the coupling results for Cu as the non-magnetic spacer layer. It may be noted that this choice of spacer layer turns the structure into a dual spin valve. As a result, there will be a contribution to the GMR from the top half of the dual spin valve. However, this effect does not detract from the validity of the measured coupling. The bottom Cu film is fixed at a thickness of 4 nm to make any contribution to the coupling from that side negligible. Only the upper Cu layer thickness is varied, and its thickness alone is responsible for the observed coupling.

The temperature dependence observed in Fig. 3 suggests that the magnetic pinholes dominate the coupling for Cu thicknesses from 0 nm to ≈ 1.5 nm and become insignificant when the Cu is thicker than ≈ 2 nm. Not surprisingly, this thickness corresponds well with what is generally used in GMR spin valves. It is commonly observed in GMR spin valves that below about 2 nm the coupling rises steeply.[6]

Conclusions

The temperature dependence of the magnetic coupling is found to be a useful approach to separating the effects of magnetic pinholes in non-magnetic spacer layers from the effects of magnetostatic coupling, such as the orange-peel effect. Test structures based on GMR spin valves are convenient for investigations of such phenomena. We find that for Cu films of ≈ 2 nm or more and for Al_2O_3 films of ≈ 0.6 nm or more magnetic pinholes do not make a significant contribution to the coupling.

References

1. J. F. Bobo, M. Piecuch, E. Snoeck, J. Magn. Magn. Mater. 126, 440 (1993); S. K. J. Lenczowski, C. Schonenberger, M. A. M. Gijs, and W. J. M. DeJonge, J. Magn. Magn. Mater. 148, 455 (1995); M. T. Kief, J. Bresowa, and Q. Leng, J. Appl. Phys. 79, 4766 (1996); H. Kikuchi, J. F. Bobo, and R. L. White, IEEE Trans. Mag. 33, 3583 (1997); F. Stobiecki, T. Lucinski, R. Gontarz, M. Urbaniak, Mater. Sci. For. 287, 513 (1998); J. F. Bobo, H. Kikuchi, O. Redon, E. Snoeck, M. Piecuch, R. L. White, Phys. Rev. B 60, 4131 (1999); T. Cohen, J. Yahalom, W. D. Kaplan, Rev. Anal. Chem. 18, 279 (1999).; D. Allen, R. Schad, G. Zangari, I. Zana, D. Yang, M. C. Tondra, and D. Wang, J. Vac. Sci. Technol. A 18, 1830 (2000); D. Allen, R. Schad, G. Zangari, I. Zana, D. Yang, M. C. Tondra, and D. Wang, J. Appl. Phys. 87, 5188 (2000); B. J. Jönsson-Åkerman, R. Escudero, C. Leighton, S. Kim, I. K. Schuller, and D. A. Rabson, Appl. Phys. Lett. 77, 1870 (2000); B. Szymanski and F. Stobiecki, Acta Phys. Pol. A 97, 535 (2000); D. Allen, R. Schad, G. Zangari, I. Zana, D. Yang, M. C. Tondra, and D. Wang, Appl. Phys. Lett. 76, 607 (2000); M. F. Gillies and A. E. T. Kuiper, J. Appl. Phys. 88, 5894 (2000); H. Boeve, J. De Boeck, and G. Borghs, J. Appl. Phys. 89, 482 (2001); D. X. Yang, B. Shashishekar, H. D. Chopra, P. J. Chen and W. F. Egelhoff, J. Appl. Phys., submitted.
2. C. L. Platt , M. R. McCartney, F. T. Parker, and A. E. Berkowitz , Phys. Rev. B 61, 9633 (2000); T. Luciński, S. Czerkas, H. Brückl, and G. Reiss, J. Mag. Mat. Mat. 222, 327 (2000).
3. W. F. Egelhoff, Jr., T. Ha, R.D.K. Misra, Y. Kadmon, J. Nir, C. J. Powell, M. D. Stiles, R. D. McMichael, C.-L. Lin, J. M. Sivertsen, J. H. Judy, K. Takano, A. E. Berkowitz, T. C. Anthony, and J. A. Brug, J. Appl. Phys., 78, 273 (1995);W. F. Egelhoff, Jr., P. J. Chen, C. J. Powell, M. D. Stiles, R. D. McMichael, C.-L. Lin, J. M. Sivertsen, J. H. Judy, K. Takano and A. E. Berkowitz, J. Appl. Phys. 80, 5183 (1996); W. F. Egelhoff, Jr., P. J. Chen, C. J. Powell, M. D. Stiles, R. D. McMichael, J. H. Judy, K. Takano, and A. E. Berkowitz, J. Appl. Phys., 82, 6142 (1997)
4. J. C. S. Kools, W. Kula, D. Mauri, T. Lin, J. Appl. Phys. 85, 4466 (1999); B. D. Schrag, A. Anguelouch, S. Ingvarsson, G. Xiao, Y. Lu, P. L. Trouilloud, A. Gupta, R. A. Wagner, W. J. Gallagher, P. M. Rice, and S. S. P. Parkin, Appl. Phys. Lett. 77, 2373 (2000).
5. J. S. Moodera, T. H. Kim, C. Tanaka, and C. H. de Groot, Phil. Mag. B 80, 195 (2000).
6. W. F. Egelhoff, Jr., P. J. Chen, C. J. Powell, M. D. Stiles, R. D. McMichael, J. H. Judy, K. Takano, and A. E. Berkowitz, J. Appl. Phys., 82, 6142 (1997)

Magnetism of Cobalt Base Artificial Lattice Films

Masataka Masuda, Shun Matsumoto, Kunihiko Taka, Naoki Yoshitake and Yasunori Hayashi
Department of Materials Science and Engineering, Faculty of Engineering, Kyushu University
6-10-1, Hakozaki, Higashi-ku, Fukuoka, 812-8581, *JAPAN*

ABSTRACT

The Co/Pd and Co/Pd artificial lattice films have attracted much interest by their special magnetization properties. We discussed the effect of the Pt, Pd layer thickness on the magnetic anisotropy, and we showed the effect of the hydrogen ion implantation on the magnetic properties of multi-layered films. The Co/Pt and Co/Pd multi-layered films were formed on Si(111) substrates with molecular beam epitaxy. We did structure analysis, magnetic domain analysis and magnetic properties evaluation with XRD, MFM and VSM, respectively. Among the series of films of 0.4nm Co layer, XRD showed that the film of 1.0nm Pt layer had a highest periodicity and that they had (111) plane orientation completely. The magnetic domain size reduced with the increase of the thickness of Pt layer. We found out that the coercivity decreased linearly as a function of the length of magnetic domain wall in the unit area. The result of VSM showed that the multi-layered films of Pt thickness of less than 2.8nm had perpendicular magnetic anisotropy. The perpendicular anisotropy energy changed by the nonmagnetic layer thickness and had a maximum value for 0.4nm Co 0.4nm/ nonmagnetic metal 1.0nm multi-layered film. After hydrogen implantation into the films, XRD showed that the lattice spacing was swelled with hydrogen dose. Also, MFM observed that the magnetic domain size reduced with the increase of the hydrogen dose. The easy axis of magnetization changed from perpendicular to parallel in the plane with the increase of the hydrogen dose. After evacuation of hydrogen at 473K, perpendicular anisotropy was partially recovered. This phenomenon suggested that the origin of magnetic anisotropy was mainly the lattice mismatch and distortion in the layer interface. But Co/Pd film was not recovered by this thermal treatment. This means that Pd made stable hydride and did not evacuate hydrogen at this temperature.

INTRODUCTION

Pd and Pt of large spin-orbit interaction show large paramagnetic susceptibility and large magnetic polarization. Accordingly, when Pd and Pt atom adjoin with ferromagnetic Co atom, the magnetic moment is caused and large magnetic anisotropy and magnetostriction are generated. Recently, the magneto-optical memory, using short wavelength blue LASER for the high-density data recording, has attracted much interest. Co/Pd, Co/Pt multi-layered films have a promise of recording device and many research about these films have been done [1]-[4]. These films have very large Kerr rotation angle for short wavelength light, and show perpendicular magnetic anisotropy [5]. For the Co layer thickness of below 1.0nm, Co/Pd and Co/Pd multi-layered films show strong perpendicular magnetic anisotropy [6]. And Co base artificial lattice films show very large Kerr rotation angle in the light of 350nm wavelength [7]. To research the structure and the misfit of interface lattice is very important for understanding the origin of perpendicular magnetic anisotropy, because the magnetostriction effect contributes largely on the

magnetic properties of the Co base artificial lattice films. The hydrogen, that is the smallest element, is easily introduced to metal and versatile to modify the interface structure of multi-layered films. In this paper, the hydrogen ion implantation was used to modify the magnetic properties and structure of the Co base multi-layered films. The artificial lattice multi-layered films of Co/Pt and Co/Pd were prepared on the Si single crystal substrate by using molecular beam epitaxy (MBE). Co base multi-layered films showed well perpendicular magnetic anisotropy. The effects of the hydrogen implantation on the magnetic properties of the multi-layered films were discussed.

EXPERIMENTAL DETAILS

By using MBE (ULVAC PHI, B8000S), the artificial lattice films of Pt/Co and Pd/Co were prepared. The pressure in the chamber during the formation of films was held below the 1.0×10^{-7}Pa. The Si single crystal (111) was used as the substrate, and substrate temperature was 473K. The layer thickness of Co, Pd and Pt was changed as the experiment variable. The hydrogen ion was irradiated to the films with the ion gun with the acceleration voltage of 3kV, and with the flux of 1.5×10^{13} ions/cm^{2}s. The sample of hydrogen irradiated was annealed at 473K in vacuum, and the structure and properties change were evaluated.

The structure of film was examined by X-ray diffraction (RIGAKU, RU-60) with the source of CuKα_1 (λ = 0.1541nm). The magnetic properties were measured by the vibrating sample magnetometer (VSM, RIKEN, BHV-50H). The magnetic domain was observed by the scanning probe microscope (SII, SPA300) in the magnetic force microscope mode (MFM).

RESULTS
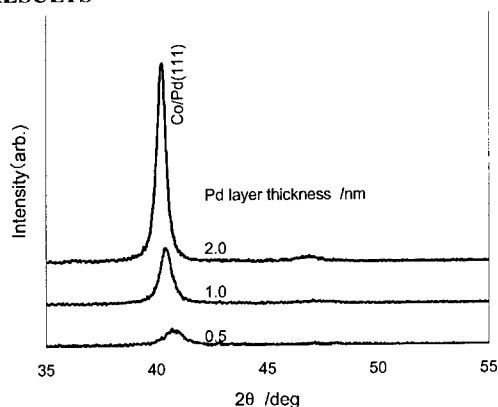
Figure 1. X-ray diffraction profiles of Co/Pd multi-layered films
Co layer thickness is 0.4nm

The X-ray diffraction profiles of Co/Pd multi-layered films are shown in Figure 1. As same as in the case of Co/Pt multi-layered films [8], the X-ray diffraction peak of Co/Pd (111) was shifted to lower angle, because the lattice constant of Pd (0.389nm) is larger than fcc-Co (0.355nm), and

the half-width of this X-ray peak decreased with the increase of Pd layer thickness. The X-ray diffraction profiles of lower angle showed that the diffraction peak reduced remarkably and layer structure became indistinct for Pd layer thickness of below 0.7nm. Contrastively, AFM observation confirmed that the interface roughness of multi-layered films increases with the layer thickness of Pd of over 1.0nm. However, it is interesting that hardly the size of crystal grain changed, even if the layer thickness of Pd increased.

The magnetization curves of (Co0.4nm/Pd1.0nm) 15 layers film is shown in Figure 2. This profile is a typical perpendicular magnetic anisotropy.
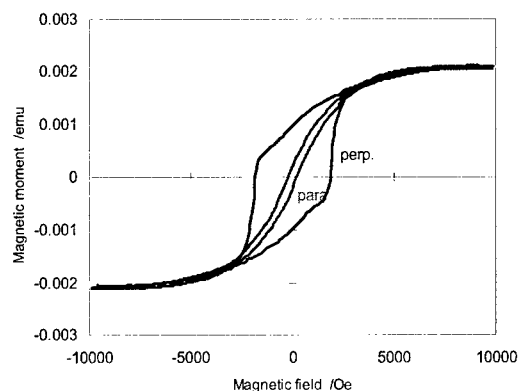
Figure 2. Magnetization curves of Co/Pd multi-layered film (Co0.4nm/Pd1.0nm) × 15 layers

The magnetic properties was affected largely by the thickness of Co layer and showed the maximum perpendicular magnetic anisotropy with about 0.4nm Co. The magnetic properties also depended on the thickness of Pt and Pd, and showed the largest perpendicular magnetic anisotropy with thickness of about 1.0nm.

As Co layer thickness changed, the magnetic domain changed largely. Figure 3 shows the MFM images of multi-layered films with Co layer thickness. As very thin Co layer, magnetic domain has island form of very large size, but the domain size decreases with the increase of the thickness of Co layer, and then, the magnetic domain becomes typical maze pattern of in-plane magnetization anisotropy.

Co0.40nm   Co0.52nm

Co1.2nm   Co2.6nm
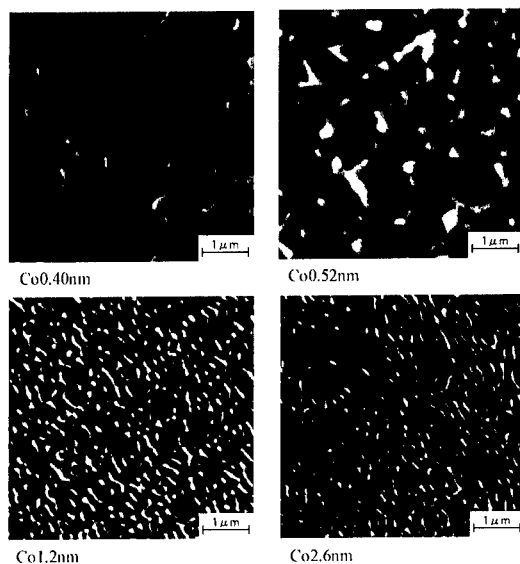
Figure 3. MFM images of Co/Pt films with the thickness of Co layer
Pt thickness is 1.0nm

The X ray profiles of Co0.4nm/Pd1.0nm multi-layered film, shown in Figure 4, illustrate that peak angle reduced and lattice spacing swelled with the hydrogen injection. As the increase of hydrogen injection quantity, the half-width of the peak increased and the shoulder of Pd hydride appeared.
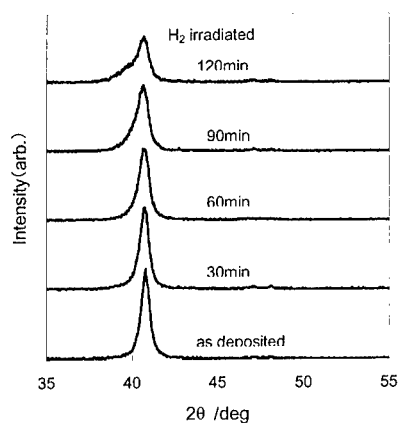
Figure 4. X-ray profiles of Co/Pd multi-layered film
(Co0.4nm/Pd1.0nm) ×15 layers

As the increase of hydrogen injection quantity, the perpendicular magnetization anisotropy energy decreased and the film became to prefer the in-plane magnetization. By vacuum annealing, the magnetic properties of Co/Pt films partially recovered to the perpendicular anisotropy, but Co/Pd films hardy recovered by the annealing.

The origins of magnetic anisotropy of Co-noble metal multi-layered films are mainly the distortion of lattice. The magnetic anisotropy caused by distortion is naturally expected to be altered by hydrogen implantation. It is possible to inject the hydrogen to the films over its solubility limit with hydrogen ion implantation. The acceleration voltage was chosen with the 'TRIM' code calculation as the peak density of hydrogen was to locate in the middle of film thickness. It is expected that the hydrogen injected diffuses easily in room temperature and migrates in a stable site. This site is estimated ordinarily to be the interface where the distortion is accumulated. It is conceivable that the magneto-elastic anisotropy decreases with the decrease of distortion of lattice, and the film changes to prefer in-plane magnetic anisotropy.

The data of MFM detects only the vertical component of the magnetic force between the probe and the film, so cannot show the magnetization direction. Figure 5 shows the comparison between MFM image and the result of Boundary Element Method calculation (BEM). The MFM profile and calculation result showed good agreement and the magnetization direction is able to estimate with MFM and BEM.
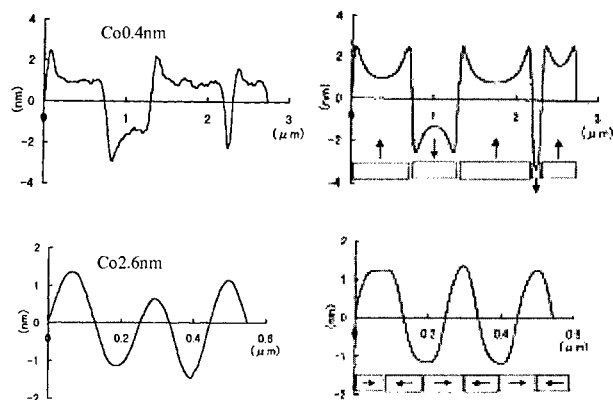
Figure 5. MFM profiles and BEM calculations
Left side: MFM, Right side: BEM

The process of magnetization can be considered as the migration of the magnetic wall. Accordingly, with the increase of domain wall length, magnetic domain size reduces, and the coercivity reduces. The magnetic domain walls were extracted from MFM image by the image processing. As shown in Figure 6, there was linear relation between the magnetic wall length and the magnetic coercivity. The coercivity decreased with the increase of the magnetic domain wall length. It is very interesting that the linear relation is consisting with the films of many couples of Co layer thickness and non-magnetic layer thickness.
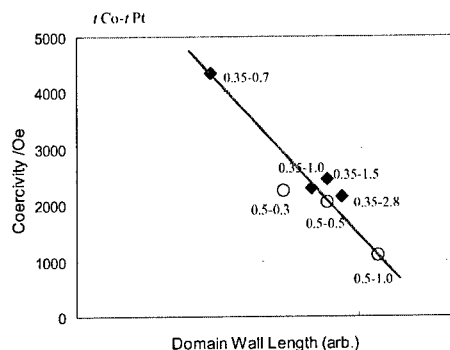
Figure 6. Coercivity and domain wall length

The thermal stability of the injected hydrogen in Co/Pd film showed the possibility of modifying the magnetic properties by hydrogen implantation. The hydrogen implantation is considered to be a new technique for the application of magnetic properties design.

CONCLUSIONS

Pt/Co, Pd/Co multi-layered films of perpendicular magnetization anisotropy were prepared with MBE. The effects of the hydrogen implantation on the structure and the magnetic properties of films were examined. The atomic mixture of interface and the change of interface distortion reduced the perpendicular magnetization anisotropy energy. The annealing after hydrogen implantation evacuated the hydrogen and increased the perpendicular anisotropy energy for Co/Pt films. For Co/Pd films, the annealing did not evacuate the hydrogen because of its thermal stability. This suggests the possibility of the magnetic properties design by hydrogen implantation.

REFERENCES

1. G.A.Bertero and R.Sinclair, *J.Appl. Phys.* **77**(1995) 3953
2. C.Train, P.Beauvillain, V.Mathet, G.Penissard, and P.Veillet, *J. Appl. Phys.* **86**(1999) 3165
3. U.Pustogowa, J.Zabloudil, C.Uiberacker, C.Blass, P.Weinberger, L.Szunyogh and C.Sommers, *Phys. Rev.* B **60**(1999) 414
4. Th-ho Wu, J.C.A.Huang, L.C.Wu, L.X.Ye and J.Q.Lu, *J. Mag. Mag. Mat.* **193**(1999)136
5. P.F.Carcia, *J. Appl. Phys.* **63**(1988) 5066
6. C.J.Lin, G.L.Gorman, C.H.Lee, R.F.C.Farrow, E.E.Marinero, H.V.Do, H.Notarys and C.J.Chien, *J. Magn. Magn. Mater.*, **93**(1991),194
7. T. Uchiyama, *Advanced Magnetics*, BAIFUUKAN (1994), 308
8. Y.Hayashi, M.Masuda, K.Tonomyo, S.Matsumoto and N.Mukai, *J. All. Comp.* **294**(1999) 463

Temperature Dependence of the Magnetoresistance of Co/Re Superlattices

Timothy Charlton[1], David Lederman[1], and Gian P. Felcher[2]
[1]Department of Physics, West Virginia University,
Morgantown, WV 26506-6315
[2]Materials Science Division, Argonne National Laboratory,
9700 South Cass Avenue, MSD/223, Argonne, IL 60439-4845

ABSTRACT

Hcp (10.0) Co/Re superlattices were grown by dc magnetron sputtering on sapphire (11.0) substrates with the [00.1] direction of the superlattice in the film plane. The temperature-dependent magnetoresistance (MR) was measured on samples patterned by photolithography from 10 K to 300 K in a 5.5 T superconducting magnet. The pattern allows the measurement of the MR with the current (I) and the magnetic field (H) parallel or perpendicular to the magnetic easy axis (c, the [00.1] direction). Measurements at 5 K on an antiferromagnetically-coupled sample shows dips in the MR near $H = 0$ when $H \parallel c$ and $H \perp I$, dips below the saturation value at H ~ 2.5 kOe for $H \parallel c$ and $H \parallel I$ configuration due to the competition between the anisotropic magnetoresistance (AMR) and the giant magnetoresistance (GMR). Since the AMR is dependent on the transport within the ferromagnetic layers, the temperature dependence yields information about the relative magnitudes of interface vs. bulk spin-dependent scattering. Our analysis shows that the GMR is anisotropic and that the spin-dependent scattering occurs predominantly at the interfaces only for certain configurations.

INTRODUCTION

Giant magnetoresistance (GMR), discovered in the late 1980's [1], which occurs in magnetic multilayers and nanoparticles, and the anisotropic magnetoresistance (AMR), extensively studied since the 1930's in bulk ferromagnetic materials [2], are effects that have been recently under intense scrutiny due to their technological applications. Only relatively recently, however, have these two effects been studied in the same system. Some previously studied systems with both AMR and GMR include Co/Cr [3], Fe/Cr [4,5], Co/Ru [6], Co/Cu [7,8] and Permalloy/Cu [9] multilayers. These include experiments which separate the AMR and GMR in the same system [7] and experiments which focus on the enhancement of the GMR by AMR in systems with magneto-crystalline anisotropy, like Co/Cr multilayers [3].

A topic of great current interest is determining the nature of the spin-dependent scattering responsible for GMR. Experiments where a monolayer or two of a magnetic material were added to the interface of a spin-valve [10] and the dependence of the GMR on interface roughness on Fe/Cr [4] show that in those systems the GMR depends strongly on scattering at the interfaces. But other studies show that the GMR depends on the film layer thickness [11], and that the GMR is dominated by bulk spin-dependent scattering [12].

Here we summarize the results of a recent, comprehensive study of the temperature-dependent magnetoresistance for a [Co (1.7 nm) / Re (0.7 nm)]$_{20}$ superlattice. The magnetoresistance, measured with the current applied in the plane of the sample, has been simulated assuming that the total magnetoresistance is the sum of a GMR and an AMR component. The AMR is known to be a result of spin-dependent scattering within the bulk of a ferromagnetic material. Hence, determining the relative amounts of bulk vs. interface spin-dependent scattering can be done by comparing the temperature dependence of the GMR contribution with that of the AMR
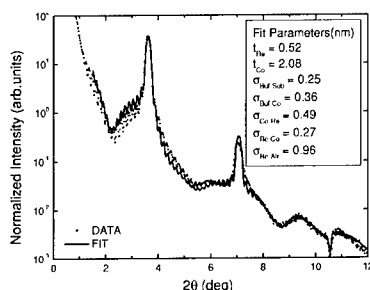
Figure 1. X-ray reflectivity of Co/Re superlattice using Cu Kα radiation. The results of the fit are shown above. The interface roughness parameters, indicated by σ, were extracted by fitting to an optical scattering model (see Ref. 13).

component. We show that when the current is applied parallel to the c-axis, the spin-dependent scattering is bulk-like, and when the current is perpendicular to the c-axis, the scattering depends on the interfaces.

EXPERIMENT

The superlattice's growth conditions, structural, and magnetic properties as well as neutron reflectivity measurements were reported previously [13,14]. In summary, the superlattice was grown via DC magnetron sputtering on Al_2O_3 (11.0) substrates with a 5.0 nm Re buffer layer. X-ray diffraction shows that the superlattice grows epitaxially in the hcp structure with the c-axis, hcp(00.1), in the film plane. Using low angle x-ray reflectivity techniques, the interface roughness between the layers was determined to be ~0.4 nm, as shown in Fig. 1. The superlattice is antiferromagnetically coupled with an in-plane magnetic easy axis parallel to the c-axis. Neutron reflectivity experiments, performed at the Intense Pulsed Neutron Source at Argonne National Laboratory, were consistent with the previous magnetic measurements and also show a gradual spin-flop transition when the external magnetic field is applied parallel to the c-axis. These
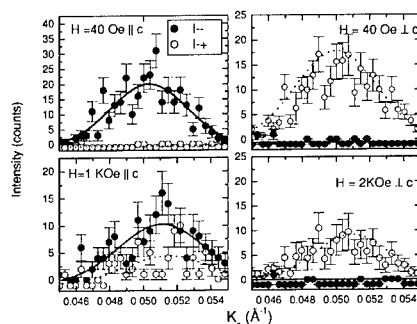
Figure 2. Non-spin flip (I--) and spin-flip (I-+) neutron scattering about the antiferromagnetic peak. The lines are fits to a Gaussian peak.

measurements were performed by scanning the antiferromagnetic peak and analyzing the spin of the scattered neutrons, as shown in Fig. 2. In this configuration, the spin-flip scattering intensity is proportional to the square of the component of the antiferromagnetic magnetization perpendicular to the applied field, whereas the non-spin-flip scattering intensity is proportional to the square of the component parallel to the field.

Magnetoresistance measurements were made using a cryostat with a 5.5 T superconducting magnet. The sample was patterned into an "L" shape using standard photolithography techniques [15]. One of the arms of the pattern was oriented parallel to the c-axis, while the other was perpendicular to it. This enabled us to apply the current both parallel and perpendicular to the magnetic easy axis on the same sample. Four-probe electrical resistance measurements using a constant current source and a nanovoltmeter were made in the following configurations: $H \parallel c / H \parallel I$, $H \parallel c / H \perp I$, $H \perp c / H \parallel I$, and $H \perp c / H \perp I$. This was done as a function of temperature from 5 K to 250 K and in an applied field H ranging from -3 T to 3 T.

RESULTS AND DISCUSSION

An important piece of information extracted from neutron reflectivity measurements is the vector direction of the magnetization in adjacent layers of cobalt with respect to the c-axis [14]. From this we can build an empirical model for the total magnetoresistance (MR) based on conventional definitions for the AMR and the GMR. It is known that the AMR depends on the angle the magnetization vector $\mathbf{M}$ makes with the sensing current $\mathbf{I}$. This dependence can be written as

$$\rho_{AMR} = \rho_{\parallel} \cos^2 \gamma(\mathbf{H}) + \rho_{\perp} \sin^2 \gamma(\mathbf{H}), \tag{1}$$

where γ is the angle between $\mathbf{M}$ and $\mathbf{I}$, $\rho_{\parallel}$ is the resistivity with $\mathbf{M} \parallel \mathbf{I}$ and $\rho_{\perp}$ is the resistivity with $\mathbf{M} \perp \mathbf{I}$.

Phenomenologically the GMR depends only on the antiferromagnetic alignment of the adjacent magnetic layers, so the GMR contribution can be written as

$$\frac{\rho_{GMR}(H) - \rho_{sat}}{\rho_{sat}} = A \left| \mathbf{M}_1(\mathbf{H}) - \mathbf{M}_2(\mathbf{H}) \right|. \tag{2}$$

Here $\mathbf{M}_1$ and $\mathbf{M}_2$ are the magnetizations of adjacent ferromagnetic Co layers, $\rho_{GMR}(H)$ is the resistivity contribution of the GMR as a function of field, ρ_{sat} is the resistivity at saturation, and A is a proportionality constant.

In order to explain the magnetotransport data below, the angles that $\mathbf{M}_1$ and $\mathbf{M}_2$ make with
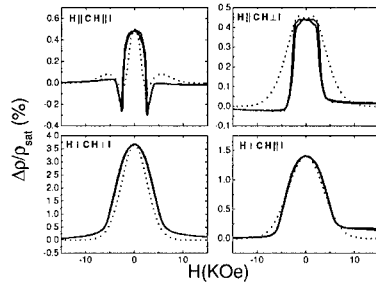
Figure 3. Magnetoresistance measurements (solid) and simulation (dotted) at 5 K. The simulation qualitatively matches the data.

respect to the current were *experimentally* determined from the neutron reflectivity measurements described above. Note that Eqn. 2 implicitly assumes a parallel resistor model where the spin-up and spin-down electrons scatter independently [16,17], and that the magnetic layers polarize the transport electrons. Eqn. 1 assumes a parallel resistor model that includes a spin-orbit interaction, which in turn causes the *s-d* electron scattering to be anisotropic [16]. The latter is the standard explanation for the existance of AMR in bulk ferromagnetic transition metals.

In Fig. 3 the MR dips at $H = 1.5$ KOe in the $H \parallel c / H \parallel I$ geometry and dips at $H = 0$ in the $H \parallel c / H \perp I$ geometry at 250 K. The MR also evolves differently as a function of temperature. We assume that $\mathbf{M_1(H)}$ and $\mathbf{M_2(H)}$ do not significantly depend on temperature since the dips in the MR remain at approximately the same field at all temperatures. This leaves all of the temperature dependence in the coefficient A and the ratio $\rho_\perp / \rho_\parallel$. By simulating the MR = AMR + GMR with the above equations, and using A and $\rho_\perp / \rho_\parallel$ as adjustable parameters, the data are qualitatively reproduced. Only one physical constraint was placed on the adjustable parameters in the simulation: that $\rho_\perp / \rho_\parallel$ must be the same for the current flowing along a given crystallographic direction because this ratio is proportional to the ratio of the spin up and spin down resistivities, which only depends on the crystallographic direction in which the current is flowing [16,17]. Our analysis shows that the interesting dips in the MR are only due to AMR [15]. The magnetoresistance of hcp(0001) oriented Co/Re multilayers has been found by other authors to be less than 2 % at 18 K [18], while our superlattices have a MR larger than 3.5 % at 5 K in certain geometries. In contrast to this previous Co/Re multilayer work, our samples are epitaxial, and therefore the AMR is more noticeable.

The existence of GMR in magnetic multilayer systems has been attributed to the matching of the band structure of the non-magnetic layer with either the spin up or spin down bands of the magnetic layer [19]. The small GMR value in Co/Ir superlattices has been blamed on the failure of the Ir bands to match with either the majority or minority spin bands of Co [20]. In the case of Co/Re, the bands of Re are similar to the spin down bands of Co [21]. This means that the GMR for Co/Re should be large, but we only find a GMR of approximately 2.5 % at 5 K. The low value of the GMR can be attributed to the large resistivity of the Re spacer. In other words, relatively few electrons traverse the Re spacer to the next Co-Re interface with out being scattered.

Notice that in Fig. 4(a) the temperature dependence of the AMR depends on the crystallographic direction that the current flows along. The GMR is usually thought to be isotropic,
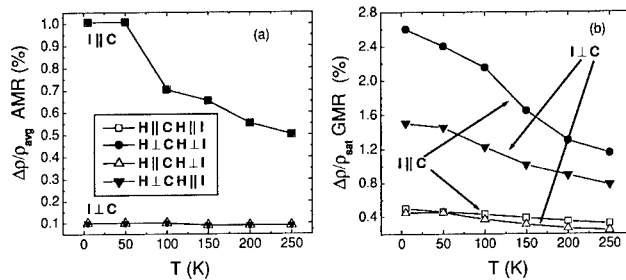
Figure 4. (a) Magnitude of the AMR $\Delta\rho_{AMR} / \rho_{avg}$, where $\Delta\rho_{AMR} = \rho_\parallel - \rho_\perp$, and (b) magnitude of the GMR $\Delta\rho_{GMR} / \rho_{sat}$, plotted as a function of temperature for different configurations.

but Fig. 4(b) shows that it is anisotropic with respect to both the field and current directions in our sample. Other authors[22] have also found the GMR to be anisotropic and to depend on the asymmetry in the spin-dependent resistivity ratio $\rho_\uparrow / \rho_\downarrow$ parallel and perpendicular to the current.

The AMR depends primarily on the transport through the ferromagnetic layers. On the other hand, in some studies the GMR depends on interface scattering [10], while in others bulk scattering has been shown to be important [12]. By comparing the temperature dependence of the GMR to the AMR (Fig. 5), one can determine whether the nature of the electron scattering is the same for the AMR and GMR. Since the AMR is known to be a result of scattering within the magnetic layers, differences between the AMR and the GMR must be due to differences in the electron scattering mechanism responsible for the two effects. In Fig. 5 the $I \parallel c$ geometry the curves are flat indicating the AMR and the GMR have a similar temperature dependence. This implies that when $I \parallel c$, bulk scattering is more important. If $I \perp c$, the temperature dependence for the GMR and AMR is different, meaning that interface scattering is more important. This is not entirely surprising given that the c-axis represents a strong crystallographic anisotropy, which leads to an anisotropic Fermi surface in the plane of the sample. This is confirmed by the inset of Fig. 5, which shows that the magnitude of the resistivity of the sample is very different in the two configurations.

Our simple empirical model, relying on $\mathbf{M}_1$ and $\mathbf{M}_2$ as functions of H determined from neutron reflectivity, does not take into account possible domain formation within the Co layers, which could alter the magnetoresistance [23]. This could explain why the model reproduces the qualitative features of the data, such as the dips near $H = 0$, but not the exact quantitative experimental results.

CONCLUSIONS

In summary, we have measured the temperature dependent magnetoresistance on a patterned, epitaxial Co/Re superlattice. We simulated the magnetoresistance and separated the AMR and the GMR effects for several temperatures. By comparing the temperature dependence of the AMR and the GMR, we find that in the $I \parallel c$ geometry the AMR and the GMR have the same temperature dependence, which implies that there is predominantly bulk scattering. In the $I \perp c$ geometry, the AMR and the GMR vary quite differently with temperature, implying that interface scattering dominates. Additionally, the GMR contribution is also found to be anisotropic. Finally, we note that other work, most notably in NiFe/Cu superlattices [24], has revealed similar behavior in terms of dips near $H = 0$ with $H \parallel c$ and $H \perp I$. We propose that the behavior observed in that instance is also due to the competition between the AMR and the GMR.
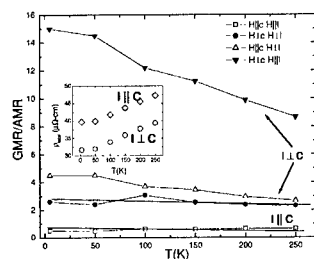
Figure 5. The ratio $\Delta\rho_{GMR} / \Delta\rho_{AMR}$ as a function of temperature. Inset is the total resistivity at $H = 0$ as a function of temperature for the $I \parallel c$ and $I \perp c$ geometries.

REFERENCES

1. M. N. Baibich, J. M. Broto, A. Fert, F. Nguyen Van Dan, F. Petroff, P. Eithenne, G. Chreuzet, A. Friedrich and J. Chazelas, *Phys. Rev. Lett.* **62**, 2472 (1988).
2. S. Chikazumi, *Physics of Magnetism* (Wiley, New York, 1964), pp. 419-421.
3. Y. D. Yao, Y. Liou, J. C. A. Huang, S. Y. Liao, I. Klik, W. T. Yang, C . P. Chang and C. K. Lo, *J. Appl. Phys.* **79**, 6533 (1990).
4. E. E. Fullerton, D. M. Kelly, J. Guimpel and I. K. Schuller, *Phys. Rev. Lett.* **68**, 859 (1992).
5. E. E. Fullerton, M. J. Conover, J. E. Mattson, C. H. Sowers and S. D. Bader, *Phys. Rev. B.* **48**, 15755 (1993).
6. A. Dina and K. Ounadjela, *J. Magn. Magn. Mater.* **146**, 66 (1995).
7. B. H. Miller, E. Y. Chen and E. D. Dahlberg, *J. Appl. Phys.* **73**, 6384 (1993).
8. J. C. A. Huang, Y. H. Lee, Y. M. Hu and T. C. Chang, *J. Appl. Phys.* **79**, 6276 (1996).
9. D. V. Dimitrov, C. Prados, C. Y. Hadjipanayis and J. Q. Xiao, *J. Magn. Magn. Mater.* **189**, 25 (1998).
10. S. S. P. Parkin, *Phys. Rev. Lett.* **71**, 1641 (1993).
11. B. Dieny, *J. Magn. Magn. Mater.* **136**, 335 (1994).
12. B. H. Miller, B. P. Stojkovic and E. D. Dahlberg, *Phys. Lett. A.* **256**, 294 (1999).
13. T. Charlton, J. McChesney, D. Lederman, F. Zhang, J. Z. Hilt and M. J. Pechan, *Phys. Rev. B.* **59**, 11897 (1999).
14. T. Charlton, D. Lederman, S. M. Yusuf and G. P. Felcher, *J. Appl. Phys.* **85**,4436 (1999).
15. T. Charlton and D. Lederman, Phys. Rev. B **63**, 94404 (2001).
16. T. R. McGuire and R. I. Potter, *IEEE Trans. Mag.* **MAG-11**, 1018 (1975).
17. I. A. Campbell and A. Fert, *Ferromagnetic Materials*, Vol. 3 (North-Holland, Amsterdam, 1982), p. 755.
18. P. P. Freitas, L. V. Melo, I. Trinadade, M. From, J. Ferreira and P. Monteiro, *Phys. Rev. B.* **45**, 2495 (1992).
19. W. H. Butler, X. G. Zhang, D. M. C. Nicholson and J. M. MacLaren, *J. Magn. Magn. Mater.* **151**, 354 (1995).
20. H. Yanagihara, K. Pettit, M. B. Salamon, E. Kita and S. S. P. Parkin, *J. Appl. Phys.* **81**, 5197 (1997).
21. D. A. Papaconstantopoulos, *Handbook of the Band Structure of Elemental Solids* (Plenum Press, New York, 1986).
22. B. Dieny, C. Cowache, A. Nossov, P. Dauguet, J. Chaussy and P. Gandit, *J. Appl. Phys.* **79**, 6370 (1996).
23. W. Folkerts, *J. Magn. Magn. Mater.* **94**, 302 (1991).
24. K. Pettit, S. Giger, S. S. P. Parkin and M. B. Salamon, *Phys. Rev. B.* **56**, 7819 (1997).

Composition-Morphology-Property Relations For Giant Magnetoresistance Multilayers Grown By RF Diode Sputtering

W. Zou, H.N.G. Wadley, X.W. Zhou, R.A. Johnson
Department of Materials Science and Engineering
University of Virginia, Charlottesville, VA 22903
D. Brownell
Nonvolatile Electronics, Inc. Eden Prairie, MN 55344

ABSTRACT

A series of experiments have been conducted to evaluate the magnetotransport properties of RF diode sputter deposited giant magnetoresistive (GMR) multilayers with either copper or copper-silver-gold nonferromagnetic (NFM) conducting layers. The study revealed that RF diode deposited multilayers utilizing $Cu_{80}Ag_{15}Au_5$ as the NFM conducting layer posses significantly superior giant magnetoresistance to otherwise identical device architectures that used pure copper as the NFM conducting layer. To explore the origin of this effect, copper and $Cu_{80}Ag_{15}Au_5$ films of varying thickness have been grown under identical deposition conditions and their surface morphology and roughness investigated. Atomic force microscopy revealed significant roughness and the presence of many pinholes in thin pure copper films. The surface roughness of the $Cu_{80}Ag_{15}Au_5$ layers was found to be much less than that of pure copper, and the alloying eliminated the formation of pinholes. Molecular statics estimates of activation barriers indicated that both silver and gold have significantly higher mobilities than copper atoms on a flat copper surface. However, gold is found to be incorporated in the lattice whereas silver tends to segregate (and concentrate) upon the free surface, enhancing its potency as a surfactant. The atomic scale mechanism responsible for silver's surface flattening effect has been explored.

1. INTRODUCTION

Metal multilayers consisting of alternating ferromagnetic (FM) and nonferromagnetic (NFM) metals sometimes exhibit large changes in their electrical resistance when a magnetic field is applied [1-10]. The effect results from a change in their spin dependent electron scattering when an applied magnetic field rotates the magnetic moment of one of the ferromagnetic layers [1-10]. Devices utilizing it are widely used as the magnetic field sensors in hard disk drive read heads [4]. Related devices are being investigated for use as magnetic random access memories (MRAM) [4]. Current GMR multilayers appear not to have achieved their performance upper bound. Reducing both the smoothness and chemical diffuseness of the interfaces in GMR multilayers appear to be particular important [2,8]. Achieving materials with a large GMR ratio at a low saturation field therefore requires the use of materials, layer thickness and deposition conditions that minimize interfacial roughness.

2.EXPERIMENTS

The study has focused upon the influence of the nonferromagnetic conducting layer composition (either Cu or $Cu_{80}Ag_{15}Au_5$) on the GMR ratio and the saturation field of RF diode sputter deposited GMR multilayers. Multilayers with either Cu or $Cu_{80}Ag_{15}Au_5$ NFM conducting layers

together with, 100, 500 and 1000A thick Cu and $Cu_{80}Ag_{15}Au_5$ single layer films were grown at Nonvolatile Electronic, Inc. (Eden Prairie, MN) using a Randex Model 2400-6J RF diode system. Briefly, the diameter of the targets was 20.32cm, the distance between substrate and target was 3.81cm, the pressure was 20mTorr and a 175W power was used for growth of all the multilayers and the Cu and $Cu_{80}Ag_{15}Au_5$ single layer films.

The architecture and compositions of the antiferromagnetically coupled multilayers are shown in Figure 1. The multilayers contained three repeated exchange coupled layer stacks. Each layer stack was a composite of two ferromagnetic layers ($Ni_{65}Fe_{15}Co_{20}$ and $Co_{95}Fe_5$) arranged so that the $Co_{95}Fe_5$ layer was at the interface with either the copper or copper alloy layer. In each case a fixed NFM conducting layer thickness of 16Å was used.
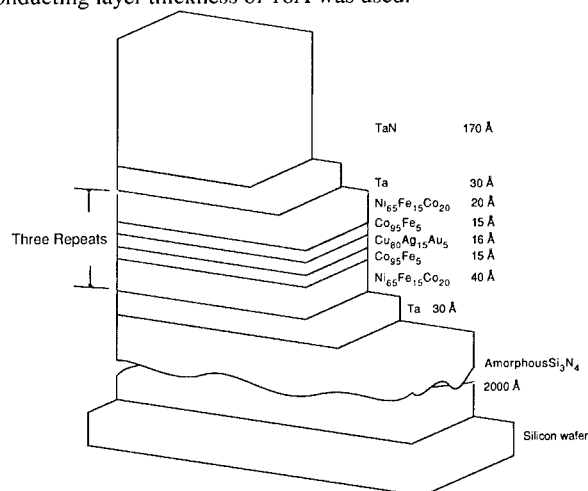
Figure 1 The GMR multilayer structure studied here. Layer compositions and thicknesses are shown. Arrows indicate the magnetic alignment of the ferromagnetic alloy layers.

3. Experimental Results

Figure 2 shows the dependence of the GMR ratio and saturation field upon the number of repeated stacks in the Cu and $Cu_{80}Ag_{15}Au_5$ conducting layer multilayers. The magnetoresistance change is usually characterized by the GMR ratio which is the resistance change scaled by the zero field resistance. The saturation magnetic field is the strength of the smallest applied magnetic field needed to achieve the GMR ratio. The results in Figure 2 show that multilayers grown with a pure Cu conducting layer exhibited no GMR effect, whereas multilayers grown with a $Cu_{80}Ag_{15}Au_5$ conducting layer had significant GMR ratios. The saturation magnetic field of the $Cu_{80}Ag_{15}Au_5$ multilayers also increased with the number of stacks. Both the GMR ratio and the saturation fields are reasonable well suited for the magnetic sensing applications [3,4,8]. Many researchers have successfully used pure Cu as conducting layer in GMR multilayers. They used a different deposition approach [4] and the Cu layer thickness was usually greater than 20Å. For the particular architecture and composition of the multilayer and RF diode deposition equipment investigated here, Cu thickness below 20Å resulted in no GMR [3].

To explore the reasons for the loss of the GMR effect, three different thickness Cu and $Cu_{80}Ag_{15}Au_5$ single layer films were grown under the same deposition conditions to the multi-layers. The surface morphology of each film was then evaluated with tapping mode atomic force microscopy (AFM), Figure 3. The scan size was 1μm x 1μm and scan rate was 1 Hz for all the films. These results revealed periodic surface roughness with an asperity width that increased with the film thickness in both types of films, Figure 3. However, the Cu films had a larger asperity widths and higher surface amplitudes than their $Cu_{80}Ag_{15}Au_5$ counterparts. Pinholes (the dark spots on the image) were present in the 100Å thick Cu film, Figure 3(d). AFM measurements indicated the average depth of the pinholes was at least 40Å. Their diameter was approximately 800Å. No pinholes were observed in CuAgAu films. Figure 3. Figure 4 shows the RMS roughness increased with the film thickness in both the Cu and $Cu_{80}Ag_{15}Au_5$ films, but the Cu films were always much rougher. The loss of the GMR effect in multilayers with a pure copper conducting layer is consistent with ferromagnetic layer coupling through pinholes in the NFM spacer layer [3].
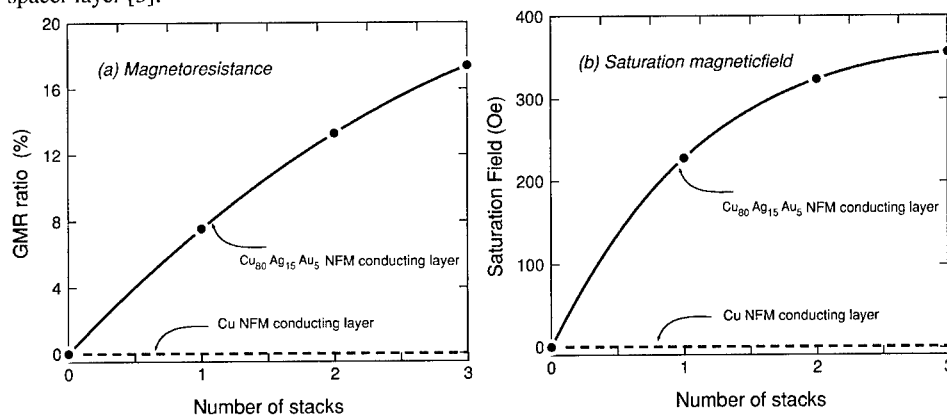
Figure 2 The dependence of (a) the GMR ratio, and (b) the saturation field upon the number of repeated multilayer stacks for Cu and $Cu_{80}Ag_{15}Au_5$ NFM conducting layers. In each case a fixed NFM conducting layer thickness of 16Å was used. Multilayers grown with a pure Cu NFM conducting layer exhibited no giant magnetoresistance. Multilayers grown with a $Cu_{80}Ag_{15}Au_5$ as conducting layer possessed significant GMR ratios.
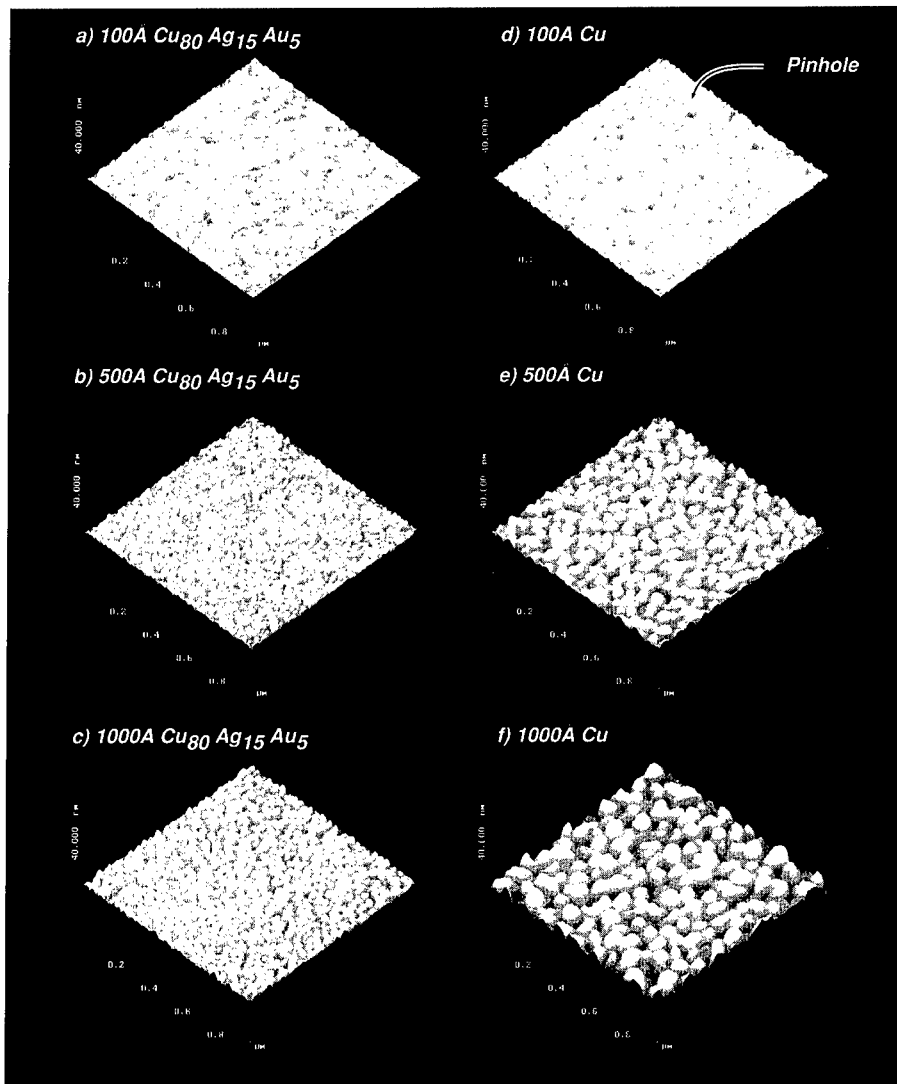
Figure 3 The topography of $Cu_{80}Ag_{15}Au_5$ and pure Cu films of different thicknesses. The growth column width increased with the film thickness for both film types. The pure Cu films have a larger growth column width, and a rougher surface compared to $Cu_{80}Ag_{15}Au_5$ films of identical thickness.
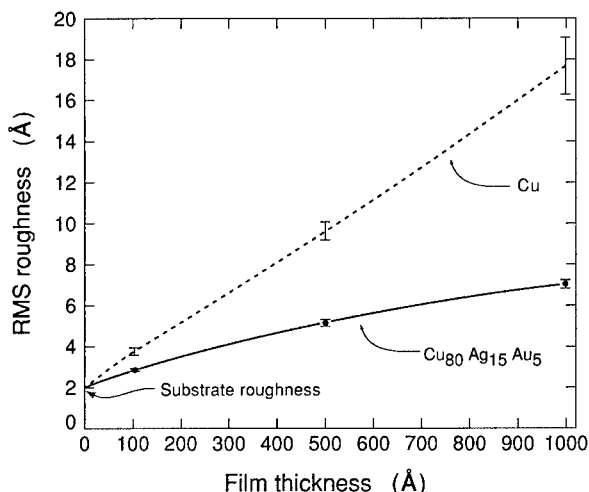
Figure 4 The RMS roughness increases with the film thickness for both Cu and Cu$_{80}$Ag$_{15}$Au$_5$ film. The pure Cu films are much rougher compare to the Cu$_{80}$Ag$_{15}$Au$_5$ films.

4. Discussion

Using the 3D EAM as a starting potential, 2D molecular statics can be used to estimates activation barriers for the atom configuration dependent migration energies [9,10]. The barrier for the hopping of Cu on a smooth close-packed Cu surface was found to be 0.25 eV. The corresponding energies for Ag and Au on such a copper surface were only 0.14 and 0.11 eV respectively. If the jump attempt frequencies are assumed identical, Ag and Au have a much higher mobility on a Cu surface than Cu atoms, Figure 5 (a). These molecular statics estimates also indicated that the Ehrlich-Schwoebel barrier for Cu depends on which atom type is attached to the edges of ledges. When the edge of the ledge is either Cu, Ag or Au, the Ehrlich - Schwoebel is 0.35eV, 0.28eV, or 0.33eV respectively, Figure 5 (b). Silver at the ledge edge reduces the Ehrlich-Schwoebel barrier for copper to approximately the barrier for hopping on a close packed surface.

These molecular statics calculations also show that it is energetically favorable (by 0.15 eV/atom) for a Au atom on a copper surface to exchange (and alloy) with a Cu atom, Figure 5 (c). They also show it is unfavorable (by 0.05 eV/atom) for Ag to exchange with copper. As a result, Au is likely to be buried in Cu whereas Ag trends to segregate to the surface which in agree with the MD simulation observations. The segregation of Ag appears beneficial since it maintains a high concentration of Ag at the surface [21-25]. This has the effect of increasing the mobility of atoms on the surface and enhances the probability that it will be attached to ledge edges where it can lower the Ehrlich-Schwoebel barrier for Cu atoms. This dramatically reduces flux shadowing and results in pinhole free films and smoother surfaces. Gold atoms also reduce the Ehrlich-Schwoebel barrier, but is not lowered as much as the silver, and no Au concentration enhancement at the surface occurs.

(a) Low Cu mobility and high Ag and Au mobility on Cu

(b) The Schwoebel barrier for Cu when the edge of the ledge is
Cu=0.35eV, Ag=0.28eV, and Au=0.33eV

(c) Ag - Cu segregation and Au - Cu exchange
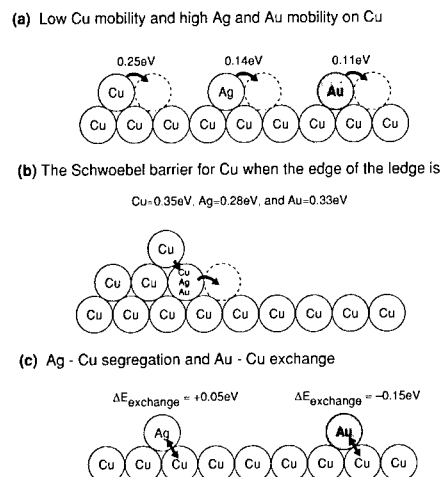
Figure 5 Alloy effects on atomic assembly. (a) low Cu and high Ag and Au mobility on Cu, (b) the Ehrlich-Schwoebel barrier for Cu when the edge of the ledge is Cu, Ag, and Au, (c) Au-Cu exchange and Ag-Cu segregation.

5. Summary

Radio frequency diode sputter deposition has been used to grow $Ni_{65}Fe_{15}Co_{20}$ /$Co_{95}Fe_5$/Cu or $Cu_{80}Ag_{15}Au_5$/$Co_{95}Fe_5$/$Ni_{65}Fe_{15}Co_{20}$ multilayers. Multilayers utilizing $Cu_{80}Ag_{15}Au_5$ as the nonferromagnetic conducting layer exhibited significant giant magnetoresistance whereas otherwise identical device architectures that use a pure copper conducting layer fail to exhibit any magnetoresistance. The cause is the AFM identified presence of pinholes in copper films but not in thin $Cu_{80}Ag_{15}Au_5$ films. Molecular statics analyses confirm that silver and gold atoms are very mobile and reduce the Ehrlich-Schwoebel barrier at a copper ledge. These changes both contribute to a smoother surface.

REFERENCES

1. P. M. Levy, J. Magn. Magn. Mater., 140-144, 485(1995).
2. J.C. S. Kools, J. Appl. Phys. 77, 2993 (1995).
3. J. Daughton, P.A. Bade, M.L. Jenson, and M. Rahmati, IEEE Trans. Magn., Vol.28, No.5, Sept. 1992.
4. G. A. Prinz, Science **282**, 1660(1998).
5. B. Dieny, et al. J. Appl. Phys. 69 (8), 15, P. 4774- 4779, April 1991.
6. W. F. Egelhoff, Jr. P. J. Chen, C. J. Powell, M.D. Stiles, and R. D. McMichael, J. Appl. Phys. 79 (5), March 1996.
7. W. F. Egelhoff, et al. J. Appl. Phys. 82 (12), 15 December 1997.
8. W. Zou, H.N.G. Wadley et al., Prepared for J. Vacuum Science and Technology.
9. H.N.G. Wadley, X. Zhou, R.A. Johnson, Mechanisms, Models, and Methods of Vapor Deposition, Progress in Materials Science, In Press, 2001.
10. R.A. Johnson, Phys. Rev. 39, 12554, 1989.

OSCILLATORY ANGULAR DEPENDENCE OF EXCHANGE BIAS FOR EPITAXIAL NiO-Co (001) BILAYERS

S. Dubourg and J.F. Bobo
LPMC, CNRS-INSA-UPS 5830 135, 31077 Toulouse Cedex 4, France

B. Warot, E. Snoeck and J.C. Ousset
CEMES-CNRS, 29 rue Jeanne Marvig 31055 Toulouse Cedex 4, France

ABSTRACT

We have sputter-deposited NiO-Co bilayers on MgO (001) substrates. NiO grows epitaxially on MgO at 900°C and subsequently the room deposited 80 Å thick Co films have a fcc crystal structure in epitaxy with the oxide underlayer. These samples were warmed up to 300° C and then zero-field or field cooled through the NiO Néel temperature (a 300 Oe magnetic field was applied along the [100] or the [110] MgO axis). Magnetic hysteresis loops were obtained by magneto-optical Kerr effect, the magnetic field being oriented in the plane of the substrate for various angles α with respect to the [100] direction. The usually expected behavior for such experiments is a smooth angular α dependence of the exchange bias H_E close to a cosine with only one sign change over 180°. The high crystallographic coherence of our NiO/Co bilayers induces a very unusual oscillatory H_E (α) dependence with several sign changes according to the NiO axis field application. Despite of the Co magnetization switching mechanism which is not a pure coherent rotation, we propose a Stoner-Wohlfhart model including four fold anisotropy and unidirectional exchange anisotropy giving a realistic description of these typical magnetic properties.

INTRODUCTION

Exchange coupling between a ferromagnetic (F) and an antiferromagnetic (AF) was first observed more than 40 years ago by Meiklejohn and Bean [1]. It is presently a subject of intense investigations in thin magnetic layers community because of its applications in magnetoresistive (MR) devices such as spin-valves and magnetic tunnel junctions (one layer of the MR device is left « free » while the other is hardened by exchange coupling with an AF). The main effect induced by this coupling is a typical shift of the ferromagnet hysteresis loop called exchange bias H_E and an increase of its coercive field H_C. In most models, the AF-F system global anisotropy is considered as a sum of uniaxial and unidirectional anisotropies. The former inducing an increase of H_C and the latter the loop shift H_E. Since the coupling is assumed to be interfacial, H_E can be expressed as:

$$H_E = \frac{J_C}{M_F t_F} \quad (1)$$

Where J_C is the AF-F interfacial exchange coupling intensity, M_F and t_F are respectively the ferromagnet magnetization and thickness. Realistic values of H_E involve the formation of domain walls in the AF during the magnetization reversal of the F layer and relate J_C to the energy of such a domain wall [2,3] instead of pure exchange between the AF and F spins at the interface. They lead to the following expression: $J_C \approx \sqrt{A_{AF} K_{AF}}$. However, the presence of structural defects like interface roughness or grain boundaries is also supposed to have a significant effect on the AF-F behavior. One can also relate J_C to the limitation of the extent of domain walls in the AF or to the presence of loose spins at the AF-F interface. Therefore, a better understanding of

the mechanism of exchange anisotropy requires AF-F systems as ideal as possible. NiO-Co epitaxial bilayers are good candidates for such investigations since NiO has a relatively high Néel temperature (525 K) and a low magnetocrystalline anisotropy, such properties are expected to lead to exchange bias effects visible at room temperature and relatively sensitive to the structural quality of the samples (a small anisotropy leads to large domain structures which are mainly expected to show up for samples with excellent crystallographic coherence). Thus this system has been chosen by our group [4][5] and others like Lai et al. [6] for [001] or [111] NiO-Co bilayers. In the present study, we will focus to magnetic cycles measured on such samples for varying angles between the anneal field direction and the in-plane applied field direction. Such a procedure was first proposed by Ambrose et al. [7]. A cosine-like dependence of H_E is expected for standard AF-F systems, the exchange field varying smoothly from $-H_{E-Max}$ to $+H_{E-Max}$ over a 180° rotation, as expected from an uniaxial/unidirectional effect. We demonstrate in this paper that, combined with the magnetocrystalline anisotropies of the F and AF layers, exchange bias may have unexpected oscillations superposed to the smooth cosine effect observed for polycrystalline samples like in ref. [9]. This behavior can be interpreted with the simple Stoner-Wohlfarth (SW) approach as the sum of unidirectional and four-fold anisotropies.

EXPERIMENTAL DETAILS

Samples were grown in a Plassys MPU 600S ultra high vacuum sputter system on epi-polished MgO (001) substrates. Substrates were first annealed for 1 hour at 900°C with a base pressure better than 5×10^{-8} mB. NiO was rf-sputtered from a facing target magnetron with a deposition rate of ≈ 0.19 Å/s. The MgO substrates were heated at 900°C during the NiO growth. The plasma was obtained from a Ar(90%)-O_2(10%) gaz mixture to prevent oxygen understoichiometry. The total working pressure during the growth was set to $P=5.6 \times 10^{-3}$ mB. The NiO thicknesses of our series of samples ranged from 335 to 1000 Å. Just after NiO deposition, the sample was cooled down in zero magnetic field down to room temperature for Co deposition. Typical Co growth conditions were achieved with a standard magnetron operated in pure Ar plasma and with a deposition rate of ≈ 0.15 Å /s. In a last step, samples were capped by a 20 Å non magnetic (Al or Mo) layer before air exposure. In-situ Reflection High Energy Electron Diffraction (RHEED) was performed at all steps of the growth (bare MgO substrates, NiO layer, Co film) with a 20 kV STAIB set-up.

After the growth, the samples surfaces were investigated by Atomic Force Microscopy with a Nanoscope III microscope in tapping mode. TEM and HREM experiments, presented elsewhere [10] were also carried out on a Philips CM30/ST working at 300kV with a point resolution of 1.9 Å to evidence the crystalline quality of the bilayers.

Then the samples were annealed from 300°C to room temperature with a 300 Oe in-plane applied magnetic field to organize the NiO spin with respect to the cobalt layer. The angle between the anneal field and the in-plane reference direction [100] is referred as ω in Fig. 1. Electron microscopy was performed before and after their thermal treatments to make sure that no structural change was induced. Finally, the magnetic properties were studied at room
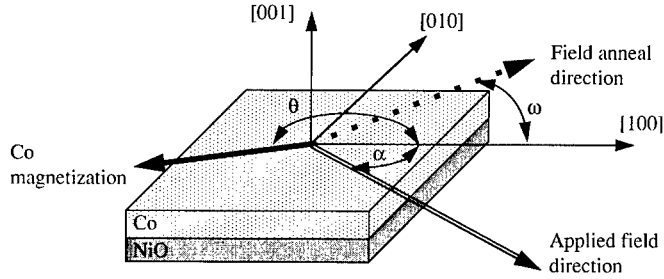
Figure 1: Configuration schematics of our orientation magnetic measurements. Angle θ represents the magnetization angle with respect to [100] axis used for Stoner-Wohlfarth modelling.

temperature by Magneto-Optic Kerr Effect (MOKE) with a polarized He:Ne laser ($\lambda = 6328$ Å). Accurate orientations of the sample in plane directions α with respect to the applied magnetic field were obtained with a goniometric sample holder. The schematic configuration of our measurements is presented in Fig. 1.

STRUCTURAL PROPERTIES

RHEED patterns, AFM scans and TEM and HREM experiments were carried out on these samples. Figure 2 shows RHEED patterns obtained for a MgO (001) bare substrate heated at 900°C prior to the NiO deposition along [100] and [110] azimuths. The same experiments are also presented after a 400 Å NiO film was deposited. The last two patterns are indicative of a smooth NiO growth with a cube-on-cube epitaxial relashionship NiO [100] (100) // MgO [100] (100). Not presented in Fig. 1, RHEED patterns on subsequently deposited Co layers reveal a similar symmetry but with a broadening of the RHEED lines due to the large misfit between NiO and Co. However, fcc cobalt structure with interface dislocations was evidenced by HREM in plane views or cross sectionnal specimens [4,5,9,10]. The surfaces are very smooth as evidenced by AFM with peak-to-peak features smaller than 15 Å.

MAGNETIC PROPERTIES

Figure 3 represents several magnetization loops obtained for a NiO(330 Å)-Co(60 Å) bilayer field-cooled along MgO [110]. Compared to a cobalt single layer, the mean coercive field increases from ≈ 40 Oe up to ≈ 500 Oe. Along the field anneal direction, the loop is shifted of $H_E \approx$ -100 Oe. Note that the maximum values of H_E are actually obtained ≈ 20-30° away from this direction. For increasing α, H_E absolute value decreases and gets a zero value close to $\alpha =$ 90-100°, then its sign gets positive from 100 to 130° and experiences a narrow negative domain between 135 and 170° followed by the expected positive values. All this behavior is summarized in Fig. 4. Note that H_C also fluctuates, evidencing four minima and maxima on 360°. This is indicative of the succession of four easy and hard axes. Thus we have simulated the experimental magnetization loops with the SW model. The bilayer energy can be decomposed as shown in Equation 2:

$$E = -HM_F \cos(\theta - \alpha) - \frac{J_C}{t_F} \cos(\theta - \omega) - K_{eff} \cos^2(2\theta) \qquad (2)$$
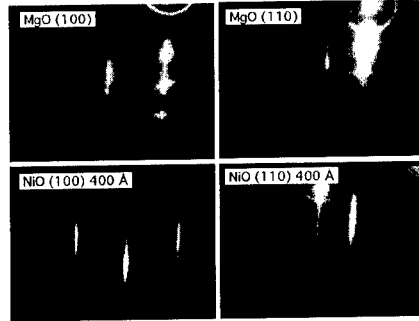
Figure 2: RHEED patterns of MgO (001) substrate prior to NiO 400 Å deposition. Pictures have been taken along both (100) and (110) azimuths.

Where the first term is the Zeeman energy of the Co layer, the second is the unidirectional exchange bias term and the third is a four-fold anisotropy term. θ is the angle between the magnetization of the Co layer and [100] axis. K_{eff} is the effective four-fold anisotropy constant. The fit was done with $\omega = 45°$ since the field anneal was done along [110]. Fit of the coercive field is not presented in Fig. 4. It yields to underestimated values. We attribute this discrepancy to the main limitation of SW model which assumes a magnetic switching by coherent rotation whereas our samples switch by a combination of coherent rotation, domain nucleation and domain wall propagation as it has been recently observed by Kerr microscopy [11]. The values used for this fit are $J_C = 7.8 \times 10^{-2}$ erg/cm^2 and $K_{eff} = 7.5 \times 10^4$ erg/cm^3. Statistics on our data collected for several thicknesses of NiO and Co yield values for J_C and K_{eff} respectively comprized between a 3×10^{-2} and 9×10^{-2} erg/cm^2 and $6 \ 10^4$ and 1×10^5 erg/cm^3. Indeed, Fig. 5 gives some insight of the validity of the SW model for the description of the oscillatory angular dependence of H_E. This figure is a grey levels image plot the bilayer magnetic energy obtained from Eq. (3) with $\alpha = 105°$ (therefore at the exchange bias oscillation position) versus the magnetization angle θ and the applied field value. The solid white line corresponds to the decreasing field switching process. The magnetization angle progressively changes from 105° to $\approx 80°$, then it switches rapidly to the opposite direction. The broken white line corresponds to the increasing field switching process. It is more vertical, signicative of an easier magnetic direction and the switching field is larger in absolute value (≈ 170 Oe). This behavior can be noticed in the marked asymmetry of the ninth magnetization loop of Fig. 3 marked with an asterisk. However, the experimental switching field values are far from the calculated ones. This discrepancy is due to the actual switching process wich involves domain nucleation and wall motion and that the basic SW approach does not take into account.

CONCLUSION
We have prepared exchange-biased NiO-Co bilayers by a combination of facing-target and standard magnetron sputtering. The epitaxial quality of our samples has allowed us to observe
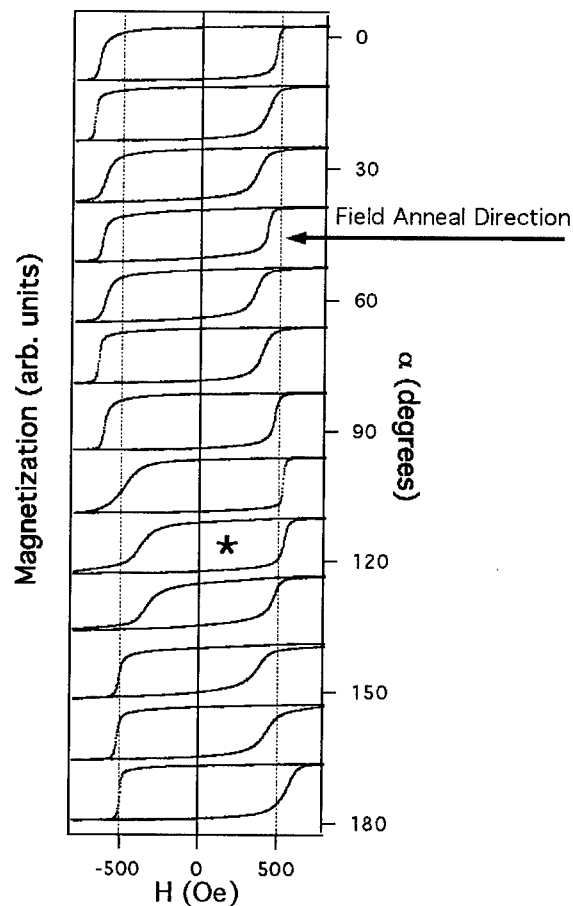
Figure 3: Magnetization loops of a NiO(330 Å)-Co(80 Å) bilayer for various angles between [100] axis and applied field direction. Note the original H_E sign changes.

original angular dependence of exchange bias. This behavior can be fully understood in terms of co-existence of uniaxial anisotropy and a four-fold extra term. The origin of the four-fold anisotropy is clearly due to the large crystallographic coherence of the samples. Such results emphasize the fundamental interest of high quality AF-F bilayers for understanding the mechanism of AF-F exchange coupling.

REFERENCES
[1] W. H. Meiklejohn and C. P. Bean, Phys. Rev. 105, 904 (1957)
[2] D. Mauri, H.C. Siegmann, P.S. Bagus and E. Kay, J. Appl. Phys. 62, 3047 (1987)
[3] A. P. Malozemoff, Phys. Rev. B 35, 3679 (1987)
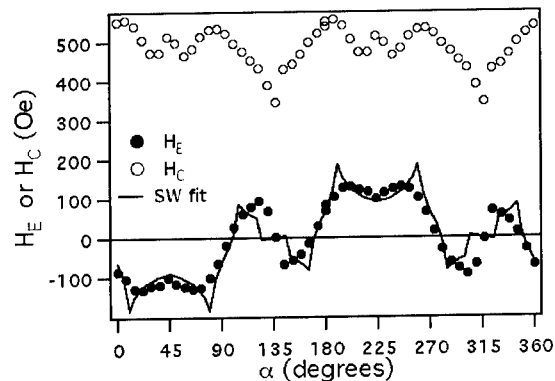
Figure 4: Angular dependence of H_C and H_E for the NiO(330 Å)-Co(60 Å) bilayer.
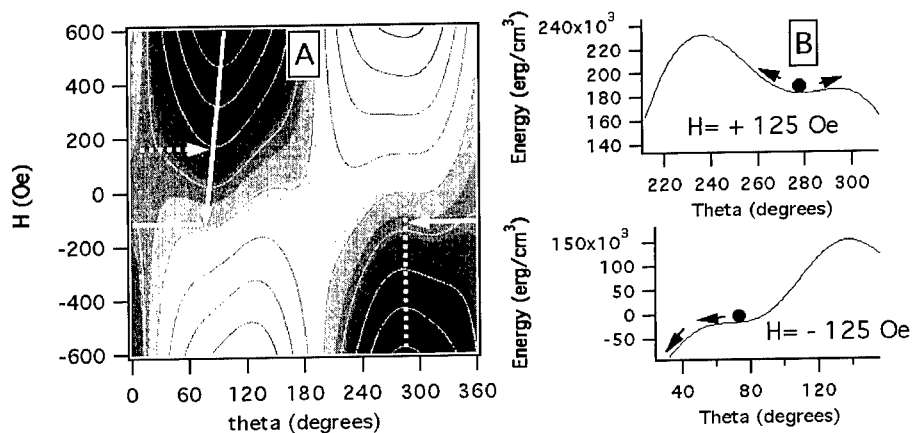
Figure 5: A: Two-dimensional grey level plot of the bilayer magnetic energy for α=105°.White lines correspond to the Co layer switching (broken line: increasing field). B: Profiles of the energy surface for H=±125 Oe evidencing the switching fields asymmetry.

[4] J.F. Bobo et al., J. Magn. Magn. Mater. 206, 118 (1999)

[5] S. Dubourg et al., J. Appl. Phys. 87, 4936 (2000)

[6] C.H. Lai, T.C. Anthony, E. Iwamura and R.L. White, IEEE Trans. Magn. 32, 3419 (1996)

[7] T. Ambrose, R. Sommer and C. Chien, Phys. Rev. B 56, 83 (1997)

[8] H. Xi, M.H. Kryder and R.M. White, Appl. Phys. Lett. 74, 2687 (1999)

[9] B. Warot et al., submitted to Symposium O, MRS Spring Meeting 2001.

[10] B. Warot et al. to be published in J. Appl. Phys.

[11] S. Dubourg, D. Hrabovsky, A.R. Fert and J.F. Bobo, to be published

Magnetic characterization of (001) and (111) Ni films epitaxially grown on MgO

R. A. Lukaszew[1], V. Stoica and R. Clarke
Randall Laboratory of Physics, University of Michigan, Ann Arbor, MI 48109
[1]Department of Physics and Astronomy, University of Toledo, Toledo, OH 43606

ABSTRACT

One interesting application of epitaxial magnetic thin films is to use them as one of the electrodes in a spin-dependent tunneling junction, in order to use the magnetocrystalline anisotropy to define the required two states of the magnetization. [1] In our preliminary work, we prepared epitaxial magnetic films on copper buffer layers grown on silicon substrates. [2] The single crystalline quality of the films was particularly evident in the magnetization hysteresis loops, showing a sharp reversal at fairly high fields (120 Oe), when the samples were magnetized along the crystallographic easy axis. One technological disadvantage in this type of samples is the chemical interaction between the metallic layers and the silicon substrate.

In order to explore the possibility of epitaxial magnetic films on less reactive substrates, we studied the growth on MgO substrates. We have shown that it is possible to obtain epitaxial (001) and (111) Ni films grown on MgO substrates. [3] In particular we observed that the crystalline quality of the films improved considerably after 10 nm of film growth. We will now present our studies on the magnetic properties of these films, particularly the azimuthal dependence of the magnetization reversal using MOKRE, correlating our finding with the structural characterization obtained with RHEED, STM and XRD.

INTRODUCTION

In general, the magnetic properties, particularly the anisotropy, of epitaxial thin films are dominated by the crystallographic structure of the metal/substrate interface as well as the surface quality. In addition, for spin-dependent tunneling devices, the roughness at the surface must be very small in order to ensure the integrity of the subsequent deposition of ultra-thin, pinhole-free insulating layers. Thus, we have considered the growth of magnetic films on MgO substrates, which can be prepared with very smooth surfaces. [3]

Here we report on the magnetic switching behavior of these thin films. Our studies reveal the existence of a second-order transition from a single-domain state to a symmetry-broken multidomain state, which leads to singularities in the switching field along specific in-plane crystallographic directions, similarly to what we have observed for epitaxial Co/Cu multilayers and Co thin films grown on silicon.

In our previous studies on Co/Cu multilayers when considering the azimuthal dependence of the coercive field, we observed the presence of singular cusps along the crystallographic hard axes, with large coercive fields values, similar to the ones observed along the easy axes. We also observed four-fold symmetry for the (001) oriented samples and uniaxial symmetry for the (111) oriented ones. In order to understand these results we developed a phenomenological model starting with the traditional coherent rotation approach. [4] Details of this model are discussed elsewhere. [5] For clarity we will point out just the main features of the model. We start by considering the free energy density. For example, for *fcc* structures in the (001) crystallographic orientation we may write:

$$E(\theta_M, H) = K_1 \cos^2(\theta_M) \sin^2(\theta_M) - H \, M_s \cos(\theta_M - \theta_H) \qquad (1)$$

where K_1 represents the magnetocrystalline anisotropy [6] M_s the saturation magnetization, H the external applied field, and θ_M (θ_H) are the angles between the Co [001] axis and the magnetization (external field), respectively. Stable orientations of the magnetization are found by minimizing $E(\theta_M,H)$. To accurately describe the free energy for each sample, the anisotropy constants were determined from separate experimental measurements using ferromagnetic resonance (FMR). [7]

For the field applied along the easy axis, the simple coherent rotation model predicts switching of the magnetization from <110> to <110)> at $H_c = \pm 2\ K_1/\ M_s$; however, the observed coercive field is much smaller. Thus we allow the system to form domains such that the moment reversal can occur at lower field by domain-wall nucleation. In this new scenario, we assume that the magnetization may "jump"[8] between two local free-energy minima when the gain in energy exceeds the cost of forming a domain wall:

$$|\Delta E| \geq E_w \tag{2}$$

E_w can be calculated straightforwardly using a standard form [9], which includes the usual exchange and anisotropy contributions. Using experimentally derived values for K_1/M_s (from FMR data), and assuming the bulk value for M_s, we were able to predict the coercive field and found it in close agreement with our experimental values.

For the (111)-oriented samples we note an interesting subtlety: the 3-fold magnetocrystalline anisotropy contribution cancels out so that any observed uniaxial symmetry is due to residual in-plane switching due for example to a weak strain-induced uniaxial contribution.

To explain the singularities in coercive field observed for the external field applied along a hard axis direction we notice that what was initially a potential local minimum in energy density (for example for $\theta_M = 0^o$) at large H, transforms to a maximum as H is decreased, and two degenerate minima start to develop in close proximity and equidistant from each side of this new maximum. A similar situation occurs for $\theta_M = 180^o$. Therefore, we see that as the external field is decreased from saturation, the system is no longer stable in the single-domain state, but a continuous transition to a multiple domain state occurs before the magnetization reversal is completed. The system spontaneously breaks up randomly in two types of symmetric domains, with the magnetization in each domain oriented along the direction of one of the two minima at each side of the hard axis direction, akin to a second-order phase transition. As the external field varies from H_{sat} to $-H_{sat}$, our model predicts that the magnetization in each domain type will at first coherently rotate. When the jumping criterion (2) is satisfied (i.e. when the energy gain exceeds the cost of forming a domain wall for each domain) the magnetization jumps to the opposite set of minima, through nucleation of domain-walls. Since twice as many walls must now be nucleated, the energy requirement is higher than it would have been without the symmetry breaking, hence the 'spikes' in the coercive field.

We have obtained direct evidence for such a domain nucleation mechanism by performing MOKE microscopy during the magnetization reversal. The data show the sudden appearance of a broad distribution of stripe domains during the reversal, consistent with our domain-wall nucleation approach. Figure 1 shows the domain configuration during the magnetic switching when the field is applied along the easy and hard directions. We notice the smooth appearance of the domain walls in the easy direction [Fig. 1(a)], consistent with one single type of domain wall. On the other hand, along the hard axis [Fig.1 (b)], the domain-walls have a zig-zag appearance,

as the magnetization must choose between the two equivalent symmetric orientations about the hard axis predicted by the model.
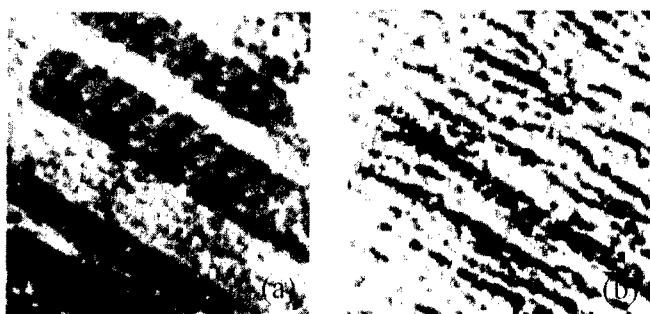
Figure 1. MOKE microscopy of a Co/Cu multiplayer. (a) Reversal of the magnetization along the easy axis, (b) reversal along the hard axis.

Thus, we have been able to qualitatively and quantitatively describe the magnetic moment switching for single crystalline Co/Cu mulatilayers and Co thin films. Our new experimental data on the magnetization reversal of epitaxial single crystal Ni films further confirms this model as will be shown below.

EXPERIMENTAL DETAILS

The Ni films were grown in an MBE VG 80 M system with a background pressure $<5 \times 10^{-11}$ torr. Ni was evaporated from a 99.999% pure source. The deposition rate was 0.5Å/sec. The substrates used in the experiment were 0.5 mm thick, 1×1 cm^2 pre-polished MgO (001) and (111) oriented single crystals, which were heat-treated in UHV at 800°C for 1 hr. The combination of flat polished substrates and the UHV heating cycle to allow the surface layers to regain crystalline order has been proven to permit growth of single crystal metal films [6] as well as exhibiting sharp reflection high-energy electron diffraction (RHEED) from the MgO surface.

Ex-situ atomic force microscopy (AFM) characterization of the annealed surfaces showed smooth surfaces with a root mean square (rms) surface roughness of 0.2nm for the (001) oriented substrates and 0.5nm for the (111) oriented ones. Prior to initiating the growth, the substrate temperature was lowered to the appropriate deposition temperature for metal growth [T $\cong$ 100 °C for (001) and T $\cong$ 300 °C for (111) oriented Ni films]. Heat transfer was by direct radiation between the heater and MgO substrate. The RHEED patterns were recorded continuously during deposition and during subsequent annealing of the films [9]. The surface morphology of the as-deposited and annealed films was determined *in-situ* with scanning tunneling microscopy [(STM) RHK model STM100]. The structural characterization of the films is extensively discussed elsewhere. [3]

DISCUSSION

Let us just review the STM studies on the (001) surface, which indicated "stripe" reconstruction, because of the possible repercussion on the magnetic properties. In order to understand this reconstruction we considered the possible effect of strain. The lattice misfit between MgO and Ni is 16%. However, it has been postulated [6] that an in-plane super-cell matching (commensuration) between the film and substrate with a_0(Ni) x 6 = 2.0446nm and a_0(MgO) x 5 = 2.1066 nm will reduce the misfit to ~0.8%. The critical thickness needed to relieve such a small strain may be quite large. Still, some authors have claimed that super-cell matching itself cannot give rise to the formation of single crystalline Ni layers, as it has been shown that in other cases interfacial periodic reconstructions can exist that allow for single crystal growth. Our observations support this. Annealing the films relaxed the surface and evidenced a reconstruction with periodicity related to the size of the postulated super-cell (i.e. 2.1 nm). [Figure 2] This type of surface reconstruction may have also an effect on the magnetic anisotropy, in the form of a weak uniaxial contribution, as will be shown below. No reconstruction was observed on the (111) oriented films after annealing.
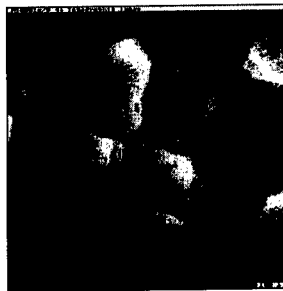
Figure2. STM image of a (001) Ni film after annealing. The bar corresponds to 10 nm.

The magnetization reversal of these films was studies with MOKE. Our setup allows the rotation of the sample in the plane of the applied field in order to facilitate studies on the azimuthal dependence of the reversal. Figure 3 shows the azimuthal dependence of the coercive field for (001) Ni films (40 nm thick) grown on MgO and further annealed. We observe the singular "spikes" along the hard axes, the four-fold symmetry due to the magnetocrystalline anisotropy, and also a weak uniaxial contribution possibly due to the "stripe" reconstruction mentioned above.

The azimuthal dependence of the (111) films didn't show any singularities, indicating that possible uniaxial contributions due to strain, steps, etc, are absent. This is consistent with the lack of observation of any type of reconstruction on the (111) surface and also with the smooth quality of the surface. The thickness of the films (in the 30-50 nm range) precludes the presence of strain, contrary to what we observed in our previous study on (111) Co/Cu multilayers. We did observe a weak three-fold anisotropy, due to the magnetocrystalline anisotropy, which was evident probably due to a slight misalignment between the plane of the sample and the applied field (Figure 4). Thus, the present data corroborates our magnetization switching model.
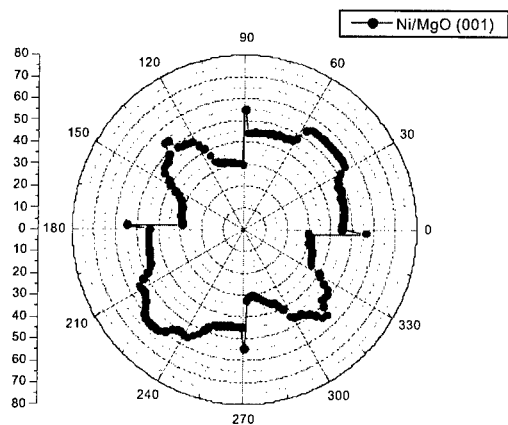
Figure 3. Azimuthal dependence of the coercive field for a (001) Ni film. The vertical axis indicates the coercive field (Oe).
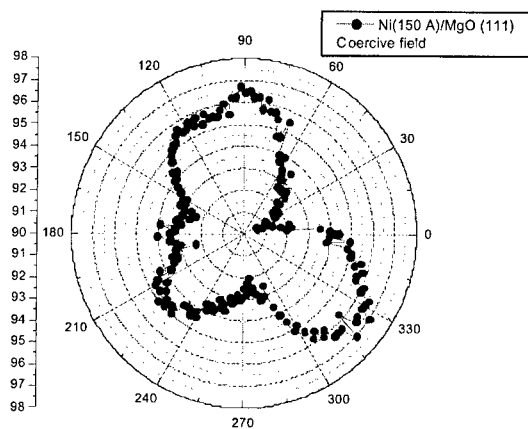
Figure 4. Azimuthal dependence of the coercive field for a (111) Ni film. The vertical axis indicates the coercive field (Oe).

References and Notes

[1]. R. A. Lukaszew, Y. Sheng, C. Uher and R. Clarke, Appl. Phys. Lett. **75**, 1941 (1999).
[2]. R. A. Lukaszew, Y. Sheng, C. Uher and R. Clarke, Appl. Phys. Lett. **76**, 724 (2000).
[3]. R. A. Lukaszew, V. Stoica, C. Uher and R. Clarke, MRS Proceedings, Fall 2000.
[4]. E. C. Stoner and E. P. Wohlfarth, *Phil. Trans. Roy. Soc.* **A-240**, 599-644 (1948). [two authors]
[5]. R. A. Lukaszew, E. Smith, R. Naik and R. Clarke, submitted to Phys. Rev. Lett. (2001)
[6]. K_1 is negative for *fcc* Co making the in-plane [001] direction a magnetic hard axis.
[7]. R. A. Lukaszew, R. Naik, K. R. Mountfield and K. R. Artman, *J. Appl. Phys.* **79**, 4787-4789 (1996). [four authors]
[8]. J. M. Florczak and E. D. Dahlberg, *Phys. Rev. B* **44**, 9338-9347 (1991). [two authors]
[9]. R. F. Soohoo, *Magnetic Thin Films*, (Harper and Row, New York, 1965); M. Prutton, *Thin Ferromagnetic Films*, (Butterworths, Washington, 1964).

EXCHANGE-BIASED NIO-CO NANOFACETED BILAYERS GROWN ON MGO (110)

S. Dubourg, J.F. Bobo
LPMC, UMR-CNRS-INSA-UPS 5830 135, 31077 Toulouse Cedex 4, France

B. Warot, E. Snoeck and J.C. Ousset
CEMES CNRS, 29 rue Jeanne Marvig 31055 Toulouse Cedex 4, France

ABSTRACT

We have sputter-grown self-organised faceted NiO-Co epitaxial bilayers on MgO(110). Due to very close lattice parameters, NiO adopts the same NaCl crystallographic structure as the substrate but it minimises its surface energy growing in a stripe-shaped morphology elongated along [001] MgO direction. The Co layers then deposited on NiO adopt a fcc structure. They consist of a set of connected nanowires whose height is about 50 Å, length is near to 1μm and lateral periodicity ≈ 100 Å. Magnetic properties of the Co layers were investigated by magneto-optical Kerr effect from 10 K to room temperature. They are dominated by a strong shape-induced uniaxial anisotropy and exchange coupling with the antiferromagnetic underlayer. Magnetisation loops recorded along the easy axis exhibit a perfect squareness and switch in a field range smaller than 10 Oe. Transverse measurements indicate that switching occurs by domain nucleation and/or domain wall propagation. On the contrary, close to the [110] hard axis, magnetic switching occurs by coherent rotation. The bi-stable Co magnetisation state along its easy axis has been used for ordering the NiO spins configuration from room temperature to 10 K. Sign and value of exchange bias induced by such a thermal treatment can be modulated thanks to a wide magnetocrystalline or local exchange path energies distributions.

INTRODUCTION

Exchange coupling between a ferromagnet (F) and an antiferromagnet (AF) was discovered more than 40 years ago by Meiklejohn and Bean [1]. This phenomenon has become a great challenge in thin magnetic layers community since it has potential applications in magnetoresistive devices such as spin-valves and tunnel junctions. The main effect induced by this coupling is a typical shift of the F hysteresis loop called exchange bias H_E and an increase of its coercive field. Ten years ago the first models predicting coherent exchange bias values were proposed by Mauri [2] and by Malozemoff [3]. Both of them point out the main rule played by domain walls in the AF and predict a $\sqrt{AK}$ dependence of H_E where A is the AF stiffness and K its anisotropy constant. These models do not only imply that the AF is completely organised after a field cooling through its Néel temperature but the exchange bias sign cannot change either when temperature is decreased further. Exchange bias is expected to follow a $\sqrt{K(T)}$ dependence. Stiles and Mc Michael [4] have recently proposed a model for polycrystalline samples in which AF grains are divided into two groups according to the $\varepsilon = J_c / \sqrt{AK}$ ratio where J_c is the average direct coupling between the AF and the F. Grains with low ε contribute to the exchange bias whereas those with high ε can induce coercive field. This theory is coherent with experimental studies made by S. Soeya et al in NiO/NiFe [5] bilayers who report that many "local domain paths" between $T_N(NiO)$ and room temperature are involved in the coupling. These paths can be "activated" reducing temperature. A better understanding of the mechanism of exchange anisotropy requires

AF / F systems as ideal as possible [6][7]. Namely, systems with controlled crystalline coherence of the AF / F interface and reduced dimension like ultra-thin films or nanostructured materials. Efforts have been done to obtain epitaxial NiO-Co bilayers by our group and others like Lai et al. [8] for [001] or[111] NiO-Co bilayers. Defect-free epitaxial systems are supposed to have perfectly flat interfaces over large distances. This is very important for exchange coupling fundamental studies since the spin-ordering in an AF changes every atomic plane. However, real systems like the above-mentioned epitaxial NiO-Co bilayers present roughness features over distances smaller than the usual F and AF domain size, which makes the interpretation of their magnetic behaviour more difficult. This issue may be solved using nanoscale-patterned bilayers. It has been demonstrated, for example, that sub micron scale patterning of continuous layers [9] involved in MTJ's leads to single-domain behaviour. The standard way for obtaining such patterned nano-objects is based on electron beam lithography and requires several steps of fabrication. An alternative way to obtain wire-like aspect ratios for patterned elements is self-organised growth or other structuration methods like the so-called atomic saw [10]. These techniques do not require lithography. Well controlled self-organised growth is expected to lead to the smallest spatial resolution of nanostructures. This way is hardly investigated and we present in this paper our recent results on exchange-biased cobalt nanowires grown on faceted epitaxial nickel oxide layers. MgO (110) single-crystal substrates were used to favour the anisotropic growth of NiO. The NiO top surface presents a roof-like morphology and the Co layers deposited on NiO form an array of connected nanowires. We demonstrate that such nanostructures exhibit a strong uniaxial shape anisotropy combined with exchange bias.

EXPERIMENTAL DETAILS

Samples were grown in a Plassys MPU 600S ultra high vacuum sputter system on epi-polished MgO (110) substrates. Substrates were first annealed for 1 hour at 900°C with a base pressure better than 5×10^{-8} mB. NiO was sputtered from a facing target magnetron with a deposition rate 0.19 Å/s on the MgO substrates heated at 800°C. In order to have the correct Ni:O stoichiometry, a mixture Ar-O$_2$ was used for NiO sputtering at P=5.6×10^{-3}mB. The NiO thickness of the samples presented in this study ranged from 335 to 1000 Å. A 40 to 160 Å -thick Co layer was deposited at 350°C with a standard magnetron at 0.15 Å /s. In order to organise the spins of the NiO layer relatively to the magnetisation of the Co layer, a 300 Oe field cooling of the as-deposited bilayer was performed in the chamber. In a last step, samples were capped by a 20 Å Mo layer before air exposure. In-situ Reflection High Energy Electron Diffraction (RHEED) was performed at all steps of the growth (bare MgO substrates, NiO layer, Co film) with a 20kV STAIB set-up. After the growth, the samples surfaces were investigated by Atomic Force Microscopy with a Nanoscope III microscope in tapping mode. For Transmission Electron Microscopy (TEM) or High Resolution Electron Microscopy (HREM) studies, the samples were prepared both in plane view (along MgO [110] zone axis) to check the in-plane epitaxial growth and film morphology, and in cross section to observe the stacking sequence along the MgO [001] zone axis. Finally, the magnetic properties were studied at room temperature by Magneto-Optic Kerr Effect (MOKE) with a polarised He:Ne laser ($\lambda = 6328$ Å).
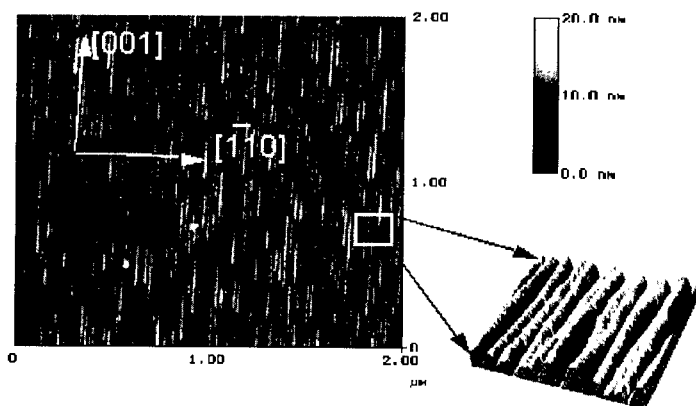
Figure 1: AFM scan of a MgO(110) / NiO(1000 Å) / Co(80 Å) / Mo(30 Å) sample over a 2×2 μm² area with enlarged 0.2×0.2 μm² view on the right

STRUCTURAL PROPERTIES

RHEED patterns, AFM scans and TEM and HREM experiments were carried out on these samples. Structural results are detailed in an other symposium [11]. Let us just point out that all these experiments confirm the NiO self-organised growth. As it can be observed in Fig 1, AFM images reveal a stripe-shaped surface elongated along [001] with symmetrical slopes of about 45° in the [-110] direction. The length of these anisotropic structures is of the order of 1μm while their width depends on the NiO film thickness. The nanostripes width is close to 80 Å for a 335 Å thick film and reaches 125 Å for a 1000 Å thick NiO layer. Quantitative AFM analysis gives a width distribution of the wires of +/- 20 Å.

MAGNETIC PROPERTIES

Magnetic properties of NiO/Co bilayers were investigated at room temperature with a magnetic field applied in the plane of the layers. They reveal a strong uniaxial anisotropy along [001] induced by the shape of the Co stripes. Longitudinal and transverse Kerr effect loops along the easy direction [001] and the hard direction [-110] are presented in Fig. 2. Along [001], they have a perfect squareness with a coercive field between 140 and 1500 Oe depending on Co layer thickness . The magnetisation loops along [001] exhibit a very sharp edge and switch in less than 10 Oe despite the Co wires shape distribution; this collective switching implies a coupling between the Co stripes indicative of a contact between each nanowire as observed by HREM. The magnetisation loops measured along [-110], therefore perpendicular to the stripes are characteristic of a hard axis. For all samples, the magnetic field required to saturate the magnetisation in this direction is at least 2200 Oe (see Table I). Transverse Kerr effect loops were also recorded, they evidence a magnetisation switching by coherent rotation if the magnetic field is applied along the [-110] hard axis. Along the easy [001] axis, the small transverse signal is indicative of a magnetisation switching dominated by domain nucleation and/or domain wall propagation.
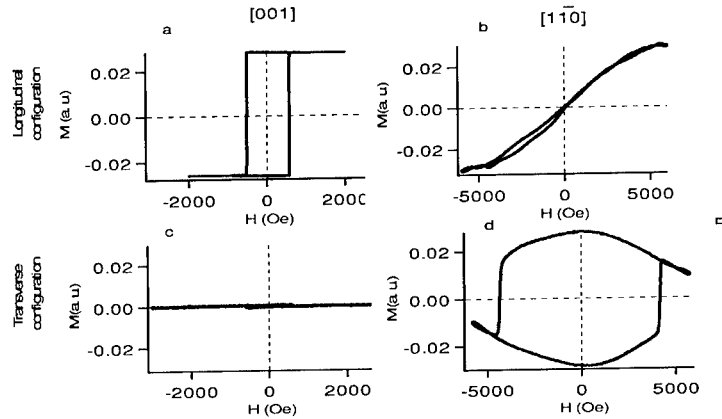
Figure 2: Kerr effect loops in longitudinal (a,b) and transverse (c,d) in-plane configuration recorded along the [001] easy axis (a,c) and the [-110] hard axis (b,d). The same scale is used for the four magnetisation loops

This explains why the easy axis coercive field is lower than the hard axis saturation field contrary to the commonly observed behaviour of uniaxial single domain particles. From the value of the saturation field along the [-110] hard axis, we estimate an uniaxial anisotropy constant of 1.4×10^6 erg/cm^3 for 160 Å of Co deposited on 335 Å of NiO and of 5.6×10^6 erg/cm^3 for 40 Å of Co deposited on 335 Å of NiO. This last value is larger than the Co hcp magnetocrystalline anisotropy along the c-axis. Therefore, we assume that the anisotropy observed in our samples is mainly due to their nanowire morphology. This is corroborated by the simple calculation of the demagnetising energy of an infinite Co cylinder which is $\pi M_{Sat}^2 = 6.16 \times 10^6$ erg/cm^3 and its saturation field is close to $\pi M_{Sat} = 8800$ Oe. Such values are almost reached for our very thin Co layer samples, confirming the strong influence of the layer morphology on the Co magnetic anisotropy. The shape anisotropy induced by the roof morphology of the cobalt layer induces a bi-stable state of the Co magnetisation. Indeed, at the remanent state only two fully saturated configurations along its easy axis are allowed. This property has been used to modify the exchange bias value according temperature. Cooling a MgO(110)/NiO(335 Å)/Co(80 Å)/Mo sample from 300°C to room temperature in a 300 Oe field along the [001] direction induces a -25 Oe exchange bias. This sample was then cut into two pieces. The first one has been cooled from room temperature to 10 K maintaining its magnetisation direction. The second one received the same thermal treatment with its magnetisation aligned along its other stable state which is [00-1]. Hysteresis loops along [001] direction were then recorded warming the samples up to room temperature. Exchange bias values measured and presented in Fig. 3. When the cobalt layer magnetisation is not reversed, exchange bias value is minimum at 10 K and reaches –60 Oe. On the contrary, when the cobalt magnetisation is reversed at room temperature, we can notice a sign change of the hysteresis loop shift which is equal to 20 Oe at 10 K. In both cases the phenomenon is reversible since the exchange bias progressively reaches its room temperature value during the warm up.
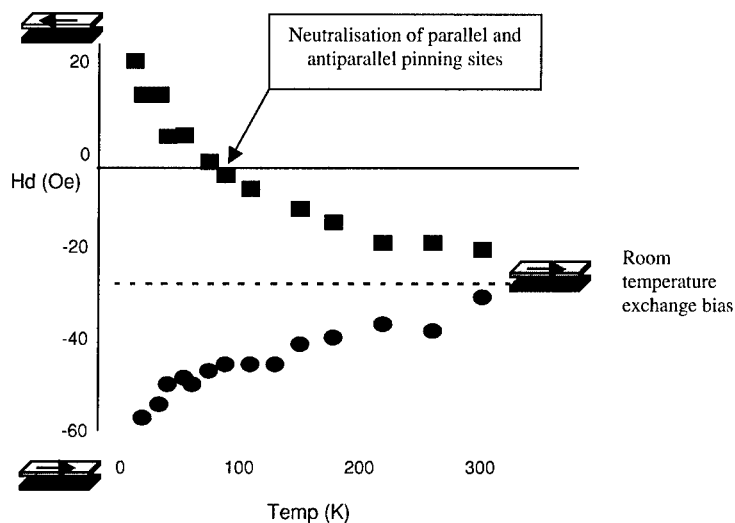
Figure 3: exchange bias temperature dependence according to the cobalt layer magnetisation direction

DISCUSSION

This phenomenon can be explained extending the Stiles and Mc Michael [4] model to our epitaxial samples. Assuming a wide distribution of the $J_c/\sqrt{AK}$ rate, the antiferromagnetic layer can be divided in local domain paths which contribute to the exchange bias or to irreversible motion of domain wall within NiO layer. Cooling down the sample, AF magnetocrystalline anisotropy will increase and reach a temperature at which a given domain path will become "active". This temperature is called local blocking temperature. The initial field cooling has organised all the domain paths whose blocking temperatures are comprised in the range [300°K - 525°K].
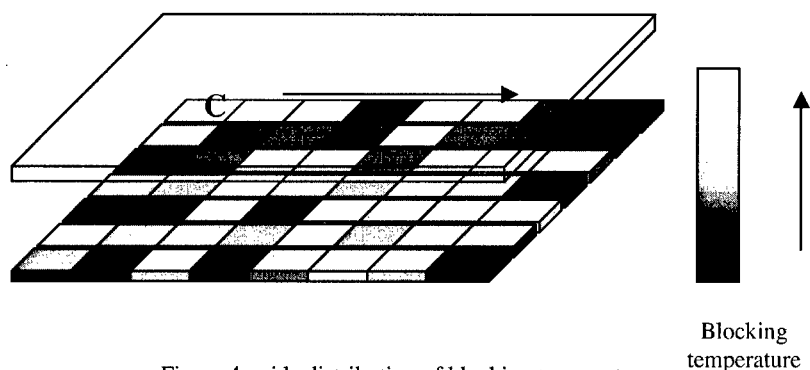
Figure 4: wide distribution of blocking temperature

During the second cooling, low blocking temperature paths have be activated in the same or in the opposite direction to the initial cooling according to cobalt magnetisation direction. Warming up the sample will progressively disable domain paths and reach the same exchange bias value at room temperature induced by high blocking temperature domain paths. Note that an equilibrium between parallel and antiparallel domain paths is obtained near 80 K when the cobalt magnetisation is reversed after the initial cooling. This is mentioned in Fig.3 as a neutralisation temperature. Such distribution has been previously observed by Soeya at al. [5] on polycristalline NiO/NiFe samples. They conclude that higher blocking temperature density is very close to the global blocking temperature near 215°C. In our samples the distribution is wider and spreads down to 10 K at least. The main teaching of this experiment is that models which describe the NiO magnetic structure as completely frozen just under its Néel temperature are not fully realistic. H_E value and the NiO magnetic organisation depend on temperature and on the cobalt magnetisation orientation (if the applied magnetic field is low enough to prevent AF spin-flop).

CONCLUSION

We have prepared exchange-biased NiO-Co bilayers by a combination of facing-target and standard magnetron sputtering. The growth of NiO on MgO(110) leads to a roofed surface with (100) and (010) nanofacets. The Co overlayers adopt this morphology and can be considered as connected nanowires with a strong uniaxial shape-induced anisotropy. The bi-stable Co magnetisation state along its easy axis has been used for ordering the NiO spins configuration from Néel temperature to 10°K. Sign and value of exchange bias induced by a thermal treatment can be modulated thanks to a wide magnetocrystalline or local path blocking temperature distributions.

REFERENCES

[1] W. H. Meiklejohn and C. P. Bean, Phys. Rev. 105, 904 (1957)
[2] D. Mauri, H.C. Siegmann, P.S. Bagus and E. Kay, J. Appl. Phys. 62, 3047 (1987)
[3] A. P. Malozemoff, Phys. Rev. B 35, 3679 (1987)
[4] M. D. Stiles and R. P. Mc Michael, Phys. Rev. B 59, 3722 (1999)
[5] S. Soeya, T. Imagawa, K. Mitsuoka and S. Narishige, J. Appl. Phys. 76, 5356 (1994)
[6] J.F. Bobo, S. Dubourg, E. Snoeck, B. Warot, P. Baules, and J.C. Ousset, JMMM 206, 118 (1999)
[7] S. Dubourg, N. Nègre, B. Warot, E. Snoeck, M. Goiran, J.C. Ousset and J.F. Bobo J. Appl. Phys. 87, 4936 (2000)
[8] C.H. Lai, T.C. Anthony, E. Iwamura and R.L. White, IEEE Trans. Magn. 32, 3419 (1996)
[9] B.D. Schrag, A. Anguelouch, G. Xiao, P.Trouilloud, Y.Lu, J. Gallagher and S.S.P. Parkin J. Appl. Phys. 87, 4682 (2000)
[10] H. Jaffrès, L. Ressier, K. Postava, A. Schuhl, F. Nguyen Van Dau, M. Goiran, J.P. Redoulès, J. P. Peyrade and A.R. Fert, JMMM 184, 19 (1998)
[11] B. Warot, E. Snoeck, P. Baulès, J. C. Ousset, M. J. Casanove, S. Dubourg and J. F. Bobo, J. Crystal Growth 224, 309 (2001); Symposium O 4.2 MRS Spring meeting 2001

EXCHANGE COUPLING AND SPIN-FLIP TRANSITION OF $CoFe_2O_4/\alpha\text{-}Fe_2O_3$ BILAYERED FILMS

Tatsuo Fujii, Takuya Yano, Makoto Nakanishi and Jun Takada
Department of Applied Chemistry, Faculty of Engineering, Okayama University,
Tsushima-naka 3-1-1, Okayama 700-8530, Japan

ABSTRACT

$CoFe_2O_4/\alpha\text{-}Fe_2O_3$ (ferrimagnetic / antiferromagnetic) bilayered films were prepared on $\alpha\text{-}Al_2O_3$(102) single-crystalline substrates by helicon plasma sputtering. A well-crystallized epitaxial $\alpha\text{-}Fe_2O_3$(102) layer was formed on the substrate, while $CoFe_2O_4$ grown on $\alpha\text{-}Fe_2O_3$ (102) was a polycrystalline layer with a (100)-preferred orientation. The $\alpha\text{-}Fe_2O_3$(102) films without $CoFe_2O_4$ layers clearly showed a spin-flip transition at about 400 K. The spins aligned perpendicular to the film plane at room temperature changed their direction within the film plane above 400 K. However the $\alpha\text{-}Fe_2O_3$ base layers of $CoFe_2O_4/\alpha\text{-}Fe_2O_3$ bilayered films did not show any spin-flip transition. The $CoFe_2O_4$ layer on $\alpha\text{-}Fe_2O_3$ had a large in-plane magnetic anisotropy, while the spin axis of the $\alpha\text{-}Fe_2O_3$ (102) base layer was directed perpendicular to the film plane. The magnetization of ferrimagnetic $CoFe_2O_4$ layers was coupled perpendicularly to the spin axis of anitiferromagnetic $\alpha\text{-}Fe_2O_3$ layers due to the exchange coupling at the interface between $CoFe_2O_4$ and $\alpha\text{-}Fe_2O_3$.

INTRODUCTION

Exchange coupling at an interface between ferromagnetic (FM) and antiferromagnetic (AFM) layers has received much attention mainly due to the technological applications in such devices as spin-valve sensors. It stabilizes a magnetic direction of the FM layer and functions as a bias field in the magnetic hysteresis loop. Recently, full micromagnetic calculations suggested the existence of the 90° FM - AFM coupling at the interface [1]. However the fundamental origin of exchange coupling between magnetic materials, especially magnetic oxide materials, is still unclear. $\alpha\text{-}Fe_2O_3$ is one of candidates for the AFM materials fabricated in the spin-valve sensors [2,3]. The spin valves partly consisting of $\alpha\text{-}Fe_2O_3$ have high thermal stability and large magneto-resistance ratio. By the way, one of the present authors found that epitaxial $\alpha\text{-}Fe_2O_3$ (102) films on $\alpha\text{-}Al_2O_3$(102) had an unique spin-flip transition [4]. The transition takes place at about 400 K, much higher than the Morin transition temperature (260 K) of the bulk crystal. The spin axis lying within a film plane above 400 K turns perpendicular to the film plane below the transition temperature.

There are a few studies on the exchange coupling between oxide materials with the FM/AFM bilayered structure [5]. Most of practical FM oxides are exactly ferrimagnetic. Microscopic spin configurations at the interface between oxide systems could be different from the ones between metallic systems. We prepared well-crystallized $\alpha\text{-}Fe_2O_3$ and $CoFe_2O_4$ bilayered films by using helicon plasma sputtering technique [6]. $CoFe_2O_4$ is a typical ferrimagnetic material with an inverse spinel structure. Structural properties and magnetic interactions between ferrimagnetic $CoFe_2O_4$ (FM) and $\alpha\text{-}Fe_2O_3$ (AFM) layers were discussed. If the exchange coupling at the $CoFe_2O_4/\alpha\text{-}Fe_2O_3$ interface was strong enough, magnetic properties of the $CoFe_2O_4$ layer should be influenced by the spin-flip transition of the $\alpha\text{-}Fe_2O_3$ layer or vice versa.

EXPERIMENT

Helicon plasma sputtering is a powerful technique to prepare high-quality multilayered films with sharp interfaces [7]. It has some advantages in comparison with conventional rf magnetron sputtering, such as high deposition rate stability and low plasma damage to the film surface. A helicon plasma cathode consists of a conventional rf magnetron cathode and a rf coil for a helicon wave. Fig.1 shows a schematic drawing of the helicon plasma sputtering system we used. Two targets for helicon cathodes were made of sintered α-Fe_2O_3 and CoO, respectively. The base pressure of the system was 10^{-7} Pa. Before sputter deposition an α-$Al_2O_3(102)$ substrate was annealed in vacuum at about 973 K for 1 hour in order to obtain a clean and well-ordered surface. α-Fe_2O_3 base layers with the thickness of 100 nm were sputtered on the substrate at the substrate temperature of 673 K. $CoFe_2O_4$ layers with several thicknesses ranging from 25 to 200 nm were then deposited on α-Fe_2O_3 at 773 K by simultaneous sputtering from both targets, to control the deposition rate ratio between α-Fe_2O_3 and CoO. The deposited films were characterized by reflection high energy electron diffraction (RHEED), x-ray diffraction (XRD), scanning probe microscopy (SPM), vibrating sample magnetometer (VSM), conversion electron Mössbauer spectroscopy (CEMS), and energy dispersive X-ray spectroscopy (EDS).

RESULTS AND DISCUSSION

Typical XRD and RHEED patterns of α-Fe_2O_3 films deposited on α-Al_2O_3 (102) single-crystalline substrates are shown in figs. 2(a) and (b), respectively. Epitaxial relationship between the α-Fe_2O_3 layer and the α-Al_2O_3 substrate can clearly be seen in both XRD and RHHED patterns. The XRD pattern had only a reflection from the film indexed as α-$Fe_2O_3(204)$ at the side of an intense α-Al_2O_3 (204) reflection. The sharp streak lines in the RHEED pattern indicated an atomically flat surface of the layer. Both α-Fe_2O_3 and α-Al_2O_3 have a corundum structure with a small lattice misfit of +5.8 %. This could be a reason why the well-crystallized and atomically flat α-Fe_2O_3 layers were epitaxially formed on the α-Al_2O_3 substrates.
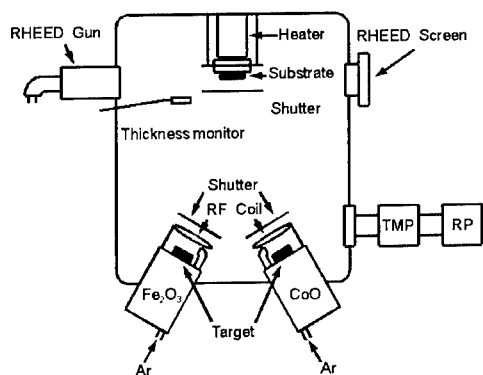
Figure 1. Schematic drawing of helicon plasma sputtering system we used. The helicon cathodes consist of conventional rf magnetron cathodes and rf coils.
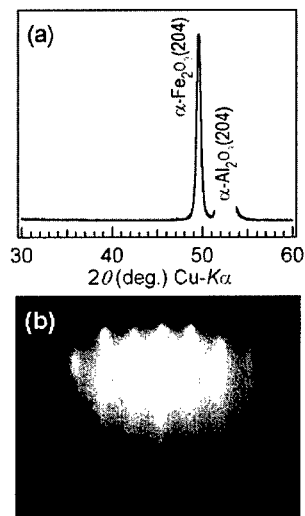
Figure 2. *(a) XRD and (b) RHEED patterns of an α-Fe₂O₃ film deposited on an α-Al₂O₃ (102) substrate.*
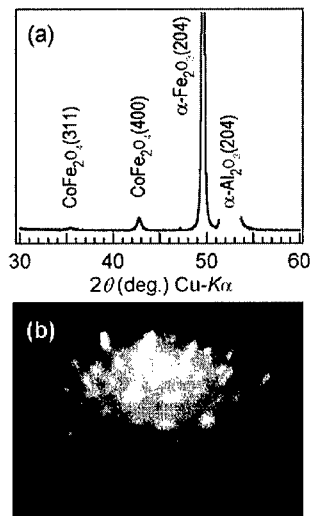
Figure 3. *(a) XRD and (b) RHEED patterns of a CoFe₂O₄/α-Fe₂O₃ bilayered film deposited on an α-Al₂O₃ (102) substrate. Thicknesses of the CoFe₂O₄ and the α-Fe₂O₃ layers were 200 and 100 nm, respectively.*

Figs. 3(a) and (b) are typical XRD and RHEED patterns of $CoFe_2O_4/Fe_2O_3$ bilayered films, respectively. The XRD pattern of the $CoFe_2O_4/Fe_2O_3$ bilayered film had two reflections from the $CoFe_2O_4$ layer indexed as $CoFe_2O_4(311)$ and (400) in addition to the reflection from the α-Fe_2O_3 (204) base layer. The relative peak intensity ratio of $CoFe_2O_4(400)$ to (311) was considerably large, in comparison with that of the $CoFe_2O_4$ bulk pattern with random orientation [8]. The $CoFe_2O_4$ layer formed on α-$Fe_2O_3(102)$ had strong (100)-preferred orientation. In crystallographic aspects, the α-$Fe_2O_3(102)$ surface has a pseudo-square structure though the α-Fe_2O_3 crystal has hexagonal corundum structure. The $CoFe_2O_4(100)$ layer with cubic spinel structure could be formed on the α-Fe_2O_3 (102) base layer. However the lattice misfit between them is very large, about -17%. The RHEED pattern of $CoFe_2O_4$ on α-$Fe_2O_3(102)$ was spotted and complicated. The $CoFe_2O_4$ layers in bilayered films were poly-crystallized and had (100)-preferred orientation. Moreover, chemical formula of the $CoFe_2O_4$ layer analyzed by EDS was $Co_{0.7}Fe_{2.3}O_4$.

The spin direction of α-Fe_2O_3 layers on α-$Al_2O_3(102)$ was easily determined by CEMS. The CEMS spectrum of α-Fe_2O_3 generally exhibited six lines due to the nuclear Zeeman splitting from a large internal magnetic field. Relative peak intensity ratio of the sextet is expressed theoretically as a function of an angle (θ) between the γ-ray direction and the spin direction

$$3:\frac{4\sin^2\theta}{1+\cos^2\theta}:1:1:\frac{4\sin^2\theta}{1+\cos^2\theta}:3.$$
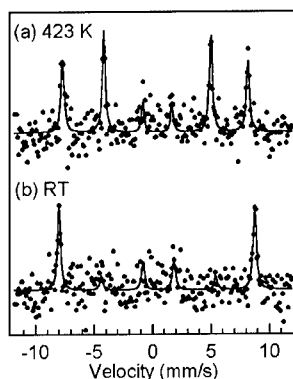
Figure 4. CEMS spectra of an α-Fe₂O₃(102) film deposited on α-Al₂O₃ (102) measured at (a) 423 K and (b) room temperature.
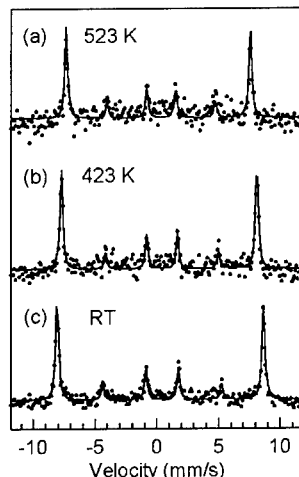
Figure 5. CEMS spectra of a CoFe₂O₄/α-Fe₂O₃ bilayered film on α-Al₂O₃ (102), measured at (a) 523 K, (b) 423 K, and (c) room temperature. Thicknesses of the CoFe₂O₄ and α-Fe₂O₃ layers were 25 and 100 nm, respectively.

CEMS spectra of an α-Fe_2O_3(102) film without a $CoFe_2O_4$ covering layer are shown in fig. 4 as a function of the temperature. The spectra had the intensity ratio of nearly 3:0:1:1:0:3 at 300 K and 3:4:1:1:4:3 at 423 K. The spin axis of the α-Fe_2O_3 (102) film was abruptly changed from the perpendicular direction ($\theta=0°$) to the in-plane direction ($\theta=90°$) at about 400 K.

Besides the intensity ratio of the CEMS spectra of the $CoFe_2O_4/\alpha$-Fe_2O_3(102) bilayered film did not show any temperature dependence, even when the α-Fe_2O_3(102) layer was covered by a very thin, 25 nm-thick, $CoFe_2O_4$ layer. All spectra of the α-Fe_2O_3(102) base layer had the intensity ratio of about 3:0:1:1:0:3 as shown in fig. 5. The α-Fe_2O_3 layer covered by $CoFe_2O_4$ did not show the spin-flip transition. The spin direction in α-Fe_2O_3 was fixed perpendicular to the film plane over the all temperatures.

In-plane and out-of-plane magnetization curves of the $CoFe_2O_4/\alpha$-Fe_2O_3 bilayered films were also measured at various temperatures. Figs. 6(a) and (b) show room temperature magnetization curves of the 200 nm-thick $CoFe_2O_4$ films without and with the α-Fe_2O_3(102) base layers, respectively. No uniaxial magnetic anisotropy nor exchange bias field was induced in the $CoFe_2O_4$ layers, when they did not have the α-Fe_2O_3 base layers. $CoFe_2O_4$ is known to have a large magnetocrystalline anisotropy along the <100> direction [8]. The (100)-oriented $CoFe_2O_4$ layers could have domain structures magnetized along the in-plane [100] and [010] and the out-of-plane [001] directions. The large coercivity was, thus, observed in both in-plane and out-of-plane hysteresis loops.

On the other hands, the $CoFe_2O_4$ layers deposited on the α-Fe_2O_3(102) base layers had a large in-plane magnetic anisotropy. The exchange bias field of about 200 Oe was induced. The spin
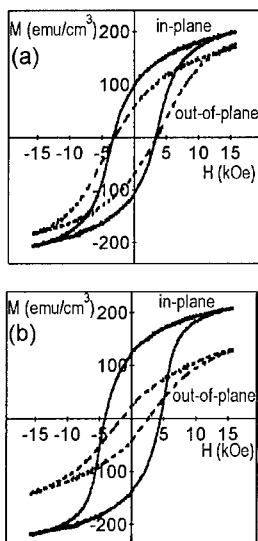
Figure 6. In-plane and out-of-plane magnetization
curves of (a) a 200 nm-thick CoFe₂O₄ film deposited
on α-Al₂O₃(102), and (b) a CoFe₂O₄ (200 nm)
/α-Fe₂O₃ (100 nm) bilayered film on α-Al₂O₃ (102).
The magnetization curves were measured at room
temperature

axis of the α-Fe$_2$O$_3$ base layers was directed perpendicular to the film plane as discussed above. The magnetization of the CoFe$_2$O$_4$ (FM) layers was exactly coupled perpendicularly to the spin axis of the α-Fe$_2$O$_3$ (AFM) layers. The 90° FM-AFM coupling observed in CoFe$_2$O$_4$/α-Fe$_2$O$_3$ bilayered films was in good agreement with the theoretical result reported by Koon [1]. The large in-plane anisotropy of the CoFe$_2$O$_4$ layers was probably induced by the 90° coupling with the α-Fe$_2$O$_3$ layers and it should suppress the spin-flip transition of the α-Fe$_2$O$_3$ layers irreversibly.

SUMMARY

Exchange coupling between a ferrimagnetic CoFe$_2$O$_4$ layer and an anitiferromagnetic α-Fe$_2$O$_3$ layer was examined to prepare CoFe$_2$O$_4$/α-Fe$_2$O$_3$ bilayered films. (100)-oriented CoFe$_2$O$_4$ layers were formed on well-crystallized epitaxial α-Fe$_2$O$_3$(102) layers deposited on α-Al$_2$O$_3$(102) single-crystalline substrates. The α-Fe$_2$O$_3$(102) films without CoFe$_2$O$_4$ layers clearly showed the spin-flip transition at about 400 K. The spin axis lay within the (102) plane of α-Fe$_2$O$_3$ at high temperatures but became almost normal to the plane at low temperatures. However the α-Fe$_2$O$_3$(102) layers covered by CoFe$_2$O$_4$ layers did not show any spin-flip transition. The spin axis of the α-Fe$_2$O$_3$(102) base layers was fixed on the perpendicular to the films. Magnetic hysteresis loops of CoFe$_2$O$_4$/α-Fe$_2$O$_3$ bilayered films indicated that a large in-plane magnetic anisotropy and an exchange bias field were induced in the films. The 90° coupling at the interface between ferrimagnetic and antiferromagnetic materials was directly observed in the CoFe$_2$O$_4$/α-Fe$_2$O$_3$ system fabricated entirely of oxides.

ACKNOWLEDGEMENT

REFERENCES

1. N. C. Koon, Phys. Rev. Lett., **78**, 4865 (1997).
2. N. Hasegawa, A. Makino, F. Koike, K. Igarashi, IEEE. Trans, Magn., **32**, 4618(1996).
3. H. Sakakima, Y. Sugita, M. Satomi, Y. Kawawake, J. Magn. Magn. Mat., **198-199**, 9 (1999).
4. T. Fujii, M. Takano, R. Katano, Y. Isozumi, Y. Bando, J. Magn. Magn. Mat., **135**, 231 (1994).
5. P. J. van der Zaag, A. R. Ball, L. F. Feiner, and R. M. Wolf, P. A. A. van der Heijden, J. Appl. Phys., **79**, 5103 (1996).
6. T. Fujii, T. Yano, M. Nakanishi, J. Takada, in *Proceedings of the 8th International Conference on Ferrites* (Kyoto, 2000) in press.
7. X. Wang, H. Matsumoto, Y. Someno, T. Hirai, Appl. Phys. Lett., **72**, 3264 (1998).
8. JCPDS, *Powder Diffraction File*, **22**-1086.
9. J. Smit, H.P.J. Wijn, *Ferrites*, Philips Technical Library, Eindhoven, the Netherlands, 1959, p.162.

Micromagnetics to Nanomagnetics—
The Next Step

Computational Modeling For Magnetic-Sensor-Based Three-Dimensional Visualization Of Microcracks

Leonid Muratov, David Lederman, and Bernard R. Cooper
West Virginia University, Morgantown, WV 26506-6315

ABSTRACT

The presence of cracks, phase segregation, or even submicron-sized grain boundaries creates a disruption of the magnetic field response to an externally applied electrical current running through the material. These effects can be detected through the magnetic field leakage in the external near-surface region. Using a computer model of an array of magnetic tunnel junction detectors, magnetic "signatures" of various faults and/or material borders and domains have been calculated using finite element analysis and portrayed by icons. We have considered a number of typical cracks and flaws, of different dimensions and orientations, within the bulk of the component. The database of "signatures" thus generated allows fast recognition of faults and generation of their images in real time. Significant efforts have been made to provide an adequate three-dimensional visualization of the shape and distribution of microcracks, the magnetic field lines, and delineation of the position of the faults in relation to the surface.

INTRODUCTION

A major problem in aircraft maintenance is the effect of wear and tear on major components. For example, cracks emanating from bolt holes on structural components or turbine blades, located below the surface, appear after years of use. These cracks can cause catastrophic damage if they are not detected sufficiently early. Non-destructive evaluation (NDE) and identification (NDI) methods allow early detection of subsurface cracks and corrosion, so that the damaged components can be replaced or repaired. Current methods used for NDE have difficulties in detecting very small cracks, on the order of a tenth of a millimeter or less, which form below the surface.

Our approach consists of fabricating an array of magnetic transistor detectors. The advantage of having an array over a single detector is that the magnetic leakage can be detected simultaneously at different points in space. By modeling the signals from all of the array components simultaneously (a generalized sort of triangulation), it is possible to obtain a three-dimensional image of the cracks and faults. This work focuses on a "proof of concept", and considers the possibility of detecting a small fringing magnetic field originating from faults and distinguishing among different types of faults.

MAGNETIC TUNNEL JUNCTION DETECTOR

Magnetic tunneling junction (MTJ) technology is applicable to the present problem because of its great sensitivity in probing the magnetic response of the metallic components to an applied current. If the material is completely homogenous, the resulting magnetic signal is also homogeneous. However, in the presence of phase segregation, cracks, or even submicron-sized grain boundaries, there is a disruption of the normal magnetic flux pattern of the material, causing a leakage field to appear.[1] This field usually has strong gradients that can be detected with these sensitive magnetic sensors.

The sensor used for NDI must be able to map the fringing magnetic fields due to cracks and other faults inside metals. This information can be used by a computer model to recreate a three-dimensional image of faults. The principle of this approach was recently tested using an array of conventional copper microloop pickup coils to detect cracks inside the walls of metal ducts in

nuclear reactors.[2] MTJ's provide a fundamental advantage with respect to this conventional technology in that their bandwidth of operation is much greater, they operate at much lower frequencies, and their sensitivity is greater. MTJ's also provide a way of measuring the direction and magnitude of the in-plane leakage field, because the magnitude of the conductance in each MTJ is proportional to $(1-\cos\theta)$, where θ is the angle between the magnetization vectors of the two ferromagnetic layers.[3] MTJ's are also superior to giant magnetoresistance (GMR) sensor technology for fabricating sensor arrays. Normally, GMR sensors are operated with the current flowing in the plane of the film; otherwise, the resistivity is too low and difficult to measure. This geometry makes the measurement of individual array components almost impossible to make. In contrast, MTJ sensors have a much lower conductivity, making the measurement of each component possible.

The array of MTJ detectors can be fabricated using standard photolithographic techniques. A sketch of such an array is shown in Fig. 1. Each of the MTJ's composing the array provides a local measure of the magnitude and direction of the magnetic field.

MTJ's are composed of two ferromagnetic, metallic layers separated by an insulating, nonmagnetic layer. As current is driven from one ferromagnetic layer to the other, where one of the

Side View
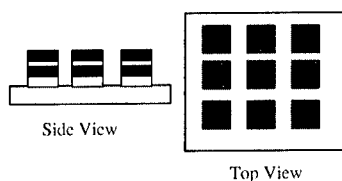
Top View

Figure 1 Side and top views of a 3 by 3 MTJ detector array. In reality, the array would have many more elements.

layers acts as an electron spin polarizer, whereas the other acts as an analyzer. The tunneling probability between these two layers is strongly dependent on the relative orientations of the magnetizations of the layers.[4] It is necessary to pin the magnetization of the polarizer, whereas the analyzer magnetization must rotate easily in small magnetic fields. This can be done by using the phenomenon of exchange bias, where an antiferromagnetic layer is deposited next to the polarizer, hence pinning its magnetization[3].

As mentioned above, it is imperative that the direction of the magnetic leakage field as well as its magnitude is known. This can be achieved if the MTJ response is linear, non-hysteretic, and sensitive to small fields. Biasing the unpinned ferromagnetic layer with a dc field at $90°$ to the pinned layer can do this.[5]

MEASUREMENTS

In order to examine an aircraft component (a sample undergoing NDE) for the presence of faults, a magnetic field should be introduced into the system. For paramagnetic materials, such as aluminum and most superalloys used in engines, an externally applied electrical current can be used to generate the magnetic field. Suppose that the area where the electrical current exists is much smaller than the characteristic size of the sample undergoing NDE. In this case, the magnetic field depends only on the properties of the material being scanned below the measuring tool (array of MTJ's), and does not depend on the shape of the sample or on the position of the measuring tool on the top surface of the component. Therefore, this magnetic field can be compen-

sated by applying an external magnetic field in such a way that, in a fault free environment, the resulting magnetic field is zero at the location of the MTJ sensors.

If there is a fault in the sample, a deviation of the current flowing through the sample will cause a distortion of the magnetic field. The magnitude of the fringing flux will be proportional to the signal measured by each detector, and the shape of the leakage field will depend on the shape of the fault. (Note that sensors can measure only a component parallel to the magnetization of the pinned layer. Rotating the detector by 90° would yield the other component.) Because the detector is composed of an array of MTJ's, a two-dimensional image of the flux lines can be obtained. The applied current can also be rotated by 90° to provide in-plane resolution. In order to improve the depth profiling capabilities, the distance between the detector and the sample can be varied by mounting the array on a precision x-y-z stage.

COMPUTATIONAL MODELING

In order to calculate the magnetic response produced by a fault one needs to know the electrical current inside and outside this fault, including its boundaries. For simplicity, we assume that there is no electrical current inside a crack and that it has simple, very thin boundaries. A simple estimate can be obtained if the relaxation of the electrical current around the fault is neglected. In this model, one can either set the conductivity tensor in the crack area to zero or equivalently, apply an effective current with magnitude equal to the initial current, but flowing in the opposite direction inside the crack. The fringing field (the deviation of the magnetic field from its initial distribution in a fault free material) is just the magnetic field produced by this effective current.

Considering a uniform current of 1A/mm^2 and using the Biot-Savart law, one can estimate that a 50 μm wide crack, located 2 mm below the surface, will generate a field of ~3 mOe at the surface. An effect of the same magnitude can be also produced by a 100 μm cubic void at the same depth. Because of the high sensitivity of the MTJ detectors, this should translate into a sizeable change in conductivity of approximately 0.1 - 0.5 %.

The presence of a fault would cause an increase in the current density in the areas surrounding the fault, which in turn produces a screening effect and therefore reduces the resulting fringing magnetic field. Accurate calculations of the magnetic field should include this relaxation of the current flowing around the fault. We used a finite-element (FE) analysis of the current distribution around faults to calculate these effects. In the finite-element approximation, a continuous function of the solution of a partial differential equation is replaced by a sum of piecewise functions, each of them being defined within a small volume (finite element). Since the work of Lord et al[6], the FE analysis of the magnetic flux leakage from various flaws in materials has become an established[2] technique.

For our purposes, we can further simplify the problem by considering only a dc current, and calculate the redistribution of the electrical current inside material composed of conducting and non-conducting phases. Our calculations were based on FEM software developed at NIST[7] and available without cost.

The NIST FEM software is designed to compute the linear electrical properties of digital images of random materials. This program takes advantage of the existence of the variational principle for the linear conductivity problem. In order to find an equilibrium distribution of currents in the system, the power (energy dissipation per unit time) is minimized with respect to the voltages at the vertices of the finite elements. An externally applied electrical field is included through the boundary conditions. Only a few modifications to this program were required in or-

der to describe the present problem and to have a convenient interface with the visualization software.

The initial distribution of the electrical current in a fault-free sample depends on the way the current is introduced to the system. The details of the experimental design are not been finalized at this time; therefore, there is no reason to choose a specific configuration of the current. For
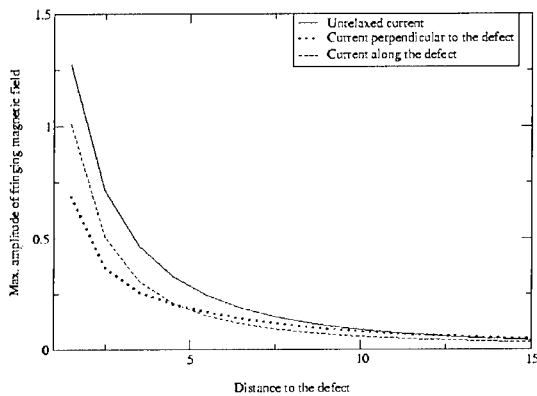
Figure 2. Effect of current relaxation around the fault on the resulting magnetic field. The fault dimensions are 10x1x1 units, it is always parallel to the surface where magnetic field is measured and is placed at various distances from this surface.

simplicity, we have considered a uniform external current. In this configuration, it was found that it is sufficient to consider a relatively small system composed of ~35,000 elements (41x41x21). A calculation of the current takes about one second of the CPU time on AMD Athlon based PC or Compaq Alpha workstation. Test calculations on a much larger system (80x80x40) did not reveal any significant changes.

For the results reported here, the observation plane was always considered at Z=0, with the electrical current running along the Y axis. Therefore, the magnetic field has the strongest component (the only component in fault-free environment) in the X direction.

FEM calculations showed that the redistribution of the electrical current plays an important role. For example, when a rod-like crack located close to the surface with a long side perpendicular to the electrical current, the resulting magnetic field is one half of the magnetic field obtained by a simple zeroing of the current inside the crack area (Figure 2). In this geometry, the current that flows around the crack deviates significantly toward the surface where, due to its proximity to the sensor, it contributes significantly to the fringing field. At the same time, when the fault is deep enough, this current is directed mainly toward the surface and it does not contribute to the X projection of the magnetic field measured immediately above the fault (generally, the magnetic response is the strongest at this point), as depicted in Fig. 2. When the same rod-like fault extended parallel to the direction of the current, the relaxation current is much smaller, but it is also extended in the Y direction, and contributes to the X projection of the magnetic field. Therefore, the screening effect is larger when the current is parallel to the longest axis of a deep fault.
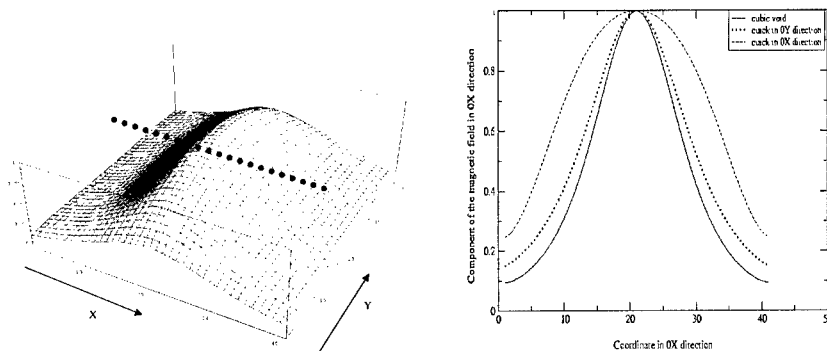
Figure 3. The left panel shows the amplitude of the fringing magnetic field generated by a crack with dimensions of 27x1x1 units. The crack is located in the center of XY plane, 10 units below the surface and it is extended along Y axis. The right panel shows the amplitudes of the fringing magnetic field generated by a crack when it is parallel and perpendicular to the current and by a cubic void of 3x3x3 units located at the same depth. The field is calculated using FEM along the dotted line as is shown in the left panel. For both panels, the external current is running in Y direction.

Information about the shape of the fault can be extracted from the 2-d profile of the magnetic field. For simplicity, we first discuss the measurements along two lines on top of an extended rod-like fault. The change in the X component of the magnetic field along the line perpendicular to the applied current and located on top of the center of this modeled crack is shown on Figure 3. When the long axis of the fault is parallel to the current, the measured magnetic field looks similar, but not identical to the response from a cubic void of the same volume (see Fig. 3). When the fault is extended in the direction perpendicular to the current (this can be achieved by rotating the MTJ array and the source of the current), the measured profile looks much different (dashed line on the Fig.3). The fact that magnetic response depends on the mutual orientation of the electrical current and the fault can be used to determine the fault orientation.

The length of the fault that generated profiles shown on Fig. 3 is large in comparison with the distance from the fault to the surface. When the fault is buried deep below the surface (as is the one used for Figs. 2 and 4), measurements that are more extensive are required. However, even in this case, the fringing magnetic field is still dependent on the angle between the current and the long axis of the fault. This is illustrated in Fig. 4, which is a 2-D map of the fringing field (much like the one that would be measured by the MTJ sensor), and shows the large difference between the two configurations.

Knowledge of the magnetic field on the surface of the volume containing a complex fault is not sufficient to uniquely determine the exact shape of the fault. Therefore, empirical information about faults should be used. For example, we can assume that a simple crack can be described by six parameters: three dimensions, two orientation angles, and the depth from the surface. These parameters can be found using a least-squares fit of the calculated to the measured

magnetic fields. The initial guess about the shape of the structure (is it a simple crack or not) can be made by comparing the measured pattern to a library of "signatures" of possible and common faults. We plan to consider a variety of possible faults that will include both cracks and flaws, of different dimensions and orientations, within the bulk of the component. In addition, we will treat faults introduced by such items as bolts and screws (e.g., mini-cracks around bolt holes).

Even a simple two-dimensional figure, such as Fig. 4, is difficult to present on paper or on a flat computer screen. A mutual orientation of a surface of the sample, array of detectors and faults is extremely difficult to depict in an understandable way. Considering a characteristic size of faults ~100 $\Box$m and a detector size 0.5 mm, then in a sample of several centimeters long, many faults could be detected. In order to understand their relative positions, it is necessary to
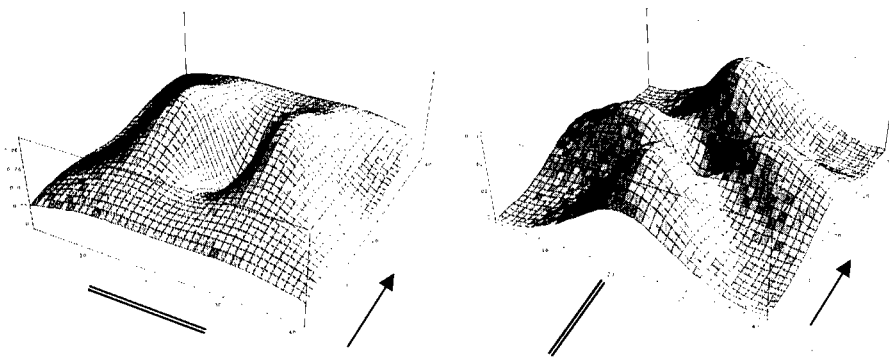
Figure 4. Magnetic signature of the rod-like crack with dimensions 10x1x1 units parallel to the surface and located 10 units below the surface. The height of plots is related to the in-plane component of the magnetic field perpendicular to the external current. In order to illuminate the differences, a normalized magnetic field generated by the point fault located at the same depth is subtracted from the both plots. An arrow shows the direction of the external current. The double line indicates the orientation of the crack, which is located directly underneath of the centers on the panels.

employ advanced visualization techniques. Volume imaging in three dimensions is the key to our approach. We have adopted a multilayer hierarchy of volume visualization capability. Relatively simple problems are addressed at any location by using inexpensive stereo-ready graphics cards and corresponding eyeware available for PC's. Viewing of complex images at an ImmersaDesk, and/or at a portable CAVE-like system driven by NT or Linux PC can provide a significant increase of viewing quality.

CONCLUSION

Our initial modeling and experimental measurements have shown that it is possible to determine the shape and position of crack-like faults underneath the surface using an array of magnetic tunneling junction detectors. Our simulations showed that a fault located at a depth comparable to its size can be categorized and identified, while faults located deeper can be located, it is more difficult to determine their shapes.

REFERENCES

[1] D. Jiles, Magnetism and Magnetic Materials, 2nd Edition (Chapman & Hall, London, 1998).

[2] M. Ueseka, K. Hakuta, K. Miya, K. Aoki, and A. Takahashi, "Eddy-Current Testing by Flexible Microloop Magnetic Sensor Array", IEEE Trans. Magn. 34, 2287 (1998).

[3] J. S. Moodera, L. R. Kinder, T. M. Wong, and R. Meservey, "Large magnetoresistance at room temperature in ferromagnetic thin film tunnel junctions", Phys. Rev. Lett. 74, 3273 (1995)

[4] M. Julliere, Phys. Lett. 54A 225 (1975).

[5] M. Tondra, J. M. Daughton, D. Wang, R. S. Beech, A. Fink, and J. A. Taylor, J. Appl. Phys. 83, 6688 (1998).

[6] J.Hwang, and W.Lord, Finite Element Modeling Field /Defect Interactions, Journal of Testing and Evaluation 3 (1975) 21-23.

[7] Garboczi, E. J. "Finite Element and Finite Difference Programs for Computing the Linear Electric and Elastic Properties of Digital Images of Random Materials". NISTIR 6269; 211 p. December 1998.

MAGNETO-RESISTANCE AND INDUCED DOMAIN STRUCTURE IN TUNNEL JUNCTIONS

M. Hehn, O. Lenoble, D. Lacour and A. Schuhl
Laboratoire de Physique des Matériaux, UMR CNRS 7556, B.P. 239,
54506 VANDOEUVRE LES NANCY Cedex, France.

C. Tiusan, D. Hrabovsky* and J.F. Bobo*
IPCMS, 23 rue du Loess, 67037 STRASBOURG Cedex, France.
* LPMC, 135 Av. de Rangueil, 31077 Toulouse Cedex, France

ABSTRACT

Magnetization reversals in sputtered Co electrodes of a magnetic tunnel junction are studied using transport measurements, magneto-optic Kerr magnetometry and microscopy. Using the tunnel magneto-resistive effect as a probe for micromagnetic studies, we first evidence the existence of an unexpected domain structure in the soft Co layer. This domain structure originates from the duplication of the domain structure of the hard Co layer template into the soft layer via ferromagnetic inter-electrode coupling. A detailed analysis of the kerr microscopy images shows that all features appearing in the variation of tunnel resistance as a function of the applied field are associated to the domain phase evolution of each electrode. By tailoring the magnetic properties of the hard Co layer, we have demonstrated that the appearance of the domain duplication is driven by the magnetic anisotropy of the hard layer. Finally, a brief theoretical description of the domain duplication process allows us to extract the main parameters governing the effect.

INTRODUCTION

The increasing interest in magnetic tunnel junctions (MTJs) for spin electronic devices requires the understanding and the control of the magnetic properties of their ferromagnetic (FM) electrodes. A coupling between the two electrodes of the MTJ takes usually place due to their proximity. These interactions between a magnetically hard (reference) and a soft (detection) layer are of particular importance as they influence the reversal characteristics of the FM layers, and thus, the magneto-resistive behavior of the tunnel device. We illustrate explicitly the effect of the magneto-static coupling on the transport and magnetic properties of those systems.

EXPERIMENTAL DETAILS

For this purpose, we prepared Glass/Co(10nm)/Al(e_{Al} nm, t_{ox} mn)/Co(e_{Co} nm)/ Co*(20nm) cross like tunnel junctions by using sputtering and *ex situ* changed shadow masks. Details on the junction fabrication (oxidation process to make the AlOx tunnel barrier, geometry for CCP measurements...) can be found elsewhere [1,2]. When Co is deposited at low Ar pressure (5×10^{-3} mbar), the grain diameter is less than 2nm and the magnetization reversal of a Co(10nm) layer is sharp with nucleation and propagation of domain walls [3]. In addition, this low pressure process leads to the appearance of an anisotropy axis due to the geometry of the deposition. When the Ar pressure increases up to an optimum, equal to 1.5×10^{-2} mbar, the grain size and the coercive field increase up to a maximum. In this case,

the magnetization behavior is consistent with a reversal occurring through the appearance of ripples domain structures [4]. More important, the magnetic anisotropy stabilized at low pressure completely disappears. Then, in a single Co^*(20nm) layer where Co^* is relative to high Ar pressure, magnetization reversal occurs only by rotation and the magnetization cycle is fully isotropic in the plane of the sample. When high and low Ar pressure deposited Co films are associated in a single hard layer, the Co(5nm)/Co^*(20nm) bi-layer is anisotropic and has a medium coercive field. The soft anisotropic Co layer is exchange biased by a layer composed of low interacting grains which reversal occurs with the appearance of ripple type domain structure. As a result, magnetization reversal in the case of Co/Co^* occurs by nucleation and propagation of domains which is hindered. Finally, the magnetic properties of the hard layer can be tuned by changing e_{Co} in the Co(e_{Co} nm)/Co^*(20nm) stack and when they are chosen to be anisotropic, the easy magnetization axis of the soft layer and hard bilayer are parallel.

DISCUSSION

Tunnel magneto-resistance measurements have been shown to be highly sensitive to local magnetization fluctuations in the electrodes in contact with the barrier [5]. This sensitivity has been used in this study as a first step to predict the duplication of the hard layer domain structure template in the soft layer. Complete (—) and Minor(-•-, -o-) TMR loops are shown in figure 1 for a sample Co(10nm)/Al(1.2 nm, ox 30s)/Co(5 nm)/Co^*(20nm). After saturation at 850 Oe, the applied field along the easy axis of the soft Co(10nm) layer is decreased down to H_{sat} = –850 Oe or H_{rev} and the step sequence is reversed in the positive field direction. When the field H is decreased down to H_{sat}, the TMR cycle is symmetric and holds two resistance jumps as presented in figure 1 (—). It reveals clearly two resistance states even if after the reversal of the soft Co layer at H_0 a gradual increase of resistance is observed before the plateau. When H_{rev} = -100 Oe (figure 1 (....)), the minor cycle appears to be shifted by a field of -17 Oe, the ferromagnetic coupling field H_f existing between the two electrodes. When the field is decreased down to H_{rev} between –105 and –125 Oe and reversed again in the positive field direction, the resistance of the junction remains constant between H_{rev} and H_1. In the positive quadrant of the loop, three resistance jumps with different signs appear at some fields named H_1, H_2 and H_3. Particularly interesting is the fact that for applied fields between H_1 and H_2, the resistance of the junction is close to the resistance measured when the magnetizations of the two magnetic electrodes are in a parallel configuration. Therefore, on each side of the barrier, the magnetizations are locally parallel even if the hard magnetic layer is far from magnetic saturation. As a consequence, the domain structure of the hard Co layer must be duplicated in the soft Co layer.
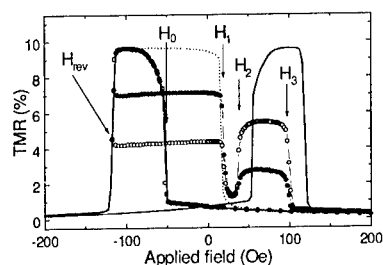
Figure 1. Complete (-) and minor (o,•, ...) magneto-resistance cycles measured on a Co(10nm)/Al(1.2nm,ox30s)/Co(5nm)/Co^*(20nm) tunnel junction.
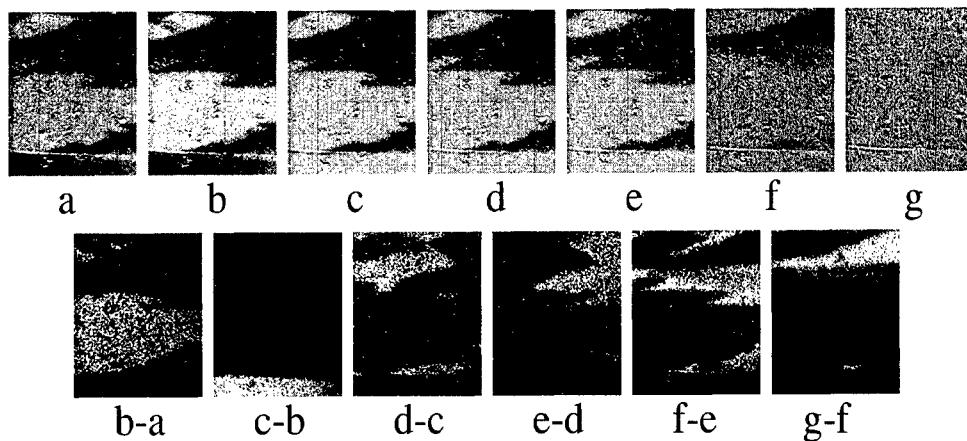
Figure 2. (i) Kerr images a to g : evolution of the domain structure measured by Kerr microscopy in the junction (upper part of each image, above the white line) and in the soft Co electrode (lower part of each image). The images a to e show the evolution around the duplication state.

(ii) Kerr images (b-a) to (g-f) : insight of the domain structure evolution is obtained from the difference of two successive Kerr images. The image (b-a) is obtained from the difference of images b and a. The white areas correspond to regions which have switched their magnetization.

(iii) Magneto-resistance cycle : field intensities corresponding to the Kerr images have been reported on this cycle.

a: 25 Oe
b: 26 Oe
c: 32 Oe
d: 39 Oe
e: 41 Oe
f: 100 Oe
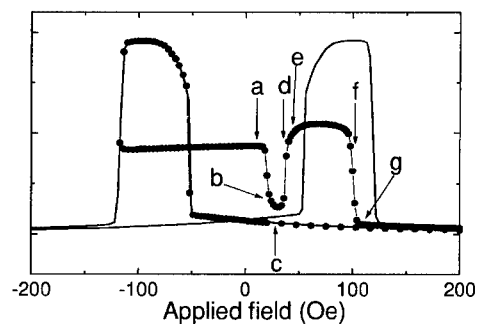
Kerr microscopy has been used to provide a direct proof of the domain duplication. Its depth sensitivity allows to visualize the evolution of the domain structure in the junction surface area for the two magnetic electrodes. The sample is first saturated by applying a magnetic field of +200 Oe. Then, it is decreased down to -120 Oe. With this field, the soft layer has totally switched (in the electrode and in the junction) and a domain structure appears in the hard layer. At this step, the applied field is increased in the positive direction and the domain structure remains unchanged up to +25 Oe. The domains which are oriented in the saturating field direction are bright while the domains which have switched appear with a dark contrast (figure 2a). By increasing the magnetic field, we can observe several changes in the Kerr images at some fields $H_{1,2,3}$, the same as given for figure 1.

From 25 Oe to 26 Oe, around H_1, an evolution of the contrast can be observed in the junction area since the bright domains become brighter. Indeed, figure 2 (b-a) confirms clearly that only these regions are affected. This change is due to the switch of the soft electrode magnetization in regions located over domains in the hard electrode with magnetization oriented in the positive saturating field direction. These regions, regions A in figure 3, are those which experience an effective local magnetic field equal to $H + |H_f|$ where $|H_f|$ is the local additional stray field due to the bright domains in the hard electrode. So, these regions switch at a field H_1 whose value is lower than the intrinsic coercive field of the soft layer H_c (figure 3b). From 26 Oe to 32 Oe, no change of the domain structure in the junction could be observed while the magnetization of the soft electrode outside the junction has totally switched at H_c. From 32 Oe to 41 Oe, around H_2, the changes of the domain structure are confined to the dark regions of the junction which become brighter. This evolution depicted in figure 2 (d-c and e-d) is attributed to the reversal of regions in the soft electrode which have not switched at H_1. These regions, regions B in figure 3, are those which experience an effective local magnetic field equal to $H - |H_f|$ where $-|H_f|$ is the local additional stray field due to the dark domains in the hard electrode. So, these regions switch at a field H_2 whose value is higher than H_c (figure 3c). Above 41 Oe, the main changes of contrast are easily attributed to the reversal of the hard layer.

Duplication of the domain structure relays on the distribution of magnetic coupling fields which can locally increase or decrease the applied field and so on the domain structure of the hard electrode. By reducing e_{Co} to zero, magnetization reversal of the single Co^* layer occurs only by rotation and the magnetization cycle is fully isotropic in plane. Thus, the domain is completely different. Regions with main magnetization oriented in the negative direction do not coexist with regions with main magnetization oriented in the positive field direction. Instead, clockwise and counterclockwise rotations of neighboring magnetic grains lead to the appearance of 360° domain walls parallel to the external field axis.
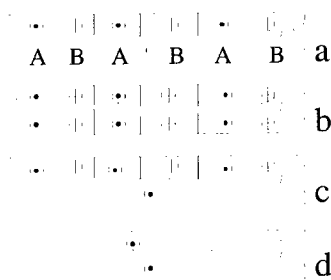
Figure 3. Sketch showing the evolution of the domain structure in each magnetic layer, the soft Co layer (bottom layer, white) and the hard Co/Co^* layer (top layer, gray scale). The symbols $\odot$ and $\otimes$ represent the main magnetization in each domain (oriented perpendicular to the paper sheet) respectively opposite and along the positive saturating field (applied along $\odot$).
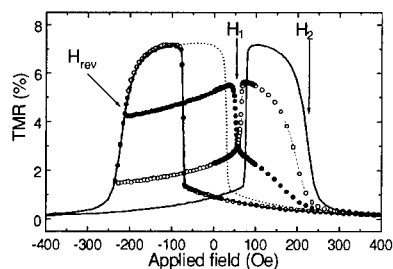
Figure 4. Complete (-) and minor (o,•, ...) magneto-resistance cycles measured on a Co(10nm)/Al(1.2nm,ox30s)/Co(5nm)/Co*(20nm) tunnel junction.

The magnetization of each grain or of each region with extension less than the exchange correlation length points in the direction of the negative applied field. In fact, for a given value of H_{rev}, the cosine of the angle between the local magnetization and the applied field, and therefore the stray field parallel to the applied field, has the same sign all over the hard electrode volume. Then, all the regions of the Co soft electrode are submitted, along the external field axis, to the same effective field equal to $H + H'_f$ since component of the stray field perpendicular to the applied field does not contribute for the reversal (H'_f is the ferromagnetic field coupling between the two electrodes). The value of H'_f increases from a negative value to a positive value when H_{rev} decreases as can be seen in figure 4. Indeed, H'_f follows a law similar to the cosine of the angle between the magnetization and the applied field at H_{rev}. This cosine law is also reflected in the shape of the TMR curve after reversal of the Co soft electrode. So, since the stray field of the hard layer domain structure along the applied field direction has the same sign all over the hard layer volume, no duplication could be observed.

To estimate the stability of the walls in each magnetic layer, we propose a simplified model sketched in figure 5. In this model, two magnetic layers are ferromagnetically coupled through a non magnetic layer, the magnetization of each layer is aligned with the applied field (either parallel or anti-parallel). We consider that non reversed domains exist in the hard layer which have a total surface area Δ. The domain walls have a length or perimeter λ, an energy per unit surface area σ_1 and no lateral extension. Let us call t_1 and t_2 the thicknesses of each magnetic layer, M_{s1} and M_{s2} the saturation magnetizations and J_F the interlayer coupling constant. When duplication occurs, the domains created in the soft layer 2 have a total surface area Δ and domain walls have an energy per unit surface area equal to σ_2.
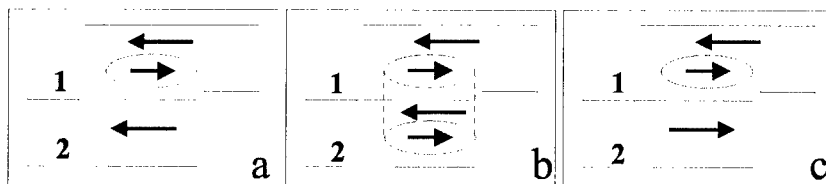
Figure 5. Three drawings showing the different magnetic configurations during the duplication process. In each box, the sheet 1 contains the magnetic configuration of the hard layer while the sheet 2 contains the one of the soft layer. The positive direction is oriented from the left to the right.

Comparing the energies of those different states, it appears that the magnetic state with a duplicated domain structure in layer 2 can exist if

$$J_F \geq \frac{\sigma_2 \lambda t_2}{4}\left[\frac{1}{\Delta}+\frac{1}{S-\Delta}\right]$$

This equation is of particular importance because it shows that depending on the parameters of the hybrid multilayer stack, a minimum coupling strength is needed that duplication occurs. By changing the thickness of the alumna barrier, we can experimentally tune the strength of J_F. We have shown that in our samples, the minimum coupling field is around 6 Oe.

CONCLUSIONS

In conclusion, we have studied the effect of the hard layer magnetic domain structure duplication in the soft layer in a magnetic tunnel junction. First evidence of the effect is given by the conventional tunnel transport measurements which interpretation has been confirmed using Kerr microscopy. It is shown that duplication occurs through the distribution of magnetic coupling fields which can locally increase or decrease the applied field. Indeed, removing those fluctuations by tuning the magnetic properties of the hard layer cancels the duplication. Finally, the influence of the hybrid multilayer stack parameters is discussed and a minimum coupling field of around 6 Oe is needed that duplication occurs in our tunnel junctions.

ACKNOWLEDGMENTS

REFERENCES

1. M. Hehn, O. Lenoble, D. Lacour, C. Féry, M. Piécuch, C. Tiusan and K. Ounadjela, Phys. Rev. B **61**, 11643 (2000).
2. M. Hehn, O. Lenoble, D. lacour, A. Schuhl, Phys. Rev. B **62**, 11344 (2000).
3. O. Lenoble, M. Hehn, D. lacour, A. Schuhl, D. Hrabovsky, J.F. Bobo, B. Diouf, A.R. Fert, Phys. Rev. B **63**, 11643 (2001).
4. D. V. Berkov and N. L. Gorn, Phys. Rev. B **57**, 14332 (1998).
5. C. Tiusan, T. Dimopoulos, M. Hehn, V. Da Costa, Y. Henry, H. A. M. van den Berg and K. Ounadjela, Phys. Rev. B **61**,580 (2000).
6. D. Lacour, M. Hehn, O. Lenoble, A. Schuhl, C. Tiusan and K. Ounadjela, 'Domain duplication in ferromagnetic sandwiches', submitted to J. of Appl. Phys.

Materials for Magnetic Devices

Multilevel Magnetoresistance in a Structure Consisting of two spin-valves

Kebin Li, Yihong Wu[1], Jinjun Qiu, Guchang Han, Zaibing Guo, and Towchong Chong
Data Storage Institute, DSI Building, 5 Engineering Drive 1, Singapore 117608
[1]Department of Electrical and Computer Engineering, National University of Singapore, 10 Kent Ridge Crescent, Singapore 119260

ABSTRACT

The magnetic and electrical properties as well as the structural characteristics have been studied on a series of samples with structure substrate $(Sub)/SV(1)/Al_2O_3 5nm/SV(2)$. Here, SV(1) is either CoFe/IrMn based spin-valve (SV) such as Ta5/NiFe2/IrMn8/CoFe2/Cu2.6/CoFe2/Ta5 (thicknesses are in nanometers) bottom SV or Ta5/NiFe2/CoFe1.5/Cu2.6/CoFe2/FeMn10/Ta5 top SV and SV(2) is Ta5/NiFe2/CoFe1.5(or 2)/Cu2.6/CoFe2/IrMn8/Ta5 top SV. SV(1) and SV(2) in the structure are decoupled by a Al_2O_3 layer with 5nm in the magnetic properties, however, they are in parallel connection in the electrical properties. In a sample with structure Sub/Ta5/NiFe2/IrMn8/CoFe2/Cu2.6/CoFe2/Ta5 /$Al_2O_3$5/Ta5/NiFe2/CoFe2/Cu2.6/CoFe2/IrMn8/Ta5, five magnetoresistance states which are related to five magnetization states have been observed after the sample was annealed at T=220 °C with a field strength of 1T under high vacuum because of different interlayer coupling fields (H_{int}) in the top and bottom CoFe/IrMn based SVs (H_{int} is about 12.21 Oe in the top CoFe/IrMn SV and 29.3 Oe in the bottom CoFe/IrMn based SV). In a sample with structure Sub/Ta5/NiFe2/CoFe1.5/Cu2.6/CoFe2/FeMn10/Ta5/$Al_2O_3$5/Ta5/NiFe2/CoFe1.5/Cu2.6/CoFe2 /IrMn8/Ta5, since the blocking temperature of the CoFe/FeMn based SV (T_b is about 150 °C) is lower than that of CoFe/IrMn based SV (T_b is about 230 °C), the spins can be easily engineered and therefore various magnetoresistance states can be obtained when the sample is magnetically annealed at different temperatures in a proper annealing sequence. By properly selecting materials and controlling the magnetically annealing conditions, multilevel giant magnetoresistance (MR) magnetic random access memory (MRAM) cell can be realized, which will significantly improve the MRAM data storage density without increasing any additional processing complexity.

INTRODUCTION

Multiple value storage is considered as a promising technique for increasing the storage density of magnetic random access memories (MRAMs). In order to implement this technique, one must first identify a suitable cell structure featuring a multi-step response in the magnetoresistance (MR) versus magnetic field curve. Such a structure has been once reported in a NiFe/Cu/NiFeCo/Cu/NiFeCo/Cu/Co pseudo-spin-valve (PSV).[1] However, the MR ratio of the PSV is rather small which may limit its applications in large scale MRAMs. In this paper, we report a new structure that consists of two electrically isolated and magnetically decoupled CoFe/IrMn spin-valves or CoFe/FeMn spin-valves. Multiple distinctive steps associated with different magnetization states have been successfully observed in the MR response curves. The potential application of this structure in multiple value MRAMs will be discussed.

EXPERIMENTAL DETAILS

The sample was fabricated by using a multiple chamber ultra-high vacuum (UHV) sputtering system operating at a base pressure of 5×10^{-10} Torr. The use of inductively coupled plasma makes it possible to deposit the thin films at a low process pressure (about 1mTorr). The sample was deposited on a 4" round Si(100) substrate coated with a 100nm-thick thermally oxidized SiO_2 layer. A typical layer structure is as follows: Ta5/NiFe2/IrMn8/CoFe2/Cu2.6/CoFe2/Ta5/ Al_2O_35/Ta5/NiFe2/CoFe2/Cu2.6/CoFe2/IrMn8/Ta5. The UHV sputtering system was configured with four processing chambers which makes it possible to deposit the whole structure without breaking the vacuum. During deposition of the magnetic layers, a magnetic field with a strength of 100 Oe is applied along a certain direction parallel to the film surface. The 5nm-thick Al_2O_3 layer was thick enough to magnetically decouple and electrically isolate the bottom and the top spin-valves, though the two would be electrically connected during the magnetoresistance measurement due to the penetration of the probes vertically through the spin-valve structure. The magnetic properties and MR curves were measured with a vibrating sample magnetometer equipped with a MR measurement fixture. Annealing was conducted in a commercial high-vacuum magnetic annealing oven at a base pressure lower than 8×10^{-7} Torr for 2 hours at 220 °C with a field strength of 10 kOe. The crystal structure of SVs was characterized by XRD.

RESULTS and DISCUSSIONS

The resistance versus magnetic field (R-H) and magnetization versus magnetic field (M-H) were measured on annealed SVs, (a)Sub/Ta5/NiFe2/CoFe2/Cu2.6/CoFe2/Ta5/Al$_2$O$_3$ (SV1),
(b) Sub/Al$_2$O$_3$5/Ta5/NiFe2/IrMn8/CoFe2/Cu2.6/CoFe2/Ta5 (SV2),
(c) Sub/Ta5/NiFe2/CoFe1.5 /Cu2.6/CoFe2/FeMn10/Ta5/Al$_2$O$_3$ (SV3),
(d) Sub/Al$_2$O$_3$5/Ta5/NiFe2/CoFe1.5/Cu2.6/CoFe2 /IrMn8/Ta5 (SV4),
(e) Sub/Al$_2$O$_3$5/Ta5/NiFe2/CoFe2/IrMn8/CoFe2/Cu2.6/CoFe1.5/NiFe2/Ta5 (SV5), and,
(f) Sub/Ta5/NiFe2/FeMn10/CoFe2/Cu2.6/CoFe1.5/NiFe2/Ta5 (SV6). Due to limit of paper length, only four of them are shown in Fig.1. But the interlayer coupling field between the free FM layer and the pinned FM layer across the spacer layer H_{int} and a coercivity field H_c of the free layer , which are defined as in Ref.[2], exchange coupling field H_{ex} as well as MR ratio for these six single SVs are summarized in Table(1). The overall properties of these single SVs are comparable to that published [3-7]. It is worth of noting that for FeMn-based SV, H_{ex} is about 490 Oe for top type and 500 Oe for bottom type, corresponding to the exchange coupling energy $J_k \sim 0.13$ erg/cm^2 (M_s=1300emu/cm^3 is assumed). Such high exchange coupling energy observed in the FeMn/CoFe SV should be attributed to the better (111) texture structure of γ-FeMn crystallite formed in the SV as shown in Fig.2(a). From XRD results, the (111) texture structure of γ-FeMn crystallite was overlapped with NiFe(111)/CoFe(111), indicating the lattice mismatch between them is very small. Both top SV and bottom SV show that (111) texture structure of γ-FeMn was well formed, there is no distinct difference between them. The XRD patterns of a single top IrMn SV, a single bottom IrMn SV and a composite SV (CSV1) are shown in Fig.2(b) after magnetically annealed.

Figure 3(a) shows the M-H loop measured on an electrically isolated and magnetically decoupled dual SV with structure Sub/Ta5/NiFe2/IrMn8/CoFe2/Cu2.6/CoFe2/Ta5/Al$_2$O$_3$5/
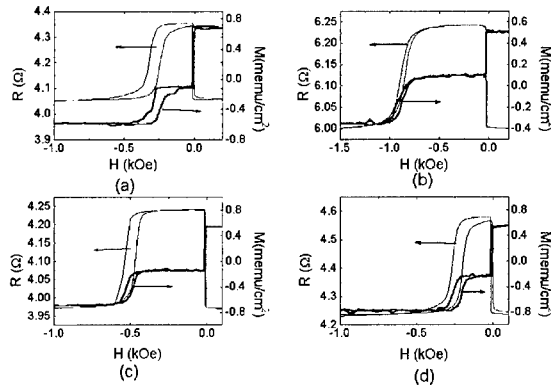
Fig.1 R-H and M-H curves for magnetically annealed (a) SV1, (b) SV2, (c) SV3, and (d) SV4
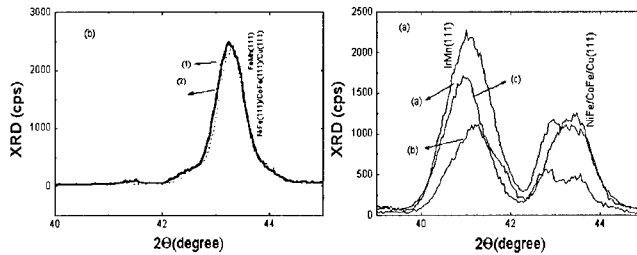
Fig.2 (a) XRD patterns of annealed (1) Sub/Ta5/NiFe2/CoFe1.5/Cu2.6/CoFe2/FeMn10/Ta5, and, (2) Sub/Ta5/NiFe2/FeMn10/CoFe2/Cu2.6/CoFe1.5/NiFe2/Ta5 SVs. The (111) texture structure of γ-FeMn is overlapped with NiFe(111)/CoFe(111)/Cu(111). There is no distinct difference between the top CoFe/FeMn and bottom FeMn/CoFe. Fig.2(b) XRD pattern of (a) a bottom spin-valve, (b) a top spin-valve, and (c) a new structure consists of a top SV and a bottom SV separated by a 5nm-thick Al_2O_3 layer after magnetically annealed.

Ta5/NiFe2/CoFe2/Cu2.6/CoFe2/IrMn8/Ta5 (termed as CSV1). When an applied magnetic field is applied along the pinning direction, the magnetizations of the free layer and the pinned layer in the CSV1 are parallel to the sweeping field axis. As the field strength increases in the opposite direction, the free layer in the top part changes its magnetization direction at -12.2 Oe and the total magnetizations drop to a lower state. The magnetizations drop to another lower state when the free layer of the bottom part starts to change its magnetization direction at -29.36 Oe. After that, it keeps a constant until the magnetic field increases to about -260 Oe at which the pinned layer of the top part changes its magnetization direction, too. Hence the total magnetizations become negative. When the field strength increases to about 865 Oe, the magnetizations jump to a higher step and become saturation. Five different magnetic states are schematically illustrated in the figure. The thickness of the arrow indicates the strength of the magnetic field that is required to flip the magnetization direction of the ferromagnetic layers.

Table (1) Some basic parameters obtained from R-H and M-H curves measured on several single IrMn-based SVs and FeMn-based SVs.

	H_{int}(Oe)	H_c(Oe)	H_{ex}(Oe)	M_s(NiFe)(emu/cm^3)	M_s(CoFe) (emu/cm^3)	MR(%)
SV3	12.0	3.0	500	725±50	1300±70	6.75
SV4	8.7	6.3	234	780±50	1203±70	8.16
SV5	24.4	2.9	764	760±50	1112±70	4.74
SV6	30.7	2.2	490	739±50	1070±70	3.94
SV1	10.1	2.8	278	785±50	1179±70	7.55
SV2	27.0	2.1	896	200±50	1013±70	4.09

As it is expected, there are five magnetoresistive states observed in the MR curve shown in Fig. 3(b). The resistance (R) is at the lowest level when the magnetization is at state one. At the second magnetization-state, R increases to a higher step because the top part is at the highest resistance-state due to the antiparallel alignment of the magnetization in the free layer and the pinned layer. At the third magnetization-state, both the top and bottom parts are at the highest resistance-state, so R reaches to the highest step. At the fourth magnetization-state, the total resistance drops to a lower step because the resistance in the top part is at the lowest level due to the parallel alignment of the magnetizations in the free and pinned ferromagnetic layers. And at the fifth magnetization-state, the total resistance is at the lowest state again.
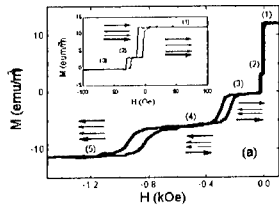
Fig.3(a) M-H loop for CSV1, five magnetization states are clearly shown in the figure. The arrows indicate the spin direction. The insert is the minor M-H loop
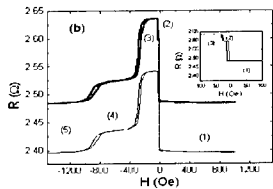
Fig.3(b) MR curve of CSV1. The thinner line are fitted by using a parallel connection of the resistance of the top SV and that of the bottom SV shown in Fig.1 (a), and (b).

The dotted lines in the Fig.3(b) was fitted by using a simple parallel connection of the resistance of the top SV and that of the bottom SV shown in Fig.1. All the features observed in the MR curve of the CSV1 are perfectly reproduced except that the fitted resistance is smaller than the measured data. The discrepance in resistance between them comes mainly from one addition 5 nm Ta layer used in the single top spin-valve and one addition Al_2O_3 layer used in the single bottom structure. The good agreement between the fitted and measured data suggests that the unique magnetoresistance characteristics observed in CSV1 should result from the simply parallel connection of two SVs used in the electrically isolated and magnetically decoupled dual SV.

Multiple steps have also been observed in the magnetoresistance response curve of SV with structure Ta5/NiFe2/CoFe1.5/Cu2.6/CoFe2/FeMn10/Ta5/Al2O35/Ta5/NiFe2/CoFe1.5/Cu2.6 /CoFe2/IrMnIrMn8/Ta5 (termed as CSV2). Since the blocking temperature of the CoFe/FeMn SV is different from that of IrMn/CoFe SV[5,8], the exchange coupling orientation of

CoFe2/FeMn10 and CoFe2/IrMn8 can be either set in the same direction or in the opposite direction. Fig.4 shows the MR curves of CSV2 when the exchange coupling orientation of CoFe/FeMn and CoFe/IrMn was set in the same direction. The dotted line shown in the Fig.4 was fitted by a simple parallel connection of R-H curves of top CoFe/IrMn and CoFe/FeMn SVs shown in Fig.1 (c) and (d). Again, the electrical properties of CSV2 are the electrical properties of two SVs in parallel connection.
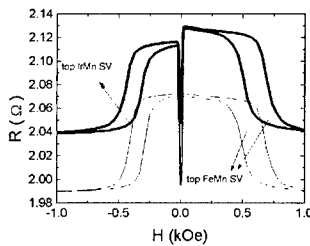
Fig.4 R-H curve for CSV2 when the exchange coupling orientation of CoFe/FeMn and CoFe/IrMn was set in the same direction. The dotted line shown in the Fig.4 was fitted by a simple parallel connection of R-H curves of top CoFe/IrMn and CoFe/FeMn SVs shown in Fig.1 (c) and (d).
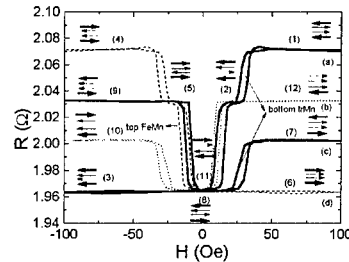
Fig.5 Minor R-H loops of an annealed composite CSV3. Twelve magnetization states are illustrated in the figure, which are corresponding to four different magnetoresistance states (a), (b), (c) and (d). The arrows represent the magnetization of each FM layers in the structure.

Multiple magnetoresistance levels were also observed in a composite SV with structure Sub/Ta5/NiFe2/CoFe2/IrMn8/CoFe2/Cu2.6/CoFe1.5/NiFe2/Ta5/Al$_2$O$_3$5/Ta5/NiFe2/CoFe1.5/Cu2.6/CoFe2/FeMn10/Ta5 (termed as CSV3). The minor R-H loops of annealed CSV3 are shown in Fig5. The thicker solid line is corresponding to the minor R-H loop of CSV3 when the exchange coupling orientation of two SVs were set at the same direction (along the negative direction of the external magnetic field axis). The thinner solid line is corresponding to the minor R-H loop of CSV3 when the exchange coupling orientation of two SVs were set in the opposite direction. Where, the exchange coupling orientation of the top CoFe/FeMn was set along the positive direction of the external magnetic field axis, while the exchange coupling orientation of the bottom IrMn/CoFe was set along the negative direction. The thicker dotted line is corresponding to the minor R-H loop when the exchange coupling orientation of two SVs were set along the positive direction of the external magnetic field axis. The thinner dotted line is corresponding to the minor R-H loop of CSV3 when the exchange coupling orientation of the top CoFe/FeMn was set along the negative direction of the external magnetic field axis, while it was set along the positive direction in the bottom IrMn/CoFe SV. Although there are four different magnetoresistance levels shown in Fig.5, twelve different magnetization states are indicated in the figure, which are illustrated in the Fig.5, too. In fact, magnetization states (1) and (4) in which the magnetization of the free FM and pinned FM layers are in anti-parallel alignment both in the bottom IrMn/CoFe SV and top CoFe/FeMn SV, are corresponding to the same magnetoresistance state (a). Magnetization states (2), (5), (9) and (12), where the magnetizations of the free FM and pinned FM layers are in parallel alignment in the bottom IrMn/CoFe SV while they are in anti-parallel alignment in the top CoFe/FeMn SV, are corresponding to the

same magnetoresistance state (b). Magnetization states (7) and (10) in which the magnetizations of the free FM and pinned FM layers are in anti-parallel alignment in the bottom IrMn/CoFe SV while they are in parallel alignment in the top CoFe/FeMn SV, are corresponding to the magnetoresistance state (c). Magnetization states (3), (6), (8), and (11), in which the magnetizations of the free FM and pinned FM layers are in parallel alignment both in the top CoFe/FeMn SV and bottom IrMn/CoFe SV, are corresponding to the same magnetoresistance state (d).

These twelve magnetization states illustrated in Fig.5 can be individually distinguished based on the field dependence of the resistance. Hence, in principle, four magnetization states can be used as information storage if only two free FM layers in the composite spin-valve are used as storage layers. One can define the magnetization state (1) as "11" where the magnetization of both free FM layers are in parallel alignment along the positive direction. One can also define the state (2) as "01" where the magnetization of the free FM layer in the bottom IrMn/CoFe spin-valve is parallel to the negative direction while the magnetization of the free FM layer in the top FeMn/CoFe spin-valve is parallel to the positive direction. And so on so forth, two bits with four states can be finally stored and read out in one storage cell. If three FM layers are used as information storage, in principle, three bits with eight states can be stored and read out in one storage cell.

CONCLUSIONS

In summary, multiple magnetoresistance states have been successfully demonstrated in an electrically isolated and magnetically decoupled dual spin-valve structure. By properly choosing the FM and AFM materials used in the new structure, the spins of the free FM and pinned FM layers can be engineered as desired. Such kind of new structure is expected to be used as a MRAM cell in which multiple magnetization states can be stored and read out, hence the data storage density will be significantly improved without increasing any additional processing complexity.

REFERENCES

[1] Won-Cheol Jeong, Byung-Il Lee, and Seung-Ki Joo, J. Appl. Phys. **85**, 4782(1999)
[2] K.-S. Moon, R.E. Fontana, Jr., and S. S. P. Parkin, Appl. Phys. Lett. **74**, 3690 (1999)
[3] Hiromi Niu Fuke, Kazuhiro Saito, Yuzo Kamiguchi, Hitoshi Iwasaki, and Masashi Sahashi, J. Appl. Phys. **81**, 4004(1997)
[4] Geoff Anderson, Yiming Huai, and Lena Miloslawsky, J. Appl. Phys. **87**, 6989(2000)
[5] A. J. Devasahayam, P. J. Sides, and M.H.Kryder, J. Appl. Phys. **83**, 7216(1998)
[6] S. -F. Cheng and P. Lubitz, J. Appl. Phys. **87**, 4927(2000)
[7] Hiromi N. Fuke, Kazuhiro Saito, Masatoshi Yoshikawa, Hitoshi Iwasaki, and Masashi Sahashi, Appl. Phys. Lett. **75**, 3680(1999)
[8] G. Choe and S. Gupta, Appl.Phys.Lett. **70**, 1766(1997)

Laser ablated pure non-crystalline Co thin films for inductors for ultra-high frequencies

V. Madurga, J. Vergara, C. Favieres
Departamento de Física. Universidad Pública de Navarra. Campus Arrosadía. E-31006
Pamplona. Spain.

ABSTRACT

Non-crystalline Co thin films have been prepared by pulsed laser ablation deposition. From the M-H hysteresis loops measurements, a soft magnetic behavior is observed. Néel type magnetic domain walls are observed in the as-deposited films. The spontaneous magnetization, M_s (T = 300 K), is $\approx$ 860 emu/cm^3. After annealing at 500 °C, M_s (T = 300 K) is $\approx$ 1460 emu/cm^3. The extrapolated to zero K resistance decreases almost two orders of magnitude from the as deposited samples to the crystallized heated at 500 °C ones. A trilayer Co/Cu/Co has shown a real part magnetic susceptibility of 120 at 100 MHz. In the 100 MHz to 1 GHz frequency range, a perpendicular bias magnetic field increased this value up to 270, remaining almost constant for all range.

INTRODUCTION

Ferromagnetic elements in the amorphous state have attracted interest from both the theoretical and the applied points of view [1-9]. Different techniques have shown the possibility of producing these kind of materials; in particular, the pulsed laser ablation deposition method, PLAD, is one of the most versatile method for preparing non-crystalline solids [7] and thin films of pure ferromagnetic elements at room temperature [8-9], exhibiting interesting magnetic and electrical properties.

Since years, there has been interest in developing thin film soft ferromagnetic materials appropriated for high frequency (f >100 MHz) applications, as for example, for electromagnetic devices as a high frequency field-amplifying component, e.g., in read-write heads for magnetic disk memories for computers [10-12]. Some of the most desirable properties in these materials are high saturation magnetization, low magnetic coercitivy, high magnetic permeability and high electrical resistivity.

In this work we show that non-crystalline PLAD Co thin films - films made up of one element only -, are very suitable for high frequencies applications because they exhibit, at room temperature, such magnetic and electrical properties mentioned above.

EXPERIMENTAL

Non-crystalline Co thin films were prepared by PLAD, using a stainless-steel chamber (Neocera) at 10^{-5} mbar pressure. A pulsed Nd: YAG laser, λ=1024 nm, 20 Hz repetition rate, with 4 ns pulses, energy 300 mJ per pulse, was used. A polished circular disk, 20 mm in diameter, of pure Co (Goodfellow metals, 99.999%) was used as the target, which was rotated at 32 rpm. The area of the laser beam on the target was 2 mm^2. Pure Si (111) substrates, 2 x 25

mm^2, were used for depositing the CoCuCo sandwiches and 4 x 4 mm^2 substrates were used for the pure Co films deposition. The substrates, which were rotated at 120 rpm, were situated at 70 mm from the target. The deposition time was 30 min., thus obtaining samples ≈ 250 nm thick. After deposition, some samples were annealed at temperatures up to 700 °C for 10 minutes in an inert atmosphere.

Trilayers Co/Cu/Co were also fabricated by this technique. For this purpose, two different targets were placed into the chamber: one of Co and one of Cu. The Co layers were deposited in accordance with the above described procedures. The intermediate Cu layer was deposited using a circular pure Cu (Goodfellow metals, 99.999%) target, 20 mm in diameter, that was also rotated at 32 rpm. The deposition time was 120 min., thus obtaining a layer 0.5 μm thick.

X- ray analysis were performed with a diffractometer (XRD-3000 Seifert), using Mo anode and a grazing incidence geometry. A graphite secondary monochromator was placed just before the detector.

We performed different magnetic measurements. We measured the Magnetooptical Transverse Kerr Effect, MOKE. The diameter of the light spot was 0.5 mm. An EG&G Vibrating Sample Magnetometer, VSM, was used for measurements at room temperature and in magnetic fields up to 1 Tesla, and a Superconducting Quantum Interference Device, SQUID, was used for measuring in magnetic fields up to 5 Tesla.

The Bitter technique was applied in analyzing magnetic domain configurations. Improved contrast and pattern resolution were achieved by applying a magnetic field perpendicular to the sample's plane, in order to polarize the colloidal suspension.

The electrical resistivity, ρ, of the Co thin films was measured by a conventional four probes system. The dependence of ρ on temperature was studied from room temperature up to 500 °C. These measurements were performed in a furnace where an Ar atmosphere was kept to avoid oxidation processes in the samples.

The susceptibility spectra of the films was measured both with a LCZ meter (Keithley 3322) in the frequency range from 100 Hz to 100 kHz and also with a network analyzer (HP 8753D) in the range from 100 kHz to 1 GHz. In the low frequency range (up to 100 kHz) the susceptibility of our films was determined by measuring the change of inductance of a pick up coil, when the sample was inserted in it and after applying an external bias magnetic field. In the high frequency range, the magnetic susceptibility was measured using a strip-loop device – 40 mm long, 8 mm wide and 3 mm high - mounted on a standard SMA connector. The changes of the impedance of the fixture when the sample was inserted in it were measured with the network analyzer. In both situations, at low and at high frequencies, an external bias magnetic field, created by a pair of Helmholtz coils, was applied in the plane of the sample and perpendicular to the ac magnetic field inside the pick up coil or inside the strip-loop fixture.

RESULTS AND DISCUSSION

Microstructure

X-ray diffractograms were performed on the as-deposited as well as on the annealed Co thin films. For the as-deposited samples, the analysis showed none of the peaks characteristic of crystalline structures, see figure 1(a). However, for the samples heat treated at 500 °C in an Ar atmosphere for 10 min., a superposition of both Co fcc and Co hcp crystalline diffraction pattern

was observed exclusively, as shown in figure 1(b); only the first peak centered at ≈17 deg. in figure 1(b) could be due to some Co oxide present in the sample.

Magnetic and electrical properties

The MOKE measurements revealed a bistable soft magnetism. Figure 2 shows two MOKE hysteresis loops, M-H, obtained when an in plane magnetic field is applied along the longitudinal easy direction and perpendicular to the longitudinal direction respectively: an easy coercive field of 1.7 Oe and a weak in plane magnetic anisotropy, anisotropy field of 12 Oe, were measured.
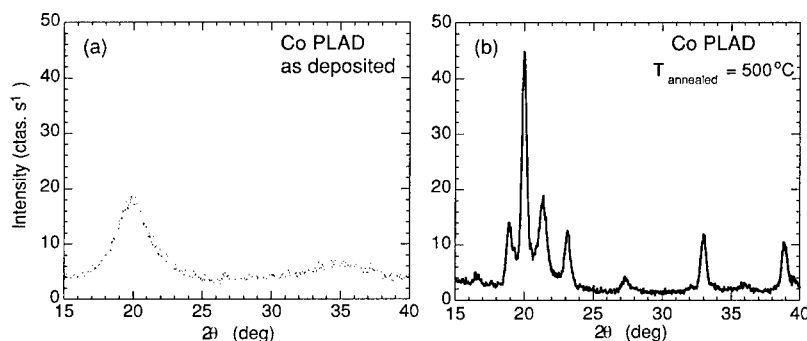
Figure 1. X-ray diffractograms from the Co thin films: (a) as-deposited: none of the peaks characteristic of crystalline structure are observed; (b): after 10 min. at 500 ^{0}C. A superposition of both Co fcc and Co hcp crystalline diffraction pattern was observed exclusively; only the first peak centered at ≈17 deg. could be due to some Co oxide.
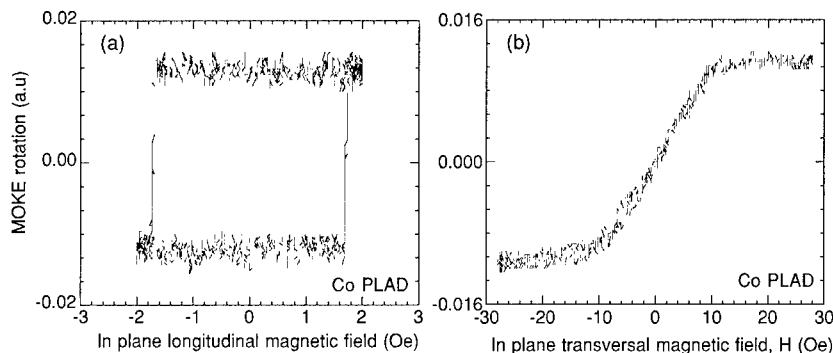
Figure 2. MOKE hysteresis loops, M-H, obtained when an in plane magnetic field is applied along (a) the longitudinal easy direction and (b) perpendicular to this easy longitudinal direction.

From VSM measurements, it is confirmed that for the as-deposited sample the coercive field is $\approx$ 1.7 Oe, as it is shown in figure 3(a). The inset in this figure shows the measurements of M-H performed in a SQUID in fields up to 5 Tesla. It is seen that the spontaneous magnetization, M_s, at room temperature is 860 emu/cm^3. When the samples are annealed at 500 ^{0}C, M_s increases to 1460 emu/cm^3, see figure 3(b). This M_s value corresponds to the value of M_s, at room temperature, of pure crystalline Co.
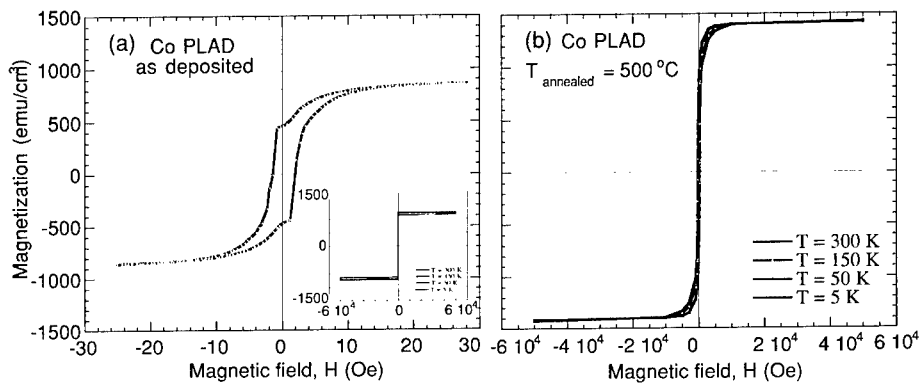
Figure 3. (a)VSM measurement for the as-deposited sample. The coercive field is $\approx$ 1.7 Oe and M_s(T = 300 K) = 860 emu/cm^3. The inset shows the SQUID measurements at 5 Tesla.; (b) SQUID measurements for the sample annealed at 500 ^{o}C, M_s (T = 300 K) =1460 emu/cm^3. Note that the vertical scale is the same in the two graphics (a) and (b).

The magnetic domains structure corresponding to the as-deposited Co thin films are shown in figure 4(a,b). The Bitter patterns show Néel type magnetic domain walls. This irregular shape of the domain walls can be attributed to a weak in plane anisotropy and to a local deviation of the magnetization from its average orientation. Figure 4(c,d) is a schematic representation of the structures observed in figure 4(a,b), indicating the direction of M_s, inside each domain.

Figure 5 shows the dependence of the electrical resistivity on temperature, R(T). Note that the resistance decreases almost two orders of magnitude from the as-deposited sample to the sample heat treated at 500 ^{o}C. It can be also seen two irreversible jumps in the resistance, associated with the irreversible changes in the microstructure of the films occurring when they are annealed.

Inductive behavior

At low frequency, f=100 Hz, the value of the magnetic susceptibility of square 4 mm long Co samples was 1200. As the frequency of the ac magnetic film increases, the motion of the magnetic domain walls is hindered, and consequently the magnetic susceptibility decreases to 200 at 100 kHz. In this situation, see figure 6(a), the application of a perpendicular bias magnetic field contributes to create a preferential orientation of the magnetization in the Co film,
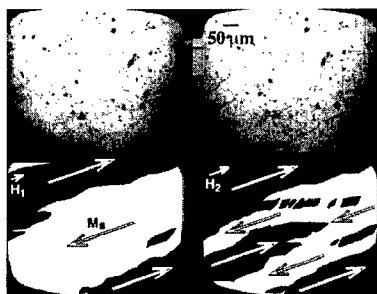
Figure 4.(a,b) Magnetic domains for the as-deposited films; a magnetic field changes the domains structure; (c, d) schematic picture of both photos.
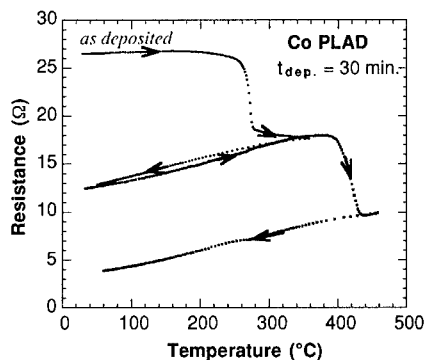
Figure 5. Dependence of the resistance on temperature of Co PLAD thin films. The arrows indicate the direction in which the measurements were done.
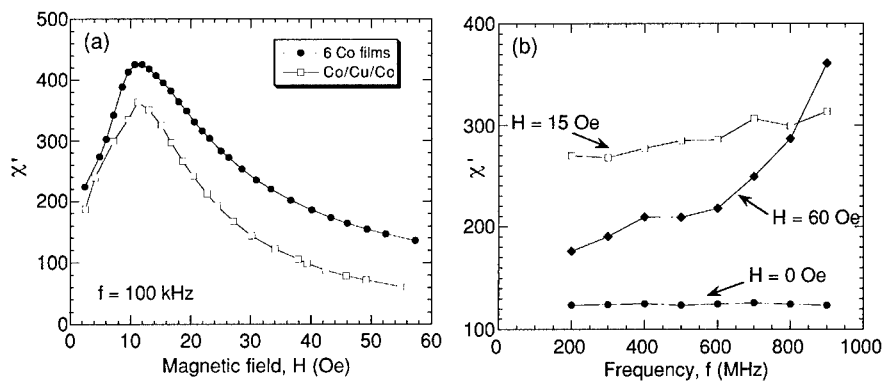
Figure 6.(a). Evolution of χ' with a dc magnetic field at f= 100 kHz, corresponding to two different systems: six Co films and a trilayer Co/Cu/Co, respectively; (b) high frequency behavior of the trilayer for different bias magnetic field.

along the direction of this bias field. In this situation, the ac magnetic film produces a coherent spin rotation towards the direction of the ac field, and this rotation mechanism gives rise to an increase of the magnetic susceptibility, up to 450 in our Co films. Further increments of the bias field tend to fix the magnetization along the dc magnetic field direction and the susceptibility decreases again.

The susceptibility was measured up to 1 GHz, see figure 6(b). The real part of the susceptibility, χ', shows a slight frequency dependence, which could be due either to a measuring artifact as the copper strip-loop exhibits a resonance at 1.3 GHz, and also to the effect of ferromagnetic resonance of Co films. χ' of our Co films is of the same order than χ' in other magnetic films , i.e. $\chi' \approx 1000$, for Co-Zr [10], $\chi' \approx 500$ for Co-Nb-Zr [11], or $\chi' \approx 200$ for Fe-Cr-Ta-N[12].

CONCLUSIONS

PLAD non-crystalline Co thin films showed a soft magnetic behavior: an easy coercive field of 1.7 Oe and an in plane magnetic anisotropy, $\approx$ 12 Oe, were exhibited. The value of the spontaneous magnetization at room temperature was, M_s (T = 300 K) $\approx$ 860 emu/cm^3. After annealing at 500 °C, M_s (T = 300 K) $\approx$ 1460 emu/cm^3. The extrapolated to zero K resistance decreased almost two orders of magnitude from the as deposited samples to the heat treated at 500 °C. Due to their soft magnetic properties, high M_s, high values of the magnetic susceptibility at high frequencies and high electrical resistivity, these films were suitable for ultra high frequencies applications. The magnetic susceptibility was 200 at 100 kHz. The application of a perpendicular bias magnetic field increased the magnetic susceptibility up to 450. In the 100 MHz to 1 GHz frequency range, the real part of the susceptibility remained almost constant and its value was similar to those of the Co-Zr, Co-Nb-Zr and Fe-Cr-Ta-N compounds.

ACKNOWLEDGMENTS

REFERENCES

1. M. R. Bennett and J. G. Wright. *Phys. Letters*. **38A**, 419 (1972).
2. E. W. Lee. *Physica B & C*. **86-88**, 781 (1977).
3. Tanaka, S. Takayama. *J. Phys: Condens. Matter* . **4**, 8203 (1992).
4. H. Magnan, D. Chandesris, G. Rossi, G. Jezequel, K. Hricovini, J. Lecante. *Phys. Rev. B*. **40**, 9989 (1992).
5. Y. Kakehashi. Mater. *Sci. Eng. A* , **179-180**, 62 (1994).
6. M. Liebs, K. Hummler, M. Fahnle. *Phys. Rev. B*. **51**, 8664 (1995).
7. Y. Hiroshima, T. Ishiguro, I. Urata, H. Ohta, M. Tohogi, Y. Ichinose. *J. Appl. Phys.* **79**, 3572 (1996).
8. V. Madurga, J. Vergara, I.P. Landazábal, R.J. Ortega, C. Favieres in *Advanced Hard And Soft Magnetic Materials*, edited by M. Coey et al. (Mat.Res. Soc.Proc. **577**, Pittsburg, PA, 1999) pp. 599-604.
9. C. Favieres and V. Madurga. *J. Non.Crys. Solids,* (2001) (in press)
10. A. Fessant, J. Gieraltowski, J. Loaec, H. Le Gall, A. Rakii. IEEE. Trans. Mag, **29**, 82 (1993)
11. V. Korenivski, R. B. van Dover, P. M. Mankiewich, Z. -X. Ma, A. J. Becker, P. A. Polakos, V. J. Fratello. IEEE. Trans. Mag., **32**, 4905 (1996).
12. S. Jin, W. Zhu, R. B. van Dover, T. H. Tiefel, V. Korenivski. Appl. Phys. Lett., **70**, 3161 (1997).

Magnetostriction and Microstructure of As-Deposited and Annealed Co Thin Films

Winfried Brückner, Michael Hecker, Jürgen Thomas, Detlev Tietjen, and Claus M. Schneider
Institute for Solid State and Materials Research Dresden, D-01171 Dresden, Germany

ABSTRACT

The magnetostriction of as-sputtered and annealed 400 nm thick Co films has been studied in longitudinal and transverse magnetic fields. The appreciable change of the magnetostriction behavior after annealing above 250 °C is correlated to grain growth and to the related change of the texture (from nearly randomly distributed hcp-Co crystallites to a c-axes texture perpendicular to the film plane). The magnetostriction behavior in the annealed samples cannot be explained by a domain magnetization within the film plane. It is assumed that a rotation of the spontaneous magnetization out of the film plane occurs due to the development of a perpendicular magnetic anisotropy.

INTRODUCTION

Cobalt thin films are of great interest as soft magnetic single layers as well as in magnetic multilayers, e.g., Cu/Co multilayers [1]. Due to the magnetoelastic coupling, the magnetostriction also affects the magnetic anisotropy. Deposition conditions and post-growth annealing may have a profound influence on the microstructure and therefore also on the magnetostrictive state.

The present contribution is focussed on the magnetostriction in sputtered 400 nm thick Co films in the as-deposited state and after annealing up to 450 °C. The results are correlated to findings of microstructural analyses concerning phase formation, texture, and grain morphology. The results are complemented with studies of: (i) the stress development as an indicator for microstructural processes as well as a factor in the magnetoelastic coupling, and (ii) the longitudinal magneto-optical Kerr effect (MOKE) for the characterization of the surface magnetization of the films.

EXPERIMENTAL DETAILS

The films were deposited by magnetron sputtering onto rotating oxidized 3-inch silicon wafers at room temperature. The deposition conditions were: base pressure 1×10^{-6} mbar, sputtering pressure 4×10^{-3} mbar Ar, and sputtering power 150 W for a 4-inch target. The film thickness was measured using a Dektak stylus profiler after wet-chemical etching of an edge into the film, and was determined to be 399 nm.

For the annealing procedure, the coated substrate was cut into slabs of 55 mm × 7 mm. The heat treatment was combined with in-situ stress measurements under high vacuum (1×10^{-5} mbar) using a sensitive laser-optical stress-measurement system described elsewhere [2]. The heating and cooling rate amounted to 4 K/min and the isothermal annealing was done at 150, 250, 350, and 450 °C for 2 h. The annealed slabs were cut into smaller samples for all other measurements.

The magnetostriction was determined by a laser-optical measurement of the substrate deflection in an applied magnetic field using a two-beam free-sample set-up described elsewhere [3]. The deflection δ of the substrate at the position of the laser beams (having a distance l of 25 mm)

with respect to the sample center was determined in longitudinal ($\parallel$) and transverse ($\perp$) magnetic fields H applied always within the film plane.

X-ray diffraction (XRD) investigations were performed using a Philips-XPert diffractometer with CuK_α radiation, Eulerian cradle, and thin-film equipment. Scans with symmetrical beam, grazing incidence, and pole-figure cuts were measured.

The transmission electron microscopy (TEM) studies employed cross-sectional specimens. The preparation was carried out by means of a focused ion beam (FIB) technique. For TEM observations, a PHILIPS CM20FEG was employed in imaging and diffraction mode. Grain-size distributions were determined from measurements in bright and dark field image modes.

RESULTS

The stress-temperature curves $\sigma(T)$ during the annealing (Fig. 1) reveal initial irreversible stress changes already above 150 °C and more distinct changes above 250 °C. Similar to CuNi thin films [4,5], the irreversible tensile stress contributions are expected to be the result of material densification due to grain-boundary relaxation and elimination (grain growth is proved by TEM, see below). No feature associated with a martensitic transformation from a hexagonal-closed-packed (hcp) to a face-centered-cubic (fcc) phase at about 400 °C, as it was reported in the literature for ≥500 nm thick Co films [6], was observed in our $\sigma(T)$ curves.

The magnetostrictive deflection during the second magnetization loop (Fig. 2) shows distinct changes between the as-deposited and the annealed state. For as-deposited samples (as well as for T_{max}=150 °C), a soft magnetic behavior with a hysteresis of about 10 kA/m is mainly observed and the deflections $\delta_\parallel$ and $\delta_\perp$ are of opposite sign. Full saturation of the deflection signal was reached only above 200 kA/m. For the samples with T_{max}=350 °C and 450 °C, the films show a hard magnetic behavior without remarkable hysteresis, the magnetostriction response being not nearly as saturated at 500 kA/m, and the deflections $\delta_\parallel$ and $\delta_\perp$ are relatively high and both negative. The curves for the sample with T_{max}=250 °C indicate a transition between the soft and hard magnetic case. The reason for these changes and the calculation of the magnetostriction value given at the right-hand axis of Fig. 2 will be discussed below. Experimental magnetostriction data, being in many points similar to our results, were also reported for 165 nm thick Co films [7].
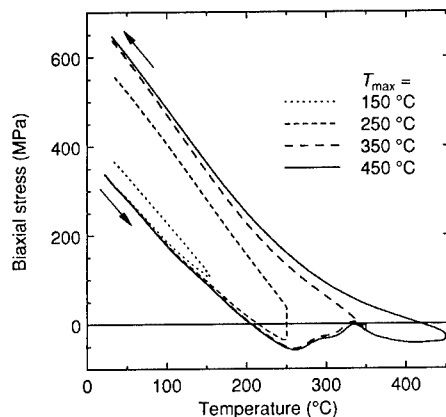
Figure 1. Stress development during annealing of Co thin films at various temperatures.
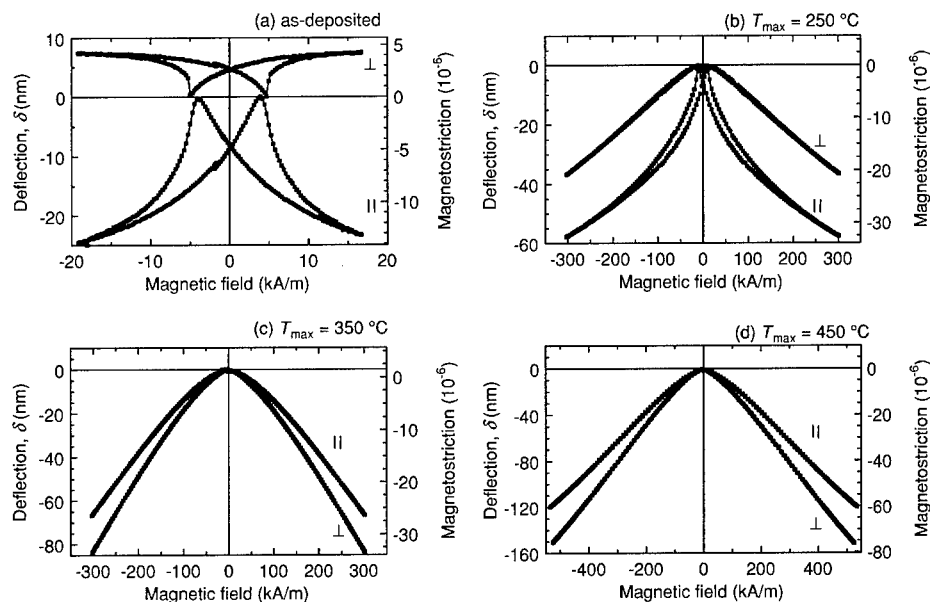
Figure 2. Magnetostrictive deflection and magnetostriction in longitudinal ($\parallel$) and transverse ($\perp$) magnetic fields during the second magnetization loop. The behavior changes strongly during annealing at $T_{max} \geq 250$ °C.
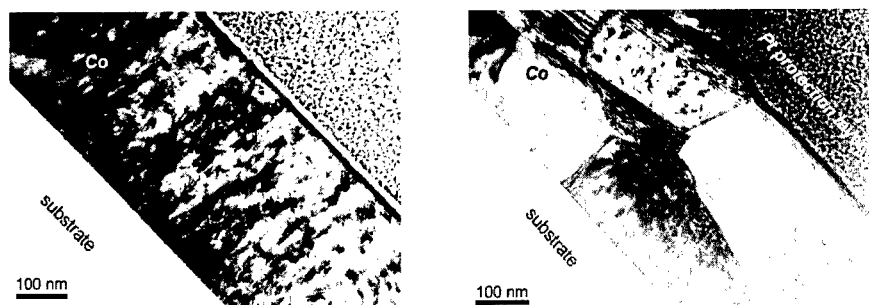
Figure 3. Cross-sectional TEM micrographs of Co thin films (FIB specimen preparation). Left: as-deposited state, right: after annealing at 450 °C. Grain growth is observed during annealing.

Two representative cross-section TEM images in Fig. 3 demonstrate the microstructural evolution during the annealing procedure. In the as-deposited state, small columnar grains with a mean diameter of 30 nm and a length of 80 nm dominate the morphology. These grains were found to grow at 250 °C starting at the film-substrate interface. For $T_{max} = 350$ °C and 450 °C, all

original small grains are converted into large grains. The average lateral grain dimension amounts to 650 nm for $T_{max} = 450$ °C. Such a secondary recrystallization was also reported for CuNi(Mn) thin films [5].

The XRD measurements of all samples show patterns (Fig. 4) representative of hcp Co. In the as-deposited state, broad reflections occur indicating small grains with (100), (001), and (101) planes parallel to the surface (lattice parameters: $a = 0.2507$ nm and $c = 0.4067$ nm). The reflection intensity relations correspond nearly to a random orientation distribution, however, with a weak preference of the hexagonal c-axis perpendicular to the film plane. Furthermore, texture measurements showed an additional weak (101) texture. During annealing, the texture strongly changes. After annealing at and above 350 °C, only a c-axis texture is found in the XRD scans. Further measurements indicate an additional small fraction of face-centered-cubic crystallites, which show a (111) texture after annealing.

Two examples of MOKE results are given in Fig. 5. An isotropic magnetic behavior within the film plane was confirmed by measurements in different azimuthal directions. A close correspondence of the magnetostrictive deflection curves ("layer-bulk" effect) to the MOKE curves (surface related signal down to about 10 nm) is ascertained. Note, that the hysteresis loop of the annealed sample reflects a hard-axis behavior for the in-plane magnetization.
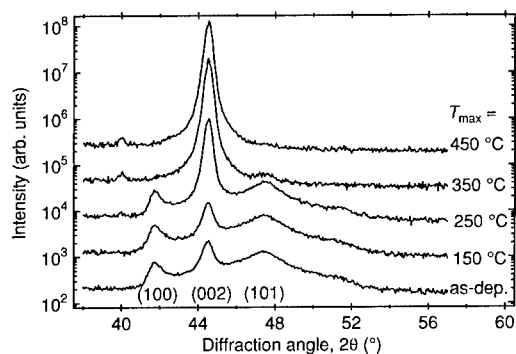
Figure 4. Reflections of hcp-Co as measured by XRD for the as-deposited and annealed Co films (annealing temperature T_{max}, as indicated). The increasing abundance of c-axis texture component is indicated by the intensity changes of the reflections.
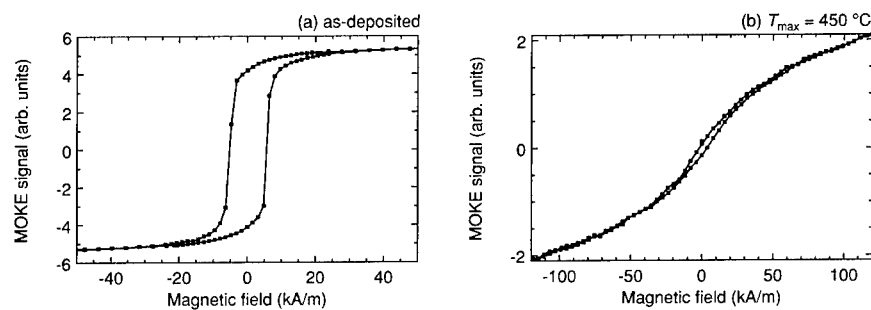
Figure 5. MOKE signals of the as-deposited and an annealed (450 °C) Co film demonstrate the surface magnetization behavior. Main features correspond to the deflection changes in figure 2.

DISCUSSION AND CONCLUSIONS

The microstructural studies have shown that the as-deposited film is polycrystalline, weakly textured, whereas the annealed state with $T_{max}>250$ °C is c-axis textured. Because the annealed state is more definite than the as-deposited one, only the annealed state is considered in the following. To discuss the magnetostriction behavior, (i) the influence of the texture on the magnetostriction and (ii) the correlation between magnetostriction and substrate deflection will be considered, and (iii) the experimental results will be compared to model calculations.

In the first approximation for hexagonal materials, the following equation describes the saturation magnetostriction in a single crystal with the material parameters λ_A, λ_B, λ_C, and λ_D:

$$\lambda_{\alpha\beta} = \lambda_A \left[(\alpha_1\beta_1 + \alpha_2\beta_2)^2 - (\alpha_1\beta_1 + \alpha_2\beta_2)\alpha_3\beta_3 \right] + \lambda_B \left[(1 - \alpha_3^2)(1 - \beta_3^2) - (\alpha_1\beta_1 + \alpha_2\beta_2)^2 \right]$$
$$+ \lambda_C \left[(1 - \alpha_3^2)\beta_3^2 - (\alpha_1\beta_1 + \alpha_2\beta_2)\alpha_3\beta_3 \right] + 4\lambda_D (\alpha_1\beta_1 + \alpha_2\beta_2)\alpha_3\beta_3 \tag{1}$$

where the measuring direction has the direction cosines α_1, α_2, and α_3 and the magnetic field, β_1, β_2, and β_3 [8]. The direction cosines refer to a cubic reference system with x and z along the hexagonal [100] and [001] direction, respectively. The magnetostriction reference is related to the ideally demagnetized state (IDS) with a regular three-dimensional domain distribution along the easy directions.

If the demagnetized state corresponds to the IDS, one obtains the longitudinal and transverse magnetostriction, $\lambda_{\parallel}$ and $\lambda_{\perp}$, for a c-axis-textured film from Eq. (1) [9]. It is

$$\lambda_{\parallel,\text{text}}^{\text{IDS}} = \lambda_A \qquad\qquad \lambda_{\perp,\text{text}}^{\text{IDS}} = \lambda_B \tag{2}$$

In thin films, however, one has an initial magnetic state (IMS), which departs from the IDS. Therefore, one has an initial change of the dimension of the sample. Considering a film with magnetic moments under a fixed angle Θ to the plane's normal, Schelp et al. [9] obtained for the magnetostriction of the IMS (in relation to the IDS)

$$\lambda_{\text{IMS}}^{\text{IDS}} = \frac{1}{2}(\lambda_A + \lambda_B)\sin^2\Theta \tag{3}$$

The extreme cases are $\Theta=90°$ and $\Theta=0°$ for in-plane and perpendicular spontaneous magnetization. The magnetostriction responses of the thin films as measured from the saturated state in relation to the state without magnetic field ($H=0$) are given by

$$\lambda_{\parallel} = \lambda_{\parallel}^{\text{IDS}} - \lambda_{\text{IMS}}^{\text{IDS}} \qquad\qquad \lambda_{\perp} = \lambda_{\perp}^{\text{IDS}} - \lambda_{\text{IMS}}^{\text{IDS}} \tag{4}$$

In thicker magnetic films, one has mostly an in-plane magnetization. But for films with strong magnetic anisotropy, the magnetization may also rotate out-of plane.

In the general case, the relation between magnetostriction and substrate deflection is complicated and no practicable equations exist, because of the tensor character of both elastic properties and magnetostriction [10]. The most complicated case with still manageable efforts is the case of isotropic mechanical properties of film and substrate and anisotropic magnetostrictive strains in two perpendicular directions within the film plane [11]. In this case one obtains a linear equation set between the deflections $\delta_{\parallel}$ and $\delta_{\perp}$ and the magnetostrictive strains $\lambda_{\parallel}$ and $\lambda_{\perp}$. For the simplified case of equal Poisson's ratios of film and substrate, the equation set decouples, and one finds:

$$\lambda_{\parallel,\perp} = \frac{4}{3}\frac{E_s}{E_f}\frac{t_s^2}{t_f}\frac{1}{l^2}\delta_{\parallel,\perp} \tag{5}$$

where E and t are Young's modulus and thickness of film (f) and substrate (s), respectively. Using Eq. (5), $E_f = 210$ GPa for (polycrystalline) Co, $E_s = 148$ GPa as an average in the Si (100) plane, and $t_s=380$ µm, the magnetostrictive strain values given in the right-hand axes of Fig. 2 were calculated.

For a comparison between theory and experiment one can use Eqs. (2) – (4) and the material parameters of single-crystalline hcp Co, i.e., $\lambda_A = -50\times10^{-6}$, $\lambda_B = -107\times10^{-6}$, $\lambda_C = 126\times10^{-6}$, and $\lambda_D = -105\times10^{-6}$ [12]. The saturation magnetostriction values of a c-axis-textured film in relation to the IMS are: $\lambda_{\parallel} = -52\times10^{-6}$, $\lambda_{\perp} = 52\times10^{-6}$ and $\lambda_{\parallel} = -50\times10^{-6}$, $\lambda_{\perp} = -107\times10^{-6}$ for in-plane and perpendicular initial magnetization, respectively. Comparing to the experimental results of Fig. 2, one has to take into account the incomplete saturation of the c-axis-textured films. Already within a qualitative (sign-wise) comparison, one may speculate that the magnetization in the IMS is not confined to the film plane but may have a strong out-of-plane component at least.

A c-axis-textured Co film should be expected to develop a perpendicular crystalline anisotropy. This may result in a rotation of the magnetization in the $H=0$ state into the direction perpendicular to the film plane, e.g., via formation of stripe domains [13] or with a perpendicular magnetization [9]. For further insight into the spontaneous magnetization behavior, measurements of the domain structure by means of Kerr microscopy and of the magnetization behavior in large magnetic fields applied within and perpendicular to the film plane are now under investigation.

ACKNOWLEDGMENTS

REFERENCES

[1]   D.H. Mosca, F. Petroff, A. Fert, P.A. Schroeder, W.P. Pratt Jr., and R. Laloee, *J. Magn. Magn. Mat.* **94**, L1 (1991).
[2]   V. Weihnacht, W. Brückner, and C.M. Schneider, *Rev. Sci. Instrum.* **71**, 4479 (2000).
[3]   W. Brückner, C. Lang, and C.M. Schneider, *Rev. Sci. Instrum.* **72**, (2001) (in press).
[4]   W. Brückner, V. Weihnacht, W. Pitschke, J. Thomas, and S. Baunack, *J. Mater. Res.* **14**, 1286 (1999).
[5]   W. Brückner, W. Pitschke, S. Baunack, and J. Thomas, *J. Mater. Res.* **15**, 1062 (2000).
[6]   H.Th. Hesemann, P. Müllner, O. Kraft, and E. Arzt in *Thin Films: Stresses and Mechanical Properties VIII*, edited by R. Vinci, O. Kraft, N. Moody, P. Besser, and E. Shaffer II, (Mater. Res. Soc. Symp. Proc. **594**, Warrendale, PA, 2000) pp. 219-224.
[7]   E. Klokholm and J. Aboaf, *J. Appl. Phys.* **53**, 2661 (1982).
[8]   Landolt-Börnstein, *Zahlenwerte und Funktionen* (Springer, Berlin, 1962), vol. II/9, pp.1-123ff.
[9]   L.F. Schelp, A.D.C. Viegas, M. Carara, and J.E. Schmidt, *J. Magn. Magn. Mat.* **139**, 59 (2000).
[10] E. du Tremolet de Lacheisserie, *Magnetostriction* (CRC, Boca Raton, FL, 1993) pp. 43ff.
[11] E. van de Riet, *J. Appl. Phys.* **76**, 584 (1994).
[12] *Magnetic properties of metals*, edited by H.P.J. Wijn (Springer, Berlin, 1991) p.14.
[13] A. Hubert and R. Schäfer, *Magnetic Domains* (Springer, Berlin, 1998) pp. 177 ff.

Microstructure and Magnetic Properties of Co-CoO Nanocomposite Films

Jae-Young Yi, G. A. Hirata* and M. L. Rudee
Material Science and Engineering, University of California, San Diego,
La Jolla, CA 92093, U.S.A.
*CCMC-UNAM, Ensenada, B.C., 22860, Mexico

ABSTRACT

The effect of exchange anisotropy on nanosize Co particles was studied in Co-CoO nanocomposite thin films for possible applications for magnetic storage media. XRD analyses showed nanosize hcp Co particles and (111) textured CoO phase. A broken columnar structure was observed in cross-section TEM images. Very large room temperature coercivity (~1 kOe) was observed and believed to be due to a shape effect and possible local exchange coupling. Large exchange anisotropy at low temperatures and linear type temperature dependence were explained by finite size effects and thermal relaxation of the CoO particles. A slow decrease of thermoremanent moment (TRM) with temperature and large TRM at room temperature indicated that the exchange anisotropy significantly modified the anisotropy energy barrier of the Co crystallites in the CoO matrix. The results indicated that the exchange anisotropy could be used to stabilize nanosize ferromagnetic particles.

INTRODUCTION

The particle sizes of magnetic storage media in computer hard disk drives continuously decrease to satisfy the demand of higher areal density. Reducing the sizes is important not only for smaller bit size but also for high signal to noise ratio. As particle size decreases thermal stability becomes a critical issue. The thermal stability is addressed by the ratio of anisotropy energy to thermal energy [1,2]. There have been many different approaches to improve the thermal stability [3,4,5]. Basically they are based on how to increase the magnetocrystalline anisotropy energy in order to enhance the overall energy barrier against thermal fluctuation. In this study, exchange anisotropy was explored as an additional anisotropy source. We investigated this effect on nanosize ferromagnetic particles. The exchange anisotropy was observed when ferromagnetic (FM) materials were coupled to antiferromagnetic (AFM) materials through a field cooling process. Exchange anisotropy could enhance the magnetic stability of fine ferromagnetic particles by exchange coupling. Meiklejohn and Bean, discoverers of the exchange anisotropy, were first to mention that the exchange anisotropy constant could be the same order of magnitude as the crystalline anisotropy of cobalt for a specific case [6]. So far most studies were conducted in FM/AFM bilayer or multilayer systems because of the simplicity of the structure and the ease to formulate the results. Since exchange anisotropy has a interfacial characteristic and a fine particle has a large surface area, it would be interesting to investigate the exchange anisotropy in fine particle systems.

EXPERIMENTS

Co-CoO composite films were prepared by co-sputtering from separate Co and CoO targets. CoO is antiferromagnetic material and the Néel temperature is 297 K. Co-SiO$_2$ films were also deposited as a reference system. Prior to deposition the base pressure was better than 5×10^{-7} Torr and Ar pressure was kept at 2 mTorr during sputtering process. The sputtering power of each target was carefully controlled to obtain desired Co volume fractions. The films were deposited onto Si substrates at room temperature. The microstructure of the films was investigated using X-ray diffraction (XRD) and transmission electron microscopy (TEM). The magnetic properties were measured using an alternating gradient force magnetometer (AGM) and a superconducting quantum interference (SQUID) magnetometer.

RESULTS AND DISCUSSION

Figure 1 shows X-ray diffraction patterns (Co K$_\alpha$, λ=1.7902 Å, 1.8 kW) of the Co-CoO films with different Co volume fractions. The relative intensities of Co and CoO were gradually changed as the volume fractions of each phase were changed. As for the CoO phase only (111) peak was observed, indicating textured structure along the direction. As the volume fraction of the Co phase increased, three peaks were developed. They were identified as hcp Co phase. No evidence of fcc Co phase was found. The Co and CoO crystallite sizes were calculated from XRD peak broadening using the Scherrer formula after correcting for instrumental broadening. As the Co volume fraction increased from 31 % to 51 % the Co particle sizes increased from 34 Å to 62 Å whereas the CoO particle sizes decreased from 105 Å to 68 Å. Typically particle sizes are proportional to the volume fraction in a granular structure.
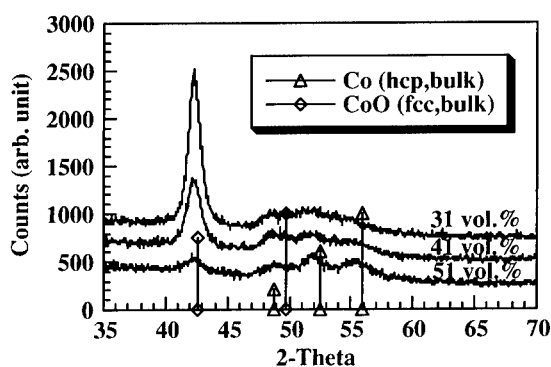
Figure 1. XRD patterns of the Co-CoO specimens with different Co volume fractions. The patterns are vertically shifted for clarification.

Figure 2-(a) and (b) show TEM cross-section images of the Co-SiO$_2$ and Co-CoO film, respectively. Spherical Co particles surrounded by SiO$_2$ matrix were observed in the Co-SiO$_2$ film. However, for the Co-CoO film, because both Co and CoO are crystalline phases, it was difficult to distinguish one from the other. In general columnar type structures were observed. From tilting experiments in the TEM, it was believed that each column was consisted of Co and CoO crystallites rather than one phase.

(a)   (b)
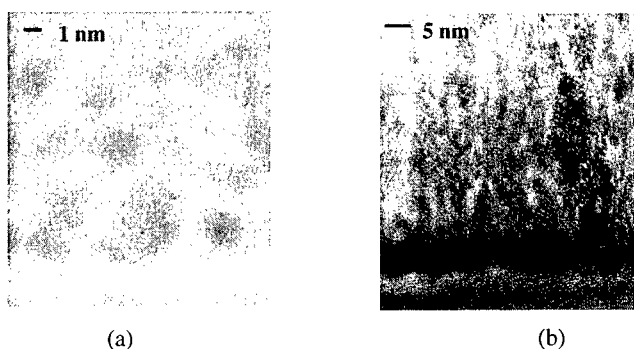
Figure 2. Cross-section TEM images of (a) Co-SiO$_2$ and (b) Co-CoO films.

Figure 3 shows magnetic hysteresis loops of the Co-SiO$_2$ and Co-CoO films measured at room temperature using AGM. Both films had about 30 volume percent of Co. The Co-SiO$_2$ film exhibited no coercivity and zero remanant magnetization, indicating superparamagnetic behavior of the Co particles. However the Co-CoO film showed unusually large coercivity, about 1 kOe.
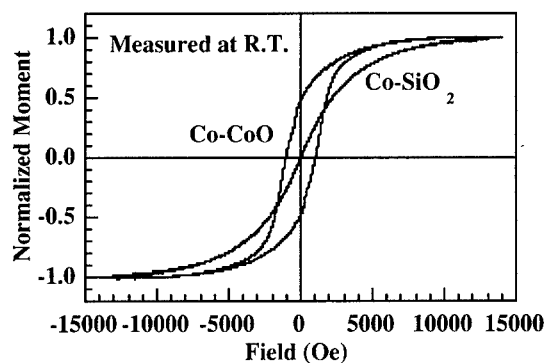
Figure 3. Magnetic hysteresis loops of the Co-SiO$_2$ (29 vol.% Co) and Co-CoO (31 vol.% Co) films.

One of possible explanations is a shape effect. As seen in TEM images the crystallites in the Co-CoO film appeared to be slightly elongated normal to the film plane. This would provide shape anisotropy to Co particles in the CoO matrix. Another possible source would be local exchange coupling of the Co particles to the CoO matrix. Even if exchange anisotropy is not expected at room temperature (Néel temperature of CoO is 293 K.), the Co particles could be locally exchange coupled to the CoO matrix. This had the same effect as increasing the volume of the particles. Therefore more energy would be required to rotate the magnetization of the Co particles.

To examine exchange anisotropy, the Co-CoO films were cooled down in a 5.5 T field from room temperature to 10 K. Large loop shifts were observed in all the Co-CoO films. Figure 4 shows the exchange anisotropy fields (H_e) as a function of temperature of the Co-CoO films with different Co volume fractions. The 31 vol. % of Co specimen exhibited the largest H_e at all temperatures and the H_e decreased as the Co volume fractions increased. The H_e almost linearly decreased with temperature in all compositions and vanished at lower temperatures than the Néel temperature of bulk CoO. This was a very different observation than the observation in the Co/CoO bilayer structure. In the Co/CoO bilayer structure TRM decreased with temperature below 100 K but remained at a constant value up to 200 K, and then decreased to zero at room temperature [7]. Finite size effects were considered as a possible mechanism for our observation. In the Co-CoO composite films, the CoO particle sizes were calculated to be about 68 ~ 105 Å. In this size range, due to the lack of internal structure, some of surface spins of the CoO particles would not be fully compensated and this would be attributed to the exchange anisotropy [8,9]. The continuous decrease of the H_e as a function of temperature can be understood by the superparamagnetic blocking and relaxation phenomena of the finite size CoO crystallites.
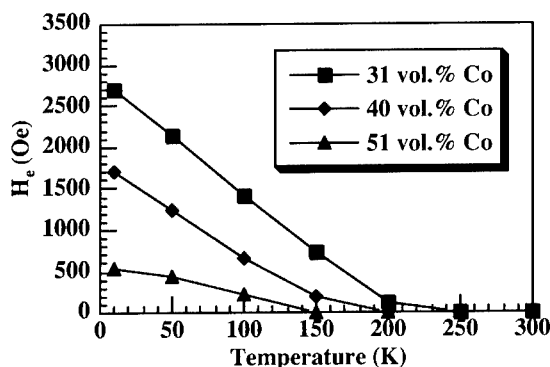
Figure 4. Exchange anisotropy field (H_e) of the Co-CoO films as a function of temperature.

The thermoremanent moment (TRM) and reverse TRM (R-TRM) of the Co particles was measured to investigate the relative effects of anisotropy and thermal energy. The moments were measured in zero field as temperature increased, after field cooling (+6 T) the specimens from 390 K to 10 K. Figure 5 shows the TRM and R-TRM curves of the Co-SiO$_2$ and Co-CoO

films. For the Co-SiO$_2$ film the effective anisotropy energy barrier is mostly due to the volume magnetocrystalline anisotropy. Since the Co particle sizes were estimated only ~30 Å at this volume fraction, the magnetization of the particles were easily disturbed by thermal energy, showing zero magnetization above 70 K. However, the Co-CoO film with the same amounts of Co exhibited very different behavior. The exchange anisotropy significantly modified the overall anisotropy energy barrier so that the Co particles seemed to have more resistance to thermal fluctuation.

To examine unidirectional characteristics of the exchange anisotropy, so called, reverse TRM (R-TRM) curves were also measured. In these measurements, after field cooling the specimen in a positive direction (+6 T) in the same way as the TRM measurement, the field direction was reversed to -6 T, then the magnetization was measured with temperature. If the system is dominated by uniaxial anisotropy, TRM and R-TRM curves should be the same except for the sign (+ or -) regardless of the cooling field direction. As expected the curves from the Co-SiO$_2$ film were exactly symmetric along a temperature axis, indicating the anisotropy energy barrier of the Co crystallites in the SiO$_2$ matrix had a uniaxial characteristic. Obvious differences in TRM and R-TRM indicate that unidirectional exchange anisotropy significantly altered the anisotropy energy barrier.
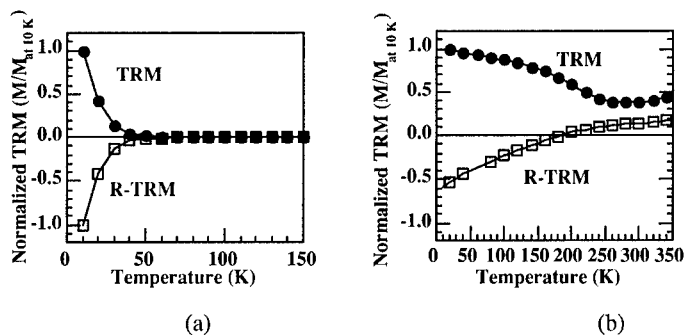
Figure 5. Normalized TRM and R-TRM curves of the (a) Co-SiO$_2$ and (b) Co-CoO films.

CONCLUSION

The effects of exchange anisotropy on the nanosize Co particles were studied in sputter deposited Co-CoO films. A very large coercivity (~1kOe) was observed at room temperature. Finite size effects of the CoO particles were introduced to explain linear type temperature dependence of the H$_e$, and lower blocking temperature than T$_N$. Large TRM and asymmetric TRM and R-TRM curves indicate that the exchange anisotropy modified the anisotropy energy barrier of the Co particles in the CoO matrix.

REFERENCES

1. P. L. Lu and S. H. Charap, *J. Appl. Phys.* **75**, 5768 (1994)
2. P. L. Lu and S. H. Charap, *IEEE Trans. Magn.* **30** (6), 4230 (1994)
3. A. Moser and D. Weller, *IEEE Trans. Magn.* **35** (5), 2808 (1999)
4. D. Weller and A. Moser, *IEEE Trans. Magn.* **35** (6), 4423 (1999)
5. D. Weller, A. Moser, L. Folks, M. E. Best, Wen Lee, M. F. Toney, M. Schwickert, J. -U. Thiele, M. F. Doerner, *IEEE Trans. Magn.* **36** (1), 10 (2000)
6. W. H. Meiklejohn and C. P. Bean, *Phys. Rev.* **105** (3), 904 (1957)
7. K. Takano, R. H. Kodama, A. E. Berkowitz, W. Cao and G. Gareth, *Phys. Rev. Lett.* **79**, 1130 (1997)
8. L. Néel, *Comp. Rend. Acad. Sci.* **252**, p. 4075 (1961); **253**, p. 9, 203 (1961); **254**, 598 (1962)
9. W. J. Schuele and V. D. Deetscreek, *J. Appl. Phys.* **33** (3), suppl., 1136 (1962)

Iron Manganites Synthesis by the Soft Chemistry Method

Herve Coradin, Sophie Guillemet-Fritsch, Fabrice Agnoli, Philippe Tailhades and Abel Rousset
Centre Interuniversitaire de Recherche et d'Ingenierie des Materiaux, UMR CNRS 5085,
LCMIE, Universite Paul Sabatier, 118 route de Narbonne 31062 Toulouse, France

ABSTRACT

The iron manganites $Fe_xMn_{(3-x)}O_4$ synthesis by soft chemistry method have been studied. The main difficulty is to obtain single phase spinel with high Mn content ($0.4 < x < 1.3$). Oxalate precursor powders of these materials with controlled shape and nanoscopic size have been prepared. The precursors are then heat treated with a $H_2/H_2O/N_2$ gas mixture at low temperature. The resulting stoechiometric spinels are metastable phases with high specific surface area and are highly reactive toward oxygen. Therefore, these oxide can be oxidized in air at low temperature in order to produce mixed valence defect manganites $Fe_xMn_{(3-x)}O_{4+\delta}$ with a good reproducibility on the oxygen content. Although, some problems persist for the higher Mn contents, as the oxygen partial pressure for the reduction must be controlled precisely in order to produce the stoechiometric spinel at low temperature. The development of a low temperature reduction system, with oxygen partial pressure controlled by oxygen electrochemical pumping, is in progress.

INTRODUCTION

Manganese iron oxides with spinel structure has applications in magnetic recording media and electronic devices. Previous works carried on in our Laboratory have shown that it is possible to enlarge the well known properties of these materials, using metastable nanoparticles synthesized by soft chemistry at low temperature [1, 2]. Recently, the interest of these materials has greatly increased with the discovery of hard magnetic properties in metastable manganese ferrites. These properties are due to the distortion of the Mn^{3+} cations in the spinel structure by the Jahn-Teller effect [3]. The same bulk ferrites (without Cobalt) are well known to be soft magnetic materials. Moreover, magneto resistance effects have been found in similar spinel phases [4].

The aim of this work is to improve the synthesis of iron manganites $Mn_{(3-x)}Fe_xO_4$, using thermodynamical approach and a new experimental setup. First, we describe precisely the synthesis method ("soft chemistry") to obtain nanosized particles with controlled shape. Different characterizations of the precursor and the oxide powders are presented. We point out the difficulties to prepare stoechiometric oxides powders with high Mn content at low temperature, and present a new experimental process to overcome theses difficulties. The phase diagram of the Fe/Mn/O system [5] shows that the spinel phase can be obtained in air at temperature above 950°C. Only a few works have been published on the synthesis of this stoechiometric spinel at low temperature [3,6,7]. Probably, the difficulty to obtain the stoechiometric spinel at low temperature is due to, the need of a better control of the reduction atmosphere, the weak crystallinity of the samples and the immiscibility gap described by Masson [8] for the natural "wredenburgite".

EXPERIMENTAL

Synthesis

The preparation of $Mn_{(3-x)}Fe_xO_4$ is done by a soft chemistry process [9]. The precursors are mixed manganese iron oxalate obtained by the co-precipitation of manganese and iron chlorides with oxalic acid, according to Eq.(1):

$$(3-x) \; MnCl_2,4H_2O + x \; FeCl_2,4H_2O + 3 \; H_2C_2O_4,2H_2O \rightarrow 3 \; [Mn_{(3-x)}Fe_x]_{1/3}C_2O_4,2H_2O + 6 \; HCl + 12 \; H_2O \tag{1}$$
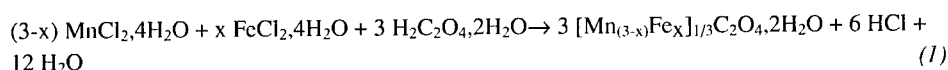
The chemical and the kinetic parameters of the reaction have to be well controlled. The metallic salts are dissolved in a mixed water, hydrochloric acid and ethylene glycol solution. The oxalic acid is dissolved in a 2-propanol solution with a concentration equal to the solubility limit at room temperature in this alcohol. The dissolution has to be made just before the precipitation in order to prevent the formation of an ester. The solution containing the salts, is quickly poured in the acid solution with a peristaltic pump. The pump is used to increase the saturation of the solution in order to favor the germination versus grain growth and to increase the number of germination sites. Such precipitation environment, with low dielectric constant allows the synthesis of mixed small size oxalate particles [10].

The precipitates are filtered, washed with distilled water in order to eliminate the remaining chlorides (tested by silver nitrate), washed by ethanol and dried overnight at 80°C. The powder is then grinded and sieved.

The next step of the process is the thermal decomposition of the oxalate precursor. The heating rate has to be low in order to keep the particle morphology (pseudomorphic transformation). Then the phase is reduced to obtain the stoechiometric spinel. The heat treatment of reduction is performed under a $H_2\backslash N_2\backslash H_2O$ mixture (flow rate ratio of 1%\49%\50% respectively) at 300°C for 5 hours. Then the samples are treated at 560°C for 2 hours in nitrogen in order to increase the crystallinity.

Analysis

A SIEMENS D501 diffractometer, equipped with a SiLi counter using $Cu_{K\alpha}$ radiation ($\lambda=0.15418$ nm) was used for the XRD analysis. Chemical analyses were performed by plasma emission spectrometry. TEM observations and microprobe analysis were made by a JEOL 2010 with a video acquisition card. The UTHSCSA ImageTool software has permitted to carry on the image analysis for granulometric distribution for a minimum of 100 particles.
Thermogravimetric analysis (TGA) was performed using a SETARAM TAG 24 apparatus and DTA by a SETARAM TAG92. Magnetic measurements have been done at room temperature with a hysteresismeter M2000 (S2IS), which allows a maximum applied magnetic field of 25 kOe. Samples were packed with a density of about 0.5 g/cm^{-3}.

RESULTS AND DISCUSSION
Precursor oxalate powders
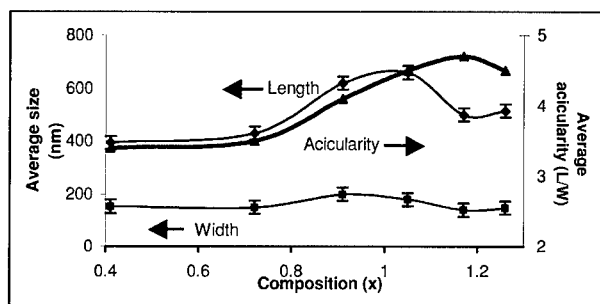
Figure 1 : Morphological evolution of the $(Mn_{(3-x)}Fe_x)_{1/3}C_2O_4$, $2H_2O$ oxalate as a function of composition

The oxalate particles obtained have a needle-like shape for the whole composition. The particles length and width have been determined for the different compositions (see figure 1). The size of the needles slightly changes with the composition. When the iron content varies from 0.4 to 1 the particles length increases from 400 to 600 nm. For the richer iron content, the length decreases again. The granulometric distribution shows a monomodal distribution for all the samples. These analyses prove that the particles morphology is controlled, but can slightly change with the Mn content.

The XRD patterns indicate (see figure 2) that the oxalate crystallize in the β iron oxalate structure described by Deyrieux [11]. The variation of the cell parameters is characteristic of a solid solution accorded to Vegard's law. When the concentration of manganese is high ($x < 0.9$) a small amount of manganese oxalate α is detected. However, the granulometric distribution is monomodal and electronic probe analysis shows an increasing Mn content at the edge of the particles. Therefore, the secondary phase observed is due to heterogeneous secondary germination, located at the edge of the particles.
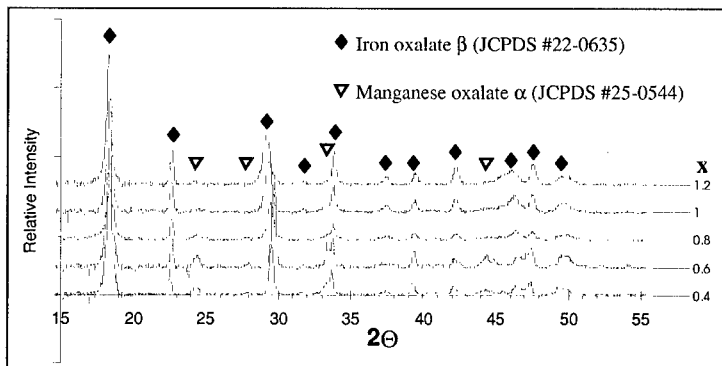
Figure 2: X-ray diffraction pattern of $(Mn_{(3-x)}Fe_x)_{1/3}C_2O_4$, $2H_2O$
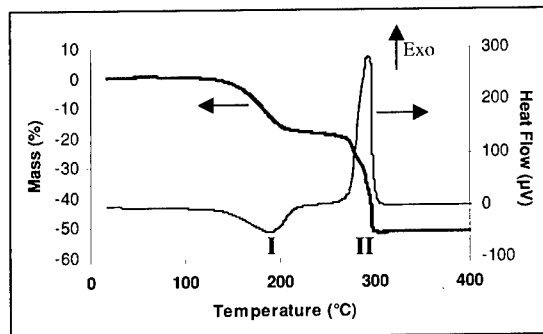
Figure 3: Thermogravimetric analysis of $(Mn_{1.7}Fe_{1.3})_{1/3}C_2O_4, 2H_2O$

The thermogravimetric analysis in air indicates that the decomposition take place in two steps for the whole composition (see figure 3). The first step (I) is endothermic and corresponds to the dehydration of two water molecules. The second step (II) is exothermic and is attributed to the decomposition of the oxalate with the release of three moles of CO and one of CO_2, according to:

$$2 (Mn_{(3-x)}Fe_x)_{1/3}C_2O_4, 2H_2O \rightarrow \alpha\text{-}(Fe_x Mn_{(3-x)})_{2/3}O_3 + 3 CO + CO_2 + 2H_2O \qquad (2)$$
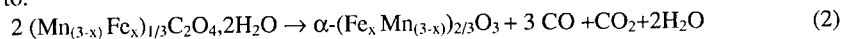
For the whole composition, the stable phase in air at 600°C is $\alpha\text{-}(Mn_{(3-x)}Fe_x)_{2/3}O_3$, so a reductive atmosphere should be used in order to obtain the spinel phase.

The exact description of the thermal treatment is given in the experimental procedure. The oxide particles have a stick shape (see figure 4). This observation indicates that the transformation is pseudomorphic. The size of the cristallite is approximatly 50 nm length and 25 nm width. This shape anisotropy is well known to favour an increase in coercive field [12].

The synthesized oxides are very reactive with oxygen due to their high division state (Sw = ~30 m^2/g). Then, the cations in the spinel structure can be oxidized in air, even at low temperature (T~200°C). The oxidation treatment leads to vacancies phases with mixed valences. Because the oxides are reactive enough, each cation can be oxidized at a given temperature [13]. Then, the analysis of the derivative thermogravimetric analysis signal can be used to quantify the cation content on the tetragonal and the octahedral sites of the spinel structure.

Figure 4 : TEM image of $Mn_{1.7}Fe_{1.3}O_4$

Cationic distribution and magnetic properties

This analysis has been performed on the stoechiometric spinel of composition x = 1.3 and gives the following cationic distribution [3]:

$$Mn^{2+}_{0.73} Fe^{3+}_{0.27} [Mn^{2+}_{0.27} Fe^{3+}_{0.95} Mn^{3+}_{0.78}] O^{2-}_4$$
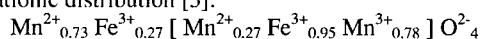
This cationic distribution is closed to the cationic distribution of an oxide of same composition, made at high temperature (T=1100 °C) and analyzed by Mossbauer technique [14,15]. The coercive field of the stoechiometric spinel prepared for our work, was 100 Oe (~0.8 kA.m^{-1}). This stoechiometric spinel phase has been oxidized for 2 hours at 275°C in air and quenched, then analyzed again. The structural formula was estimated to be:

$$Mn^{2+}_{0.73} Fe^{3+}_{0.27} [Mn^{2+}_{0.09} Fe^{3+}_{0.95} Mn^{3+}_{0.96}] O^{2-}_{4.09}$$
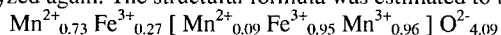
At this temperature, only the Mn^{2+} ions in octahedral sites have been oxidized into Mn^{3+} ions. The coercive field was measured at 2500 Oe (~ 200 kA.m^{-1}), is closed to the coercive field determined by A. Agnoli [3].

Thermodynamic calculations for a new reduction process

Finally, thermodynamic calculations has been done on the pure phases of the Fe-Mn system in order to better understand the difficulties to synthesize stoechiometric spinel phases. Thermodynamic data has been collected from Fritsch et al. [16] for the Mn-O system, Laberty et al. [17] for the Fe-O system an from Knacke et al. [18] for the other data.

Calculation results are presented on an Ellingham diagram (Figure 5). The stability domain of the single bulk oxides and the partial pressure of air, nitrogen and the $H_2 \backslash N_2 \backslash H_2O$ gas mixture are reported. The partial pressure of the gas mixture is located in the stability domain of Fe_3O_4, so this process is well adapted to obtain pure stoechiometric iron spinel even with low Mn content. It is confirmed with the diagram of the stability region of $MnFe_2O_4$ versus oxygen [19].

However, this gas mixture is also located in the stability domain of the wurstite MnO. Therefore, with higher Mn content the wurstite phase appears as a second phase during the reduction process. For high Mn content, the oxygen partial pressure should be around 10^{-20} atm. at low temperature (T~500°C). The $H_2 \backslash N_2 \backslash H_2O$ mixture can't be used to produce this stoechiometric spinel at low temperature, because the water content in the gas should be huge compared to nitrogen content to prevent wurstite formation during the process. For the same reason, it is difficult to use a $CO \backslash CO_2$ mixture.
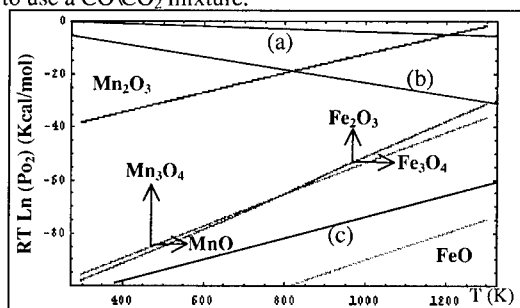
Figure 5: Calculated Ellingham diagram of the Mn-Fe system, oxygen partial pressure of air (a), nitrogen (b) and the 1% $H_2 \backslash 49\%$ $N_2 \backslash 50\%$ H_2O mixture (c)

A new reduction process has been thought to produce the correct gas mixture: the electrochemical oxygen pump [20]. Previous studies dedicated to this electrochemical oxygen pump have shown that it is possible to create reducing atmospheres with 0.2 atm $<P_{O_2}<10^{-20}$ atm using a starting gas containing a few content of O_2, H_2 or CO [21].

CONCLUSIONS

Needle shape manganese iron oxides $Mn_{(3-x)}Fe_xO_4$ powders have been synthesized by a "chimie douce" technique. This process allows to control perfectly the morphology and the size of the particle powder. The coercive field of an oxide of composition x = 1.3 with such characteristics was measured at 2500 Oe. The difficulty to produce higher Mn content spinel can be explained by the thermodynamical behaviour of these oxides. A new device, using electrochemical oxygen pump is in progress of development and it is believed that it should be well adapted to produce high Mn content stoechiometric spinel with a good reproducibility.

REFERENCES

[1] P. Tailhades, B. Gillot, A. Rousset, *J. Phys.IV France*, 7, C1-249 (1997)
[2] P. Tailhades, C. Villette, A. Rousset, G. U. Kulkarni, K. R. Kannan, C. N. R. Rao, M. Lenglet, *J. Solid State Chem.*, **141**, 56 (1998)
[3] F. Agnoli, B. Albouy, P. Tailhades, A. Rousset, *C.R. Acad. Sci. Paris*, t.2, Série II c, 525 (1999)
[4] E. Rezlescu, N. Rezlescu, *J. Magn. Magn. Mater.*, **193**, 501 (1999)
[5] D.G. Wickham, *J. Inorg. Nucl. Chem.*, **31**, 313 (1969)
[6] P. Holba, M.A. Khilla, S. Krupicka, *J. Phys. Chem. Solids*, **34**, 387 (1973)
[7] S. Guillemet-Fritsch, S. Viguié, A. Rousset, *J. Solid State Chem.*, **146**, 245 (1999)
[8] B. Mason, *Geol. Föreh. Stockholm Föerh*, **65**, 97 (1943)
[9] P. Mollard, A. Collomb, J. Devenyi, A. Rousset, *I.E.E.E Trans. Mag.*, **11**, 3, 894 (1975)
[10] A. Rousset, P. Mollard, C. Bonino, M. Gougeon, P. Tailhades, *European Patent*, EP 86 905 853.7.
[11] Deyrieux, Peneloux, *Bull. Soc. Chim. Fr.*, 2675 (1969)
[12] E. C. Stoner, E. P. Wohlfarth, *Phil. Trans. R. Soc. London Ser.*, **A240**, 599 (1948)
[13] B. Gillot, M. El Guendouzi, P. Tailhades, A. Rousset, *Reactivity of Solids*, **1**, 139 (1986)
[14] T. Battault, R. Legros, A. Rousset, *J. Eur. Ceram. Soc.*, **15**, 1141 (1995)
[15] B. Gillot, M. Laarj, S. Kacim, *J. Mater. Chem.*, **7**, 5, 827 (1997)
[16] S. Fritsch, A. Navrotsky, *J. Am. Ceram. Soc.*, **79**, 7, 1761 (1996)
[17] C. Laberty, A. Navrotsky, *Geoch. Cosm. Acta*, **62**, 17, 2905 (1998)
[18] O. Knacke, O. Kubachewski, K. Hesselmann, *Thermochimical Properties of Inorganic Substances*, Spinger-Verlag (1991)
[19] G. Bonsdorf, K. Schäfer, K. Teske, H. Langbein, H. Ullmann, *Solid State Ionics*, **110**, 73 (1998)
[20] J. Besson, C. Deportes, M. Kleitz, *French Patent*, 1.580.819 (1969)
[21] Y. K. Agrawal, D. W. Short, R. Gruenke, R. A. Rapp, *J. Electochem. Soc.*, **121**, 3, 354 (1974)

Modification of the magnetic properties of longitudinal thin-film media by ion-beam irradiation

Jason D. Wright[1] and Kannan M. Krishnan
Materials Sciences Division, Lawrence Berkeley National Laboratory
Berkeley, CA 94720
[1]Department of Materials Science, University of California, Berkeley
Berkeley, CA 94720

ABSTRACT

The modification of conventional longitudinal recording media by ion-beam irradiation is of both scientific and technological interest. In particular, patterning by irradiation through a stencil mask at the 50 nm length scale may fulfill the promise of a commercially viable patterned media architecture. In this context, the magnetic properties and microstructural evolution of high-coercivity longitudinal thin film media were investigated after ion-beam irradiation. TRIM simulations were used to calculate the depth profiles and damage distributions as a function of energy and dose for carbon, nitrogen, and chromium ions and three different media (C, Cr, no capping layer). Corresponding implantations were carried out and hysteresis curves were measured using a vibrating sample magnetometer (VSM). Using chromium ion implantation at 20 keV, both remanence and coercivity were reduced to zero, i.e., rendering the ferromagnetic thin film paramagnetic, at doses as low as 1×10^{16} cm^{-2}. For C$^+$ implantation at 20 keV, remanence and coercivity were also reduced to varying extent up to doses of 5×10^{16} cm^{-2} after which further irradiation had no effect. Slight decreases in remanence and coercivity were observed for 20 keV N$_2{}^+$ irradiation. XRD measurements indicate that the hexagonal cobalt alloy phase remains intact after irradiation. The physical and magnetic domain structures at the surface were assessed by atomic force and magnetic force microscopy. Combined with the development of a suitable stencil mask, such chromium ion implantation can be used to develop a viable patterned media with nanoscale dimensions, consisting of locally defined ferromagnetic and paramagnetic regions. This work is in progress.

INTRODUCTION

Improvements in the ability to carefully control the magnetic properties of thin films have made significant contributions to the recent 60% growth rate in the areal bit density of magnetic recording media. Historically, these improvements have been associated with reductions in grain size and advances in grain isolation (made necessary by statistical noise constraints requiring a certain number of grains per bit). The superparamagnetic effect, a grain size limit that renders magnetic moments unstable with respect to thermal fluctuations, represents a fundamental roadblock to the current regime of media development. Since the magnetic properties of interest in such recording systems occur in the near-surface region, ion beam processing may be an appropriate means of asserting yet further control over the important physical, chemical and magnetic microstructures of these films. Baglin et al.[1] have previously reported the loss of uniaxial anisotropy and

an increase in coercivity in Permalloy thin films with irradiation by a number of ion species at MeV energies.

Modifying the properties of ferromagnetic thin films is both of scientific and technological interest. If an ion-beam process that induces a ferromagnetic-to-paramagnetic transition ($M_s \rightarrow 0$) can be identified at room temperature, patterning through a stencil mask at the 50 nm length scale may fulfill the promise of a commercially viable patterned media architecture. For example, Chappert et al.[2] and Weller et al.[3] have reported local variations in coercivity and easy magnetization axis in Co/Pt multilayers via light ion irradiation near the MeV energy range.

In this research, we investigate the effect of Cr^+, C^+, and N_2^+ irradiation on the magnetic properties of a commercial CoCrPt thin-film media. Our approach is to introduce structural and chemical changes by systematically varying the ion species and qualities of the protective cap layer. Protective overcoats in commercial media range in thickness up to 250 Å. Controlling the amount of energy absorbed by cap layer atoms will change the ion range and damage profiles. Furthermore, a certain number of these carbon and chromium atoms will recoil, coming to rest within the CoCrPt layer. The saturation magnetization of CoCr-alloys is well known to decrease with Cr enrichment, approaching zero at roughly 25 at% Cr [4]. Diffusion of carbon atoms into CoCr-alloys has also been shown to decrease M_s [5]. Both species reduce the Curie temperature of cobalt alloys. It is reasonable to expect that C^+ and Cr^+ implantation into CoCrPt thin films will result in similar compositional effects. Nitrogen ions, in the form of the relatively inert N_2^+, should introduce large numbers of target displacements through collision cascade dynamics. The resulting expansion of the lattice may weaken the exchange interaction by increasing the ratio of interatomic separation to $3d$-orbital radius, as predicted by the Bethe-Slater curve [6-8].

EXPERIMENT

Commercial thin-film recording media, prepared by dc magnetron sputtering on aluminum disk substrates, were obtained courtesy of Seagate Recording Media (Fremont, CA). The complete film structure was $Al/Ni_{77}P_{23}(>0.5 \ \mu m)/Cr_{83}Ta_{17}(320$ Å$)/Co_{72}Cr_{18}Pt_{10}(100$ Å$)$, as determined by Rutherford backscattering spectrometry. Thin cap layers of Cr and C defined additional variations of the media based on the film structure mentioned above. These films were machined and backside thinned to produce 8 mm disk samples. The in-plane and plane normal magnetic hysteresis curves were characterized along the circumferential orientation of the original disk by using a vibrating sample magnetometer (VSM) with saturating fields of ±14 kOe. The structural properties of the as grown films were determined using XRD. TRIM[9] simulations were used to model and optimize the irradiation process for C^+, N_2^+ and Cr^+ irradiation in the C/Cr capped and uncapped media. Corresponding implantations were carried out at 20 keV incident energy; structural and magnetic properties as a function of ion dose were characterized by XRD and VSM. Atomic force (AFM) and magnetic force microscopy (MFM) was performed on a Digital Instruments Nanoscope Dimension 3000 Scanning Probe Microscope in tapping LiftMode®. The probe tip was etched Si tip sputter coated with a CoCr thin film.

RESULTS

Figure 1 shows the TRIM concentration and damage event profiles as a function of depth for 20 keV C^+, N_2^+ and Cr^+ implantation in the Cr capped media. The composition and thickness of the cap layers influence these distributions by absorbing energy from energetic ions. The TRIM results were used to determine optimum irradiation conditions and cap layer thickness based on the twin goals of delivering a peak concentration of either ions or damage events within the magnetic layer. The concentration and damage profiles of chromium and nitrogen ions, respectively, peak within the magnetic layer. In order to study all ion species at constant incident energy, larger doses were selected for C^+ implantation. TRIM was also used to relate the physics of ion-solid interactions to observed changes in magnetic properties.

As determined by VSM, the coercivity (H_c) and saturation magnetization (M_s) as a function of ion species, dose, and cap layer are plotted in Figure 2 for incident energies of 20 keV. The magnetization was completely in-plane. Both M_s and H_c decreased with dose in all cases, in contrast with the results of Baglin et al.[1], who observed increasing H_c. The rate of decline is quite different for each respective ion species. Chromium ions caused the most dramatic change in magnetic properties; both H_c and M_s were reduced to zero (within instrument sensitivity) at doses as low as 10^{16} Cr^+ cm^{-2}. Carbon ions achieved similar, although incomplete, reductions in magnetic properties but at higher doses. These observations are consistent with the chemical effects expected from adding C or Cr into a CoCr-alloy. The much weaker response to nitrogen ions suggests that ion-induced lattice disruption does not play a dominant role here.

From Figure 2 it is also apparent that cap layers play an important role in the evolution of magnetic properties with dose. Both coercivity and saturation magnetization decline more rapidly in capped film structures. This behavior is most striking for C^+ and Cr^+ irradiated systems and is perhaps explained by the transfer of energy from incident ions to the cap layer, leading to shallower depth profiles which retain more implanted species within the magnetically active $Co_{72}Cr_{18}Pt_{10}$ layer. Ion-beam mixing might also
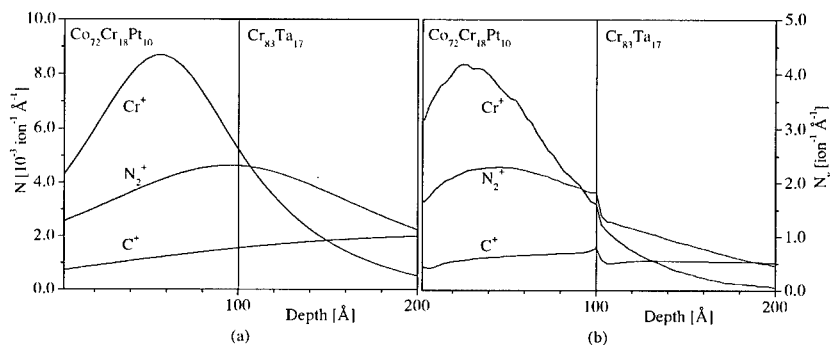
Figure 1. TRIM simulations of (a) projected range and (b) damage distributions for 20 keV ion implantation in $CoCrPt/Cr_{cap}$ media (cap layer not shown).
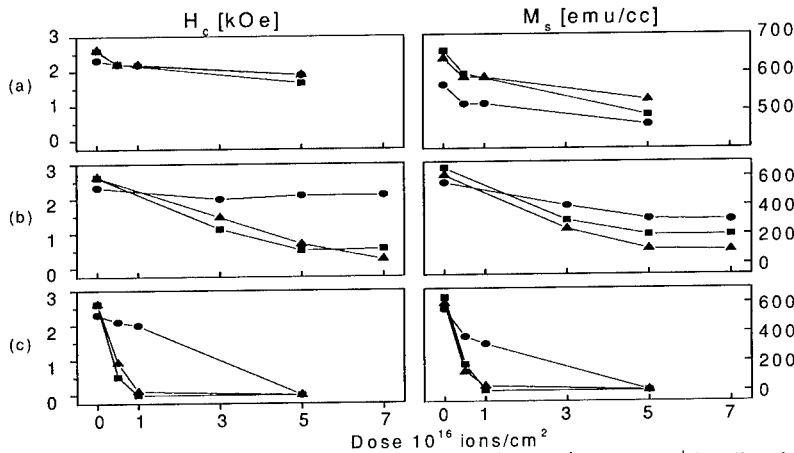
Figure 2. Magnetic properties of 20 keV (a) N_2^+, (b) C^+ and (c) Cr^+ irradiated films in uncapped (circles), C_{cap}, (squares), and Cr_{cap} (triangles) media.

lead to more rapid accumulation of Cr and/or C as recoiling cap layer atoms near the interface come rest within the magnetic layer.

It is noteworthy that M_s and H_c evolve in a similar manner with dose of C^+, N_2^+, and Cr^+; moreover, the parallel decline of these properties suggests the uniaxial magnetocrystalline anisotropy constant K_u of the CoCrPt phase declines even more rapidly than M_s. While M_s and K_u are fundamental material properties, H_c is microstructure-sensitive, scaling as $H_c \propto 2K_u / M_s$ [10]. For chromium ion implanted films, the implied decrease in K_u is agrees with Iwasaki et al. [11], who reported the intrinsic magnetocrystalline anisotropy constant in sputtered CoCr thin films declined with Cr content from 37×10^5 erg cm^{-3} (10 at% Cr) to 1.3×10^5 erg cm^{-3} (25 at% Cr).

X-ray diffraction scans for equivalent doses of 20 keV C^+, N_2^+, and Cr^+ irradiated films with Cr cap layers are shown in Figure 3, demonstrating the CoCrPt phase generally retains $(11\overline{2}0)$ texture without change in lattice spacing. These scans prove that the observed changes in magnetic properties are not due to successive removal of cap and magnetic layer by sputtering. The 0.396% compression (Cr^+ ions) and 1.67% expansion (C^+ ions) of the Cr (002) planes may be due to the respective accumulation of displacement events or carbon ions within the CrTa adhesion layer, as predicted by TRIM simulations (Figure 1).

Figure 4 shows AFM and MFM images of as grown and 20 keV 3×10^{16} Cr^+ cm^{-2} irradiated Cr_{cap} media in a remanent magnetization state. The AFM/MFM image pairs represent topographic and magnetic data taken from identical regions of the sample surface. The lines of vertical contrast in the AFM scans represent mechanical texturing along the circumferential direction of the disk. The AFM signal may be characterized by the rms surface roughness, which increases from 1.21 to 1.46 nm with implantation.

Although MFM does not directly measure the surface magnetization, the contrast, a stray field mapping above the as grown media, certainly suggests the presence of domains. Likewise, the lack of MFM contrast from the irradiated sample implies the
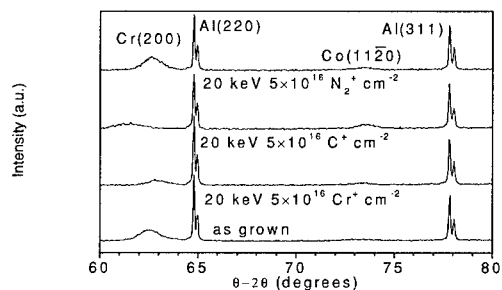
Figure 3. XRD θ-2θ scans of as grown and irradiated CoCrPt/Cr$_{cap}$ media.

absence of magnetic moment in the near surface region. These MFM images are consistent with expectations based on earlier magnetic property measurements (Figure 2), and represent further evidence for a ferromagnetic-to-nonmagnetic transition of the CoCrPt layer.

CONCLUSIONS

The effect of 20 kV C^+, N_2^+ and Cr^+ implantation on CoCrPt ferromagnetic thin films was characterized by VSM, XRD, and scanning probe microscopy (AFM/MFM). Both M_s and H_c decreased in parallel with dose for all species. The magnitude of response
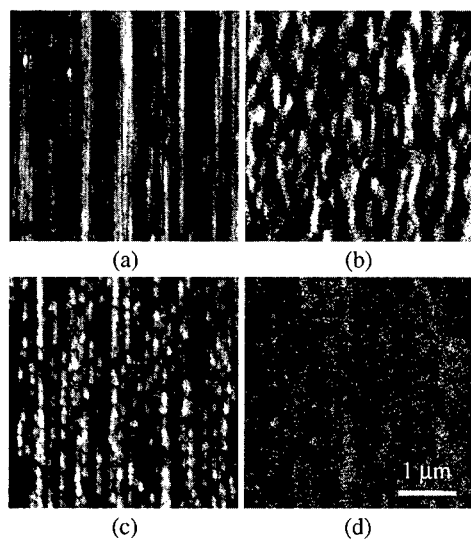
Figure 4. Scanning probe microscopy of CoCrPt/Cr$_{cap}$ media: (a) AFM and (b) MFM of as grown samples; (c) AFM and (d) MFM of 20 kV 3×10^{16} Cr$^+$ cm^{-2} samples.

followed the series $N_2^+ < C^+ < Cr^+$ and was greatest for samples with protective cap layers. We have shown that, for 20 keV Cr^+ ion implantation at doses as low as 10^{16} ions cm^{-2}, the magnetization of $Co_{72}Cr_{18}Pt_{10}$ longitudinal media exhibits essentially paramagnetic behavior. The mild increase in surface roughness revealed by AFM suggests the post-irradiation surface state remains compatible with small read head-media fly heights. Although there is some evidence pointing to chemical, rather than structural, effects, TEM characterization of the physical, chemical and magnetic microstructures is required to further elucidate the mechanisms of ion-induced magnetic property changes. Combined with the development of a suitable stencil mask, such chromium implantation might be used to fabricate a viable patterned media, which would consist of locally defined regions of ferromagnetic and nonmagnetic character. This work is in progress.

ACKNOWLEDGMENTS

REFERENCES

1. J.E.E.E. Baglin, M.H. Tabacniks, R. Fontana, A.J. Kellock, and T.T. Bardin, Materials Science Forum **248-249**, 87-93 (1996).
2. C. Chappert, H. Bernas, J. Ferre, V. Kottler, J.-P. Jamet, Y. Chen, E. Cambril, T. Devolder, F. Rousseaux, V. Mathet, and H. Launois, Science **280** (5371), 1919-1922 (1998).
3. D. Weller, J.E.E.E. Baglin, A.J. Kellock, K.A. Hannibal, M.F.A. Toney, G.A. Kusinski, S.A. Lang, L. Folks, M.E. Best, and B.D. Terris, Journal of Applied Physics **87** (9 pt. 1-3), 5768 (2000).
4. M. Doerner, T. Yogi, D. Parker, and T. Nguyen, IEEE Transactions on Magnetics **29** (6), 3667-3669 (1993).
5. J. Chang and K. Johnson, IEEE Transactions on Magnetics **34** (4), 1567-1569 (1998).
6. J. Slater, Physical Review **35**, 509 (1930).
7. J. Slater, Physical Review **36**, 57 (1930).
8. H. Bethe, Handbuch der Physik **24**, 595 (1933).
9. J. Ziegler, J. Biersack, and U. Littmark, *The Stopping and Range of Ions in Solids.* (Pergamon Press, Inc., New York, 1985) p. 1.
10. B. Cullity, *Introduction to Magnetic Materials.* (Addison-Wesley, Menlo Park, California, 1972) p. 233
11. S. Iwasaki, K. Ouchi, and N. Honda, IEEE Transactions on Magnetics **16**, 1111 (1980).

Improvement of crystallographic characteristics of CoCrTa thin film using double underlayer

Y.J.Kim*, S.H.Kong**, S.Nakagawa**, M.Naoe** and K.H.Kim*
*School of Electrical & Electronic Eng., Kyungwon Univ., Kyunggi-do 461-701, Korea
**Dept. of Physical Electronics, Tokyo Institute of Technology, Tokyo 152-8522, Japan

ABSTRACT

High c-axis oriented CoCr-based thin films are expected for ultra-high density recording media in perpendicular magnetic recording system. In order to improve dispersion angle of c-axis of CoCr-based for perpendicular magnetic recording media, we prepared trilayered film with double underlayer using New Facing Targets Sputtering apparatus. The thickness of magnetic layer CoCrTa and double underlayer, such as interlayer Pt, paramagnetic CoCr, underlayer Ti was fixed 50nm and 20nm respectively. In order to prepare the thin film, we fixed argon gas pressure 1mTorr, substrate temperature 250°C and input current 0.5A. The crystallographic characteristics of CoCrTa layer with varying interlayer thickness (0- 20nm) have been investigated. By the result, the CoCrTa trilayered thin film with interlayer Pt showed good c-axis orientation 3.45° and 3.62° at thickness 5nm and 10nm respectively. However, CoCrTa thin film using interlayer paramagnetic CoCr showed 8.28° and 8.62° at thickness 5nm and 10nm respectively.

INTRODUCTION

Perpendicular magnetic recording [1] is regarded as a candidate for achieving ultra-high density above 100Gbits/in^2 [2]. Among the rest thin films of Co-Cr alloy with thickness of several tens of nanometers are known as most compatible media due to easiness of thin film preparation, and control of coercivity and saturation magnetization. In these thin film media of Co-Cr alloy the most important things are realization of being low-noise and high recording density. To overcome these, it is necessary to be thinner the thickness of ferromagnetic recording layer, and necessary to be finer grains. However, because of the formatted initial layer that exhibited to bad perpendicular characteristics, it should be improve magnetic characteristic of magnetic layer and be thinner the initial layer as much as a possible [3]. In this study, the effects of inserting interlayer to CoCrTa/Ti doublelayer media for perpendicular magnetic recording are observed.

EXPERIMENTAL DETAILS

Films were prepared by using the New Facing Targets Sputtering apparatus with box type sputtering units. FTS [4,5] was in which substrate was located apart from plasma, so called

plasma free, and could restrain bombardment to substrate from γ-electron and negative ion as high-energy particles and maintain the stable electrical discharge at low gas pressure. Forming the magnetron mode with varying location of a permanent magnet, NFTS [6] can confine plasma effectively and expand efficiency area of target. Also, FTS can prepare the thin film that has a good compositional segregation and spinodal decomposition. Ti [7] as underlayer, CoCrTa as magnetic layer, and an interlayer of Pt and paramagnetic CoCr were deposited on Si substrate. The background pressure was 5×10^{-7} Torr. The substrate temperature fixed at 250°C. Sputtering processing was performed at input current 0.2 A under Ar gas pressure of 1 mTorr. The thickness of magnetic layer and underlayer were 50 nm and 20 nm respectively. To investigate the effect of annealing, postannealing was carried in vacuum of 5×10^{-6} Torr at 100-500°C for 1hour. Magnetic properties were measured by using a vibrating sample magnetometer (VSM), and the crystalline orientation of the film was investigated by X-ray diffractometer. The surface of film was observed by atomic force microscopy (AFM).

DISCUSSION

Figure 1 shows XRD patterns of prepared films on variation of interlayer thickness. Diffraction intensity of Co (002) of CoCrTa/[Pt/Ti] was five times stronger than CoCrTa/[CoCr/Ti] and CoCrTa/Ti. This result suggests that crystalline growth of Pt is well at high temperature and Pt promote crystalline growth of CoCrTa layer deposited on it.
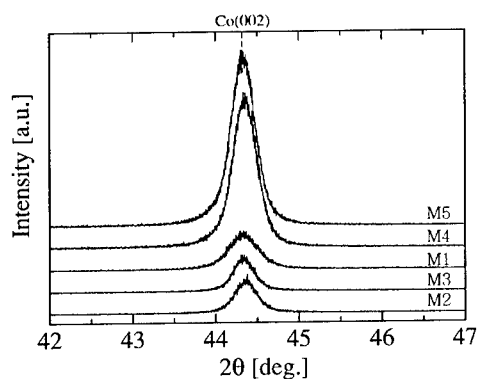
Figure 1. XRD patterns of prepared films on variation of interlayer thickness

Table 1. Perpendicular coercivity $H_{c\perp}$, in-plane coercivity $H_{c//}$ and dispersion of the c-axis orientation $\Delta\theta_{50}$ of prepared thin film.

Media	Layer Structure	$H_{c\perp}$ [kOe]	$H_{c//}$ [kOe]	$\Delta\theta_{50}$ [deg.]
M1	CoCrTa/Ti (20)	1.67	0.398	5.69
M2	CoCrTa/[CoCr (10)/Ti (10)]	1.03	0.432	8.62
M3	CoCrTa/[CoCr (5)/Ti (15)]	1.32	0.552	8.28
M4	CoCrTa/[Pt (10)/Ti (10)]	1.91	0.372	3.62
M5	CoCrTa/[Pt (5)/Ti (15)]	1.98	0.344	3.45

* Number of parentheses shows thickness of film

Table 1 shows perpendicular coercivity $H_{c\perp}$, in-plane coercivity $H_{c//}$ and dispersion of the c-axis orientation $\Delta\theta_{50}$ of prepared thin film.

Dispersion of the c-axis orientation $\Delta\theta_{50}$ of CoCr-based thin films with the c-axis perpendicular to the film plane was evaluated from the full width at half maximum o f the rocking curve of Co(002) peak.

$H_{c\perp}$, $H_{c//}$ and $\Delta\theta_{50}$ of prepared thin film with Pt interlayer exhibit a good value compared with that of paramagnetic CoCr layer. This result is due to superior matching between Pt (111) plane and CoCrTa (002) plane than paramagnetic CoCr deposited on Ti underlayer. Figure 2 shows AFM images of CoCrTa/[Pt/Ti] and CoCrTa/[CoCr/Ti] trilayered film at interlayer 5nm thickness. Scan size is 1×1μm. As shown in Figure 2, crystalline grain of magnetic layer of trilayered film with Pt interlayer was explicitly observed than paramagnetic CoCr.
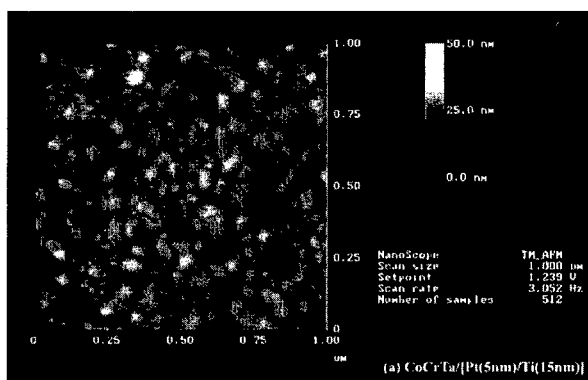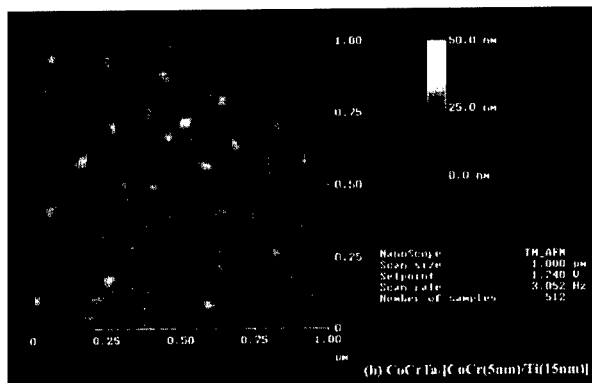
Figure 2. AFM images of (a) CoCrTa[Pt(5nm)/Ti(15nm)] and (b) CoCrTa[CoCr(5nm)/Ti(15nm)] trilayered film(R_a: (a) 1.816nm, (b) 1.274nm).

The effect of crystallographic and magnetic characteristics on varying annealing temperature was investigated. Figure 3 shows XRD patterns of trilayered film with interlayer of Pt on annealing temperature. For all of the prepared samples, it was observed that peak of crystalline plane of CoCrTa was moved at T_a 500°C. The reason for this behavior was exposed due to crystalline size that was affected by distance between planes. Figure 4 shows dependence of $H_{c\perp}$ and $\Delta\theta_{50}$ on annealing temperature. $\Delta\theta_{50}$ slightly decrease with increasing annealing temperature. However, at T_a is above 300°C, $H_{c\perp}$ drops rapidly.
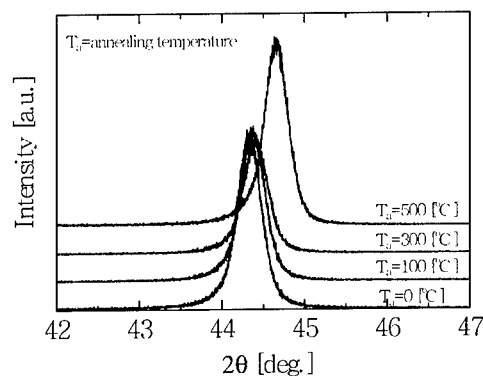
Figure 3. XRD patterns of CoCrTa/[Pt/Ti] trilayered thin film on annealing temperature.
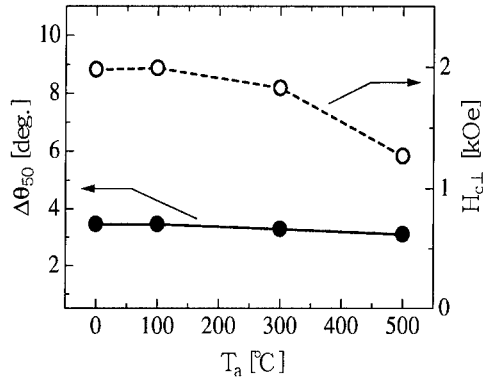
Figure 4. Dependence of $H_{c\perp}$ and $\Delta\theta_{50}$ of CoCrTa/[Pt/Ti] trilayered thin film on annealing temperature.

At first, making Pt element diffusing into Pt element into CoCrTa layer through annealing treatment, this experiment was intending to form CoCrPtTa crystallite with high perpendicular coercivity. However, perpendicular coercivity $H_{c\perp}$ was decreased due to segregation structure of magnetic layer according to homogenized with increasing annealing temperature.

Figure 5 shows AFM images of CoCrTa/[Pt(5nm)/Ti] for as-deposited and postannealed at 500°C. Average crystalline size was 34.02nm and 36.36nm respectively.
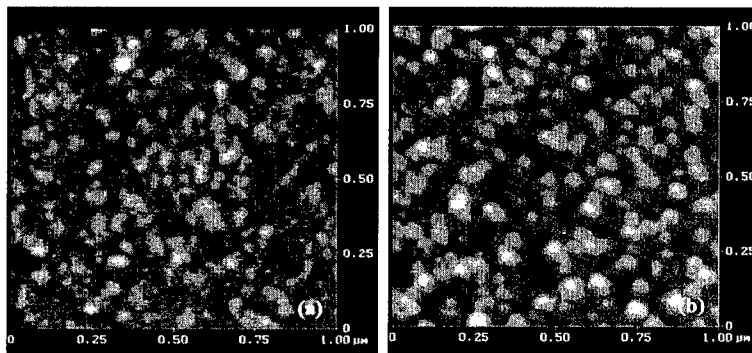
Figure 5. AFM images of as-deposited and postannealed at 500°C of CoCrTa/[Pt(5nm)/Ti] trilayered thin film. (a) as-deposited(R_a=1.816nm) (b) postannealed(500°C)(R_a=2.399nm)

CONCLUSIONS

We prepared CoCr-based trilayered thin film with varying interlayer thickness using the New Facing Targets Sputtering System. As a result, trilayered thin film with Pt interlayer shows good value of perpendicular coercivity and dispersion angle of c-axis compared with the film with CoCr interlayer. Also, trilayered film with 5nm of interlayer thickness had higher perpendicular coercivity $H_{c\perp}$ and had lower dispersion of the c-axis orientation $\Delta\theta_{50}$ than 10nm of interlayer thickness. Especially, trilayered film with Pt interlayer thickness of 5nm exhibited high perpendicular coercivity value about 2kOe and dispersion of the c-axis orientation 3.45°. That means epitaxial growth is achieved due to superior crystalline orientation of Pt and Ti layer at high temperature and matching between CoCrTa magnetic layer and Pt layer deposited on those. So, it was improved crystallographic and magnetic characteristics by inserting interlayer to CoCr-based thin film alloy.

A Crystallographic characteristic of CoCrTa/[Pt/Ti] trilayered film was improved about 3.1° of $\Delta\theta_{50}$ at annealing temperature 500°C. But, for effect of the interference between grain lattice, perpendicular coercivity was decreased.

REFERENCES

1. S.Iwasaki and K.Ouchi, *IEEE Trans. Magn.*, **MAG-14**, 5, 849 (1797)
2. S.Nakagawa, K.Takayama, A.Sato and M.Naoe, *IEEE Trans. Magn.* **35**, 2739 (1999)
3. C.Byun, E.M.Simpson, J.M.Siversen and J.H.Judy, *IEEE Trans. Magn.*, **MAG-21**, 1453 (1985)
4. Y.Nimura, Y.Kitamoto, S.Nakagawa and M.Naoe, *IEEE Trans. Magn.*, **23**, 2464 (1987)
5. K.H.Kim, S.H.Kong, I.H.Son, M.Naoe and S.Nakagawa, *Applied Surface Science*, **169**, 409 (2001)
6. S.Kadokura, M.Naoe, *J. Magn. Magn. Mater.*, **193**, 114 (1999)
7. O.Kitakami, K.Ojima, Y.Ogawa, T.Maro and H.Fujiwara, *IEEE Trans. Magn.*, **MAG-23**, 5, 27197 (1996)

Co/Pd Multilayer Based Recording Layers For Perpendicular Media

Dmitri Litvinov,* Thomas A. Roscamp[1], Timothy Klemmer,
Mei-Ling Wu, J. Kent Howard, and Sakhrat Khizroev
Seagate Research, Pittsburgh, Pennsylvania 15203
[1]Roscamp Engineering, Woodlane Park, Colorado 80866

ABSTRACT

The results of the experimental study of CoX/Pd multilayer based recording layers for perpendicular recording media are presented. The perpendicular magnetic recording media with multilayer recording layers and high moment soft underlayers were deposited by magnetron sputtering. It is shown how a favorable microstructure of the multilayer films can be achieved by the use of the appropriate buffer layers. The effects of boron addition to the cobalt layer in a multilayer recording layer is described. The feasibility of the aging process that leads to the reduced exchange coupling in the multilayer recording layer, is demonstrated. It is shown that boron addition to the cobalt layer accelerates the aging process.

INTRODUCTION

As the storage industry ramps the areal bit densities at increasingly higher rates, thermal instabilities in recording media begin to manifest themselves[1]. Perpendicular recording technology[2] while being technically close to conventional longitudinal recording and the least difficult technology to make the transition to if necessary[3, 4, 5, 6], addresses the issue of thermal stability for areal bit densities exceeding 100Gbit/in^2 [7].

Several candidates for the perpendicular media recording layers are being considered. Hexagonal single layer CoCr-based alloys are among the strongest candidates due to a wealth of knowledge about material properties accumulated over the years using these alloys for longitudinal media. The major drawback in using hcp Co alloys is the difficulty in achieving the high remanent squareness, preferably equal to one. Remanent squareness of less than one leads to substantial DC noise and potential thermal instabilities. L10 phases of CoPt, FePt, etc. suffer from the lack of knowledge of how to control the microstructure and magnetic properties. These highly attractive materials due to their high magnetic anisotropy can play an important role in the future magnetic recording technologies if the mentioned above technical difficulties are resolved.

An alternative approach is to use Co and Co-alloy based multilayers[8, 9, 10]. In this set of materials, the magnetic anisotropy is controlled by interfacial effects between Co and Pt or

*E-mail:dmitri.litvinov@seagate.com

Pd non-magnetic (but highly polarizable) spacer layers. The multilayers form an attractive class of materials since they exhibit high remanent squareness and easily controlled magnetic anisotropy with both aspects being critical for the thermal stability.

EXPERIMENTAL DETAILS

The media films were deposited by magnetron sputtering onto AlMg/NiP substrates at room temperature. The following general perpendicular media structure was utilized [substrate/buffer/soft underlayer/buffer/multilayer/overcoat]. $Ni_{45}Fe_{55}/Ta/FeAlN$ was used as a soft underlayer. Indium oxide doped with 10 wt% of tin oxide (ITO) was used as a seed/buffer layer to control the microstructure of the $(CoX/Pd)_N$ multilayer recording layer[8]. Tantalum was used as a buffer for Co/Pd multilayer films as well for comparison. Both pure Co and Co doped with 4% of boron were used in a multilayer structure. The multilayer films were deposited in 30mTorr of Kr. A 5nm hydrogenated carbon $(C:H_x)$ overcoat was used as a protective wear-resistive layer.

Single pole recording heads with the pole tip made of $Ni_{45}Fe_{55}$ alloy with a $4\pi M_S$ of 16kG and GMR based readers were used to test the media. The track width was $0.8\mu m$. Autocorrelation signal-to-noise (ACSN) ratio using a pseudo-random bit pattern covering spectral density from 0 to 200kfci was used as a signal-to-noise ratio (SNR) measurement technique.

A custom built polar Kerr magnetometer was used to measure the M-H loops. The structure of the films was determined using a Philips X-Pert Pro X-ray diffractometer and transmission electron microscopy (TEM)[11]. The compositional distribution of the films was studied by electron energy loss spectroscopy (EELS).

INFLUENCE OF ITO BUFFER LAYER ON THE MCROCSTRUCTURE AND ON THE MAGNETICS OF MULTILAYER FILMS

It is important to emphasize the role of ITO buffer layers on the microstructure and resulting magnetic properties of multilayer films. Figure 1 compares plain-view TEM micrographs of the multilayer films deposited on Ta and ITO seed layers. The morphologies of the two films are distinctly different. In the case of the Ta buffer layer, a usual polycrystalline granular structure is observed while in the case of the ITO buffer layer, the films appear to consists of agglomerates of grains that are surrounded by either different density or different elemental composition material. EELS revealed that the intergranular material is a CoPd alloy with substantially lesser density than the material that makes the body of the columns/grains.

The cross-sectional TEM micrograph shown in Fig. 2 compares the Co/Pd multilayer films grown on ITO and Ta buffer layers. The Co/Pd multilayer on ITO buffer exhibits two clearly distinct layers: a continuous film to about 1/4 of the film thickness followed a film represented by columns, or grain agglomerates, surrounded by lower density material regions. In contrast, the Co/Pd multilayer films grown on Ta buffer layer appears to have a continuous structure.

One can expect that the double-layer structure of the multilayer films would have a strong influence on the magnetic properties of the films and, ultimately, on the recording
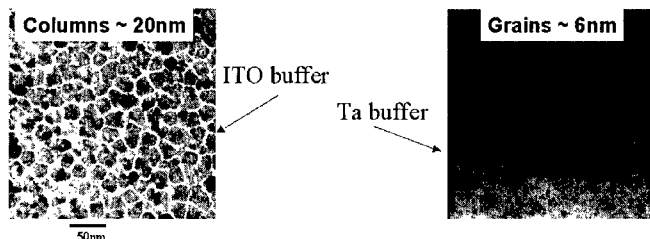
Figure 1: Bright field plain-view TEM images of Co/Pd multilayer films on Ta and ITO buffer layers.

performance of the media that utilizes such multilayers as recording layers. The distinctly different microstructures of the two layers will result in different magnetic properties of the two layers. Reduced exchange coupling is expected between the columns which are surrounded by lower density material while the bottom continuous layer is expected to be strongly exchanged coupled within the layer.

Figure 3 compares M-H loops of multilayer films grown on Ta and ITO buffer layers. In the case of a Co/Pd multilayer film deposited on a Ta buffer layer, the film is continuous and can be expected to be substantially exchange coupled. This strong exchange in the multilayer film grown on a Ta buffer is demonstrated in Fig.3 where mostly collective magnetization reversal takes place at essentially the same external field value (very high value of the slope in the reversal region). In the case of a Co/Pd multilayer film deposited on a ITO buffer layer where 3/4 of the film consists of exchange decoupled magnetic columns, the shape of the hysteresis loop is dramatically different, with a clearly finite slope of the magnetization reversal region and a drastically boosted coercivity value.

It is commonly believed that in multilayers the magnetic anisotropy is controlled by the interfacial effects between the layers and for that reason is called surface anisotropy. No significant crystalline texture was observed using X-ray diffraction in Co/Pd multilayer films grown on a ITO buffer, which further supports the view that the anisotropy arises predominantly from interfacial effects in the multilayer films (See Fig. 4.) This is in contradiction to previously published data where authors correlated the presence of < 111 > crystallographic texture in Co/Pd multilayers with the increase of magnetic anisotropy[12].
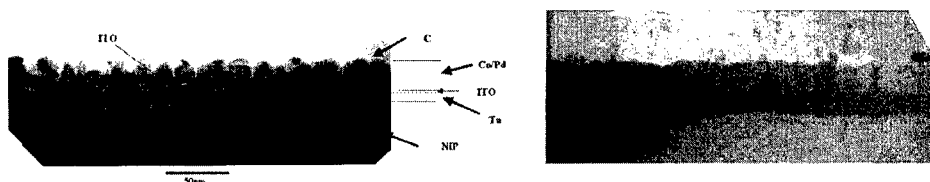
Figure 2: Cross-section TEM image of Co/Pd multilayer film on ITO buffer layer (left) and of Co/Pd multilayer film on Ta (right).
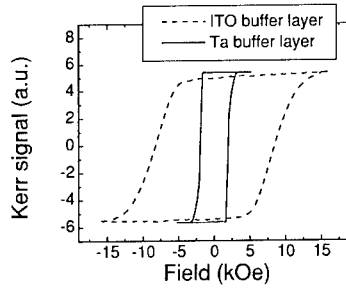
Figure 3: M-H loops for the multilayer films grown in ITO and Ta buffer layers.
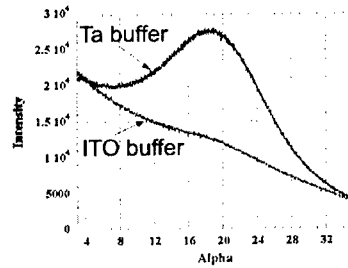
Figure 4: X-ray (111) rocking curves for Co/Pd multilayers grown on Ta and ITO buffer layers.

To further illustrate the importance of the correct microstructure of the multilayer films that the ITO buffer layer provides, the recording performance of the two multilayer based media (with Ta and ITO buffer layers) were studied. Figure 5 compares roll-off curves and SNR of the two media. A substantial improvement of the recording performance of the media with the ITO buffer layer is observed vs. media in which Ta is used as a buffer layer for the Co/Pd multilayer recording layer.

EFFECTS OF BORON ADDITION TO COBALT LAYER

Figure 6 compares roll-off curves and SNR of Co/Pd and CoB/Pd multilayer based perpendicular media. A clear improvement in both SNR and roll-off curves is observed with the boron addition. TEM studies of the multilayer microstructure did not reveal any measurable variation in the column size distribution leading to the conclusion that the most likely role of boron is of an additive facilitating better exchange decoupling of the magnetic columns.
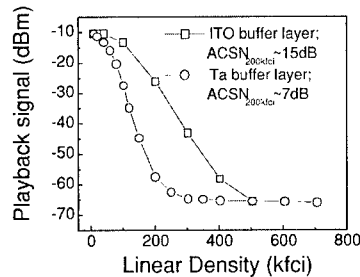
Figure 5: Roll-off curves and SNR for the media with ITO and Ta buffer layers for Co/Pd multilayer structure.
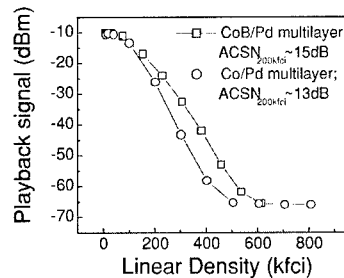
Figure 6: The effect of boron addition to the Co layer in the Co/Pd multilayer recording layer.

AGING EFFECTS

The recording performance of as deposited films was compared to the recording performance of the films exposed to ambient conditions for 180 days. As shown in Fig. 7 which compares the two sets of data, improved SNR and roll-off curves that extended to higher linear densities were observed in the "aged" films. One of the likely explainations of the observed improvement in the recording performance is preferential oxidation of the column boundaries as the lower density material in the grain boundaries facilitates oxygen and/or water vapor diffusion. Since no measurable aging effect was observed in Co/Pd multilayers without boron additions, one can conclude that boron additions act as a precursor for accelerated column boundary oxidation. Although 180 day aging is clearly not a manufacturable process, the observed aging phenomenon suggests feasible routes for improving the multilayer media performance via accelerated aging techniques such as aging in an oxygen rich environment at elevated temperatures.
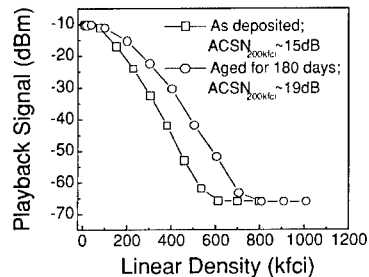
Figure 7: The Influence of the aging process on the recording performance of the multilayer based media.

SUMMARY

In summary, the effects of an ITO buffer on microstructure and magnetic properties of Co/Pd multilayer films has been studied. It was shown that boron additions improve the recording performance of Co/Pd multilayer based media. Furthermore, it is shown that boron works as a precursor in the aging of the CoB/Pd multilayer structures, helping to further improve the recording performance of multilayer based media.

References

[1] S. H. Charap, IEEE Trans. on Magn. **33**, 978 (1996).

[2] S. Iwasaki and Y. Nakamura, IEEE Trans. on Magn. **13**, 1272 (1977).

[3] D. A. Thompson, J. Magn. Soc. Jap. **21**, 9 (1997).

[4] S. Khizroev, M. Kryder, Y. Ikeda, K. Rubin, P. Arnett, M. Best, and D. Thompson, IEEE Trans. on Magn. **35**, 2544 (1999).

[5] D. Litvinov, M. Kryder, and S. Khizroev, J. Magn. Magn. Mater. **232**, 84 (2001).

[6] S. Khizroev and D. Litvinov, Perpendicular systems above 100 Gbit^2 density, presented at Joint MMM-Intermag 2001 in San Antonio, TX; to be published in *IEEE Tans. on Magn.*

[7] N. H. Bertram and M. Williams, IEEE Trans. on Magn. **36**, 4 (1999).

[8] T. K. Hatwar and C. F. Brucker, IEEE Trans. on Magn. **31**, 3256 (1995).

[9] K. Ho, B. Lairson, Y. Kim, G. Noyes, and S. Sun, IEEE Trans. on Magn. **34**, 1854 (1998).

[10] K. Takano, E. Fullerton, G. Zeltzer, A. Moser, and D. Weller, CoCr/Pt and CoB/Pt multilayers as perpendicular recording media, presented at MMM Conference in San Jose (1999).

[11] A. Roy, D. Laughlin, T. Klemmer, J. K. Howard, S. Khizroev, and D. Litvinov, J. Appl. Phys. **89**, 7531 (2001).

[12] W. Peng and J. Judy, Co/Pd & Co/Pt Superlattice on InSn Oxide Seed Layer for Perpendicular Recording, 1999, proceedings of 15th MINT Research Review, Univeristy of Minnesota.

In-Situ Characterization Of Ultra-Small Magnetic Junctions Made By Electrochemical Techniques

A. Sokolov, J.R. Jennings, C-S Yang, J. Redepenning[1] and B. Doudin
Department of Physics and Astronomy, [1] Department of Chemistry
University of Nebraska-Lincoln, Lincoln NE 68588-0111, U.S.A.

ABSTRACT

Electrochemical impedance spectroscopy is used to characterize the growth of NiO over Ni electrodes. We find a limited increase of thickness and a significant increase of porosity of the oxide as a function of time and anodization potential. Conductance measurements performed on Ni/NiO/Co junctions of 30 nm diameters indicate the presence of a Coulomb blockade at low temperatures and small bias. Tunneling is observed at higher bias. Small magnetoresistance ratios (1%) are found.

INTRODUCTION

Synthesis of a metal/insulator/metal system by electrochemical techniques is presented. We use template methods to make ultra-small ferromagnetic tunnel junctions, of interest for studying magnetoresistive sensors. The conductance of a ferromagnet/insulator/ferromagnet system is modified when switching the magnetic alignment of the two ferromagnetic contacts between parallel and antiparallel configurations [1, 2]. This junction magnetoresistance is of interest for making new types of magnetic sensors and memories [3]. The electrochemical technique we use is an original method for making such structures, and junctions with areas as small as 0.008 μm^2 can be prepared and investigated. Our first results showed remarkably large magnetoresistance (MR) effects in such junctions, and a model of conductance governed by impurity states in the barrier has been put forward [4]. Theoretical models of interplay between Coulomb blockades and tunnel magnetoresistance have been published recently [5 - 7]. In light of these models, our goal is to investigate the extent to which the MR in our systems is due to thermally enhanced sequential tunneling, co-tunneling [5] or spin accumulation [6, 7].

In-situ investigations during the synthesis of the insulating barrier are helpful in understanding and in controlling the morphological and electrical properties of the oxide barrier. We modulate the electrochemical process necessary to grow the barrier with an AC excitation. By monitoring the frequency dependent response of the system to this excitation, we can thus monitor and quantify the growth of the insulating oxide in-situ. Electrochemical impedance spectroscopy (EIS) is a well-established characterization method, and we can take advantage of the abundant literature on corrosion studies to compare our results with those obtained for other dielectric layers on conductors in electrochemical baths [8]. Under appropriate experimental conditions we are able to decouple the impedance of the electrochemical bath from the impedance due to the oxide coating. Correlation between the electric conductance of the metal-insulator-metal system and the EIS of the metal/insulator electrode gives a clearer picture of the morphology of the insulating oxide.

EXPERIMENTAL

Polycarbonate track-etched membranes were used as templates for the electrodeposition of wires with lengths of 7 µm and diameters as small as 30 nm [9]. Ni half-wires were plated using a Watt's bath. Anodization of Ni was performed in 0.075 M sodium borate and 0.3 M boric acid solution [10]. The Co overlayer was plated using a non-aqueous bath comprised of 0.1M cobalt chloride (anhydrous) in dimethylformamide or ethylene glycol. Deposition of the cobalt overlayer was performed in a nitrogen atmosphere (containing less than 3 ppm of oxygen and water) to eliminate side reactions possible during the Co plating [4].

EIS studies were performed in the sodium borate bath during the anodization process. A frequency response analyzer coupled with an electrochemical interface was used to record the spectrum. Figure 1 shows a theoretical EIS spectrum of a thin dielectric coating of a metal, with the corresponding equivalent circuit. Extensive literature can be found on the subject [11]. At high frequencies the kinetics of the redox processes (elements R1, C1 and R2a) dominate the response. This is manifested by a high-frequency half-circle in the Nyquist plot (Figure 1). In mid range frequencies, the dielectric thin film contributes through elements R2b, R3 and CPE1 to the second half-circle of the spectrum. The constant phase element expresses a frequency-dependent capacitance that is observed for very thin films. In detailed analysis, deviations from perfect capacitance can be interpreted in terms of film porosity. At low frequency, the dominant mass transfer process is represented by the lumped elements W1 (Warburg impedance), R4 and CPE2. Ex-situ electrical connections were made to single wires by monitoring the deposition current as described previously[12]. Low temperature investigations were performed in a helium cryostat under magnetic field of ± 10 T range.
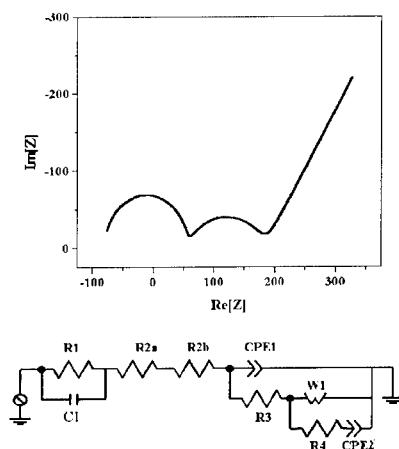
Figure 1. Nyquist plot of a theoretical electrochemical impedance spectrum, with the related equivalent circuit. The dielectric coating is represented by the lumped elements R2b, CPE1 and R3.

RESULTS

Systematic measurements of the EIS spectrum of Ni/NiO systems were performed as a function of time and anodization potential. Figure 2 shows the evolution of the spectrum with time. The half circle at mid-range frequencies (between and 1 kHz and 100 kHz typically) can be attributed to the presence of a dielectric layer on the electrode surface; however, care should be exercised in making a quantitative interpretation of the data. In-situ EIS is advantageous because the insulator of interest can be characterized as it is grown. Unfortunately, the impedance of the bath is convolved with that of the circuit elements of interest. For example, the low impedance values found at low frequencies are associated with mass transfer processes. As a result, reliability of absolute values for the insulator properties is decreased when chemical processes occur. Qualitative information can be obtained by measuring the time evolution of the EIS response at a frequency (e.g., 5 kHz) where changes in the dielectric properties of the barrier are particularly evident. After a rapid initial growth phase that occurs over a few tens of seconds, the capacitance associated with the oxide barrier increases slowly with anodization time. Figure 3 demonstrates the influence of the anodization potential on the capacitance. The imaginary part of the impedance *decreases* as the potential of the anode is made more positive. It also *decreases* with increased anodization time. The related increase in capacitance indicates an increase in the effective area of the oxide and a limit to the maximum thickness that can be achieved. In other words, we find that the porosity of the nickel oxide increases with time and anodization potential. This result confirms previous studies of anodized nickel that suggest the presence of a thin NiO film of a few atomic layers which becomes more porous upon extended anodization [13]. After plating the top Co half-wire, we investigated the current-potential response of a series of samples at low temperatures (Figure 4). We observed a systematic decrease of the sample conductance when increasing the anodization potential. At low bias a majority of the sample showed a low conductance that can be attributed to blocking of electron flow by an electrostatic energy $E_c = e^2/2C$, where C is the capacitance between the blocking island and current source and drain. At the limit of zero temperature, no current flows for voltage bias smaller than e/2C.
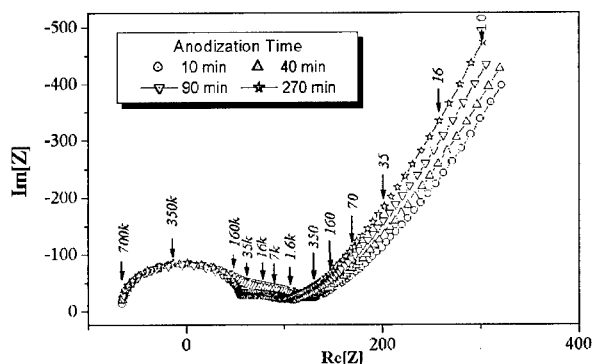
Figure 2. The observed impedance spectrum of anodized Ni for several anodization times.
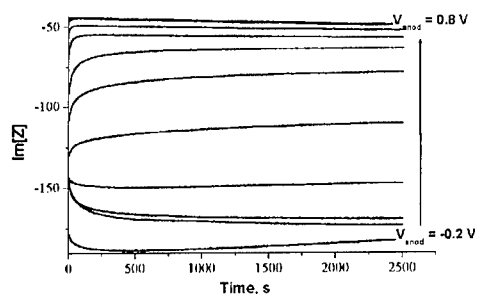
Figure 3. Time evolution of the imaginary part of the impedance at 5 kHz, for several anodization potential values. In a first approximation −Im(Z) can be interpreted as the inverse of the oxide film capacitance.
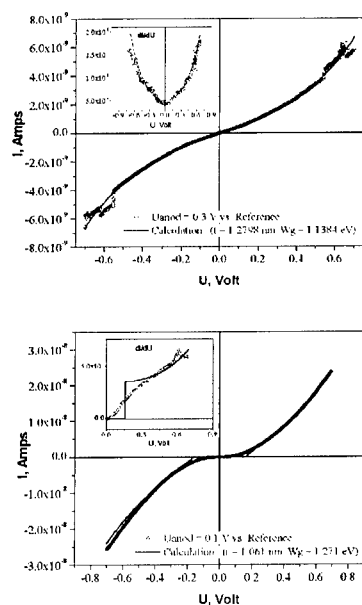
Figure 4. IV curves of Ni/NiO/Co nanowires of 30 nm diameters. Inserts are derivatives of the curves, with the corresponding fittings using tunneling (left) of Coulomb blockade at low bias and tunneling at high bias (right).

One can express the current due to tunneling through a barrier of width t and height W_g, by the equation

$$ J = \frac{e}{2\pi h}\frac{1}{t^2}\left\{\left(W_g - \frac{eV}{2}\right)Exp\left[-Ct\left(W_g - \frac{eV}{2}\right)^{1/2}\right] - \left(W_g + \frac{eV}{2}\right)Exp\left[-Ct\left(W_g + \frac{eV}{2}\right)^{1/2}\right]\right\} $$

which corresponds to a quadratic conductance versus voltage in first approximation [14]. Values of t and W_g are fit to the above equation in the set of four samples shown in Figure 4. A value of 0.008 μm^2 is used for the area of all the junctions. This is a rough estimate corresponding to the geometric cross-section area of the nanowires. The porosity of the oxide increases this value, but filamentary conduction will occur through a limited fraction of the junction, reducing its effective area. The barrier thickness and height contribute exponentially to the conductance, and fitted values of typically 1 eV for the barrier height and 1 nm for its thickness account for the whole set of investigated samples.

No significant change of conductance with temperature is expected for a tunneling barrier of energy height much larger than kT. The significant conductance variation we observe

at temperatures higher than a few tens of K (Figure 5) is inconsistent with the simple model presented above. The electronic conductance of our junctions increases when the temperature is increased, apparently because intermediate energy levels become thermally accessible. Consequently, at "high" temperatures, a semiconductor-type conduction plays the dominant role. The classical expression is of the form:

$$ J = V(N_0 N_d)^{1/2} Exp\left(-\frac{W_d - eV}{2k_B T}\right), \text{ where } N_0 \equiv 2\left(m_e k_B T / h^2\right)^{1/2} $$

where N_d is the donor concentration and W_d is the donor activation energy. To summarize, our samples show three conduction regimes: a Coulomb blockade regime at low voltage bias and low temperatures, a tunneling regime at high voltage bias and low temperatures, and a regime at high temperatures where conduction is mediated by defects in the barrier.

Magnetoresistance measurements are shown in Figure 6. We found small MR amplitudes, rapidly decreasing with voltage bias. These values are reminiscent of results found on NiO junctions made by vacuum techniques [15], and do not reach the large values previously found on larger nanowires (diameter 80 – 100 nm). A possible explanation is the lower conductance of this new series of samples, making the process of co-tunneling very unlikely [5]. The enhancement of the MR is therefore of low probability and we find that a sequential tunneling thermally enhanced through a Coulomb blockade does not show large MR effects.
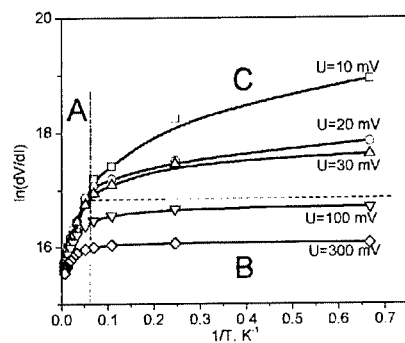
Figure 5. Temperature evolution of the conductance, measured at several different voltage bias. The conduction regimes are indicated by A: Coulomb blockade, B: tunneling, C: semiconducting.
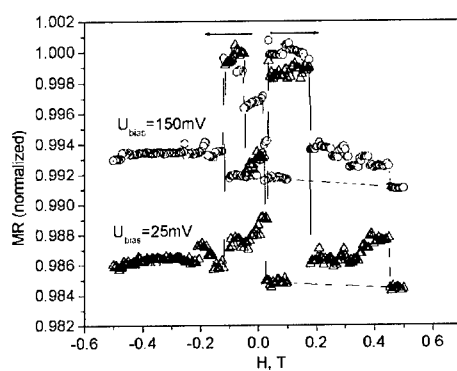
Figure 6. Magnetoresistance curves at 5 K, for two different voltage bias. The resistance is normalized to the antiparallel state value.

REFERENCES

1. M. Julliere, *Phys. Lett.* **54A**, 225 (1975).

2. J. S. Moodera, L. R. Kinder, T. M. Wong and R. Meservey, *Phys. Rev. Lett.* **74**, 3273 (1996)

3. W. J. Gallagher, S. S. P. Parkin, Yu Lu, X. P. Bian, A. Marley, K. P. Roche, R. A. Altman, S. A. Rishton, C. Jahnes, T. M. Shaw and Gang Xiao, *J. Appl. Phys.* **81**, 3741 (1997).

4. B. Doudin, S. Gilbert, G. Redmond, J.-Ph. Ansermet, *Phys. Rev. Lett.* **79**, 933 (1997).

5. S. Takahashi and S. Maekawa, *Phys. Rev. Lett.* **80**, 1758 (1998).

6. J. Barnas and A. Fert, *Phys. Rev. Lett.* **80**, 1058 (1998)

7. A. Brataas, Y. V. Nazarov, J. Inoue and G. E. Bauer, *Phys. Rev. B* **59**, 93 (1999).

8. J. R. Macdonald, *Impedance spectroscopy: emphasizing solid materials and systems*, John Wiley & Sons, New York, (1987).

9. C. R. Martin, *Science* **266**, 1961 (1994)

10. B. MacDougall and M. J. Graham, *J. Electrochem. Soc.* **128**, 2321 (1981).

11. M. Duprat, Ed. *Electrochemical Methods in Corrosion Research*, Materials Science Forum, Vol 8 (1986).

12. J.E. Wegrowe, S.E. Gilbert, D. Kelly, B. Doudin, J.-Ph. Ansermet *IEEE Trans. on Mag.* **34**, 903 (1998).

13. G. Dagan, W.-M. Shen and M. Tomkiewicz, *J. Electrochem. Soc.* **139**, 1855 (1992).

14. J. G. Simmons, *J. Appl. Phys.* **34**, 1793 (1963)

15. T. Miyazaki and N. Tezuka, *J. Mag. Mag. Mater.* **151**, 403 (1995).

Spins in Semiconductors

Epitaxial Growth of Dilute Magnetic Semiconductors: GaMnN and GaMnP

Mark E. Overberg, Cammy R. Abernathy, Stephen J. Pearton, Fred Sharifi [1], Arthur F. Hebard [1], Nineta Theodoropoulou [1], Stephan von Molnar [2], Madjid Anane [2], and Peng Xiong [2]
Department of Materials Science and Engineering, University of Florida, Gainesville, FL 32611, U.S.A.
[1]Department of Physics, University of Florida, Gainesville, FL 32611, U.S.A.
[2]Department of Physics and MARTECH, Florida State University, Tallahassee, FL 32306, U.S.A.

ABSTRACT

Epitaxial growth of the dilute magnetic semiconductors GaMnP and GaMnN has been investigated by Gas Source Molecular Beam Epitaxy (GSMBE). GaMnP films grown with < 4.5% Mn show the preferential formation of the second phases MnP and $Mn_{5.64}P_3$, resulting in only a slight deviation from purely diamagnetic behavior. GaMnN films grown on both Al_2O_3 and Metal-Organic Chemical Vapor Deposition (MOCVD) derived GaN surfaces show strong ferromagnetism when grown with either C codoping or at elevated temperatures to raise the concentration of n-type carriers. Comparable GaMnN films grown under conditions which produce highly resistive material show only paramagnetism, indicating the importance of carrier concentration on the resulting magnetic behavior. The formation of second phases was not observed in the GaMnN material for Mn concentrations less than 9%.

INTRODUCTION

Since the invention of the transistor, all facets of semiconductor electronics technology have been based upon the exploitation of the electron charge. Currently, a large research effort is centered upon methods to also exploit the property of electron spin. For many years it has been hypothesized that "spintronic" devices that utilize the quantum properties of the electron spin wavefunction will allow great advances in the development of electro-optic switches, ultra-sensitive magnetic field sensors, and particularly, quantum-based logic and memory for high speed computation[1-3]. However, its has been found that directly mating electronic materials (semiconductors) with spin materials (ferromagnetic metals) leads to interfacial problems due to the dissimilar nature of the materials' crystal structure, bonding, physical, and chemical properties[4]. Another solution is the dilute magnetic semiconductor (DMS), which consists of a semiconductor host heavily doped with a magnetic ion. A DMS material could permit direct integration with current semiconductor devices. Several theories have been presented on the nature of DMS-related ferromagnetism[5,6]. In the theory based upon a bound magnetic polaron (BMP) model, predicted Curie temperature (T_C) values are presented for 5% Mn in various III-V and II-VI semiconductors with a concentration of free holes equal to 3.5×10^{20}/cm^3 [6]. To date, the best experimental T_C values for InMnAs, GaMnSb, and GaMnAs reasonably agree with theory, but are still well below room temperature[7-9]. The III-V DMS material GaMnN is predicted to have a T_C well above room temperature, while the material GaMnP is expected to be

more compatible with Si devices due to its close lattice matching. GaMnN has been produced in a powder form, but its application is limited[10]. In this paper, we demonstrate for the first time the thin film growth of the DMS materials GaMnP and GaMnN.

EXPERIMENTAL PROCEDURE

Films were grown by GSMBE in an INTEVAC Gas Source Gen II on In-mounted substrates. GaMnN films were grown on either (0001) Al_2O_3 substrates upon which a 20 nm low temperature AlN buffer layer ($T_g = 435°C$) was applied, or on MOCVD grown n-GaN layers on Al_2O_3 substrates. GaMnP films were grown on epi-ready (100) GaP substrates. The Al for the low temperature buffer layer was provided by a dimethylethylamine alane source. Shuttered effusion ovens charged with 7 N Ga and 4 N Mn provided the group III and the magnetic dopant fluxes. The C dopant was provided via a CBr_4 bubbler using 6 N He as the carrier gas, the CBr_4 being pyrolized at the substrate surface. GaMnP:C was grown with a CBr_4 flux sufficient to produce a hole concentration of $2.7 \times 10^{20}/cm^3$ in GaP. The CBr_4 flux was held constant in all of the GaMnP growth runs. Reactive nitrogen for the GaMnN films was provided by an SVT RF plasma source operating at 375 W of forward power and a gas flow rate of 3 sccm N_2. Reactive phosphorous for the GaMnP films was provided by thermally cracked PH_3, at a flow rate of 1 sccm and a cracker temperature of 1050°C. X-ray diffraction (XRD) measurements were performed in a Philips APD 3720 powder diffractometer. Compositional information was provided by Auger Electron Spectroscopy (AES) in a Perkin-Elmer PHI 6600 system. Magnetic measurements were performed in a Quantum Design SQUID MPMS system. All Hall measurements were taken at room temperature in a custom built system using a 0.8 T electromagnet. Curie temperatures for ferromagnetic films were estimated by comparing the field cooled and zero field cooled curves at 500G.

RESULTS AND DISCUSSION

The Mn concentration in GaMnP was found to increase with increasing Mn cell temperature for Mn concentrations up to 8%. Growth temperature, T_g, was found to play a significant role in determining the number and type of phases found. At $T_g = 600°C$ the Mn was found by XRD to incorporate as GaMnP and as MnP, which is orthorhombic. As T_g is reduced, the layers exhibit a mix of GaMnP, MnP and $Mn_{5.64}P_3$, which is hexagonal. For $T_g \leq 400$, $Mn_{5.64}P_3$ was found to be present in all of the films. In light of the multi-phase nature of these films it is not surprising that polycrystalline RHEED patterns were observed for all growth temperatures.

Electrically, Mn is expected to behave as a deep acceptor in GaP as it does in the case of GaMnAs. However, as the Mn concentration is increased, the hole concentration was found to decrease from the $2.7 \times 10^{20}/cm^3$ in the GaP:C to $3 \times 10^{18}/cm^3$ for an Mn concentration of 2.1%. Mn concentrations $\geq 4.2\%$ produced semi-insulating films. It is possible that the reduction in hole concentration is due to the presence of the Mn_xP_y phases which are expected to be metallic. Magnetic measurements of the sample with 2.1% Mn and $p=3 \times 10^{18}/cm^3$ showed a very slight deviation from pure diamagnetism in the M vs H data, as shown in Figure 1. Initial estimates suggest a T_C of ~50K. In light of the RHEED and XRD data it is likely that the magnetic behavior is due to the Mn_xP_y phases.
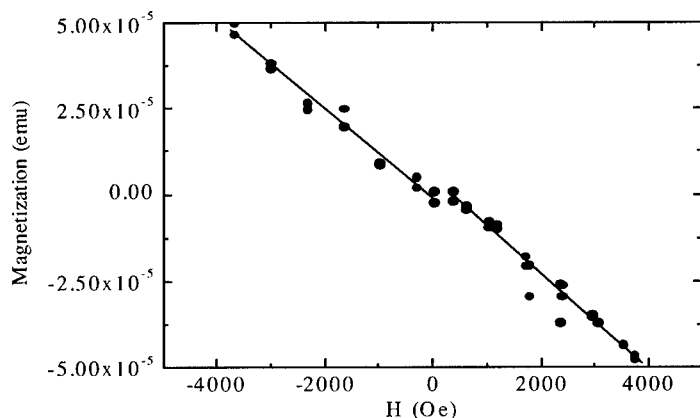
Figure 1. Magnetic characterization of GaMnP:C grown at 400°C. XRD indicates presence of MnP and $Mn_{5.64}P_3$ in addition to GaMnP:C.

Significantly better results were obtained with GaMnN. Because of the high vapor pressure of Mn, a lower growth temperature, 750°C, was used than is normally employed for growth of GaN in this system. Even this reduced temperature is significantly higher than is typically used for formation of III-Mn-V alloys. AES analysis showed the Mn incorporation to be linear with Mn cell temperature for Mn concentrations in the range of ~ 1.1% to 43.1%, as shown in Figure 2. The high concentrations that could be achieved suggest that in spite of the high vapor pressure, the Mn sticking coefficient is adequate even at elevated GaN growth temperatures. An XRD standard was grown using only Mn and the nitrogen plasma. The stable Mn_xN_y phase was found to be Mn_4N. However, when GaMnN films with concentrations less than 9% were examined, no evidence of this or any other Mn-containing phase could be found except for GaMnN. At very high Mn fluxes, additional MnGa phases were observed, suggesting that the metal flux exceeded the nitrogen flux in these films, resulting in the formation of metal rich phases. RHEED analysis showed evidence of 3D or polycrystalline structure. Increasing the growth temperature to 865°C improved the crystal quality, as evidenced by the appearance of a RHEED pattern that was a mixture of streaky and spotty patterns.

The GaN grown at T_g = 750°C was n-type with an electron concentration, n, of n $\cong$ $4 \times 10^{19}/cm^3$. This large undoped background is believed to be due to a large concentration of nitrogen vacancies. As the Mn concentration was increased in the single-phase material, the GaMnN became increasingly resistive. This is in keeping with the expectation of a deep Mn acceptor that would serve to compensate the shallow nitrogen vacancy donor. At the very high Mn concentrations, Mn $\approx$ 47%, the films become conductive, presumably due to formation of the MnGa phases. It was found that the electron concentration could be increased either through the addition of carbon at the lower T_g, or by increasing the growth temperature. Using a CBr_4 flux previously calibrated to produce a carbon concentration of $\sim 10^{20}/cm^3$, an electron concentration in the GaMnN of $5 \times 10^{18}/cm^3$ was obtained. Under these growth conditions carbon typically produces highly resistive material. The fact that n-type GaMnN was observed suggests that the carbon is behaving as an amphoteric dopant in this material. Increasing the T_g to 865°C also
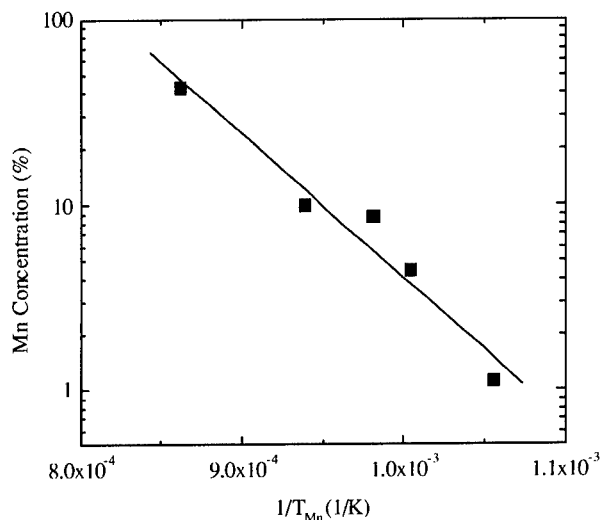
Figure 2. Variation of Mn concentration in GaMnN grown at 750°C as a function of reciprocal Mn cell temperature.

produced conductive GaMnN with n~1.5×10^{19}/cm^3. In this case the higher electron concentration is believed to be due to an increase in the nitrogen vacancy concentration caused by enhanced loss of nitrogen from the surface during growth at the higher temperature.

Magnetically, the higher carrier concentrations appear to be beneficial as the highly resistive films only show paramagnetic behavior. A rough estimate of these films shows a moment of 3.9 Bohr magnetons per Mn, suggesting that a significant fraction of the Mn ions are substitutional. In the conductive single-phase films, clear hysteresis was observed at 10 K, as shown in Figure 3, indicative of a ferromagnetic material. It was found that, at least for the lower T_g of 750°C, growing on an MOCVD buffer produced a higher saturation magnetization, M_s~2×10^{-5} emu vs. 4 $\times 10^{-6}$ emu. This suggests that crystallinity plays a significant role in the magnetization since the MOCVD buffer is expected to produce superior growth. However, the T_c for both films was estimated to be ~ 100K, independent of the crystal quality. The more conductive material grown at 865°C showed similar behavior, though with a much higher saturation magnetization of 2×10^{-4} emu. The T_c was again estimated to be ~100K, and thus was not strongly affected by the change in carrier concentration. The appearance of ferromagnetism in samples both with and without C eliminates the formation of Mn-C complexes as the source of the ferromagnetic behavior in the samples grown at 750°C.
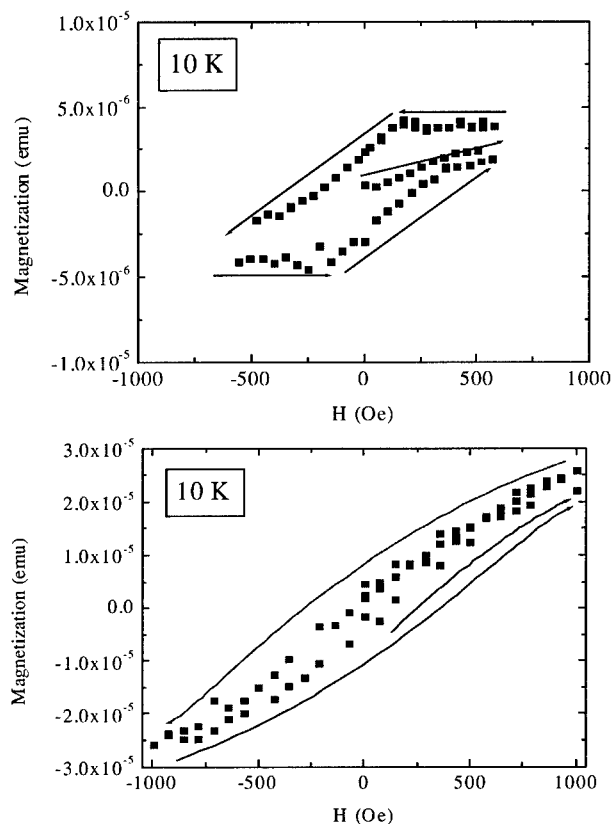
Figure 3. 10K magnetic characterization of GaMnN grown at 750°C on sapphire (top) or on an MOCVD buffer (bottom).

CONCLUSIONS

Synthesis of GaMnP and GaMnN by gas-source molecular beam epitaxy was investigated. For the case of GaMnP suppression of undesired Mn-containing phases was found to be extremely difficult. These second phases result in poor crystallinity as evidenced by RHEED and are most likely responsible for the slight deviation from pure diamagnetism observed in the M vs. H. data. GaMnN was found to be much more amenable to growth with single-phase material obtained for Mn concentrations up to 8%. The background electron concentration was found to drop as the Mn concentration was increased, resulting in semi-insulating material which showed only paramagnetic behavior when analyzed magnetically. Increasing the electron concentration either via the addition of carbon or by increasing the growth temperature produced ferromagnetic films with an estimated Curie temperature of ~100K. While improving the crystallinity and

increasing the electron concentration increased the saturation magnetization, they did not appear to strongly affect the Curie temperature. It is expected that increasing this parameter substantially will require the addition of Mg to produce a hole mediated Mn-Mn exchange interaction rather than an electron mediated Mn-Mn exchange interaction.

ACKNOWLEDGEMENTS

REFERENCES

(1) G. Prinz and K. Hathaway, Phys. Today **48**, 24-25 (1995).

(2) D. DiVencenzo, Science **270**, 255-261 (1995).

(3) D. Deutsch, Proc. R. Soc. Lond. A **400**, 97-117 (1985).

(4) M. Tanaka, J. Crys. Growth **201/202**, 660-669 (1999).

(5) B. Lee, T. Jungwirth, and A. H. MacDonald, Phys. Rev B **61** (23), 15606-15609 (2000).

(6) T. Dietl, H. Ohno, F. Matsukara, J. Cibert, and D. Ferrand, Science **287**, 1019-1022 (2000).

(7) H. Ohno, Science **281**, 951-956 (1998).

(8) H. Munekata, A. Zaslavsky, P. Fumagalli, and R. J. Gambino, Appl. Phys. Lett. **63** (21), 2929-2931 (1993).

(9) F. Matukura, E. Abe, and H. Ohno, J. Appl. Phys. **87** (9), 6442-6444 (2000).

(10) M. Zajac, R. Doradzinski, J. Gosk, J. Szczytko, M. Lefeld-Sosnowska, M. Kaminska, A. Twardowski, M. Palczewska, E. Grzanka, and W. Gebicki, Appl. Phys. Lett. **78** (9), 1276-1278 (2001).

Ferromagnetic and Structural Properties of Mn-Implanted p-GaN

N. Theodoropoulou[1], A.F. Hebard[1], M.E. Overberg[2], C.R. Abernathy[2], S.J. Pearton[2], S.N.G. Chu[3] and R.G. Wilson[4]

[1]Department of Physics, University of Florida, Gainesville, FL 32611
[2]Department of Materials Science and Engineering, University of Florida, Gainesville, FL 32611
[3]Bell Laboratories, Lucent Technologies, Murray Hill, NJ 07974
[4]Consultant, Stevenson Ranch, CA 95131

ABSTRACT

High doses ($10^{15} - 5 \times 10^{16}$ cm^{-2}) of Mn$^+$ ions were implanted into p-GaN at ~350°C and annealed at 700-1000°C. At the high end of this dose range, platelet structures of Ga$_x$Mn$_{1-x}$N were formed. The presence of these regions correlated with ferromagnetic behavior in the samples up to ~250K. At low doses, the implantation led to a buried band of defects at the end of the ion range.

There is tremendous interest in structures involving the manipulation of the spin of the electron in addition to its charge for switching and memory devices with new functionality.[1-10] Applications for these spintronic devices are envisioned in communications technology, data processing and storage and in photonics. It has been demonstrated in a number of semiconductors (including GaMnAs, InMnAs and ZnMnSe) that quantum spin states are quite robust and can be transported over very large distances (>100 μm in some cases).[1-10] The ferromagnetism in dilute magnetic III-V semiconductors is carrier-induced and is still far from completely understood.[11,12] The Curie temperature (T$_C$) in these materials is believed to be governed by the interaction between localized ferromagnetic clusters (bound magnetic polarons). Recent calculations[12] suggest that wide bandgap semiconductors may have T$_C$ values well above those for GaMnAs (110K)[10] and InMnAs (<35K)[10]. In particular GaMnN with ~5 at. % Mn, and high hole concentrations is predicted to have a T$_C$ exceeding 300K.[12] At present, little is known about doping GaN with Mn, although some initial results have been published on n-type Ga$_x$Mn$_{1-x}$N single crystallites with paramagnetic behavior.[13-15]

In this paper, we report on the magnetic properties of p-GaN implanted with high doses (3-5 at.%) of Mn. Under optimized annealing conditions we observe platelet regions with the same lattice structure as GaN, but different lattice constant, which give rise to Moire fringes and multiple diffraction in transmission electron microscopy analysis. These regions, which appear to be Ga$_x$Mn$_{1-x}$N, produce ferromagnetic behavior with a T$_C$ of ~250K. Thus, selected-area Mn-implantation into GaN may be useful for creating spin-injection contact regions.

The GaN samples were grown by Metal Organic Chemical Vapor Deposition on c-plane sapphire substrates. A low temperature (540°C) GaN buffer was grown first (250Å) followed by 4μm of undoped GaN and 0.5μm of p-GaN (Mg-doped) with a room temperature hole concentration of 2×10^{17}-cm^{-3}. Mn$^+$ ions were implanted at an energy of 250keV and doses from $10^{15} - 5 \times 10^{16}$ cm^{-2} at an approximate dose rate of 8×10^{12} cm$^{-2} \cdot$s^{-1} to produce average volume concentrations from ~0.1-5 at.% in the top ~2000Å of the GaN. The samples were held at 350°C during implantation to avoid amorphization.[16-18] Subsequent annealing at 700-1000°C was performed for 5 mins under flowing N$_2$ gas with the samples face-down on GaN wafers. The

structural properties of the implanted material were examined by double crystal x-ray diffraction (XRD), and 200 kV transmission electron microscopy (TEM) with selected area diffraction analysis. The magnetic properties were measured in a Quantum Design PPMS SQUID magnetometer. The hole density after implantation and annealing was $\leq 10^{16}$ cm^{-3}.

Figure 1 shows TEM cross-sectional views of the GaN implanted with ~0.1 (top) or ~3 at.% Mn (center and bottom) and annealed at 700°C. For the low-dose case (top) the implanted regions contains a relatively large density of lattice defects resulting from agglomeration of point defects created by the nuclear stopping processes of the implanted ions. These samples showed only paramagnetic behavior. By sharp contrast, the samples implanted at higher doses show large (≤ 200Å diameter) platelet structures in addition to a buried band of damage at the end of range of the Mn ions. The end-of-range region is heavily-damaged single crystal. The platelet structures are shown in higher magnification at the bottom of Figure 1. Similar structures that were on average slightly larger in diameter (≤ 250Å) were observed in the high dose samples annealed at 1000°C.

Figure 1. TEM micrographs taken under dark-field conditions of GaN after Mn$^+$ implantation and subsequent annealing at 700°C. The doses were 10^{15} cm^{-2} (top) or 5×10^{16} cm^{-2} (center and bottom) at 250 keV. The scales on the top two micrographs are 200Å long, while in the bottom micrograph the scale is 100Å long. The sample surface is at the top of each micrograph.

GaMn(3%)N
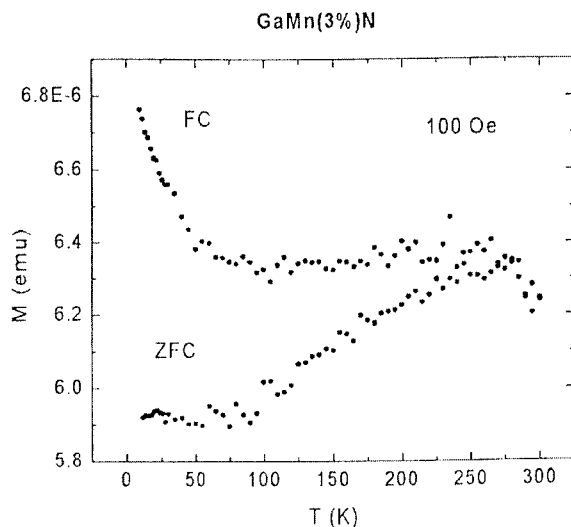
Figure 2. ZFC and FC magnetization as a function of temperature for GaN implanted with ~3 at. % Mn and annealed at 700°C.

The higher dose samples ($\geq$ 3 at.% Mn) displayed a ferromagnetic behavior persisting to ~250 K as shown in Figure 2 for zero-field cooling (ZFC) and field-cooling (FC) conditions. There is also a contribution present with a Curie temperature of ~ 50 K, whose origin we have not identified. The difference between these plots essentially subtracts a large diamagnetic background. As further evidence of ferromagnetic behavior, Figure 3 shows that hysteresis was observed in the magnetic moment of the 3 at. % Mn sample. Assuming the ferromagnetism originates from the platelet structures, we can roughly estimate the saturation magnetization to be approximately 3.8 ± 1.3 Bohr magnetron per Mn. An alternative explanation could be that the GaMnN has a Curie temperature of 50 K, and superparamagnetic clusters of MnGa or some alloy thereof are present with size below the 20 Å resolution of TEM. The splitting of the FC/ZFC curve could then be attributed to the presence of these clusters with a blocking temperature of 250 K.

Numerous authors have reported on the creation of submicron MnGa and MnAs ferromagnetic crystallites in GaAs by Mn^+ implantation and subsequent heat treatment. [19-23] Both of these phases have T_C values above room temperature (eg. GaMn has T_C's between 450-800 K depending on the amount of Mn in the alloy). In addition, ferromagnetic MnAs nanoclusters embedded in GaAs can be created by annealing of $Ga_{1-x}Mn_xAs$ films. [24] In some cases, $MnGa_xAs_y$ phases are observed in addition to the MnGa and MnAs phases [23], indicating that under some conditions it is possible to form ferromagnetic ternary phases. Note that for these GaAs experiments the Mn implants were performed at room temperature, in contrast to our use of elevated substrate temperatures which should reduce the point defect density.
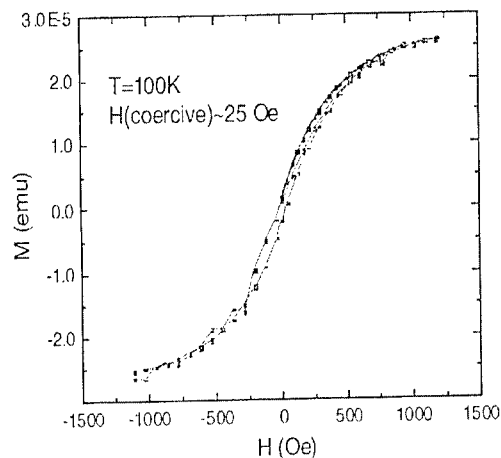
Figure 3. Hysteresis measured at 100K in the magnetic moment of a sample implanted with ~3 at. % Mn and annealed at 700°C.

Figure 4 shows a plan view TEM micrograph of a 5 % at. Mn implanted sample (top), along with selective area diffraction pattern (bottom). The sample was thinned from the backside and the data are typical of all samples implanted with 3-5 at. % Mn and annealed at 700°C or 1000°C. Electron diffraction did not show any 4-fold symmetry patterns, which would be expected to be present if either tetragonal (GaMn, $Mn_{0.6}Ga_{0.4}$, Mn_3N_2) or cubic (Ga_5Mn_8. Mn_4N, $Ga_{7.7} Mn_{2.3}$) phases were formed. The diffraction pattern shows multiple diffraction spots around those of GaN with a 6-fold symmetry, indicating the platelet regions are $Ga_x Mn_{1-x}N$ with the same lattice structure as GaN but with a different (smaller) lattice constant which gives rise to the Moire fringes and multiple diffractions. This was confirmed by a qualitative simulation of [0001] double diffraction for a stack of two hcp lattices with different lattice constants, in analogy for a previous analysis of the cubic system GaAs on InP.[25] Similar diffraction results were obtained from cross-section samples, confirming that the Al_2O_3 substrates play no role. The only possible hexagonal phase present could be Mn_3Ga, but this was not found either in x-ray diffraction spectra or in energy dispersive x-ray spectroscopy analysis of the platelets. In the latter case, the probe beam was too large to get an exact composition for the platelets. Also, we could not apply Vegard's law due to the non-uniform composition in the Mn-implanted region. Moreover, we could expect the samples to display T_C values above room temperature if the binary GaMn phases were present.

In conclusion, high-dose Mn^+ implantation at elevated temperatures into p-GaN appears to be a promising method for producing ferromagnetic behavior and may be useful for creating selective-area spin-injection regions in device structures. The observed Curie temperature is below theoretical predictions, but may be affected by the low hole density in heavily implanted
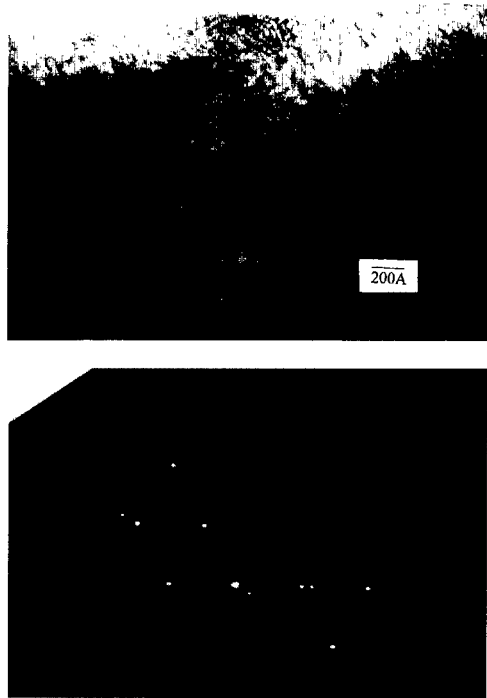
Figure 4. Plan view TEM micrograph of 5 at. % Mn-implanted GaN (dose 5×10^{16} cm^{-2} at 250 keV) sample annealed at 1000°C (top) and selected area diffraction pattern (bottom). The scale is 200Å long.

p-GaN. Considerable work needs to be done to understand the solubility limits of Mn under these conditions and the thermal stability of the phases created.

ACKNOWLEDGMENTS

REFERENCES

1. D.D. Awschalom and J.M. Kikkawa, *Physics Today* **523**, 33 (1999).
2. J.M. Kikkawa and D.D. Awschalom, *Science* **287,** 473 (2000).
3. G.A. Prinz, *Science* 282, 1660 (1998).
4. B.T. Jonker, Y.D. Park, B.R. Bennett, H.D. Cheong, G. Kioseoglou and A. Petrov, *Phys. Rev.* **B62**, 8180 (2000).
5. Y.D. Park, B.T. Jonker, B.R. Bennett, G. Itskos, M. Furis, G. Kioseoglou and A. Petrov, *Appl. Phys. Lett.* **77**, 3989 (2000).
6. F. Fiederling, M. Kelm, G. Reuscher, W. Ossau, G. Schmidt and A. Waag, *Nature* **402**, 787 (1999).
7. Y. Ohno, D.K. Young, B. Beschoten, F. Matsukura, H. Ohno and D.D. Awschalom, *Nature* **402**, 790 (1999).
8. an early review of the field is given in, F. Holtzberg, S. von Molnar and J.M.D. Coey, *Handbook of Semiconductors Vol. 3*, ed. S.P. Keller (North-Holland, Amsterdam 1980).
9. a review of hybrid ferromagnet-semiconductor research is given in M. Johnson, IEEE Spectrum 37, 33 (2000); J. Vac. Sci. Technol. A16, 1806 (1998).
10. H. Ohno, *J. Mag. Mag. Mater.* **200**, 110 (1999).
11. J. Konig, H.H. Lin and A.H. MacDonald, *Phys. Rev. Lett.* **84**, 5628 (2000).
12. T. Diehl, H. Ohno, F. Matsukura, J. Cibert and D. Ferrand, *Science* **287**, 1019 (2000).
13. *W. Gebicki, J. Strzeszewski, G. Kamler, T. Szczyko and S. Podsiado, Appl.* Phys. Lett. **76**, 3870 (2000).
14. M. Zajac, R. Doradzinski, J. Gosk, T. Szczyko M. Palczewska, G. Grzanka, M. Lefeld-Sosnowska, W. Gebicki, M. Kaminska and T. Twardowski , *Appl. Phys. Lett.* **78**, 1276 (2001).
15. T. Szyszko, G. Kamler, B. Strojek, G. Weisbrod, S. Podsicask, L. Adamowicz, W. Gebicki, A. Twardowski, J. Szcztko and K. Sikorski (to be published).
16. S.O. Kucheyev, J.S. Williams, J. Zou, C. Jagadish and G. Li, *Appl. Phys. Lett.* **77**, 3577 (2000).
17. S.O. Kucheyev, J.S. Williams, C. Jagadish, V.S.J. Craig and G. Li, *Appl. Phys. Lett.* **78**, 1373 (2001).
18. S.O. Kucheyev, J.S. Williams, C. Jagadish, J. Zou and G. Li, *Phys. Rev.* **B62**, 75100(2000).
19. J. Shi, J.M. Kikkawa, R. Proksch, T. Schaeffer and D.D. Awschalom, *Nature* **377**, 707 (1995).
20. J. Shi, J.M. Kikkawa, D.D. Awschalom, G. Medeiro-Riberio, D.M. Petroff and K. Babcock, *J. Appl. Phys.* **79,** 5296 (1996).
21. J. DeBroeck, R. Osterholt, A. Van Euch, H. Bender, C. Brynseraede, C. Van Hoof and G. Borghs, *Appl. Phys. Lett.* **68**, 2744 (1996).
22. P.J. Wellman, J.M. Garcia, J.L. Feng and P.M. Petroff, *Appl. Phys. Lett.* **71**, 2532 (1997).
23. C. Chen, M. Cai, X. Wang, S. Xu, M. Zhang, X. Ding and Y. Sun, *J. Appl. Phys.* 87, 5636 (2000).
24. H. Akinaga, S. Miyaniski, K. Tanaka, W. Van Roy and K. Onodera, *Appl. Phys. Lett.* **76**, 97 (2000).
25. S.N.G. Chu, *J. Appl. Phys.* **66**, 520 (1989).

CHALCOPYRITE MAGNETIC SEMICONDUCTORS: AN AB–INITIO STUDY OF THEIR STRUCTURAL, ELECTRONIC AND MAGNETIC PROPERTIES

S. PICOZZI[†], A. CONTINENZA[†], W. T. GENG[§], Y. J. ZHAO[§] and A. J. FREEMAN[§]

† INFM – Dip. Fisica, Univ. L'Aquila, 67010 Coppito (L'Aquila), Italy
§ Dept. of Phys. and Astron. and Materials Research Center[1], Northwestern University, Evanston, IL 60208 (U.S.A.)

ABSTRACT

Stimulated by recent experimental observations of room–temperature ferromagnetism of $Mn_xCd_{1-x}GeP_2$, we investigate the structural, electronic and magnetic properties of these systems as a function of Mn concentration by means of first–principles density-functional-theory-based codes. Moreover, we investigate the effect of the anion substitution (P vs As) in Mn-rich chalcopyirites. Our calculations indicate that the antiferromagnetic alignment is the most stable ordering for all the systems studied, at variance with that experimentally reported. Moreover, we find that there is a slight reduction of the total magnetic moment per Mn atom from ~ 5 μ_B in all the Cd-rich P-based chalcopyrites to ~ 4 μ_B in the Mn rich $MnGeP_2$ and $MnGeAs_2$ systems.

INTRODUCTION AND COMPUTATIONAL DETAILS

A great effort is being devoted to explore new, advanced magnetic semiconductors for spintronics applications[1], based on crystal structures that transcend the limitations (defect formation and too low operating temperatures) of the magnetic zinc-blende systems explored so far (e.g. $Mn_xGa_{1-x}As$). Within this framework, the chalcopyrites seem to be good candidates; the expected advantage of these systems is that Mn can readily substitute for the type–II cations, as has been demonstrated for $II_{1-x}Mn_xVI$ alloys with x up to 1.0 without defect formation, due to the natural tendency of Mn to adopt a +2 valence state.

Recently, Medvedkin et al. [2] deposited a Mn overlayer in vacuum on the surface region of a $CdGeP_2$ crystal, followed by a solid phase reaction at elevated temperatures. A relevant finding of Medvedkin et al. is the room temperature ferromagnetism in highly doped $Mn_xCd_{1-x}GeP_2$ - which constitutes a tremendous improvement from the T_C of 110 K found in $Mn_xGa_{1-x}As$ at $x = 5.3$ %. Moreover, their photoluminescence spectrum at 20 K shows a peak around 3.2 eV, from which they proposed a Mn induced enhancement of the energy gap of $CdGeP_2$ ($E_g = 1.83$ eV). This is quite different from the III-V alloys, in which Mn is known to reduce the band–gap [7].

In order to understand the magnetic interaction in chalcopyrite semiconductors, we investigated $Mn_xCd_{1-x}GeP_2$ for various x and $MnGe(V)_2$ where V = As, P with the full-potential linearized augmented plane wave (FLAPW)[3] method. This is one of the most accurate ab–initio methods, in which there is no artificial shape approximation for the wave functions, charge density and potential. For all atoms, the core and valence states are treated fully– and semi–relativistically (i.e. without spin orbit coupling), respectively. The muffin tin

---

(MT) radii for Cd, Ge, Mn are set to 2.3 a.u.; 2.0 and 1.8 a.u. are used for As and P, respectively. An energy cut off of 9.0 Ry was employed for the wave function expansion in the interstitial region, whereas a 49 Ry cut–off was used for the charge density and potential.

For all the systems studied, we used the generalized gradient approximation (GGA) functional of Perdew-Burke-Ernzerhof [5] rather than the bare local density approximation (LDA) exchange–correlation functional [6], within density functional theory; the GGA was proved to give better agreement with available experimental structural data for Mn pnictides [8] and is therefore likely to describe more accurately the Mn rich chalcopyrites.

STRUCTURAL DETAILS

Let us first focus on the structural details. Recall that the chalcopyrite differs from the zincblende crystal structure by a doubling of the unit cell along a four fold axis, rendering the system body centered tetragonal. Through total energy calculations, we fully optimized the $MnGeAs_2$ system, obtaining $a = 5.83$ Å, $c/a = 1.95\pm0.05$ and $u \sim 0.25$. The estimated numerical uncertainty on the η value can be ascribed to the very small effect on the total energy due to the tetragonal deformation (i.e. $\eta = c/2a \neq 1$) around the η equilibrium value. Our optimized structural values are in good agreement (within 0.5 % on the a lattice constant) with the values predicted by the "conservation of tetrahedral bonds" (CTB) plus $\eta = \eta_{tet}$" theory discussed in Refs. [9]. In our work, Pauling's tetrahedral radii were chosen as 1.48, 1.22, 1.22 and 1.10 Å for Cd, Ge, As and P respectively; the Mn tetrahedral radius, derived from the Mn chalcogenides is 1.41 Å. With these values, we obtained $a = 5.86$ Å and $c/a \sim 1.9$. The good agreement for the As-based chalcopyrite suggests that the "CTB plus $\eta = \eta_{tet}$" rule may even hold for the similar P-based $MnGeP_2$ system; we therefore used $a = 5.67$ Å, $c/a = 1.9$. Regarding the $MnCdGeP_2$ structures[10], we interpolated the lattice constants (a and η) from the experimental values for $CdGeP_2$ and the "CTB plus $\eta = \eta_{tet}$" value for $MnGeP_2$. This approximation is equivalent to Vegard's law and works well in this system. For instance, it is reported by Medvedkin et al. [2] that the lattice constant decreases to 5.7 Å when the Mn concentration becomes greater than Cd, which means x in the range of 50 % to 53 % since the maximum x is 53 % in the experiment. Our interpolated lattice constant for $x=0.5$ is 5.71, which is different from experiment by only 0.4 %. Moreover, in the $MnCdGeP_2$ systems, we optimized the internal degrees of freedom using both the $Dmol^3$[4] (i.e. density functional theory for molecules and 3-dimensional periodic solids) and the FLAPW codes. More accurate details about the structural properties of $Mn:CdGeP_2$ can be found in Ref. [10].

We focused on the dependence of the electronic and magnetic properties in semiconducting chalcopyrites as a function of i) the type V anion (i.e. P vs As) in Mn rich systems and ii) the Mn concentration ($x = 0.25$, 0.5 and 1).

THE $MnGeV_2$ (V = As, P) SYSTEMS

Let us first discuss the effects due to the anion species by comparing some relevant properties in $MnGeP_2$ and $MnGeAs_2$ shown in Table 1. As for the antiferromagnetic (AFM) configurations, we considered a 1x1 chalcopyrite "spin superlattice" along the [001] direction. We find that both the P-- and As–based systems largely prefer the AFM alignment, since the AFM is much lower in energy than the ferromagnetic (FM) structures. Let us now consider

Table 1: Comparison of relevant structural and magnetic properties of $MnGeP_2$ and $MnGeAs_2$.

	$MnGeP_2$		$MnGeAs_2$	
	FM	AFM	FM	AFM
Total energy (meV/Mn)	0	-160	0	-60
μ_{Mn} (Bohr magn.)	3.55	3.55	3.74	3.68
Total spin moment/Mn (Bohr magn.)	4.0	-	4.3	-
Mn-anion bond length (Å)	2.44	2.43	2.52	2.51
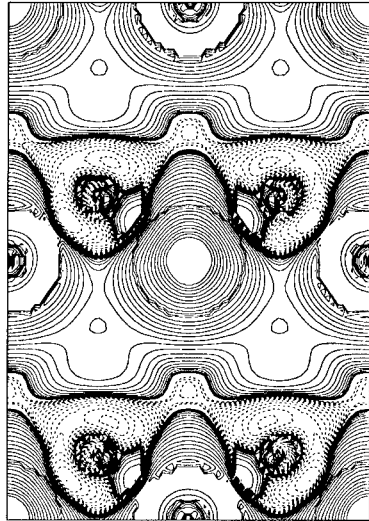
Figure 1: Spin density of ferromagnetic $MnGeAs_2$, plotted in the [110] plane. Positive (negative) spin-density is represented by solid (dashed) lines.
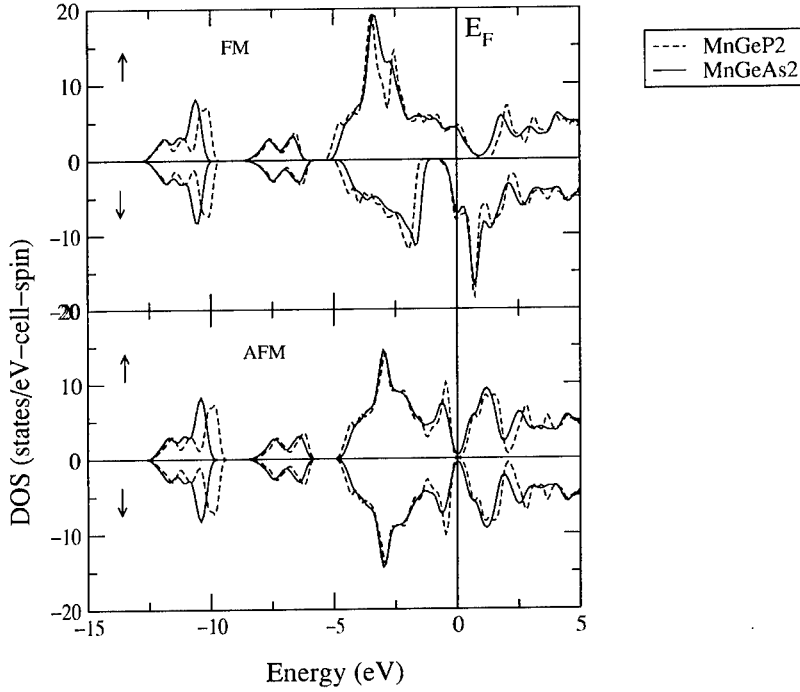
Figure 2: Total density of states of $MnGeP_2$ (dashed line) and $MnGeAs_2$ (solid line) for FM (upper panel) and AFM (lower panel) ordering. The zero of the energy scale denotes the Fermi level.

the magnetic moments. In this case, Mn substitutes a type-II cation; we would therefore expect a magnetic moment close to 5.0 μ_B. However, note that the local moment relative to the free Mn atom ($\mu_0 = 5$ μ_B in the d^5 configuration) is reduced due to the mixing of the unoccupied Mn $d^\downarrow$ bands with the occupied p bands by the $p - d$ hybridization. Note that in both As- and P-based chalcopyrites, the Mn induced FM moment at Ge sites gives positive contributions, while both P and As have a very small induced magnetic moment within the muffin tin sphere. As an example, we plot in Fig. 1 the spin–density in $MnGeAs_2$ in the [110] plane; it is evident that a negative spin density is present around the As atom, even though there is a positive spin density along the bond.

Let us now discuss the electronic properties of the $MnGeAs_2$ and $MnGeP_2$ systems. In Fig. 2 the spin-resolved total density of states for the FM and AFM alignments is reported. Let us first focus on the FM alignment, whose main features are: i) around -12 eV we find the hybridized Ge s and, mostly, anion s bands; ii) the structure around -7 eV has a similar

Table 2: Relevant structural, electronic and magnetic properties in $Mn_xCd_{1-x}GeP_2$ for various Mn concentrations. The $x = 0.5$ and 1.0 are 1x1 "spin-superlattices" ordered along the [001] direction, whereas the $x = 0.25$ is ordered along the [100] direction.

x	0.25		0.5		1.0	
	FM	AFM	FM	AFM	FM	AFM
MnP bond length (Å)	2.43	2.43	2.44	2.43	2.44	2.43
Total energy (meV/Mn)	0	-30	0	-35	0	-160
Total spin moment/Mn (Bohr magn.)	~5	-	~5	-	$\sim4.$	-
Energy gap (eV)	0.16	0.58	-	0.49	-	0.71

origin, with a more marked Ge s character; iii) the states at higher energy ($i.e$ from -5 eV to +5 eV) have a mixed character. In particular, it is evident that the Mn $d^\uparrow$ states are almost totally occupied (c.f. feature peaked at around -3.4 eV in the spin up DOS), whereas the $d^\downarrow$ states are mainly unoccupied and hybridized with the p anion states. (c.f. feature going from -0.8 eV, peaked at around 0.5 eV and then up to 5 eV in the spin down DOS). The pronounced feature in the spin–down DOS from -5 eV to -0.8 eV is mainly due to hybridization between Ge p and anion p states. We can estimate a d exchange splitting of about 4 eV. Neither the spin-up nor the spin-down density of states show a gap, therefore resulting in a metallic system; on the other hand, there is a small gap in the spin-down DOS at around -0.8 eV (between the Ge-anion p bands and the Mn d states) which could lead to half–metallicity, possibly by proper modifications in the lattice constants. The main difference between As and P anions stems from the higher hybridization [8] with the Mn d bands, shown by an almost rigid shift of the P (Mn) features towards lower (higher) binding energies with respect to the As case. As for the AFM DOS, we can outline features similar to the FM case. We still find a metallic character, even though a depletion of states is present just around the Fermi level, suggesting a starting gap opening effect. This difference with respect to the FM case is related to the i) less evident hybridization between Mn $d^\uparrow$ with anion $p^\uparrow$ states and ii) totally unoccupied Mn $d^\downarrow$ antibonding states.

THE $Mn_xCd_{1-x}GeP_2$ STRUCTURES

Let us now focus on the effect of Mn vs Cd substitution for Cd in the P based chalcopyrites. We report in Table 2 the relevant structural, electronic and magnetic properties of these systems. First of all, note that the AFM alignment is the most stable for all Mn concentrations, although the energy difference between FM and AFM configurations is strongly reduced with respect to the Mn-rich chalcopyrite. These results are not in agreement with the experimental observations[10], that found $Mn_xCd_{1-x}GeP_2$ to be a room-temperature ferromagnet. The reason for this disagreement is not clear. In our calculations, $Mn_xCd_{1-x}GeP_2$ is an ideal periodic bulk structure, while in experiment it is a surface doped system with Mn concentration that decays from the surface to the bulk. To resolve this discrepancy, a more thorough and careful experimental characterization is called for. As for the total spin moment, we note that the Mn induced moment on the Cd atom is positive and this is likely to justify the higher total moment for $x = 0.25$, 0.5 than for $x = 1.0$ systems.

Finally, we focus on the energy gap in $Mn_xCd_{1-x}GeP_2$. Recall that within GGA we obtain strongly underestimated band gaps, with respect to experimental values; for example, we obtain 0.93 eV for the $CdGeP_2$ crystal, to be compared with the experimental value of 1.83 eV. In the AFM state, the energy gap decreases to 0.49 eV for $x = 0.5$, although it goes up to 0.71 eV for $x = 1.0$. In all cases, the energy gap of $Mn:CdGeP_2$ does not exceed that of pure $CdGeP_2$. In the FM state, there is no energy gap except for $x = 0.25$. Therefore, the effect of Mn doping on the energy gap in $CdGeP_2$ is similar to that in $Mn_xGa_{1-x}As$, where a reduction of the energy gap of the host semiconductor is found. This disagrees with the experimental observation of Medvedkin et al.[2], showing an increase of the energy gap upon incorporation in $CdGeP_2$.

CONCLUSIONS

The recently reported room temperature ferromagnetism in $Cd_{1-x}Mn_xGeP_2$ was investigated for $x = 1.0$, 0.5 and 0.25 using the FLAPW and DMol codes, within the generalized gradient approximation to the density functional theory. Moreover, we have compared the $MnGeAs_2$ and $MnGeP_2$ systems, in terms of structural, electronic and magnetic properties. At variance with recent experimental observations, we find that the total energy of the AFM state is always lower than the corresponding FM state for all the systems studied. The total magnetic moment per Mn atom is close to 5 μ_B for the Cd-rich P-based systems, whereas it is reduced in the Mn-rich P- and As-based chalcopyrites.

References

[1] H. Ohno, Science **281**, 951 (1998); Y. Ohno, D. K. Young, B. Beschoten, F. Matsukura, H. Ohno and D. D. Awschalom, Nature (London), **402**, 790 (1999).

[2] G. A. Medvedkin, T. Ishibashi, T. Nishi, K. Hayata, Y. Hasegawa and K. Sato, Jpn, J. Appl. Phys. **39**, L949 (2000).

[3] E. Wimmer, H. Krakauer, M. Weinert and A. J. Freeman, Phys. Rev. B **24**, 864 (1981); H.J.F.Jansen and A.J.Freeman, Phys. Rev. B **30**, 561 (1984).

[4] B. Delley, J. Chem. Phys. **113**, 7756 (2000); B. Delley, ibid. **92(1)**, 508 (1990).

[5] J. P. Perdew, K. Burke and M. Ernzerhof, Phys. Rev. Lett. **77**, 3865 (1996).

[6] L. Hedin and B. I. Lundqvist, J. Phys. C. **4**, 2062 (1971).

[7] Yu-Jun Zhao, W. T. Geng, K. T. Park and A. J. Freeman, Phys. Rev. B (accepted).

[8] A. Continenza, S. Picozzi, W. T. Geng and A. J. Freeman, submitted to Phys. Rev. B.

[9] J. E. Jaffe and A. Zunger, Phys. Rev. B **29**, 1882 (1984); S. C. Abrahams and J. L. Bernstein, J. Chem. Phys. **59**, 5415 (1973).

[10] Y. J. Zhao, W. T. Geng, A. J. Freeman and T. Oguchi, to be published on Phys. Rev. B.

SYMPOSIUM U

Soft Magnetic Alloys
and Ferrites

Ferromagnetic properties and Nanocrystallization behavior of Amorphous $(Fe_{0.99}Mo_{0.01})_{78}Si_9B_{13}$ Ribbons

Xiang-Cheng Sun[1,*], J. A. Toledo[1], S. Galindo[2] and W. S. Sun[3]

[1]Prog. Molecular Simulation, Instituto Mexicano del Petroleo, Lazaro Cardenas 152[#], 07730, D.F. Mexico   *E-mail: sun@imp.mx; Fax: +525-3336239
[2]ININ , Km.36.5, Carr. Mexico-Toluca, C.P.52045, Edo. de Mexico, Mexico.
[3]Institute of Metal Research, CAS, Shenyang, 110015, P. R. China

ABSTRACT

Ferromagnetic properties and nanocrystallization process of soft ferromagnetic $(Fe_{0.99}Mo_{0.01})_{78}Si_9B_{13}$ ribbons are studied by transmission electron microscope (TEM), X-ray diffraction (XRD), Mössbauer spectroscopy (MS), differential scanning calorimeters (DSC) and magnetization measurements. The Curie and crystallization temperature are determined to be $T_C=665K$ and $T_x = 750K$, respectively. The T_x value is in well agreement with DSC measurement results. X-ray diffraction patterns had shown a good reconfirm of two metastable phases $(Fe_{23}B_6, Fe_3B)$ were formed under in-situ nanocrystallization process. Of which these metastable phases embedded in the amorphous matrix have a significant effect on magnetic ordering. The ultimate nanocrystalline phases of α-Fe (Mo, Si) and Fe_2B at optimum annealing temperature had been observed respectively. It is notable that the magnetization of the amorphous phase decreases more rapidly with increasing temperature than those of nanocrystalline ferromagnetism, suggesting the presence of the distribution of exchange interaction in the amorphous phase or high metalloid contents.

INTRODUCTION

The very good promising bulk soft magnetic nanocrystalline (NC) materials, FeSiB based Finemet---are two phase alloys consisting of very fine BCC solid solution grains (typically with a diameter of about 10-15nm) embedded in a remaining amorphous matrix [1-5]. Yoshizawa [4] and co-workers revealed that the presence of small additions of Cu and Nb to some FeSiB-based alloys could allow the creation of two-phase materials by the devitrification, which showed superior soft magnetic properties. This effect was caused by the homogeneous precipitation of bcc α-Fe(M) nanocrystals embedded in the ferromagnetic amorphous matrix. Moreover, the addition of Cu, Nb had great influence on the formation of nanocrystalline materials by changing the crystallization behavior [3]. It can be expected that, study of crystallization of Fe-based metallic glasses containing transitional element additives will also benefit the development of new types of materials.

In the present work, by using transmission electron microscopy (TEM), differential scanning calorimeters (DSC), and X-ray diffraction (XRD), a study on nanocrystallization behavior had been carried out for $(Fe_{0.99}Mo_{0.01})_{78}Si_9B_{13}$ amorphous ribbons with a little amount of Mo element. Furthermore, intrinsic ferromagnetic properties were also studied using Mössbauer spectroscopy (MS) and vibrating sample magnetometer (VSM) techniques.

EXPERIMENT

Amorphous $(Fe_{0.99}Mo_{0.01})_{78}Si_9B_{13}$ (at%) alloy ribbons of 30mm width and about 25 μm thickness, were prepared by the melt-spinning techniques [6]. The transmission electron micrographs (TEM) were obtained with a JEOL-JEM100 EX electron microscopes, equipped with an *in situ* heating holder inside the electron microscope. The Mössbauer spectra were recorded using a conventional spectrometer of the electromechanical type with a $^{57}Co/Rh$ source. Differential scanning calorimetric measurements of the as-quenched ribbons were performed on a differential scanning calorimeter (DuPont 2000 Thermal Analysis DSC-2) using different heating rates under Ar gas atmosphere. X-ray diffraction (XRD) were carried out on a Simiens x-ray diffactometer (Cu, Kα radiation, λ=0.15418nm), Rietveld refinement was used to identify different phases. Magnetization measurements were carried out using a vibrating sample magnetometer (VSM) operating with applied magnetic fields up to 3600Oe from 16K to room temperature.

RESULTS and DISCUSSION

It should be noted that, two critical temperature points, crystallization temperature T_x and the Curie temperature T_c, usually determine the microstructure and their magnetic properties for Fe-based soft amorphous alloys. Consequently, it become very important to know this two critical temperature before our studying on $(Fe_{0.99}Mo_{0.01})_{78}Si_9B_{13}$ amorphous ribbons.

Fig. 1(a) shows the differential scanning calorimeters (DSC) thermal analysis for as-quenched ribbons samples at a heating rate of 10K/min. Two exothermic peaks are observed at around 768K and 803K, indicating this is typical primary crystallization process, in other words, two crystallization processes (nucleation and growth) took place, the around maximum of the first peak 750K reaches the crystallization temperature T_x for this $(Fe_{0.99}Mo_{0.01})_{78}Si_9B_{13}$ amorphous alloy.
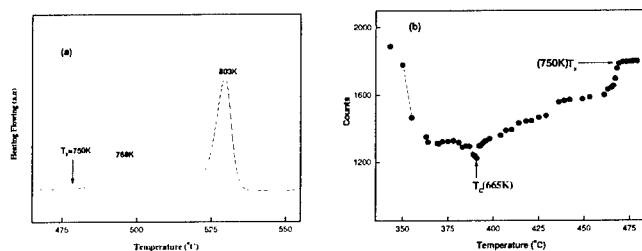
Figure 1 (a) DSC pattern at heating rate of 10K/min.   Figure 1 (b). The Curie temperature determination using Mössbauer spectrometer

In order to determine the Curie temperature T_c, the velocity transducer of the Mössbauer spectrometer was set at zero velocity and counts were recorded for a fixed counting time, 15s, while the temperature was raised at a rate of 1K/min from 400K to 780K. The results are shown in Fig. 1 (b). The Curie temperature is determined to be 665K. As the temperature is further increased, the counts rate increase slowly due to the second-order Doppler effect [8],

and increase until 750K, then keep unchanged. In other words, the amorphous $(Fe_{0.99}Mo_{0.01})_{78}Si_9B_{13}$ alloy has reached the crystallization temperature $T_x =750K$, the amorphous state gradually transformed into the nanocrystalline phases. Both T_x and T_c values are in good agreement to previous measurements [6,7].
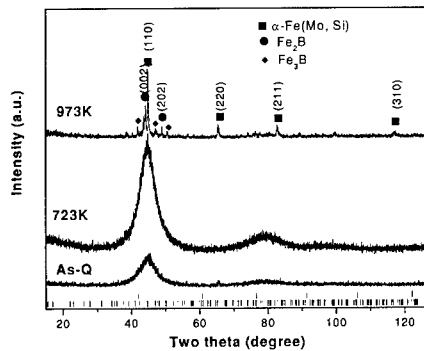
Figure 2   XRD patterns for as-quench $(Fe_{0.99}Mo_{0.01})_{78}Si_9B_{13}$ ribbon and two samples after 723K and 973K annealed treatments, respectively.
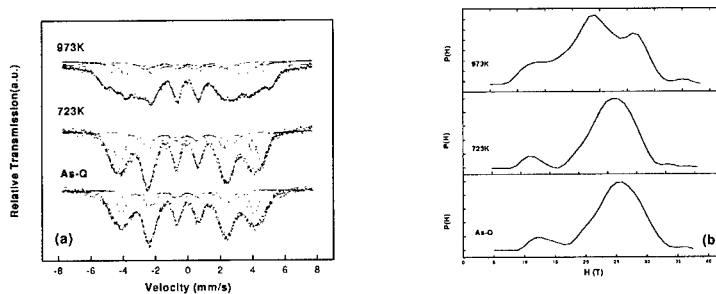
Figure 3   Mössbauer spectra (a) and hyperfine field distributions (b) for $(Fe_{0.99}Mo_{0.01})_{78}Si_9B_{13}$ ribbon and two samples after 723K and 973K annealed treatments, respectively.

Fig. 2 shows the XRD patterns for amorphous ribbon and two samples after 723K and 973K annealed treatments. It is clear to note that the as-quenched sample is in the amorphous state. On the heating the as quenched sample at 723K ($T_c<T< T_x$), very similar XRD pattern to amorphous state appears. However, very few metastable $Fe_{23}B_6$ (bcc), and Fe_3B (bct) borides phases are found using Rietveld XRD refinement analysis [6,7]. And from the following Mössbauer spectra (Fig.3(b)), hyperfine field value is also seen to increase compared with amorphous sample. This phenomenon is mainly due to the internal strain

relaxation and short-range order that is induced by thermal treatment. On the another hand, after annealed the sample at temperature 973K than T_x ($T> T_x$), nanocrystalline phases (α-Fe(Mo, Si), Fe_2B, Fe_3B) are observed in the XRD pattern. Two main nanophases, α-Fe(Mo, Si) (bcc) and Fe_2B (bct), can be clearly identified.

The Mössbauer spectra and hyperfine field distribution of amorphous ribbon and the samples after 732K and 973K annealed treatment were shown in Fig.3 (a) and Fig.3 (b), respectively. And the fitted Mössbauer parameters of amorphous ribbon and the annealed samples were shown in table 1. The Mössbauer spectrum of amorphous $(Fe_{0.99}Mo_{0.01})_{78}Si_9B_{13}$ exhibits a magnetic pattern with a hyperfine magnetic field of 250 KOe and the broad lines are to be expected in view of the disordered atomic arrangements, in which the strength of the hyperfine interactions change from site to site due to the structurally inequivalent Fe environment. However, after annealed the amorphous sample at $T_C<T< T_x$, very few metastable $Fe_{23}B_6$ (bcc), and Fe_3B (bct) borides phases appeared, and the hyperfine field value (Fig.3 (b)) was also found to increase. It is expected that the observed increase in the hyperfine fields could be originated from the occurrence of the short-range order through redistribution of atoms and changes of its relative position in metastable Fe_3B(bct) and $Fe_{23}B_6$(bcc) phases during structural relaxation. Nevertheless, after annealed the amorphous sample at $T > T_x$, the Mössbauer spectrum consisted of two main magnetic patterns due to two nanophases, which confirmed by former XRD patterns of Fig.2. From Table 1, according to the literature reports [8, 9], the magnetic hyperfine field pattern of 308KOe and 246KOe belongs to bcc α-Fe(Mo, Si) solid solutions and bct Fe_2B boride, respectively.

In particular, the magnetization of the amorphous $(Fe_{0.99}Mo_{0.01})_{78}Si_9B_{13}$ have been measured at $H_{app} = 3.6$ KOe at various temperatures from 16K to RT. The results are shown in Fig. 4. It is clear that the magnetization $M(T) / M(0)$ of the amorphous phase decreases more rapidly with reduced temperature T/T_C than those of α-Fe(Mo,Si) and Fe_2B nanocrystallines, which indicating the presence of the distribution of exchange interaction in the amorphous phase or high metalloid contents. And the saturation magnetization of the as-quenched amorphous materials extrapolated to 0K is found to be 2.01 μ_B/Fe atom. This value is smaller than the 2.22 μ_B of bcc Fe [10], suggesting that electron transfer from the metalloid atoms to the d band of the Fe atoms occur.

Table 1. The fitted Mössbauer parameters for $(Fe_{0.99}Mo_{0.01})_{78}Si_9B_{13}$ amorphous alloy and after different annealed treatment (H_{hf} is the magnetic hyper fine field, ΔE_Q is the quadrupole splitting, δ is the isomer shift and refers to α-Fe)

Annealed temperature (K)	H_{hf} (KOe)	δ (mm/s)	ΔE_Q (mm/s)
300	250.9±0.06	0.107±0.02	0.00±0.01
723	257.2±0.06	0.077±0.02	0.00±0.01
923	308.9±0.06	0.111±0.01	0.00±0.01
923	246.3±0.06	0.05±0.02	0.12±0.02
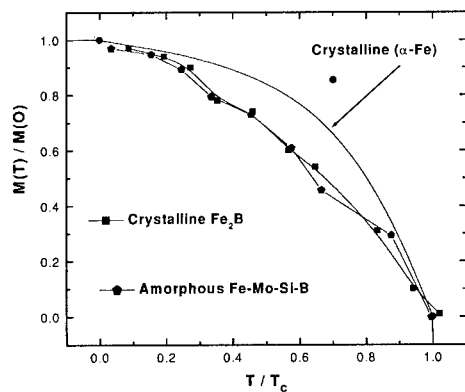
Figure 4. Reduced magnetization vs reduced temperature of the amorphous $(Fe_{0.99}Mo_{0.01})_{78}Si_9B_{13}$ ribbon and the α-Fe(Mo,Si) and Fe_2B nanocrystallines.
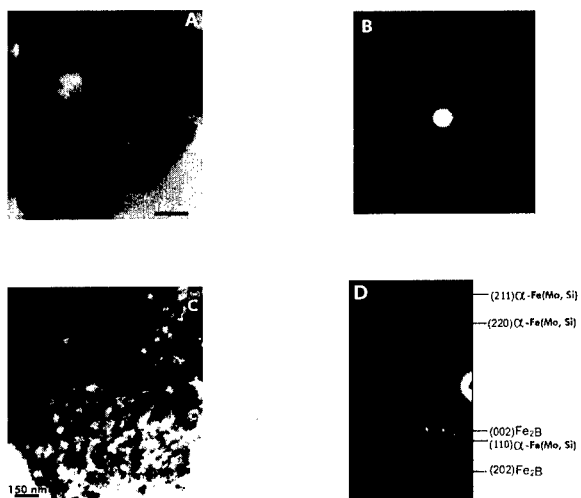
Figure 5 (a, b, c, d) Typical TEM morphologies and selected area electron diffraction for Fe-Mo-Si-B amorphous and nanocrystalline phases

Typical TEM images of the Fe-Mo-Si-B amorphous state and nanocrystalline alloy at annealing temperature, $T_a = 973K$ $(T > T_x)$, is shown in Fig.6 (a, b, c, d). From Fig.6 (c), small almost spherical nanometer grains precipitated homogeneously are observed. The selected area electron diffraction (Fig.6 (d)) patterns confirms that the randomly distributed nanocrystalline phases are crystalline α-Fe(Mo, Si) (bcc) and Fe_2B (bct) with a random orientation. Which is in good agreement with above XRD and Mössbauer analysis results.

CONCLUSIONS

Nanocrystalline Fe-Mo-Si-B alloys with different nanometer grain sizes have been successfully prepared by means of the *in situ* amorphous crystallization method. Two main nanophases are formed after full crystallization of the amorphous $(Fe_{0.99}Mo_{0.01})_{78}Si_9B_{13}$ alloy. The XRD pattern, M[]ssbauer spectra and in situ TEM observations suggest that the observed nanophases are the α-Fe(Mo, Si) (bcc) solid solution and the Fe_2B (bct).

The Curie temperature (T_c) and crystallization temperature (T_x) have been determined to be 665K and 750K using DSC thermal analysis and Mössbauer spectroscopy measurements. The reduced magnetization $M(T)/ M(0)$ of the amorphous phase decreases more rapidly with reduced temperature T/T_C than α-Fe(Mo, Si) and Fe_2B nanocrystalline ferromagnetism, this kind of rapid decrease can be described in terms of either a distribution of exchange interaction in the amorphous phase or high metalloid contents.

ACKNOWLEDGMENTS

REFERENCES:

1. J. C. Rawers, R, A. McCune and A. Adams, *J. Mater. Sci. Lett.* **7**, 958 (1988)
2. A, Hernado, P. Marin, M. Vazquez, J. M. Barandiaran, and G. Herzer, *Phys. Rev.* **B58**, 366 (1998).
3. X. D. Liu, J. T. Wang and B. Z. Ding, *J. Mater. Sci. Lett.* **12**, 1108 (1993)
4. Y. Yoshizawa, S. Oguma and K. Yamauchi, *J. Appl. Phys.* **64**(10), 6044 (1988)
5. M. Bario, C. Antonione, P. Allia, P. Tiberto and F. Vinai, *Mater. Sci. Eng.* **A179**, 572 (1994).
6. X. D. Liu, K. Lu, and Z. Q. Hu, *Mater. Sci. Eng.* **A179/180**, 386 (1994)
7. H. Y. Tong, J. T. Wang, H. G. Jiang and K. Lu, *J. Non-Cryst. Solids* **150**, 444 (1992)
8. M. B. Sterns *Phys. Rev.* **129**, 1136 (1963)
9. C. S. Kim, S. B. Kim, J. S. Lee and T. H. Noh, *J. Appl. Phys.* **79**(8) 5459 (1996)
10. R. S. Tebble and D. J. Craik, *Magnetic Materials* (Wiley-Interscience, NewYork, 1969), P. 51

Ferromagnetic Resonance On Metallic Glass Ribbons

M. Chipara, M. Toacsen[1], M. Sorescu[2]

Department of Physics and Astronomy, University of Nebraska, Lincoln, NE 68588-0111.
[1]Institute for Physics and Technology of Materials, Bucharest, PO BOX MG-7, Romania.
[2]Physics Department, Duquesne University, Pittsburgh, Pennsylvania 15282-0321, USA.

ABSTRACT

Ferromagnetic resonance data on metallic glasses, at room temperature, in X band, are discussed. The spectra were decomposed into two Lorentzian lines and the angular dependence of their main parameters (line width and position) is fully analyzed. It is proved that the usual approaches are not able to describe accurately the experimental data. This behavior is ascribed to the misalignment of the magnetization with respect to the external magnetic field, and successfully tested by using a "relaxed" resonance condition that allows a small misalignment of the magnetization relative to the external magnetic field.

INTRODUCTION

Metallic glasses are available as ribbons produced by rapid quenching from the melt. They exhibit both metallic and soft magnetic features and present high mechanical strength and hardness. Striped domain morphology is obtained [1] by annealing the metallic glass in external magnetic fields, confined within the plane of the ribbon. Magnetostrictive transducers are produced from metallic glasses, as the magnetomechanical coupling is usually large. Under the effect of the external magnetic field, the domain wall motion has a negligible contribution to the reorientation of the magnetization in an external magnetic field [1]. The free energy of a magnetic material, of unit volume, is [2]:

$$F = -\vec{M}\vec{H} + K_1(\alpha_1^2\alpha_2^2 + \alpha_1^2\alpha_3^2 + \alpha_2^2\alpha_3^2) + K_2(\alpha_1^2\alpha_2^2\alpha_3^2) + \alpha_1^2 K_1^U + \alpha_1^4 K_2^U +$$
$$+ (N_X M_X^2 + N_Y M_Y^2 + N_Z M_Z^2) + E'(\lambda, \sigma, NM^2) \tag{1}$$

The terms occurring in this equation are associated with (in the order of appearance) are: The Zeeman energy, the first and second order cubic magnetocrystalline anisotropy, the first and second order uniaxial anisotropy, the demagnetizing effects, the magnetostriction and higher order contributions. M is the magnetization, H the intensity of the applied magnetic field, K_1 and K_2 the cubic magnetocrystalline anisotropy constants, K_1^U and K_2^U the uniaxial magnetocrystalline anisotropy constants, and α_i (i =1,2,3) the direction cosines of the magnetization with respect to the coordinate axes. In the derivation of (1), only the diagonal components of the demagnetizing tensor N ($N_{jj} = N_j$ where j = X, Y, Z) were considered. The last term, E', depends on the magnetostriction constants λ, stresses σ demagnetizing factor N and on the direction of the magnetization, M. It was introduced to take into consideration stress and magnetostriction effects. The position of the ferromagnetic resonance line is given by [2, 3]:

$$\left(\frac{\omega}{\gamma}\right)^2 = H_{eff}^2 = \frac{(1+\varepsilon^2)^{1/2}}{M^2 \sin^2 \theta_0}\left[\left(\frac{\partial^2 F}{\partial \theta^2}\right)\left(\frac{\partial^2 F}{\partial \varphi^2}\right) - \left(\frac{\partial^2 F}{\partial \theta \partial \varphi}\right)^2\right] \tag{2}$$

$$\left(\frac{\partial F}{\partial \theta}\right)_{\theta=\theta_0} = 0 \qquad\qquad \left(\frac{\partial F}{\partial \varphi}\right)_{\varphi=\varphi_0} = 0 \tag{3}$$

The derivatives of the free energy are estimated at equilibrium ($\theta=\theta_0$, $\varphi=\varphi_0$). The damping associated with the time evolution of the magnetization in an external magnetic field is introduced by ε. Within the thermodynamic approach, the peak-to-peak line width of the ferromagnetic resonance spectrum, H_{PP} is [2]:

$$H_{pp} \propto \Delta H = \frac{\varepsilon\gamma}{M}\frac{1}{\left(\dfrac{d\omega}{dH}\right)}\left[\left(\frac{\partial^2 F}{\partial \theta^2}\right) + \frac{1}{\sin^2 \theta_0}\left(\frac{\partial^2 F}{\partial \phi^2}\right)\right] \tag{4}$$

EXPERIMENTAL

Ferromagnetic resonance (FMR) investigations on some amorphous magnetic ribbons ($Fe_{40}Ni_{38}Mo_4B_{18}$-2826 MB, $Fe_{78}B_{13}Si_9$-2605 TCA and $Fe_{66}Co_{18}B_{15}Si$-2826 CO) have been performed using a JES-ME-3X spectrometer, operating in the X band ($\approx$ 9 GHz).
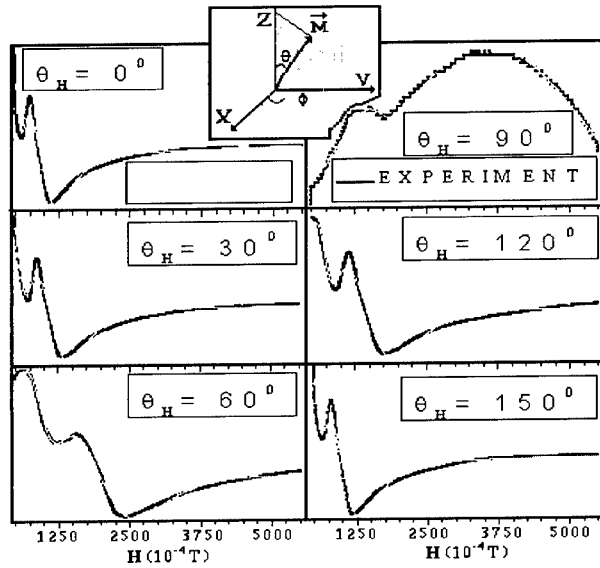
Figure 1. The FMR spectra of METGLASS 2605 TCA at different orientations.

The angular dependence of the resonance lines, for an out of plane configuration (i.e. the static external field is normal to the plane of the ribbon-see the inset of Figure 1), at room temperature, was investigated in detail. The FMR spectrum of the amorphous magnetic ribbons (which is in fact the derivative of the absorption line [2, 5]) has been successfully deconvoluted into two Lorentzian lines, for any composition and most orientations of the magnetic ribbon relative to the external magnetic field (see Figure 1), using the relation [5]:

$$I(X) = \frac{32I^{(1)}\frac{(H - H_{res}^{(1)})}{H_{PP}^{(1)}}}{\{3 + 4[\frac{(H - H_{res}^{(1)})}{H_{PP}^{(1)}}]^2\}^2} + \frac{32I^{(2)}\frac{(H - H_{res}^{(2)})}{H_{PP}^{(2)}}}{\{3 + 4[\frac{(H - H_{res}^{(2)})}{H_{PP}^{(2)}}]^2\}^2} + P_1 + P_2 H \quad (5)$$

Where $H_{res}^{(1)}$ and $H_{res}^{(2)}$ are the resonance field for the low and high field components, $I^{(1)}$ and $I^{(2)}$ are the components of the resonance line amplitude for the low and high field components, $H_{PP}^{(1)}$ and $H_{PP}^{(2)}$ are the resonance line width for the low and high field components, respectively. The parameters P_1 and P_2 allow for a linear base line correction. The possibility to decompose the resonance spectrum into symmetric Lorentzian lines indicates that the contribution of skin effects is negligible.

The position and width of the high field resonance line is sensitive to the orientation of the film relative to the external magnetic field. The low field resonance line position, $H_{res}^{(1)}$ cannot be recorded for all orientations, as it occurs at very small magnetic fields. However, the deconvolution allows, at most orientations, an accurate estimation of the resonance line parameters for both lines. The resonance line position was noticed at the lowest magnetic field if the external magnetic field is parallel to the plane of the sample. As may be observed from Figure 1, starting to rotate the sample, from this orientation, the resonance field position is increased until a maximum is reached in the perpendicular configuration (external field normal to the plane of the sample). In this case, the resonance line position is given by [2, 4]:

$$H_{eff}^2 = H^2 + H(4\pi M_S + 2H_{K1} - 2H_{K2}) + H_{K1}(4\pi M_S + H_{K1} - H_{K2}) \quad (6)$$

As the FMR studies on metallic glasses concern materials with a magnetocrystalline anisotropy smaller by 2 orders of magnitude than the demagnetizing effects [4], taking into account that g $\approx$2.0, it is possible to have an estimation of $4\pi M_s$ by neglecting the contribution of these terms. The values of $4\pi M_s$, associated with the high field line are: 2.13 T (2605 TCA), 6.53 T (2826 CO) and 2.07 T (2826 MB). These values are of the correct order of magnitude, with the exception of sample 2826 CO. The same calculus for the low field lines result in 1.1 T (2605 TCA), 1.09 T (2826 CO) and 1.08 T (2826 MB). The following relation gives the resonance line position for the parallel configuration:

$$H_{eff} = H - 4\pi M_S + H_{K2} - (1/2)H_{K1} \quad (7)$$

Neglecting the contribution of the magnetocrystalline anisotropy the estimated values of $4\pi M_S$ associated with the high field lines, are 0.095 T (2605 TCA), 0.19 T (2826 CO) and 0.12 T (2826 MB). The value of the resonance field corresponding to the low field line cannot be

described by the expressions (6) and (7), whereas for the high field line a qualitative agreement is met for the parallel configuration (excepting the 2605 SC1 sample). The low field resonance cannot be considered as an AFMR line as neither the phase of the resonance line, nor the position is consistent with this hypothesis [4]. The strongest deviation from the theoretical expectations is noticed when the sample is perpendicular on the magnetic field. It was concluded that the deviation of the magnetization from the direction of the external magnetic field is stronger in the perpendicular configuration, due to the shape anisotropy. Under these circumstances, the underlying approximations used to derive the relations (6) and (7) are not fulfilled. From the physical point of view, this implies that the sample is not fully saturated, at the resonance field. In order to test this hypothesis, an expression for the angular dependence of the resonance line, supposing a small misalignment of the magnetization along the external magnetic field, was derived.

$$H_{1,2} = -[2H_{K,2}(3\sin^2\theta_H \cos^2\theta_H - \cos^4\theta_H) + M(N_\perp - N_K)\cos 2\theta_H] \pm$$

$$\pm \{[2H_{K,2}(3\sin^2\theta_H \cos^2\theta_H - \cos^4\theta_H) + M(N_\perp - N_K)\cos 2\theta_H]^2 + \lambda H_{eff}^2\}^{1/2} = 0$$

$$(8)$$
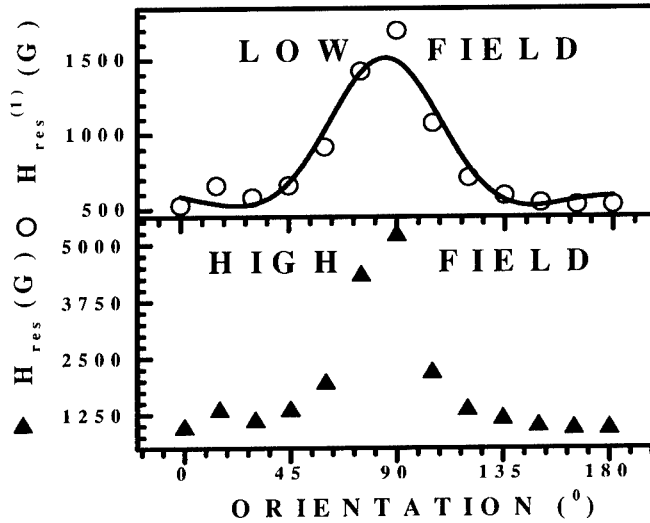
Figure 2. The angular dependence of the resonance line position, for the sample 2605 TCA.

Where λ is a constant of the order $\sin\theta/\sin\theta_H$ that allows an estimation of the magnetization misalignment, θ is the orientation of the magnetization with respect to the OZ axis and θ_H is the orientation of the external magnetic field with respect to the same axis. Actually, only θ_H is known and θ may be estimated by using an appropriate model. The resonance line position was

derived supposing an uniaxial magnetocrystalline field and the corresponding H_{KI} term has been absorbed in the parallel demagnetizing term $N_\parallel = N_K - H_{KI}/4\pi M_S$.

The best fit obtained using the relation (9) is represented by thick curves in Figure (2). Although the agreement is good, the largest deviation between the prediction based on equation (9) and the experimental data is noticed when the external magnetic field is perpendicular on the ribbon. That indicates that although a significant improvement was obtained, the misalignment of the magnetization with respect to the external magnetic field, in this configuration, is not very small. Neglected the effect of mosaicity, the angular dependence of the resonance line width is roughly identical with the angular dependence of the resonance line position, up to a multiplicative constant, that is equal to the dampening of the magnetization, ε. As may be observed, from Figure 3, such dependence is qualitatively supported by the experimental data. The largest deviation is noticed in the perpendicular configuration and may be due to the fact that this oversimplified picture assumed that the dampening of the magnetization is independent on the misalignment between the external magnetic field and the magnetization of the sample. The damping constants are, up to the same multiplicative factor equal to 0.429 (2605 TCA), 0.503 (2826 MB) and 0.765 (2826 CO).

The origin of the second line is not obvious. In ferromagnetic experiments, two or more solutions are possible and therefore, several resonance lines may be observed. The possibility of a stripe structure of magnetic domains, the mosaicity or the texture may also induce the split of the resonance line into several components. As this behavior is related to a dependence of the
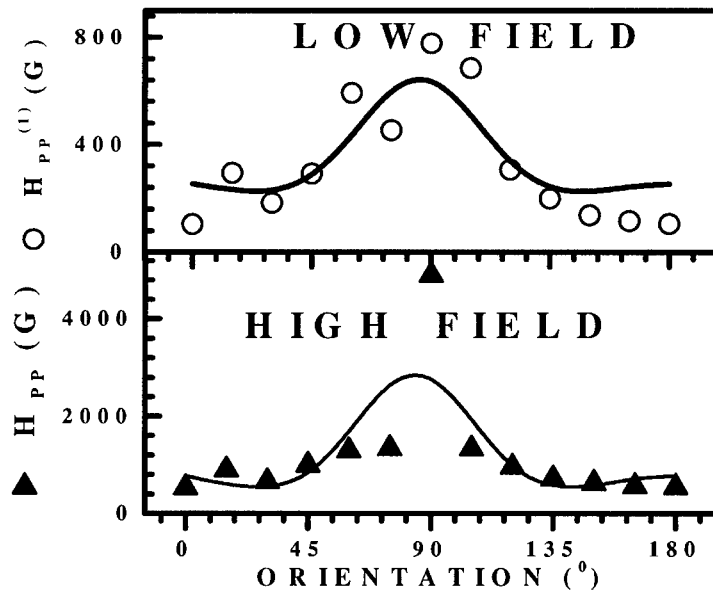
Figure 3. The angular dependence of the resonance line width, for the sample 2605 TCA

ferromagnetic resonance spectra in a plane normal to the film, it seems reasonable to suppose that long spin waves with components normal to the film are excited. Two main mechanisms would induce a discontinuity in the shift of the resonance field, in the perpendicular configuration. The first is related to the impossibility of the magnetization to point along the external magnetic field. This behavior is due to the demagnetizing field and appears in not fully saturated samples. In magnetic wires and stripes, the magnetostatic interactions would shift also to infinity the resonance field in the perpendicular configuration (magnetic field normal on the wire). In the general case, although the enhancement of magnetostatic interaction reduces the coercive field, an increase of the saturation field is expected. This increase in the saturation field amplifies the contribution of the demagnetizing term and makes difficult the alignment of the magnetization along the external field, in the case in which the external magnetic field is normal on the ribbon [6].

DISCUSSIONS

Ferromagnetic resonance studies on magnetic glasses reveals the presence of at least two symmetric Lorentzian lines, and indicates the absence of skin effect. The angular dependence of the resonance line reflects that the magnetization is not perfectly along the external magnetic field, mainly if the external magnetization is normal to the plane of the film. This is due to the demagnetizing field. An expression for the angular dependence of the resonance field, supposing a small misalignment of the magnetization relative to the external magnetic field was proposed and successfully tested. The large value estimated for this misalignment of the magnetization suggests a supplementary contribution due to stripe like structure of the sample with magnetostatic interactions among these stripes. From the angular dependence of the resonance line width, the dampening constant is estimated. However, the correlation between the predictions and the experimental results is only qualitative as in order to avoid calculus complications it was supposed that the dampening constant is independent on the magnetization misalignment.

REFERENCES

1.   L. T. Kabacoff, J. Appl. Phys. **53**, 8098 (1982).
2.   S. V. Vonsovskii, *Ferromagnetic Resonance*, (Pergamon Press, Oxford 1966) p. 22.
3.   Ch. Kittel, *Introduction to Solid State Physics*, seventh edition, (John Wiley & Sons, New York, 1996) p.503.
4.   J. F. Cochran, K. Kyrtie and B. Heinrich, J. Appl. Phys. **53**, 2261 (1982).
5.   C. P. Poole, Jr. and H. A. Farach, *The Theory of Magnetic Resonance*, (Wiley-Science, New York, 1972) p. 364-395.
6.   U. Ebels, P.E. Wigen, and K. Ounadjela, J. Mag. Mag. Mat. **177-181**, 1239 (1998).

Characterization of Softmagnetic Thin Layers using Barkhausen Noise Microscopy

Jochen Hoffmann[1], Norbert Meyendorf[1], Iris Altpeter[2]
Center for Materials Diagnostics, University of Dayton,
Dayton, OH 45469-0121, U.S.A.
Fraunhofer Institute for nondestructive Testing IZFP,
Saarbruecken, Germany

ABSTRACT

Ferromagnetic materials are essential for data recording devices. For inductive or magnetoresistive (MR) sensors softmagnetic thin layer systems are used. Optimal performance of these layers requires homogeneous magnetic properties, especially a pronounced uniaxial magnetic anisotropy. Furthermore, microstructural imperfections and residual stresses influence the magnetic structure in the layer system.

Barkhausen Noise Microscopy enables the characterization of such thin layers. By cycling the magnetic hysteresis of ferromagnetic material electrical voltages (the Barkhausen noise) are induced in an inductive sensor. Miniaturization of the sensor and the scanning probe technique provides resolution down to few micrometers. Two materials were examined in terms of their structure, thickness, residual stresses and heat treatment condition: Sendust, used in inductive sensors and nanocrystalline NiFe, used in MR-sensors. In quality correlations to Barkhausen noise parameters were found. For representative sample a quantification of residual stress distribution could be established employing X-ray stress analysis.

INTRODUCTION

Currently there are several sophisticated methods available to image and characterize the magnetic structure of ferromagnetic thin layers. Especially Magnetic Force Microscopy MFM and Kerr-optical measurements are very popular. For dynamic magnetization processes ferromagnetic resonance spectroscopy or Brillouin scattering are frequently used. An important issue is the influence of mechanical properties, e.g. residual stress on the magnetic performance of the layer system. Residual stresses in such layers are due to non-optimized process conditions, undesired phase transitions or insufficient ductile adaptation to the substrate. They deteriorate the signal to noise ratio and thus the sensor sensitivity. Barkhausen Noise Microscopy provides the possibility to characterize mechanical and magnetic properties of softmagnetic layers both with high accuracy and lateral resolution.

EXPERIMENTAL DETAILS

By tracing the hysteresis curve of a ferromagnetic material, electrical impulses are induced in an electromagnetic inductive probe: the magnetic Barkhausen noise. Barkhausen events occur when domain wall movement has to overcome microstructural obstacles. Usually most noise activity can be measured in the vicinity of the coercivity H_C. The main parameters derived from the Barkhausen noise signal are the Barkhausen noise maximum M_{MAX} and the coercive field
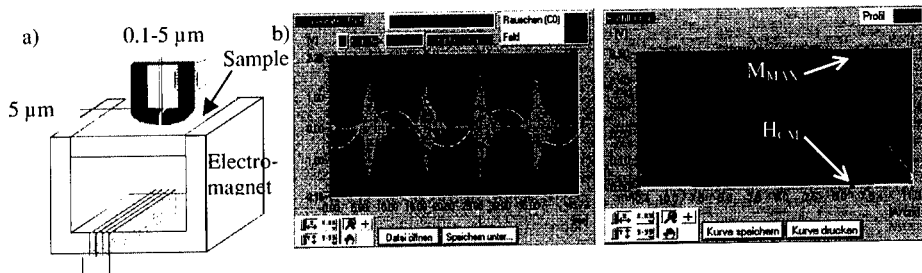
Figure 1. a) Schematic of miniaturized inductive sensor   b) Barkhausen noise signal

strength H_{CM}, which is the position of M_{MAX} within the magnetic field H (Fig. 1b) [1]. The Barkhausen Noise and Eddy Current Microscope (BEMI) enables the measurement of both Barkhausen noise and eddy currents [2]. A very efficient manipulation system precisely guides the miniaturized sensors to a positional accuracy of 1 µm across the surface to be tested. The sensors include ferrite cores with narrow air gaps (0.1 to 5 µm) that provide small exchange areas between sample and sensor and thus the possibility to map the Barkhausen noise with high lateral resolution down to 10 µm (Fig. 1a).

Two materials were examined: (i) Sendust (84.9 wt% Fe, 9.6 wt% Si, 5.5 wt% Al) used as layer material in inductive sensors, especially in data write units. Sendust achieves its best magnetic performance within a layer thickness range of 1-5 µm. However, it is necessary to anneal the sputtered material to obtain ordered intermetallic structures that provide the desired uniaxial magnetic anisotropy [3]; (ii) multi-layer systems of nanocrystalline NiFe used in magneto-resistive read sensors. This material can operate below a thickness of 20 nm providing the possibility of higher data density [3].

RESULTS

The magnetic properties of softmagnetic layers are significantly influenced by the layer thickness. This is exemplary shown for the coercivity in fig. 2a (H_C from hysteresis - and H_{CM} from Barkhausen noise measurements). The coercivity increases dramatically from 0.5 µm to 0.1 µm layer thickness.

The same thickness dependence can be observed for the residual stress states which can be explained with the high strain the first atomic layers of sputtered material has to endure due to the attachment to the substrate. The resulting stress can relax with increasing thickness. This mechanical property change will have an influence on the magnetic parameters (Figure 2 shows indirect the almost linear relation between stress and coercivity with respect to the film thickness), but basically the drastic change in coercivity is due to the change from Bloch wall - to Néel wall structures with decreasing thickness. Thus, BEMI measurements enable fast and easy determination of the threshold thickness for this phenomenon [4].

Using soft magnetic layers in read/write sensors requires homogeneous structural and magnetic properties, e.g. coercivity. Thus local variation of the H_{CM} parameter is an important

information for the use and optimization of magnetic layer systems. The H_{CM}-surface scan on a NiFe multi-layer system is shown in Fig. 3a. For comparison, Fig. 3b shows the H_C-values determined using a Kerr BH-Looper over the same area (5 x 5 measurement points). It is clearly apparent that there is good qualitative agreement between the results obtained [3,5,6].

a)

b)
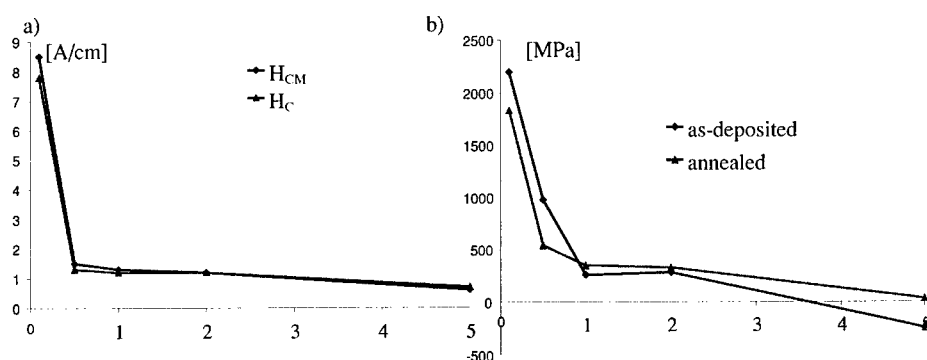
Figure 2. a) coercivity and b) residual stress as functions of Sendust layer thickness

Microstructure and texture of the magnetic layer can be significantly affected by changes in the growth condition of the column-like crystals. A possible method of manipulating this growth is applying an interface layer on the substrate prior to magnetic layer deposition. Coercivity, permeability and residual stresses of the magnetic layer can be varied over a broad range. Figure 4 shows SEM images of broken Sendust cross sections sputtered onto ceramic substrates. The ceramics were previously sputtered with either Cr- or SiO_2-interface layers. The images clearly show differences in the resulting crystalline structure of Sendust.

a)
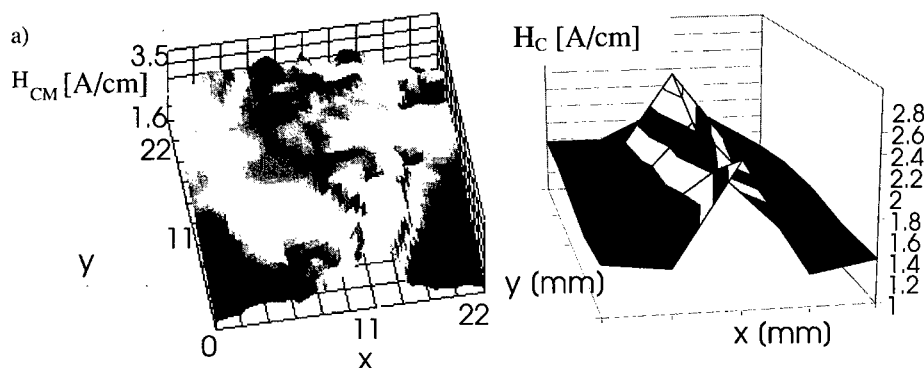
Figure 3. Mapping of coercivity (NiFe multi-layer system)
a) Barkhausen noise H_{CM}-scan   b) H_C-scan with Kerr BH-Looper

The clear dependence between Barkhausen profile and used interface layer is of great value for the processing of such magnetic layers. Figure 4 also shows the Barkhausen noise amplitude

as a function of time for 2 μm and 8 μm Sendust-layers sputtered either on Cr-layer or a SiO_2-layer. For the latter undesired high coercivity and low M_{MAX} can be observed. Specific individual structural properties of the coatings such as their microstructural condition (phase proportion, grain size) and residual stress apparently affect the domain wall movement in a very significant and characteristic way. The noise profile permits controlling the growth conditions of soft magnetic layers to be during manufacturing [3,5,6].
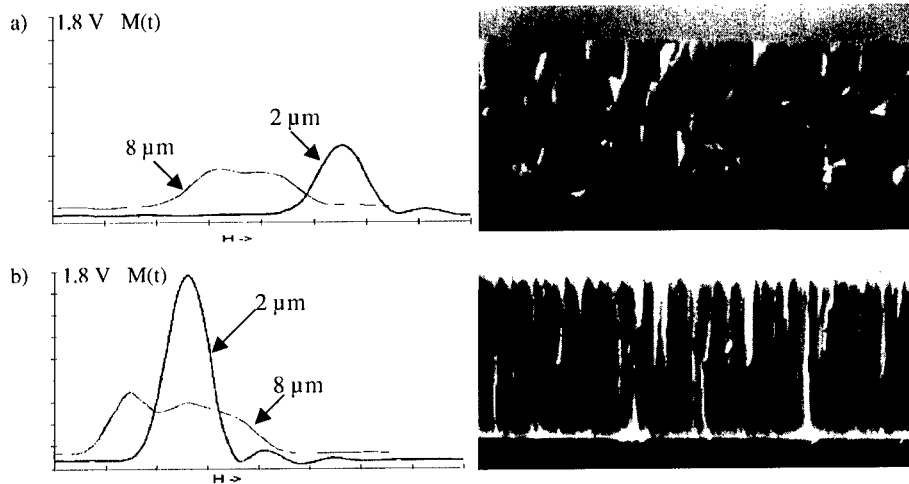
Figure 4. Barkhausen noise over time and cross section SEM images for Sendust-layers of 2 μm and 8 μm   a) with SiO_2 interface layer   b) with Cr interface layer

The effect of tensile and compressive stresses on the Barkhausen amplitude is a result of the partial ordering processes taking place within the magnetic structure. The coercive field strength (magnetic hardness) generally increases with increasing mechanical hardness. For quantitative nondestructive hardness or residual stress measurements, the magnetic test parameters must be calibrated with the help of mechanical hardness or stress measurements [1].

Using X-ray diffraction, it was possible to make a number of residual stress measurements on a single specimen (diameter of the X-ray beam: approx. 100 μm). Figure 5 shows a M_{MAX}- scan compared to the X-ray scan of the exact same area (2×2 mm^2) on a annealed Sendust sample (layer thickness: 2 μm). The two images show almost identical structures. In addition, both the residual stress values and the M_{MAX}-values within this area have comparably high gradients (310 – 396 MPa and 2.26 – 3.84 V). Thus, the BEMI enables fast and highly resolved qualitative (and with proper calibration) quantitative determination of the residual stress distribution across a thin soft magnetic layer [3,5,6,7].
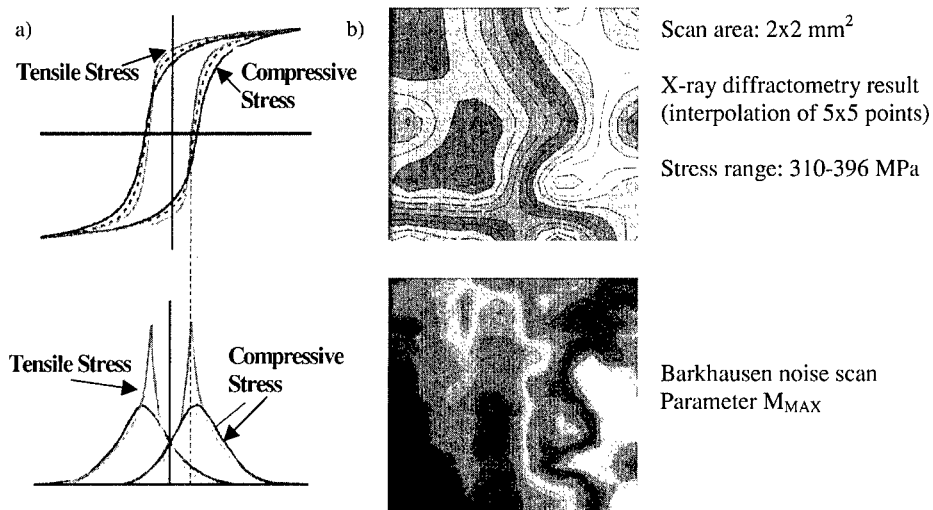
Figure 5. a) Stress influence on magnetic properties
b) Mapping of M_{MAX} compared to X-ray stress analysis on 5 µm thick Sendust

SUMMARY

Barkhausen Noise Microscopy (BEMI) provides high potential for improving the development and manufacturing of new magnetic materials. It can be used to optimize the processing parameters used during processing of thin ferromagnetic layers. The efficiency of Barkhausen noise microscopy was demonstrated on a series of thin softmagnetic materials.

The BEMI could be used to provide important information about the microstructure or the magnetic hardness of these materials. It was possible to distinguish between Bloch- and Néel wall domain structures by evaluating the coercivity of the respective samples. Using the BEMI a quick and highly localized qualitative, and by calibrating the results with by X-ray diffraction quantitative, determination of the residual stress present in Sendust samples can be obtained. Investigations carried out on Sendust-coatings with different coating structures show that the BEMI allows the examination of structural differences resulting from the use of different types of intermediate layers, such as SiO_2 and Cr.

ACKNOWLEDGEMENTS

References

1. W. Theiner, I. Altpeter, "Stress Analysis using magnetic Effects", *Handbook for Stress Measurement* (VDI-Verlag, Düsseldorf, Germany, 1989).

2. I. Altpeter, W. Theiner, M. Gessner, European Patent EPO 595 117B1, (4 April 1994).

3. J. Hoffmann, "Characterization of ferromagnetic Thin Films using electromagnetic Techniques", MS. Thesis, University of Saarland, Germany (1998).

4. A. Ashida and M. Hattori, "Structure and magnetic Properties of Sendust/Under-Layer Films", *IEEE Trans. Magn.* **5**, 445-450 (1990).

5. J. Hoffmann, I. Altpeter, M. Kopp, H. Grimm, W. Nichtl-Pecher, "Characterization of thin Ferromagnets using Barkhausen Noise Microscopy", *Practical Metallography* **37**, 261-270, (2000).

6. I. Altpeter, J. Bender, J. Hoffmann, M. Kopp, D. Rouget, Final Report of the Fraunhofer-Institute for nondestructive Testing IZFP to project 03N80003B7 initiated by the German Federal Department for Science and Technology (Saarbrücken, Germany, 1998).

7. I. Altpeter, J. Hoffmann, W. Nichtl-Pecher, "Detection of Residual Stresses and Nodular Growth in Ferromagnetic Layers with Barkhausen and Acoustic Microscopy", *Proceedings of 8th International Symposium on Nondestructive Characterization of Materials* (Boulder, CO, 1997).

Magnetic Permeability and Relaxation Frequency in High Frequency Magnetic Materials.

M.I. Rosales, H. Montiel and R. Valenzuela
Institute for Materials Research, National University of Mexico
P.O. Box 70-360, Mexico D.F., 04510 Mexico.

ABSTRACT

An investigation of the frequency behavior of polycrystalline ferrites is presented. It is shown that the low frequency dispersion ($f < 10$ MHz) of permeability is associated with the bulging of pinned domain walls, and has a mixed resonance-relaxation character, closer to the latter. It is also shown that there is a linear relationship between the magnetocrystalline anisotropy constant, K_1, and the relaxation frequency. The slope of this correlation depends on the grain size. Such a relationship could allow the determination of this basic parameter from polycrystalline samples.

INTRODUCTION

Many electronic devices such as switched-mode power supplies involve [1] the use of magnetic materials with high magnetic permeability ($\mu_{rel} \geq 1000$) at high frequencies ($f \geq 10$ MHz). The active magnetization processes in the 1 - 50 MHz frequency range have been found to be domain wall movements and spin rotation [2,3]. At frequencies higher than ~50 MHz, domain walls become unable to follow the excitation field, and only spin rotation remains. Recent studies [3,4] associate a resonance character to the permeability dispersion of domain walls. We think, however, that a more detailed investigation is needed. In this paper we present a study of the frequency behavior of polycrystalline Ni-Zn ferrites, with the aim of progressing also on the understanding of the influence of grain size on the relaxation frequency.

EXPERIMENTAL TECHNIQUES

Polycrystalline ferrite samples in the formula $Ni_xZn_{1-x}Fe_2O_4$ (with $x = 0.30, 0.35$ and 0.40) were prepared by the ceramic method, from the reactive grade oxide reagents NiO, ZnO and Fe_2O_3. The initial wet milling of raw materials was followed by press in the shape of toroids and sintering for various combinations of time and temperature (6-96 h at 1150 °C). The furnace atmosphere was oxidizing (100% O_2 at 1 atm) in order to reduce the possibility of reduction of ferric to ferrous ions, which would reduce the electric resistivity and therefore would increase the frequency losses. Their grain size was determined by counting on scanning electron microscopy (SEM) micrographs of selected surfaces.

Real and imaginary impedances were measured in a system [2] including an HP 4192 A Impedance Analyzer controlled by a PC computer. Measurements were carried out in the 5 Hz-13 MHz frequency range at temperatures from 110 to 450 K. Real and imaginary permeability

values were calculated from impedances by using the relationship $\mu^* = KL^* = (j/\omega)Z^*$, where μ^* is the complex permeability, K is a geometrical constant (for toroids), L^* is the complex inductance, ω is the angular frequency ($\omega = 2\pi f$), j is the basis of imaginary numbers ($\sqrt{-1}$) and Z^* is the complex impedance. Note that the presence of j leads to a cross-over of values, since the real part of inductance (and therefore of real permeability) is given by the imaginary value of impedance, and conversely, the imaginary part of permeability depends on the real part of impedance. Our system allows to obtain up to 94 permeability values at discrete frequencies in less than 3 min.

EXPERIMENTAL RESULTS AND DISCUSSION

Real and imaginary permeabilities, μ' and μ'' respectively, as a function of frequency of the excitation field appear in figure 1. A clear dispersion appears, indicated in the real permeability by the decrease from a given value at low frequencies toward a lower value at higher frequencies, and by a maximum in the imaginary permeability. The complex plane, or Cole-Cole plot, where the imaginary permeability is plotted as a function of real permeability, exhibits a locus of points with the tendency to a semicircle.
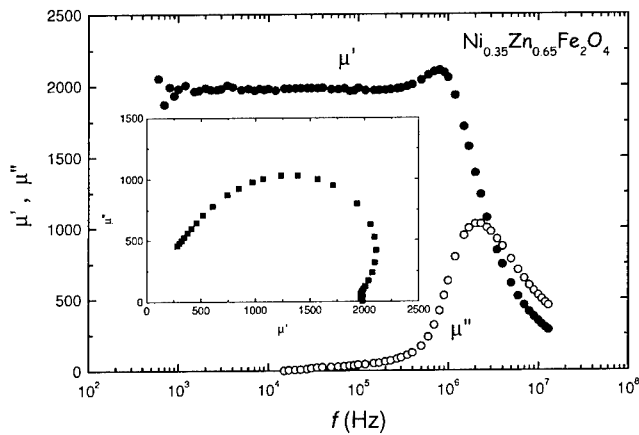
Figure 1. Spectroscopic plots of the real and imaginary parts of permeability for $x = 0.35$ ferrite. In inset, the Cole-Cole plot.

Simple dispersions typically can have either a resonant or a relaxation character. Resonant systems possess a natural frequency of vibration. If a general equation of motion is considered,

$$m \, d^2x/dt^2 + \beta \, dx/dt + \alpha \, x = F(t) \tag{1}$$

where m is the effective mass, x the displacement, β the damping coefficient, α the restoring term and $F(t)$ the excitation force, then it can be shown that a resonance dispersion occurs if the effective mass, m, is comparable to the damping term, β. The resonance frequency is then given by:

$$\omega_s = 2\pi f_s = (\alpha / m)^{1/2} \tag{2}$$

When a resonant system is submitted to an excitation of increasing frequency going through such natural frequency, the resonance appears in μ' plots as a large peak followed by a vertical drop down to the negative part of μ', finally recovering a zero value. In μ'', the resonant dispersion appears as a strong maximum. These behaviors have been observed in the case of ferromagnetic resonance in many magnetic materials, and a typical example appears in Ref. [5]. It can be shown that in complex plots, where μ'' is plotted as a function of μ' (also known as Cole-Cole plots), a resonance exhibits a full circle [6].

In a relaxation dispersion, damping is stronger than the effective mass ($m \ll \beta$) the inertia term can be neglected, and the solution of Eq. (1) simplifies to:

$$\omega_x = 2\pi f_x = \alpha / \beta \tag{3}$$
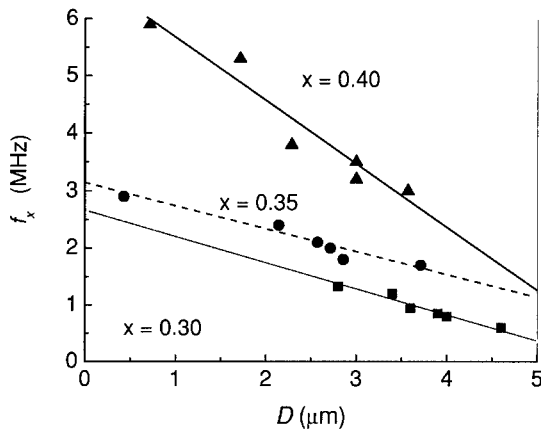
Figure 2. Linear relationship between relaxation frequency and grain size for the studied compositions.

a) ━━━ 10 μm   b) ━━━ 10 μm
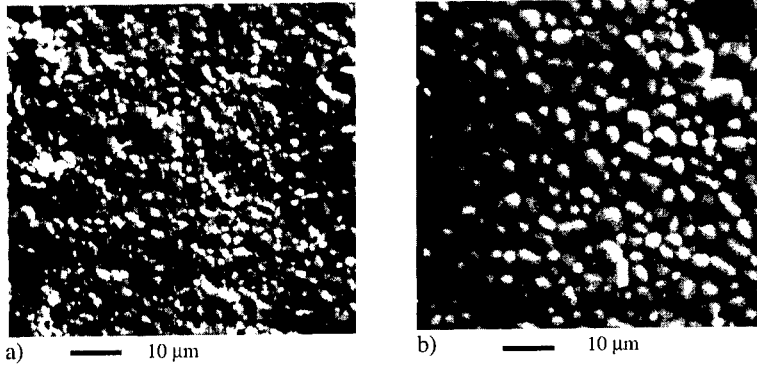
Figure 3. Typical microstructure of samples, for a). 6 h, b). 96 h of thermal treatment ($x = 0.35$).

In this case, the dispersion appears in μ' as a simple decreasing and in μ'' as a maximum at the relaxation frequency, ω_x ($\omega_x = 2\pi f_x$), and the Cole-Cole plot shows a semicircle. At this point, we can establish that the dispersion shown by our samples is closer to a relaxation than to a resonance, and use the relaxation frequency, f_x, in the following.

The relaxation frequency depends not only on the intrinsic parameters of ferrites, but also on the granular structure, as shown in figure 2, where a linear correlation is observed between the average grain size, D, and the f_x. Figure 3 shows the typical microstructure of samples sintered for 6 and 96 hr, in this case for composition $x = 0.35$.
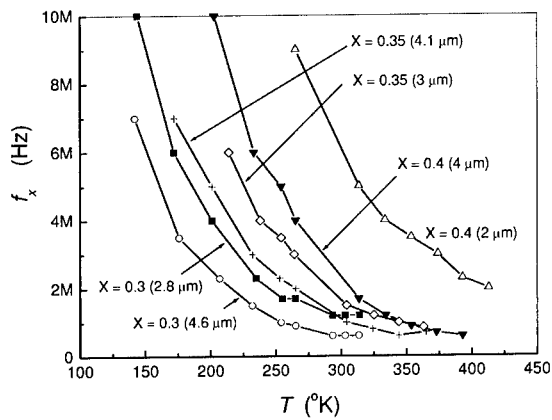
Figure 4. Thermal behavior of relaxation frequency for the studied compositions.
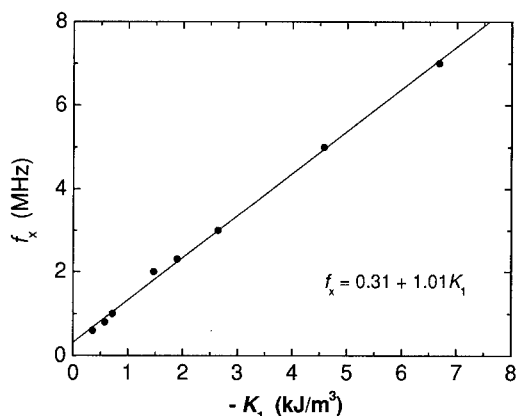
Figure 5. Relaxation frequency (f_r) as a function of anisotropy constant (K_1).

It is interesting to look at the thermal behavior of the relaxation frequency, as shown in figure 4. The decrease observed reminds in a way the decrease observed in the case of the magnetocrystalline anisotropy constant, K_1, for the case of $x = 0.35$, where single crystals were prepared [7]. When this data is plotted as a function of relaxation frequency (for each temperature), it has been shown that a linear relationship is obtained [2,8]. These results are presented in figure 5 for composition $x = 0.3$. However, the grain structure or grain size distribution has a strong influence on the relaxation frequency; a particular relationship is observed for each sample (with a different granulometry), figures 3 and 4. In order to "normalize" by average grain size, D, we have plotted $f_x D$ against the temperature, which leads to a single relationship for each composition, figure 6. In this way, the effect of grain size is taken into account.

CONCLUSIONS

We have analyzed the character of the dispersion observed in the permeability of polycrystalline ferrites and shown that it is closer to a relaxation than to a resonance. We have also shown the dependence of relaxation frequency on the grain size, as well as the effects of the latter on the relationship between magnetocrystalline anisotropy and relaxation frequency.

ACKNOWLEDGMENTS
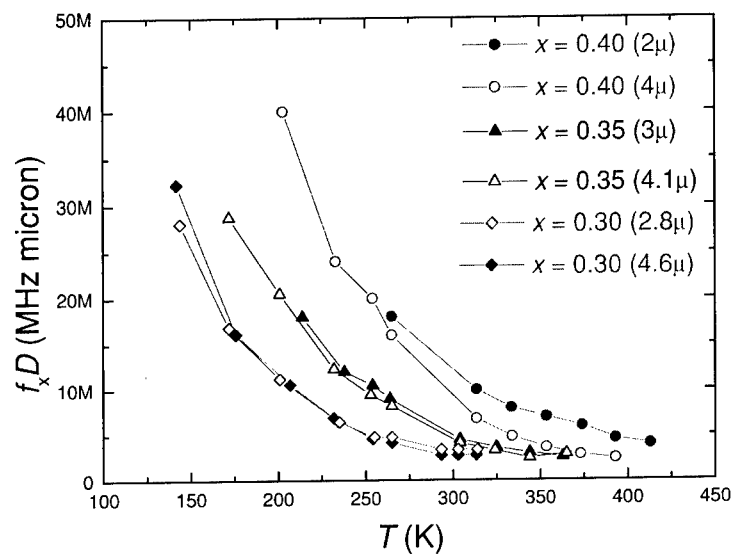
Figure 6. "Normalization" of the thermal behavior of relaxation frequency by the average grain size.

REFERENCES

1. R. Valenzuela, *Magnetic Ceramics*, Cambridge University Press p. 255 (1994)
2. M.I. Rosales, E. Amano, M.P. Cuautle and R. Valenzuela, *Mat. Sci. Eng.* **B49**, 221 (1997).
3. T. Nakamura, *J. App. Phys.* **88**, 348 (2000).
4. T. Nakamura, T. Tsutaoka and K. Hatekamaya, *J. Magn Magn. Mat.* **138**, 319 (1994).
5. R. Valenzuela and J.T.S. Irvine, *J. Appl. Phys.* **72**, 1486 (1992).
6. P. Ciureanu, C. Aykel, M.R. Britel, D. Ménard, L.G.C. Melo, A. Yelon, R. Valenzuela and P. Rudkowski, *Proceedings of the 1999 Asia-Pacific Microwave Conference, Singapore*, Dec. 2-5, **vol. 3** p. 876 (2000).
7. B. von Groenou and J.A. Schulkes, *J. App. Phys.* **38**, 1133 (1967).
8. R. Valenzuela and J.T.S. Irvine, *J. Magn Magn. Mat.* **160**, 386 (1996).

Hard Bulk Magnets

Effect of Composition and Processing on the Microstructure and Magnetic Properties of 2:17 High Temperature Magnets

W. Tang, Y. Zhang, D. Goll[1], H. Kronmüller[1] and G. C. Hadjipanayis
University of Delaware, Dept. of Physics & Astronomy, Newark, DE 19716, USA
[1]Max-Planck Institut für Metallforschung, D-70569 Stuttgart, Germany

ABSTRACT

A comprehensive and systematic study has been made on $Sm(Co_{bal}Fe_vCu_yZr_x)_z$ magnets to completely understand the effects of composition and processing on their magnetic properties. The homogenized $Sm(Co,Fe,Cu,Zr)_z$ magnets have a featureless microstructure. A cellular/lamellar microstructure develops after 2-3 hours of aging at 800-850°C, but the coercivity increases only after a subsequent slow cooling to 400°C. During cooling, diffusion takes place and Cu is concentrated in the 1:5 cell boundaries and Fe in the 2:17R cells. This dilutes the magnetic properties of the 1:5 phase and causes domain wall pinning/nucleation at the cell boundaries. Higher ratio z leads to larger cells as expected due to the larger amount of the 2:17 phase. For a fixed Cu content, this translates to a larger amount of Cu in the 1:5 cell boundaries, and therefore, to a higher coercivity. Magnets without Cu but with Zr have a lamellar and a cellular like microstructure. In Zr free samples, however, a larger amount of Cu is needed to form the cellular microstructure. This cellular microstructure is unstable with prolonged isothermal aging. A uniform and stable cellular/lamellar microstructure is only observed in alloys containing both Cu and Zr. A higher aging temperature T_{ag} leads to larger cells and higher coercivity as explained above. The results of all these studies clearly show that the amount of Cu in the 1:5 cell boundaries controls both the coercivity and its temperature dependence leading to positive and negative temperature coefficients of coercivity in low and high Cu content alloys, respectively.

INTRODUCTION

$Sm(Co,Fe,Cu,Zr)_z$ permanent magnets are characterized by large anisotropy fields and high Curie temperatures which make them suitable candidates for high temperature applications [1, 2]. The optimum properties of the magnets are obtained after a lengthy heat treatment consisting of homogenization at a temperature T_h (1160-1190°C), slightly below the sintering temperature, followed by an aging at temperatures T_{ag} between 800-850°C, and a subsequent slow cooling to 400°C. Their high coercivity originates from a complex microstructure consisting of a superposition of cellular (2:17 cells and 1:5 cell boundaries) with a lamellar structure known as the Z phase. Cu is found to be concentrated in the 1:5 cell boundaries and Zr in the Z phase. According to Ray [3], Cu stabilizes the $Sm(Co, Cu)_5$ phase in the presence of Fe and Fe stabilizes the 2:17R phase in the presence of Cu. The $Sm_2(Co,Fe)_{17}$ cells are mainly responsible for the large saturation magnetization while the $Sm(Co, Cu)_5$ cell boundaries pin the domain-walls [4]. Lorentz microscopy studies [5, 6] clearly showed wavy domain walls following the 1:5 cell boundaries, indicating domain wall pinning at the latter. The Zr-rich lamella phase is believed to provide diffusion paths for Cu segregation and thus to form uniform $Sm(Co,Cu)_5$ cell boundary phase, which leads to high coercivity [7].

The $Sm(Co_{bal}Fe_vCu_yZr_x)_z$ magnets represent a complex system with four compositional variables (x, y, v, z) and five heat treating variables (T_h, t_h, T_{ag}, t_{ag}, dT/dt). We have recently undertaken a comprehensive and systematic study (MURI Project) on cast alloys and sintered magnets to understand the effects of composition (z, x, y, v) and processing on their magnetic hardening behavior, particularly on H_{ci} and its temperature dependence. These studies led to the development of new high temperature magnets with controlled temperature dependence of H_{ci} (including an abnormal temperature dependence of coercivity $H_c(T)$ in some magnets) [8-10] having a record value of 10 kOe at 500°C [11]. From these studies, we are able to finely tune the microstructure and microchemistry of the Sm-Co magnets through adjustments in the composition and processing parameters, and design magnets for various applications. In addition, the discovery of the abnormal temperature behavior has posed a new challenge about how to explain their magnetization reversal mechanism. This paper summarizes our studies on the effect of composition and processing on the microstructure and magnetic properties, and discuss the magnetization reversal mechanism with respect to the $H_c(T)$ of $Sm(Co_{bal}Fe_vCu_yZr_x)_z$ magnets.

EXPERIMENTAL PROCEDURES

Cast samples with nominal composition $Sm(Co_{bal}Fe_vCu_yZr_x)_z$ with x=0-0.1, y=0.048-0.168, v=0-0.3 and z=7.0-9.0 were prepared by arc-melting. All the samples were solutionized (homogenized) at 1170-1190°C. The aging heat treatments were carried at temperatures in the range of 700-900°C. The isothermal aging time was varied from 0.5 to 24h. After isothermal aging, the samples were subjected to either a quenching to room temperature or to a slow cooling to 400°C. In addition, some samples were cooled to intermediate temperatures and then quenched to room temperature. The room temperature magnetic properties were measured using an Oxford vibrating sample magnetometer (VSM) with a maximum applied field of 5 T. The high temperature magnetic properties were measured using a high temperature VSM with an applied field of 20 kOe. Microstructure analysis was carried out using a JEOL JEM-2000 FX transmission electron microscope (TEM). Nanoprobe chemical analysis was carried out using JEOL 2010 FEG with 1nm resolution.

RESULTS AND DISCUSSION

Compositions required for the formation of cellular/lamellar microstructure

Binary Sm-Co alloys with composition close to that of 2:17 magnets do not show the cellar/lamellar microstructure. Figure 1 shows the microstructure of the stoichiometric $Sm_{11}Co_{89}$ and $Sm_{14}Co_{86}$ samples without Cu and Zr addition. The microstructure of $Sm_{11}Co_{89}$ sample mainly consists of the 2:17 phase with many dislocations present [see Fig. 1 (a)]. With increasing Sm content (i. e. decreasing ratio z) in the alloys, a certain amount of 1:5 phase is observed besides the 2:17 phase as seen in Fig. 1(b). However, the cellular microstructure is not yet formed. When x=2.5 at.% Zr is added, the lamellar structure is observed with an incomplete cellular microstructure (see Fig. 2). However, the coercivity of the sample is almost zero due to the lack of a large gradient in domain wall energy across the 1:5 boundaries. In Zr free

$Sm(Co_{bal}Fe_{0.1}Cu_y)_{8.5}$ magnets with $y=0.088$, the cellular/lamellar microstructure is not formed. A rod or needle-like 1:5 phase is distributed in the 2:17 matrix instead (Fig. 3a). If the Cu content y is increased to 0.168, a very fine (35 nm) cellular microstructure is formed with a maximum $H_{ci}=5.6$ kOe after aging (Fig. 3b). However, the cell size cannot be uniformly grown and finally breaks down with further aging [9]. As it will be seen later, in order to obtain a high coercivity, a uniform cellular and lamellar microstructure is required and this is the result when both Cu and Zr are present in Sm-Co alloys.
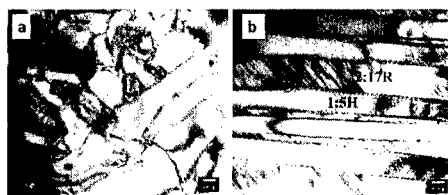
Figure 1. TEM micrographs of $Sm_{11}Co_{89}$ (a) and $Sm_{14}Co_{86}$ (b) samples.
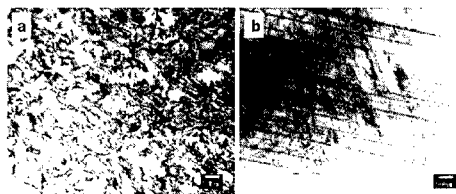
Figure 2. TEM micrographs of a $Sm_{11}Co_{86.5}Zr_{2.5}$ sample. (a) perpendicular, and (b) parallel to the c-axis of the 2:17 phase
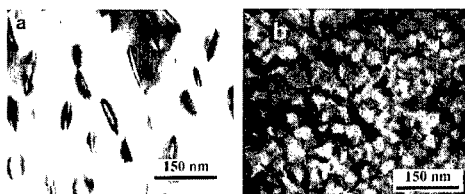
Figure 3. The TEM cellular microstructures for the $Sm(Co_{bal}Fe_{0.1}Cu_y)_{8.5}$ magnets with (a) $y=0.088$ and (b) 0.168, respectively.

Effect of ratio z

Ratio z defines the ratio of TTM/Sm (TTM=total transition metal). According to the phase diagram [12], magnets with a low ratio z (i.e. high Sm content) would be expected to have more of the $Sm(Co,Cu)_5$ cell boundary phase. Figure 4 shows the cellular microstructure of $Sm(Co_{bal}Fe_{0.224}Cu_{0.08}Zr_{0.033})_z$ magnets with $z=7.0$, 8.5 and 9.1 obtained by TEM (magnets with $z>8.5$ have a small amount of Co present). It is clear that when the ratio z increases from 7.0 to

8.5 and 9.0, the average cell size increases to 88, 108 and 237 nm, respectively. For a fixed Cu content, a larger cell size results in a larger amount of Cu in the 1:5 cell boundaries. This leads to a larger gradient in domain wall energy across the cell boundaries resulting in a stronger domain wall pinning, and gives rise to a higher coercivity. For high z the cellular microstructure is not complete and the coercivity deteriorates. Figure 5 shows the temperature dependence of intrinsic coercivity of $Sm(Co_{bal}Fe_{0.1}Cu_{0.088}Zr_{0.04})_z$ magnets with different ratio z. It is seen that the magnets with lower z have better $H_c(T)$. In addition, an abnormal $H_c(T)$ is observed in the magnets with z=7.0. Both of these effects will be discussed later.
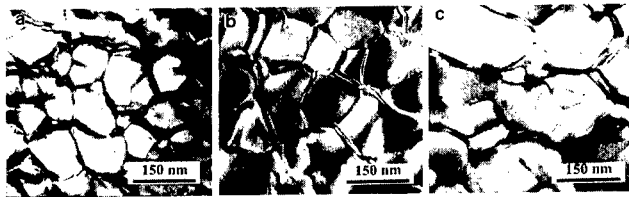
Figure 4. The cellular microstructure of $Sm(Co_{bal}Fe_{0.224}Cu_{0.08}Zr_{0.033})_z$ magnets with (a) z=7.0, H_{ci}=15 kOe, (b) z=8.5, H_{ci}=35 kOe and z=9.1, H_{ci}=8 kOe.
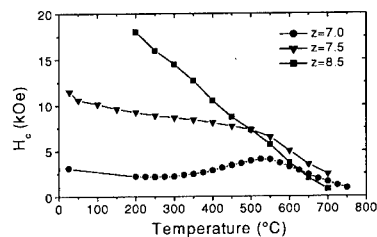
Figure 5. The temperature dependence of intrinsic coercivity H_{ci} of $Sm(Co_{bal}Fe_{0.1}Cu_{0.088}Zr_{0.04})_z$ magnets with different ratio z.

Effect of Cu

Cu content has the most important effect on the microstructure and magnetic properties of the magnets. Figure 6 shows the dependence of intrinsic coercivity H_{ci} and saturation magnetization M_s of $Sm(Co_{bal}Fe_{0.1}Cu_yZr_{0.04})_z$ magnets (y=0.048-0.168, z=7.5 and 8.5) on the Cu content. M_s decreases while H_{ci} increases with increasing Cu content. It is noted that the H_{ci} of the magnets with z=8.5 reaches a maximum of about 40 kOe when the Cu content x is 0.088. However, for the magnets with z=7.5, H_{ci} continues to increase with increasing the Cu content y up to 0.168. The TEM microstructure of $Sm(Co_{bal}Fe_{0.1}Cu_yZr_{0.04})_z$ magnets [11] shows that the cell size decreases slightly with increasing Cu content with a stronger dependence in the case of high ratio z. The average cell size decreases from 120 to 75 nm with increasing the Cu content from 0.048 to 0.168. Our nanoprobe chemical analysis results (see Fig. 16 in the section of magnetic hardening) show that Cu is concentrated at the cell boundaries and Cu content increases with increasing the Cu content of the magnets. Because the magnet with low ratio z has a smaller

cell size, the proportion of the cell boundaries is larger. More Cu is needed to obtain a large domain wall gradient across the cell boundaries. Even when the Cu content is up to 0.168, the coercivity has not yet reached its maximum. The temperature dependence of $Sm(Co_{bal}Fe_{0.1}Cu_yZr_{0.04})_{7.5}$ magnets with different Cu content y is shown in Fig. 7. The magnets with lower Cu content have lower room temperature coercivity but exhibit a better $H_c(T)$.
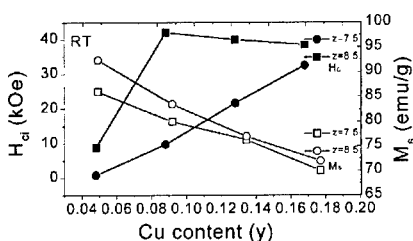
Figure 6. The dependence of saturation magnetization M_s and intrinsic coercivity H_{ci} on the Cu content in $Sm(Co_{bal}Fe_{0.1}Cu_yZr_{0.04})_z$ magnets (y=0.048-0.168, z=7.5 and 8.5).
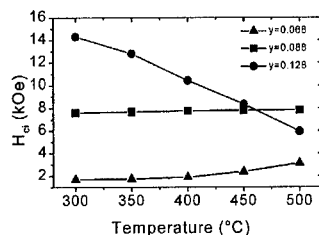
Figure 7. The temperature dependence of intrinsic coercivity H_{ci} of $Sm(Co_{bal}Fe_{0.1}Cu_yZr_{0.04})_{7.5}$ magnets with different Cu content.

Effect of Zr

Although many studies in the past have examined the role of Zr [3, 7, 13, 14], yet its effect is not fully understood. Figure 8 shows the optimized intrinsic coercivity H_{ci} as a function of Zr content in $Sm(Co_{bal}Fe_{0.1}Cu_{0.088}Zr_x)_{8.5}$ magnets at 25 and 500°C, respectively. At room temperature, the coercivity is below 2 kOe for the sample without Zr. However, with increasing Zr content, the coercivity dramatically increases and reaches a value of around 40 kOe for x in the range from 0.015 to 0.06. When x>0.06, the coercivity begins to decrease. At 500°C, although the coercivity is below 10 kOe for all magnets, it still gradually increases with increasing x up to 0.06 and then it decreases significantly.
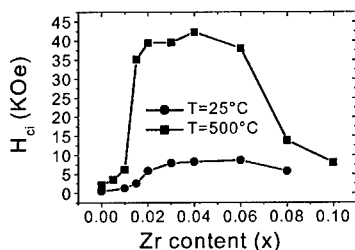
Figure 8. Effect of Zr on the coercivity of $Sm(Co_{bal}Fe_{0.1}Cu_{0.088}Zr_x)_{8.5}$ magnets at 25 and 500°C

Figure 9 shows TEM cellular microstructures for the $Sm(Co_{bal}Fe_{0.1}Cu_{0.088}Zr_x)_{8.5}$ magnets with (a) x=0.005, (b) 0.04 and (c) 0.08, respectively. With increasing x from 0 to 0.08, the microstructure gradually changes from the 2:17 matrix along with a needle-like 1:5 phase [Fig. 3(a)] to an incomplete cellular [Fig. 9(a)], and finally a uniform cellular, while the cell size decreases, first slightly and then quickly, from 120 to 35 nm. On the other hand, the density of lamella phase increases, first quickly and then slightly, from 0.024 to 0.062 nm^{-1} [15, 16]. When the Zr content is further increased to over 0.08, a 2:7 phase is formed leading to a decrease in coercivity [17].
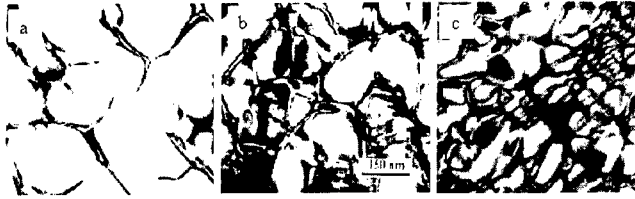
Figure 9. The TEM cellular microstructures for the $Sm(Co_{bal}Fe_{0.1}Cu_{0.088}Zr_x)_{8.5}$ magnets with (a) x=0.005, (b) 0.04 and (c) 0.08, respectively.

Figure 10 shows the effect of isothermal aging time on the coercivity of $Sm(Co_{bal}Fe_{0.1}Cu_{0.088}Zr_x)_{8.5}$ magnets with different Zr content. Because Zr helps the redistribution of Cu at the cell boundaries, the development of high coercivity with the isothermal aging time strongly depends on the Zr content in magnets.

As mentioned before in Zr-free magnets with higher Cu content, a fine cellular microstructure is observed which becomes highly non-uniform with aging. After the addition of Zr and Cu in the magnets, a normal microstructure consisting of rhombohedral $Sm_2(Co,Fe)_{17}$ cells surrounded by a Cu-rich hexagonal $Sm(Co,Cu)_5$ cell boundary phase is always formed. These results indicate that the lamellar phase formed by adding Zr stabilizes a uniform cellular microstructure with the right microchemistry for high coercivity [9].
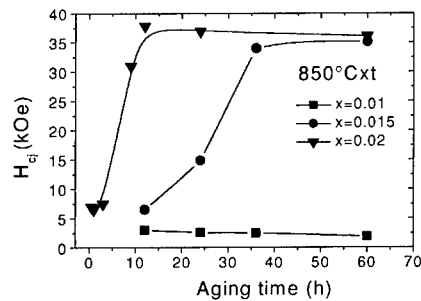
Figure 10. The coercivity as a function of aging time for $Sm(Co_{bal}Fe_{0.1}Cu_{0.088}Zr_x)_{8.5}$ magnets with different Zr content.

Effect of Fe

Iron has a significant effect on the high temperature magnetic properties of $Sm(Co,Fe,Cu,Zr)_z$ magnets. Some studies [17, 18] suggested that the high temperature performance of SmCo 2:17 magnets can be improved by decreasing the Fe content. Our results show that for some compositions the addition of a certain amount of Fe is necessary to develop a uniform cellular microstructure with a larger cell size and thus a high coercivity. The TEM studies for $Sm(Co_{bal}Fe_vCu_{0.128}Zr_{0.02})_{7.0}$ magnets with different v (see Fig. 11) show that the magnet with low Fe content has a smaller but non-uniform cell size (The average cell size is 48 nm). With increasing the Fe content v up to 0.2, the cell size increases to 120 nm but becomes uniform because Fe substitutes in the 2:17 phase. As explained earlier, for a fixed Cu, this leads to a larger Cu content in the 1:5 cell boundaries and therefore, to a higher coercivity. When the Fe content is further increased up to 0.25, the cell size continuously increases up to 180 nm and becomes inhomogeneous. The cellular structure starts deteriorating and this leads to the decrease of coercivity. In the $Sm(Co_{bal}Fe_vCu_{0.078}Zr_{0.033})_{8.3}$ magnet with higher ratio z [19], because the original cell size is large, the addition of Fe does not have a significant effect on the microstructure and coercivity.
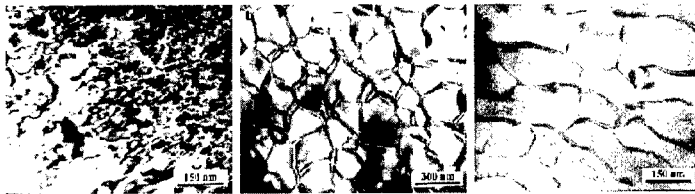
Figure 11: TEM micrographs of $Sm(Co_{bal}Fe_vCu_{0.128}Zr_{0.02})_{7.0}$ magnets (a) v=0, (b) v=0.02 and (c) v=0.25.
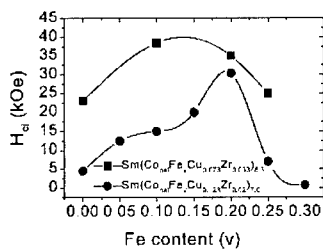
Figure 12. The effect of Fe content on the intrinsic coercivity H_{ci} of magnets with different compositions.
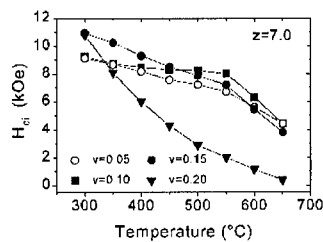
Figure 13. The temperature dependence of intrinsic coercivity H_{ci} of $Sm(Co_{bal}Fe_{0.1}Cu_{0.128}Zr_{0.02})_{7.0}$ magnets with different Fe.

Figure 12 shows the effect of Fe content on the magnetic properties of magnets with different compositions. Although a maximum of coercivity exists with Fe content, the coercivity of $Sm(Co_{bal}Fe_vCu_{0.128}Zr_{0.02})_{7.0}$ magnet with a low ratio z is more sensitive to the Fe content. More Fe is needed to develop a high coercivity. The $H_c(T)$ of $Sm(Co_{bal}Fe_vCu_{0.128}Zr_{0.02})_{7.0}$ magnets with different Fe content (see Fig. 13) show that the coercivity of all magnets always decreases with increasing temperature. However, the $H_{ci}(T)$ curves for the magnets with higher Fe content are steeper. This is probably due to the lower anisotropy K of the 2:17 matrix phase and its stronger temperature dependence $K(T)$, because of the lower Curie temperature of the 2:17 matrix phase.

Effect of aging temperature and time

Figure 14 shows the dependence of coercivity H_{ci} on the aging temperature T_{ag} in a $Sm(Co_{bal}Fe_{0.1}Cu_{0.088}Zr_{0.04})_{8.5}$ magnet. It can be seen that the magnet aged at 850°C has an optimal coercivity. The TEM image shows that the magnet aged at 750°C has a smaller cell size (70 nm). Additional data about the microstructure and coercivity of sintered $Sm(Co,Fe,Cu,Zr)_{6.4}$ magnets with different aging temperature is listed in Table 1. Although the Cu concentration at the cell boundaries is almost the same with different aging temperature, the difference of microstructure parameters, especially the thickness of cell boundaries, results in a different coercivity. A higher T_{ag} leads to larger cells and thicker cell boundaries and thus leads to higher coercivity. It is reasonable to assume that an increase of T_{ag} over 850°C leads to a further increase and final deterioration of the cell size, and thus it leads to a reduction in coercivity.
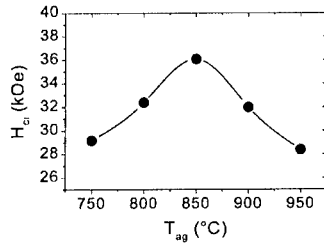
Figure 14: Dependence of coercivity H_{ci} on the aging temperature T_{ag} in a $Sm(Co_{bal}Fe_{0.1}Cu_{0.088}Zr_{0.04})_{8.5}$ magnet.
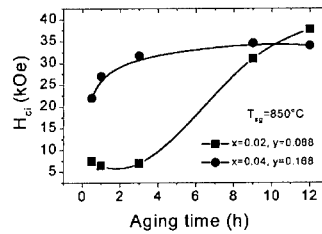
Figure 15. The dependence of intrinsic coercivity H_{ci} on the aging time for $Sm(Co_{bal}Fe_{0.1}Cu_yZr_x)_{8.5}$ magnets with different Cu and Zr content.

Figure 15 shows the dependence of coercivity on the aging time for $Sm(Co_{bal}Fe_{0.1}Cu_yZr_x)_{8.5}$ magnets with different Cu and Zr content. For the magnet with low Cu and Zr content, an optimal coercivity is developed only after aging at 850°C for over 9h, followed by the slow cooling. However, the development of coercivity for the $Sm(Co_{bal}Fe_{0.1}Cu_{0.168}Zr_{0.04})_{8.5}$ magnet is not sensitive to the isothermal aging time at 850°C. The magnet develops a coercivity of over 21 kOe even after aging at 850°C for 0.5h, followed by a slow cooling to 400°C. This suggests that higher Cu content along with a certain amount of Zr permits the rapid formation of the right microstructure and microchemistry during aging and thus it leads to the observed high coercivity [10]. These results are also consistent with the studies on the evolution of microstructure and nanoscale composition [21], which shows that a perfect cellular/lamellar microstructure is formed

after aging for 2h at 850°C, while Cu diffusion at the cell boundaries mainly occurs during a slow cooling stage.

Table I. Effect of aging temperature on the microstructure parameters and coercivity of a sintered Sm(Co,Fe,Cu,Zr)$_{6.4}$ magnet.

T_{ag} (°C)	H_{ci} (kOe)	Cell size (nm)	Boundary width (nm)	Density of lamella (nm)	Cu content in cell boundary (nm)
700	6.5	50	6.5	0.046	14.4
800	13	105	11	0.061	15.7

Magnetic hardening

Recently our extensive studies show that the distribution and amount of Cu at the 1:5 cell boundaries is the predominant factor in controlling the pinning strength or magnetization reversal and therefore the coercivity and its temperature dependence. Figure 16 shows a typical element profile along the cell boundary obtained by nanoprobe chemical analysis for the Sm(Co$_{bal}$Fe$_{0.1}$Cu$_{0.128}$Zr$_{0.02}$)$_{7.5}$ magnet. Cu mainly concentrates at the 1:5 cell boundaries and increases from 13.8 to 33.8 at. % with Cu increasing from 0.068 to 0.128.
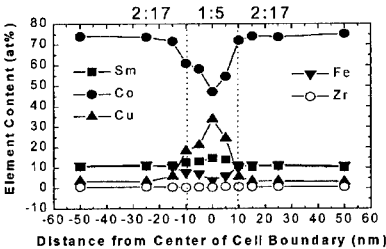
Figure 16. An element profile along the cell boundary for Sm(Co$_{bal}$Fe$_{0.1}$Cu$_{0.128}$Zr$_{0.02}$)$_{7.5}$ magnet.
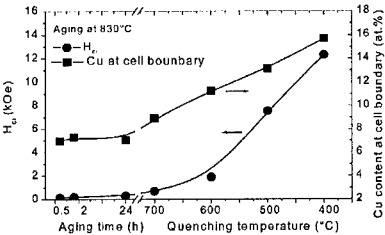
Figure 17: The evolution of Cu at cell boundaries and coercivity with heat treatment.

Figure 17 shows the evolution of Cu at the cell boundaries and coercivity with heat treatment. It can be seen that the development of coercivity closely follows the changes of Cu content at the cell boundaries. A large Cu gradient at the cell boundaries is obtained by the low temperature slow cooling close to 400°C, which then leads to large coercivities. These results further confirm that the Cu content plays an important role in the development of coercivity. In addition, the $H_c(T)$ study on Cu-free Sm$_{11}$Co$_{86.5}$Zr$_{2.5}$ sample shows that an abnormal $H_c(T)$ exits, and is reversible with temperature. Because the sample is Cu-free, the abnormal $H_c(T)$ should be caused due to the presence of cellular microstructure. Therefore, the abnormal $H_C(T)$ is related to both the presence of cellular microstructure and distribution of Cu at cell boundaries.

Figure 18 show the $H_C(T)$ for Sm(Co$_{bal}$Fe$_{0.1}$Cu$_y$Zr$_{0.04}$)$_{7.0}$ magnets with different Cu content. These magnets have the cellular/lamellar structure. It can be seen that the room temperature coercivity increases with increasing Cu content. The abnormal $H_C(T)$ is observed in the magnets with lower Cu content. Additionally, it is noted that the temperature of the peak coercivity at high temperature decreases with increasing Cu content. Figure 19 shows the temperature dependence

of anisotropy constant K_I for some 1:5 and 2:17 compounds (after [22-24]). Because Cu mainly goes into the 1:5 boundary phase, it is assumed the K_I of 2:17 phase remains constant with increasing Cu content. It has been shown that the K_I of the 1:5 phase gradually decreases with increasing Cu content, leading to the gradual reduction of the critical temperature T_{cr}, where K_I (1:5)=K_I (2:17). The abnormal H_c(T) behavior can be explained by using both the pinning and nucleation models.
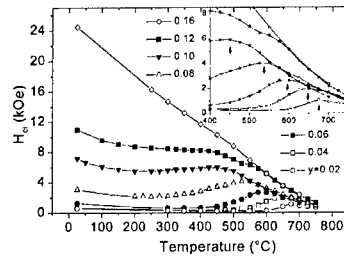
Figure 18. Temperature dependence of coercivity for $Sm(Co_{bal}Fe_{0.1}Cu_yZr_{0.04})_{7.0}$ magnets with different Cu content.
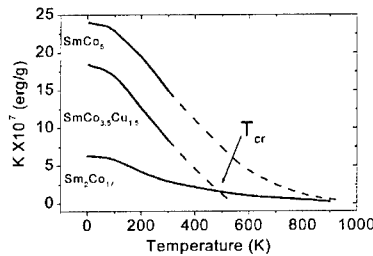
Figure 19. Temperature dependence of anisotropy K for 1:5 and 2:17 compounds [22-24].

According to the two-phase pinning mechanism [25], the coercivity is proportional to the $\Delta\gamma$ between the domain-wall energies $\gamma=4(AK_I)^{0.5}$ for the two phases, where $\Delta\gamma=\gamma_{2:17}-\gamma_{1:5}$, A is the exchange stiffness. If the Cu content is low, below a critical temperature T_{cr}, the γ(1:5) is higher than γ(2:17) leading to a relatively weak repulsive pinning. Above T_{cr}, the γ(1:5) is lower than γ (2:17) leading to an attractive pinning with an increase in coercivity. Moreover, with increasing Cu content, T_{cr} moves in the direction of low temperature, which leads to the shift of peak coercivity to lower temperature (see Fig. 18). If the Cu content is sufficiently high, the γ(1:5) is lower than γ(2:17) at any temperature range. Therefore, the abnormal H_C(T) disappears and the coercivity monotonically decreases with increasing temperature. However, this model predicts a minimum value of coercivity at T_{cr} (There may be a distribution of T_{cr} due to the inhomogeneous microchemistry at cell boundaries.). This, however, could not be observed in our experimental data. Our results show that the abnormal H_c(T) behavior is observed in magnets with a wide range of Cu content (0-0.12). These results suggest that the coercivity is controlled by

magnetization reversal in magnetically isolated 2:17 cells at $T_c(1:5)<T<T_c(2:17)$, where T_c is the Curie temperature.

In the Sm-Co magnets, each 2:17 cell is partially or totally surrounded by the 1:5 boundary phase. In this case, the coercivity and its temperature dependence are mainly determined by the anisotropy of the 2:17 phase and its temperature dependence. The 1:5 cell boundary controls the strength of magnetization reversal nucleation with different Cu content or temperature. Figure 20 shows a schematic representation of a single cell under different conditions. When the Cu content is very low, the 2:17 cells are not entirely surrounded by 1:5 boundaries and thus are not completely isolated by the 1:5 cell boundaries [Fig.20(a)], leading to a low coercivity. With increasing Cu content, a uniform cellular microstructure is observed and the 1:5 boundary becomes close to nonmagnetic, resulting in complete magnetic isolation of the 2:17 cells [Fig. 20(b)] and thus a high room temperature coercivity. On the other hand, the magnetic transformation of the 1:5 boundaries caused by increasing temperature is similar to that by increasing Cu content. At $T>T_c$ (1:5), the 2:17 cells are completely isolated and this results in an increase of coercivity. Because the increase of Cu content leads to the reduction of T_c (1:5), the temperature of the peak coercivity at high temperature decreases with increasing Cu content (see Fig. 18). After the 2:17 phase has been isolated at room temperature, the abnormal behavior disappears and the coercivity monotonically decreases with increasing temperature because of thermal activation and $K(T)$ dependence.

(a) $T<T_{c\,1\,5}$ or lower Cu   (b) $T>T_{c\,1\,5}$ or higher Cu
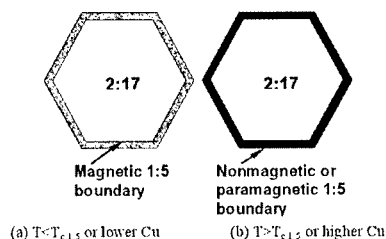
Figure 20. Schematic representation of the 1:5 cell boundaries under different conditions.

CONCLUSIONS

The coercivity and its temperature dependence in $Sm(Co_{bal}Fe_vCu_yZr_x)_z$ magnets are very sensitive to the composition and processing parameters, which in turn affect the microstructure and microchemistry of the magnets. All of these effects lead to a change of the cell size, which in turn leads to a variation of the amount of Cu concentration in the $Sm(Co,Cu)_5$ cell boundaries. The distribution and amount of Cu at the 1:5 cell boundaries is the predominant factor in controlling the magnetization reversal and therefore the coercivity and its temperature dependence. The addition of Zr stabilizes a uniform cellular microstructure with the right microchemistry for high coercivity. The addition of a certain amount of Fe is necessary to develop a uniform cellular microstructure with a larger cell size and thus a high coercivity. The isothermal aging temperature and time mainly change the microstructure parameters, including the cell size, boundary thickness, and density of lamella. The increase of the Cu and Zr content assists in the development of the right microstructure and microchemistry with high coercivity. The temperature dependence of coercivity of magnets with different Cu content cannot be

completely explained by the traditional domain-wall pinning models based on the difference in domain wall energy between the Cu substituted 1:5 and the 2:17 phases. The coercivity and its temperature dependence may also be explained by the nucleation of reversed domains in magnetically isolated Sm_2Co_{17} cells.

ACKNOWLEDGEMENTS

REFERENCES

1. A. E. Ray and S. Liu, *J. Mater. Eng. Perform*, **1**, 183(1992).
2. G. C. Hadjipanayis, in *Rare earth iron permanent magnets*, edited by J. M. D. Coey (Oxford University Press, Inc., New York, 1996).
3. A. E. Ray, *J. Appl. Phys.*, **55**, 2094(1984).
4. K. Kumar, *J. Appl. Phys.*, **63**, R13(1988).
5. J. Fidler and P. Skalicky, *J. Magn. Magn. Mater.*, **30**, 58(1982).
6. R. K. Mishra, G. Thomas, T. Yoneyama, A. Fukino, and T. Ojima, *J. Appl. Phys.***52**, 2517(1981).
7. L. Rabenberg, R. K. Mishra, and G. Thomas, *J. Appl. Phys.*, **53**, 2389(1982).
8. J. F. Liu, T. Chui, D. Dimitar, and G. C. Hadjipanayis, *Appl. Phys. Lett.* **73**, 3007(1998).
9. W. Tang, Y. Zhang, and G. C. Hadjipanayis, *J. Appl. Phys.*, **87**, 5308(2000).
10. W. Tang, Y. Zhang, and G. C. Hadjipanayis, *Appl. Phys. Letter.*, **77**, 421(2001).
11. J. F. Liu, Y. Ding, Y. Zhang, D. Dimitar, F. Zhang, and G. C. Hadjipanayis, *J. Appl. Phys.*, **85**, 5660(1999).
12. L. Cataldo, A. Lefevre, F. Ducret, M.-Th. Cohen-Adad, C. Allibert, and N. Valignat, *J. Alloys Compd.*, **241**,216(1996).
13. M. Katter, J. Weber, W, Assmus, P. Schrey, and W. Rodewald, *IEEE Trans. Magn.* **32**, 4815(1996).
14. M. V. Satyanarayana, H. Fujii, and E. Wallace, *J. Appl. Phys.* **53**, 2374(1982).
15. W. Tang, Y. Zhang, and G. C. Hadjipanayis, *J. Magn. Magn. Mater.* **212**, 138(2000).
16. W. Tang, Y. Zhang, and G. C. Hadjipanayis, *J. Appl. Phys.*, **87**, 399(2000).
17. S. Liu and E. P. Hoffman, *IEEE Trans. Magn.*, **32**, 5091(1996).
18. C. Chen, M. S. Walmer, and M. H. Walmer, *J. Appl. Phys.*, **83**, 6706(1998).
19. J. F. Liu, Y. Ding, and G. C. Hadjipanayis, *J. Appl. Phys.*,**85**, 1670(1999).
20. H. Kronmuller, in *Magnetic hysteresis in novel magnetic materials*, NATO ASI Series, 338(1997).
21. Y. Zhang, W. Tang, and G. C. Hadjipanayis, *Proceedings of the sixteenth international workshop on rare earth magnets*. pp167-177, Sept. 14, 2000, Sendai, Japan.
22. B. Barbara and M. Uehara, *IEEE Trans. Magn.*, **12**, 997(1976).
23. A. V. Deryagin, *J. Physique*, **40**, 165(1979).
24. A. S. Ermolenko, *IEEE Trans. Magn.*, **12**, 992(1976).
25. J. D. Livingston, *J. Appl. Phys.*, **46**, 5259(1975).

Effect of Iron Substitution on the High-temperature Properties of Sm(Co,Cu,Ti)$_z$ Permanent Magnets

Jian Zhou, Ralph Skomski, and David J. Sellmyer
Department of Physics and Astronomy and Center for Materials Research and Analysis
University of Nebraska, Lincoln, NE 68588
Wei Tang and George C. Hadjipanayis
Department of Physics and Astronomy, University of Delaware, Newark, DE 19716

ABSTRACT

Recently, Ti-substituted Sm-Co permanent magnets have attracted renewed attention due to their interesting high-temperature coercivity. Our presentation deals with the effect of iron substitutions on the magnetic properties of the materials. X-ray diffraction shows that the investigated Sm(Co,Fe,Cu,Ti)$_z$ materials (z = 7.0 - 7.6) are two-phase magnets, consisting of 1:5 and 2:17 regions. The iron content affects both the coercivity and the magnetization. Depending on composition and heat treatment, some samples show a positive temperature coefficient of the coercivity in the temperature range from 22 °C to 550 °C. Moderate amounts of iron enhance the room-temperature coercivity. For example, the room-temperature coercivity of Sm(Co$_{6.0}$Fe$_{0.4}$Cu$_{0.6}$Ti$_{0.3}$) is 9.6 kOe, as compared to 7.6 kOe for Sm(Co$_{6.4}$Cu$_{0.6}$Ti$_{0.3}$). At high temperatures, the addition of Fe has a deteriorating effect on the coercivity, which is as high as 10.0 kOe at 500 °C for Sm(Co$_{6.4}$Cu$_{0.6}$Ti$_{0.3}$). The room-temperature magnetization increases on iron substitution, from 73 emu/g for Sm(Co$_{6.4}$Cu$_{0.6}$Ti$_{0.3}$) to 78 emu/g for Sm(Co$_{6.0}$Fe$_{0.4}$Cu$_{0.6}$Ti$_{0.3}$). The observed temperature dependence is ascribed to the preferential dumbbell-site occupancy of the Fe atoms.

INTRODUCTION

The demand for permanent magnets with high-temperature applications above 450 °C has attracted much attention in recent years. Usually, the best room- temperature permanent magnets are made by Nd-Fe-B since it has a relatively high saturation magnetization and moderate intrinsic coercivity. These two properties lead to a high energy product (BH)$_{max}$, which is a key figure of merit for a hard magnet. However Nd-Fe-B has large temperature coefficients of H$_c$ and B$_r$. Therefore, (BH)$_{max}$ drops below 10 MGOe when T > 200 °C, and even more for higher temperatures, which makes it unsuitable for high-temperature applications. Another type of commercially available permanent magnets is 2:17-type Sm-Co magnets. The complicated heat-treatment of Sm(Co, Fe, Cu, Zr)$_z$ leads to a cellular microstructure that is Fe-containing SmCo-2:17 phases surrounded by Cu-rich SmCo$_5$ grain boundaries. Zr plays a key role in the formation of this type of structure by helping the precipitation of the Cu-rich phase. Although the maximum energy product of Sm$_2$Co$_{17}$ is not as high as that of the Nd-Fe-B at room temperature, the low temperature coefficients of H$_c$ and B$_r$ make the energy product larger at elevated temperature, which makes the 2:17 type Sm-Co based magnets a good choice for high-temperature applications [1, 2].

Our previous studies have been focused on SmCo-based alloys with Ti-substitution and their possible use as high temperature permanent magnets [3, 4]. An abnormal temperature dependence of coercivity has been found and an explanation for that has been given. An H$_c$ of

12.3 kOe at 500 °C has been obtained. However, the relatively low magnetization limits the attainable energy product of these alloys. This paper reports on the Fe effects of substitution for Co on both coercivity and magnetization.

EXPERIMENTAL METHODS

Sm(Co, Fe, Cu, Ti)$_z$ (Z= 7.0-7.6) are prepared by arc melting the starting element materials under flowing argon. The composition is represented in the form of Sm(Co$_{z-x-y-v}$Fe$_x$Cu$_y$Ti$_v$) where x= 0 – 1.0, y = 0.4-0.9, and v = 0.25, 0.3. The as-melted samples are heat treated following a procedure similar to that of the Sm$_2$TM$_{17}$ magnets: homogenization at 1165 °C for 3 hours, annealing at 825 °C for 8 hours, slow cooling under a rate of 1 °C/min till 550 °C, and holding there for another 8 hours. Aligned samples are made by mixing ground powders with high-temperature cement in a 1.4 T field until solidification. X-ray diffraction is used for the determination of the crystal structure. SQUID magnetometer and high-temperature VSM are used to obtain magnetization data.

RESULTS AND DISCUSSION

The as-melted samples show the disordered 1:5 structure and after annealing the cellular-like microstructure forms, which contains a 5-10 nm thick grain-boundary Cu-rich 1:5 phase and a main phase with the 2:17 structure and with an average grain size of around 70 nm. This was shown in our previous work [3].

Table I shows the room temperature M$_s$, M$_r$, and H$_c$ values for different Cu and Fe contents (TM/Sm ratio z = 7.6). All data show that additional Fe helps to increase M$_s$. For low Cu content (Cu = 0.6), more Fe decreases H$_c$. For high Cu content value, large coercivities are obtained and some samples are not saturated in a field of 55 kOe.

Z=7.6	Ms (emu/g)			Mr (emu/g)			Hc (kOe)		
Fe \ Cu	0.6	0.7	0.8	0.6	0.7	0.8	0.6	0.7	0.8
0	70	66	63	48	41	43	10.6	7	30
0.4	78	77	68	60	64	45	8.7	18.2	23
0.7	82	N/s	N/s	39	N/s	N/s	4.5	N/s	N/s
1.0	89			58			3.8		

Table I. Room temperature M$_s$, M$_r$ and H$_c$ of SmCo$_{7.3-x-y}$Fe$_x$Cu$_y$Ti$_{0.3}$. (N/s means not saturated at 55 kOe)

For some particular compositions, a certain amount of Fe can increase both H$_c$ and M$_s$. Figure 1 shows the temperature dependence of coercivity for the series of SmCo$_{6.4-x}$Fe$_x$Cu$_{0.6}$Ti$_{0.3}$. For x ≤ 0.7, the samples show a positive temperature coefficient of coercivity (TCC). We see that on Fe substitution for Co the room temperature coercivity reaches a maximum at a certain Fe
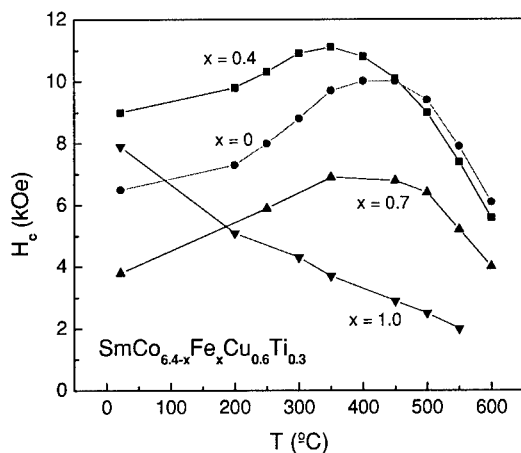
Figure 1. Temperature dependence of coercivity of $SmCo_{6.4-x}Fe_xCu_{0.6}Ti_{0.3}$.
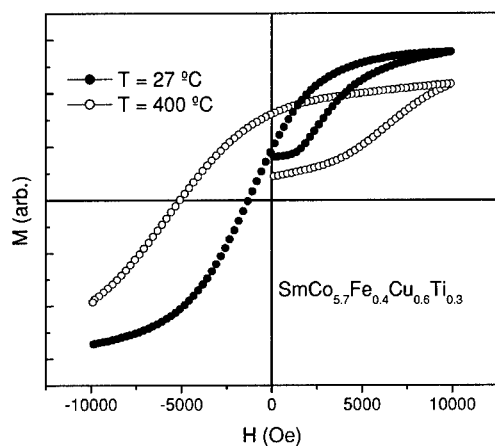
Figure 2. Typical loops for a sample with positive TCC at room temperature and 400 °C.

amount, then decreases while the TCC remains positive. On further addition of Fe, the TCC becomes negative and also the coercivity drops to a relatively low level. The positive TCC has been explained by a model in terms of domain-wall-pinning mechanism in a two-phase magnet [4].

As in the case of conventional SmCo 2:17 magnets, Fe substitutes for Co and most likely enters the main 2:17 phase in the cellular structure, and also stabilizes the 2:17 phase at the
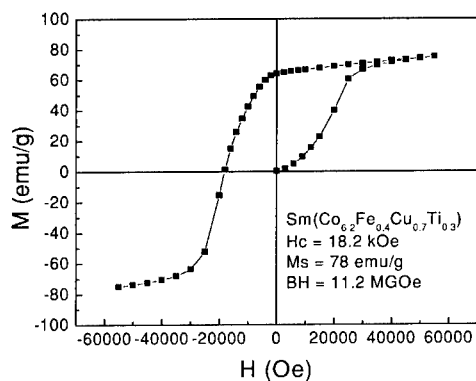
Figure 3(a). Hysteresis loop of $SmCo_{6.2}Fe_{0.4}Cu_{0.7}Ti_{0.3}$ at room-temperature.
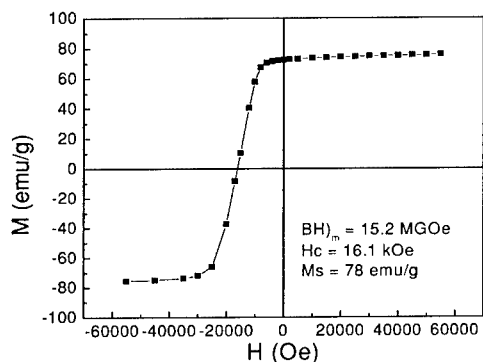
Figure 3(b). Hysteresis loop of aligned $SmCo_{6.2}Fe_{0.4}Cu_{0.7}Ti_{0.3}$ sample at room-temperature.

presence of Cu [5]. The increase of the room-temperature coercivity due to Fe is explained by the preferential dumbbell-site occupation of Fe in the 2:17 structure [6]. This enhances the anisotropy of the 2:17 phase and results in a higher coercivity as compared to the Fe-free sample. Figure 2 shows typical loops for a sample with positive TCC at room temperature and 400 °C. Even though at 400 °C the sample is not saturated, it is obvious that the coercivity increases with increasing temperature. This is due to the different temperature dependence of the two phases (1:5 and 2:17). A detailed explanation of this mechanism has been given elsewhere [4].

Figure 3(a) shows the room-temperature loop of a sample, whereas 3(b) shows the same sample after alignment. The energy product has been improved by alignment from 11.2 MGOe to 15.2 MGOe. The demagnetization curve of the $SmCo_{6.2}Fe_{0.4}Cu_{0.7}Ti_{0.3}$ bulk sample at room temperature and 500 C is shown in Fig. 4. A coercivity of 7.3 kOe and an energy product of 5.3 MGOe is obtained. Noticing that the grains in the sample are randomly oriented, a higher energy product is anticipated in aligned or sintered magnets. Because we do not have a high temperature
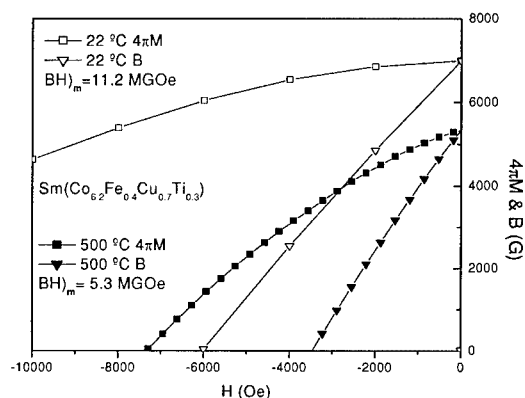
Figure 4. Demagnetization curves for $SmCo_{6.2}Fe_{0.4}Cu_{0.7}Ti_{0.3}$ bulk sample.

epoxy that can withstand 500 °C, no results for aligned samples have been obtained at this temperature until now. Further investigations on sample alignment are still under way, but the good property shown in bulk sample makes the material promising for high-temperature application as a permanent magnet.

Figure 5 shows the change of coercivity at room temperature and 500 °C. We can see that for Fe = 0.7, the high-temperature coercivity remains around 8.5 kOe. This makes it possible to increase remanence by introducing certain amount of Fe without losing too much coercivity. That will lead to obtain an energy product value around 10 MGOe at 500 °C.

Figure 6 shows the demagnetization curves for $SmCo_{6.0}Fe_{0.4}Cu_{0.6}Ti_{0.3}$ at different temperatures. The increase in H_c is obvious and an H_c of 9 kOe is obtained at 500 °C.

CONCLUSIONS

Fe substitution for Co enhances the magnetization of Sm-Co-Cu-Ti and, for some compositions, the coercivity. The latter is due to the preference of the Fe occupation of dumbbell site in the 2:17 phase. The room-temperature coercivity of $Sm(Co_{6.0}Fe_{0.4}Cu_{0.6}Ti_{0.3})$ is 9.6 kOe, as compared to 7.6 kOe for $Sm(Co_{6.4}Cu_{0.6}Ti_{0.3})$. However, larger Fe amounts (Fe$\geq$1.0) will decrease the coercivity at both room temperature and elevated temperature. An H_c of 9.0 kOe is obtained at 500 °C. The substitution of Fe for Co helps increase the magnetization at all the temperatures, which leads to a higher energy product than that of Fe-free samples. A $(BH)_{max}$ of 11.2 MGOe and 5.3 MGOe in a $SmCo_{6.2}Fe_{0.4}Cu_{0.7}Ti_{0.3}$ bulk sample is obtained at room temperature and 500 °C, respectively. A large increase of $(BH)_{max}$ is anticipated in aligned samples. These properties make this material a promising candidate for high-temperature applications.

ACKNOWLEDGEMENT
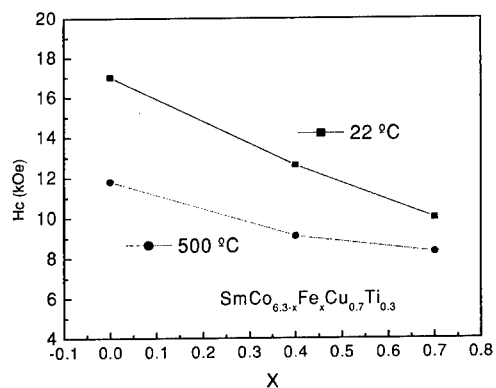
Figure 5. Coercivities of $SmCo_{6.3-x}Fe_xCu_{0.7}Ti_{0.3}$ at room temperature and 500 °C.
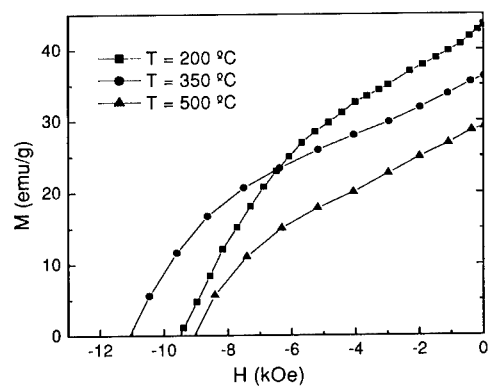
Figure 6. Demagnetization curves of $SmCo_{6.0}Fe_{0.4}Cu_{0.6}Ti_{0.3}$ at different temperatures.

REFERENCES

1. Christina H. Chen, Marlin S. Walmer, Michael H. Walmer, Sam Liu, G. Edward Kuhl, and Gerard K. Simon, *Advanced hard and soft magnetic materials*, edited by M. Coey *et al.* (Mater. Res. Soc. Proc. **577**, San Francisco, CA 1999) pp.277-287.
2. J. F. Liu, Y. Ding, and G. C. Hadjipanayis, *J. Appl. Phys.* **85**, 1670 (1999).
3. J. Zhou, R. Skomski, C. Chen, G. C. Hadjipanayis, and D. J. Sellmyer, *Appl. Phys. Lett.* **77**, 1514 (2000).
4. J. Zhou, R. Skomski, and D. J. Sellmyer, *IEEE Trans. Magn.*, **37**, (2001) (in press).
5. A. E. Ray, *J. Appl. Phys.* **55**, 2094 (1984).
6. Kaplesh Kumar, *J. Appl. Phys.* **63**, R13 (1988).

Nanocrystalline and Nanostructured High-Performance Permanent Magnets

D. Goll, W. Sigle, G.C. Hadjipanayis[1] and H. Kronmüller
Max-Planck-Institut für Metallforschung, Heisenbergstr. 1, D-70569 Stuttgart, Germany
[1] University of Delaware, Newark, U.S.A.

ABSTRACT

The rather complex correlation between the microstructure and the magnetic properties is demonstrated for two types of high-quality RE-TM permanent magnets (pms), namely nanocrystalline $RE_2Fe_{14}B$ (RE = Nd,Pr) and nanostructured $Sm_2(Co,Cu,Fe,Zr)_{17}$ pms. The detailed analysis of this correlation for both pm materials leads to a quantitative comprehension of the hardening mechanism enabling the optimization of their magnetic properties and temperature dependences. In the case of $RE_2Fe_{14}B$, isotropic bonded pms are fabricated showing maximum energy products in the order of 90 kJ/m³. In the case of $Sm_2(Co,Cu,Fe,Zr)_{17}$, magnets with excellent high-temperature magnetic properties are tailored. Hereby, the investigations in addition provide important clues to the evolution of the characteristic microstructural and magnetic properties and to the role of the involved elements.

INTRODUCTION

Modern high-quality permanent magnets (pms) are based on RE-TM intermetallic compounds of rare earth (RE = Nd,Pr,Sm) and transition metals (TM = Fe,Co) [1–4]. With these compounds outstanding intrinsic magnetic properties, large magnetocrystalline anisotropy constants $K_1 > 10^6$ J/m³, large spontaneous polarizations $J_S > 1.2$ T and Curie temperatures $T_C > 250°C$ as well as optimized microstructures can be realized. A large spontaneous polarization is a prerequisite for high remanences J_R, whereas a large magnetocrystalline anisotropy constant may result in large coercivities both ensuring high maximum energy products $(BH)_{max} \leq J_R^2/(4\mu_0)$ $(\mu_0 = 4\pi \cdot 10^{-7}$ Vs/Am) as long as the condition $\mu_0 H_C > 0.5 J_R$ holds. The ternary systems $RE_2Fe_{14}B$ (RE = Nd,Pr) [5] are currently considered to be the highest performance pm materials at all because of their very large spontaneous polarization of 1.6 T resulting in maximum energy products $(BH)_{max}$ up to 15 times larger than for ferrites. The only disadvantage of such magnets are their comparatively low Curie temperatures of $T_C \approx 300°C$. Nevertheless, nanocrystalline magnetic materials of this system have opened a new class of pm materials which are optimally suitable for high-performance polymer bonded magnets. Pms which supply the highest $(BH)_{max}$ values at elevated temperatures (beyond which $RE_2Fe_{14}B$ is no longer viable) are based on the quintary system $Sm_2(Co,Cu,Fe,Zr)_{17}$ [5]. With such magnets coercivities as large as 1 T can be realized even at 500°C which makes them suitable for high temperatures [6,7].

For a further improvement of the performance of polymer bonded magnets and the high-temperature magnetic properties, especially the temperature stability of the coercivity, the most important prerequisite for both hard magnetic materials is the detailed analysis of the hardening mechanisms and in the case of $Sm_2(Co,Cu,Fe,Zr)_{17}$ additionally of its formation. It is nowadays generally accepted that in $RE_2Fe_{14}B$ based materials the nucleation mechanism governs the coercivity, whereas in Sm_2Co_{17} based materials domain wall pinning processes are dominant. For both hardening mechanisms the coercivity is well-described by the following global formula [8]:

$$\mu_0 H_C = \mu_0 \alpha \frac{2K_1}{J_S} - N_{eff} J_S \tag{1}$$

with the microstructural parameters α and N_{eff} describing the effect of the real microstructure, i.e. all deviations from the ideal crystal structure. Some recent results concerning the interpretation of hardening mechanisms in nanocrystalline or nanostructured pms will be discussed in the following sections.

EXPERIMENTAL

There are two principal processing routes for manufacturing high-quality pms – sintering and melt-spinning leading to microcrystalline (anisotropic) and nanocrystalline (isotropic) microstructures, respectively. Our studies were performed on nanocrystalline exchange coupled $Pr_2Fe_{14}B$ type melt-spun ribbons and polymer bonded specimens made out of them as well as on sintered and melt-spun $Sm_2(Co,Cu,Fe,Zr)_{17}$ type pms. For the melt-spun ribbons master alloys of different nominal compositions have been prepared by arc melting from the constituent elements and a FeB prealloy in the case of PrFeB. By using the melt-spinning technique the ingots were directly quenched into nanocrystalline ribbon flakes whereby in all cases the processing conditions were optimized. For the polymer bonded magnets the melt-spun ribbons were crushed into powder (powder particle size: $1-40\,\mu m$) and then industrially fabricated into isotropic bonded magnets (density 6.0 g/cm^3) by mixing the powder with a polymer (4.5wt% epoxy resin, 0.5wt% Zn-stearat) followed by compression molding the resulting compound at a pressure of 7 t/cm^2 without a magnetic field. For the sintered samples a commercial solution heat treated sintered magnet of the nominal composition $Sm(Co_{bal}Cu_{0.07}Fe_{0.22}Zr_{0.04})_{7.4}$ has been taken. For the annealing procedures the samples have been wrapped into Ta foils and sealed in quartz tubes with Ar.

For the microstructural investigations different types of electron microscopy have been used: 1. (High resolution) transmission electron microscopy HRTEM (Philips CM200) for imaging the morphology and crystal lattices of the microstructure. 2. Lorentz microscopy (Philips CM200) in the Fresnel and Foucault mode for visualizing the domain wall pattern. 3. High resolution energy dispersive X-ray analysis (EDX) in a dedicated scanning TEM (VG HB501) to determine the chemical compositions of the three phases involved. Due to the very high spatial resolution of 1 nm the latter technique can be also used to measure compositional changes between different phases. Here, it should be noticed, that such profiles are a convolution of the real chemical profile and the resolution function of the probe. The magnetic measurements were performed in a vibrating sample magnetometer (PAR VSM) with a maximum field of 9 T. The external field was corrected by the demagnetization field ($\mu_0 H = \mu_0 H_{ext} - NJ$) with the macroscopic demagnetization factor N of the order of 0.01 (ribbons) and 0.33 (bonded/bulk magnets), respectively. The magnetic field was applied parallel to the ribbon direction or to the texture axis.

NANOCRYSTALLINE MAGNETS

Nanocrystalline hard magnets on the basis of $RE_2Fe_{14}B$ are suitable for tailoring magnets with definite properties of the hysteresis loop. Based on the ternary phase diagram three types of nanocrystalline pms with different microstructures have been developed (see figure 1) – magnets with RE excess (decoupled magnets), stoichiometric magnets and magnets with overstoichiometric Fe (composite magnets) [9–16].

Decoupled Magnets $RE_2Fe_{14}B$ / RE   Stoichiometric Magnets $RE_2Fe_{14}B$ Composite Magnets $RE_2Fe_{14}B$ / Fe
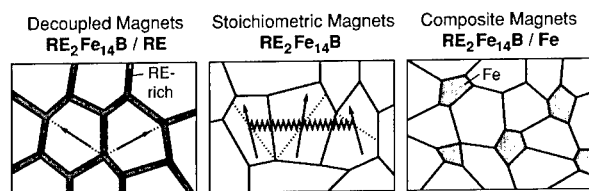
Figure 1. Schematic microstructures (remanent state) for the three different types of nanocrystalline $RE_2Fe_{14}B$ based magnets (RE = Nd,Pr).

Exchange coupled magnets

Whereas in decoupled magnets the hard magnetic grains are isolated by a RE-rich paramagnetic intergranular layer limiting the remanence to rather low values, i.e. $J_R \leq 0.5\,J_S$, the rema-
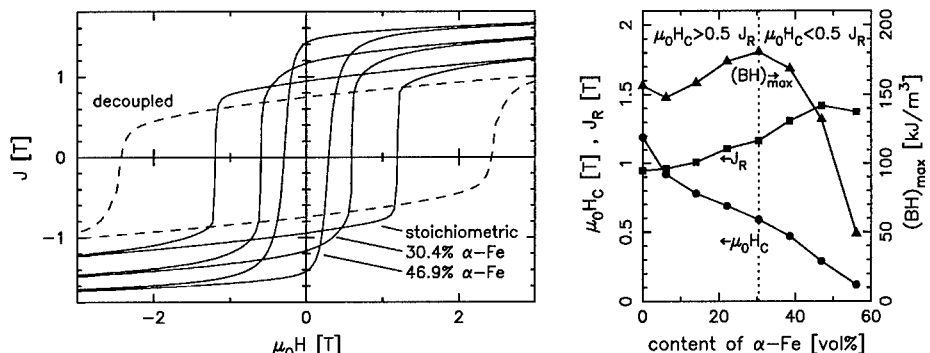
Figure 2. Room temperature hysteresis loops of PrFeB based pms: $Pr_{15}Fe_{78}B_7$ (decoupled grains), $Pr_{12}Fe_{82}B_6$ (stoichiometric, exchange coupled grains), $Pr_8Fe_{87}B_5$ (30.4% α-Fe) and $Pr_6Fe_{90}B_4$ (46.9% α-Fe) (composite, exchange coupled grains) *(left)*. Magnetic properties of composite PrFeB pms measured at room temperature as a function of excess α-Fe *(right)*.

nence and therefore $(BH)_{\mathrm{max}}$ are significantly increased in exchange coupled magnets (stoichiometric and composite) due to the effect of exchange coupling between the grains. In stoichiometric magnets the hard magnetic grains are directly connected and therefore magnetically coupled by exchange interactions, i.e. the polarization direction underlies a smooth transition from the easy axis of one hard magnetic grain to the easy axis of another one on the scale of the so-called Bloch wall width $\delta_{\mathrm{B}} = \pi (A/K_1)^{0.5} = \pi l_{\mathrm{K}}$ (A: exchange constant, l_{K}: exchange length) which is in the order of 4 nm for $RE_2Fe_{14}B$. Or, in other words, within the wall width δ_{B} a magnetic texture is induced with the texture axis parallel to the original saturation polarization (i.e. the direction of the initially applied field). Since only this exchange coupled volume fraction causes the remanence enhancement the grain size should be smaller than four times the exchange length l_{K} in order to notice an efficient remanence enhancing effect macroscopically [17]. In composite magnets beside the hard magnetic $RE_2Fe_{14}B$ grains nanocrystalline soft magnetic α-Fe grains occur as a consequence of the overstoichiometric α-Fe leading to a further significant increase of the remanence. In this case, remanence enhancing is due to exchange coupling among the grains and to the large spontaneous polarization of α-Fe ($J_{\mathrm{S}} = 2.15$ T) which drastically intensifies the magnetic texturing effect. For a complete exchange hardening and therefore excellent hard magnetic properties it is imperative that the grain size of the soft magnetic grains is in the order of the Bloch wall width δ_{B} of the hard magnetic phase.

Figure 2 illustrates the enormous effect of exchange coupling by comparing the room temperature hysteresis loops of the different types of nanocrystalline PrFeB based magnets with each other. Additionally, figure 2 summarizes the changes of the room temperature magnetic properties with varying α-Fe content. For an iron excess of 30.4% the observed J_{R} is 1.17 T, i.e., an increase of 51% as compared to the isotropic value of 0.78 T and $(BH)_{\mathrm{max}}$ amounts to 180.7 kJ/m^3. With increasing α-Fe concentration besides the remanence enhancement the coercivity decreases continuously. However, as long as the condition $\mu_0 H_{\mathrm{C}} > 0.5 J_{\mathrm{R}}$ is fulfilled, $(BH)_{\mathrm{max}}$ increases. Otherwise, $(BH)_{\mathrm{max}}$ is restricted by irreversible demagnetization processes. For stoichiometric $Pr_{12}Fe_{82}B_6$ the average grain size amounts to 20 nm whereas in the case of the $Pr_8Fe_{87}B_5$ composite magnet a mixture of hard magnetic $Pr_2Fe_{14}B$ grains (grain size 20–30 nm) and soft magnetic α-Fe grains (grain size $\approx$ 15 nm) is found [11].

Polymer bonded magnets

Exchange coupled grain structures are optimally suitable for the industrial fabrication of polymer bonded magnets because of their high $(BH)_{\mathrm{max}}$ values and their low RE content compared to

conventional magnets which reduces the cost of the raw materials and improves the corrosion resistance. With bonded magnets which are characterized by low brittleness, low electric conductivity and their isotropy any desired shape can be prepared directly. In figure 3 the room temperature hysteresis loops of polymer bonded pms can be seen in comparison with the loops of the corresponding ribbon material using a stoichiometric and a composite alloy. It is obvious from this, that the rectangularity or squareness of the hysteresis loops is reduced for bonded magnets which may be due to the large number of ribbons used for powderizing with their magnetic properties varying slightly. Nevertheless, in both cases the coercive field corresponds approximately to that of the as melt-spun ribbons. Despite the reduction of the remanence for bonded pms due to the diluting effect of the polymer $(BH)_{max}$ values up to $90 \, kJ/m^3$ can be received.
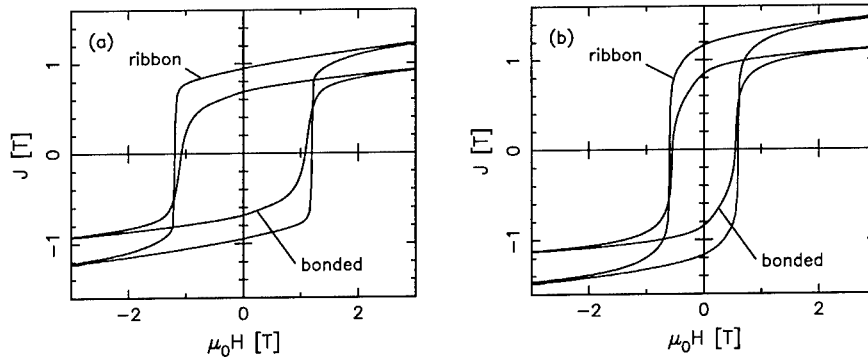
Figure 3. Room temperature hysteresis loops of polymer bonded powders compared to the corresponding ribbon material: (a) $Pr_2Fe_{14}B$ (stoichiometric pm) and (b) $Pr_2Fe_{14}B/30.4vol\%$ α-Fe (composite pm).

Coercivity mechanism

As shown in figure 4 (left), the temperature stability of the coercivity is better for the exchange coupled magnets (including polymer bonded magnets) than for the decoupled magnet. Using eq. (1) the temperature dependence of the coercivity can be analyzed quantitatively within the framework of the theory of micromagnetism. For nanocrystalline (nucleation hardened) magnets, the microstructural parameter α in general is composed of three subparameters ($\alpha = \alpha_K \alpha_{ex} \alpha_\psi$) [8, 18], namely α_K which describes the effect of the grain boundaries where the magnetocrystalline anisotropy is reduced ($\alpha_K \approx 0.8$) and α_{ex} taking into account the effect of the exchange coupling between neighbouring grains ($\alpha_{ex} = 1$ for decoupled magnets). The parameter α_ψ denotes the effect of misaligned grains and can be substituted in the case of isotropic magnets by the minimum nucleation field $H_N^{min} = \alpha_\psi 2K_1/J_S$, since the most unfavourably oriented grains (misorientation angle $\psi \approx 45°$) govern the whole demagnetization process. H_N^{min} is determined by the intrinsic material parameters J_S, K_1 and K_2 which are well-known from single crystals. If the nucleation model is valid, plotting the experimental data $\mu_0 H_C/J_S$ versus the theoretical values should yield a straight line with slope $\alpha_K \alpha_{ex}$ and ordinate intersection $(-N_{eff})$ in the case of temperature independent microstructural parameters. In figure 4 (right) the results of this evaluation are represented for the three different types of nanocrystalline PrFeB magnets and in addition for the bonded magnets made from stoichiometric and 30.4% excess iron ribbons, respectively. In fact, in all cases an approximately linear behaviour is observed, i.e., the dominant process for the magnetization reversal is the nucleation of reversed domains.

In general, the $\alpha_K \alpha_{ex}$ and N_{eff} values of the composite magnets are significantly smaller than for the decoupled magnet. The decrease of $\alpha_K \alpha_{ex}$ reflects the decrease in the coercivity and can

be attributed to the low anisotropy constant of α-Fe and to the exchange coupling between the grains inducing cooperative demagnetization processes of clusters of grains. On the other hand, the decrease in N_{eff} is caused by a more spherical grain shape and by a reduction of local stray fields at the edges and corners of the grains due to the smoothing effect of the exchange interaction at the grain boundaries. It is of interest to note that the microstructural parameters $\alpha_K \alpha_{ex}$ and N_{eff} for the bonded magnets are nearly the same as for their fully dense counterpart.
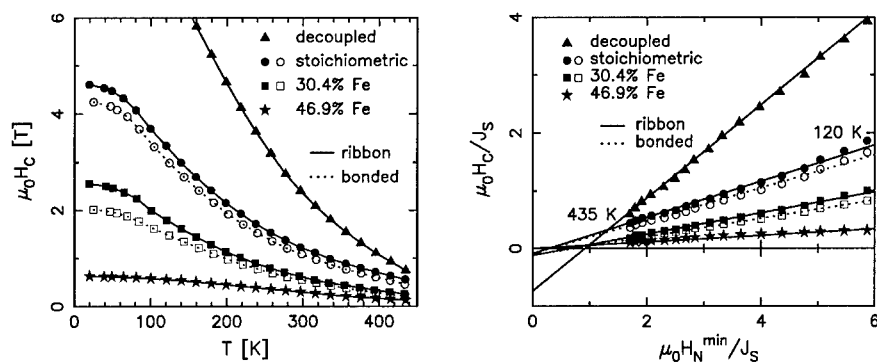
Figure 4. (*Left*) Temperature dependence of the coercivity. (*Right*) $\mu_0 H_C / J_S$ versus $\mu_0 H_N^{min} / J_S$ plot to determine the microstructural parameters for different nanocrystalline PrFeB pms. Decoupled: $\alpha_K \alpha_{ex} = 0.8$, $N_{eff} = 0.74$, stoichiometric: $\alpha_K \alpha_{ex} = 0.32$, $N_{eff} = 0.09$, stoichiometric/bonded: $\alpha_K \alpha_{ex} = 0.29$, $N_{eff} = 0.09$, composite (30.4% Fe): $\alpha_K \alpha_{ex} = 0.18$, $N_{eff} = 0.12$, composite (30.4% Fe)/bonded: $\alpha_K \alpha_{ex} = 0.16$, $N_{eff} = 0.12$, composite (46.9% Fe): $\alpha_K \alpha_{ex} = 0.06$, $N_{eff} = 0.00$.

NANOSTRUCTURED PERMANENT MAGNETS

Sm$_2$(Co,Cu,Fe,Zr)$_{17}$ magnets owe their outstanding magnetic properties exclusively to their complicated nanostructure (figure 5) consisting of three different phases: 1. Fe-rich pyramidal cells of the rhombohedral (R) 2:17 structure. 2. Cu-rich cell boundaries of the hexagonal (H) 1:5 structure. 3. Zr-rich lamellar platelets of the hexagonal 2:17 structure. The nanostructure develops in a self-organized process inside the μm-scaled grains during a complex three-step annealing
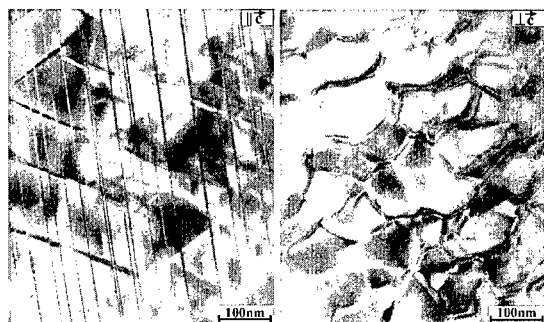
Figure 5. TEM micrographs of the nanostructure of a Sm$_2$(Co,Cu,Fe,Zr)$_{17}$ based sintered magnet. (*Left*) Rhombic structure observed parallel to the c-axis. (*Right*) Hexagonal network observed perpendicular to the c-axis.

procedure composed of homogenization, isothermal aging and slow cooling and causes a pinning type hardening mechanism, i.e., repulsive (or attractive) pinning of domain walls at (in) the 1:5 cell walls.

Evolution mechanism

It is generally agreed, that homogenization is required to obtain a single-phase 1:7 precursor alloy, i.e. a partly disordered R2:17 structure. This first step of the annealing procedure has been performed commercially at about 1200°C and will not be subject of the paper. During isothermal aging at 800°C the morphology of the nanostructure develops completely. As illustrated in figure 6 (left), this second step of the heat treatment is characterized by a continuous increase of the cell size and the lamellae density up to 110 nm and 0.043/nm after aging for 16 h, respectively, whereas the subsequent slow cooling procedure down to 400°C (cooling rate 1°C/min) followed by quenching to room temperature does not affect the morphology any more. It should be mentioned that the higher the aging temperature T_a is chosen, the larger the cell size is, however, the density of the lamellae increases only slightly. Our systematic study could solve the long lasting debate concerning the exact sequence of transformations by means of which the precursor alloy separates into the three phases present in the microstructure of the aged alloy. As proposed by Maury et al. [19] the ordering of the R2:17 phase induces the formation of the cell boundary phase whereas the platelet phase is generated less rapidly leading to a further ordering of the R2:17 phase. Hence, the results of Ray and Liu [20] according to which the lamellar Z-phase is created before the cell boundary phase could not be confirmed.

One of the most striking phenomena of the 2:17 based pms is the fact that after the isothermal aging the coercive field is only of the order of 0.1 T although the morphology of the three phases is fully developed. For receiving significant coercivity values slow cooling to lower temperatures ($< 650°C$) is absolutely necessary. In figure 6 (right) the annealing procedure is correlated with the coercive field and the (effective) magnetocrystalline anisotropy constant measured at room temperature. As will be shown in the following, the development of the typical hard magnetic properties has both chemical and structural reasons. The microchemical changes determined by using EDX which occur during aging are summarized in figure 7 for the matrix phase, the cell boundary phase and the lamellar Z-phase. It is obvious from this, that the lamellae are formed during the isothermal annealing at 800°C where they even develop their final chemical composition. Consequently, the evolution of the typical hard magnetic properties cannot be attributed to the lamellae as Katter [21] mistakenly presumed. In contrary, the chemical composition of the 1:5 cell boundary phase is mainly developed during the cooling procedure. Actually, during isothermal aging there is only a
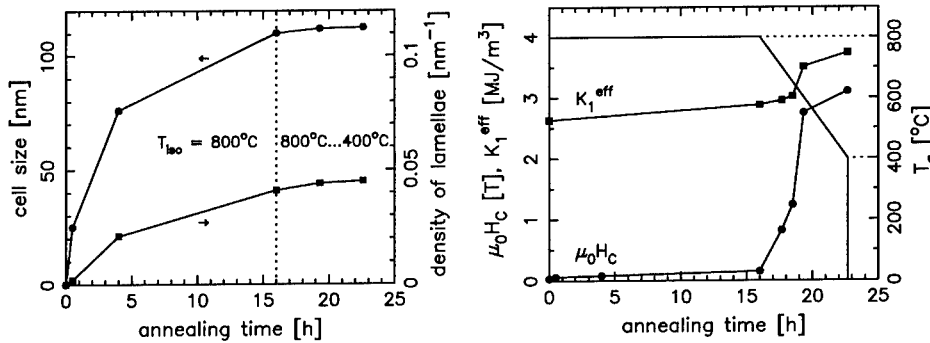
Figure 6. Evolution of the microstructural and hard magnetic properties for a sintered $Sm(Co_{bal}Cu_{0.07}Fe_{0.22}Zr_{0.04})_{7.4}$ pm during the aging program: (*Left*) Morphology of the microstructure. (*Right*) Coercivity $\mu_0 H_c$ and (effective) magnetocrystalline anisotropy constant K_1^{eff}.
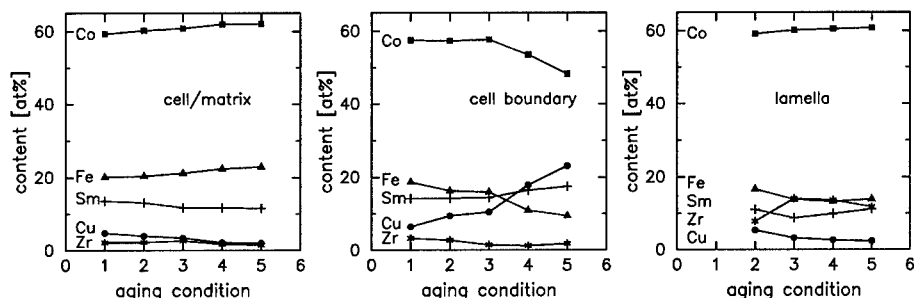
Figure 7. Chemical compositions (absolute accuracy $\pm(0.5-1.5)$ at%) of the cells, cell boundaries and lamellae determined by EDX for the $Sm(Co_{bal}Cu_{0.07}Fe_{0.22}Zr_{0.04})_{7.4}$ sintered magnet in different stages of the complex heat treatment: 1: $T_a = 800\,°C / t_a = 0.5\,h$, 2: $T_a = 800\,°C / t_a = 4\,h$, 3: $T_a = 800\,°C / t_a = 16\,h$, 4: same as 3 but cooled to $600\,°C$ and 5: final state.

weak tendency for an enrichment of Cu or a depletion of Fe found, while during cooling the amount of Cu (Fe) increases (decreases) substantially in this phase by a factor of 3 (2) compared to state 1. Simultaneously, the Cu content decreases within the cells, whereas the Fe content increases. In addition, the development of the elemental profiles within the cell and the cell wall is characterized by a sharpening of the transition region between the 2:17 and the 1:5 phase as can be seen for Cu from figure 8 (left) for the different aging conditions. The distribution of all five elements after the slow cooling procedure down to $400\,°C$ is represented in figure 8 (right). Hereby, it is noteworthy, that Zr, Co and Fe are diluted within the cell walls. From a structural point of view, the slow cooling is also necessary for the development of the hexagonal 1:5 crystal structure of the cell walls. Although almost from the beginning of the isothermal aging, i.e. as soon as a cellular-like structure becomes visible, a 1:5 stoichiometry is obtained for the cell boundary phase, its crystal structure is not formed during isothermal aging. This is supported by X-ray diffraction spectra received before and after the cooling procedure. In order to detect [0 0 n] reflexes of high intensity in the diffraction spectra the samples were prepared perpendicular to the c-axis. According to figure 9 and table I after the isothermal heat treatment the following phases could be identified: rhombohedral and hexagonal Sm_2Co_{17}, rhombohedral Sm_2Co_7 and hexagonal Sm_5Co_{19}. However, the $SmCo_5$ phase is not present in this state. After cooling down to $400\,°C$ the Sm_2Co_7 and Sm_5Co_{19} phases have nearly vanished, but in addition besides the Sm_2Co_{17} phases (cells and lamellae) the $SmCo_5$ phase
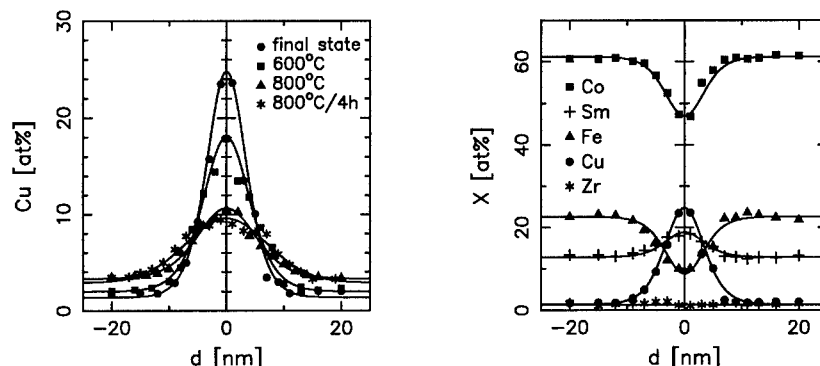
Figure 8. EDX profiles in the vicinity of a 2:17/1:5 phase boundary: (*Left*) Cu profiles as a function of the annealing program. (*Right*) Profiles of the elements Sm, Co, Cu, Fe and Zr for the final state.
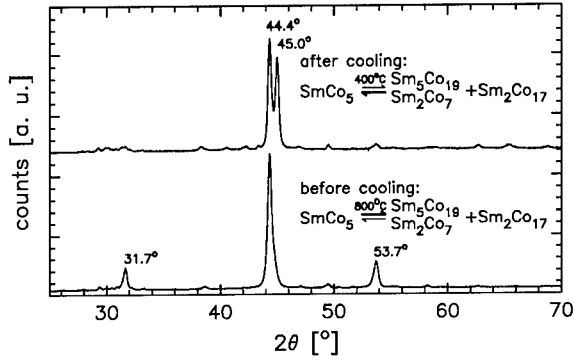
Figure 9. X-ray diffraction spectrum (CuK_α-radiation, $\lambda = 1.5406$ Å) of the $Sm(Co_{bal}Cu_{0.07}$ $Fe_{0.22}Zr_{0.04})_{7.4}$ sintered pm prepared perpendicular to the c-axis (before and after the slow cooling procedure).

Phase	[h k l]	d^{theo} [Å]	d^{exp} [Å]	$2\theta^{exp}$ [°]
$SmCo_5$	[0 0 2]	1.989	2.013	45.0
$SmCo_{3.3}Cu_{1.7}$	[0 0 2]	2.012	2.013	45.0
Sm_2Co_{17} (R)	[0 0 6]	2.029	2.039	44.4
Sm_2Co_{17} (H)	[0 0 4]	2.041	2.039	44.4
Sm_2Co_7 (R)	[0 0 13]	2.806	2.820	31.7
Sm_5Co_{19} (H)	[0 0 19]	1.698	1.705	53.7

Table I. The lattice parameters d^{exp} determined from the diffraction peaks ($2\theta^{exp}$) marked in figure 9 in comparison with the reference data d_{theo} [22,23].

(cell walls) now appears. This behaviour reflects the eutectoid decomposition reaction of binary $SmCo_5$ into Sm_5Co_{19}, Sm_2Co_7 and Sm_2Co_{17} at 800°C [24] and the substantial decrease of this decomposition temperature to lower temperatures if some of the Co in $SmCo_5$ is substituted by Cu [25]. Consequently, according to these results the development of the typical hard magnetic properties during the cooling procedure is a complex process where by the diffusion of Cu into the cell walls and the decreasing temperature the thermodynamic phase equilibrium is shifted to the 1:5 phase.

Coercivity mechanism

According to the above results, it is the cell wall and not the lamellar Z-phase which is directly involved in the coercivity mechanism. Using Lorentz microscopy, the magnetic domain wall pattern (md) can be visualized (figure 10). These studies cleary show the zig-zag pinning of the domain walls (dw) along the elongated 1:5 cell boundaries, which is not affected by the lamellae present. Nevertheless, the lamellae are the most important prerequisite for a good stability of the precipitation structure. Indeed, according to high-resolution TEM studies the transition between the different phases is comparatively sharp and a large coherency of the various crystal lattices is observed despite their different lattice parameters (figure 11 (left)). Obviously, the occuring internal stresses are reduced by the lamellar Z-phase. This is suggested also by the fact that in Zr-free samples the lamellar phase does not exist and only Cu-rich ellipsoidal precipitations are found (figure 11 (right)), resulting in rather low coercivities. The pinning type hardening mechanism becomes also evident from the values for the microstructural parameters $\alpha_{K,pin}$ and $\alpha_{\psi,pin}$ obtained from $\mu_0 H_C / J_s$ versus $2\mu_0 K_1 / J_s^2$ plots according to eq. (1) and from the dependence of
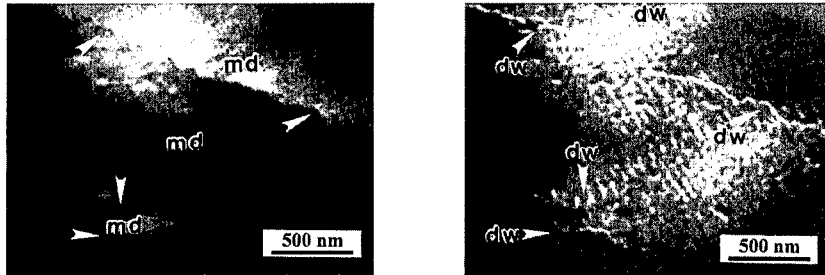
Figure 10. Lorentz microscopy images of a fully heat treated $Sm(Co_{bal}Cu_{0.07}Fe_{0.22}Zr_{0.04})_{7.4}$ sintered magnet: Foucault mode (left), Fresnel mode (right).

the coercivity of the misalignment angle ψ using Kerr microscopy, respectively. In fact, the parameter $\alpha_{K,pin}$ which is a measure for the strength of the domain wall pinning centers amounts to $0.1 - 0.4$ for fully heat treated samples depending on the aging conditions (figure 12 (left)) and for the parameter $\alpha_{\psi,pin}$ the typical $1/\cos\psi$ behaviour with increasing ψ is found, i.e. $\alpha_{\psi,pin} \geq 1$ (figure 12 (right)).

From the elemental profiles of figure 8 (right) the compositions of the pure phases are known. Hence, for the pure phases the intrinsic magnetic properties can be determined [26,27]. When these results are correlated as can be seen in figure 13 the schematic crystal energy profile proposed by Kronmüller [28] could be confirmed quantitatively. Accordingly, in the present case the cell walls act as repulsive barriers for domain walls since their domain wall energy is much larger than that of the 2:17 cells ($\gamma^{1:5} = 0.032$ J/m^2, $\gamma^{2:17} = 0.020$ J/m^2). The coercivity of 2:17 based pms can be analyzed quantitatively on the basis of micromagnetic models. Hereby, one takes advantage of theories which has been developed by several authors in terms of the continuum model [29] and of the Heisenberg model [30] to describe the pinning behaviour of domain walls by planar defects. According to that, a first approximation of the coercive field may be obtained from the maximum change in the domain wall energy with position. Supposing a linear increase of the wall energy over the range r_0 the coercivity may be written as

$$\mu_0 H_c = \mu_0 \frac{1}{2J_s} \frac{d\gamma}{dz}\bigg|_{max} = \mu_0 \frac{1}{2J_s} \frac{|\gamma^{1:5} - \gamma^{2:17}|}{r_0} . \tag{2}$$

Within the range $r_0 \approx 2$ nm the intrinsic material parameters vary between the cells and the cell boundaries. The sample under consideration yields a coercivity of $\mu_0 H_c = 2.7$ T at room tem-
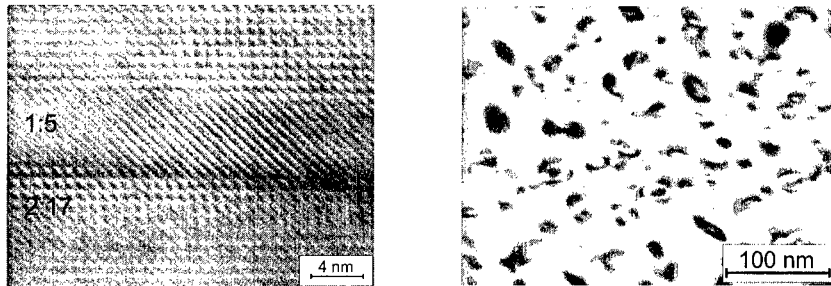
Figure 11. (*Left*) High-resolution TEM micrograph of the phase boundary between the cell (2:17) and the cell wall (1:5). (*Right*) Microstructure of a fully heat treated Zr-free $Sm(Co_{bal}Cu_{0.08}Fe_{0.1})_{8.5}$ alloy.
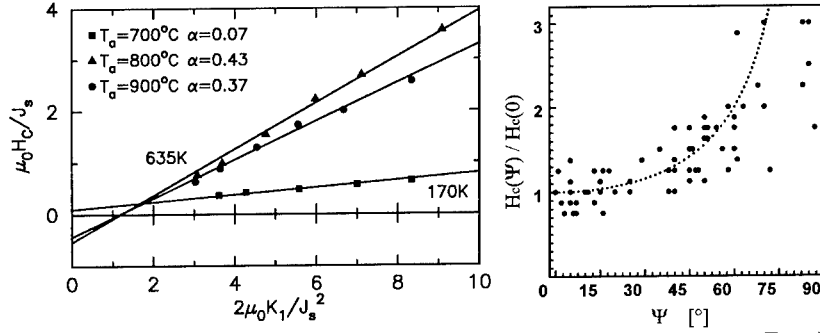
Figure 12. Microstructural parameters of a fully heat treated $Sm(Co_{bal}Cu_{0.07}Fe_{0.22}Zr_{0.04})_{7.4}$ sintered pm. (*Left*) Pinning strength $\alpha = \alpha_{K,pin}$ as function of the aging temperature T_a. (*Right*) $\alpha_{\psi,pin}$.
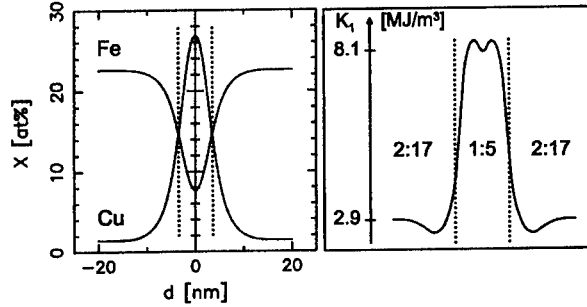
Figure 13. Calculated profile of the magnetocrystalline anisotropy constant K_1 in the vicinity of a 2:17/1:5 phase boundary using the results of the (deconvoluted) EDX Cu-profile.

perature and of 1.1 T at 200°C agreeing rather well with the measured temperature dependence of the coercivity. In a second approximation which is closely related to the first one the transition region between the 2:17 and the 1:5 phase is described by n individual lattice planes of distance $d = 0.2$ nm. Each plane i is characterized by a local anisotropy constant K_1^i and an exchange constant $A^{i,i+1}$ between neighbouring planes. Minimizing the total energy of this planar configuration results in:

$$\mu_0 H_C = \mu_0 \frac{\pi}{3\sqrt{3}} \frac{2K_1}{J_s} \frac{1}{\cos\psi_0} \frac{d}{\delta_B} \left| \sum_{i=1}^{n-1} \frac{A}{A^{i,i+1}} - \frac{K_1^i}{K_1} \right| \tag{3}$$

where the material parameters A and K_1 and the domain wall width δ_B refer to the matrix phase. From eq. (3) we derive the microstructural parameter

$$\alpha_{K,pin} = \frac{\pi}{3\sqrt{3}} \frac{d}{\delta_B} \left| \sum_{i=1}^{n-1} \frac{A}{A^{i,i+1}} - \frac{K_1^i}{K_1} \right| . \tag{4}$$

For a numerical evaluation of $\alpha_{K,pin}$ we assume $A^{i,i+1} \approx A$ because both phases have similar Curie temperatures. An approximate value of $\alpha_{K,pin}$ can be estimated under the assumption of

a linear increase of K_1' from K_1 to $3K_1$ which extends over $n = 10$ layers. For the wall width $\delta_B = \pi(A^{2:17}/K_1^{2:17})^{0.5}$ we receive with $A^{2:17} = 9.5 \; 10^{-12}$ J/m and $K_1^{2:17} = 2.91$ MJ/m^3 $\delta_B = 5.7$ nm. From eq.(4) we then obtain $\alpha_{K,pin} = 0.35$ in agreement with the experimental value of ≈ 0.4. Accordingly, the two expressions for estimating the coercivity lead to a rather accessible explanation of the temperature coefficients of the coercivity. In general, the temperature stability of the coercive field is better for Cu-poor cell walls than for Cu-rich ones [6,16]. This is due to the fact that in the Cu-poor case the equilibrium of the decomposition reaction mentioned above is not completely shifted to the left so that the 1:5 phase is diluted by the remaining phases resulting in a reduction of its intrinsic magnetic parameters and therefore showing over a large temperature range a similar K_1 (and therefore γ) behaviour as the 2:17 cell phase (figure 14 (left)). The Cu content of the cell walls is influenced by both the Cu content of the sample itself and the cell size. Usually, if the cell size is small which can be realized by a low Fe content, a high Zr content and a smaller TM:RE ratio z ($z \leq 7.0$) the Cu content of the cell walls is also small. Similarly, magnets which have not been heat treated optimally (T_a too low, t_a too short) also show smaller cell sizes and therefore less Cu in the cell walls. In contrast, in the Cu-rich case the equilibrium is completely shifted to the left leading to a entirely different temperature behaviour of the wall energies $\gamma^{1:5}$ and $\gamma^{2:17}$ and therefore to a strongly negative temperature coefficient of the coercivity according to eq.(2) and eq.(3). In any case, at low temperatures the pinning is repulsive and changes to an attractive one at temperatures between 400 K and 700 K depending on the Cu content. The smaller the Cu content of the cell walls the higher the temperature of the cross-over and the Curie temperature of the 1:5 phase. Although the coercivity is determined by the difference in the domain wall energies, $\mu_0 H_C$ never becomes zero at the temperature of the cross-over. This is because $\Delta\gamma$ does not become equal zero everywhere in the cell walls at the same temperature due to local fluctuations of the 1:5 composition. Consequently, as the crossing angle β is larger for Cu-rich samples, $\mu_0 H_C(T)$ is not influenced by the cross-over. However, as in Cu-poor samples β is very small the crossing manifests in an anomalous (positive) temperature coefficient. As soon as the 1:5 phase reaches its Curie temperature (which is always smaller than that of the 2:17 phase) it seems to be possible that the pinning behaviour changes to a nucleation behaviour with the cells magnetically isolated by the paramagnetic 1:5 boundaries. This behaviour was observed by Tellez-Blanco et al. [31]. In figure 14 (right) the temperature dependence of the coercivity is presented for some fully heat treated melt-spun pms for which a very similar behaviour concerning microstructure and magnetic properties can be realized after applying an appropriate annealing procedure [32]. To illustrate impressively the suitability of 2:17 type Sm-Co based pms for high temperature applications the temperature behaviour is compared to three other common pm materials, namely Nd$_2$Fe$_{14}$B, a Sr ferrite and AlNiCo.
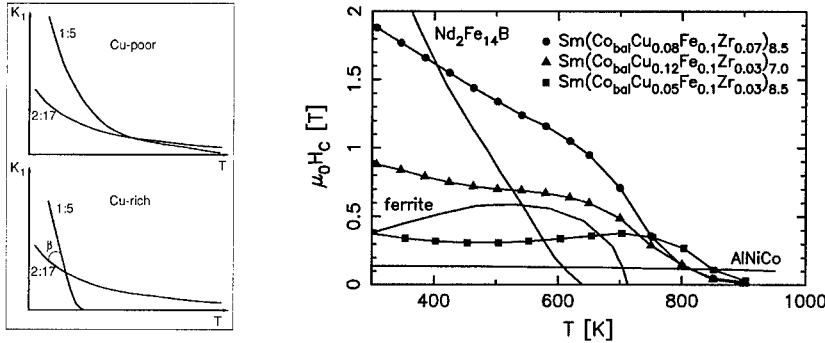
Figure 14. Temperature dependence of the magnetocrystalline anisotropy constant schematically (*left*) and of the coercivity of different fully heat treated melt-spun pms compared to other common pm materials (*right*).

ACKNOWLEDGEMENT

REFERENCES

[1] K.J. Strnat, G. Hoffer, J.C. Olsen, W. Ostertag, J.J. Becker, J. Appl. Phys. **38**, 1001 (1967).
[2] J.J. Croat, J.F. Herbst, R.W. Lee, F.E. Pinkerton, J. Appl. Phys. **55**, 2078 (1984).
[3] M. Sagawa, S. Fujimura, M. Togawa, Y. Matsuura, J. Appl. Phys. **55**, 2083 (1984).
[4] G.C. Hadjipanayis, R.C. Hazzleton, K.R. Lawless, J. Appl. Phys. **55**, 2073 (1984).
[5] K.H.J. Buschow, in *Handbook of Magnetic Materials*, ed. K.H.J. Buschow (Elsevier, North-Holland-Amsterdam), Vol. 10 (1997) 463.
[6] J.F. Liu, Y. Zhang, Y. Ding, D. Dimitrov, G.C. Hadjipanayis, in *Proceedings of the 15th International Workshop on REM and their applications*, Dresden, Germany, ed. L. Schultz, K.H. Müller (1998) 607.
[7] C.H. Chen, M.S. Walmer, M.H. Walmer, S. Liu, E. Kuhl, G. Simon, *J. Appl. Phys.* **83**, 6706 (1998).
[8] H. Kronmüller, in *Supermagnets, hard magnetic materials*, Kluwer, Dordrecht, eds. G.J. Long, F. Grandjean (1991) 461.
[9] A. Manaf, R.A. Buckley, H.A. Davies, M. Leonowicz: *J. Magn. Magn. Mater.* **101**, 360 (1991).
[10] J. Bauer, M. Seeger, A. Zern, H. Kronmüller: *J. Appl. Phys.* **80**, 1667 (1996).
[11] D. Goll, M. Seeger, H. Kronmüller: *J. Magn. Magn. Mater.* **185**, 49 (1998).
[12] E.F. Kneller, R. Hawig, *IEEE Trans. Magn.* **27**, 3588 (1991).
[13] A. Manaf, M.A. Al-Khafaji, P.Z. Zhang, H.A. Davies, R.A. Buckley, W.M. Rainforth, *J. Magn. Magn. Mater.* **128**, 307 (1993).
[14] W. Gong, G.C. Hadjipanayis, R.I. Krause, *J. Appl. Phys.* **75**, 6649 (1994).
[15] H. Kronmüller, R. Fischer, M. Bachmann, T. Leineweber, *J. Magn. Magn. Mater.* **203**, 12 (1999).
[16] D. Goll, H. Kronmüller, *Naturwissenschaften* **87**, 423 (2000).
[17] H. Kronmüller, R. Fischer, M. Seeger, A. Zern, *J. Phys. D* **29**, 2274 (1996).
[18] H. Kronmüller, in *Proc. 11th Int. Symp. Magnetic Anisotropy and Coercivity in Rare Earth – Transition Metal Alloys*, Sendai, Japan, eds. H. Kaneko et al. (2000) S83.
[19] C. Maury, L. Rabenberg, C.H. Allibert, *phys. stat. sol. (a)* **140**, 57 (1993).
[20] A.E. Ray, S. Liu, in *Proceedings of the 12th International Workshop on REM and Their Applications*, Canberra, 1992, p.552.
[21] M. Katter, J. Weber, W. Assmus, P. Schrey, W. Rodewald, *IEEE Trans. Magn.* **32**, 4815 (1996).
[22] International Centre for Diffraction Data, U.S.A.: Powder Diffraction File.
[23] Y. Khan, *Z. Metallkd.* **65**, 489 (1974).
[24] H.H. Stadelmeier, B. Reinsch, G. Petzow, *Z. Metallkd.* **89**, 2 (1998).
[25] A.J. Percy, *J. Less Common Met.* **51**, 153 (1977).
[26] E. Lectard, C.H. Allibert, R. Ballou, *J. Appl. Phys.* **75**, 6277 (1994).
[27] D. Goll, W. Sigle, G.C. Hadjipanayis, H. Kronmüller, in *Proc. 16th Int. Workshop on RE-Magnets and their Applications*, Sendai, Japan, eds. H. Kaneko et al. (2000) 61.
[28] H. Kronmüller, K.D. Durst, W. Ervens, F. Fernengel, *IEEE Trans. Magn.* **20**, 1569 (1984).
[29] H.R. Hilzinger, *Appl. Phys.* **12**, 253 (1977).
[30] H.R. Hilzinger, H. Kronmüller, *Phys. Letters* **51A**, 59 (1975).
[31] J.C. Tellez-Blanco, X.C. Kou, R. Grössinger, E. Estevez-Rams, J. Fidler, B.M. Ma, in *Proc. 14th Int. Workshop on RE-Magnets and their Applications*, World Scientific, Singapore, eds. F.P. Missell et al., 707 (1996).
[32] D. Goll, I. Kleinschroth, W. Sigle, H. Kronmüller, *Appl. Phys. Lett.* **76**, 1054 (2000).

Magnetic and Microstructural Aspects of the Bulk Metallic Glassy Materials $Nd_{60}Fe_{30}Al_{10}$

N. H. Dan, N. X. Phuc, V. H. Ky, N. M. Hong
Institute of Materials Science, NCST, Hoang Quoc Viet Str., Hanoi, Vietnam

N. Chau, N. H. Luong, C. X. Huu
Center for Materials Science, Department of Physics, Hanoi National University, Nguyen Trai Str., Hanoi, Vietnam.

R. W. McCallum, M. J. Kramer, A. S. O'Connor, K. W. Dennis
Ames Laboratory, USDOE and Department of Materials Science and Engineering,
Iowa State University, Ames, IA 50011, USA

L. H. Lewis
Materials and Chemical Sciences Division, Energy Sciences and Technology Dept., Brookhaven National Laboratory, Upton, New York 11973-5000, USA

L. D. Tung
International Training Institute for Materials Science, 1 Dai Co Viet Str., Hanoi, Vietnam

ABSTRACT

The ferromagnetic bulk metallic glass (BMG) $Nd_{60}Fe_{30}Al_{10}$ system exhibits extremely large coercivities at low temperature and moderate coercivities near room temperature. The magnetic hardness, as best evidenced by the onset of magnetic irreversibility, was studied in bulk suction-cast and melt-spun alloys with the nominal composition $Nd_{60}Fe_{30}Al_{10}$. Systematic x-ray diffraction studies of the degree of crystallinity performed as a function of position within the bulk suction-cast samples is found to correlate with the variation in the room-temperature magnetic hysteresis character. X-ray diffraction data clearly shows the presence of both crystallites and amorphous material on the samples' outmost surfaces; the amorphous phase content increases with distance into the cast sample. These results underscore the importance of solidification conditions and attendant nanophase selection, on the resultant magnetic properties of this class of alloys.

INTRODUCTION

The ferromagnetic bulk metallic glass composition $RE_{60}Fe_{30}Al_{10}$ (RE=Nd or Pr) has generated considerable interest of both applied and fundamental nature by virtue of its appreciable coercivity at room temperature [1]. The presence and magnitude of this reported coercivity, up to 0.4 T at room temperature, is an apparent contradiction to the conventional understanding of the relationship between nanostructure and coercivity in nominally amorphous materials. An additional challenge associated with study of this class of materials is the difficulty of reproducing the results reported in various laboratories around the world [2-6]. This latter challenge indicates that the material preparation conditions, such as the purity of the starting materials, the prealloy state [7] and the solidification condition, all influence the

resultant magnetic properties. To further clarify the relationship between microstructure and magnetic properties in this class of materials, systematic studies of the position-dependent degree of crystallinity with the suction-cast rods were correlated with the room-temperature magnetic response. The considerable variation in magnetic response with degree of crystallinity underscores the importance of solidification conditions, and attendant nanophase selection, on the resultant magnetic properties of this class of alloys.

EXPERIMENTAL DETAILS

Investigations into both the temperature- and field-dependent character of the coercivity and into the relationships between the microstructure and the room-temperature coercivity were carried out on bulk suction-cast and melt-spun forms of $Nd_{60}Fe_{30}Al_{10}$ made from the elements Nd (2-9's purity), Fe (4-9's purity) and Al (4-9's purity). The alloy ingots were used to prepare two forms of the samples: melt-spun ribbons were formed on a copper single-wheel roller operated at various circumferential speed and hence with with various quenching rates, and rods that were suction-cast into copper molds of various rectangular cross-sections. The dimensions of the rod samples were height $z_0 \approx 60$ mm, width $y_0 \approx 10$ mm and thicknesses $x_0 \approx 1$, 1.5 or 3 mm. All rods were sectioned and polished parallel to the (y_0,z_0) sample plane. The phase constitution and degree of crystallinity of both forms of sample were assessed with room-temperature Cu-K_α x-ray diffraction (XRD). While materials melt-spun at high circumferential wheel speeds proved to be x-ray amorphous, the most meaningful data was obtained from partially-crystalline samples quenched at lower wheel speeds. The results obtained from the partially-crystalline samples were extrapolated to explain the results manifest in more amorphous samples.

The magnetic characterization was performed in an Ar atmosphere with a vibrating sample magnetometer both on the melt-spun ribbons and on 1 mm^3 cubic-shaped specimens taken from the center of the thickest cast rod. The applied field was in the range -15 kG $\leq H_{appl} \leq +15$ kG and was applied parallel to the long axis of the ribbons; the temperature range of measurement varied from 100 K $-$ 600 K. The magnetic response of the bulk cube specimen showed no dependence on orientation with respect to the magnetic field. After raising the temperature well above the temperature range where the materials exhibit hysteresis, magnetization versus temperature measurements were made using both zero-field-cooled (ZFC) and field-cooled (FC) measurements which diverge at a temperature T_{irr} marking the appearance of irreversible magnetic behavior, Fig. 1. The divergence of the ZFC and FC measurements at T_{irr} is most easily understood in terms of the normalized field, $H_n=H_{appl}/H_c(T)$ where H_{appl} is the applied field and $H_c(T)$ is the temperate-dependent coercivity of the magnetically hardest phase present in the sample. In the ZFC measurement, the field is applied at the lowest temperature and the sample magnetization follows the initial magnetization curve. As the temperature is increased at fixed applied filed H_{app}, the normalized field H_n increases as $H_c(T)$ decreases so that the magnetization response moves to a higher value along the temperature-dependent initial magnetization curve. For the FC measurement, H_n starts at a value which effectively saturates the sample and then H_n decreases as $H_c(T)$ increases with decreasing temperature so that the magnetization moves down the first-quadrant demagnetization curve. Thus the difference between the ZFC and FC curves represents the difference between the initial magnetization curve and the demagnetization curve for the applied field and temperature. In other words T_{irr}, the temperature at which $M_{ZFC} = M_{FC}$, corresponds to the temperature where the width of the hysteresis loop closes at H_{appl}. For a

hypothetical sample consisting of a paramagnetic phase combined with a hard magnetic phase with coercivity $H_{c(Hard)}$ that is independent of temperature, H_{irr} is also independent of temperature while it is clear that H_c of the sample is strongly dependent on temperature do to the temperature dependence of the paramagnetic fraction. Thus, due to the multiple magnetic phase behavior of the samples studied, T_{irr} is considered to be a more consistent measure of magnetic hysteresis than the value of the coercivity. T_{irr} was followed as a function of applied field for a melt-spun ribbon sample quenched at 30 m/sec and for a sample of the drop-cast material of 1 mm thickness, Fig. 1 inset.

RESULTS AND DISCUSSION:

The ZFC and FC magnetization measurements were performed on both melt-spun and bulk cast rod specimens of $Nd_{60}Fe_{30}Al_{10}$; representative results obtained at an applied field of 0.5 kG are displayed in Fig. 1. Strictly speaking the measurement fields are not equivalent due to the large differnce in demagnetization factor between the two samples. However this effect should lower T_{irr} in the bulk sample so that the actual difference in curves is enhanced over that which is measured. The departure from magnetic reversibility occurs at approximately 450 K for the bulk cast sample and around 325 K for the melt-spun ribbon at the measuring field of 0.5 kG. The difference in the onset of the magnetic irreversibility temperature in the two samples must be due to microstructural differences (including significant fluctuations in chemical composition in the disordered matrix) originating from the two solidification methods, as the nominal compositions
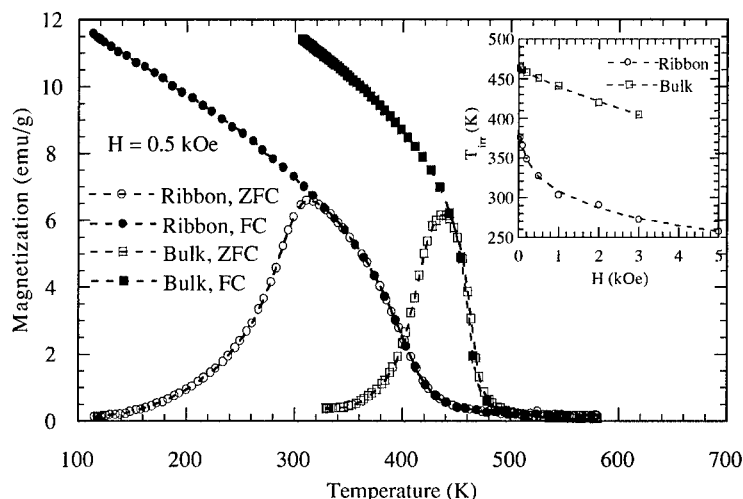
Figure 1. Magnetization data obtained at 0.5 kG in the zero-field-cooled (M_{ZFC}) and the field-cooled (M_{FC}) states from samples of the $Nd_{60}Fe_{30}Al_{10}$ in the form of ribbons melt-spun at 30 m/sec and cast rods of 1 mm diameter. The inset shows the field dependence of the onset temperature (T_{irr}) of the magnetic irreversibility temperature.

are the same. The origins of the differences in the onset of magnetic irrevsibility noted in the two different forms of the composition $Nd_{60}Fe_{30}Al_{10}$, Fig. 1, were pursued with systematic studies of the variation of the microstructure and magnetic properties in the bulk rods. Representative x-ray diffraction results are presented in Figs. 2 and 3. Significant varia- tion the of microstructure with position within the sample appears in ribbon melt-spun at 25 m/s with thickness ~ 40 μm. The surfaces of the ribbons were investigated separately: the "wheel side" surface, which describes the ribbon surface that was in direct contact with the quenching wheel and the "free side" ribbon surface that was exposed to the quenching atmosphere. As shown in Fig 2, the broad diffraction peak observed for the wheel-side surface at $2\theta \approx 30°$ is sharper than the corresponding peak for the ribbon free-side surface. This observation motivated study of the position-dependent microstructure and corresponding magnetic properties for samples of millimeter-scale thickness.
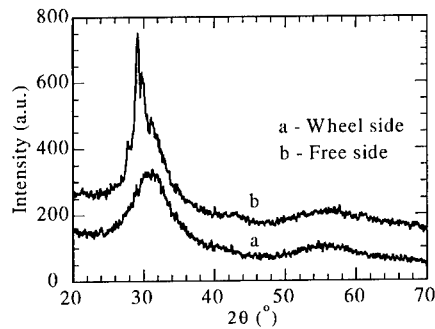
Figure 2. XRD patterns of Nd-Fe-Al ribbon melt-spun at 25 m/s.
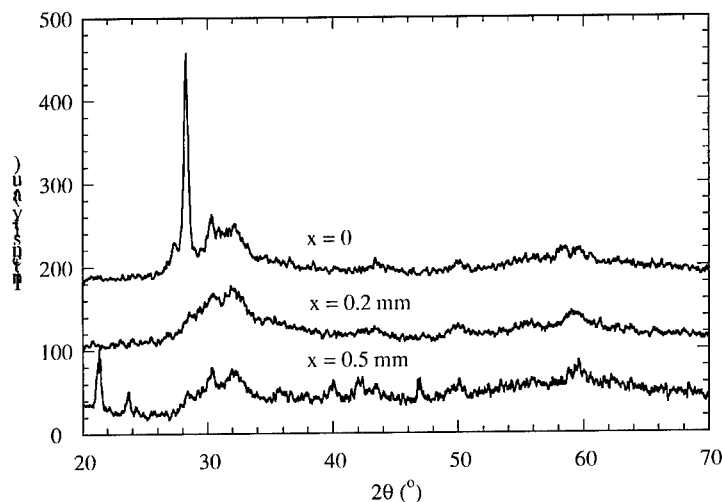
Figure 3. XRD patterns taken from cast rod of diameter 1 mm at depths x = 0 (cast surface), x = 0.2 mm and x = 0.5 mm. Note that the sample assumes a more amorphous character with increasing depth in the rod.
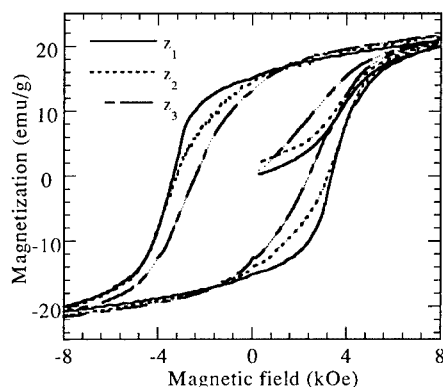
Figure 4a). Room-temperature hysteresis loops of 1-mm thick cast rod sample for specimens sectioned at various height z positions.
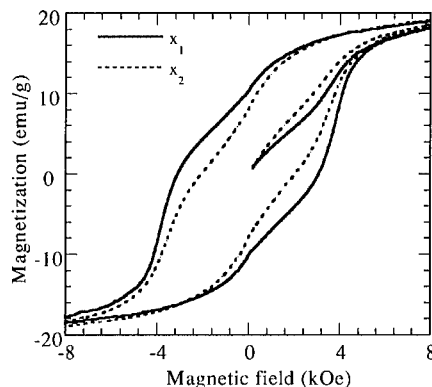
Figure 4b). Room-temperature hysteresis loops for specimens sectioned from the outermost (x_1) and innermost (x_2) position of 3-mm-thick cast rod.

XRD scans reveal a variation of crystallinity with respect to position within the suction-cast samples, Figure 3. The original cast surfaces of all rods are revealed to be partially crystalline. Systematic magnetic investigation from samples taken from at a variety of depths within the cast samples show a variation of hysteretic character that reflects the variation of crystallinity, as discussed above. The magnetic data of Fig. 4a) contradict the XRD data of Fig. 3 by demonstrating the existence of small but signficant differences in the microstructure along the length (z-direction) of the cast rod. More pronounced differences in the magnetic properties are found along the sample thickness (Fig. 4b)) as expected from the XRD data. An interesting question is why the outer sections of the cast specimen exhibit a larger coercivity than do inner sections (Fig. 4b)). Clearly the data presented above concerning different forms (*i.e.*, melt-spun ribbons *vs.* cast rods) of the BMG composition $Nd_{60}Fe_{30}Al_{10}$ suggest that the solidification conditions, and attendant nanophase selection, greatly influence the magnetic properties. Heat flow patterns are quite different in the various casting techniques investigated during the course of this study. The presence of significant crystallization on the free surface of the single-roller melt-spun ribbons (Fig.2) indicates that the cooling rate at this surface is suffciently slow to allow nucleation and growth of the pre-existing nanoscale clusters [7]. Analogously, the initial cooling rate near the mold wall is insufficient to prevent nucleation and growth at the starting composition. In the bulk samples there is an apparent contradiction to conventional understanding of solidification behavior because the interior of the sample contains less crystalline material than the exterior. However the cooling rate is suffcently slow in during the casting process to allow for bulk diffusion to occur during cooling. This effect causes the exterior of the sample to become partially crystalline and causes the composition of the remaining liquid becomes more Nd-rich as is required by mass balance. It appears that the glass-forming ability of the remaining liquid composition is greater than that of the initial composition.

The origin of this behavior is related to the equilibrium ternary phase diagram and will be discussed in another paper.

In summary, we have shown that the use of x-ray diffraction analyses can reveal clearly the presence of microsized crystallites in the outermost and innermost regions of the suction-cast rods of $Nd_{60}Fe_{30}Al_{10}$ BMG-type alloy. The effects of solidification-related changes in the liquid composition are demonstrated to significantly alter the glass-forming ability of the melt. The attendant magnetic measurements demonstrate that the cast samples are inhomogenous not only along their thickness but also along their height, $i.e.$, along the distance from the bottom of the mold to the top. The differences in the degrees of crystallinity and phase proportions found in the samples of identical composition but processed by the two different solidification methods — melt-spinning and suction casting — lie in the time scale over which diffusion is possible during solidification.

ACKNOWLEDGMENTS

REFERENCES
[1]. A. Inoue, T. Zhang and A. Takeuchi, Mat. Trans. JIM **37** (2) (1996) 99.
[2]. A. Inoue, T. Zhang and A. Takeuchi, IEEE Trans. Magn. **33** (1997) 3814;
[3]. K. V. Rao, Dept. of Condensed Matter Physics, The Royal Institute of Technology, Stockholm, Sweden, presented at the Spring MRS Research Society Meeting, San Francisco, CA April 5-8, 1999.
[4]. A. Inoue, T. Zhang and A. Takeuchi, Met. and Mat. Trans. **29A** (1998) 1779.
[5]. Y. Li, J. Ding, S. C. Ng and X . Z. Wang, J. Magn. Magn. Mat. **187** (1998) 273.
[6]. J. Ding, Y. Li and X. Z. Wang, J. Phys. D: Appl. Phys. **32** (1999) 713.
[7]. A. S. O'Connor, L. H. Lewis, R. W. McCallum, K. W. Dennis, M. J. Kramer, D. T. K. Anh, N. H. Dan, N. H. Luong and N. X. Phuc, Proc. of the 16th Intern. Workshop on Rare Earth Magnets, Sendai, Japan, Sept. 10-14 (2000) 475.

Investigations on the Magnetic Properties of High-Coercivity $(Nd_{1-x}Fe_x)_{90}Al_{10}$ Bulk Amorphous Alloys

N. Lupu, H. Chiriac, A. Takeuchi[1] and A. Inoue[1]
National Institute of Research and Development for Technical Physics,
47 Mangeron. Blvd., Iasi, RO 6600, Romania
[1]Institute for Materials Research, Tohoku University,
2-1-1 Katahira, Aoba-Ku, Sendai 980-8577, Japan

ABSTRACT

Bulk rods with diameters up to 3 mm prepared by suction casting and respectively mould casting and melt-spun amorphous ribbons with thicknesses in the range 25 – 150 μm with compositions $Nd_{90-x}Fe_xAl_{10}$ (x = 35; 40; 45; 50) were investigated by XRD, DSC and magnetic measurements in the temperature range 5 – 600 K. The microstructure and magnetic properties are strongly dependent on the cooling rate, preparation process and Fe content. The large values of the coercive field, which amount to 320 kA/m in the as-cast state as well as the increase with decrease of the temperature and cooling rate result from the formation of very small metastable or nonequilibrium magnetic clusters.

INTRODUCTION

The interest in glass-forming alloys, which vitrify at relatively low cooling rates from the molten state, compared with conventional rapidly quenched metallic glasses has grown in the last years. Owing to their resistance to crystallization, these easy-glass forming alloys can be cast in bulk shape with dimensions of millimeters. However, no results on bulk amorphous alloys with ferromagnetic properties at room temperature have been reported earlier than 1995 [1].

Recently, it has been found that Nd-Fe-(Al,Si) ternary amorphous alloys are formed in a wide range of compositions by melt spinning and mould casting technique and exhibit large coercive fields at room temperature [2,3]. Their magnetic behavior indicates that they are structurally glasses but magnetically granular with coercive fields as high as 8.4 T at low temperatures in an applied field of 30 T [4]. These results are in contradiction to those found in conventional $Nd_2Fe_{14}B$ ternary amorphous alloys, in which the amorphous microstructure gives rise to soft magnetic characteristics with negligible coercivities, but they are in agreement with the high coercivities obtained in the past for Nd-Fe binary amorphous alloys.

We performed investigations on the glass formability, thermal stability and magnetic properties of $Nd_{90-x}Fe_xAl_{10}$ melt-spun amorphous ribbons with thicknesses between 25 and 150 μm and cast amorphous rods up to 3 mm in diameter produced by mould casting and suction casting techniques, respectively, in order to clarify the relationship between microstructure and coercivity in these bulk amorphous alloys.

EXPERIMENTAL DETAILS

$Nd_{90-x}Fe_xAl_{10}$ master alloys with $x = 35; 40; 45; 50$ were prepared from Fe (99.99 %), Nd (99.9 %) and Al (99.99%) in an arc furnace under Ar atmosphere, and re-melted several times for homogenisation. Ribbons with thicknesses between 25 and 150 μm and widths of 3 to 5 mm were obtained by single roller melt-spinning method in vacuum or in Ar atmosphere, at surface velocities of the Cu wheel ranging from 30 to 2.5 m/s. Bulk amorphous alloys with diameters up to 3 mm were formed in a wide composition range of 35 to 50 at. % Fe by mould casting and suction casting techniques.

The structure of the samples was checked by X-ray diffraction (XRD) using Cu-Kα radiation. For the ribbons, the structure was checked on both sides as well as on powders obtained by milling the ribbons, while structural investigations on cast rods were performed using powders obtained after crushing the rod in small pieces and then milling.

Magnetisation measurements above room temperature, at applied magnetic fields limited to 1.6 T, were carried out using a Vibrating Sample Magnetometer (VSM). The magnetisation and coercive field below room temperature (5 – 300 K) were studied using a Superconducting Quantum Interference Device (SQUID) Magnetometer in external magnetic fields not exceeding 1 T. Each sample was thermally demagnetised prior to recording each measurement.

RESULTS AND DISCUSSION

The largest diameter obtained for an amorphous rod is 3 mm for nominal composition $Nd_{55}Fe_{35}Al_{10}$, and glass forming ability decreases by increasing the Fe content. XRD patterns indicate also fully amorphous structures for ribbons with thicknesses below 100 μm and for rods with diameters less than 1 mm, regardless of their Fe content. The increase of the Fe content over 45 at. % results in the on-set of crystallization in melt-spun ribbons thicker than 100 μm.

These alloys crystallize through a single exothermic reaction and exhibit very large values for the reduced crystallization temperature (T_x/T_m) of 0.87 to 0.92, as it can be seen in figure 1 $(T_x$ and T_m are the crystallization and eutectic melting temperatures, respectively). The amount of the crystallization energy (the area under the exothermic peak) is higher for melt-spun ribbons in comparison with the rods that contain a higher amount of Fe due to the more disordered amorphous structure developed in the first ones. It is worth to note that in contradiction with the results obtained for other amorphous alloys, neither endothermic peak nor glass transition temperatures are evidenced for Nd-Fe-based amorphous alloys. The crystallization energy doesn't change significantly as a function of the Fe content for $Nd_{90-x}Fe_xAl_{10}$ thin ribbons 30 μm thickness, whereas for cast rods it strongly decreases with the increase of the Fe content as a consequence of the decrease of the glass-forming ability. This behavior is explained by the insufficient cooling rates assured by the casting techniques for the alloys with larger contents of Fe and indicates a strong correlation between the composition, the cooling rate and the glass-forming ability for Nd-Fe-based ternary amorphous alloys.
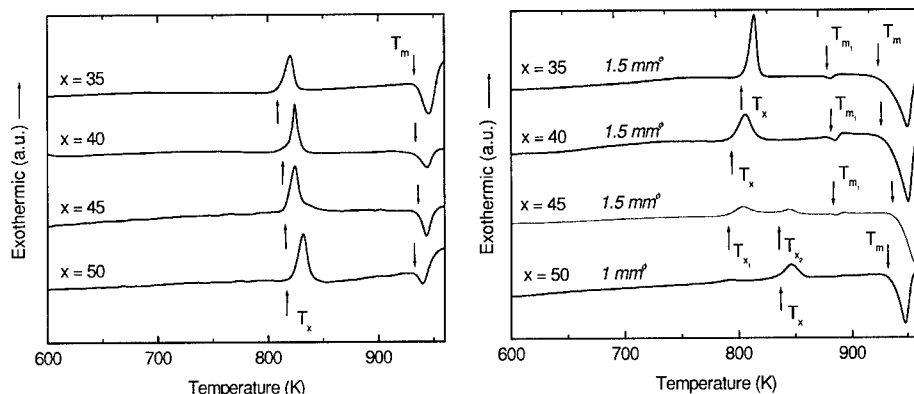
Figure 1. DSC curves plotted for $Nd_{90-x}Fe_xAl_{10}$ melt-spun ribbons and cast rods as a function of Fe content

$Nd_{90-x}Fe_xAl_{10}$ (x = 35 – 50) amorphous alloys exhibit large coercive fields at room temperature, even for low applied fields, regardless of their thickness and preparation techniques. In figure 2 are presented comparatively the hysteresis loops as a function of the Fe content for 3 different kinds of $Nd_{90-x}Fe_xAl_{10}$ samples: fully amorphous thin ribbons 25 μm in thickness (a), fully amorphous (x = 35; 40) and for comparison, partially vitrified (x = 50) thick ribbons with a thickness of about 120 μm (b) and fully amorphous cast rods 1 mm in diameter (c). The magnetization increases about 2 times by increasing the Fe content from 35 to 50 at. %, regardless of the amorphous samples shape, the same behavior being observed for high fields (up to 10 T). The coercive field presents a strong dependence on the composition. One observes that the on-set of crystallization in the $Nd_{40}Fe_{50}Al_{10}$ thick ribbon results in the decrease of the magnetization, while the coercive field has almost the same value as those obtained for fully amorphous thick ribbons with a less content of Fe because of the existence of the amorphous residual phase. Thus, the large coercive fields of Nd-Fe-based ternary bulk amorphous alloys are related to the existence of the amorphous phase, its disappearance leading to the drastically decrease of the coercive field and moreover, to the disappearance of the ferromagnetic properties [5]. The decrease of the Fe content results in the decrease of the coercive field of about 2 times for thin amorphous ribbons and in its increase of about 2 times for amorphous cast rods. For thick amorphous ribbons the coercive field is almost the same, regardless of the Fe content. For higher external fields (larger than 3 T) the coercive field doesn't change significantly with the Fe content for each different type of ribbon or for cast rods.

The large values of the coercive field can be explained by assuming the existence of very small Fe-Nd magnetic clusters dispersed in the amorphous matrix, whose size approaches a single magnetic domain, in agreement with the previous results obtained for melt spun Nd-Fe amorphous alloys [6]. The high values obtained for coercive fields of the thick amorphous ribbons comparatively with thin ones are related to the more relaxed microstructure developed in the first ones. The microstructure is more homogenous in amorphous rods due to their dimensions and lower cooling rates and consequently the values obtained for coercive field are smaller than for the thick ribbons. The difference in the absolute value of the coercive field as a

function of the amorphous samples' thickness results from the volume rate between Fe-Nd magnetic clusters and the homogenous Nd-rich matrix through the cooling rate.
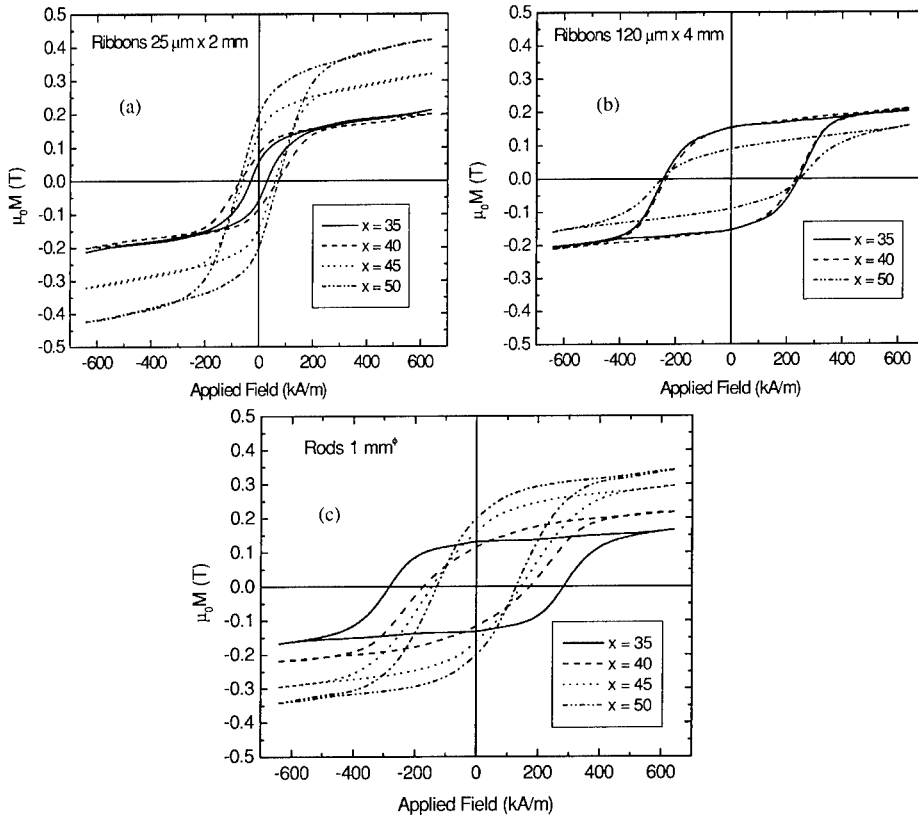
Figure 2. M-H hysteresis loops of $Nd_{90-x}Fe_xAl_{10}$ melt-spun ribbons 25 and respectively 120 μm in thickness and cast rods 1 mm in diameter, at room temperature

In order to obtain more information on the magnetic coupling in short range ordered magnetic structures existent in $Nd_{90-x}Fe_xAl_{10}$, the type of interactions as well as their influence on the coercive fields, the dependence of the magnetisation and coercive field was carried out at low temperatures (between 5 and 300 K). Figure 3 presents the dependence on temperature of the magnetization and coercive field for $Nd_{90-x}Fe_xAl_{10}$ thin amorphous ribbons, thick amorphous or partially vitrified ribbons, and amorphous cast rods. The humps appearing in the coercive field over a narrow range (150-220 K) for amorphous ribbons containing a large amount of Nd (over 50 at. %) and for cast rods in the entire range of compositions suggest the existence of one pronounced anisotropy of the magnetic clusters. The decrease of the coercive field with the temperature is similar to that obtained for similar crystalline compounds and is believed due to a

change of the size of the magnetic clusters domains, which probably approach to the superparamagnetic regime.
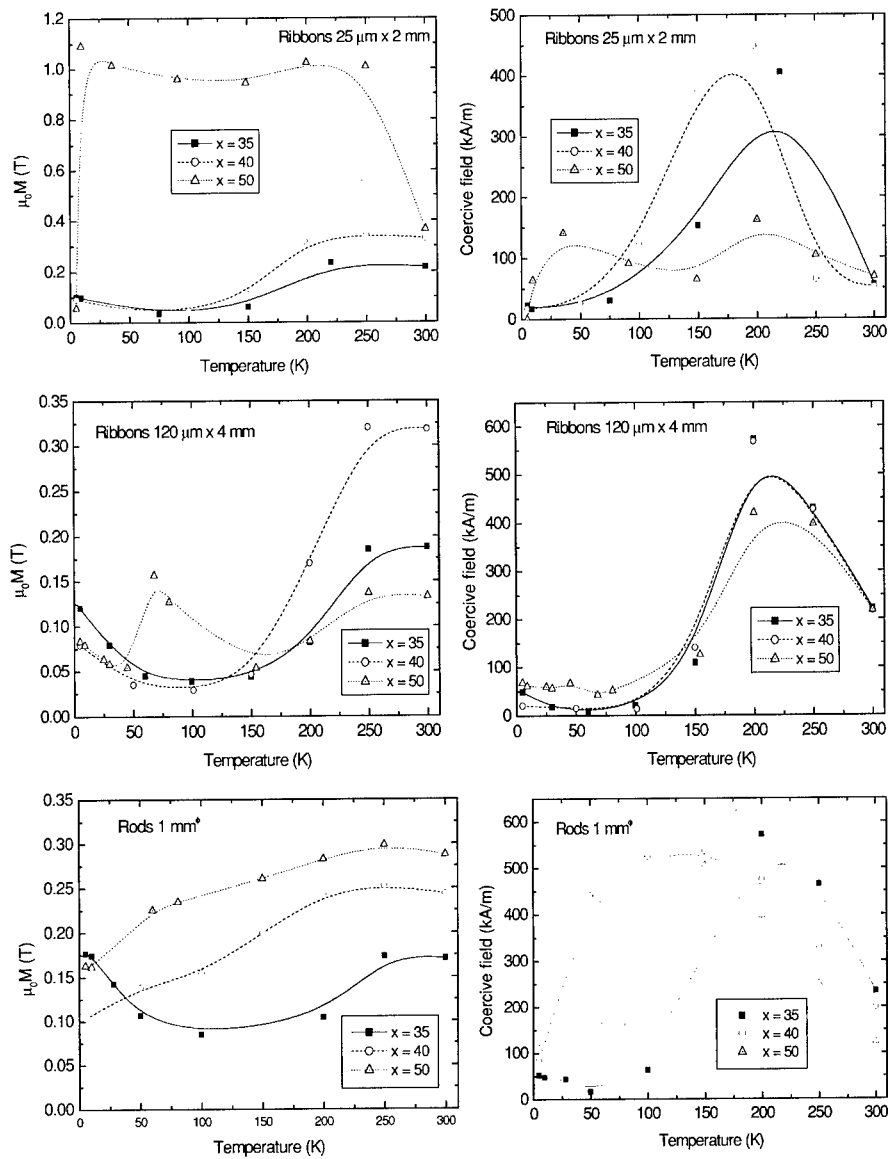
Figure 3. Temperature dependence of the magnetization at 1 T and coercive field for $Nd_{90-x}Fe_xAl_{10}$ amorphous ribbons and cast rods as a function of the Fe content

Due to the more homogenous structure existent in the thin ribbons the clusters size is smaller and consequently the interactions between them are not so stronger. The behaviour is typical for a spin-glass system with random configuration of the magnetic spins, in which thermal activation energy is enough to destroy the magnetic order. The coexistence of two types of magnetic order: long-range ferromagnetic order which gives the macroscopic behaviour, and short range ordered structures which determines the large values of the coercive fields in Nd-Fe-based bulk amorphous alloys is proved by the differences between zero-field-cooled and field-cooled magnetization curves and was reported elsewhere [7]. From the temperature dependence of the coercive field for $Nd_{40}Fe_{50}Al_{10}$ thin amorphous ribbon 25 μm in thickness one observes the existence of two maximum for the coercive field: one around 200 K which is similar to that obtained for the other bulk amorphous samples and the new one around 25 K, whose origin is unknown, but probably is caused by the larger amount of Fe which determines a more homogenous topological and magnetic structure. It is worth to note that the coercive field for this ribbons in the as cast state is the smallest one measured for $Nd_{90-x}Fe_xAl_{10}$ amorphous alloys with x=35~50. The magnetization increases with the temperature increase, this increase being more pronounced for thin ribbons 25 μm in thickness containing the largest amount of Fe in composition.

From the data presented here, it can be seen that the high coercivities obtained for $Nd_{90-x}Fe_xAl_{10}$ amorphous alloys at room temperature and their dependence on cooling rate and the preparation technique result from the formation of very small metastable or nonequilibrium magnetic clusters. The magnetic response of the Nd-rich matrix and Fe-Nd clusters phase are very different and very sensitive to any change in temperature and external field. Although these materials are currently below those considered necessary for economic viability, the mechanism that governs their unusual magnetic properties may be very interesting for basic research and consequently for finding new magnetic materials with granular structures for applications.

ACKNOWLEDGMENTS

REFERENCES

1. A. Inoue and J.S. Gook, Mater. Trans., JIM **36**, 1282 (1995); **36**, 1427 (1995).
2. A. Inoue, T. Zhang, and A. Takeuchi, IEEE Trans. Magn. **33**, 3814 (1997).
3. H. Chiriac, N. Lupu, F. Vinai, E. Ferrara, A. Stantero, J. Magn. Magn. Mater. **226-230**, 1379 (2001).
4. K.V. Rao, R. Ortega, J. Nogues, J. S. Munoz, A. Inoue, presented at 1999 MRS Spring Meeting, San Francisco, CA, 1999 (unpublished).
5. H. Chiriac, N. Lupu, J. Non-Crystalline Solids **287**, 135 (2001).
6. J.J. Croat, IEEE Trans. Magn. **MAG-18**, 1442 (1982).
7. H. Chiriac, N. Lupu, Physica B: Physics of Condensed Matter **299**, 293 (2001).

Hard Ferrites/Colossal Magneto-Resistance Materials

Direct and Real-Time Observation of Sub-Micron Domain Dynamics in Magnetically Biased Strontium Ferrite Permanent Magnets by Room Temperature Scanning Micro-Hall Probe Microscopy

Adarsh Sandhu, Naoji Iida, Hiroshi Masuda[1], Ahmet Oral[2], and Simon J. Bending[3]

Department of Electrical and Electronic Engineering, Tokai University,
1117 Kitakaname, Hiratsuka-shi, Kanagawa 239-1292, Japan.
[1]Toei Kogyo Ltd, 8-13-1, Tadao, Machida, Tokyo, 194-0035, Japan.
[2] Department of Physics, Bilkent University, 06533 Ankara, Turkey.
[3] Department of Physics, University of Bath, Claverton Down, UK.

ABSTRACT

A room temperature scanning micro-Hall probe microscope (RT-SHPM) was used for imaging stray magnetic field fluctuations at the surfaces of strontium ferrite permanent magnets (SFM) in the presence of external bias fields. The RT-SHPM enables the extremely fast, non-invasive, and quantitative measurement of localized surface magnetic fields on the sub-micron-scale. A 0.8 x 0.8 μm^2 GaAs/AlGaAs micro-Hall probe (300K Hall coefficient =0.3Ω/G; field sensitivity=0.04 G/$\sqrt{Hz}$) with an integrated STM tip for precise vertical positioning was used as a magnetic field sensor. External bias fields (H_{ex}) of up to 2700 Oe were applied parallel to the easy and hard axes of thermally demagnetized SFMs. Sample areas of up to 50x50 μm were imaged at a height of 0.3 μm above the SFM surface for each H_{ex}, with scan speeds of approximately one frame/second (128x128 pixels) enabling quasi-real time imaging in synchronization with bias field changes. RT-SHPM images of surfaces normal to the easy axis of demagnetized samples at H_{ex}=0, clearly showed the presence of 8-15 μm sized domains and stray magnetic field fluctuations of ±200G; images of surfaces normal to the hard axis showed 20 μm sized domains with magnetic field fluctuations of ±100G. Pronounced domain movement and rotation was observed for surfaces normal to the easy axis at bias fields above 700 Oe applied along the easy axis. A good correlation was found between domain movement and vibrating sample magnetometer hysteresis measurements. The RT-SHPM system was demonstrated to be a valuable tool for the direct and non-invasive study of micro-magnetic phenomena in ferromagnetic materials.

INTRODUCTION

The development of ferromagnetic materials for high performance permanent magnets requires a fundamental understanding of the behavior magnetic domains in external bias fields.

To-date, magnetic force microscopy (MFM) has been extensively used for imaging magnetic domains of a wide range of materials [1]. However, it has been found that the interpretation of MFM images can be complicated due to artifacts arising from the MFM tip field [2]. The situation is even more complex when the MFM imaging is carried out in the presence of external bias fields [3].

In this paper we describe the unique features of a new versatile room temperature scanning Hall probe microscope (RT-SHPM) system used for the direct, non-invasive, and quantitative imaging of domains at the surface of strontium ferrite permanent magnets in the presence of large external magnetic fields.

EXPERIMENTAL

Figure 1 is a schematic diagram of the RT-SHPM system used in this study [4]. It consists of a GaAs/AlGaAs micro-Hall probe (HP) mounted onto a piezoelectric scanning tube (PZT) at a tilt angle of 1.5° with respect to the sample surface. A scanning tunnelling microscope (STM) tip is integrated adjacent to the HP for precise vertical positioning. The coil is used for calibrating the
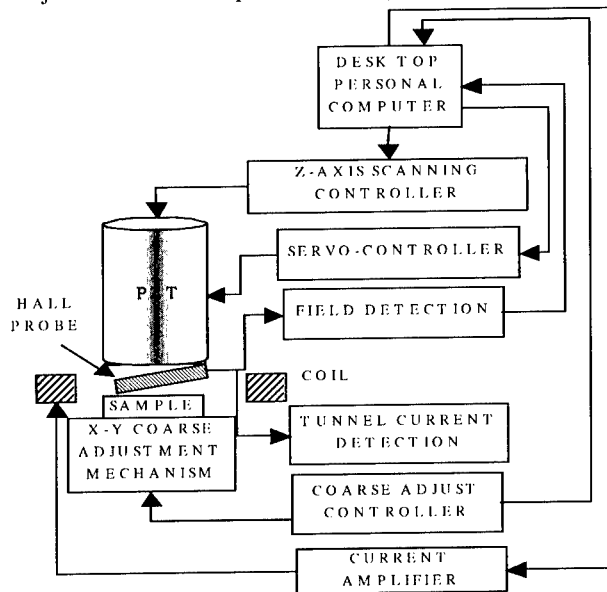
Figure 1. Schematic of the main components of the Room Temperature Scanning Hall Probe System

Hall probe. Magnetic imaging was carried out by scanning the HP over the surface of the sample while simultaneously measuring changes in Hall voltage that are proportional to fluctuations of the perpendicular component of the stray magnetic field emanating from the surface. All measurements were made at a height of 0.3μm above the sample surface.

The unique features of the RT-SHPM include: (i) the tilt angle between the HP and sample surface is precisely adjusted using an electronic angle sensor coupled to the PC control software; (ii) coarse sample approach is achieved by a high resolution motorized z-stage with a 25 mm range; (iii) scan range up to 50x50 μm^2; (iv) the use of electrodes on the reverse-side of the Hall probe chip carrier for electrical connection of the Hall bar and STM tip to the control and biasing electronics; (v) data acquisition with a choice of 3 modes including the *STM/SHPM mode* where scanning is carried out while simultaneously monitoring STM tip tunnel current thus enabling topographic imaging and the *real time mode*, where a 128 x 128 pixel scan is possible in about 1 second. The HP was fabricated by photolithography using a GaAs/AlGaAs heterostructure grown by MBE with a two dimensional electron gas density of 2 x 10^{11} cm^{-2} and mobility of 400,000 cm^2/Vs, at 4.2K. The Hall probe was located 13 micrometers away from the chip corner that was coated with a thin gold layer to act as the STM tip. The Hall probe had an active area of ~ 0.8 x 0.8 μm^2, a room temperature Hall coefficient of the HP was 0.3Ω/G and a field sensitivity of 0.04 G/√Hz. The STM tip was not coupled to the Hall bar thus reducing noise during measurement. A Hall drive current of 3 μA was used for all the measurements. A unique set of program routines were developed for the static and animated 3D visualization of SHPM data using Interactive Data Language [5].

The samples studied were cut from a strontium ferrite permanent magnet (SFM) and surfaces normal to the easy and hard axes polished until the undulations were less than 0.2 μm as measured by the STM tip integrated with the HP. Typical dimensions of the resulting samples were 5x5mm with a thickness of 400 μm. The external stepped bias fields (H_{ex}) were applied using a neodymium iron boride permanent magnet incorporated into the RT-SHPM system enabling bias fields of up to 2700 Oe to be applied perpendicular to the polished surfaces. The use of a permanent magnet for applying external bias fields eliminates sample heating problems associated with electromagnets. The external fields were applied in regular steps and the RT-SHPM scan carried out in synchronization at one frame/second (128x128 pixels). The SF samples were also characterized using a vibrating sample magnetometer (VSM) to compare the RT-SHPM results with conventional macroscopic measurements methods.

RESULTS AND DISCUSSION

There was no observable correlation between the STM topography and magnetic images for any of the samples studied. Figure 2 shows representative 50x 50 μm scans (surface normal to the easy axis) of the variation of surface magnetic field fluctuations with increasing H_{ex} along the

| 300 | 850 | 1250 | 1850 | 2250 | 2700 |
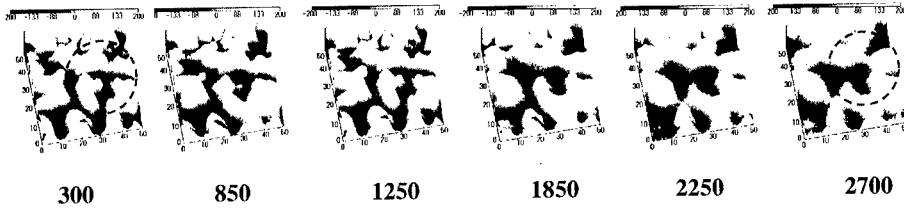
Figure 2. External bias field (Oe) dependence of RT-SHPM images (50x50μm) for SFM initially in the demagnetized state.   Image surface is normal to the easy axis

| -300 | -850 | -1250 | -1850 | | -2250 |
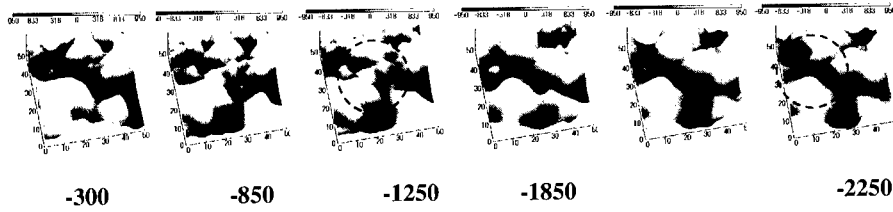
Figure 3. External bias field (Oe) dependence of RT-SHPM images (50x50μm) for SFM initially in the remanent state. Image surface is normal to the easy axis.
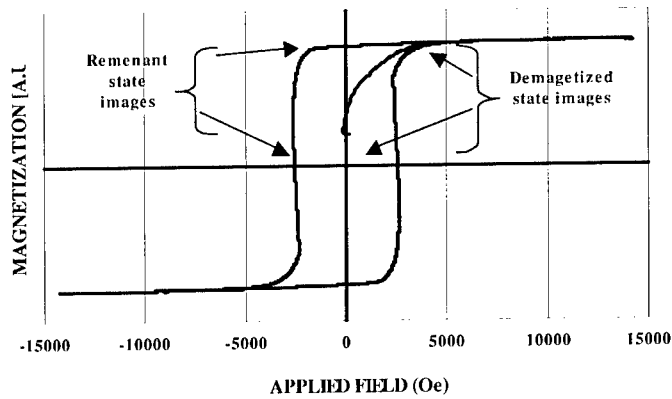
Figure 4. VSM magnetization curve along the easy axis of the SFM

easy axis of a SFM initially in a demagnetized state. Figure 3 shows the images for a sample initially at the remanent state as H_{ex} was increased to –2700 Oe along the easy axis. The black and white regions in the RT-SHPM images represent domains with magnetizations into and out

| 300 | 850 | 1250 | 1850 | 2250 | 2700 |
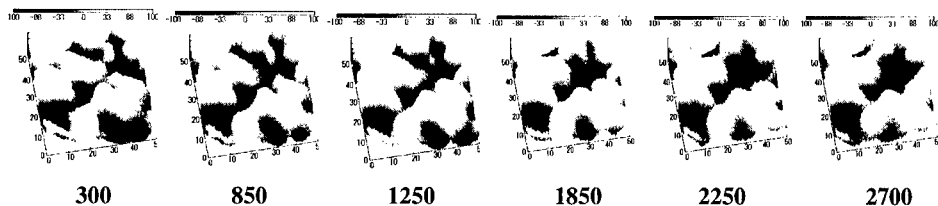
Figure 5. External bias field (Oe) dependence of RT-SHPM images (50x50μm) for SFM initially in the demagnetized state. . Image surface is normal to the hard axis.

| -300 | -850 | -1250 | -1850 | -2250 | -2700 |
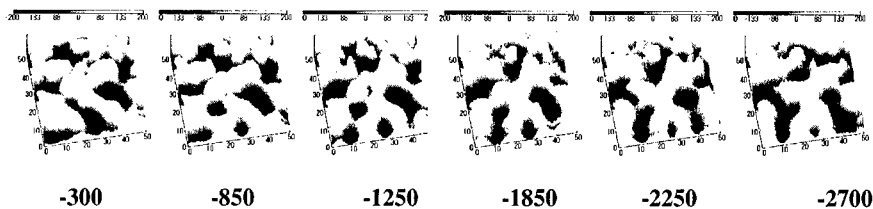
Figure 6. External bias field (Oe) dependence of RT-SHPM images (50x50μm) for SFM initially in the remanent state. Image surface is normal to the hard axis.
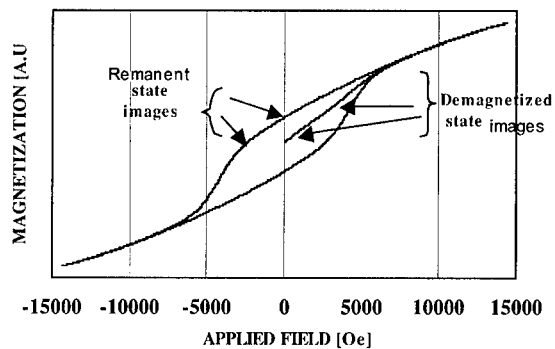
Figure 7.   VSM magnetization curve along the hard axis of the SFM

of the plane of the paper. The corresponding VSM hysteresis loop is shown in figure 4. Figures 5 and 6 show the H_{ex} dependence of RT-SHPM images of surfaces normal to the hard axis starting at the demagnetized and remanent states, respectively. Figure 7 is the VSM loop along the hard axis.

The RT-SHPM images show magnetic regions on the sample with magnetization perpendicular to its surface due to the existence of clusters of multi-domain grains. The SFM samples used in this study were produced by a process involving sintering and had grain sizes ranging between 2-10 micrometers [6,7]. A comparison of the RT-SHPM images in figures 2 and 5 at H_{ex} = 300 Oe shows the domains of samples along the easy axis to be smaller (5~10 μm) than those along the hard axis (~20 μm). These differences can be attributed to differences in the size of grains along these two orthogonal directions as has also been observed in other materials used for fabricating permanent magnets [8]. The RT-SHPM images also reveal the size of domains to vary with H_{ex}. An example of domain movement followed by rotation can be seen in the regions marked by broken circles in figures 2 and 3. The changes in the gray scale contrast indicate changes in direction of the magnetization of the domains due to the external bias. The movement and rotation of the domains was particularly pronounced in the case of SFM surfaces normal to the easy axis. These microscopic observations correlate with VSM measurements, where a rapid change in magnetization is observed along the easy direction (figure 4) but the contrary when H_{ex} was applied along the hard axis (figure 7). The surface stray magnetic fields measured by the RT-SHPM (shown by the gray scale above the images) were greater along the easy axis than the hard axis in both the demagnetized and remanent states. A detailed micro-magnetic evaluation of these results is in progress and the results will be reported elsewhere.

CONCLUSION

The RT-SHPM system was demonstrated to be a valuable tool for the direct, quantitative and non-invasive observation of localized stray magnetic field fluctuations at the surface of ferromagnetic materials in the presence large external bias fields. In order to further improve the range of applications and performance of the RT-SHPM, we are currently working on the fabrication of Hall probes with a higher spatial resolution and the incorporation of magnets for applying external fields greater than one Tesla.

REFERENCES
[1] A. Hubert, and R. Schafer, *Magnet Domains*, (Springer , 1998), pp.78-86.
[2] H.Mamin, D. Rugar, J.E. Stern, R Fontana, and K. Kasiraj, *Appl. Phys. Lett.* **55**, 318, (1989)
[3] R. Proksch, E. Runge, P.K. Hansma, S. Foss, and B. Walsh, *J. Appl. Phys.* **78**, 3303, (1995).
[4] A. Sandhu, H. Masuda, A. Oral, S.J. Bending, *ICF-8*, Kyoto, Sept., 17-21, (2000).
[5] Research Systems Inc., 4990 Pearl East Circle, Boulder, USA.
[6] H. Taguchi, F. Hirata, T. Takeishi and T. Mori, Proceeding of *ICF-6*, 1118, (1996).
[7] D. Livingston, *J. Appl. Phys.* **57**, 4137, (1985).
[8] L. Folks, R. Street and R.C. Woodward, *Appl. Phys. Lett.* **65**, 910, (1994).

Advances in the Low Temperature Preparation and Structural Characterization of Lanthanum Strontium Manganite Powder

Sophie Guillemet-Fritsch, Hervé Coradin, Antoine Barnabé, Christophe Calmet, Philippe Tailhades and Abel Rousset

Centre Inter-universitaire de Recherche et d'Ingénierie des Matériaux (CIRIMAT)/ UMR CNRS 5085, LCMIE,

Université Paul Sabatier, Bât. 2R1-118, Route de Narbonne 31062, Toulouse Cedex, France

ABSTRACT

Perovskite oxides of formula $La_{1-x}Sr_xMnO_3$ have been obtained by the thermal decomposition of precursor powders. Two different kinds of precursors, carbonates and citrates have been prepared by low temperature, i.e., "chimie douce" technique. The careful control of the chemical and the hydrodynamic parameters during the synthesis process allows obtaining nice homogeneous and small size particles (80 nm for the ex-carbonates and 30 nm for ex-citrates). Pure perovskite phase is observed after a low temperature thermal treatment, from 550 °C. The structure of these oxides is either rhombohedral or cubic and depends on the strontium content, the temperature and the partial pressure of oxygen during the thermal treatment. The Mn-O distances and the Mn-O-Mn angles are directly related to the amount of Mn^{4+} content.

INTRODUCTION

In recent years, the doped perovskite manganites such as $La_{1-x}Sr_xMnO_3$ have attracted growing attention due to the colossal magnetoresistance (CMR) properties. Several studies have shown that the microstructure, such as grain size, plays a very significant role in the intrinsic properties [1,2]. The synthesis methods are very important to obtain polycrystalline materials with specific microstructure.

Traditional way of processing is usually the mixing of oxides, hydroxides or carbonates, followed by high temperature (T > 1000 °C) processing. Consequently, the materials obtained with these methods are constituted of large particles with low surface area. "Soft chemistry" techniques have been developed in order to obtain - at lower temperature - the same materials as the one observed at high temperature with the ability to control the particle size, the surface area and the stoichiometry of the powders [3]. The advantages of using powders of reduced grain size to prepare ceramics or thick films is the increase of the reactivity and the possibility of lowering the sintering temperature. The homogeneity is a very important parameter for having reproducible properties. Our previous studies performed on spinel manganites have evidenced the influence of the powder quality on the final material properties [4, 5].

The electronic properties are related to the mixed valence state Mn^{3+}/Mn^{4+} that leads to mobile charge carriers. Low temperature synthesis allows moreover a larger oxidation state [6]. It was also observed that high oxygen ionic conductivity correlates with a cubic or an orthorhombic structure [7,8]. The coefficient of non stoichiometry δ depends on the temperature of thermal treatment and on the oxygen partial pressure [9]. The highest values of δ have been obtained for low temperature synthesis technique [10]. Many recent studies indicate that the $LaMnO_{3+\delta}$ compounds exhibit different structural types as orthorhombic $Pnma$, rhombohedral $R\bar{3}c$, monoclinic $P\frac{2_1}{c}$ or cubic $Pm\bar{3}m$ phases [10-15]. These phase transitions continue to exist when the pure $LaMnO_{3+\delta}$ is doped with divalent Sr^{2+} cations [16,17].

The aim of this work is to synthesize, by "chimie douce" technique, lanthanum strontium manganite powders of controlled characteristics (size, composition, homogeneity, surface area). These oxides are obtained from thermal decomposition of precursors (carbonates and citrates) powders. The structural evolution of $La_{1-x}Sr_xMnO_{3+\delta}$ is studied for various compositions (x = 0.10, 0.30 and 0.50), temperature and atmosphere of the thermal treatment of decomposition (T = 600, 900 and 1250°C under air or O_2 flow).

EXPERIMENT

The powder morphology was observed with a JEOL 2010 transmission electron microscope. The thermal decomposition of the precursors was examined by thermogravimetric analyses (TGA) (SETARAM TAG 24 apparatus, accuracy < 10^{-6} g). The structure was determined by X-ray diffraction analysis : the powder X-ray diffraction (PXRD) data was collected with a SEIFERT XRD-3003-TT diffractometer using Cu-Kα radiation (in the range $10° \leq 2\theta \leq 140°$ in increments of 0.02°). The Rietveld method implemented in the program FULLPROF [18] has been used for nuclear structure refinement. Plasma emission spectrometry was used to determine the chemical composition of the oxides. The specific surface area was determined using a Micrometrics Accusorb 2100^E, defined by the Brunauer, Emmet and Teller (BET) method.

Temperature programmed desorption analyses (TPD) were studied by thermogravimetry, gas chromatography and mass spectroscopy. The sample was first degassed (1 Pa) at room temperature for 1 h, and then the system was filled with Ar. A flow of 15 cm^3min^{-1} was allowed to pass through the reactor. During the experiment, the temperature was linearly increased (with a heating rate of 5°Cmin^{-1}). Every 120 s, the gas flowing out of the reactor was sampled and analyzed by gas chromatography (SHIMADZU GC-8A chromatograph fitted with a molecular sieve 13X column and a thermal conductivity detector). These analyses provided the oxygen concentration in the flowing gas, and the integration of these data over time gave the total amount of oxygen released during the experiment.

RESULTS

Carbonate route

Carbonates are obtained by the co-precipitation of an aqueous solution of the metallic salts (lanthanum nitrate $La(NO_3)_2$, $6H_2O$, strontium nitrate $Sr(NO_3)_2$ and manganese nitrate $Mn(NO_3)_2$, $6H_2O$) with ammonium carbonate. The concentrations of the salts and of the precipitating agent are respectively 3 mol.l^{-1} and 0.4 mole.l^{-1}. The salts and the ammonium carbonate are dissolved in distilled water. The solution containing the ammonium carbonate is poured in the solution containing the metallic salts. The aging time is 30 minutes. The so obtained particles are carefully washed and dried. The thermal decomposition was then followed by TGA (**Figure 1**) and by mass spectrometry. Four phenomena can be observed. The first reaction (I) is an endothermic one and corresponds to the departure of water molecules. The next 3 steps respectively noticed at 420 °C, 720 °C and 880 °C are exothermic and were identified as the decomposition (departure of CO_2 and CO) of the simple carbonates (La and Mn). The initial powder is probably constituted of an intimate mixture of lanthanum carbonate and manganese carbonate. The strontium is substituted either in one or the other carbonate. TGA analyses show that the single phase oxide should be obtained from 880 °C.
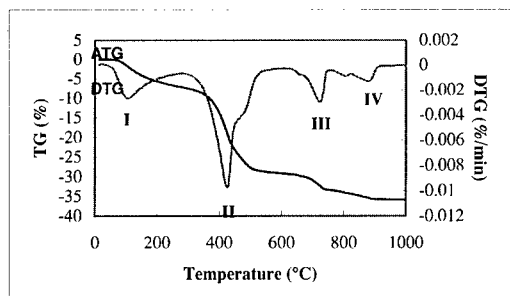
Figure 1. TGA and DTA curves of La-Sr-Mn carbonate decomposition
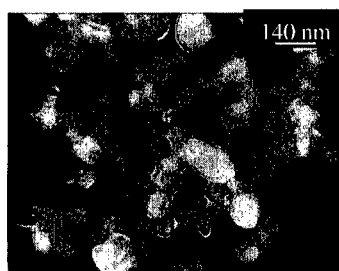
Figure 2. TEM micrograph of ex-carbonate $La_{1-x}Sr_xMnO_3$ obtained at 1000 °C.

TEM observations (**Figure 2**) of an oxide of composition $La_{0.68}Sr_{0.28}Mn_{1.04}O_4$ prepared at 1000 °C show that the oxide particles have a nice regular shape. The crystallite size determined from the broadening of the X-Ray diffraction patterns is approximately 80 nm. It does not vary as a function of the strontium content.

Citrate route

This method of synthesis has been developed by Szabo [19]. It allows obtaining oxides with the perovskite structure at moderate temperature. The synthesis of the mixed citrate needs first to synthesis the simple citrates, La citrate, Sr citrate and Mn citrate. Lanthanum and strontium citrates are prepared by the following procedure. 0.2 moles of lanthanum (strontium) nitrate are dissolved in 600 ml of water. The solution is poured in a solution of dihydrogeno-citrate dissolved in water. The solution is mixed during 1 hour and then passed through a centrifuge for 10 minutes. Thermogravimetric analyses show that the 2 citrates have the respective formula : $La(C_6H_5O_7)$, $3.5 H_2O$ and $Sr_3(C_6H_5O_7)_2$, $3.5 H_2O$. A different procedure is used for the synthesis of manganese citrate. 0.5 moles of MnO_2 are poured in an aqueous solution containing an excess of 0.5 moles of citric acid $C_6H_8O_7$, $6 H_2O$. According to Szabo [19], there is a formation of intermediate Mn^{4+} able to oxidize citric acid into acetone. The manganese ion resulting from this reaction reacts with the excess of citric acid to form the insoluble $Mn(C_6H_5O_7)$, H_2O citrate. Then, the mixed La-Sr-Mn citrate is obtained after the dissolution of the simple citrates in hot ammoniacal solution. The solution is then evaporated and grounded. TGA and TPR analyses show that the heating of citrates leads to dehydration (noted I and II) and to a release of CO and CO_2 (III) (**Figure 3**). The decomposition is over at 530 °C. The oxide powder is constituted of particles of approximately 30 nm (**Figure 4**).

The specific surface area was determined as a function of the thermal treatment temperature. This method of synthesis allows obtaining a specific surface area varying from 30 to 2 m^2/g as the temperature increases from 550 °C to 1000 °C. The values obtained in this work are 50 % higher than the one reported after firing precursors prepared using the Pechini process [20].
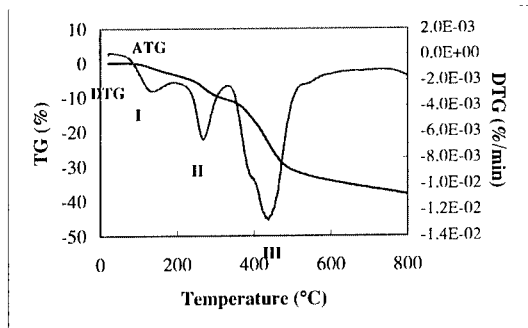
Figure 3. TGA and DTA curves of La-Sr-Mn citrate decomposition
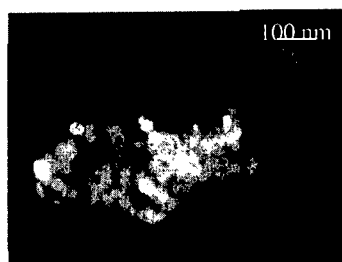
Figure 4. TEM micrograph of an ex-citrate $La_{1-x}Sr_xMnO_3$ oxide obtained at 800 °C

The structural evolution of the ex-citrates $La_{1-x}Sr_xMnO_{3+\delta}$ oxides with x = 0.10, 0.30 and 0.50 has been studied for various temperature and atmospheres (T = 600, 900 and 1250°C under air or O_2 flow). θ-2θ PXRD diffractograms are registered for all the samples. The results of the structural refinements are systematically connected to the Mn^{4+} content in the samples. Additional samples of different composition and prepared at various temperature and atmosphere need to be done to complete this study and correspond to the on going research work.

For these compounds, all the structures exhibit rhombohedral or cubic symmetries with the $R\bar{3}c$ and $Pm\bar{3}m$ space groups respectively : no distorted perovskite phase due to a Jahn-Teller effect is observed. Lattice parameters, Mn-O distances and Mn-O-Mn angles are resumed in **Table I**. In these symmetries, MnO_6 octahedra are always regular with 6 equal Mn-O distances. Therefore, Mn-O distances are an appropriate parameter to characterize the structural evolution of this series as shown in the **Figure 5** where the Mn-O distances obtained by PXRD structural refinements are plotted versus the Mn^{4+} content determined by TPD. The Mn-O-Mn angles are also presented in order to confirm the decrease of the distortion from a rhombohedral $(a^-a^-a^-)$ tilted structure with Mn-O-Mn < 165° to a cubic $(a^0a^0a^0)$ one where Mn-O-Mn = 180°, according to the Glazer tilt system notation [21]. This results confirm that the lattice parameters are very sensitive to changes in the oxygen content in these pseudo-cubic perovskite compounds : for the same Sr doping ratio $La_{0.90}Sr_{0.10}MnO_{3+\delta}$, we can stabilize with the 1250°C/air decomposition conditions a really highly tilted structure with Mn-0-Mn equal to 163° and a nearly cubic cell with the 700°C/O_2 conditions.

• The 1250°C/air compound corresponds to the limit of the tilt angle of the rhombohedral phase : no oxide presenting a rhombohedral symmetry with a more tilted Mn-O-Mn angle has been reported in the literature. Systematically, for more tilted Mn-O-Mn angle, a distortion, due to Jahn-Teller effect, appears and generates a structural transition to orthorhombic symmetry. The lattice parameter of the 1250°C/air compound reduced to the primary a_P cubic perovskite is very close to the x = 0.10 single crystal synthesized at 1200°C by A. Urushibara et al. [22] which is orthorhombic. A less oxidizing atmosphere during the precursors decomposition (i.e. a lower Mn^{4+} content in the sample) can also tend to the orthorhombic phase. This rhombohedral to orthorhombic transition has been reached for an oxide obtained at 700°C in N_2 atmosphere.

Synthesis conditions	Chemical Composition	Oxygen Content $3+\delta$	% Mn^{4+}	Space Group	Lattice Parameters (Å)	Mn-O distance (Å)	Mn-O-Mn angle (°)
1250°C/air	$La_{0.86}Sr_{0.09}Mn_{1.05}$	3.04	16	$R\bar{3}c$	a = 5.529(1) c = 13.352(1)	1.966(3)	163(1)
900°C/air	$La_{0.86}Sr_{0.09}Mn_{1.05}$	3.07	22	$R\bar{3}c$	a = 5.5171(2) c = 13.3598(6)	1.960(3)	165(1)
600°C/air	$La_{0.86}Sr_{0.09}Mn_{1.05}$	3.10	28	$R\bar{3}c$	a = 5.4993(4) c = 13.3552(6)	1.952(2)	167(1)
900°C/air	$La_{0.69}Sr_{0.28}Mn_{1.03}$	3.02	31	$R\bar{3}c$	a = 5.4967(6) c = 13.3602(9)	1.947(2)	169(1)
600°C/air	$La_{0.69}Sr_{0.28}Mn_{1.03}$	3.03	33	$R\bar{3}c$	a = 5.4932(6) c = 13.351(1)	1.946(3)	169(1)
600°C/O₂	$La_{0.86}Sr_{0.09}Mn_{1.05}$	3.14	35	$R\bar{3}c$	a = 5.487(1) c = 13.323(3)	1.940(3)	171(1)
900°C/air	$La_{0.49}Sr_{0.41}Mn_{1.09}$	3.01	42	$Pm\bar{3}m$	a = 3.8643(2)	1.932(1)	180
600°C/air	$La_{0.49}Sr_{0.41}Mn_{1.09}$	3.03	46	$Pm\bar{3}m$	a = 3.8641(3)	1.932(1)	180

Table I. Lattice parameters for the ex-citrates $La_{1-x}Sr_xMnO_{3+\delta}$ oxides. The rhombohedral parameters are indicated with hexagonal axes. Estimated standard deviations are in parentheses.
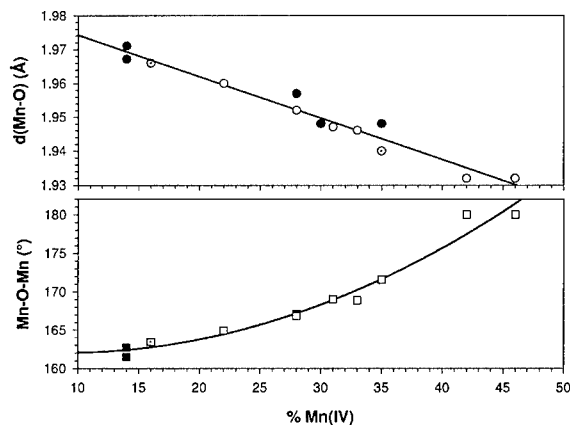
Figure 5. Mn-O distances and Mn-O-Mn angles as a function of Mn^{4+} content for ex-citrates $La_{1-x}Sr_xMnO_{3+\delta}$ (with x ≈ 0.10, 0.30 and 0.50) and for T = {1250°C/air, 900°C/air, 600°C/air and 600°C/O₂}. The white points correspond to this work and the black points correspond to the references [10,15,20].

- For the 900°C/air, 600°C/air, 600°C/O₂ compounds, we can observe a decrease of the Mn-O distances coupled with an increase of the Mn-O-Mn angle leading to a less tilted phase as the Mn^{4+} increases. The symmetry is always rhombohedral even in the 600°C/O₂ compound. The constant decrease of the distortion is strongly correlated to the Mn^{4+} content : for the same Sr doping ratio, the Mn^{4+} content can be simply reduced to the oxygen non-stoichiometry δ in $La_{0.90}Sr_{0.10}MnO_{3+\delta}$ formula : the MnO_6 tilt system tends to decrease with the increase of Mn^{4+} and

finally attempts the perfect cubic cell for $Mn^{4+} \geq 45\%$. The Mn-O distances also decrease and tend to 1.93Å. This value corresponds to the ideal cubic perovskite cell ($a_P \approx 3.86$Å) and also to the sum of the ionic radii of Mn^{4+} (rMn^{4+}_{VI}=0.53Å) and O(-II) (rO^{2-}_{VI}=1.40Å) [23].

- The two others oxides (x = 0.30 and x = 0.50) confirm this Mn^{4+} dependence. In these cases, the total Mn^{4+} content is mostly due to the initial Sr doping ratio rather than the non-stoichiometry in oxygen : δ value decreases and tends to 0 when x increases. The two compounds $La_{0.49}Sr_{0.41}Mn_{1.09}O_{3+\delta}$ are cubic.

CONCLUSION

Lanthanum strontium manganite powders have been prepared by a "Chimie douce" process. Homogeneous particles of controlled size, size distribution and morphology have been obtained. Both the surface area and the oxygen content can be adjusted. The structure (symmetry, Mn-O distances, Mn-O-Mn angles) strongly depends on the Mn^{4+} content in the sample.

REFERENCES

1. L.E. Huesco, F. Rivadulla, R.D. Sanchez, D. Caeiro, C. Jardon, C. Vazquez-Vazquez, J. Rivas, M.A. Lopez-Quintela, *J. Magn. Magn. Mater.* 189, 321 (1998).
2. N. Zhang, W.P. Ding, W. Zhong, D.Y. Du, *Phys. Rev. B* 56, 8138 (1997).
3. J. Twu, P.K. Gallagher « *Properties and applications of perovskite-type oxides* » ed. by L.G.Tejuca, J.L.G. Fierro, (1993).
4. S. Fritsch, J. Sarrias, M. Brieu, J.J. Couderc, J.L. Baudour, E. Snoeck and A. Rousset, *Solid State Ionics* 109, 229 (1998).
5. C. Chanel, S. Guillemet-Fritsch, J. Sarrias and A. Rousset, *Int. J. Inorg. Mat.* 2, 24 (2000).
6. I. Maurin, P. Barboux, Y. Lassailly, J.P. Boilot, *Key Engineering Materials* 132-136, 1357 (1997).
7. Butler V., Catlow C.R., Fender B.E.F., Harding J.H., *Solid State Ionics* 8, 109 (1982).
8. Cook R.L., Sammells A.F., *Solid State Ionics* 45, 311 (1991).
9. J.A.M. Van Roosmalen, E.H.P. Cordfunke and R. B. Helmholdt, *J. Solid State Chem.* 110, 100 (1994).
10. M. Verelst, N. Rangavittal, C.N.R Rao, and A. Rousset, *J. Solid State Chem.* 104, 74 (1993).
11. Q. Huang; A. Santoro; J.W. Lynn; R.W.Erwin; J.A. Borchers; J.L. Peng; R.L. Greene, *Phys. Rev. B* 55, 14987 (1997).
12. J.AM. Van Roosmalen; P.Van Vlaanderen; E.H.P. Cordfunke; W.L. IJdo, D.J.W. IJdo, *Solid State Chem.* 114, 516 (1995).
13. J. Rodríguez-Carvajal, M. Hennion; M. Moussa; A.H. Moudden; L. Pinsard; A. Revcolevschi, *Phys. Rev. B* 57, R3189 (1998).
14. J. Töpfer, J.B. Goodenough, *J. Solid State Chem.* 134, 117 (1997).
15. C. Ritter, M.R. Ibarra; J.M. De Teresa; P.A. Algarabel; C. Marquina, J. Blasco, J. García; S. Oseroff, S.W. Cheong *Phys. Rev. B* 56, 8902 (1997).
16. J.F. Mitchell, D.N. Argyriou, C.D. Potter; D.G. Hinks, J.D. Jorgensen, S.D. Bader, *Phys. Rev. B* 54, 6172 (1996).
17. L. Pinsard, A. Revcolevschi; J. Rodríguez-Carvajal, *J. Alloy Compd* 262-263, 152 (1997).
18. J. Rodriguez-Carvajal, *Abstracts of the Satellite Meeting on Powder Diffraction of the XV Congress of the IUCr, Toulouse, France*, 127 (1990).
19. G. Szabo, *Thesis*, Lyon (1969).
20. Y-H. Huang, Z-G. Xu, C-H. Yan, Z-M. Wang, T. Zhu, C-S. Liao, S. Gao, G-X. Xu, *Solid State Comm.* 114, 43 (2000).
21. A.M. Glazer, *Acta Cryst. B* 28, 3384 (1972), *Acta Cryst. A* 31, 756 (1975).
22. A. Urushibara, Y. Moritomo, T. Arima, A. Asamitsu, G. Kido, Y.Tokura, *Phys. Rev. B* 51, 14103 (1995).
23. R.D. Shannon, *Acta Cryst. A* 32, 751 (1976).

Studies on Crystal Structure and Magnetic Scaling Behavior of Perovskite-Like (La₁₋ₓPbₓ)MnO₃ System with $x = 0 - 0.5$

Ting-Sheng Huang, Chiung-Hsiung Chen and Ming-Fong Tai
Department of Physics, Chung Cheng University,
160 San-Hsing, Ming-Hsiung, Chia-Yi 621, Taiwan, R. O. C.

ABSTRACT

The magnetic critical behaviors in the perovskite-like (La₁₋ₓPbₓ)MnO₃ series with $x = 0.0 \sim 0.5$ are studied by means of dc magnetic measurements. All the samples crystallize in the rhombohedral unit cell with a $R\,\overline{3}C$ space group ($a \sim 0.54$ nm and $c \sim 1.33$ nm). The detailed crystallographic parameters of all the samples are obtained by the refinements of the powder x-ray diffraction data using the Rietveld method. The substitution effect of Pb^{2+} ions on La^{3+} sites induces a mixed-valence state of Mn^{3+}/Mn^{4+} and enhances magnetic transition temperature in the (La₁₋ₓPbₓ)MnO₃ system. The transition temperature T_C increases with the Pb content from 225 K as $x = 0$ to 355 K as $x = 0.5$. The canonical spin-glass behaviors in low fields and the scaling behaviors of magnetic physical quantities are clearly observed in all our samples. The values of the related critical exponents and the scaling functions of magnetic data are close to those of the conventional spin glass systems.

INTRODUCTION

The rich physical properties in the perovskite-like (Ln₁₋ₓAₓ)MnO₃ series (Ln = trivalent rare earths, A = divalent alkali metals, $e.g.$ Ca, Sr, Ba, and Pb) have attracted many interests since the discoveries of the colossal magnetoresistance (CMR) effect [1,2]. Many anomalous phenomena, including high negative magnetoresistance ratio, metal-insulator transitions and anomalous lattice expansions $etc.$, are found in the vicinity of the critical point. Despite much efforts made, the nature of this magnetic critical behavior is still not clear. An extensive study of flux-growth single crystals of (La₁₋ₓPbₓ)MnO₃ series with $0.2 \leq x \leq 0.4$ has been carried out by some groups [1,3-5]. The metallic conductivity was observed below the Curie transition point T_C and a negative magnetoresistance effect of ~ 20 % at $H = 1$ T was found in the vicinity of T_C. C. W. Serale $et\ al.$ [3-5] suggested that a fully spin-polarized d band is involved in the ferromagnetic ordering process of the Pb-doping manganese. Very few researches have been working out on this system since 1970. In this paper we report the detailed studies of the crystal structure, magnetic properties and scaling behaviors of the perovskite-like (La₁₋ₓPbₓ)MnO₃ manganese.

EXPERIMENTAL DETAILS

Samples (La₁₋ₓPbₓ)MnO₃ with $x = 0 - 0.5$ were prepared using a conventional powder solid-state reaction method. Stoichoimetric amounts of high-purity La_2O_3, Pb_3O_4, and MnO_2 raw powders were homogenously mixed and completely ground, thus the mixed samples were fired to 1000 - 1300°C and hold at the same temperature for 12 hours. The heated samples were cooled to low temperature and removed, reground, and reheated at the same temperature for an addition 24 h. The processes were repeated at least three times until the samples are of a single

Table I. Selected crystallographic and magnetic parameters of $(La_{1-x}Pb_x)MnO_3$ samples with x = 0 – 0.5. Numbers in the parenthesis are errors of the least significant digit.

Pb content x	Crystal System: Trigonal, a hexagonal axes Space group: $R\bar{3}c$, $\alpha = \beta = 90°$, $\gamma = 120°$				Volume of unit cell	Magnetic transition point		Effective moment (μ_B)	
	a (Å)	c (Å)	d_x (g/cm^3)	R_{wp} (%)	V_{cell} (Å^3)	T_c (K)	θ_p (K)	μ_{FM}	μ_{PM}
0.0	5.5008(5)	13.276(6)	5.35	10.47	347.90(8)	225	240	3.35	4.59
0.1	5.5033(3)	13.293(4)	5.54	12.47	348.66(2)	271	293	3.48	5.65
0.2	5.5019(9)	13.293(3)	5.74	13.10	348.49(0)	275	270	3.44	4.78
0.3	5.5037(1)	13.334(6)	5.91	12.02	349.79(1)	350	341	3.19	5.17
0.4	5.5217(3)	13.404(3)	6.03	12.27	353.92(6)	358	347	3.20	5.43
0.5	5.4842(2)	13.383(0)	6.32	13.14	348.57(9)	355	353	3.15	5.41

phase. The thoroughly reacted powders were pressed into pellets during the last sintered process. All heated processes were progressed at ambient atmosphere and used warm-up and cooling rates of 300°C/h.

X-ray powder diffraction (XRD) data were collected with a Rigaku Rotaflex RTP500RC powder X-ray diffractometer using Cu $K\alpha$ radiation and a secondary graphite monochromator from 20° to 100° with a step size of 0.02° in $2\theta/\theta$ scanning mode and a counting rate of 5 sec/step. The XRD patterns were refined by a Riqas program based on the Rietveld analysis technique. Magnetic measurements were performed on using an Oxford MagLab magnetometer and a Bruck Vibrating Sample magnetometer (VSM) systems for $T < 300$ K and $T > 300$ K, respectively. The zero-field cooling (ZFC) and field cooling (FC) magnetization curves were carried out under various dc external fields H from 0 – 5 T. Isothermal magnetic hysteresis loops at various temperatures were also obtained in applied fields up to 5 T.

RESULTS AND DISCUSSION

XRD data of all the samples showed single-phase patterns, which are described well by an rhombohedral (trigonal) unit cell with space group $R\bar{3}c$ rather than an orthorhombic unit cell with space group $Pbnm$. Detailed crystallographic data extracted from the refinement results of XRD data were listed in tables I - III. The results show that there was almost no Pb lossing during the sample preparation procedures and the compositions of all atoms were consistent with the original stoichoimetries. Lattice parameters, Mn-O bond length and Mn-O-Mn bond angle as a function of the Pb content are drawn in figure 1. Lattice parameters a and c slightly vary as $x \le$ 0.3, then suddenly increas at $x \sim 0.4$, but slightly decrease again as $x = 0.5$, as shown in Figure 1(a). The bond length between Mn and O ions is found a small oscillating variation as $x < 0.4$, then abruptly becomes short as $x = 0.5$. The dependence of the bond angle of Mn-O-Mn on x is found an inverse variation. The change of the La/Pb ratio is not only to change the average ion radius $<r_A>$ in the La/Pb sites, but also to affect the average radius of the transition metal ions $<r_{Mn}>$ in the Mn^{3+}/Mn^{4+} site. In perovskite-structure oxides, the ionic radius of Pb^{2+} (1.49 Å) is larger smaller than that of La^{3+} (1.36Å), but the ionic radius of Mn^{4+} is 0.53 Å is smaller than that

of Mn^{3+} (0.645 Å). So it is possible that both the $<r_A>$ and the ratio of Mn^{4+}/Mn^{3+} increases with increasing x, however, $<r_{Mn}>$ decreases. As a result that the variation of the lattice constants a and c with the Pb content does not obey a simple linear relation of the Vegard's law. In addition, the chemical order or charge order may occur for certain special compositions such that allow to have very complex relations between the crystallographic parameters and the Pb content.

Table II. Summary of the room-temperature XRD refinements of $(La_{1-x}Pb_x)MnO_3$ samples with x = 0-0.5 using a Riqas program based on the Rietveld analysis technique. Numbers in the parenthesis are errors of the least significant digit.

Crystal System: Trigonal, hexagonal axes					
Space group $R\bar{3}c$ (NO.167), $\alpha = \beta = 90°$, $\gamma = 120°$, Z = 6					
Atomic positions: La/Pb (6a), Mn^{3+}/Mn^{4+} (6b), O (18e)					
La/Pb (0.00, 0.00, 0.75), Mn^{3+}/Mn^{4+} (0, 0, 0), O (x, 0.00, 0.25)					
Pb content	Ion	X	Y	Z	B	N
---	---	---	---	---	---	---
x = 0.0	La^{3+}	0	0	0.75	1.14	1.00
	Mn^{3+}	0	0	0	0.20	1.00
	O^{2-}	0.5567(1)	0	0.25	2.93	1.10
x = 0.1	La^{3+}	0	0	0.75	0.08	0.88
	Pb^{2+}	0	0	0.75	0.10	0.10
	Mn^{3+}	0	0	0	0.13	0.98
	Mn^{4+}	0	0	0	0.20	0.10
	O^{2-}	0.5512(4)	0	0.25	1.69	1.00
x = 0.2	La^{3+}	0	0	0.75	0.06	0.78
	Pb^{2+}	0	0	0.75	0.10	0.20
	Mn^{3+}	0	0	0	0.30	0.97
	Mn^{4+}	0	0	0	0.06	0.20
	O^{2-}	0.5540(5)	0	0.25	1.98	1.19
x = 0.3	La^{3+}	0	0	0.75	0.67	0.69
	Pb^{2+}	0	0	0.75	0.65	0.30
	Mn^{3+}	0	0	0	0.40	0.75
	Mn^{4+}	0	0	0	0.20	0.30
	O^{2-}	0.4552(4)	0	0.25	1.22	1.07
x = 0.4	La^{3+}	0	0	0.75	0.59	0.52
	Pb^{2+}	0	0	0.75	0.64	0.41
	Mn^{3+}	0	0	0	0.99	0.70
	Mn^{4+}	0	0	0	0.20	0.40
	O^{2-}	0.4618(7)	0	0.25	2.06	1.04
x = 0.5	La	0	0	0.75	0.26	0.49
	Pb	0	0	0.75	0.30	0.50
	Mn^{3+}	0	0	0	0.29	0.57
	Mn^{4+}	0	0	0	0.20	0.50
	O^{2-}	0.5355(4)	0	0.25	1.30	1.07

Table III. Bond angles of both Mn-O-Mn and O-Mn-O bonds and bond lengths of Mn-O bond of $(La_{1-x}Pb_x)MnO_3$ samples with $x = 0$ - 0.5.

Sample	Mn-O-Mn Bond Angle (degrees)	O-Mn-O Bond Angle (degrees)	Mn-O Bond Length (Å)
$LaMnO_3$	161.77°	180° (91.27°)	1.9601
$La_{0.9}Pb_{0.1}MnO_3$	163.43°	180° (91.11°)	1.9573
$La_{0.8}Pb_{0.2}MnO_3$	162.54°	180° (91.17°)	1.9591
$La_{0.7}Pb_{0.3}MnO_3$	167.65°	180° (90.86°)	1.9544
$La_{0.6}Pb_{0.4}MnO_3$	168.51°	180° (90.67°)	1.9578
$La_{0.5}Pb_{0.5}MnO_3$	168.47°	180° (90.43°)	1.9463
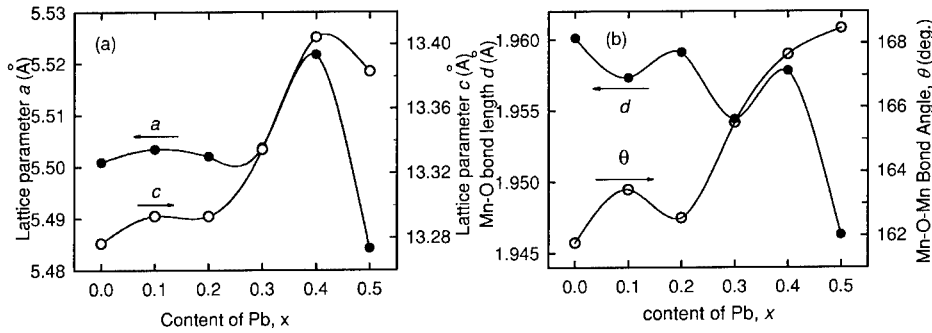
Figure 1. Lattice parameters a and c as a function of Pb contration x. (b) Dependence of Mn-O bond length and Mn-O-Mn Pb content. All lines are drawn to guide the eyes.

Some magnetic parameters of $(La_{1-x}Pb_x)MnO_3$ samples, including the ferromagnetic critical point T_C and Curie-Weiss transition temperature θ_p and effective magnetic moment per Mn site in FM and PM states, μ_{FM} and μ_{PM}, were determined from dc magnetization and inverse susceptibility versus temperature in an external field. These parameters are listed in table I. The substitution effect of Pb^{2+} ion on La^{3+} site in this system induces a mixed-valence state of Mn^{3+}/Mn^{4+} and enhances the ferromagnetic transition temperature. Although the dependence of transition temperature with x presents an oscillating variation, both T_C and θ_p trend to linearly increase with x, as shown in the inset plot of figure 2(a). The transition temperature T_C increases with the Pb content from 225 K as $x = 0$ to 355 K as $x = 0.5$, but an anomalous reduce at $x = 0.3$ Both curves are similar to the variation trend of Mn-O-Mn bond angle in figure 1(b). The effective magnetic moments per Mn site in both FM and PM states vary in the ranges of 3.3 ± 0.3 μ_B and 5.5 ± 0.5 μ_B, respectively. Based on the comparison between crystal parameters and magnetic parameters shown in figures 1 and 2, the variation trends of those magnetic quantities with the Pb doping apparently depends upon the results of the crystallographic variation.
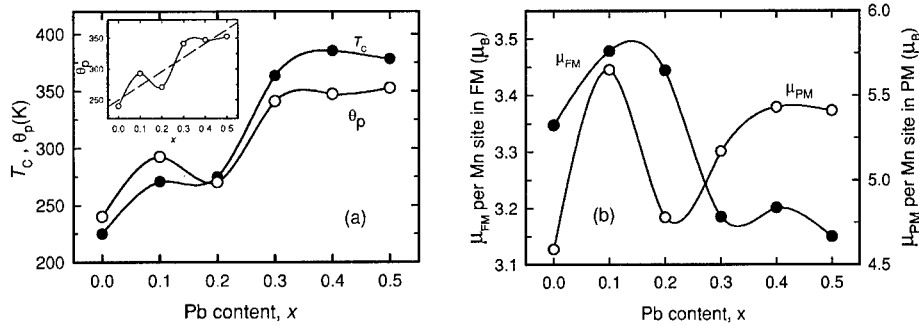
Figure 2. (a) Ferromagnetic and paramagnetic transition temperatures as a function of Pb content, $T_C(x)$ and $\theta_P(x)$. (b) Saturation and effective magnetic moments per Mn site vs Pb content. All curves serve as guide lines to the eyes.

For a well-defined magnetic phase transition the scaling theory [6-8] predicts that magnetic susceptibility χ, determined by the experimental $M(T)$ data in figure 3(a), exhibits a scaling relation as follows:

$$\chi - \chi_0 = \frac{C}{T - \theta_p}(1 - q) = \frac{C}{T}[1 - |t|^\beta f_\pm(H^2/|t|^{\beta+\gamma})], \tag{1}$$

$$q(t,H) = |t|^\beta f_\pm(H^2/|t|^{\beta+\gamma}), \tag{2}$$

$$q|t|^{-\beta} = f_\pm(H^2/|t|^{\beta+\gamma}), \tag{3}$$

where t is the reduced temperature $t = (T - T_0)/T_0$ with T_0 being certain transition temperature (T_C for a FM/PM transition or T_g for a SG transition). q is the order parameter as functions of T and H and the scaling functions f_+ and f_- apply for $t > 0$ (in PM phase) and $t < 0$ (in FM or SG phase),
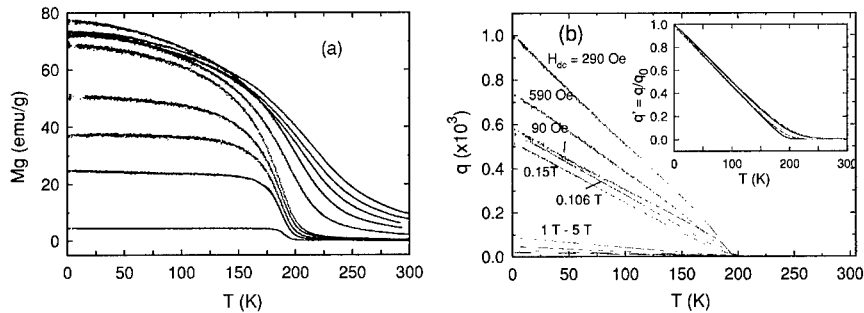
Figure 3. (a) Temperature dependence of FC magnetization, and (b) temperature dependence of order parameter of LaMnO₃ compound in 10 various applied fields: 0.009 - 5 T. The inset plot shows the normalized order parameter as a function of temperature.
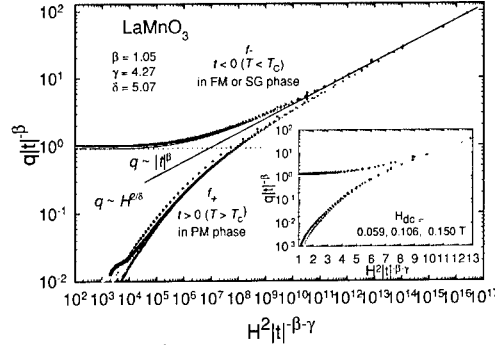
Figure 4. Log-log plot of $q|t|^\beta$ vs $H^2|t|^{-(\beta+\gamma)}$ of LaMnO$_3$ compound for data in $H = 1, 2, 3, 4$ and 5T. Inset plot shows the same plot for data in $H = 0.059, 0.105$ and 0.15 T. All data obtained in the ranges $2 \le T \le 305$ K collapse two scaling relation f_+ and f_- as Eq. (3).

respectively. For our LaMnO$_3$ sample, the values of the critical exponents $\beta = 1.05 \pm 0.1$, $\delta = 5.07 \pm 0.3$ and $\gamma = 4.3 \pm 0.5$ are derived by fitting $q(t) \sim q_0|t|^\beta$, $q(H) \sim q_0'H^{2/\delta}$ and $\delta = 1 + \gamma/\beta$. These exponents are similar to those found in conventional spin glasses. The β value is very close to the predicted value of the mean field theory, $\beta = 1$. Using these critical exponents, $C = 1.81 \times 10^{-2}$ cm^3/g·K, $\chi_0 = 0$ and $\theta_p = 213.3$ K all data of $M(T)$ in various fields give a plot of $q|t|^{-\beta}$ vs $H^2|t|^{-\beta-\gamma}$ shown in figure 3. All of the q data collapse onto two curves, that is, the scaling functions $f_+(x)$ for $t > 0$ ($T > T_0$, in the PM phase) and $f_-(x)$ for $t < 0$ ($T < T_0$, in the FM phase). For $t < 0$, $q|t|^{-\beta}$ approaches a constant (~ 1) for small $H^2|t|^{-\beta-\gamma}$ (the dashed line in figure 4). The solid line of $q \sim H^{2/\delta}$ with $\delta = 4.68$ in figure 4 demonstrates the asymptotic behavior for $T \to T_0$. The shapes of both the scaling functions are also quite similar to those observed in most conventional spin glasses.

ACKNOWLEDGMENTS

REFERENCES

1. J. M. D. Coey, M. Viret and S. von Molná, *Advances in Physics* **48**, 167 (1999).
2. C. Frontera, J. L. García-Muñoz, A. Llobet, M. Respaud, J. B. Broto, J. S. Lord and A. Planes, *Phys. Rev.* **B62**, 3381 (2000).
3. C. W. Searle and S. T. Wang, *Can. J. Phys.* **47**, 2703 (1969); **48**, 2023 (1970).
4. A. H. Morrish, B. J. Evans, J. A. Eaton and L. K. Leung, *Can. J. Phys.* **47**, 2691 (1969).
5. L. K. Leung, A. H. Morrish and C. W. Searle, *Can. J. Phys.* **47**, 2697 (1969).
6. F. C. Chou, N. R. Belk, M. A. Kastner, and R. J. Birgeneau and A. Aharony, *Phys. Rev. Lett.* **75**, 2204 (1995); B. Barbara, A. P. Malozemoff and Y. Imry, *Phy. Rev. Lett.* **47**, 1852 (1981).
7. A. P. Malozemoff, S. E. Barnes and B. Barbara, *Phy. Rev. Lett.* **51**, 1704 (1983).
8. N. Moutis, I. Panagiotopoulos, M. Pissas, and D. Niarchos, *Phys. Rev.* **B59**, 1129 (1999).

Influence of Domain Structure on Magnetoresistance in Perovskite Manganite Grain Boundary Junctions

Robert Gunnarsson[1], Anatoli Kadigrobov[1,2], Zdravko Ivanov[1]
[1]Department of Microelectronics and Nanoscience, Chalmers University of Technology and Göteborg University, SE-412 96 Göteborg, Sweden
[2]B. I. Verkin Institute for Low Temperature Physics & Engineering, Kharkov, Ukraine

ABSTRACT

We have been able to deduce a temperature dependence of the built-in potential in $La_{2/3}Sr_{1/3}MnO_3$ grain boundary junctions. This has been performed by trimming a single grain boundary down to $1\mu m$ width with a focused ion-beam. We can thereby see the impact of single domain walls on the magnetoresistance and the current-voltage characteristics. We have also demonstrated the effect of averaging as we increased the number of junctions.

INTRODUCTION

Since the discovery of colossal magnetoresistance (CMR) [1] in perovskite manganites these materials have attracted a lot of scientific attention. The interest is mainly due to their potential for technical applications, but also because of the many intriguing and complex properties. Grain boundaries (GBs) in manganites form magnetic junctions giving a tunnelling-like magnetoresistance response, both in granular films [2] and in bi-crystal films [3-7]. Bi-crystals have previously successfully been applied to study the colossal magnetoresistance of single manganite grain boundaries [3-7]. It has been shown that the Julliere model is not directly applicable to charge transport across manganite GBs [5,6] since the main origin of charge transport perpendicular to the grain boundary is not a direct tunnelling [4]. It has also been shown by magnetic force microscope that a grain boundary pins a magnetic domain wall [8].

The previous studies have focused on large-angle grain boundaries ($\geq 24°$), and the impact of single magnetic domains has previously not been thoroughly studied. Our previous study of noise in a multidomain structure [7] revealed an additional contribution originating from the GB region. Hence the motivation for our present work is to study the influence of junction width on its transport properties. This is achieved by decreasing the size of the grain boundary junctions (GBJs) in consecutive steps. Therefore we have studied the magnetoresistance (MR) and current-voltage (IV) dependence of a single low-angle GB as well as a GB array, and the dependences as function of width of the GBJ. This allows us to describe the magnetoresistance of single domain magnetic tunnel junctions.

EXPERIMENTAL DETAILS

On a $LaAlO_3$ bi-crystal substrate with symmetric misorientation angle of $8.8°$ a $La_{2/3}Sr_{1/3}MnO_3$ film was grown by pulsed laser deposition. In this process a stoichiometric target was ablated by an excimer laser (KrF, $\lambda=248nm$) with an energy density of $\sim 1.4J/cm^2$. During deposition the substrate was held at $740°C$ in an oxygen pressure of $0.4mbar$. A high degree of epitaxy of the 90nm-thick film was verified by x-ray θ-2θ and ϕ-scans in a Bragg-Brentano diffractometer. The film was then patterned with photolithography and Ar-ion milling into a meander with 101 GB crossings, each $6\mu m$-wide. Such a layout allows us to measure across one, two and three as well as one hundred GBJs. The MR properties were measured in a helium-cooled cryostat with a variable temperature insert and a

superconducting magnet. In all measurements the magnetic field was in the plane of the film and the MR was measured with a bias current of 10μA. The high-field MR has been deduced from the zero-field and field cooled resistance measurements, while the low-field MR was measured at specific temperatures.

To study the behaviour of junction width we have trimmed one of the junctions. The trimming was performed in a focused ion-beam (FIB) with Ga-ion source. The junction was trimmed in two steps, the first FIB-process left a grain boundary junction 2μm wide and 20 μm long, while in the second FIB-process the junction was trimmed down to 1μm width. The junction geometry is shown in figure 1.

RESULTS

We estimate the temperature of the paramagnetic-ferromagnetic transition, the T_C, to be around 360K for a single 6μm wide grain boundary junction (figure 2). After trimming the junction the high-field MR as well as the resistance curves are shifted down with about 50K, which indicates a T_C just above 300K. This can be related to a heating or Ga contamination during the FIB-process. From figure 2 it is also clear that the onset of the grain boundary MR decreases as the GBJ is narrowed. As the junction is trimmed from 6μm to 2μm the onset decreases from 300K to 250K. Further trimming to 1μm results in a slight further decrease of the onset temperature. The temperature dependence of the grain boundary MR seems to be similar regardless of the width of the junction.The MR curves become smoother, as shown in figure 3a, when the number of GBs is increasing. The MR for a single GB is step-like, involving a few (5 to 10) resistance levels. Even though the effect is weak with the field perpendicular to the GB the step-like behaviour is clearly seen as the field is applied parallel to the GB. The effect of averaging, i.e. smoothing the MR by measuring several GBs, is therefore also most clear with the magnetic field parallel to the grain boundary. We note that the field for the MR peak does not change as more GBJs are included. On the other hand the maximum grain boundary magnetoresistance (MR*) decreases when increasing the number of GB included in the measurements.Trimming a grain boundary junction resulted in a decrease in the number of resistance-steps as illustrated in figure 3b. Roughly the average number of steps decreased from about 7 for the 6μm wide junction to 2-3 steps for the 2μm and 1μm wide junctions. The experiments did not reveal any specific temperature dependence for the number of resistance-steps, it is basically constant in the entire temperature range.
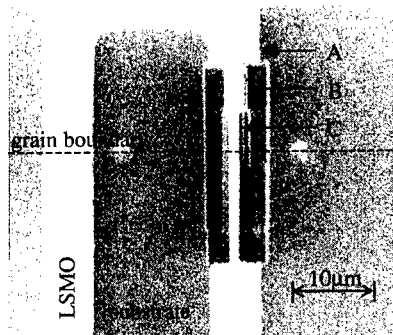
Figure 1. A secondary electron image of the trimmed junction after the second FIB-process. The grain boundary is indicated by the dashed line and the electrode is marked 'LSMO'. The width at 'A' is the original one-6μm, the width at 'B'-2μm and 'C' marks the trimmed '1μm' junction.
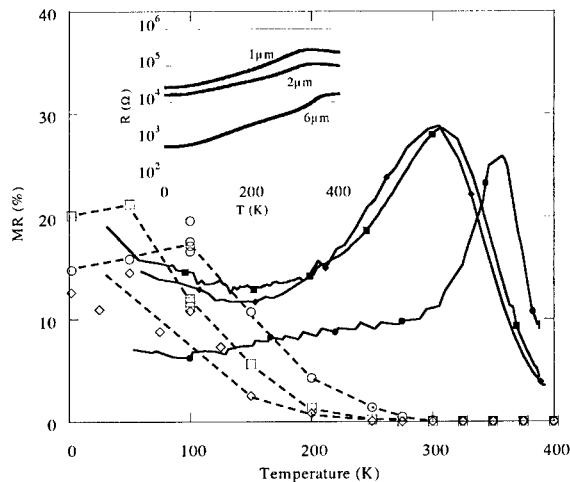
Figure 2. Temperature dependence of high-field (5T, solid lines) and low field (~Hc, open markers) magnetoresistance for a single GBJ with 6μm (circles), 2μm (boxes) and 1μm (diamonds) width. At 100K the magnetoresistance was measured several times, this is indicated by several open markers. The dashed lines are guides for the eye. The inset shows the temperature dependence of the resistance for the GBJs.

DISCUSSION

The grain boundary magnetoresistance effect in perovskite manganites is different from the colossal magnetoreistance observed in the same materials. In the kind of devices studied here both effects are present but have different temperature dependences. The grain boundary magnetoresistance has an onset at temperatures lower than the bulk Curie temperature and increases as the temperature falls. The IV-characteristics follows the same temperature dependence.

The resistance-area product of a manganite domain wall has previously been estimated to be about $10^{-13}\Omega m^2$ [9]. For the 1μm trimmed junction the cross section will be $\sim 10^{-13}m^2$, which results in a domain wall resistance of 1Ω. The latter is much smaller than the resistance measured in our experiments and hence the main voltage drop is due to dislocations or distortions at the GB. We believe, based on the results from the MR measurements (figure 3b), that we have been able to distinguish the influence of single domains on the MR and hence the impact of single domains on the IV characteristics of the junction.

In the IV-characteristics there seem to be two different regions. At low voltages the current goes as V^α where $\alpha=1$-2, which is consistent with suggested quantitative models [4,6] for the current transport across the GB region: Gross et al [6] suggested a Glazman-Matveev [10] based theory which includes tunnelling through the GB region via localised states resulting in a voltage dependence of $\alpha=1$ (plus extra terms of the order of $\alpha=7/3$). On the other hand Todd et al [5] suggested to employ the Simmons model [11] which results in $\alpha=1$ (plus extra terms of the order of $\alpha=3$). In this voltage range we have too few data points to distinguish between
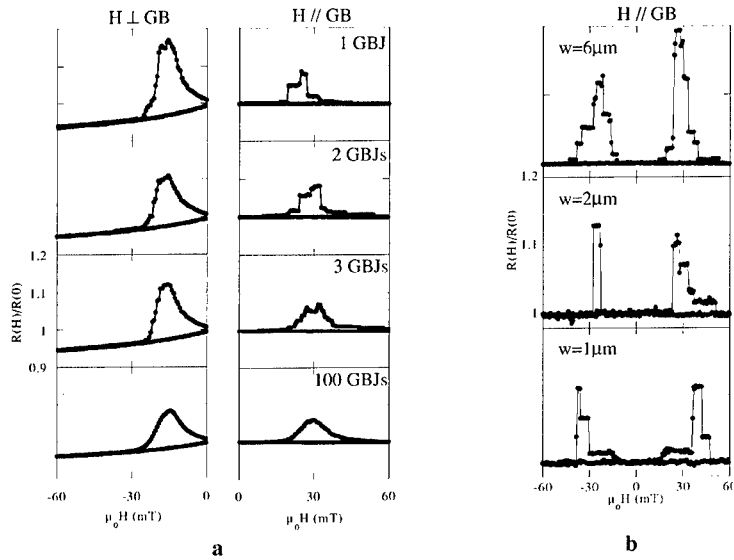
Figure 3. a) Magnetoresistance for 1, 2, 3 and 100 GBJ (6μm wide), the left column was measured with a magnetic field perpendicular to the grain boundary (H ⊥ GB) while the right column displays the MR with a field parallel to the grain boundary (H // GB). Since magnetoresistance is symmetric for positive and negative magnetic fields, only one part of the curve is displayed here. All plots are in the same scale.
b) Single grain boundary magnetoresistance for the trimmed junction with 6, 2 and 1μm width. Data for both subfigures are taken at 100K.

the suggested models. None of them is valid at high bias voltages where the voltage becomes comparable to the potential barrier.

For high voltages the IV-curve is linear up to 5V where the Joule heating effect starts to influence transport properties. This also suggests that the linear part can be extrapolated to zero bias-current that would give an estimate of the built-in potential, V_{bi}, discussed by Gross et al [6]. This assumption is valid at least within the error of a pre-factor. The measured potential and hence V_{bi} decreases down to zero at about the Curie temperature, see figure 4. This strengthens the argument that the non-linearity has a magnetic origin.

CONCLUSIONS

By employing several as well as single grain boundary junctions we have been able to demonstrate the effect of magnetoresistance averaging in a granular manganite film. Then by trimming a single grain boundary junction we have been able to deduce the temperature dependence of the magnetic potential barrier. The latter differs from the temperature dependence of the grain boundary MR observed in the same sample. Thus, despite the fact that they both have magnetic origin, the non-linearity of IV-curves for manganite GBJs and the grain boundary MR does not describe the same physical effect.
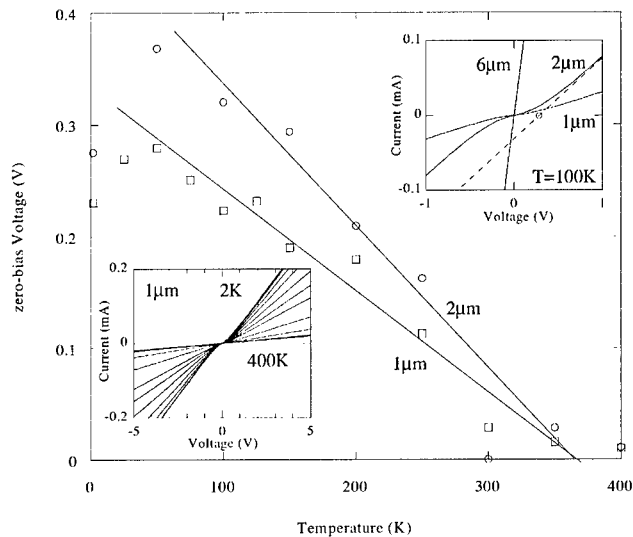
Figure 4. Zero-bias voltage drops linearly with temperature to become zero at roughly the Curie temperature. The 2μm and 1μm wide junctions are represented by open circles and open boxes respectively, the lines are guides for the eye. The upper inset show the IV-characteristics at 100K for the 6μm, 2μm and 1μm wide junctions. The zero-bias voltage is deduced from the linear part (indicated by a dashed line and a circle at zero current). The influence of temperature on the IV-characteristics is shown in the lower inset with IV-curves at 2K, 25K, 50K, 75K, 100K, 125K, 150K, 200K, 250K, 300K, 350K, 400K.

ACKNOWLEDGEMENTS

REFERENCES

1. R. von Helmolt, J. Wecker, B. Holzapfel, L. Schultz, and K. Samwer, *Phys. Rev. Lett.* **71**, 2331 (1993); S. Jin, T.H. Tiefel, M. McCormack, R.A. Fastnacht, R. Ramesh, and L.H. Chen, *Science* **264**, 413 (1994).
2. H.Y.Hwang, S.-W. Cheong, N.P. Ong and B. Batlogg, *Phys.Rev. Lett.* **77**, 2041 (1996); A. Gupta, G.Q. Gong, Gang Xiao, P.R. Duncombe, P. Lecoeur, P.Trouilloud, Y.Y. Wang, V.P. Dravid and J.Z. Sun, *Phys. Rev. B* **54**, R51629 (1996).
3. N.D. Mathur, G. Burnell, S.P. Isaac, T.J. Jackson, B.-S. Teo, J.L. MacManus-Driscoll, L.F. Cohen, J.E. Evetts and M.G. Blamire, *Nature* **387**, 266 (1997); K. Steenbeck, T. Eick, K. Kirsch, K. O'Donnell and E. Steinbeiβ, *Appl. Phys. Lett.* **71**, 968 (1997).
4. N.K. Todd, N.D. Mathur, S.P. Isaac, J.E. Evetts and M.G. Blamire, *J. Appl. Phys.* **85**, 7263 (1999).

5. W. Westerburg, F. Martin, S. Friedrich, M. Maier and G. Jakob, *J. Appl. Phys.* **86**, 2173 (1999).
6. R. Gross, L. Alff, B. Büchner, B.H. Freitag, C. Höfener, J. Klein, Yafeng Lu, W. Mader, J.B. Philipp, M.S.R. Rao, P. Reutler, S. Ritter, S. Thienhaus, S. Uhlenbruck and B. Wiedenhorst, *J. Magn. & Magn. Mater.* **211**, 150 (2000); C. Höfener, J.B. Philipp, J. Klein, L. Alff, A. Marx, B. Büchner and R. Gross, *Europhys. Lett.* **50**, 681 (2000).
7. R. Mathieu, P. Svedlindh, R. Gunnarsson and Z.G. Ivanov, *Phys. Rev. B* **63**, 132407 (2001).
8. Yeong-Ah Soh, G. Aeppli, N.D. Mathur and M.G. Blamire, *Phys. Rev. B* **63**, 020402(R).
9. N.D. Mathur, P.B. Littlewood, N.K. Todd, S.P. Isaac, B.-S. Teo, D.-J. Kang, E.J. Tarte, Z.H. Barber, J.E. Evetts and M.G. Blamire, *J. Appl. Phys.* **86**,6287 (1999).
10. L.I. Glazman and K.A. Matveev, *Sov. Phys. JETP* **67**, 1276 (1988).
11. J.G. Simmons, *J. Appl. Phys.* **34**, 1793 (1963); ibid, *J. Appl. Phys.* **34**, 2581 (1963).

Magnetic Properties and Scaling Behavior in Perovskite–like $La_{0.7}(Ba_{1-x}Pb_x)_{0.3}CoO_3$ System

Chiung-Hsiung Chen, Ting-Sheng Huang and Ming-Fong Tai
Department of Physics, Chung Cheng University,
160 San-Hsing, Ming-Hsiung, Chia-Yi 621, Taiwan.

ABSTRACT

In this study, we used x-ray diffraction patterns and dc magnetic measurements to investigate the crystallographic structure, magnetic properties and scaling behavior of the distorted perovskite $La_{0.7}(Ba_{1-x}Pb_x)_{0.3}CoO_3$ ($0 \leq x \leq 0.5$) system with a constant ratio of Co^{4+}/Co^{3+}. Samples with $x = 0.0$ and 0.1 were crystallized in the cubic structure with $a \sim 7.76$ Å whereas samples with $x \geq 0.2$ were crystallized in an orthorhombic $Pbnm$ space group with $a \sim b \sim 5.50$ Å and $c \sim 7.85$ Å. For all our samples the spin-glass-like behavior were observed in low temperature and low field ranges. The Pb^{2+} substitution on Ba^{2+} site does not significantly affect the ferromagnetic transition temperature T_C, but does introduce large variation in the magnetic strength. In both the ferromagnetic and paramagnetic states the minimum values of the average effective moments provided by every Co ion occur at $x = 0.3$. We also observed the scaling behaviors of magnetic data in all samples. The derived values of the critical exponents (β, γ, δ) were consistent with those predicted by mean field theory and a three-dimensional Heisenberg model.

INTRODUCTION

The discoveries of high-T_c superconductivity in cuprates and great magnetoresistance (MR) in manganates have initiated intensive investigations of the $(La_{1-x}A_x)TO_3$ compounds (A = Ca, Sr, Ba, Pb; T = $3d$ transition metal) [1-3]. In the Co-based perovskite-like oxides the competition between the crystal-field splitting and the intra-atomic Hund's coupling of Co ions lead to a variety of magnetic and electronic phase transitions among the high-, intermediate- and low-spin configurations of Co^{3+} and Co^{4+} ions. The $(La_{1-x}A_x)CoO_3$ system also displays many new and unusual behaviors open to study. Such as orbital and charge ordering phenomena as well as large changes in the electrical, magnetic, and structural properties, driven by small variations of composition, temperature, magnetic field, or pressure. However, many of these properties are still not understood completely.

In some transition-metal oxides, such as Tl- and Bi-based high-T_c superconducting cuprates, the addition of a small Pb amount can reduce the sintering temperatures and the process times as well as stabilize the required structures with special physical properties. In addition, because Pb ions does not contribute significant magnetic signal in solids and have very similar chemical properties to the divalent alkali earth ions, the substitution of Pb atom on the alkali earth atom can be used to study the disorder effects of chemical, orbital, charge, or magnetic moment. In this report, we investigated the substitution effect of Pb^{2+} ions for Ba^{2+} ions on the structural and magnetic properties in the distorted perovskite $La_{0.7}(Ba_{1-x}Pb_x)_{0.3}CoO_3$ ($x \leq 0.5$) system with a fixed ratio of Co^{4+}/Co^{3+}. The short-range ferromagnetic order and the scaling behavior have been studied in this series.

EXPERIMENTAL DETAILS

We prepared $La_{0.7}(Ba_{1-x}Pb_x)_{0.3}CoO_3$ samples with $x = 0 - 0.5$ using a standard powder solid-state reaction method. Stoichiometric amounts of high-purity La_2O_3, $BaCO_3$, Pb_3O_4, and Co_3O_4 raw powders were homogenously mixed and completely ground. After that, the samples were fired to 1150°C and hold at the same temperature for 12 hours. The heated samples were cooled to low temperature and removed, reground, and reheated at the same temperature for an addition 24 hours. The processes were repeated at least three times until the samples are of a single-phase. The thoroughly reacted powders were pressed into pellets during the last sintered process. All heated processes were progressed at ambient atmosphere and used warm-up and cooling-down rates of 300°C/h. We collected X-ray powder diffraction (XRD) data with a MAC MPX^3 powder X-ray diffractometer using Cu $K\alpha$ radiation and a secondary graphite monochromator. A step-scan mode with a step size of $\Delta 2\theta = 0.002°$ were selected in a $2\theta/\theta$ scanning from 20° to 100° using a counting rate of 5 sec/step. We further refined all XRD patterns by using a Riqas program based on an analysis technique of the Rietveld method. Dc magnetic measurements were performed with an Oxford MagLab magnetometer. The zero-field cooled (ZFC) and field cooled (FC) magnetization curves were carried out under various dc external fields H from $0 - 5$ T. Isothermal magnetic hysteresis loops at various temperatures were also obtained in applied fields of up to 5 T.

RESULTS AND DISCUSSION

We assessed the phases of all the samples by XRD patterns and all the samples were of single phase. The samples of $x = 0$ and 0.1 were crystallized in a cubic unit cell with $a \sim 7.76$ Å, whereas samples with $x \geq 0.2$ were crystallized in the orthorhombic $Pbnm$ space group with $a \sim 5.46$ Å, $b \sim 5.50$ Å, $c \sim 7.85$ Å. The refinement results appear that all Pb ions are divalent, not tetravalent and the ratios of Co^{4+}/Co^{3+} keep at a constant value in this series. When the Ba^{2+} ions are partially substituted by the Pb^{2+} ions, only slight differences in lattice parameters, distances, and angles among the atoms induce. The results may be contributed to a small difference in the ionic radii of Pb^{2+} and Ba^{2+} ions as well as very little changes in compositions. The crystallographic refinements of all the XRD data have been reported elsewhere in details [5,6].

Figure 1 shows that the temperature dependence of FC and ZFC magnetization in $H = 1$ kOe for all the samples. The ferromagnetic transition temperature T_C was determined from the inflection point of the $M(T)$ curve. The remarkable feature of magnetic properties of this series is the appearance of short-range ferromagnetic interactions. This is confirmed by observing a spin-glass-like behavior in low temperature and low field ranges. In the low applied fields both the ZFC and FC magnetization curves split at temperatures below a so-called irreversibility temperature, T_r ($\leq T_C$), comparing those curves in figures 1(a) and 1(b). The irreversibility temperature decreases with increasing external field and the difference between the ZFC and FC $M(T)$ curves in $T < T_r$ also decreases with increasing temperature and field. Both the ZFC and FC $M(T)$ resemble substantially in the range of $T \geq T_r$ and implying the reversibility of magnetization. In addition, the low-field ZFC $M(T)$ clearly shows a sharp cusp at a so-called spin freezing (or spin-glass transition) temperature, T_g, where it attains a maximum magnetization, as demonstrated in figure 1(b). As the strength of external magnetic field increases, T_g also shifts to a lower temperature and the cusp in the ZFC $M(T)$ is smeared out to broad maximum. These
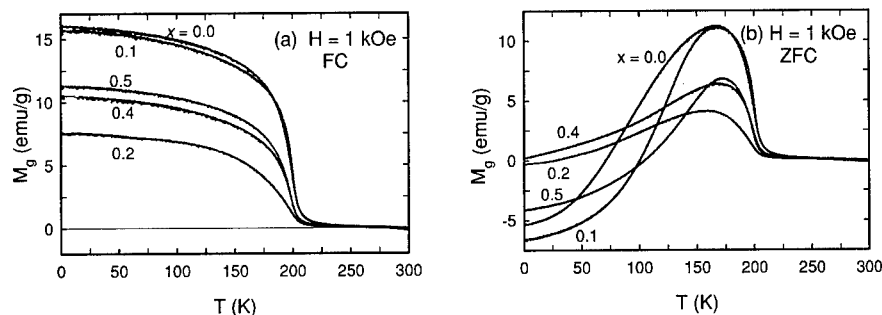
Figure 1. (a) Field-cooling and (b) zero-field-cooling magnetizations *vs* temperature in $H = 1$ kOe for $La_{0.7}(Ba_{1-x}Pb_x)_{0.3}CoO_3$ compounds with $x = 0 - 0.5$.

phenomena are identifying features of a spin glass or a glass-cluster state.

The variations of T_C, θ_p, T_g, and T_r in a fixed field with the Pb content x are displayed in figure 2. The limited changes in these characteristic temperatures were obtained as x varies from 0 to 0.5: $T_C = 206$ K $\pm$ 2 K, $\theta_p = 205$ K $\pm$ 10 K, $T_g(H = 1$ kOe) $= 166$ K $\pm$ 3 K and $T_r(H = 1$ kOe) $= 183$ K $\pm$ 5 K for $0 \le x \le 0.5$. Although a structural phase transition occurring in $0.1 < x < 0.2$, the Pb substitution on Ba does not strongly affect those magnetic related temperatures. Thus, we propose that the major factor affecting the ferromagnetic transition temperature in this series is the ratio of Co^{4+}/Co^{3+}, not by the ratio of Pb/Ba. The ratio of the mixed-valence Co ions, which is controlled by the ratio of $(Ba^{2+} + Pb^{2+})/La^{3+}$, determines the concentration of the hole-type carriers and further impinges on the electronic and magnetic properties in these cobaltates.

The magnetization at temperatures above T_C obeys well a Curie-Weiss relation of $\chi = \chi_0 + C/(T-\theta_p)$ in our measuring fields. Here, C is the Curie constant, θ_p the paramagnetic Curie-Weiss temperature, and χ_0 the temperature-independent term of susceptibility. In this series the major contribution to the magnetization arises from the $3d$ cobalt ions, very few contributions from the
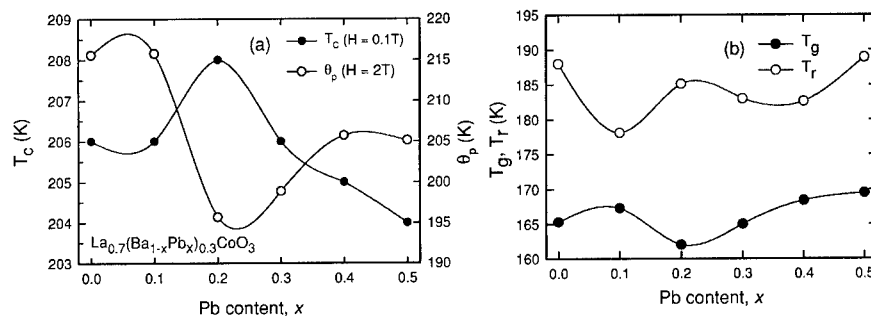
Figure 2. (a) Ferromagnetic transition temperature T_C and Curie-Weiss paramagnetic temperature θ_p versus Pb content, and (b) spin-glass transition temperature T_g and reversible temperature T_r versus Pb content for $La_{0.7}(Ba_{1-x}Pb_x)_{0.3}CoO_3$ system.
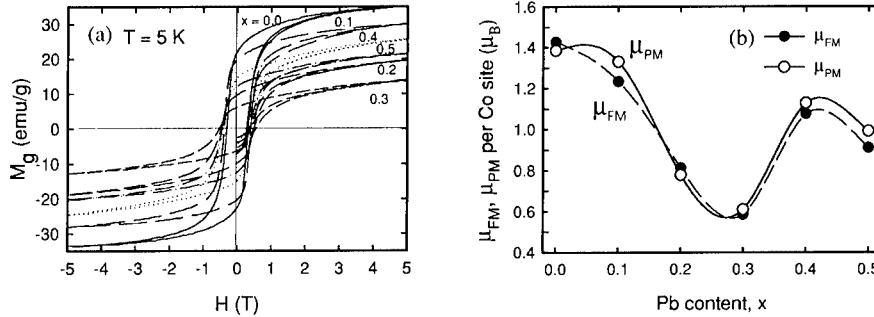
Figure 3. (a) Magnetic hysteresis loops at $T = 5$ K, and (b) dependence of the average effective moment per Co site in a FM and PM phase upon Pb content for $La_{0.7}(Ba_{1-x}Pb_x)_{0.3}CoO_3$ series.

other ions, even Pb and Ba ions. So the value of C is used to calculate the average effective moment per Co ions, μ_{PM}, in the paramagnetic state.

Figure 3(a) displays the magnetic hysteresis loops, $M(H)$, at $T = 5$ K for all our samples. The saturation magnetic moment in the low-temperature magnetic ordering phase, μ_{FM}, is estimated by the saturation magnetization in the $M(H)$ loop at low temperature ($T = 5$ K) or is determined by the low-temperature magnetization of the FC $M(T)$ curve in a high field ($H = 4$ T). As shown in figure 3(b) both μ_{PM} and μ_{FM} for each sample appear very slight difference and have the same dependence on Pb content. The μ_{PM} and μ_{FM} decrease with increasing Pb content from ~1.4 μ_B as $x = 0$, follow by attaining a minimum value of about 0.6 μ_B at $x = 0.3$, then increase as $x = 0.4$ and slightly decrease again as $x = 0.5$. We consider that the addition of Pb ions may changes the degree of chemical disorder and in advance changes the ordering of magnetic moments. As a result it may lead to the average effective magnetic moments in both ferromagnetic and paramagnetic phases to vary with the Pb concentration. The kind of the oscillating variation may be attributed to the competition between the size effect of the ionic radii and the effect of chemical and/or charge disorder. The further investigation of this variation is in progress.

In general, a well-defined equilibrium phase transition is expected to show scaling behavior. The scaling theories [1,6-9] predict that magnetic susceptibility χ (= M/H) exhibits a scaling relation as follows:

$$\chi - \chi_0 = \frac{C}{T - \theta_p}(1 - q) = \frac{C}{T}[1 - |t|^\beta f_\pm(H^2/|t|^{\beta+\gamma})], \tag{1}$$

$$q(t,H) = |t|^\beta f_\pm(H^2/|t|^{\beta+\gamma}), \tag{2}$$

$$q|t|^{-\beta} = f_\pm(H^2/|t|^{\beta+\gamma}), \tag{3}$$

In these equations t is the reduced temperature $t = (T - T_0)/T_0$ with T_0 being a certain magnetic transition temperature. The T_0 may be T_C for a FM/PM transition and may be T_g for a SG transition. The q in equations (2) and (3) is as functions of T and H. If a well-defined magnetic phase transition exits, these equations will present two different scaling functions: f_+ for $t > 0$ in a PM state and f_- for $t < 0$ in a FM/SG state, respectively. Since we did not observe a significant relaxation effect, the magnetic data are considered to be in equilibrium states for all our samples.
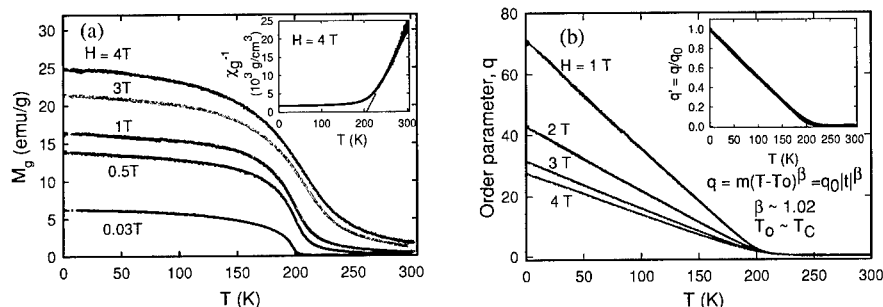
Figure 4. (a) FC magnetization versus temperature in various applied fields for the sample of $x = 0.4$. Inset plot: Inverse susceptibility versus temperature in $H = 4$ T. (b) Order parameter q as a function of temperature, T, in various fields show linear relations. Inset plot presents the temperature dependence of the normalized order parameter in all the external fields.

This behavior is observed mostly in high-quality single crystals or thin films, but scarcely in polycrystalline samples. However, all our samples present this scaling behavior. In this report, we use the sample of $x = 0.4$ as a typical example for discussing the scaling behavior in detail. The universal property of the other samples in our series has been reported elsewhere [6].

Figure 4(a) and 4(b) display the temperature dependencies of the FC magnetization and the order parameter, $M(T)$ and $q(T)$, in various external fields ranging from 0.03 to 4 T. The $q(T)$ curves are extracted from the experimental data of $\chi(T) = M(T)/H$ during the FC measurements using equation 1 and the parameters of $\theta_p = 205.7 \pm 0.3$ K, $C = 4.35 \times 10^{-3} \pm 3.2 \times 10^{-5}$ cm^3·K/g and $\chi_0 \sim 0$. The used parameters are obtained by fitting the $\chi(T)$ experimental data in $H = 4$ T to the Curie-Weiss relation $\chi_0 + C/(T-\theta_p)$ as shown in the inset plot of figure 4(a).

Obviously, figure 4(b) appears that q linearly decreases with increasing temperature in a wide low temperature and field ranges. The inset plot in figure 4(b) displays the normalized $q(T)$, *i.e.* $q'(T) = q(T)/q_0$, where q_0 is the extrapolated value of q at $T = 0$ K. For $T < T_0$, the $q'(T)$ curves for various fields all collapse to an universal straight line of $q' = |T - T_0|$. Here T_0 is considered as a certain transition temperature as described above. In general, we can also say that the order parameter well obeys a power-law relation of $q_0|t|^\beta$ with the reduced temperature $t = (T_0 - T)/T_0$. All $q(T)$ curves in various applied fields give the average fitting values of $\beta = 1.05 \pm 0.01 \sim 1$ and $T_0 = 208$ K ± 2 K. The fitting value of T_0 is very close to the value of T_C as H approaches zero. This result is consistent to the prediction of the mean-field theory in which the powder-law relation has an exponent of $\beta = 1$ and is strictly a linear relation. This result clearly confirms that the magnetic behavior of this compound in temperatures below and even close to the critical point can be described well by the mean-field theory. The same result is usually observed in some conventional spin glass systems and some strong ferromagnetic systems.

We are interested in the magnetic behavior near the critical point T_C. The field dependence of q can be calculated from the experimental $M(H)$ curves using equation 1. It also shows a power-law relation of $q = q_0'H^{2/\delta}$ in high fields. For $q(H)$ at $T = 5$ K a fitting parameter of $\delta = 2.80 \pm 0.01$ was obtained as $H > 0.3$ T. This δ value gives a critical exponent of $\gamma = 3.87 \pm 0.02$
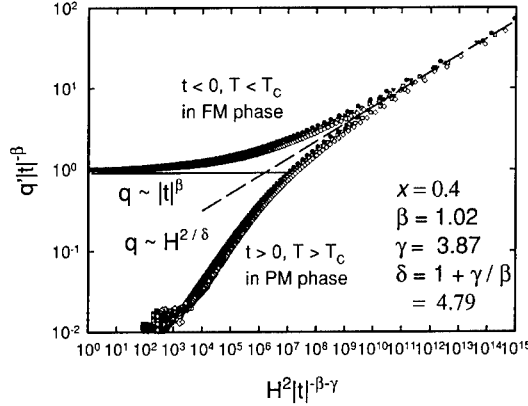
Figure 5. Log-log plot of $q|t|^{-\beta}$ vs $H^2|t|^{-\beta-\gamma}$ of the sample of $x = 0.4$. All magnetic data in the ranges of $2 \le T \le 300$ K and 1 T $\le H \le 4$ T collapse to two curves f_+ for $t > 0$ and f_- for $t < 0$, which clearly demonstrates the scaling relations in equation 3.

based on the relation of $\delta = 1 + \gamma/\beta$. For demonstrating the scaling behavior, the log-log plots of $q|t|^{-\beta}$ versus $H^2|t|^{-\beta-\gamma}$ in various fields (0.03 T – 4 T) as shown in figure 5 are obtained by using the derived values of $\beta = 1.05$, $\gamma = 3.87$, and $T_0 = 208$ K. All of the q data collapse onto two curves. One is the scaling functions $f_+(x)$ for $t > 0$ ($T > T_C$, in the PM phase) and the other is $f_-(x)$ for $t < 0$ ($T < T_C$, in the FM phase). For $t < 0$, $q|t|^{-\beta}$ approaches a constant (~ 1) for small $H^2|t|^{-\beta-\gamma}$ as indicates in the dashed line in figure 5. The line of $q \sim H^{2/\delta}$ with $\delta = 2.80$ as the solid line in figure 5 demonstrates the asymptotic behavior for $T \to T_C$. The shapes of both the scaling functions are also quite similar to those observed in the most conventional ferromagnetic materials. These values of critical exponents are between those predicted by the mean field theory and those derived by a three-dimensional Heisenberg model [1, 6-9].

In summary the scaling behavior in our compounds has some approximations as follows:

(1) For high $T > T_C$ ($t > 0$), equation 1 reduces to the Curie-Weiss relation [$\chi = \chi_0 + C/(T - \theta_p)$] and q gradually approaches to zero with increasing temperature. For all our $La_{0.7}(Ba_{1-x}Pb_x)CoO_3$ samples, the value of χ_0 is so small that it can be neglected.

(2) For $T \to T_C$ or a large H, $i.e.$, $H^2|t|^{-(\beta+\gamma)} >> 1$ ($H^2 >> |t|^{(\beta+\gamma)}$), a power form of $q \sim H^{2/\delta}$ with $\delta = 1 + \gamma/\beta$ (as the dashed line in figure 5) is used to describes the field dependence of the order parameter near the magnetic transition point T_C.

(3) As temperature is far away the critical transition point T_C or $H \to 0$, the value of $H^2|t|^{-(\beta+\gamma)}$ becomes a relative small value. Thus, $q \sim |t|^\beta$ for $t < 0$. It means that $f_-(0)$ approaches to a nonzero constant as the solid line in figure 5. While $f_+(0)$ approaches to zero for $t > 0$ as described in the above situation.

CONCLUSIONS

The striking features of the spin glass behavior and the scaling behavior have been studied in the perovskite-like $La_{0.7}(Ba_{1-x}Pb_x)CoO_3$ oxides with $x = 0 - 0.5$. The Pb^{2+} substitution on Ba^{2+} ions does not significantly affect the ferromagnetic transition temperature T_C, which is determined mainly by the ratio of Co^{4+}/Co^{3+}. But the addition of Pb ions leads to a change in the chemical and magnetic disorder, and induces a large variation in the magnetic strength.

ACKNOWLEDGMENTS

REFERENCES

1. J. M. D. Coey, M. Viret and S. von Molná, *Advances in Physics* **48**, 167 (1999).
2. M. F. Tai, Y. Y. Lee and J. B. Shi, *J. Mag. Magn. Mater.* **209**, 148 (2000).
3. N. Gayathri, A. K. Raychaudhuri, S. K. Tiwary, R. Gundakaram, A. Arulraj and C. N. R. Rao, *Phys. Rev.* **B56**, 1345 (1997).
4. R. Caciuffo, D. Rinaldi, and Barucca, J. Mira, J. Rivas, M. A. Señarís-Rodríguez, P. G. Radaelli, D. Fiorani and J. C. Goodenough, *Phys. Rev.* **B59**, 1068 (1999); D. N. H. Nam, K. Jonason, P. Nordblad, N. V. Khiem and N. X. Phuc, *Phys. Rev.* **B59**, 4189 (1999).
5. C. H. Chen, T. S. H, Y. L. Shieh and M. F. Tai, submitted to *J. Mag. Magn. Mater.* (2001).
6. Chiung-Hsiung Chen, *Thesis of Master Degree*, National Chung Cheng University, Taiwan (July, 2001).
7. F. C. Chou, N. R. Belk, M. A. Kastner, and R. J. Birgeneau and A. Aharony, *Phys. Rev. Lett.* **75**, 2204 (1995); B. Barbara, A. P. Malozemoff and Y. Imry, *Phy. Rev. Lett.* **47**, 1852 (1981).
8. A. P. Malozemoff, S. E. Barnes and B. Barbara, *Phy. Rev. Lett.* **51**, 1704 (1983).
9. N. Moutis, I. Panagiotopoulos, M. Pissas, and D. Niarchos, *Phys. Rev.* **B59**, 1129 (1999).

**Magnetic Nanoparticles,
Nanowires and Arrays**

Magnetic Properties of Self-Assembled Fe Nanoparticle Arrays

D. Farrell, S. Yamamuro, and S. A. Majetich
Dept. of Physics, Carnegie Mellon University
Pittsburgh, PA 15213, U.S.A.

ABSTRACT

The magnetic properties of multilayer arrays of Fe nanoparticles were compared with those of frozen, dilute suspensions of the same particles. The array sample displayed larger coercivity in both hysteretic and remanent magnetization measurements. However, the derivative of the remanent magnetization curve shows a much broader switching field distribution for the arrays than for the dilute sample. Magnetic relaxation measurements show the convergence of the time dependent properties of the samples at large times, and much more rapid relaxation in the arrays at short times.

INTRODUCTION

Dipolar interactions have long been known to affect the switching fields of nanoparticles [1]. However, with a large distribution of interparticle distances, these effects have been difficult to quantify. Improved synthetic methods have made it possible to prepare monodisperse magnetic nanoparticles that self-assemble into arrays [2, 3]. Here we reexamine the effect of dipolar interactions in these nanoparticle arrays, which lend themselves to numerical computation of the dipolar fields.

In this paper we present experimental results showing how the switching fields of the arrays differ from those of a dilute sample made from the same nanoparticles. The magnetic properties are measured at low temperatures so that the particles do not move. At room temperature these particles are superparamagnetic, but at low temperature hysteresis is observed.

EXPERIMENTAL

Monodisperse Fe nanoparticles were prepared under an argon atmosphere. 4 mg of platinum acetylacetonate was dissolved in 15 mL of octyl ether in the presence of 150 mg of the reducing agent 1,2-hexadecanediol. The solution was then warmed to 100 °C and 0.2 mL of $Fe(CO)_5$ was added. The heating continued until the solution reached 280 °C, at which point the heating mantle was removed and the solution was heated again to 260 °C. While heating the platinum salt is reduced to form platinum clusters, onto which iron atoms from the thermally decomposed $Fe(CO)_5$ preferentially deposit. The solution was cooled, and an additional 15 mL of octyl ether was added. At 100 °C 1.5 mL of $Fe(CO)_5$ was added, and the heating continued to 260 °C. The amount of iron added determines the final size of the particles; for these experiments, the average particle size was 8 nm. However, the large arrays were formed preferentially from particles 6 nm in

diameter; larger particles were confined to the edges of the arrays. The fluid was kept under an inert atmosphere, and 0.025 mL each of the surfactants oleylamine and oleic acid were added to the cooled solution. Ethanol was added to precipitate the iron particles, and after decanting the supernatant the particles were redispersed in hexane. The concentration of surfactant in the solvent was kept constant throughout the washing procedure.

The structural properties of the resulting particles were characterized by transmission electron microscopy (TEM). Here a TEM grid was dipped into the solution and suspended in an argon atmosphere to dry. The grids were then imaged in a Philips EM420 electron microscope (120 kV accelerating voltage) to reveal the particle array structures.

For magnetic characterization, two types of sample were prepared. Dilute suspensions of the particles were prepared by diluting the ferrofluid to one-tenth the original concentration. The estimated final concentration was 0.8 mg/mL (0.01% volume, assuming a density of 7.86 g/mL). The dilute fluid was placed into a glass ampoule, which was sealed under argon. The array sample consisted of ten stacked, particle-coated TEM grids. TEM screening verified the presence of arrays and uniformity of coating over the grids. The plane of the grids was *perpendicular* to the field direction within the Quantum Design MPMS2 SQUID magnetometer.

The samples were magnetically characterized by regular and remanent hysteresis loops, and by magnetic relaxation measurements. All measurements were performed at 10 K. For the hysteresis loops, the field was applied and the magnetic moment of the sample was measured; after each at-field measurement, the field was applied and turned off, and the remanent moment M_r was measured. The at-field measurements form the regular hysteresis loop, and the zero field measurements form the remanent hysteresis loop. In magnetic viscosity or relaxation measurements, the sample was first saturated at 50 kOe. The field was then reduced to zero, or a reverse field equal to the coercivity H_c was applied. The moment of the sample was measured at 90 – 600 sec time intervals over a ten hour period at this field. For the array sample it was necessary to correct for the large diamagnetic signal arising from the carbon coated copper TEM grids. The diamagnetic contribution was estimated by calculating the slope of the straight line data acquired at fields above 35 kOe. This contribution was subtracted prior to data analysis.

RESULTS AND DISCUSSION

We assume that the samples were identical except for the effect of magnetic dipolar interactions between particles. For the array sample, the center-to-center particle spacing was approximately 9 nm as measured by TEM [4]. The sample consisted of mainly hexagonally close packed structural domains of Fe nanoparticles, typically ~100 nm across and several layers thick. For the dilute sample, the average particle spacing estimated from the mass concentration was greater than 500 nm.

Comparison of regular and remanent magnetization loops show higher coercivities for the arrays (760 Oe) than the dilute sample (300 Oe). However, these measurements include rotational effects, which are absent from the remanent

magnetization curves shown in Figure 1. Here, H_c was 2760 Oe for the arrays and 550 Oe for the dilute sample.

The increased H_c in the arrays sample suggests that the dipolar interactions stabilize the particles against magnetization reversal. The fringe fields of the surrounding particles create a local field $\mathbf{H}_{loc}$, and the effective field $\mathbf{H}_{eff} = \mathbf{H}_{loc} + \mathbf{H}_{applied}$. Magnetically isolated, uniaxial monodomain particles with their easy axes parallel to $\mathbf{H}_{applied}$ will all switch at the same field $\mathbf{H}_{sw}$ [5]. This leads to a perfectly square hysteresis loop with a delta function switching field distribution.

We can see how the larger coercivity arises from dipolar interactions. Assume that a particle switches its magnetization direction when $\mathbf{H}_{eff} = \mathbf{H}_{sw}$, and that $\mathbf{H}_{eff}$ depends on the distribution of the surrounding particle moments. At saturation the particle moments are aligned with the applied field, perpendicular to the plane of the TEM grid, as shown in Figure 2a. The fringe field of one particle causes a destabilizing local field at its neighbors, but $\mathbf{H}_{loc}$ is small compared with $\mathbf{H}_{applied}$. As soon as the field is removed, the particle moments begin to reorient. In the absence of an external field the lowest energy configuration for a two-dimensional lattice will have the magnetic moments in the plane of the lattice [6]. Within the plane the dipolar interactions favor the formation of chains of particles, and neighboring chains have opposite moment directions, as shown in Figure 2b. Once chains have formed the local field will be in-plane. Near neighbor calculations estimate this field to be on the order of 2500 Oe. Only when the applied field is larger than this do the particle moments switch to lie perpendicular to the TEM grid. The arrays studied here have multiple layers and finite structural domains, so their behavior will be somewhat more complex than that shown in Figure 2. However, there is clearly rapid relaxation of the magnetization associated with dipolar interactions in the arrays.

The switching field distribution was found from the derivative of the remanent hysteresis loop, dM_r/dH, as shown in Figure 3. The dilute sample dM_r/dH curve is broadened with respect to a delta function. The breadth could arise from several sources. Our particles are not uniaxial and they have randomly oriented easy axes. Some particles in the dilute sample may be closely associated, though the average spacing is large. The
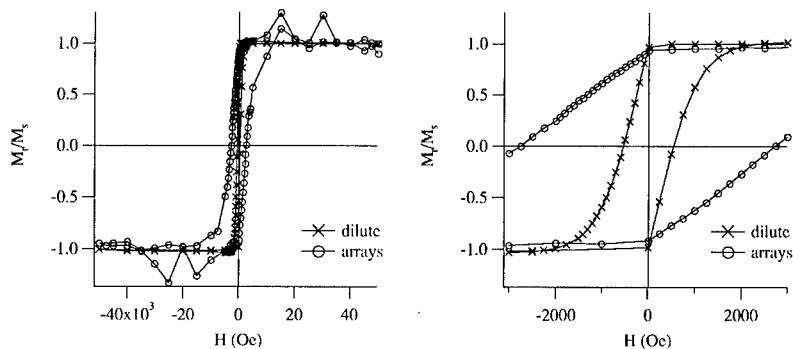
Fig. 1. Remanent magnetization loops taken for dilute and arrays samples of 6 nm Fe nanoparticles at 10 K. The magnetizations are normalized to the saturation values.
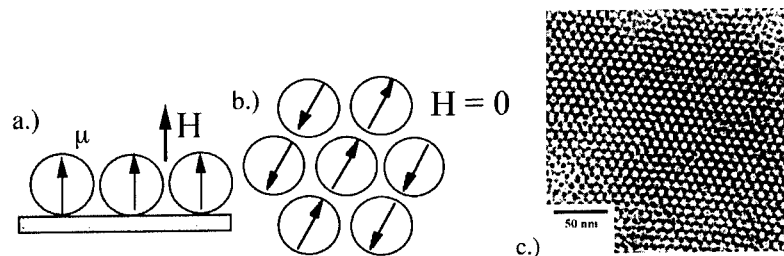
Fig. 2. a.) Nearest neighbor moments at saturation, with the field normal to the plane of the TEM grid. b.) Equilibrium orientation of nearest neighbor moments in zero field. c.) TEM image of Fe multilayer, showing hexagonal symmetry. Dark spots represent phase contrast of overlapping particles; light spots are regions with less particle overlap.

arrays have an even broader switching field distribution, indicating a broader distribution of energy barriers than in the dilute sample. Variation of the local field over the area of the sample leads to a range of local fields, and therefore switching occurs over a range of applied fields. Even though the arrays have a larger coercivity, they contain many particles with low barriers to switching of the magnetization direction.

For the arrays, the switching field distribution will depend not only on the distribution of easy axis orientations, but also on the uniformity of particle environments and array orientations with respect to the field. A distribution of switching fields will arise from the distribution of hexagonal array orientations. In addition, the local field will be very different for particles near grain boundaries than for those located within a domain. Greater structural uniformity of the arrays should narrow the switching field distribution, as should crystallographic alignment of the particles.
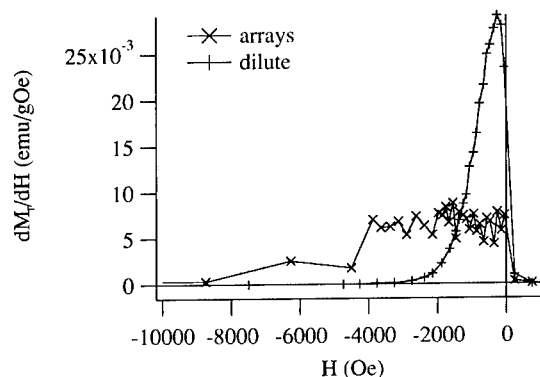
Fig. 3. Switching field distributions for dilute and arrays samples of Fe.

A second way to characterize the distribution of energy barriers is through magnetic relaxation measurements (Figure 4). This distribution causes the magnetization to decay logarithmically in time, so that $M = M_0 - S\ln(t/t_0)$ [7, 8]. Here, M_0 is the initial magnetization at field, S is the slope of the line, and t_0 is the time of the initial measurement. By different choices of the initial time t_0 the value of the magnetization intercept M_0 is changed, but the value of the slope S is not.

Figure 4 shows the magnetic relaxation of the arrays and the dilute sample both at zero field and at the coercivity of the regular hysteresis loop. The dilute samples show logarithmic decay at all times, but the arrays have a dramatic drop in the magnetization at early times, followed by logarithmic decay. Figure 5 illustrates the magnetic viscosity S found from the slope of the plots of Figure 4. S is larger at the coercivity than at zero field, as expected [9]. The larger relaxation rate in the arrays seems at first to be inconsistent with the greater coercivity, relative to the dilute sample. We postulate that the rapid initial relaxation arises due to chain formation like that in Figure 2b. Once the chains have formed, the dipolar local fields prevent further switching until much greater
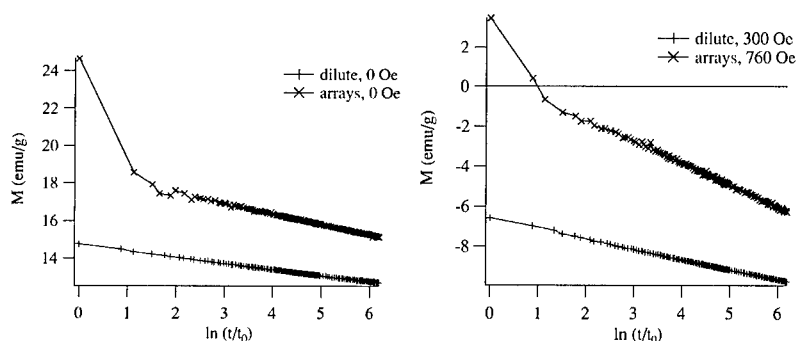
Fig. 4. M vs. ln (t/t_0) at 10 K. Left: H = 0; Right: arrays, H = 760 Oe; dilute, H = 300 Oe.
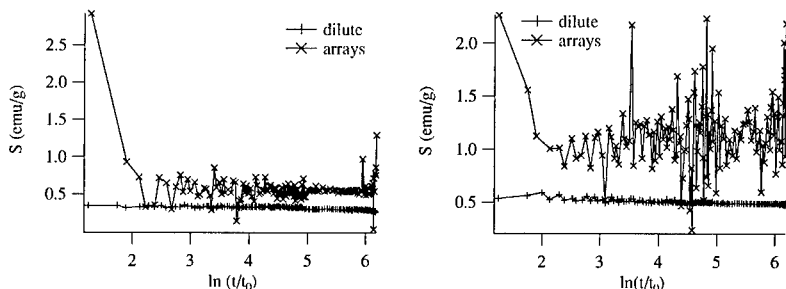
Fig. 5. S versus ln (t/t_0). Left: H = 0; Right: arrays, H = 760 Oe; dilute, H = 300 Oe.

fields are applied. Because the particles are not crystallographically oriented when the arrays are self-assembled, there is a broad range of switching fields for chain formation. The long time behavior may be dominated in both samples by the distribution of energy barriers associated with variations in the easy axis orientations of the particles [10].

CONCLUSIONS

The results of magnetic measurements on samples of Fe nanoparticles in frozen, dilute suspensions and ordered in hcp arrays indicates the effect of a local field arising from dipole interactions between Fe particles. Based on simulations of TEM images, the particles studied here had 6 nm cores and a spacing of 3 nm between the surfaces of the iron cores. The self-assembled iron nanoparticle arrays have a larger coercivity than a dilute sample of the same nanoparticles. The enhanced coercivity can be understood qualitatively in terms of the average local field due to dipolar interactions with neighboring particles. The arrays also have a much broader distribution of switching fields than the dilute sample. Magnetic relaxation measurements show comparable relaxation rates for the arrays and dilute samples at long times, but much more rapid relaxation in the arrays over a short time period. This is attributed to the rapid formation of chains of dipoles following the application of a reverse field.

ACKNOWLEDGMENTS

REFERENCES

1. B. D. Cullity, *Introduction to Magnetic Materials* (Addison-Wesley, Reading, MA, 1972), p. 387.
2. S. Sun. C. B. Murray, D. Weller, L. Folks, and A. Moser, *Science* **287**, 1989 (2000).
3. C. Petit, A. Taleb, and M. P. Pileni, *J. Phys. Chem.* **103**, 1805 (1999).
4. S. Yamamuro, D. Farrell, S. A. Majetich, MRS Symposium Proceedings, Fall 2000, paper D10.8.
5. E. C. Stoner, F. R. S. and E. P. Wohlfarth, Phil. Trans. Roy. Soc. **240**, 599 (1948).
6. G. Mukhopadhyay, P. Apell, and M. Hanson, J. Magn. Magn. Mater. 203, 286 (1999).
7. R. Street and J. C. Woolley, Proc. Phys. Soc. *A* **62**, 562 (1949).
8. R. W. Chantrell, M. Fearon, and E. P. Wohlfarth, Phys. Stat. Sol. (a) **9** , 213 (1986).
9. S. A. Majetich and E. M. Kirkpatrick, IEEE Trans. Mag. **33**, 3721 (1997).
10. K. D. Humfeld, A. K. Giri, S. A. Majetich, and E. L. Venturini, IEEE Trans. Mag. (in press, 2001).

Magnetization reversal and magnetic anisotropy of Fe, Ni and Co nanowires in nanoporous alumina membranes

M. Kröll[1], L. J. de Jongh[2], F. Luis[2], P. Paulus[2], G. Schmid[3]
[1]Physics Department, Trinity College Dublin, Dublin 2, Ireland
[2]Kamerlingh Onnes Laboratory, Leiden University, P.O. Box 9506, 2300 RA Leiden, The Netherlands
[3]Institut für Anorganische Chemie, Universität GH Essen, Universitätsstr. 5-7, 45117 Essen, Germany

ABSTRACT

The magnetization reversal and magnetic anisotropy of Fe, Ni and Co nanowires is studied at low temperatures. All nanowires show a strong shape anisotropy with the easy axis being parallel to the long axis of the wires. Co nanowires additionally show a temperature dependent magnetocrystalline anisotropy along the hexagonal c-axis, which is directed nearly perpendicular to the long axis of the wires, as is confirmed by X-Ray diffraction measurements [1] and reported by Strijkers et al. who performed NMR measurements on samples prepared in a similar way [2]. Therefore, at low temperatures and for large wire diameters a competition between magnetocrystalline and shape anisotropies can be observed. Co wires with a small diameter, however, do not show a significant magnetocrystalline anisotropy. Fcc-Co, which is only known as a high-temperature Co modification and which does not have a large magnetocrystalline anisotropy constant, becomes the predominant Co modification here [1,3]. Investigations on the size dependence of the switching field for Fe and Ni nanowires provide information about the magnetization reversal process, which takes place via a nucleation of small magnetic domains probably at the end of the wires, and subsequent propagation of the domain wall along the wire.

INTRODUCTION

Nanostructured materials are of considerable interest because of many new possible applications in different fields such as information technology, biotechnology, medicine or environmental engineering. Scientifically they are interesting because the physical properties of a material can change significantly if its lateral dimensions are reduced down to the nanometer scale. These changes can occur if the size of at least one dimension is reduced down to a regime comparable, for example to that of the DeBroglie wavelengths of electrons, the excitation wavelengths of phonons or magnons, or the domain wall width D_W as regards ferromagnetic materials. A cylindrical particle with a diameter smaller or comparable to D_W and a length that is much larger than D_W can be considered to be one-dimensional.

One-dimensional nanostructures can be built by performing chemical or electrochemical reactions in the pores of a suitable host or matrix material. As matrix material polycarbonate membranes [4], zeolites [5] or alumina membranes [6] may be used.

We chose nanoporous alumina membranes as the template material because they are easily accessible by anodic oxidation of high purity aluminum in polyprotic acids, they are chemically and physically stable and their properties (pore diameter, thickness) can be easily varied. Metals can be plated into the pores using a simple AC plating procedure.

The nanowires thus achieved can be considered as being one-dimensional if their diameter is in the order of 10-50 nm. Since the pore diameter, and therefore the wire diameter, can be varied between 5 and 250 nm by the above mentioned method the nanowires produced here fulfill this condition.

The magnetization of one-dimensional Fe, Ni and Co wires is investigated here. Fe and Ni show a strong shape anisotropy for all wire diameters and all temperatures investigated. The easy axis lies parallel to the long axis of the wire. For Co, however, there is a strong competition between the shape anisotropy and a magnetocrystalline anisotropy. This magnetocrystalline anisotropy, which is well-known for hcp-Co with an easy axis perpendicular to the long axis of the wire, can be found in pores with a rather large pore diameter at low temperatures. At increasing temperatures the magnetocrystalline anisotropy becomes less important and the shape anisotropy predominates. In smaller pores hcp-Co is substituted bit by bit by fcc-Co which does not show a significant magnetocrystalline anisotropy. Therefore, Co wires with a small diameter do not show a competition between shape and magnetocrystalline anisotropy anymore.

Magnetization reversal in one-dimensional ferromagnets has been widely investigated. For wires having a diameter D smaller than $\sqrt{\pi} D_W$ rotation in unison was predicted to be the responsible magnetization reversal process, whereas wires having a larger diameter than $\sqrt{\pi} D_W$ should reverse via a curling mode [7,8]. In both cases all spins are reversed simultaneously. Other reversal mechanisms including the formation of domain walls are also discussed [9,10]. Investigations on the temperature dependence of the coercive field for Fe and Ni wires that help to identify the responsible magnetization reversal process for different wires diameters are presented here.

EXPERIMENTAL DETAILS

Nanoporous alumina membranes are prepared by anodizing aluminum foils (99.8 %) in polyprotic acids like sulfuric acid, phosphoric acid or oxalic acid at 0°C and a constant anodizing voltage. The pore diameter achieved depends nearly linearly on the anodizing voltage applied (approx. 1.2 nm/V). In order to clean and make a smooth surface the aluminum foils are treated with chromic acid and electropolished in a mixture of concentrated phosphoric and sulfuric acid (11:7 (v/v)) prior to the anodizing. The pore diameters achieved here range between 6 and 50 nm.

Metal plating is performed using an AC plating procedure. The aluminum that is not consumed during the anodizing and that is still underneath the membrane serves as an electrode during the metal plating. Graphite may be used as a counter electrode. The plating voltage used for all metals is 16 V (50 Hz).

Magnetic measurements were performed using a SQUID magnetometer at temperatures between 3 and 300 K and in fields between –5 and +5 T.

DISCUSSION

Figure 1 shows a TEM picture of a cross-sectioned alumina membrane filled with Ni. It is clearly visible that the Ni wires propagate parallel to each other.
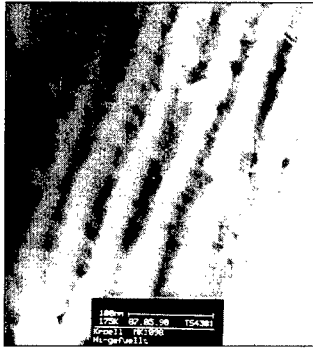
Figure 1. TEM picture of a 20 V alumina membrane filled with Ni (cross section)

The magnetization curves of Fe and Ni wires with an average diameter of 12 nm are shown in figure 2. An almost square shape of the curves can be observed when the magnetic field is applied parallel to the long axes of the wires whereas hardly any hysteresis can be seen when the magnetic field is directed perpendicular to the long axes. This indicates a strong shape anisotropy for both Fe and Ni wires, i.e. there are two stable orientations for the magnetic moments namely, pointing parallel and antiparallel to the long axis of the wire. These orientations are separated by an energy barrier. The shape anisotropy can be observed independent of the wire diameter.

For finite cylinders the coercive field B_{c0} at $T = 0$ K is predicted to be independent of the wire diameter D if the magnetic moments are reversed via rotation in unison

$$B_{c0} = \frac{\mu_0}{2} M_{sb} \qquad (1)$$

where M_{sb} is the saturation magnetization of the bulk. If the magnetization is reversed via a curling mode, however, the coercive field B_{c0} depends on D [7,8]

$$B_{c0} = 0.54\mu_0 M_{sb} (\frac{\sqrt{\pi}D_W}{D})^2 \qquad (2).$$

Figure 3 shows the measured coercive fields as a function of $D/(\pi^{1/2}D_W)$ with $\pi^{1/2}D_W = 11$ nm and 39 nm for Fe and Ni respectively [3]. For large wire diameters the measured values follow the predicted curve for the curling process. For small wire diameter the value for $2B_{c0}/\mu_0 M_{sb}$ remains nearly constant as predicted for the rotation in unison but is a factor of 3 too low. For small wire diameters the magnetization reversal mechanism needs to be modified. Investigations on the temperature dependence of the coercive field, the magnetic relaxation and the magnetic viscosity, not presented here, [3] gave evidence for a mechanism including the nucleation of a magnetic domain and a following propagation of the domain wall along the wire. The domain is likely to be formed near structural defects or at the ends of the wire.
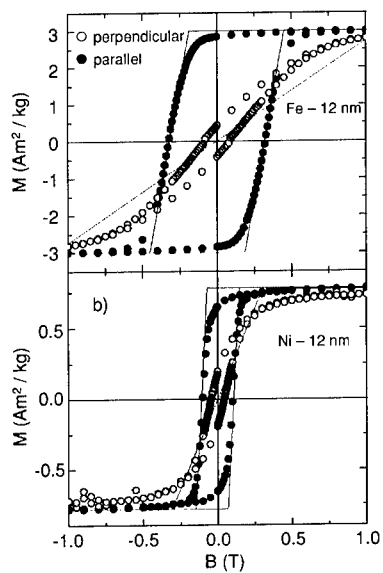
Figure 2. Magnetization curves of 12 nm Fe and
Ni wires indicating a strong shape anisotropy
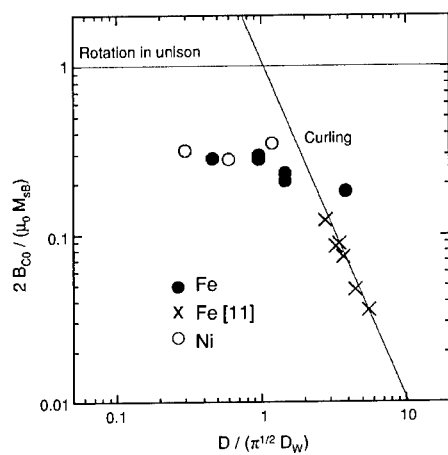
Figure 3. Size dependence of the coercivity for Fe and Ni nanowires (data
from Ref [11] are included for wire diameters larger than those used in this work)

Apart from the shape anisotropy Co nanowires show a temperature and size dependent magnetocrystalline anisotropy along the hexagonal c-axis, which is directed nearly perpendicular to the long axis of the nanowire [1,2]. Therefore, at low temperatures wires with a large pore diameter show a hysteresis in the magnetization curve for both the magnetic field applied parallel and perpendicular to the long axes of the wires (cf. Fig. 4). At room temperature, however, the magnetocrystalline anisotropy constant becomes significantly smaller than at 5 K. This causes the loss of the hysteresis in the magnetization curve when the magnetic field is applied perpendicular to the long axes of the wires. Furthermore, the magnetocrystalline anisotropy becomes less important if the wire diameter is decreased. This can be attributed to the fact that in all the wires a mixture of fcc-Co and hcp-Co can be found. The amount of fcc-Co increases if the pore diameter decreases [1,2]. Fcc-Co, however, does not show a significant magnetocrystalline anisotropy. This in turn leads to a prevailing shape anisotropy in Co wires with a small diameter even at low temperatures. It is not yet understood what causes the amount of fcc-Co, which in the bulk is only known as a high temperature Co modification, to increase in small pores. However, intensive EXAFS and WAXS studies on this subject are in progress .
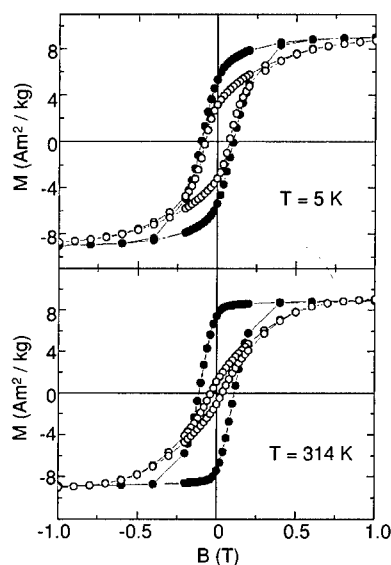
Figure 4. Magnetization curves for Co nanowires (D = 50 nm) at two different temperatures

CONCLUSIONS

Extensive studies on the magnetization reversal process in one-dimensional Fe and Co wires have been performed showing that for small wire diameters, i.e. diameters in the range of the domain wall widths, the magnetization reversal process takes place including the formation of small domains at imperfections or at the ends of the wires followed by the propagation of the

domain walls along the wire. In Fe and Ni wires the shape anisotropy predominates, whereas Co wires show a competition between this shape anisotropy and a magnetocrystalline anisotropy. The magnetocrystalline anisotropy (with the easy axis nearly perpendicular to the long axis of the wire) is temperature and size dependent. In small Co wires and at elevated temperatures the shape anisotropy predominates, whereas in large pores and at low temperatures the shape and magnetocrystalline anisotropy constants nearly equal each other. A decreasing amount of hcp-Co in favor of fcc-Co in small pores is determined by EXAFS and WAXS spectroscopies. This causes a reduction of the magnetocrystalline anisotropy strength in small pores.

ACKNOWLEDGMENTS

REFERENCES

1   R. E. Benfield, D. Grandjean, J. C. Dore, Z. Wu, M.. Kröll, T. Sawitowski and G. Schmid, Structure of metal nanowires in nanoporous alumina membranes studied by X-ray diffraction, (2001) (in press)

2   G. J. Strijkers, J. H. J. Dalderop, M. A. A. Broeksteeg, H. J. M. Swagten and W. J. M. de Jonge, Structure and magnetization of arrays of electrodeposited Co wires in anodic alumina, *J. Appl. Phys.* **86 (9)**, 5141-5145 (1999)

3   P. M. Paulus, F. Luis, M. Kröll, G. Schmid and L. J. de Jongh, Low temperature study of the reversal mode and the magnetic anisotropy of Fe, Ni and Co wires in alumite, *J. Magn. Magn. Mater.* **224**, 180-196 (2001)

4   G. A. Ozin, Nanochemistry: Synthesis in Diminishing Dimensions, *Adv. Mater.* **4 (10)**, 612-649 (1992)

5   C. L. Bowles and G. A. Ozin, Self-Assembling Frameworks: Beyond Microporous Oxides, *Adv. Mater.* **8 (1)**, 13 (1996)

6   D. Routkevitch, A. A. Tager, J. Haruyama, D. AlMawlawi, M. Moskovits, J. M. Xu, Nonlithographic Nano-Wire Arrays: Fabrication, Physics, and Device Application, *IEEE T. Electron. Dev.* **43 (10)**, 1646-1658 (1996)

7   E. H. Frei, S. Shtrikman and D. Treves, Critical Size and Nucleation Field of Ideal Ferromagnetic Particles, *Phys. Rev.* **106**, 446-455 (1957)

8   A. Aharoni, S. Shtrikman, Magnetization Curve of the Infinite Cylinder, *Phys. Rev.* **109**, 1522-1528 (1958)

9   H.-B. Braun, Thermally Activated Magnetization Reversal in Elongated Ferromagnetic Particles *Phys. Rev. Lett.* **71**, 3557-3560 (1993)

10   J. E. Knowles, Magnetization Reversal by Flipping, in Acicular Particles of γ-Fe$_2$O$_3$, *J. Magn. Magn. Mater.* **61**, 121-128 (1986)

11   G. T. A. Huysmans, J. C. Lodder and J. Wakui, Magnetization curling in perpendicular iron particle arrays (alumite media), *J. Appl. Phys.* **64**, 2016 (1988)

Stability of Magnetic States in Patterned Materials

Martha Pardavi-Horvath
The George Washington University, Department of Electrical and Computer Engineering,
Washington, D.C. 20052, U.S.A.

ABSTRACT

The stability of the individual elements of a two-dimensional (2D) regular array of single domain particles is investigated. The variance in the statistical distribution of up- and down switching fields of the elements leads to premature switching for the low coercivity particles, and incomplete overwriting for the high end of the distribution. The distribution of the interaction fields from surrounding elements on a 2D array depends the saturation magnetization of the elements, their packing density, and the recorded information. The non-ellipsoidal shape of the elements leads to reduced switching fields as a result of non-collinear magnetization around the corners and edges. The thermal stability of 2D arrays, switching by (incoherent) rotation of the magnetization, is enhanced compared to bulk/contiguous media, due to the lack of low energy barrier domain wall motion processes. However due to the fast decrease of the anisotropy, stability at elevated temperatures is still a problem. Experimental data for a model 2D square array of single crystalline, strongly uniaxial, single domain garnet particles illustrate the effects on stability of statistics, shape, and thermal excitation.

INTRODUCTION

The interest in regular two-dimensional (2D) arrays of small magnetic particles is motivated by their potential as the next generation of high density magnetic recording media. The stability of the magnetic states of a 2D patterned magnetic system is an important practical problem with interesting fundamental aspects. The stability of the magnetic state of the individual *elements* and the *system*, as a whole, is determined by material parameters, the statistical distribution of the se parameters, shape and size of the elements, geometry of the array, and by the reversal mode.

The shape of the elements depends on the technology of preparation, it can be elliptical [1] , or flat rectangular [2], or even conical [3]. The elements (bits in recording) should have two stable magnetic states, separated by an energy barrier, high enough to prevent erroneous switching, but low enough to make (over)writing possible. The easy direction can be either in-plane, or normal to the plane of the array. Perpendicular recording mode is preferred because of higher packing density. The elements of a 2D array are single domain particles. Ideal single domain particles would switch by coherent rotation, similar to the Stoner–Wohlfarth mode [4]. However, although the elements on the 2D arrays do not have any domain walls, the magnetization state is not uniform due to the presence of corners and edges. As a result, the switching mode is of incoherent rotation. Any interaction between the elements will influence the switching field. The elements are separated by nonmagnetic areas, thus the interaction between them is purely magnetostatic, and it depends on the shape, the separation between the elements, and the saturation magnetization.
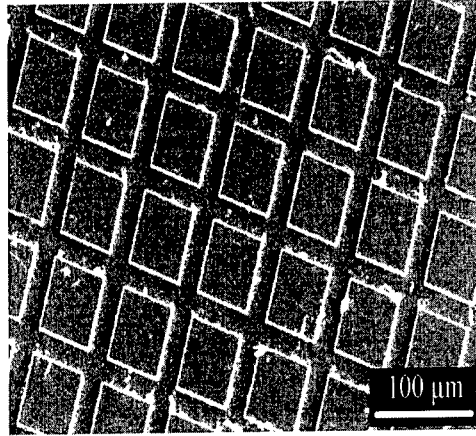
Figure 1. Scanning electron microscope (SEM) photo of a part of an epitaxial garnet wafer with the 2D square array of 40 μm x 40 μm x 3 μm particles (Courtesy of Zofia Vertesy, HAS, Budapest, Hungary).

Assuming a modest 10 Gb/cm^2 recording density, the center-to-center distance between adjacent bits is about 100 nm, including the separating "groove". A 100 Gb "disk" of this medium has an area of about 10 cm^2. For flawless operation, it is required that all the elements behave the same way. The most critical characteristics of the elements is the switching field H_{sw}, because it is very sensitive to many parameters of the system, including magnetization, anisotropy, array geometry, shape, size, defects, stress, temperature, etc. The major technological challenge for recording on 2D arrays of small particles is how to keep the switching field distribution for 10^{11} particles as narrow as it is required by the recording system? One of the main potential problems lies in the statistical distribution of the parameters of the elements on the array. The lowest switching fields will cause bit errors, while the high end of the distribution will prevent (over)writing.

In the following, the role of the statistical distribution of the properties of the elements, geometrical (shape and size) effects, interaction effects between the elements, switching modes, and temporal and thermal effects on system stability will be in examined. These effects are demonstrated on a model system of a 2D array of single crystal, single domain garnet particles.

EXPERIMENTS

Two-dimensional square arrays of 40 μm to 60 μm square, 3 μm thick garnet particles of substituted $Y_3Fe_5O_{12}$ (YIG) were etched from an epitaxially grown single crystalline film to study the magnetization process of a system of magnetically small, highly uniaxial, single domain magnetic particles. The separation between particles is about 1/3 of the lateral dimension. Figure 1. shows a detail of the photolithographed and etched LPE garnet wafer with the 2D square array of 40 μm x 40 μm x 3 μm particles.
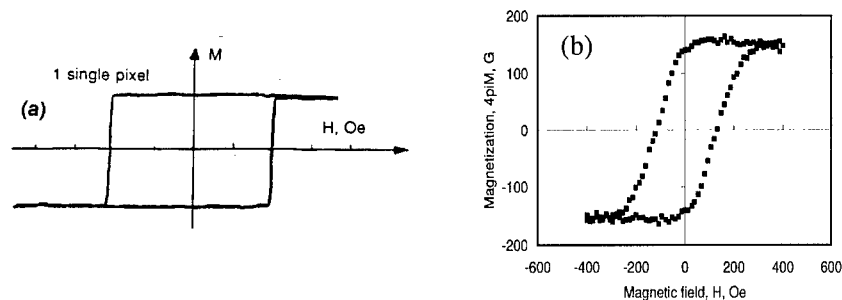
Figure 2. Hysteresis loop of an individual particle of Fig. 1., measured magnetooptically (a), and major hysteresis loop of about 3,000 particles, measured at T=50° C in a VSM (b).

Although the physical size of these garnet particles is relatively large, they satisfy the requirements of magnetic smallness: they are single domain due to a very strong uniaxial anisotropy, $H_k = 2.2$ kOe, combined with a very low magnetization, $4\pi M_s = 160$ G, resulting in a uniaxiality of $Q = H_u / 4\pi M_s \geq 10$. The easy direction of the magnetization is perpendicular to the surface of the particles. Each particle has only two stable states of the magnetization, "up" and "down". The hysteresis loop of the individual particles is rectangular, and the squareness of the major hysteresis loop of thousands of particles $S = M_r/M_s = 1$. The coercivity along the major hysteresis loop at room temperature is $H_c = 285$ Oe.

The epitaxial garnet films are of extremely high quality single crystals, and as a result, it is expected that interactions with defects do not influence the magnetization process. Another advantage of this system is its optical transparency and high magnetooptical activity. Individual hysteresis loops of hundreds of particles, and major and minor loops of assemblies of particles were measured in an optical magnetometer, with optoelectrical detection and simultaneous visual observation. Statistics of the switching fields, coercivities, and interaction fields were determined from the measured data. Mean values for over 3,000 particles (5x5 mm^2 samples) were measured by a VSM [5].

DISCUSSION

Statistical stability
Coercivity distribution

For an ensemble of a large number of particles, the statistical distribution of properties is very important. Without considering the standard deviation, the mean values for magnetic properties, geometry, interactions, can be misleading, of these quantities. The weakest link of a system is determined not by mean values of significant parameters, but their variance. The
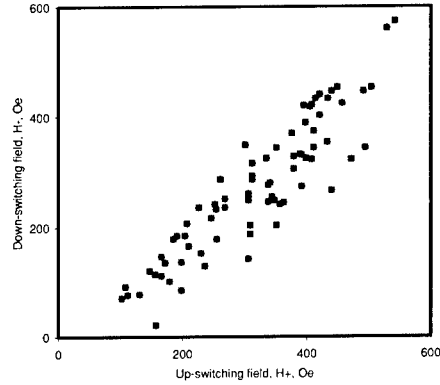
Figure 3. Measured distribution of the up- and down-switching fields H⁺ and H⁻ of individual particles on the 2D array.

statistical distribution of the magnetic characteristics of individual particles was measured on the model system of single domain garnet particles. Figure 2. shows a hysteresis loop for a single particle, and the major hysteresis loop for thousands of particles. The up- and down switching fields (H^+ and H^-) of individual particles were determined from the individual hysteresis loops of over 200 individual particles, resulting in the switching field distribution, shown in Figure 3.

This 2D system of small particles can serve as a nearly ideal system for Preisach hysteresis models [5-7]. The Preisach model assumes that the major hysteresis loop is originating in the statistics of switching of individual particles, each characterized by a shifted rectangular hysteresis loop. The width of each individual loop is the measure of the coercivity of the given particle, while the shift is due to the interaction with the surrounding particles. The coercivity of individual particles is the halfwidth of the hysteresis loop:

$$H_c = (H^+ + H^-)/2 \qquad (1)$$

The measured up- and down switching field data can be converted into a coercivity-interaction field plot, where the distribution of both can be clearly seen, as shown in Fig.4. The measured switching fields span a surprisingly broad range of about 600 Oe. The distribution of coercivities is Gaussian with $H_c = (288 \pm 112)$ Oe. The mean value corresponds to the major loop coercivity of a large number of particles. The standard deviation of H_c, $\sigma_c = 112$ Oe reflects the range of the strength of the defects, contributing to the coercivity. However, according to the Gaussian distribution, the probability to find H_c values at $3\sigma_c$ is still finite. As a result, there will be particles switching too early, at very low fields, and particles at the high end of the H_c distribution, resisting switching within the nominal field of the device operation.
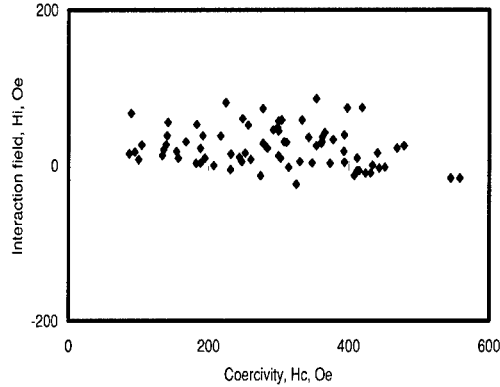
Figure 4. Distribution of coercivities, H_c and interaction fields, H_i of individual particles, calculated from the data of Fig. 3.

Interaction field distribution

The second contribution to switching field distribution originates in the *interaction fields*, H_i, between the particles, manifested in the shift of the individual hysteresis loops by the effective field from the neighbors:

$$H_i = (H^+ - H^-)/2. \tag{2}$$

The shift of the hysteresis loops of individual particles is due to the interaction with the surrounding particles. This interaction is entirely magnetostatic, and it arises from the "demagnetizing" or "magnetizing" effects of the neighbors. The average interaction field for the data in Fig. 3 and Fig. 4 is $H_i = 23.4$ Oe, with a standard deviation of $\sigma_i = 25.2$ Oe [8-10]. For a perpendicular 2D medium the interaction field differs from the usual 3D particulate material case. Depending on the state of the neighbors of the actual particle to be switched (i.e. a bit in recording), the interactions can be "magnetizing" or "demagnetizing", causing switching at much lower or higher fields than the coercivity of the particle. For example, a central particle experiences an effective field of

$$H_{eff} = H_{appl} + H_i, \tag{3}$$

coming from the applied bias field H_{appl} and the interaction field, $H_i = \Sigma H_D$. The interaction field, in first approximation, is the *vector* sum of the demagnetizing fields from neighbors. This field, $H_D = -N_{zz} M_s$ can be very large for a high magnetization medium, and for high density (close) packing of particles. This field has been calculated by us previously by micromagnetic methods. The interaction field at a given particle, originating from all the other particles, is given by

$$H_i = 4\pi M_s N_{zz} \tag{4}$$

where

$$N_{zz} = \Sigma\Sigma D_{zz}\,(\,i,j\,) \qquad\qquad (5)$$

summing up the interactions at each point of the 2D system with all other points. The sign of $D_{zz}(i,j)$ is determined by the state of particle j. In fact, N_{zz} corresponds to the usual demagnetizing tensor element.The measured up-switching field of a particle is equal to:

$$H^+ = H_{c0} - H_i \qquad\qquad (6)$$

where H_{c0} is the coercivity without interactions [11, 12]. It was shown that in the calculations the interactions with the surrounding particles can be truncated at the 3rd coordination shell. The effect of the state of the neighbors was measured, and micromagnetically calculated for 25 particles (embedded in a 9x9 array), showing that when all the 24 neighbors are switched "up", in other words, no neighbors are in the "down" state, $H_i = 86$ Oe for $H^+ = 398$ Oe, resulting in $H_{c0} = 312$ Oe for that particle, in very good agreement with experiments. To illustrate the worst case scenario, let's assume 4 nearest neighbors of a central particle, and $N_{zz} = 1$. Then, in the worst case, when all the neighbors are magnetized in the same direction as the central particle, H_{eff} can change from $(H_{appl} - 4*4\pi M_s)$ to $(H_{appl} + 4*4\pi M_s)$, i.e. by $|8*4\pi M_s|$ upon inverting the magnetization of the central particle. On a square array, the interaction is the strongest between the corners of neighboring elements. These effects can lead in one case to premature switching, in the other, to difficulty of (over)writing, thus significantly affecting the stability of digital information in 2D recording media. At the same time, around the corners, the magnetization is canted, and large in-plane interaction field component exists, acting on the neighbors, further reducing the switching field. Thus, the interaction field with the neighbors depends on the shape, density, and magnetization state of the elements i.e. the total magnetization of the array, what leads to the increase of the variance of the interaction field. This field is proportional to the saturation magnetization of the material. High M_s is preferred for a high read signal. This taken together with the requirement for high packing density results in a high interaction field. High interaction field means low stability of the magnetic state, i.e. the stability of the information on a 2D array depends on the information itself.

Switching instability due to shape effects

For perpendicular recording the most important demagnetizing tensor component is N_{zz}. For finite aspect ratio shapes, $N_{zz} \neq 1$, i.e. it differs from the thin film value. Due to the non-ellipsoidal shape of these particles, the *local* demagnetizing tensor elements, $N_{zz}(\mathbf{r})$ inside the particles should be taken into account and calculated numerically [13-16]. The resulting internal field and magnetization distribution $M(r)$ in a rectangular or cylindrical particle will be non-uniform. For a 1:1:0.1 aspect ratio particle, even in a large field, $H_{appl} = 5\pi M_s$, the magnetization will be canted at the corners and at the edges by an angle up to about 30°. The magnetization of such a particle will have a significant in-plane component. Figure 5 illustrates how the local N_{zz} values, shown across the centerline of a rectangular particle, deviate from the thin film value of 1 for different aspect ratios. It is clearly seen that even for an aspect ratio of thickness/lateral size=0.01, the decrease of N_{zz} around the corners is about 50%!
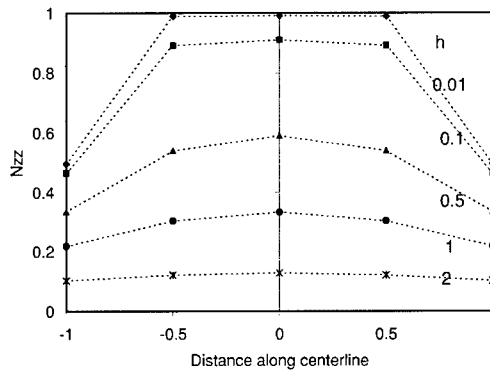
Figure 5. Shape dependence of the $N_{zz}(r)$ local demagnetizing tensor component along the centerline for unit square base columns of height $0.01 \le h \le 2$. The connecting lines serve only to guide the eye.

For a single domain particle, switching along the easy axis by the Stoner-Wohlfarth mode, the switching field is expected to be equal to the anisotropy field, $H_c = H_k$ [4]. However, in the case of non-ellipsoidal small particles $H_c \ll H_k$, indicating that the magnetization switching is not a uniform rotation process. Early micromagnetic calculations did show that the uniform rotation is always an idealization [17], later this became a fact of life [18]. The switching mode of these particles is by incoherent rotation. The switching field is significantly reduced. The dominant source of reduced switching field is the inhomogeneous internal field, resulting in a non-collinear magnetic structure around the corners and edges. Due to the canted magnetization, according to the switching asteroid, the switching starts much earlier, than it would be for a particle, uniformly magnetized along the particle normal. The canted moments are the seeds of switching. [19, 20]. The statistics of the interaction field with the surrounding particles, the lowered nucleation barriers at crystalline defects, also contribute to the observed switching field and its standard deviation. However, the main cause of the reduction in the switching field and of the switching instabilities is the non-uniform internal field.

Temporal and thermal stability

One of the major concerns about patterned media is the thermal and temporal instability of the information, due to the low anisotropy energy $E_K = KV$ of the small volume (V) particles with respect to the fluctuations of thermal energy [21, 22]. In continuous, or bulk magnetic materials, even in the case when the dominant mechanism of the magnetization change is rotation, domain wall (DW) motion processes are always present around the coercivity. The critical field for domain wall motion, compared to the anisotropy field for rotation, is several orders of magnitude lower. As a result, the probability of magnetization reversal by domain wall motion in continuous media is very high, especially around the coercivity of the major hysteresis loop. This gives rise to the characteristic maximum on the magnetic viscosity, $S=dM/d\ln t$ vs H, curves. It is assumed, that for materials where DW processes are excluded, as in the case of single domain
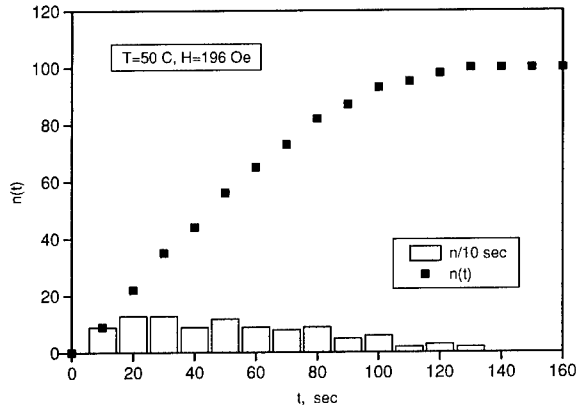
Figure 6. Rotation aftereffect for the particles on the 2D array , T=50, H=190 Oe.
n/10 – the number of particles, switched in 10 sec intervals; n(t) - the total number of
particles switched during t sec.

particles, this curve is more or less flat. There is still a statistical distribution of the switching
fields of the particles, reflected in the shape of the $S(H)$ curve, but this distribution is much
narrower than the distribution of the energy barriers for domain wall motion and rotation taken
together. Therefore, lowered sensitivity of the magnetic aftereffect to the magnetic field is
expected for a patterned recording medium of high anisotropy particles.

The particles in our model system of 2D arrays are thermally very stable, due to the high
anisotropy field, $H_K = 2$ kG. Combined with the very low magnetization, the uniaxial anisotropy
constant $K_u = 1.3*10^4$ erg/cm^3, $V = 7.5*10^{-9}$ cm^3. Thus the anisotropy barrier at room temperature
$E_K \cong 10^{-4}$ erg in $H = 0$, compared to the thermal fluctuations energy of $E_T \cong 40k_BT \cong 10^{-12}$ erg. The
lowest switching field is about 100 Oe, the highest is above 500 Oe (see Fig.4). If to assume the
worst case: i.e. that the barrier height H_b is lowered the most at the lowest switching field; the
incoherent switching volume is not the whole particle volume, but only a 0.8 μm "rim" of the
particle, where the magnetization is strongly canted (corresponding to the activation volume V_a);
the applied field is H_c; the barrier height $E_K = K_uV_a (1-H/H_b)^2 = 10^{-6}$ erg, it is still several orders
of magnitude higher than the thermal energy of $E_T \cong 40 \ k_BT \cong 10^{-12}$ erg. This is in agreement with
the experimental data, that there was no observable aftereffect on the 2D array of garnet particles
at room temperature, independent of the magnetic field, applied to lower the barrier height [23].

However, upon increasing the temperature, the anisotropy barrier is lowered, the coercivity
is decreasing (at $T = 50°C \ H_c = 164$ Oe; at $T=72°C \ H_c = 128.5$ Oe); the thermal fluctuations
increase, and it becomes possible to observe the rotational aftereffect. The magnetic aftereffect,
i.e. the time evolution of the number of particles, switched during 10 s intervals at 50°C in
$H=190$ Oe, is plotted in Fig.6. This plot reflects the distribution of the barrier heights of the
particles. At 50°C the distribution of particle's switching time is rather even. The "best" particle,
with no defects is switching the last (130 s), as it has the highest barrier. At 72°C the barriers are
much lower, the switching proceeds faster, the last observed particle switches in 70 s [24]. This
means for a future patterned recording medium, switching by rotation, the temporal and thermal

stability at room temperature is of much less concern, than for a traditional continuous thin film, where thermal relaxation due to domain wall motion processes is significant. However, the thermal stability at elevated temperatures depends primarily on the temperature dependence of the anisotropy energy. The magnetocrystalline anisotropy is usually a strong function of the temperature, decreasing as fast as $K(T) \approx M_s(T)^3$. This means that special attention should be paid to the temperature sensitivity of the switching effects in 2D patterned media above room temperature.

CONCLUSIONS

Factors, affecting the stability of the magnetic states of the elements and the system of 2D patterned media have been investigated. Regular 2D arrays of nanosize magnetic particles, having a potential application in future extreme high density magnetic recording, are now manufactured at several laboratories. The stability of the system depends on the statistical distribution of the up- and down switching fields of individual elements of the array. The mean value of the switching fields of the elements is equal to the major loop coercivity of the system. However, the standard deviation of the switching fields depends on the local effective anisotropy fields of crystalline and manufacturing defects, leading to premature switching of the particles with strong defects, and stabilizing against overwriting the "best" particles. The unexpectedly large standard deviation of the switching field distribution is a major obstacle on the road to magnetic RAMs. Introduction of a well-defined, technologically completely reproducible 'weak point" might reduce the switching field instabilities, however, at the price of a lower average switching field.

Another factor affecting stability is the (magnetostatic) interaction between magnetically separated elements. Its mean value depends on the saturation magnetization of the system, on the total magnetization of the system with up- and down magnetized elements, and on the geometry of the separation between particles. High magnetization materials and high density increases the interaction fields. The standard deviation of the interaction field depends not only on the statistical errors in the geometry of the array, but it depends also on the total magnetization of the system. This means, that for a 2D magnetic recording medium, the stability of the recorded information depends on the information itself.

The magnetic properties of these systems depend very strongly on the shape, size, and geometry of the elements. The switching of the magnetization of non-ellipsoidal particles proceeds via incoherent rotation. The internal field and the distribution of the magnetization in these particles is strongly inhomogeneous. The switching field is significantly reduced from the idealized Stoner-Wohlfarth value. The dominant source of reduced switching field is the inhomogeneous internal field, resulting in a non-collinear magnetic structure around the corners and edges, serving as starting points for magnetization reversal, even in systems, free from manufacturing and crystalline defects.

The stability against thermal excitation depends on the details of the magnetization process. The magnetization process in film and bulk materials involves both low energy barrier domain wall motion and high energy rotational processes. However, the thermal stability of single domain particles, switching by rotation, is much higher than for a continuous medium, which has a much broader switching barrier distribution, ranging from the domain wall motion coercivity up to the anisotropy field.

Experimental data for a model system of a 2D square array of single crystalline, strongly uniaxial, single domain magnetic garnet particles illustrate the effects of statistics, shape, magnetization process, and thermal relaxation effects on the of magnetic states of the system.

REFERENCES

1. S. Ganesan, C. M. Park, K. Hattori, H. C. Park, R. L. White, H. Koo and R. D. Gomez, IEEE *Trans. Magn.*, **36**, 2987 (2000).
2. Jose I. Martin, Jose L. Vicent, Jose L. Costa-Kramer, L. Menendez, Alfonso Cebollada, Jose V. Anguita, and Fernando Briones, IEEE *Trans. Magn.*, **36**, 3002 (2000).
3. C. A. Ross, T. A. Savas, H. I. Smith and M. Hwang, *IEEE Trans. Magn.*, **35**, 3781 (1999).
4. C. Stoner and E. P. Wohlfarth, *Phil. Trans. Roy. Soc. London*, **A420**,.599, (1948).
5. M. Pardavi-Horvath and G. Vertesy, *IEEE Trans. Magn.*, **30**, 124 (1994).
6. I.D. Mayergoyz, *Mathematical Models of Hysteresis*, Berlin, (Springer Verlag, 1991)
7. E. Della Torre, *Magnetic Hysteresis*, (IEEE Press, 1999).
8. M. Pardavi-Horvath, "Switching properties of a regular two-dimensional array of small uniaxial particles" *IEEE Trans. Magn.*, **32**, 4458 (1996).
9. M. Pardavi-Horvath, Guobao Zheng, G. Vertesy and A. Magni, *IEEE Trans. Mag.*, **32**, 4469 (1996).
10. M. Pardavi-Horvath, *J. Magn. Magn. Mater.*, **177-181**, 213 (1998).
11. Y. D. Yan and E. Della Torre, *J.Appl. Phys.*, **67**, 5370 (1990).
12. M. Pardavi-Horvath, Guobao Zheng, G. Vertesy and A. Magni, *IEEE Trans. Magn.*, **32** , 4469 (1996).
13. R. I. Joseph and E. Schloemann, *J. Appl. Phys.*, **36**, 1579 (1965).
14. Xiaohua Huang and M. Pardavi-Horvath, *IEEE Trans. Magn.*, **32**, 4180 (1996).
15. M. Pardavi-Horvath and Guobao Zheng, "Inhomogeneous internal field distribution in planar microwave ferrite devices" In *"Nonlinear Microwave signal processing: Towards a new range of Devices"*, Ed. R. Marcelli, Ch. 3. (Kluwer., Amsterdam, 1996) pp.41-65
16. Martha Pardavi-Horvath, Jijin Yan and J. Roger Peverley, *IEEE Trans. Magn.*, (2001) *in press*
17. N. A. Usov and S. E. Peschany, *J. Magn. Magn. Mater.*, **135**, 111 (1994).
18. W. Rave, K. Ramstöck and A. Hubert, *J. Magn. Magn. Mater.*, **183**, 329 (1998).
19. M. Pardavi-Horvath, G. Vertesy, B. Keszei, Z. Vertesy, and R. D. McMichael, *IEEE Trans. Magn.*, **35**, 3871, (1999).
20. M. Pardavi-Horvath, *J. Magn. Magn. Mater.*, **198-199**, 219 (1999).
21. S. M. Stinnett, W. D. Doyle, P. J. Flanders and C. Dawson, *IEEE Trans. Magn.*, **34**, 1828, (1998); S. M. Stinnett, W. D. Doyle, IEEE *Trans. Magn.*, **36**, 2456 (2000).
22. J.-P. Jamet, S. Lemerle, P. Meyer, J. Ferre, B. Bartenlian, N. Bardou, C. Chappert, P. Veillet, F. Rousseaux, D. Decanini and H. Launois,,*Phys. Rev. B*, **57**, 14320 (1998).
23. M. Pardavi-Horvath, G. Vertesy, B. Keszei and Z. Vertesy, *J. Appl. Phys.*, **87**, 7025 (2000).
24. Martha Pardavi-Horvath , Gabor Vertesy, and Antonio Hernando, *IEEE Trans. Mag.*, (2001) *in press*.

Synthesis and Self-Assembly of Films
Containing FeCoPt Nanoparticles

Min Chen and David E. Nikles*
The University of Alabama, Tuscaloosa,
Center for Materials for Information Technology,
Box 870209, Tuscaloosa, Alabama, 35487-0209, US
*dnikles@mint.ua.edu

ABSTRACT

$Fe_{49}Co_7Pt_{44}$ and $Fe_{40}Co_{17}Pt_{43}$ nanoparticles were synthesized by simultaneous chemical reduction of platinum acetylacetonate and cobalt acetylacetonate and thermal decomposition of iron pentacarbonyl. As-prepared the particles had a disordered face-centered cubic lattice with an average diameter of 3.2 nm and were superparamagnetic. These particles were well dispersed in a 50/50 mixture of hexane and octane. The particles self-assembled into ordered superlattices when deposited onto carbon coated Cu TEM grids or onto single crystal Si (100) substrates. After vacuum annealing (from 500°C to 700 °C), the particles transformed to the tetragonal phase. The coercivity of the film strongly depended on the composition and annealing temperature. For the $Fe_{49}Co_7Pt_{44}$ film, coercivity of 8700 Oe and a squareness of 0.75 after annealing at 700 °C for 30 minutes. XPS shows existance of oxidized iron and cobalt on the surface of film.

INTRODUCTION

Ordered superlattices of nanosize particles have received considerable attention in recent years, as they present an interest both for fundamental and potential applications. Some of methods used for preparing ordered superlattices from the liquid phase are Langmuir-Blodgett technique, [1] self-assembly by slowing evaporation of solvent [2-5], and electrophoretic deposition [6]. It has been found that formation of ordered closed-packing nanoparticle array requires the monodispersed particles and proper stabilization by surfactants. The synthesis of nanoparticles, characterized by a low size distribution, is a new challenge in solid-state chemistry. Due to their small size, nanoparticles exhibit novel material properties that differ considerably from those of the bulk solid state. Up to date, ordered self-assembly of nanocrystals has been successfully fabricated for several materials, such as Ag [2], Au [3], Fe_2O_3 [4], CoO [5].

Equatomic FePt and CoPt nanocrystals attracted high interest for the ultrahigh density magnetic hard media because they have large uniaxial magnetocrystalline anisotropies (K_u) due to their tetragonal $L1_0$ crystal structure. Recently, $(Co_{100-x}Fe_x)_{50}Pt_{50}$ thin films, with $20<x<68$, were reported to have K_u between FePt and CoPt [7]. Progress in magnetic recording density is due in part to the development of media with finer and finer grain magnetic films. It has been estimated that, if an magnetic nanocrystals with sizes down to ~3 nm, the storage density can be up to 100-1000 Gbits/in^2 [8-9]. Thin granular films of ferromagnetic materials formed by sputter deposition are already the basis of conventional rigid magnetic storage media. Recently, two chemical methods have been employed to produce magnetic cobalt nanoparticles, including

solution phase metal salt reduction in reverse micelles [10] and in organic solvent [11]. Ordered arrays of nanocrystal FePt alloy from simultaneous polyol reduction of $Pt(acac)_2$ and thermal decomposition of $Fe(CO)_5$ has also been reported [12]. However, we found any reports of the chemical synthesis and self-assembly of CoFePt nanoparticles.

EXPERIMENTAL DETAIL

Materials and synthesis

All materials were used without further purification. Iron pentacarbonyl [$Fe(CO)_5$], cobalt acetylacetonate [$Co(acac)_2$], platinum acetylacetonate [$Pt(acac)_2$], 1, 2-hexadecanediol, octyl ether, oleic acid and oleyl amine were purchased from Aldrich. Hexane and octane were from Fisher Scientific.

FeCoPt nanoparticles were prepared by simultaneous thermal decomposition of $Fe(CO)_5$ (1.0 mmol) and polyol reduction of $Co(acac)_2$ (from 0.1 to 0.25 M) and $Pt(acac)_2$ (0.5M) in organic solvent of octyl ether. $Pt(acac)_2$ and $Co(acac)_2$ were combined with 10 mL of dioctylether in a three-neck flask and dissolved at 120 °C under N_2 protection. 1,2-Hexandecanediol (390 mg) was dissolved in 10 mL of dioctylether and heated to 80°C. The dissolved 1,2-hexadecanediol, 0.13 mL of $Fe(CO)_5$, 0.16 mL of oleic acid and 0.17 mL of oleylamine were added to the above mixture of $Co(acac)_2$ and $Pt(acac)_2$ solution, respectively. Under nitrogen gas protection, the mixture solution was heated to 286°C (the boiling temperature of dioctylther). After being refluxed for 30 minutes, the reaction mixture was cooled down to room temperature. Ethanol (40 mL) was added to precipitate the particles. The particles were washed twice with ethanol to remove the excess diol and reaction byproducts, finally separated by centrifugation. The black products were purified by re-dispersing in hexane and re-precipitating by adding ethanol.

The FeCoPt particles were dispersed in 10 mL of mixture of (1:1) hexane and octane, containing 0.05mL of oleic acid and 0.05 mL of oleylamine. In order to obtain TEM image of self-assembled nanoparticles, The above surfactants stabilized FeCoPt dispersion was diluted four times with the mixture of (1:1) hexane and octane, and 0.01-0.05 mL of diluted dispersion were dropped on carbon-coated Cu TEM grids which were put on 0.3*0.3 mm^2 Si(100) waver in order to constrain the dispersion in the desired region. Samples assembled and annealed on SiO_2/Si(100) waver were also prepared for EDS, XPS, X-ray diffraction, and magnetic measurements. The as-deposited samples were annealed under vacuum (<1*10^{-7} torr) at 500 °C, 600 °C and 700 °C, respectively, for 30 minutes.

Characterization.

X-ray diffraction (XRD) data were acquired on Rigaku D/MAX-2BX Horizontal XRD Thin Film Diffractometer. Transmission electron microscopy (TEM) microphotographs were carried out on a Hitachi 8000 electron microscope operating at 200 kV. Energy Disperse spectroscopy (EDS) was obtained with a Philips XL 30 scanning electron microscope equipped with EDS. Chemical analysis was carried out with Kratos Axis 165 XPS/Auger system. Magnetic measurement was obtained with Princeton Micromag™ 2900 Alternating Gradient Magnetometor (AGM).

RESULTS AND DISCUSSION

Chemical and phase analysis of CoFePt nanopartices

The chemical composition of FeCoPt nanoparticles from EDS, table I, shows that the composition of the particles can be controlled by the relative amounts of Fe, Co and Pt charged to the reactor. The relationship is not direct as the amount of iron incorporated into the particles was less then the amount of iron pentacarbonyl charged to the reactor.

Table I. Comparison of the mole percent reactants charged to the reactor and the composition of the FeCoPt nanoparticles

Batch		Fe	Co	Pt
1	Charged	63	6	31
	Found	49	7	44
2	Charged	57	14	29
	Found	40	17	43

As-prepared the FeCoPt particles had a face center cubic lattice. The crystallite size was estimated to be 3.2 nm by analyizing the (111) peak from XRD. This number was close to the particle size of FeCoPt (3.6 nm) from TEM image. When the samples were annealed under vacuum or Ar mixed with 2% of hydrogen gas, the particles transformed to the tetragonal phase. The degree of transformation increased with annealing temperature from 500°C to 700°C. However, the samples were also sintered significantly when annealing temperature is above 600°C. After annealing at 600°C the crystallite size ($d_{crys(111)}$) of $Fe_{49}Co_7Pt_{44}$ increases to 6.0 nm and increased to 16.2 nm after annealing at 700°C.

Ordered self-assembly of as-prepared FeCoPt nanoparticles

Fig.1 (a) show the 'honeycomb' arrays of $Fe_{49}Co_7Pt_{44}$ nanoparticles on the carbon-coated TEM grids. The ordered domain can extend to 150 nm in diameter. Sometimes, we also found wire arrays on the carbon-coated Cu grids. The 'honeycomb' and wire arrays actually both come from the hexagonal close-packing (HCP, ABAB stacking) of $Fe_{49}Co_7Pt_{44}$ nanoparticles. Fig. 1b and 1c show that "honeycomb" arrays can be transformed into "wire" array for HCP structure when tilting the sample by 20°.

(a)   (b)   (c)
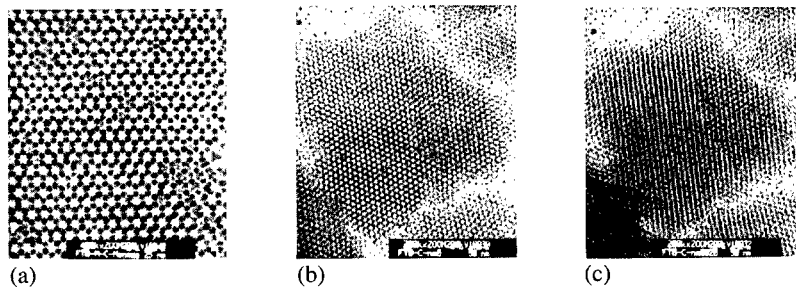
Figure 1. 'Honeycomb' ordered superlattice of $Fe_{49}Co_7Pt_{44}$ nanoparticles as-deposited on carbon-coated Cu grid. (a) magnification of 400 k, (b) magnification of 200 k when sample is not tilted and (c) when sample was tilted by 20°.

When the film thickness increases, $Fe_{49}Co_7Pt_{44}$ nanoparticles tend to self-assemble from ABAB close-stacking to ABCABC close-packing. We usually observed a mixture of ABAB and ABCABC packing (Fig. 2a) and hexagonal arrays (Fig. 2b). The calculation from the small angle electron diffraction pattern show the interparticle distance is 6.67 nm, which is about the twice of particle size.

(a)   (b)   (c)
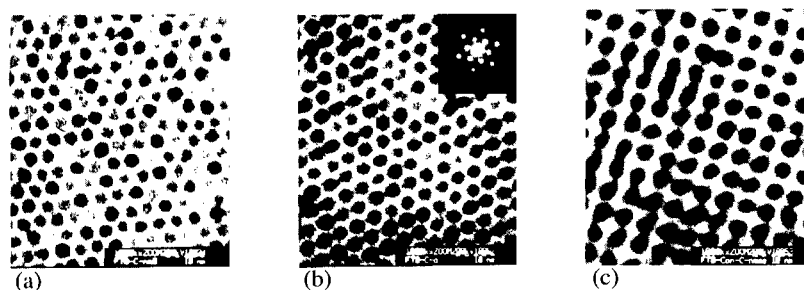
Figure 2. Ordered superlattices of CoFePt nanoparticles superlattices as-deposited on carbon-coated Cu grid. (a) & (b) Hexagonal, and (c) square nanoparticle lattice. The insert in (b) is small angle electron diffraction pattern of the sample.

Sometimes we also find square arrays for the thicker film (Fig.2c). The square arrays (more exactly, FCC particle latice) can be viewed as ABCABC close-packing of nanoparticles from [111] direction. The average interparticle distance in Fig3a and 3b is about 6.67 nm, which is 1.42 times of that in Fig. 2c (4.69 nm). This confirmed that the hexagonal and square arrays are from the same kind of stacking, but from different view direction.

Magnetic properties of FeCoPt films

Magnetic hysteresis curves were measured on an alternating gradient magnetometer. As-prepared the self-assembled FeCoPt films were superparamagnetic. After annealing under vacuum (10^{-7} torr) or Ar with 2% of H_2 gas, the films became ferromagnetic. Table II shows that the coercivity of FeCoPt film increases with annealing temperature. As the atomic percentage of cobalt increased, the coercivity decreased.

Table II. Coercivity (Oe) of self-assembled FeCoPt films (fixed annealing time for 30 minutes).

Annealing Temperature	500°C	600°C	700°C
$Fe_{48}Pt_{52}$	3970	6500	< 11600*
$Fe_{49}Co_7Pt_{44}$	2430	4500	8700
$Fe_{40}Co_{17}Pt_{43}$		3800	6590

* minor loop

CONCLUSIONS

We prepared $Fe_{49}Co_7Pt_{44}$ and $Fe_{32}Co_{21}Pt_{46}$ nanoparticles by simultaneous chemical reduction of platinum acetylacetonate and cobalt acetylacetonate and thermal decomposition of iron pentacarbonyl. As-prepared particles had an average diameter of 3.2 nm and were superparamagnetic. These nanoparticles were well dispersed in a hexanone or octane. FeCoPt tended to self-assemble into ordered arrays with either ABAB close-packing for the thin films or ABCABC close-packing for thick films while deposited onto a silica coated Cu TEM grids. The coercivity of FeCoPt film increased with annealing temperature, but decreased as the atomic percentage of cobalt increased.

ACKNOWLEDGMENTS

REFERENCES

1. J. H. Fendler, F. C. Meldrum. *Adv. Mater.* **7**, 607 (1995).
2. P.C. Ohara, J.R. Heath and W.M. Gelbart. *Angew. Chem. Int. Ed. Engl.* **36**, 1078 (1997).
3. R.P. Andres, J.D. Bielefeld, J.I. Henderson, D.B. Janes, V.R. Kolagunta, C.P. Kubiak, W.J. Mahoney and R.G. Osifchin. *Science* **273**, 1690 (1996).
4. M.D. Bentzon, J. Van Wonterghem, S. Mrup, A. Thölen and C.J.W. Koch. *Phil. Mag. B.* **60**, 169 (1989).
5. J.S. Yin and Z.L. Wang. *J. Mater. Res.* **14**, 503 (1999).
6. T. Teranishi, M. Hosoe, T. Tanaka, and M. Miyaka. *J. Phys. Chem. B.* **103**, 3818 (1999).
7. H. Kanazawa; G. Lauhoff; R. Sbiaa; T. Suzuki. *Digests of the 8th Joint MMM-Intermag Conference* Jan. 7-11 2001, p. QC-03.
8. D. Weller, A. Moser, L. Folks, M. E. Best, W. Lee, M. F. Toney, M. Schwickert, J.-U. Thiele, and M. F. Doerner, *IEEE Trans. Magn.* **36**, 10 (2000)
9. J. Numazawa and H. Ohshima. *J. Magn. Magn. Mater.* **176**, 1 (1997).
10. Taleb, A.; Petit, C.; Pileni, M. P. *Chem. Mater.* **9**, 950. (1997).
11. S. Sun and C.B. Murray. *J. Appl, Phys.* **85**, 4325 (1999).
12. S. Sun, C.B. Murray, D. Weller, L. Folks and A. Morser. *Science.* **287**, 1989 (2000).

Effects of Substrates on the Self-Assembling of FePt Nanocrystals

Min Chen and David E. Nikles*
The University of Alabama, Tuscaloosa,
Center for Materials for Information Technology,
Box 870209, Tuscaloosa, Alabama, 35487-0209, US
*dniklcs@mint.ua.edu

ABSTRACT

$Fe_{48}Pt_{52}$ nanoparticles were synthesized by the simultaneous chemical reduction of platinum acetylacetonate and thermal decomposition of iron pentacarbonyl. As-prepared the particles were spherical with an average diameter of 3 nm and a polydispersity of less than 5%. The particles were superparamagnetic and had a fcc structure. Highly ordered self-assembled supercrystals of particles were formed in TEM grids by deposition from dispersions in hydrocarbon solvents. Nanoparticles deposited on amorphous carbon-coated and SiO_2-coated Cu grids tend to assemble into small domains of hexagonal arrays. Larger domains of hexagonal arrays formed on Si_3N_4 membrane TEM grids. For thin multilayers, the FePt nanoparticles tends to assemble into hexagonal close-packed lattices (ABABAB stacking). For the thicker multilayers, ABCABC stacking was observed. Small angle X-ray reflectivity of the particles on a Si (100) substrate show highly ordered multiplanar structure with d-spacing of 6.2 nm. The coercivity of self-assembled FePt films strongly depended on the annealing temperature. After annealing at 700°C for 30 minutes, the particles transformed from FCC to "FCT" phase and the coercivity of film increased up to 11570 Oe. However, the particle size increased to 16 nm due to sintering.

INTRODUCTION

The "face-centered tetragonal" phase FePt is emerging as an important material in ultrahigh density magnetic data storage media. This phase has large uniaxial magnetocrystalline anisotropies (K_u) due to its tetragonal structure. The study of nanoscale magnetic domains are of both fundamental and pressing technical interest. The grain size of advanced recording media is rapidly being reduced to dimensions, where the magnetic materials approach the superparamagnetic limit. Development of a detailed understanding of the properties of magnetic nanocrystals is essential to the development of future magnetic recording technology. It is expected that if an ordered monolayer is formed by magnetic nanocrystals with sizes down to ~3 nm, the storage density can be up to 100-1000 Gbits/in^2 [1-2].

There are three conventional methods for magnetic material processing: vacuum sputtering, physical vacuum evaporation and molecular bean epitaxy. Chemical vacuum evaporation and electrochemical deposition are also used in processing the magnetic thin film. Progress in magnetic recording density is due in part to the development of media with finer and finer grain magnetic films [3-9].

Processing of ordered 2D or 3D structure of magnetic nanocrystalls becomes an area of great interest for the thin granular films. The synthesis of nanoparticles, characterized by a narrow size distribution, is a new challenge in solid-state chemistry. Due to their small size, nanoparticles exhibit novel material properties that differ considerably from those of the bulk

solid state. Up to date, ordered self-assembly of nanocrystals has been successfully fabricated for several materials, such as Ag [10], Au [11], Fe_2O_3 [12], CoO [13]. Recently, two chemical methods have been employed to produce magnetic cobalt nanoparticles, including solution phase metal salt reduction in reverse micelles [14] or in an organic solvent [15]. Ordered arrays of nanocrystal FePt alloy have also been reported [16], demonstrating the possibility of self-assembly of magnetic nanoparticles.

In the present paper, we try to understand the effect of substrates and other factors on self-assembly of FePt nanoparticles.

EXPERIMENTAL DETAILS

Materials and sample preparation

All materials were used without further purification. $Fe(CO)_5$, platinum acetylacetonate, octyl ether, oleic acid and oleylamine were purchased from Aldrich. Hexane and octane were purchased from Fisher Scientific.

FePt nanocrystals were processed by simultaneous thermal decomposition of $Fe(CO)_5$ and reduction of platinum acetylacetonate, $Pt(acac)_2$, in octyl ether, following Sun's procedure [16]. The particles were dispersed in a 50/50 mixture of hexane and octane, then dropped onto carbon-coated TEM grids, SiO_2 coated TEM grids or Si_3N_4 membrane window TEM grids. The solvent was allowed to evaporate. Samples were annealed under vacuum (<1 x 10^{-7} torr) at 500°C, 600°C or 700°C for 30 minutes. Samples assembled and annealed on $SiO_2/Si(100)$ wafer were also prepared for EDS, XPS, X-ray diffraction & scattering, and magnetic measurements.

Characterization

Wide angle X-ray diffraction (XRD) data were acquired on Rigaku D/MAX-2BX Horizontal XRD Thin Film Diffractometer. The small angle X-ray scattering (SAXS) data from 0.2 to 5° (2θ) were collected on Philips X'Pert system X-ray diffractometer using Cu Kα radiation and by activating beam attenuator Ni 0.125 mm (factor 151.00). A graded parabolic focusing mirror was utilized to transform a divergent X-ray beam into a quasi-parallel yet intensive incident beam with angular divergence of about 0.05°. Transmission electron microscopy (TEM) microphotographs were carried out on a Hitachi 8000 electron microscope operating at 200 kV. Energy disperse spectroscopy (EDS) were obtained with a Philips model XL 30 scanning electron microscope equipped with EDS. Chemical analysis was carried out with Kratos Axis 165 XPS/Auger system. Magnetic measurement was obtained with Princeton Micromag^{TM} 2900 alternating gradient magnetometor (AGM).

RESULTS AND DISCUSSIONS

Ordered self-assembling of as-prepared FePt nanocrystals

Figure 1 (a-d) shows the ordered monolayer of FePt nanoparticles on different kinds of TEM grids. The size distribution of FePt nanoparticleswere determined from the TEM image. The average diameter was 3 nm with a polydispersity of <5%. Magnetic measurement shows that these FePt nanoparticles were superparamagnetic. In general, FePt nanoparticles tended to self-

assemble into hexagonal monolayers. We found mutiple hexagonal domains of FePt particles on carbon-coated TEM grids and on SiO$_2$-coated TEM grids. On Si$_3$N$_4$ membrane grids the hexagonal domains were much larger, on the order of 800 nm. The nearest neighbor particle distance is in the range of 7.4-8.0 nm. The small angle electron diffraction in the insert of Fig. 1b shows a hexagonal ring. This also indicated the forming of various small domains of hexagonal arrays in different orientations. The small angle electron diffraction in the insert of Fig. 1c show hexagonal-spot pattern. The nearest neighbor particle distance is 7.6 nm. Interestingly, when the concentration of FePt is too low to form a continuous monolayer on Si$_3$N$_4$ membrane TEM grids, FePt nanoparticles still form discontinuous hexagonal arrays but in almost the same direction, as shown in Fig.1d. The carbon and SiO$_2$ coatings on TEM Cu grids are amorphous, while Si$_3$N$_4$ membrane is believed to be single crystal. The above evidence suggests the effect of substrates on the forming first layer self-assembling of nanoparticles.

(a)   (b)   (c)   (d)
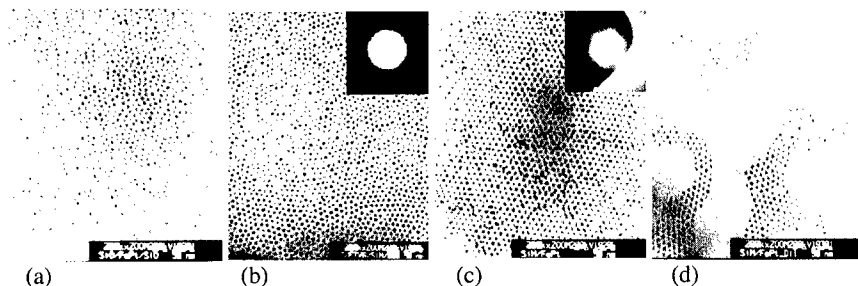
Figure 1. TEM images of ordered 2-D FePt on (a) SiO$_2$-coated Cu grid, (b) carbon-coated Cu grid, and (c) & (d) Si$_3$N$_4$ membrane TEM grids. The inserts in (b) and (d) are small angle electron diffraction patterns of samples.

For the multilayer FePt nanoparticles on different kinds of TEM grids, the TEM pictures show that "honeycomb" arrays of FePt on a carbon-coated Cu TEM grid (Fig2a) and wire superlattice on a SiO$_2$-coated Cu TEM grid (Fig. 2b). Actually, we also found "honeycomb" arrays of FePt on SiO$_2$-coated Cu grids and wire arrays on carbon-coated Cu grids. They both come from the hexagonal close-packing (HCP, ABAB stacking) of FePt. The honeycomb arrays can be transformed into wire array for HCP structure if changing the viewing from the [001] to the [211] direction. The small angle electron diffraction of "honeycomb" FePt structure confirms the hexagonal stacking with lateral d-spacing of 6.56 nm, which is twice the particle size. When the thickness of multilayer films increase, FePt nanoparticles self-assemble into square array on SiO$_2$-coated Cu grid (Fig. 2c) and highly ordered hexagonal arrays on Si$_3$N$_4$ membrane TEM grid. The square arrays (more exactly, FCC superlatice) can be viewed as ABCABC close-packing of nanoparticles from [111] direction.
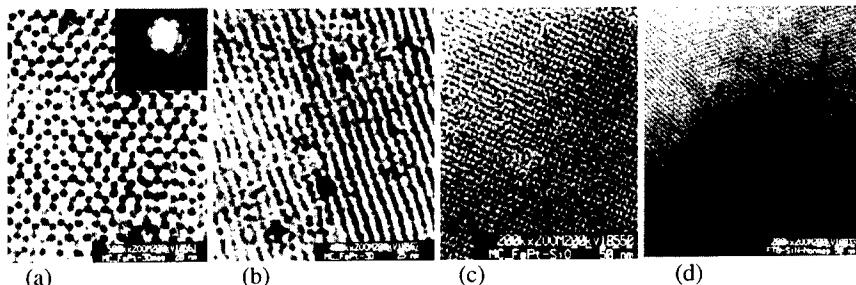
Figure 2. TEM images of ordered 3-D FePt on (a) carbon-coated Cu grid, (b)&(d) SiO_2-coated Cu grid, and (d) Si_3N_4 membrane TEM. The insert in (a) is small angle electron diffraction pattern of sample.

Small angle X-ray scattering (Fig.3) reveals the highly ordered multiplayer structure of FePt/surfactants with periodic thickness of 6.2 nm while as-depositing on $SiO_2/Si(100)$ wafer. The periodic thickness is also the d-spacing of nearest neighbor FePt layers [17]. Similar to Ref.[18], the analysis of peak positions show the FePt is likely to be HCP superlattice .
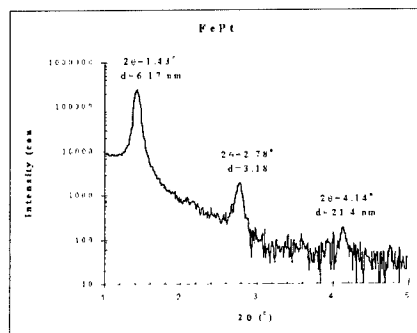
Figure 3. SAXS of ordered FePt multilayer on $SiO_2/Si(100)$ waver.

Mechanism of forming ordered assembled FePt film

The ordered HCP superlattice formation has been shown to apply to a variety of materials when the nanoparticles are stabilized by surfactant [10-16]. Molecular dynamics simulations shows that, without interparticle attraction, monodispersed hard spheres order when particle concentrations exceed a critical volume fraction of 0.49 [19]. In this case, the repulsion between particles must dominate when particles approach each other. Entropy is only the driving force for disorder-order phase transitions of hard spheres. HCP or FCC arrays are formed because they are the lowest energy state of stacking. Korgel's model shows that the balance between the interparticle attraction and the attraction between particles and the substrate (which can be tuned by solvent polarity) determines film structure, especially thickness while permitting nanoparticles to self-assemble into a HCP structure [20].

The attractive capillary force might be the main factor governing the ordering. It is reported that, for micro-size latex particles, HCP superlattice start to form when the thickness of the solvent layer approach the particle diameter during evaporation [21].

Effects of Annealing Temperature on FePt

Table I shows the temperature effect on the phase transformation, sintering and magnetic properties of FePt. When the annealing temperature increase to 500°C, FePt nanoparticles began to transform from fcc to tetragonal. The order parameter, S, was determined from the ratio of the c axis to the a axis lattice parameters as measured from x-ray diffraction. Increasing the annealing temperature increased the ordering parameter and the coercivity. The grain size was determined from the linewidth of the x-ray diffraction peaks. In our hands annealing the FePt articles resulted in significant increases in grains size.

Table I. Effect of annealing temperature on the crystallite size, ordering parameter, and magnetic properties of FePt films on silicon.

Annealing Temperature (°C)	Ordering parameter, S	Grain Size (nm)	Coercivity (Oe)
500	0.22	3.0	3970
600	0.52	7.6	6500
700	0.88	16.0	< 11600*
	$S=(1-(c/a))/(1-0.961)$		* minor loop

XPS depth profile of FePt shows that after vacuum annealing at 600°C for 30 minutes, iron is mostly in Fe (+2) state at the surface of FePt film, and in Fe (0) state in the bulk of the film. Platinum is in the metallic Pt (0) state through all the film. Fe and Pt never react with Si to form silicided FePt film even after annealing at 700°C.

CONCLUSIONS

For monolayer deposition, the as-deposited FePt tend to assembly into small domains of hexagonal arrangements nanoparticles on amorphous carbon-coated and SiO_2-coated Cu grids, while forming larger single domain of hexagonal arrangement on Si_3N_4 membrane. For the thin multilayer, the FePt nanoparticles tends to assembly into HCP (ABABAB stacking) on TEM grids (either carbon or SiO_2-coated). For the thick multilayer, FePt tends to form ABCABC close packing on TEM grids. Small angle X-ray scattering of as-deposited FePt on Si (100) substrate show highly ordered multiplayer structure with d-spacing of 6.2 nm between layers. The coercivity of self-assembled FePt film strongly depends on the annealing temperature. After annealed at 700 °C for 30 minutes, 88% of FePt nanocrystal transform from FCC to "FCT" phase, and the coercivity of film increase up to 11570 Oe with the squareness of 0.70. However, The particle size increase to 16 nm due to sintering. Processing high coercivity FePt film without significant sintering is the priority of our future work.

ACKNOWLEDGMENTS

REFERENCES

1. D. Weller, A. Moser, L. Folks, M. E. Best, W. Lee, M. F. Toney, M. Schwickert, J.-U. Thiele, and M. F. Doerner, *IEEE Trans. Magn.* **36**, 10 (2000)
2. J. Numazawa and H. Ohshima. *J. Magn. Magn. Mater.* **176**, 1 (1997).
3. E. S. Murdock, R. F. Simmons, and R. Davison, *IEEE Trans. Magn.* **28**, 3078 (1992).
4. T. Yogi and T. A. Nguyen, *IEEE Trans. Magn.* **29**, 307 (1993).
5. P.-L. Lu and S. H. Charap, *IEEE Trans. Magn.* **30**, 4230 (1994).
6. E. Grochowski and D. A. Thompson, *IEEE Trans. Magn.* **30**, 3797 (1994).
7. R. M. H. New, R. F. W. Pease, and R. L. White, *J. Vac. Sci. Technol.* **B12**, 3196 (1994).
8. D. N. Lambeth, E. M. T. Velu, G. H. Bellesis, L. Lee, and D. E. Laughlin, *J. Appl. Phys.* **79**, 4496 (1996).
9. S. H. Charap, P.-L. Lu, and Y. He, *IEEE Trans. Magn.* **33**, 978 (1997).
10. P.C. Ohara, J.R. Heath and W.M. Gelbart. *Angew. Chem. Int. Ed. Engl.* **36**, 1078 (1997).
11. R.P. Andres, J.D. Bielefeld, J.I. Henderson, D.B. Janes, V.R. Kolagunta, C.P. Kubiak, W.J. Mahoney and R.G. Osifchin. *Science* **273**, 1690 (1996).
12. M.D. Bentzon, J. Van Wonterghem, S. Mrup, A. Thölen and C.J.W. Koch. *Phil. Mag. B.* **60**, 169 (1989).
13. J.S. Yin and Z.L. Wang. *J. Mater. Res.* **14**, 503 (1999).
14. Taleb, A.; Petit, C.; Pileni, M. P. *Chem. Mater.* **9**, 950. (1997).
15. S. Sun and C.B. Murray. *J. Appl, Phys.* **85**, 4325 (1999).
16. S. Sun, C.B. Murray, D. Weller, L. Folks and A. Morser. *Science.* **287**, 1989 (2000).
17. A. County, C. Fermon and M.-P. Pileni. *Adv. Mater.* **13**, 254 (2001).
18. H. Zabel. *Appl. Phys.* A **58**, 159 (1994).
19. B. J. Alder; W. G. Hoover; and D. A. Young. *J. Chem. Phys.*, **49**, 3688 (1968).
20. B. A. Korgel and D. Fitzmaurice. *Phys. Rev. Lett.* **80**, 3531 (1998).
21. N. D. Denkov; O. D. Velev; P. A. Kralchevsky, I. B. Ivanov; H. Yoshimura; and K. Nagayama. *Langmuir*, **8**, 3183 (1992).

**Magnetic Micro- and
Nanocomposites**

The Role of Disorder in the Magnetic Properties of Mechanically Milled Nanostructured Alloys

Diandra L. Leslie-Pelecky[1], Elaine M. Kirkpatrick[1], Tom Pekarek[2], Richard L. Schalek[3], Paul Shand[4], Deborah S. Williams[1], and Lanping Yue[1]

[1]Center for Materials Research and Analysis and Department of Physics & Astronomy,
University of Nebraska, Lincoln NE 68588-0111
[2]Department of Chemistry and Physics, University of North Florida,
Jacksonville, FL 32224
[3]Composite Materials and Structures Center, Michigan State University,
East Lansing MI, 48824
[4]Physics Department, University of Northern Iowa,
Cedar Falls, Iowa 50614

ABSTRACT

Mechanical milling provides a unique means of studying the influence of grain size and disorder on the magnetic properties of nanostructured alloys. This paper compares the role of milling in the nanostructure evolution of two ferromagnets – $SmCo_5$ and $GdAl_2$ – and the subsequent impact of nanostructure on magnetic properties and phase transitions. The ferromagnetic properties of $SmCo_5$ are enhanced by short (< 2 hours) milling times, producing up to an eight-fold increase in coercivity and high remanence ratios. The coercivity increase is attributed to defect formation and strain. Additional milling increases the disorder and produces a mix of ferromagnetic and antiferromagnetic interactions that form a magnetically glassy phase. $GdAl_2$, which changes from ferromagnetic in its crystalline form to spin-glass-like in its amorphous form, is a model system for studying the dependence of magnetically glassy behavior on grain size and disorder. Nanostructured $GdAl_2$ with a mean grain size of 8 nm shows a combination of ferromagnetic and magnetically glassy behavior, in contrast to previous studies of nanostructured $GdAl_2$ with a grain size of 20 nm that show only spin-glass-like behavior.

INTRODUCTION

Mechanical milling is a high-energy deformation process that progressively introduces defect structures (dislocations and vacancies), atomic-scale chemical disorder and elastic strain energy into the initially crystalline starting powders through the shearing actions of ball-powder collisions [1,2]. Mechanical milling can be used to produce a variety of effects in intermetallic alloys due to the complex dependence of the nanostructure on milling intensity, temperature, and other factors [3]. The magnetic properties of a nanostructure depend on the intrinsic material properties, but also on grain size and grain size distribution, the magnetic character of the interphase (the region between grains), and the intergrain magnetic coupling. The challenge is to separate the different contributions to the overall magnetic properties by carefully controlling and characterizing nanostructure. The versatility of mechanical milling makes it a valuable tool for altering a material's structure and thus improving our understanding of correlations between nanostructure and magnetism.

This paper compares the magnetic behavior of two mechanically milled alloys. $SmCo_5$ and $GdAl_2$ are both ferromagnetic in their crystalline state. The goal of this paper is to understand how the nanostructure produced by mechanical milling affects the ferromagnetism and, in particular, how milling can induce a change in magnetic ordering from ferromagnetic to spin-glass-like. The first section of this paper details sample fabrication and the characterization techniques used to determine the nanostructure of the samples. Magnetic measurements are described in the second section of the paper and followed by a discussion of the correlations between nanostructure and magnetic properties.

EXPERIMENTAL DETAILS

Sample fabrication

Commercially purchased $SmCo_5$ powder (-100 mesh) was handled exclusively in an argon-filled glove box to prevent oxidation. Milling was performed in a hermetically sealed tungsten-carbide-lined vial in a SPEX 8000 mixer/mill with a 3:1 ball-to-powder mass ratio. The three milling balls were also made of tungsten carbide. Milling was stopped every 15 minutes for the first two hours and every hour thereafter to remove a small amount of powder for x-ray diffraction and magnetic measurements, and to break up powder clumps. Milling continued for a total of 30 hours in fifteen-minute intervals. Fifteen-minute rest periods between milling segments were used to minimize heating.

The starting $GdAl_2$ bulk sample was formed by arc melting Gd (99.9%) and Al (99.999%) shot in an argon atmosphere. The bulk sample was ground to a powder, then annealed at 800°C for 48 hours in a vacuum of ~10^{-6} torr. Milling was performed in a tungsten-carbide-lined vial in a SPEX 8000 mixer/mill for times up to 400 hours. A one-to-one ball-to-powder mass ratio was used with one tungsten-carbide ball. As with the $SmCo_5$, all milling and handling was performed in an argon atmosphere to minimize contamination and the sample was milled in fifteen-minute increments with fifteen-minute breaks to minimize heating.

Structural and magnetic measurements

X-ray diffraction patterns were obtained using a D-Max-B Rigaku diffractometer with Cu-K_α radiation. Bright-field transmission electron micrographs were taken using a 200 kV JEOL 2010 high-resolution microscope. Sample preparation for the $SmCo_5$ consisted of encapsulating milled powder in a room-temperature-cured epoxy and microtoming with a diamond knife to a thickness of approximately 100 nm. $GdAl_2$ powders were ultrasonicated in isopropanol and deposited on a carbon-coated Cu TEM grid.

Samples for magnetic measurements were loaded in paraffin-filled polyethylene bags in the glove box and sealed. The paraffin was melted to immobilize the randomly oriented powder particles during measurement. The polyethylene bags also protected the samples from oxidation during the transfer from the glovebox to the magnetometers. The coercivity (H_c) and remanence ratio (M_r/M_s, where M_r is the remanence ratio and M_s is the saturation magnetization) of the $SmCo_5$ were extracted from room temperature hysteresis loops.

Temperature-dependent magnetization measurements of $SmCo_5$ and $GdAl_2$ were made at fields from 100 Oe to 500 Oe using a Quantum Design MPMS SQUID magnetometer. The zero-

field-cooled (ZFC) magnetization was measured by cooling the sample to 5 K with no applied field, stabilizing the temperature, then applying the field and measuring as the temperature was increased to 300 K. The field-cooled (FC) magnetization was measured by apply the measuring field at 300 K and taking data as the sample was cooled.

Low-field magnetization measurements of $GdAl_2$ from 1 Oe to 100 Oe were made using a Quantum Design MPMS XL7 SQUID magnetometer with a magnet-reset option. The same procedure was used to measure the ZFC and FC magnetizations at low field, except that the sample was held at or above 250 K and the magnet quenched to reduce the residual field to < 0.5 Oe before cooling to 5 K and making FC and ZFC measurements as described above.

DISCUSSION

Evolution of the nanostructure

Figures 1a and 1b show the changes in the x-ray diffraction patterns with milling time for $SmCo_5$ and $GdAl_2$. The initial material in both cases has fairly sharp x-ray diffraction peaks at the same Bragg angles as those expected for the bulk materials. The annealing of the $GdAl_2$ prior to milling produces a much larger starting grain size and the diffraction peaks are correspondingly sharper. As milling time increases, the diffraction peaks of both materials become increasingly broad and diffuse, indicating grain refinement and disordering of the alloy.

The (110) $SmCo_5$ diffraction peak was Fourier decomposed and compared to a LaB_6 standard to remove instrumental broadening and contributions from the $K_{\alpha 2}$ doublet [4]. A single-profile analysis that separates linewidth broadening due to microstrain from broadening due to grain size was applied to extract the coherent diffracting crystallite size (DCS) and root-mean-squared microstrain [5]. The $GdAl_2$ data were analyzed using an integral-breadth technique after the $K_{\alpha 2}$ contributions were removed from the (111) diffraction peak.

2θ (degrees)
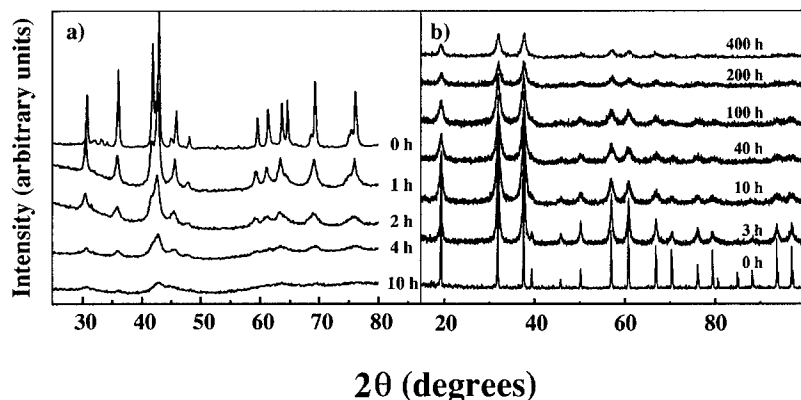
Figure 1. X-ray diffraction patterns for a) $SmCo_5$ and b) $GdAl_2$ as functions of milling time.

Figure 2 shows the DCSs as functions of milling time for the SmCo$_5$ and GdAl$_2$. The SmCo$_5$ grain size rapidly decreases from 20 nm to ~5 nm after only 4 hours of milling [6]. The GdAl$_2$ also experiences rapid reduction from its initial grain size of 90 nm, but takes considerably longer time to reach its final mean grain size of ~8 nm. The minimum attainable grain size depends on the melting temperature of the material; however, milling intensity and temperature also play important roles in determining the final grain size [7]. The structures presented are the results for two specific sets of processing parameters. Fabrication parameters can be varied to produce other nanostructures.

Transmission electron microscopy (TEM) was performed to further investigate the effects of milling on the morphology. TEM shows that the milled powder particles are close to spherical in shape, with a distribution of particle sizes. Figure 3 shows particle-size distributions from GdAl$_2$ milled for 300 hours and 400 hours. The mean grain size obtained from x-ray diffraction measurements remains constant over this range of milling times, and agrees well with the mean grain size obtained from the TEM measurements. Note that the sample preparation technique for the TEM grain-size-distribution measurement eliminates very large particles, so the possibility of there being larger single-or multi-grain particles remains.
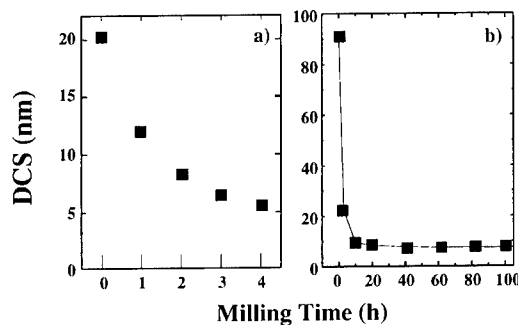
Figure 2: The dependence of coherent diffracting crystallite size (DCS) on milling time for a) SmCo$_5$ and b) GdAl$_2$.
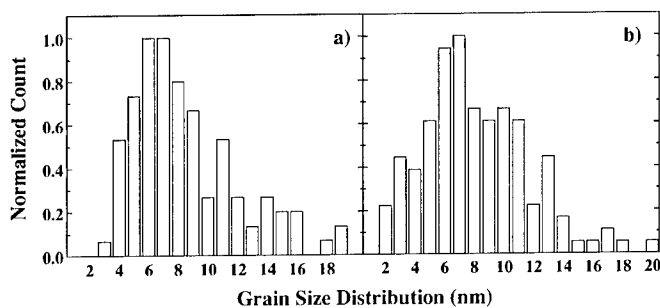
Figure 3: Particle size distribution for GdAl$_2$ milled for a) 300 hours and b) 400 hours. The mean grain size obtained from x-ray diffraction measurements is 8 nm for both samples.

Magnetic properties

Milling time is in general not a robust parameter for characterizing nanostructure due to the complex dependence of nanostructure on milling intensity, temperature, and other factors; however, SmCo$_5$ grains are refined to the limits within which a grain size can be obtained from x-ray diffraction within the first four hours of milling. We therefore must settle for parameterizing these data in terms of milling time.

Figure 4 shows the dependence of the coercivity H$_c$ and the remanence ratio M$_r$/M$_s$ on milling time for SmCo$_5$. The dependence of the coercivity on milling time appears similar to that expected for particles passing from multi-domain to single domain and finally to superparamagnetic sizes; however, the grain size changes from 20 nm to 4 nm during the period of greatest change in the magnetic properties.

Aging studies were used to probe the origin of the enhanced coercivity. The coercivity of SmCo$_5$ milled for 2 hours decreases by a factor of two over the two-week period immediately following the milling [8]. Measurements of the same samples were made every 48 hours for two weeks, with the samples stored in an Ar-filled glove box at room temperature in between measurements. The coercivity was constant after two weeks of aging. No changes in grain size were observed using x-ray diffraction; however, the diffraction peak positions shifted slightly toward higher angles as the samples aged. The large coercivity change at constant grain size eliminates grain size effects as the source of the enhanced coercivity. The shift in diffraction peak positions suggests that defects and strain play a large role in the magnetic properties. We attribute the increase in coercivity to the milling-induced defects and/or strain, which are metastable enough to be removed by room temperature annealing. The saturation magnetization decreased by only 0.1% during this time, so the coercivity decrease is not attributable to oxidation.

Figure 4 shows that the coercivity increases only during the first two hours of milling. Samples milled for longer times show lower coercivities and remanence ratios, although the remanence ratio remains above 0.5 for all milling times.
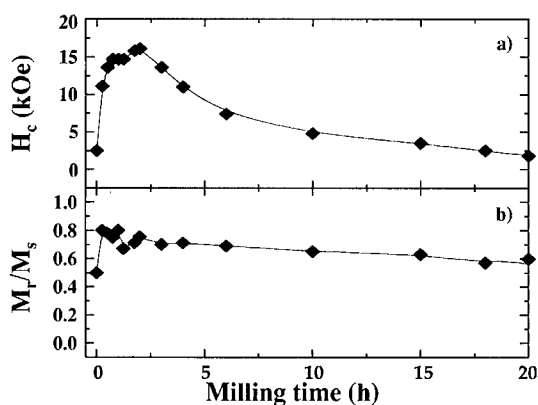
Figure 4. The dependence of a) the coercivity (H$_c$) and b) the remanence ratio (M$_r$/M$_s$) on milling time for SmCo$_5$.

Irreversibility between the field-cooled (FC) and zero-field-cooled (ZFC) low-field magnetizations increases as milling time increases. Figure 5 shows the magnetization at 100 Oe for SmCo$_5$ milled for 4 hours (top) and 15 hours (bottom). FC and ZFC magnetizations obey a $T^{3/2}$ behavior after 4 hours of milling; however, the sample milled for 15 hours shows a departure from the $T^{3/2}$ behavior at lower temperatures, and irreversibility between the FC and ZFC magnetizations. Subtracting the $T^{3/2}$ behavior shows that the remaining magnetization has a broad peak at low temperatures. Small cobalt clusters form for milling times greater than 20 hours, which prevents further investigation of the magnetically glassy phase.

Monitoring a paramagnet/ferromagnet or paramagnet/magnetic-glass transition in a high-Curie-temperature material such as SmCo$_5$ (T_c ~1000 K) is difficult because measurement at high temperatures would significantly change the nanostructure. GdAl$_2$ is a ferromagnet in its crystalline phase and shows spin-glass-like behavior when amorphous. The lower Curie temperature (T_c ~ 175 K) allows investigation of the paramagnet/ferromagnet transition without any temperature-induced nanostructure changes.

Earlier measurements of mechanically milled GdAl$_2$ showed irreversibility between the FC and ZFC magnetizations, and a broad peak spin-glass-like peak; however, the peak temperature occurs near 60 K instead of the 16 K freezing temperature found in amorphous GdAl$_2$ films [9,10]. Figure 6 shows the GdAl$_2$ zero-field-cooled magnetization at 100 Oe for milling times up to 80 hours. Unmilled GdAl$_2$ shows the characteristic ferromagnetic behavior. The transition lessens in magnitude and a broad peak near 45 K appears after 3 hours of milling. The peak continues to broaden and shifts to ~ 50 K after 80 hours of milling.
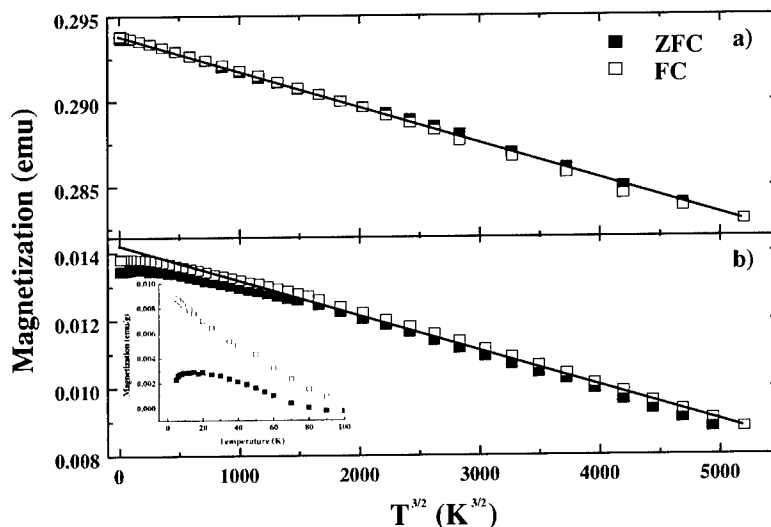
Figure 5. The field-cooled (FC) and zero-field-cooled (ZFC) magnetizations measured at 100 Oe for SmCo$_5$ milled for a) 4 hours and b) 15 hours. The FC magnetization is represented by open symbols and the ZFC magnetization is represented by solid symbols. The inset shows the FC and ZFC magnetizations for the 15-hour milled sample with the $T^{3/2}$ behavior removed.

Figure 2b shows that the GdAl$_2$ reaches its final grain size of 8 nm after 40 hours of milling; however, the magnetic properties continue to change with additional milling, despite the lack of further grain reduction. This indicates that disordering is the dominant effect of extended milling. Although the data in Figure 6 appear to show that ferromagnetism has disappeared by 80 hours of milling, measurements at lower fields reveal residual ferromagnetism. Figure 7 shows the FC and ZFC magnetizations in a field of 5 Oe for samples milled for 200 h and 300 h. The position of the peak measured in a field of 5 Oe occurs at the same temperature as the measurements at 100 Oe, in contrast to earlier reports [9,10]. As in the case of SmCo$_5$, ferromagnetic and spin-glass-like behaviors are observed, although the ferromagnetic component in GdAl$_2$ is weaker. The magnitude of the magnetization for the 300 h data is larger than for the 200 h data, which suggests that the proportion of the sample in the spin-glass-like phase
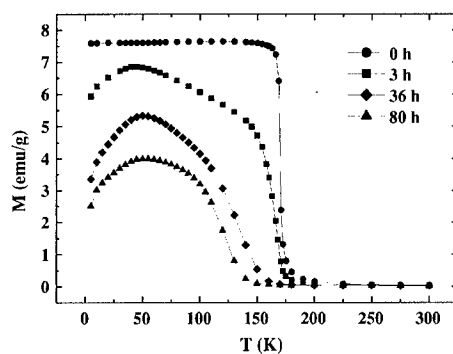
Figure 6. The dependence of the magnetization on the milling time for GdAl$_2$. All data were taken in a field of 100 Oe in the ZFC configuration.
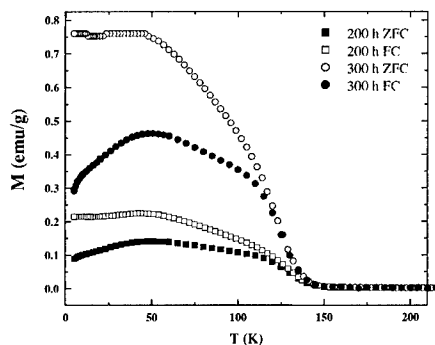
Figure 7. The dependence of the magnetization at 5 Oe on the milling time for GdAl$_2$ milled for 200 h (squares) and 300 h (circles). The ZFC data are represented by solid symbols and the FC data by open symbols.

increases with milling time. The observed behavior differs from canonical spin-glass behavior in that the separation between the FC and ZFC curves occurs at a much higher temperature than the peak temperature, and that the FC magnetization displays a large offset relative to the ZFC magnetization. Lower-field measurements indicate that the separation point between the FC and ZFC curves shown near 120 K in Figure 7 is actually coincident with a second magnetic transition. The ZFC magnetization at 1 Oe for 300-hour milled $GdAl_2$ (Figure 8) shows the presence of the second magnetic transition more clearly.

The relationship between nanostructure and magnetism

The magnetic properties of our mechanically milled $GdAl_2$ are different than those observed by Zhou and Bakker (ZB) [9,10]; however, the physical origins of the magnetically glassy behavior can be elucidated by investigating how differences in nanostructure affect magnetic properties. Mechanical milling of $GdAl_2$ has two primary effects: the introduction of quadruple-defect disorder and grain refinement. Quadruple-defect disorder results from the large difference between the sizes of Gd and Al atoms, which allows Al to substitute on the Gd sublattice, but prevents Gd from substituting on the Al lattice. ZB used low-intensity milling and started with a grain size of about 45 nm, while our experiment used high-intensity milling and a larger starting grain size of about 90 nm. The milling intensity and degree of disorder of the starting materials can significantly affect the nanostructure of the final material and thus its magnetic properties. The volume ratio of crystalline to amorphous phases, and the degree of disorder within and at the surface of the grains also play important roles in determining magnetic properties. Our results underscore the sensitivity of magnetic properties to nanostructure.

The initial stages of milling produce an exponential decrease in the crystallite size, along with the introduction of small amounts of disorder. The decrease of the Curie temperature with milling time could indicate finite size effects on the Curie temperature due to grain refinement, and/or the effect of disorder weakening the Gd-Gd exchange. Once the grain size has reached its minimum value, the dominant effect of continued milling is to increase disorder. This is consistent with changes in the magnetic properties that are observed after the mean grain size has reached a steady state.
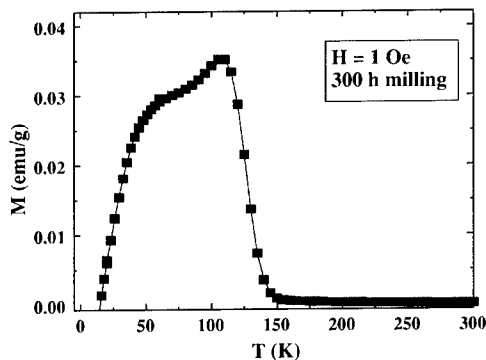
Figure 8. The magnetization of $GdAl_2$ after 300 hours of milling in a measuring field of 1 Oe.

ZB's GdAl$_2$ 'spin-glass' sample has a mean grain size of 20 nm. The majority of the atoms are in the bulk, which suggests that the broad peak in the ZFC magnetization is characteristic of grains of disordered GdAl$_2$. Finite-size effects are not expected to be significant at a grain size of 21 nm. ZB observe a feature in the ZFC magnetization near 16 K – the temperature at which amorphous GdAl$_2$ shows a freezing transition. Although ZB do not address this feature specifically, it is likely that some significantly amorphized material is present.

Although our nanostructured GdAl$_2$, with a final mean grain size of 8 nm, has a much larger fraction of atoms on surfaces or interfaces, ferromagnetic interactions remain dominant enough to produce a strong ferromagnetic transition, albeit with a lower Curie temperature than the bulk. Additional investigation of the effect of milling parameters on the final nanostructure is underway so as to produce a sample free of ferromagnetic effects.

Modder and Bakker found a combination of magnetically glassy and ferromagnetic behavior in mechanically milled GdIr$_2$ with a grain size of ~10 nm [11]. Gd and Ir are much closer in atomic diameter than Gd and Al, Gd can be transferred to the Ir sublattice and vice-versa. Ferromagnetic and spin-glass-like transitions (at 150 K and 20 K) are observed in mechanically milled GdIr$_2$. Modder and Bakker call this a re-entrant spin glass; however, it is more likely that their nanostructured GdIr$_2$ is a two-phase system, with one phase responsible for the ferromagnetic behavior and one responsible for the spin-glass-like behavior. The role of the non-magnetic element in mediating Gd-Gd coupling was cited by Modder and Bakker as important in explaining the differences in the magnetic properties of GdIr$_2$ and GdAl$_2$. Our results show that it is possible to obtain two-phase behavior similar to that found in GdIr$_2$ in GdAl$_2$ with the appropriate nanostructure.

The degree of long-range order appears to be critical to the observation and temperature of the peak in the ZFC magnetization. Magnetic and structural measurements of GdAl$_2$ thin films indicate the presence of ferromagnetic order on a length scale of 2-4 nm [12]. The observed 16 K freezing temperature of GdAl$_2$ films may be due to coupled ferromagnetic regions with random orientation. Rettori, et al. found that Gd can induce significant random anisotropy effects [13]. Amorphous Gd$_x$Al$_{1-x}$ is spin-glass-like for $x \leq 0.4$ and ferromagnetic for $0.56 < x < 0.81$. A peak in the susceptibility for $0.4 < x < 0.56$ is observed in low-field measurements; however, the same samples showed ferromagnetic behavior in high-field measurements [14]. The observation of different behaviors in the same sample can be clarified by Figures 7 and 8. The components in the two-phase system respond differently to the magnetic field. The relative amounts of each phase, the measuring field and the temperature determine whether ferromagnetic or spin-glass-like responses dominate the magnetization. Mechanically alloyed Ag$_{95}$Gd$_5$ has a spin-glass-like peak was observed near 5K that is attributed to interacting ferromagnetic Gd clusters with diameters on the order of a few nanometers [15]. These observations suggest that sample homogeneity and its effect on short-range magnetic order is critical to understanding the nature of magnetic ordering in glassy materials.

CONCLUSIONS

The properties of nanostructured ferromagnetic alloys change significantly with grain size and the amount of disorder introduced during mechanical milling. This sensitive dependence may be taken advantage of to explore the relative importance of grain size and disorder in determining magnetic properties. SmCo$_5$ exhibits enhanced coercivities and large remanence ratios when milled for short periods of time. The coercivity increase is attributed to the

formation of defects and increased strain, which can be removed by room temperature annealing. Continued milling produces irreversibility between field-cooled and zero-field cooled magnetizations at low fields, along with the appearance of a broad peak at low temperatures. Cobalt clustering results from extended milling, effectively limiting investigation of the phase responsible for the magnetically glassy behavior.

GdAl$_2$ has a lower Curie temperature (175 K) and undergoes a spin-glass-like transition in the amorphous phase, making it an ideal system in which to study the origins of magnetically glassy behavior. High-intensity milling was used to produce nanostructured GdAl$_2$ with a mean grain size of 8 nm. Magnetic measurements showed the presence of a ferromagnetic transition at 120 K and a broad peak at 50 K. The effect of disorder and intergrain interactions must be investigated to determine whether the broad peaks observed in nanostructured ferromagnets are truly indicative of spin-glass-like transitions.

ACKNOWLEDGEMENTS

REFERENCES

1) C.C. Koch, NanoStruct. Mater. **2**, 109 (1993).
2) C. Suryanrayana, Prog. Mater. Sci. **46**, 1 (2001).
3) C.C. Koch, Scripta Met. **34**, 21 (1996).
4) A.R. Stokes, Proc. Phys. Soc. London **61**, 382 (1948).
5) P. Ganesan, H.K. Kuo, A. Saavedra, and R.J. DeAngelis, J. Catal. **52**, 310 (1978).
6) Diandra L. Leslie-Pelecky and Richard L. Schalek, Phys. Rev. B **59**, 457 (1999).
7) J. Eckert, J.C. Holzer, C.E. Krill III, and W.L. Johnson, J. Mater. Res. **7**, 1751 (1992).
8) Diandra L. Leslie-Pelecky, E.M. Kirkpatrick, and R.L. Schalek, Nanostruct. Mater. **12**, 887 (1999).
9) G.F. Zhou and H. Bakker, Phys. Rev. Lett. **73**, 344 (1994).
10) G.F. Zhou and H. Bakker, Phys. Rev. B **52**, 9437 (1995).
11) I.W. Modder and H. Bakker, Phys. Rev. B **58**, 14479 (1998).
12) S.C. Hart, P.E. Wigen, and A.P. Malozemoff, J. Appl. Phys. **50**, 1620 (1979).
13) C. Rettori, D. Davidov, R. Orbach, and E.P. Chock, Phys. Rev. B **7**, 1 (1973).
14) T.R. McGuire, T. Mizoguchi, R.J. Gambino, and S. Kirkpatrick, J. Appl. Phys **49** (1978).
15) J. Tang, W. Zhao, J. O'Connor, C. Tao, and L. Wang, Phys. Rev. B **52**, 12829 (1995).

Electrochemical Deposition of FeCo Alloys and FeCo/TiO$_2$ Nanocomposites

I. Shao[a], P. M. Vereecken[a], R. C. Cammarata[a], P. C. Searson[a], and C. L. Chien[b]

[a]Department of Materials Science and Engineering
The Johns Hopkins University, Baltimore, MD 21218
[b]Department of Physics and Astronomy
The Johns Hopkins University, Baltimore, MD 21218

ABSTRACT

Electrochemical deposition of FeCo alloys with 1:1 atomic ratio has proved difficult due to cracking from high stress. By using a sulfamate electrolyte and optimizing other deposition parameters, we successfully electrodeposited high quality FeCo films of 20-25 μm in thickness and 7 mm in diameter. Using a suspension of hard oxide nanoparticles (25 nm TiO$_2$) in the electrolyte, we produced oxide-dispersion-strengthened FeCo/TiO$_2$ nanocomposite films with large grains. Enhanced strength was observed from these nanocomposites relative to pure FeCo alloys as determined from Knoop hardness measurements. In order to further improve the ductility of the alloys, vanadium has been codeposited with FeCo. Some preliminary results of FeCoV alloy deposition are reported.

INTRODUCTION

Iron-cobalt alloys near the equiatomic composition have superior soft magnetic properties with a very high saturation magnetization (24 kG), high permeability at high magnetic flux density, and low D.C. coercivity. In the field of micro-devices, such as hard disk drives, micro-actuators and micro-inductors, thin film deposition processes have to be developed to generate desirable magnetic materials. Electrochemical deposition is an important processing technology for microfabrication due to its low cost, high yield, low energy requirements, and capability for generating high-aspect-ratio features. However, electrochemical deposition of FeCo alloys has been problematic over the years.

Bulk FeCo alloys are primarily used in the manufacture of rotor and stator laminations in motors and generators for aircraft power generation applications. The inferior mechanical properties of these alloys, including low yield strength, low creep resistance, and poor ductility, inhibit many applications. Oxide dispersion strengthening can improve both yield strength and creep resistance. We have utilized electrochemical codeposition from an electrolyte containing a suspension of TiO$_2$ particles (25 nm in diameter) to produce oxide dispersion strengthened FeCo/TiO$_2$ nanocomposites. Large grain sizes of the order of 10 μm were observed for all these FeCo/TiO$_2$ films. Composition, hardness and magnetic properties were tested for these films.

EXPERIMENTAL

FeCo alloy films were deposited from an aqueous sulfamate solution of 0.75 M cobalt sulfamate (IMC Americhem) + 0.5 M iron(II) sulfamate (Strem Chemicals) + 0.4 M boric acid + 0.25 M sodium chloride + 0.025 M sodium borate + 0.025 M vitamin C + 1 g/l saccharine + 0.5 vol.% aerosol DPOS 45 surfactant (Cytec Industries) + 0.4 mM ammonium metavanadate. A small amount of vanadium was added to enhance the ductility of the alloy. Although no vanadium was detected in the deposited films (the detection limit of wavelength dispersive spectroscopy (WDS) was 0.1 wt.%), it was found that this solution produced more ductile films

than films produced from the vanadium-free electrolyte. The pH of the solution was about 4. After preparation the solution was kept under a nitrogen atmosphere at all times. The bath temperature was kept at 50 °C during deposition. Hiperco FeCo50 ($Fe_{49}Co_{49}V_2$ by weight) alloy from Carpenter Technology Corporation was used as the counter electrode. The counter electrode was separated from the working electrode with glass frit.

25 nm in diameter TiO_2 particles (Degussa P25) were added to the solution to make 0.1 vol.% TiO_2 suspensions for deposition of $FeCo/TiO_2$ nanocomposite films. The solution was stirred for at least one hour to make a stable suspension. The composition of FeCo and $FeCo/TiO_2$ films was determined by wavelength-dispersive spectroscopy (WDS), using a JXA-8600 SuperProbe. An anatase standard was used to calibrate the TiO_2 spectrum. Pure Fe, Co metal standards were used for calibration of Fe and Co spectrums. Knoop hardness was tested on all the films with a Leco M-400 microhardness tester using a load of 50 g. Magnetic hysteresis loops were measured using a vibrating sample magnetometer (VSM). Both atomic force microscopy (AFM) and scanning electron microscopy (SEM) images were used to investigate the microstructure and morphology of the films..

In order to codeposit more vanadium with FeCo, we replaced ammonium metavanadate (0.4 mM) in the solution with the more soluble vanadyl sulfate (50 mM $VOSO_4$). The FeCoV deposition solution is made of 0.5M iron sulfamate + 0.5M cobalt sulfamate + 0.4 M boric acid + 0.25 M sodium chloride + 0.025 M sodium borate + 0.025 M vitamin C + 1 g/l saccharine + 0.5 vol.% acrosol DPOS 45 surfactant (Cytec Industries) + 50 mM vanadyl sulfate. The pH was adjusted to 4 with sodium hydroxide. About 1 - 2 atomic percent of vanadium was detectable from energy dispersion x-ray spectroscopy (EDS) measurements. Hysteresis loops were measured for these FeCoV alloy films.

RESULTS AND DISCUSSIONS

FeCo alloy deposition

A series of FeCo alloy films were deposited at constant current densities of -5, -10, -20, -40, -100, -200, and -400 mA/cm^2 and at a rotation rate of 1000 rpm. The composition of FeCo as determined from WDS is plotted as a function of current density in figure 1. It can be seen that a Fe composition close to 50 at.% was achieved between -20 and -40 mA/cm^2. At higher current densities, a Fe composition of about 47 wt.%, independent of current density, was observed. At lower current densities, the film composition was strongly dependent on current density. The Fe^{2+} to Co^{2+} ratio in the solution was 2:3, whereas the ratio of Fe to Co in the deposits was about 1:1 for films formed at current densities higher than -10 mA/cm^2. Contrary to what would be anticipated from the equilibrium potentials for the single Fe^{2+}/Fe and Co^{2+}/Co redox couples (Fe is less noble than Co), Fe deposition was much faster than Co at those current densities. Such anomalous codeposition of Fe and Co is a common phenomenon for electrodeposition of iron group alloys [1].

The microstructure of the FeCo films was studied using AFM. Figure 2 shows an AFM image of an as-deposited FeCo film (-20 mA/cm^2, 1000 rpm). The deposited films were very smooth and the grain size was about 150-250 nm in diameter. Similar submicron grains were observed for all the other FeCo films deposited between -5 and -400 mA/cm^2.

Magnetic hysteresis loops were measured for these samples. The saturation magnetization was normalized to the volume of FeCo material in the film, which was calculated from the total charge passed during deposition, the film composition and the deposition efficiency for each
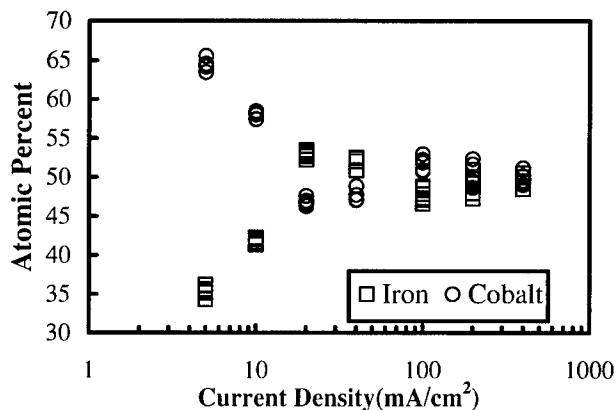
Figure 1. FeCo alloys composition as a function of deposition current density. Two samples were made at each current density. The $Fe^{2+}:Co^{2+}$ ratio in the electrolyte was 2:3.
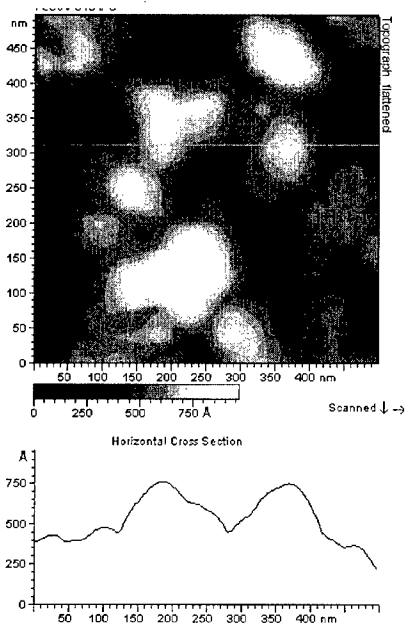
←**Figure 2.** AFM image of an as-deposited FeCo film made at -20 mA/cm^2 and 1000rpm.
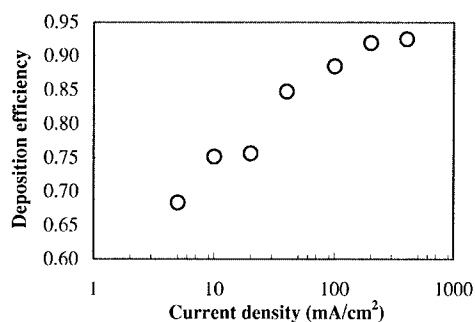
Figure 3. Deposition efficiencies of FeCo alloys versus deposition current density.

current density. Deposition efficiency is plotted as a function of current density in figure 3. It can be seen that deposition efficiency increases with increasing current density. Table 1 shows the saturation magnetization and coercivity of FeCo films together with the deposition efficiency and the film composition.

Knoop hardness tests were carried out with a load of 50 g on films polished with 0.05 μm Al_2O_3 paste. Table 1 also shows the hardness results for all FeCo films. It can be seen that hardness was not a sensitive function of film composition in the range of 33 - 51 wt.% Fe.

Table 1. Magnetic properties, deposition efficiency, and hardness of FeCo films deposited at different current densities.

Current densitym(mA/cm^2)	-5	-10	-20	-40	-100	-200	-400
Fe wt.%	33	38	51	50	46	47	47
Current efficiency	68%	75%	76%	85%	89%	92%	93%
$4\pi M_s$ (kG)	20.6	21.0	21.8	21.1	21.3	21.6	21.6
H_c (Oe)	33	29	12	16	6	6	8
Hardness (Gpa)	3.1	3.1	3.8	4.1	3.1	3.2	3.2

FeCo/TiO$_2$ deposition

A Fe / Co ratio of 1:1 was achieved for films deposited at current densities between -20 and -40 mA/cm^2. A series of FeCo/TiO$_2$ samples were deposited at a current density of -20 mA/cm^2 with different rotation rates. A concentration of 1 to 2 vol.% TiO$_2$ (25 nm in diameter) in the films was observed for films deposited from 0.1 vol.% TiO$_2$ solution. The Fe / Co ratio of these films was lower than pure FeCo alloys deposited with the same conditions and close to the electrolyte ion ratio. Apparently the presence of TiO$_2$ nanoparticles in the electrolyte inhibits the anomalous codeposition of Fe and Co as observed in the solution without TiO$_2$ particles.

Grain sizes of order of 10 μm were observed for all FeCo/TiO$_2$ nanocomposite films. Figure 4 shows a typical SEM image for an as-deposited FeCo/TiO$_2$ film deposited at 2000 rpm and -20 mA/cm^2 from 0.1vol.% TiO$_2$ solution. The average grain size was estimated to be 8 μm.

The hardness of the nanocomposite films is plotted as a function of rotation rate in figure 5. It can be seen that hardness increases as rotation rate. This is due to the increasing amount of embedded particles in the films when the rotation rate was increased. Similar behavior has been reported for the Ni/Al$_2$O$_3$ system [2].

The hardness of the electrodeposited FeCo/TiO$_2$ nanocomposites was compared to cast Hiperco FeCo alloys. The hardness of the electrodeposited FeCo/TiO$_2$ (1 to 2 vol.%) nanocomposites were on average 50% higher than the similar grain size Hiperco FeCo alloys from the Hall-Petch relation reported by Shang etc. [3].

Magnetic hysteresis loops were measured for all FeCo/TiO$_2$ films. The saturation magnetization was normalized to the volume of FeCo in the film. Figure 6 shows the magnetic hysteresis loops for a FeCo/TiO$_2$ nanocomposite film and a FeCo alloy film with a similar Fe:Co ratio. The Fe$_{40}$Co$_{60}$/TiO$_2$ film was made at -20 mA/cm^2 and 1000 rpm and the Fe$_{40}$Co$_{60}$/TiO$_2$ was made at -10 mA/cm^2 and 1000 rpm. From the figure, it is seen that the addition of TiO$_2$ slightly
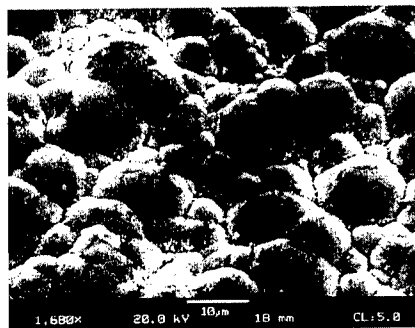
Figure 4. Scanning electron micrograph of an etched FeCo/TiO$_2$ nanocomposite film deposited from a 0.1vol.% TiO$_2$ solution at 2000 rpm and -20 mA/cm^2.

degraded the saturation magnetization, but improved the squareness of hysteresis loop. This can be attributed to a combined effect of grain size and nanoparticles incorporation.
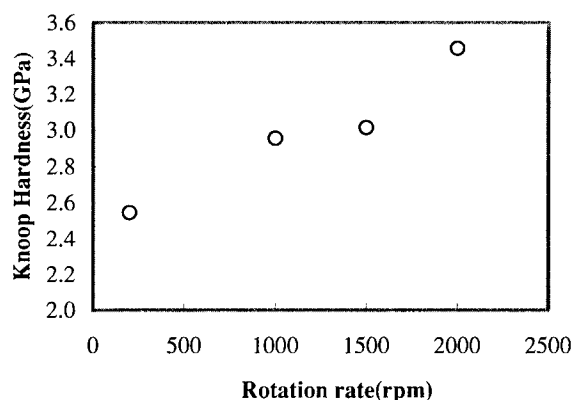
Figure 5. Hardness of the FeCo/TiO₂ nanocomposites deposited from 0.1 vol.% TiO₂ solutions.

FeCoV alloy deposition

Vanadium proved to be a very effective element that improved the ductility of FeCo alloys [4]. We attempted codepositing more V into the films by using a more soluble V salt VOSO₄. Figure 7 compares three i-U curves obtained from blank (a), V-only (b) and FeCoV (c) deposition solutions. Ammonium sulfamate replaced Fe sulfamate and Co sulfamate to make the blank solution, and VOSO₄ was added to the blank solution to make the V-only solution. All solutions were freshly made and kept under nitrogen atmosphere at all times. The i-U curve from the V-only solution shows two plateaus in the deposition stage compared to the blank solution. This may be due to the reduction of high valence V ions to lower valence V ions in the solution. By introducing Fe and Co ions into the electrolyte, we could still distinguish a similar plateau in the i-U curve. Very nice deposition and stripping peaks can be seen from figure 7 (c) from the FeCoV electrolyte.

A series of FeCoV samples with 7 mm in diameter were made at -20 mA/cm² and 1000 rpm. The samples were weighed before and after deposition to calculate the weight of the deposit. The films were smooth and highly reflective. The film composition was $Fe_{53}Co_{46}V_1$ measured with EDS. Deposition efficiency was calculated from the film weight and film composition. A value of 80% deposition efficiency was consistently obtained for all the samples. The film thickness was approximately 22 µm as calculated from the passed charged, taking into account the current efficiency.

Magnetic properties of FeCoV films were measured with VSM. A saturation magnetization value of 22 kGauss and a coercivity of 7 Oe were observed.

SUMMARY

We successfully produced high quality $Fe_{50}Co_{50}$ films electrochemically. Oxide dispersion strengthened FeCo/TiO₂ nanocomposite films were made by using FeCo electrolyte with a TiO₂ suspension. Hardness enhancement was observed due to particle incorporation. The TiO₂ particles played an important effect on the kinetics of the deposition as well as on the microstructure of the films. FeCoV alloy deposition was also perfected. Further investigation of

FeCoV codeposition and scaling-up the deposition cell to produce large samples is currently being conducted.

ACKNOWLEDGMENTS

REFERENCES

1. Abner Brenner, *Electrodeposition of Alloys*, Academic Press, 1963.
2. P.M. Vereecken, I. Shao, P.C. Searson, J. Electrochem. Soc., **147** (7), 2572-2575, (2000).
3. C.H. Shang, R.C. Cammarata, T.P. Weihs, C.L. Chien, J. Mater. Res. **15**(4), 835 (2000).
4. R.M. Bozorth, *Ferromanetism*, Institute of Electrical & Electronics, 1983.
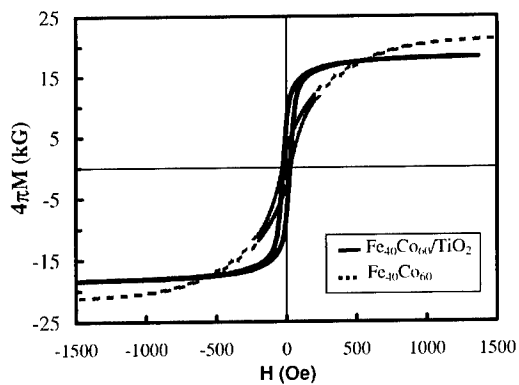
Figure 6. Magnetic hysteresis loops for $Fe_{40}Co_{60}/TiO_2$ (-20 mA/cm^2 and 1000 rpm), and $Fe_{40}Co_{60}$ (-10 mA/cm^2 and 1000 rpm) films.
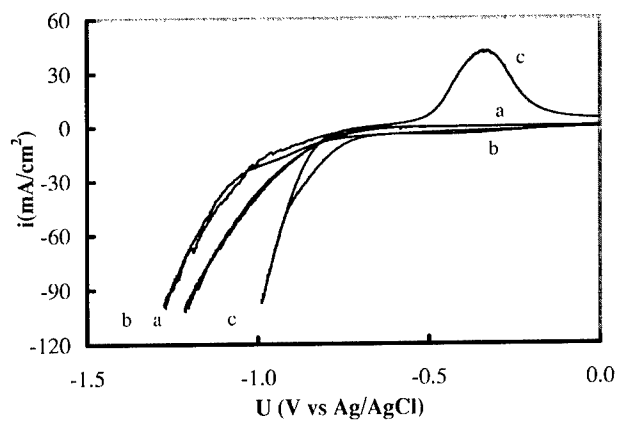
Figure 7. i-U curves from (a)blank solution, (b)V-only solution and (c) FeCoV solution.

High Strength Soft Magnetic Composites

Ronghai Yu[1], Michelle M. Corte-Real[1], Adrian Gorea[1], Libo Ren[3], Azar Parvizi-Majidi[3], and John Q. Xiao[1]

[1]Department of Physics and Astronomy, University of Delaware, Newark DE 19716, USA
[3]Department of Mechanical Engineering, University of Delaware, Newark DE 19716, USA

ABSTRACT

There has been an increasing demand for high temperature soft magnetic materials with mechanical properties better than those of existing commercial materials such as FeCo alloys. We have designed new magnetic composites by reinforcing FeCo alloys with high strength tungsten fibers. The composite materials were fabricated by electrodeposition. In general, the as-deposited composites have a relatively high coercivity H_c and low magnetic permeability μ, because of induced strain during fabrication. After appropriate thermal annealing, the composites have good soft magnetic properties, comparable to commercial bulk alloys. However, the saturation induction is reduced due to the non-magnetic inclusions. The composites also show significant enhancements in yield strength and tensile strength that increases linearly with fiber volume fraction as seen in other common composite materials. In addition, near zero creep is observed at 600 °C under a stress of 600 Mpa. The mechanical properties can be further improved by co-depositing soft magnetic material and Al_2O_3 onto the fibers. An approximately linear relationship was observed between the coercivity and volume fraction of Al_2O_3 particles. The square-root relationship was observed between the hardness and the Al_2O_3 concentration.

INTRODUCTION

There is an increasing demand for high-performance soft magnetic materials in the design of high-speed motors and generators for high temperature operation [1-5]. The mechanical strength of these materials at high temperatures is a crucial parameter in such applications. Fe-Co alloys exhibit high saturation magnetization M_s and high Curie temperatures T_c ($T_c \approx$ 900 °C) that make them potential candidates. The ordered Fe-Co alloys are excellent soft magnetic materials with negligible magneto-crystalline anisotropy K_1 [6]. However, equiatomic Fe-Co alloys are extremely brittle and other elements such as V are usually added to obtain workable materials. These additions however, significantly deteriorate the soft magnetic properties, due to the precipitation of a second phase [7-9]. Therefore, mechanical strength is achieved at the expense of magnetic performance.

We have developed new magnetic composites by reinforcing Fe-Co materials with tungsten fibers and Al_2O_3 particles. In the case of FeCo-fiber composites, the contributions to magnetic and mechanical properties come from two nearly independent entities, i.e. the FeCo matrix and fiber network, respectively. One immediate advantage of such materials is that one can optimize magnetic and mechanical properties in each entity independently, and thus no comprise between the magnetic and mechanical properties is necessitated. For further improvement in mechanical properties, hard fine particles of Al_2O_3 were dispersed in the matrix, to inhibit recrystallization and grain growth at elevated temperatures.

EXPERIMENTAL

Fiber and dispersion reinforced magnetic composites were fabricated by the electrochemical deposition of the alloys onto W fibres. An aqueous bath containing $CoSO_4 \bullet H_2O$, $FeSO_4 \bullet H_2O$, HBO_3, and saccharine [10] was used. The Al_2O_3 particles of diameter $d<0.1$ μm were mixed directly into the solution. Sulfuric acid was added to the bath to adjust the pH value to about 2.0.

Toroidal and long stripe samples were used to measure magnetic properties using a magnetic loop tracer, with a maximum field of 150 Oe. The magnetic measurements were made parallel to the long axis of the fibres. Grain sizes and precipitates were characterized by optical microscopy, SEM and TEM. The Vicker microhardness (HV) of the magnetic composites was measured using a load of 50 g for 10 s. Tensile tests were performed using an Instron mechanical tester.

RESULTS AND DISCUSSION

Room temperature magnetic hysteresis loops for the as-deposited and annealed $Fe_{50}Co_{50}$-W composites are shown in figure 1. The sample diameter was 50 μm and the diameter of the fiber was about 12 μm. In the as-deposited state, the samples are not magnetically soft and have low magnetic permeabilities and coercivities of about 16 Oe, whereas the annealed samples have good soft magnetic properties. The improvement of soft magnetic properties is related to a micro structural change during thermal annealing. First, the grain sizes increase from about 50 nm to 200 nm after heat-treatment, which reduces coercivity [11]. In addition, thermal annealing relieves the internal stress induced during the electrodeposition process. This internal stress, which causes a radial dependence of permeability, results in giant impedance effects in the as-deposited sample [12]. There are also other micro structural changes such as an increase in the structural order parameter and a decrease in the number of defects, which further enhance the soft magnetic properties.
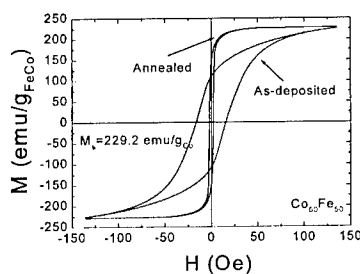
Figure 1. Magnetic hysteresis loops for the as-deposited and annealed Fe20Co80-W samples

A significant improvement of mechanical properties has been observed in these composites. In figure 2 the mechanical strength is presented as a function of the W fiber volume percent for

the annealed $Fe_{50}Co_{50}$-W samples. Both yield strength and tensile strength increase linearly with fiber volume percent as seen in other common composite materials [13]. In our sample geometry, the stress is applied on the matrix material and transferred to the W-fibers through the interface. The observation of such a composite behavior suggests good adhesion between deposited materials and W fibers. Magnetic measurements illustrated that FeCo thickness does not significantly alter the magnetic properties of the samples. More significantly, as shown in figure 3, the high temperature (600 °C) creep was found to be negligible in the FeCo-W composites. This is in contrast with commercial FeCo-based alloys, in which substantial creep takes place after about 50 hours, causing detrimental failures at high operating temperatures.
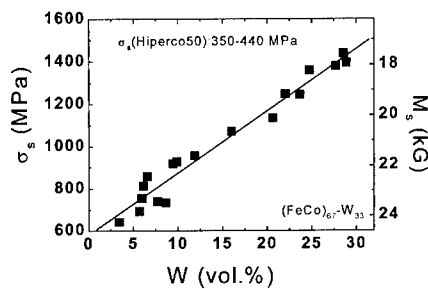
Figure 2. Mechanical strength vs. W fiber volume fraction, for annealed $Fe_{20}Co_{80}$-W composites
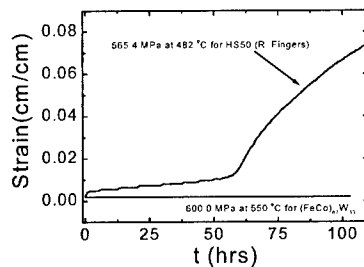
Figure 3. High temperature creep for FeCo composites in comparison with commercial FeCo bulk alloy [*]

To further enhance the mechanical properties of the soft magnetic materials, fine Al_2O_3 particles were uniformly dispersed in FeCo alloys during deposition. Figure 4 shows the dependence of H_c on the volume percent of Al_2O_3 particles of diameter of 37 nm for as-deposited

and annealed FeCo(Al$_2$O$_3$)-W samples. A reduction in coercivity H_c is seen after thermal annealing, but the heat treatment does not influence the trend of coercivity H_c as a function of the Al$_2$O$_3$ content.
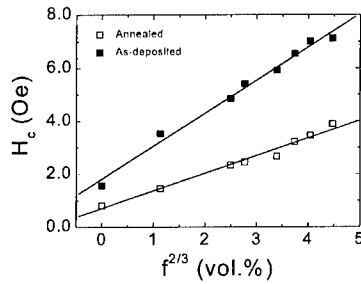
Figure 4. Coercivity vs. Al$_2$O$_3$ content in the as-deposited and annealed Fe50Co50-W samples

Kersten [14] developed a theory to explain the effect of inclusions on the magnetic properties. In his model, he assumed that spherical nonmagnetic particles of average radius r were uniformly imbedded at the corners of unit cells of an adopted simple cubic lattice with lattice constant a. In addition, the size of inclusions is assumed to be comparable to the domain wall thickness. The coercivity H_c can be expressed as:

$$H_c = 2.4 \frac{\delta_u K_1}{M_s \mu_0 r} f^{2/3} \qquad (1)$$

where f is the volume percent of the inclusions. This linear relationship between H_c and $f^{2/3}$ has indeed been observed as shown in Fig. 4. Using $\delta_w \approx \sqrt{k_B T_c / a K_1}$, where k_B is the Boltzmann constant, we estimated the domain wall thickness for Fe$_{50}$Co$_{50}$ alloy to be about $\delta_W \approx 0.26$ μm, which is comparable to the Al$_2$O$_3$ particle size.

Figure 5 shows the Vicker hardness of FeCo-Al$_2$O$_3$ composites as a function of Al$_2$O$_3$ content. The increase in hardness was found to be about a 100% for FeCo samples with 12 vol.% Al$_2$O$_3$ particles when compared with a pure a FeCo sample. A reduction of the hardness in the annealed samples is due to the increase in grain size and the relief of internal stress. A roughly linear relationship between the hardness and the cube root of the volume percent of the dispersed Al$_2$O$_3$ phase has been observed for both as-prepared and annealed samples. Dispersion hardening commonly follows the Orowen-Ashby model [15]. For the case of non-coherent spherical particles of size r, Orowen [15] proposed the mechanism where the yield stress is determined by the shear stress required to bow a dislocation line between two particles separated by a distance λ. The increase in yield stress is given by:

$$\Delta \sigma = \frac{0.13 G b}{\lambda} \ln \frac{r}{b} \qquad (2)$$

where G is elastic modulus, b is Buger vector of a dislocation. For dispersion reinforced composites, the spacing λ between particles can be estimated using: $\lambda \propto (16/f)^{1/3} r$. The hardness as a function of $f^{1/3}$ is shown in Fig. 5. The linear relationship between hardness and $f^{1/3}$ suggests that the dispersion hardenning in our samples follows the Orowen-Ashby model.
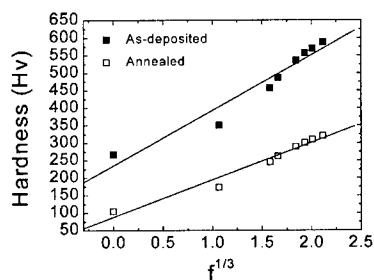
Figure 5. Vicker hardness vs. the square root of the volume fraction of Al_2O_3 content for the as-deposited and annealed $Fe_{50}Co_{50}$-W samples

CONCLUSIONS

To significantly improve the mechanical properties without significantly sacrificing the magnetic properties, we have designed and fabricated fiber and ceramic particle reinforced soft magnetic composites. Excellent mechanical properties including high yield strength and negligible creep rate at 600°C have been observed in the fabricated fiber composites. The dispersion hardness in the ceramic particle reinforced composites increases in accordance with the Orowen-Ashby model.

ACKNOWLEDGEMENT

REFERENCES

1. F. Pfeifer, and C. Raddeloff, "Soft Magnetic Fe-Ni and Fe-Co Alloys-Some Physical and Metallurgical Aspects", J. Magn. Magn. Mater., vol. 19, pp. 190-207, 1980.

2. R. H. Yu, S. Basu, Y. Zhang, and John Q. Xiao, 'Magnetic Domain and Coercivity in FeCo Soft Magnetic Alloys", J. Appl. Phys., vol. 85, pp. 6034-6036, 1999.
3. L. Li, "High Temperature Magnetic Properties of 49%Co-2%V-Fe Alloy", J. Appl. Phys., vol. 79, pp. 4578-4580, 1996.
4. R. V. Major, and V. Samadian, "Physical Metallurgy and Properties of a New High Saturation Co-Fe Alloy", J. Mater. Eng., vol.11, 1989.
5. R. H. Yu, S. Basu, Y. Zhang, A. Parvizi-Majidi, and John Q. Xiao, "Pinning Effect of the Grain Boundaries on Magnetic Domain Wall in FeCo-based Magnetic Alloys", J. Appl. Phys., vol. 85, pp. 6655-6659, 1999.
6. R. M. Bozorth, Ferromagnetism, IEEE, New York, 1991.
7. J. A. Ashby, H. M. Flower, and R. D. Rawling, "Gamma Phase in An Fe-Co-2%V Alloy", Metal Science, pp. 91-96, March 1977.
8. C. D. Pitt, and R. D. Rawling, "Microstructure of Fe-Co-2V and Fe-Co-V-Ni Alloys Containing 1.8-7.4 wt.%Ni", Metal Science, vol. 15, pp. 369-376, August 1981.
9. R. H. Yu, S. Basu, Y. Zhang, and John Q. Xiao, "Precipitation and High Temperature Magnetic Properties of FeCo-based Alloys", J. Appl. Phys., to be published.
10. R. H. Yu, L. Ren, S. Basu, K. M. Unruh, A. Parvizi-Majidi, and John Q. Xiao, "Novel Soft Magnetic Composites Fabricated by Electrodeposition", J. Appl. Phys., to be published.
11. A. Mager, Ann. Phys., vol. 6F11, pp.15, 1952.
12. R. H. Yu, G. Landry, S. Basu, and John Q. Xiao, "Magneto-impedance effect in Soft Magnetic Tubes", J. Appl. Phys., to be published.
13. A. G. Metcalfe, Interfaces in Metal Matrix composites, New York, Academic Press, 1974.
14. C. W. Chen, Magnetism and Metallurgy of Soft Magnetic Materials, North-Holland, p. 132, 1977.
15. G. E. Dieter, Mechanical Metallurgy, McGraw-Hill, p. 212, 1986.

Magnetic Properties of Transition Metal-Dendrimer Nanocomposites

Richard A. Fry, Robert D. Shull, Srinivas Uppuluri[1], and Lajos Balogh[1]
Metallurgy Division, National Institute of Standards and Technology,
Gaithersburg, MD 20899-8552, U.S.A.
[1]University of Michigan Center for Biologic Nanotechnology, University of Michigan,
Ann Arbor, MI 48109-0533, U.S.A.

ABSTRACT

Magnetic nanocomposites have been successfully prepared by encapsulating nanosized entities of iron, cobalt, and nickel compounds in poly(amido-amine) (PAMAM) dendrimer hosts. Problems related to the instability of the magnetic structures under the influence of an external electromagnetic field have been overcome by using a solid polystyrene matrix to embed the dendrimer hosts containing the magnetic guests. SQUID magnetometry measurements on these nanocomposites showed that after subtraction of the diamagnetic polymer background, at 300 K all samples exhibited paramagnetic behavior, with susceptibilities of 1.14, 1.68, and 0.70×10^{-6} m^3/kg for Fe-, Co-, and Ni-containing samples respectively. The temperature dependence for T<300 K showed typical paramagnetic behavior, with the susceptibility increasing for decreasing temperatures. Curie-Weiss (1/M vs. T) graphs displayed a linear behavior at high temperatures, with temperature axis intercepts (θ) occurring at -139 K (Fe), -16 K (Co), and 0 K (Ni). Negative deviations from Curie-Weiss behavior occurred at T<175 K for the Fe and T<25 K for the Co samples. Magnetic moments calculated from the high temperature Curie constant indicated that Fe, Co, and Ni possessed effective moments of 3.5, 4.4, and $2.8\mu_B$. The negative intercepts and the fact that these moments are larger than those expected for metallic transition metals are indicative that these species are probably present in an oxidized form. The low-temperature behavior indicates either superparamagnetic or soft ferromagnetic behavior.

INTRODUCTION

Recent improvements in the technology for materials preparation, combined with the driving force toward device miniaturization and increased magnetic storage densities, has resulted in the present capability of controlling morphology and features at the nanometer level. Correspondingly, issues relating to magnetism and magnetic anisotropy on a very small size scale have become increasingly important from perspectives of both applied technology and pure science. One of the primary objectives of this study was to develop an understanding of the magnetic behavior of low dimensional systems.

Dendrimers are a relatively new class of three-dimensional, organic molecules consisting of a small linear polymer core, surrounded by consecutive shells of interior branching units called dendritic generations, and culminating with peripheral terminal branch cells. Typically in the size range of 1 to 15 nm, these dendrimers are prepared by a synthetic route which provides exceptional control over the formation and placement of the repetitive branching units, resulting in a well-defined shape, chemistry, and structural symmetry [1-3]. This architecture creates an environment within the dendrimer molecule that facilitates trapping of guest (inorganic) species;

thus they are promising candidates as templates for the formation of polymer/inorganic nanocomposites [4]. The ability to control the size and chemistry of both interior branches and terminal groups (which may be chemically different from the interior), as well as the number of generations, makes it straightforward to manipulate the size of the trapping centers and, correspondingly, the size of the trapped species. Also, because the guest species is essentially encapsulated by the polymer dendrimer, the solubility of the overall nanocomposite is controlled by the dendrimer [5]. Therefore, normally insoluble materials such as semiconductors or metal sulfides, once encapsulated by the dendrimer, can be placed into solution, thus suggesting intriguing biological applications like targeted drug delivery and catalysis.

In recent years, a number of researchers have demonstrated the viability of using dendrimers as templates to contain predetermined numbers/clusters of metal atoms (Cu, Au, Ag, Pt, Pd) [6-10] or other inorganic compounds (CuS, CdS, Ag_2S) [11,12]. This "reactive encapsulation" method, in which the entrapped material is non-covalently bound to the dendritic polymer either by electrostatic or other physical/chemical interactions, or simply by the creation of an interpenetrating polymer network, essentially makes possible atom-by atom control in the construction of nanosized individual domains of materials [9].

Composites of magnetic materials having nanometer dimensions can possess unique properties and property combinations not easily achieved with conventional materials (e.g., both high magnetic permeability and large electrical resistivity). In fact, ferromagnetic behavior itself is strictly related to the cluster size of the individual magnetic entities. Incorporation of magnetic atoms into a dendrimer should prevent unwanted aggregation as well as providing a method for controlling the cluster size. In addition to targeted drug delivery, potential applications for such materials include magnetic imaging pigments, anti-radar coatings, microwave components, and transparent magnetic plastics.

In this work, we have synthesized magnetic-dendrimer nanocomposites of Co, Ni, and Fe. Here, we report on the temperature and field dependence of the magnetization. Ultimately, this work will provide us with a unique opportunity to examine the fundamental nature of ferromagnetism, while developing improved capabilities to engineer magnetic properties at nanometer length scales.

EXPERIMENTAL PROCEDURE

We have successfully prepared magnetic nanocomposites by encapsulating nanosized entities of iron, cobalt, and nickel in poly(amidoamine) (PAMAM) dendrimer hosts. Generation five PAMAM dendrimers were obtained from Dendritech, Inc. and solutions prepared by dispersing metal acetates and dendrimers in a polystyrene matrix. The concentrations of metal in the final matrices were determined by atomic absorption to be 0.10 wt% Fe, 0.38 wt% Ni, and 0.30 wt% Co. Specific details of the sample preparation have been reported elsewhere [9,14]. All samples gave optically clear matrices indicating particle sizes less than 50 nm. Using a solid polystyrene matrix to embed the dendrimer hosts containing the magnetic guests overcame previous problems [13] related to the instability of the magnetic structures under the influence of an external electromagnetic field. SQUID magnetometry measurements were performed in order to characterize the magnetic behavior of the nanocomposites at temperatures from 5 K to 300 K.

RESULTS AND DISCUSSION

Initial magnetization (M) versus applied field (H) measurements were performed at 300 K as follows. A sample consisting of only the dendrimer/polystyrene matrix was first examined to obtain a baseline background signal. It was, as expected, found to be strongly diamagnetic. Then the nanocomposite samples, containing both transition metal and the dendrimer/polystyrene matrix, were measured. The portion of signal due to the diamagnetic matrix was then subtracted out of the latter data, leaving only the magnetic contribution of the transition metal "suspended" within the nanocomposite. This corrected data is plotted in Figure 1. All samples exhibited paramagnetic behavior, with mass susceptibilities calculated to be 1.68, 1.14, and 0.70×10^{-6} m^3/kg for the Co-, Fe-, and Ni-containing dendrimers respectively. From the room temperature susceptibility, effective magnetic moments (μ_{eff}) for the Co, Fe, and Ni in the dendrimers were respectively calculated to be 4.4 μ_B, 3.5 μ_B, and 2.8 μ_B.
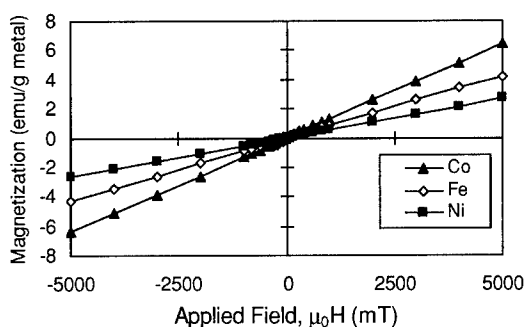
Figure 1. Magnetization versus applied field for the Co, Fe, and Ni components of the dendrimer nanocomposites, showing paramagnetic behavior at 300 K.

The temperature dependence (T<300 K) of the magnetization for the nanocomposites also showed fairly typical paramagnetic behavior, with susceptibility increasing for decreasing temperature, as shown in Figure 2(a). Curie-Weiss (1/M vs. T) graphs of the data [Figure 2(b)] displayed a linear behavior at high temperatures which when extrapolated to low temperatures indicated intercepts (θ) with the temperature axis of –139 K, –16 K, and 0 K for Fe, Co, and Ni respectively. The negative intercept values imply that both the Fe and Co particles exhibit a propensity toward antiferromagnetic interactions, while the 0 K intercept value implies that there are no interactions among the Ni particles in the composite. The slopes of the 1/M vs. T curves were also utilized to calculate effective moments for the Co, Fe, and Ni in the dendrimers. Those values were respectively 4.4 μ_B, 4.4 μ_B, and 2.8 μ_B. Note that the values for Co and Ni agree nicely with those calculated previously, while the 26 % difference in the Fe moment is presumably related to the fact that notable deviations from the linear Curie-Weiss region for Fe begin at temperatures as high as 175 K. This negative deviation from Curie-Weiss behavior also occurred for the Co samples (at T<25 K). Negative deviations from linear Curie-Weiss behavior indicate that either the magnetization is increasing faster than would be expected by the Weiss molecular field, or that the Weiss molecular field is changing with temperature. Since it does not
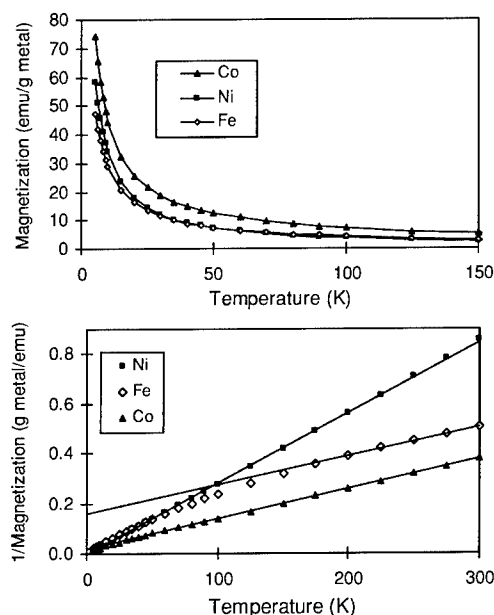
Figure 2. (a) Temperature dependence of magnetization for Co, Fe, and Ni dendrimer nanocomposites measured at constant applied field of 2000 mT while cooling; (b) (Magnetization)$^{-1}$ vs. temperature.

seem unreasonable that the extent of particle/cluster interactions could be changing with temperature, the latter alternative seems more likely. The deviations from linear Curie-Weiss behavior, combined with the negative temperature axis intercepts and the fact that the calculated effective magnetic moments are larger than those expected for metallic transition metals, are indicative that these metallic species are probably present within the composites in an oxidized form.

The low-temperature (T = 5 K) magnetization behavior for these dendrimers is shown in Figure 3. The M vs. H curves begin to approach saturation at fields >3000 mT, and at 5000 mT measured magnetization values are 76, 132, and 123 A·m^2/kg (i.e., emu/g) for Fe, Co, and Ni respectively. However, none of the samples exhibit a measurable coercive field, indicating either superparamagnetic or soft ferromagnetic behavior. Additional analysis and detailed structural characterization is underway in order to resolve this issue.

CONCLUSIONS

Magnetic nanocomposites consisting of iron, cobalt, and nickel entities in polymeric dendrimer hosts have been successfully prepared. SQUID magnetometry measurements on these nanocomposites showed that after subtraction of the diamagnetic polymer background, at 300 K
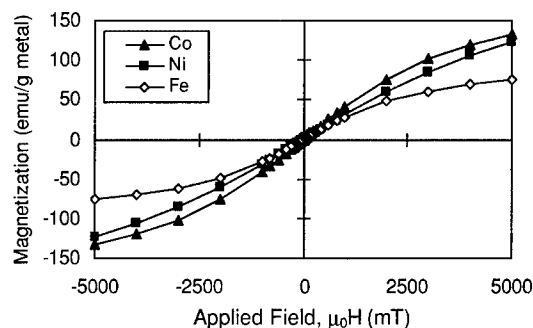
Figure 3. Magnetization versus applied field at 5 K for the Co, Fe, and Ni within dendrimer nanocomposites, showing evidence of superparamagnetic or soft ferroelectric behavior.

all samples exhibited paramagnetic behavior, with susceptibilities of 1.14, 1.68, and 0.70×10^{-6} m^3/kg and effective moments of 3.5, 4.4, and $2.8\mu_B$ for Fe-, Co-, and Ni-containing samples respectively. The temperature dependence for T<300 K also exhibited typical paramagnetic behavior. Curie-Weiss (1/M vs. T) graphs of the data displayed a linear behavior at high temperatures, which when extrapolated to low temperatures indicated intercepts (θ) with the temperature axis of –139 K (Fe), –16 K (Co), and 0 K (Ni). The negative θ values, together with negative deviations from Curie-Weiss behavior, seem to indicate a propensity toward antiferromagnetic interactions in the Fe and Co samples, particularly at lower temperatures. In addition, the fact that the calculated moments are larger than those expected for metallic transition metals is indicative that the metallic species are probably present in an oxidized form. Low-temperature hysteresis measurements exhibit approach to saturation at large fields and no coercivity, thus indicating either superparamagnetic or soft ferromagnetic behavior in these nanocomposite dendrimers.

ACKNOWLEDGMENTS

REFERENCES

1. D.A. Tomalia, *Scientific American* **272**, 62 (1995).
2. J.M.J. Frechet, *Science* **263**, 1710 (1994).
3. C. Wu, *Science News* **151**, 384 (1997).
4. L. Balogh, D.A. Tomalia, and G.L. Hagnauer, *Chem. Innov.* **30**, 19 (2000).
5. L. Balogh, D.R. Swanson, R. Spindler, and D. Tomalia, *Polym. Mater. Sci. Eng.* **77**, 118 (1997).

6. L. Balogh and D.A. Tomalia, *J. Am. Chem. Soc.* **120**, 7355 (1998).
7. M. Zhao, L. Sun, and R.M. Crooks, *J. Am. Chem. Soc.* **120**, 4877 (1998).
8. K. Esumi, A. Suzuki, N. Aihara, K. Usai, and K. Torigoe, *Langmuir* **14**, 3157 (1998).
9. L. Balogh, R. Valluzzi, K.S. Laverdure, S.P. Gido, G.L. Hagnauer, and D.A. Tomalia, *J. of Nanoparticle Research* **3**, 1 (1999).
10. F. Gröhn, B.J. Bauer, and E.J. Amis, *Abs. of Papers of the Am. Chem. Soc.* **219**, 295-POLY (2000).
11. N.C. Beck Tan, L. Balogh, S.F. Trevino, D.R. Swanson, D.A. Tomalia, and J.S. Lin, *Polymer* **40**, 2537-45 (1999).
12. K. Sooklal, L.H. Hanus, H.J. Ploehn, and C.J. Murphy, *Adv. Mater.* **10**, 1083 (1998).
13. R.D. Shull, L. Balogh, D.R. Swanson, and D.A. Tomalia, *Abs. of Papers of the Am. Chem. Soc.* **216**, 69-MACR (1998).
14. M.S. Diallo, L. Balogh, A. Shafagati, J.H. Johnson, Jr., W.A. Goddard, III, and D.A. Tomalia, *Environ. Sci. Technol.* **33**, 820 (1999).

Nanocomposite with Non-Spherical Granules – Logarithmic Field Dependence of Giant Magnetoresistance

E. Meilikhov[a], B. Raquet[b]
[a]Russian Research Center «Kurchatov Institute», 123182 Moscow, Russia
[b]Laboratoire de Physique de la Matière Condensée de Toulouse, Av. de Rangueil, 31077 Toulouse, France

ABSTRACT

Magnetoresistance of the nanocomposite $Fe_x(SiO_2)_{1-x}$ ($x \approx 0.6$) at high enough magnetic field is logarithmic function of the magnetic field. Such a dependence does not fall into the known theory of giant magnetoresistance of ferromagnetic nanocomposites. This paper examines the giant magnetoresistance of such a system in terms of a simple model where the non-ordinary quasi-logarithmic magnetic field dependence of nanocomposite magnetoresistance is related to the non-spherical granules' distribution over their shapes.

INTRODUCTION

In the present paper, we consider the giant magnetoresistance of the nanocomposite $Fe_x(SiO_2)_{1-x}$ which is the granular ferromagnetic metal in the insulator matrix with $x \approx 0.6$ (that corresponds to the metal state close to the percolation metal-insulator transition). Experiments show that at high enough magnetic fields, the resistance of the system depends logarithmically on the magnetic field. Such a dependence does not fall into the framework of the known theory of the giant magnetoresistance of ferromagnetic nanocomposites [1, 2]. We relate this discrepancy to the fact that the "traditional" theory is applied to systems with spherical granules, while real nanocomposites consist most commonly of non-spherical ones. Moreover, as a rule, there are granules of diverse non-sphericity in the system - from the strongly prolate to the strongly oblate ones. This paper examines the giant magnetoresistance of such a system in terms of a simple model where the non-ordinary semilogarithmic magnetic field dependence of nanocomposite magnetoresistance is related to the non-spherical granules' distribution over their shapes.

EXPERIMENT

Thin $Fe_x(SiO_2)_{1-x}$ films with $x \approx 0.6$ were studied. They have been prepared by the ion-beam sputtering technique in a vacuum chamber with a mosaic target consisting of Fe and SiO_2 tablets. The volume fraction x of iron has been controlled by X-ray micro-analysis. Grains' diameters vary from ~2 nm up to ~ 20 nm and the film thickness equals about 0.4 µm.

The magnetoresistance $\Delta R/R$ of the film (R is the sample resistance at a given temperature and zero magnetic field, ΔR is the resistance change at the magnetic field B) was measured within the 4.2-300 K temperature range under the action of the "long" (of ~0.1 s-duration) pulse magnetic fields up to 20 T.

Experimental field dependencies of the sample manetoresistance for various temperatures are shown in Fig. 1. In fig. 2, only those parts of those dependencies are demonstrated that relate to the high field region. In this case, the magnetoresistance is shown

as a function of the "effective" field B/T [1]. It could be seen that in the high field region the magnetoresistance is the logarithmic function of the magnetic field.
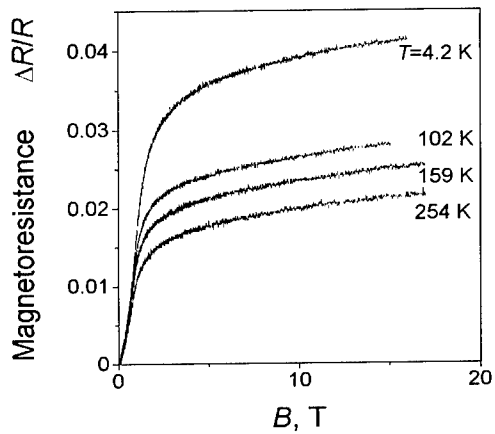
Fig. 1. Field dependencies of $Fe_x(SiO_2)_{1-x}$ nanocomposite magnetoresistance ($x \approx 0.6$) at various temperatures.
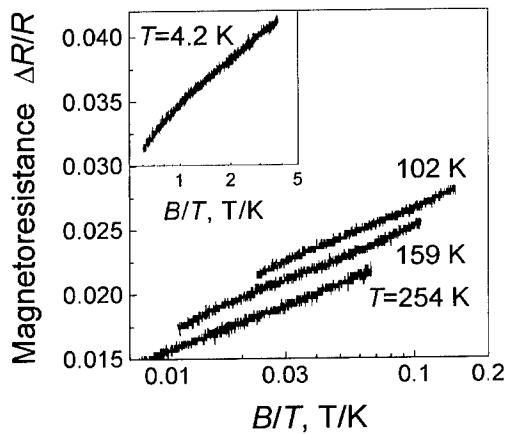
Fig.2. Log-scale field dependencies of $Fe_x(SiO_2)_{1-x}$ nanocomposite magnetoresistance ($x \approx 0.6$) at various temperatures in the high field region.

THEORY: NANOCOMPOSITE WITH NON-SPHERICAL GRANULES

The conductivity of granular metals (nanocomposites) and (in the case of ferromagnetic metals) their giant magnetoresistance are defined by tunnel intergranular electron transitions [1, 2]. However, in real systems consisting of granules of various sizes, not every

---

[1] It is known that for non-interacting spherical granules the magnetoresistance $\Delta R/R \propto M^2$, where M is the nanocomposite magnetization [2]. In the case, the latter is defined by the Langevin function (cf. Eq.(4)) which argument is the effective field B/T.

those transitions are actual: the most considerable contribution to the conductivity is due to tunnel transitions between granules of sizes close to the "optimal" one [3, 4]. For a nanocomposite consisting of *spherical* granules, such an optimal size is defined by the competition between enhanced concentration of small granules (that is typical for real systems) and reduced degree of their ionization which is the consequence of Coulomb effects. So, it is the result of the "game of survival" – there is great deal of small granules but only a few of them are charged (and therefore could contribute to the conductivity) and there is a few of big granules which all are charged. The optimal granule size is expressed by the relation [3]

$$a_{opt}(T) \approx a_0 (x/4\pi)^{1/2} (\lambda/a_0)(T/T_0)^{-5/9} \qquad (1)$$

where $kT_0 \approx (e^2/\varepsilon\, a_0)(a_0/\lambda)^{3/2} x^{-1/2}[1-(x/x_c)^{1/3}]$, a_0 is the average granule size, λ is the electron wavelength in insulator phase, ε is its dielectric constant, x is the volume fraction of the metal phase, and x_c is the percolation threshold. So, the conductance $G(T)$ of the system is controlled by the "optimal cluster" consisting of particles of the optimal size $a_{opt}(T)$ which is rearranged with temperature.

The resistance variation of the considered system under magnetic field B is defined by the magnetic field dependence of the probability of tunnel transitions between spontaneously magnetized single-domain (due to small sizes) granules. The reduced magnetoresistance $MR(B, T) = [G(0,T)-G(B,T)]/G(0,T)$ equals [4]

$$\Delta R(B,T)/R = P^2 \langle \cos\gamma \rangle^2 \qquad (2)$$

where P is the electron spin polarization in the ferromagnetic granule, γ are angles between the external magnetic field and magnetic moments of granules. Averaging is performed over the granules constituting the optimal cluster. Thus, the calculation of the magnetoresistance is reduced to the calculation of the averaged (over that cluster) $\langle \cos\gamma \rangle$ - value.

However, in the real system, granules are, generally, *non-spherical*. It means that not every values of γ- angle for a single granule are equally probable and the averaged (over time) $\overline{\cos\gamma}$ - value for a non-spherical granule is defined by its magnetic anisotropy (crystal or geometric) and the external field [5]. For an ellipsoidal granule with a high (comparing to Bohr magneton) magnetic moment,

$$\overline{\cos\gamma} = \int_0^\pi \exp[-(W_A+W_B)/kT]\cos\gamma\, d\Omega \Big/ \int_0^\pi \exp[-(W_A+W_B)/kT]\, d\Omega, \qquad (3)$$

where $d\Omega = \sin\gamma\, d\gamma\, d\phi$ is the solid angle, ϕ is the azimuth angle of granule' magnetic moment $(\cos\phi = [\cos\theta - \cos\gamma\cos\beta]/\sin\gamma\sin\beta$, θ and β are the angles between the large axis of a granule and directions of its magnetic moment and magnetic field, respectively). In Eq. (3) $W_A = W_A(\theta)$ is the magnetic anisotropy energy independent of the magnetic field, $W_B = -I_s VB \cos\gamma$ is the Zeeman energy depending on the γ- angle only, I_s is the saturation magnetization of granule' material. At high magnetic fields, $W_B \gg W_A$ and, hence,

$$\overline{\cos\gamma} = \operatorname{cth} h - 1/h \equiv L(h), \qquad (4)$$

where $h= I_s VB / kT$. That corresponds to the known Langevin model.

If the optimal cluster consisted of *spherical* granules of the size a_{opt}, then the granule volume V appearing in Eq. (4) would be the same for all granules and equal to $V=V_{opt}=(4\pi/3)$ $a^3_{opt}(T) \propto T^{-5/3}$. In this case, $\langle \cos\gamma \rangle = \overline{\cos\gamma} = L(h_{opt})$, where $h_{opt} = I_s B V_{opt}/kT \propto T^{-8/3}$. It is clear that even in this case the temperature dependence of the optimal cluster magnetic moment (which is proportional to $\langle \cos\gamma \rangle$) is not described by the Langevin model (where $h \propto 1/T$).

In the system consisting of *non-spherical* (ellipsoidal) granules, the situation is more complicate. In that case, the probability of granules' ionization is defined by their *capacity C* (which in the spherical case coincides with the granule radius). Therefore, the optimal granule size is the result of the new "game of survival" which depends on 1) the relation between the charged granules' concentration and their capacity, and 2) the dependence of the average (tunnel) distance between granules with equal capacities and their characteristic size. A granule which form is an ellipsoid of revolution has the two characteristic sizes a, b that are the lengths of its long and short axes. Which of those sizes is the characteristic one for the problem considered? It is known that the capacity of the ellipsoidal granule with the larger size of a depends slightly on its smaller size b: for the prolate ellipsoid of revolution $C=(a^2-b^2)^{1/2}$ /Arch$(a/b) \approx a/\ln(2a/b)$, while for the oblate one $C=(a^2-b^2)^{1/2}$ /arccos(a/b) (i.e., $2/\pi<C/a<1$) [6]. It means that the only essential size of an ellipsoidal granule is its larger size, and *all* granules with the larger size a close to a_{opt} are the optimal ones. Therefore, the optimal cluster consists of granules of various volumes in the range $V_{min} < V < V_{opt}$, where $V_{opt}= (4\pi/3)a^3_{opt}$ and $V_{min} = (b_{min}/a_{opt})^2 V_{opt}$ (for prolate ellipsoids) or $V_{min} = (b_{min}/a_{opt})V_{opt}$ (for oblate ellipsoids), b_{min}/a_{opt} is the minimum ratio of the respective granule' sizes which characterizes their maximum (for a given nanocomposite) elongation or flatness. If $b_{min}/a_{opt} \sim 0.1$, then the optimal cluster includes granules which volumes differ by ~100 times! Naturally, in this case, $\langle\cos\gamma\rangle \neq \overline{\cos\gamma}$ and one should perform averaging over all granules of the optimal cluster. Let $f_b(b)$ be the distribution function of the smaller sizes of the granules, and x_o is the volume fraction of the prolate granules. Then

$$\langle\cos\gamma\rangle = \int_{b=b_{min}}^{b=a_{opt}} \left\{(1-x_o)L\left[(ab^2/a^3_{opt})h_{opt}\right]+x_oL\left[(a^2b/a^3_{opt})h_{opt}\right]\right\}f_b(b)db = F(h_{opt}),$$

$$F(h_{opt}) = \int_{z_{min}}^{1} \left[(1-x_o)L(h_{opt}z^2)+x_oL(h_{opt}z)\right]f_z(z)dz, \tag{5}$$

where we introduced the distribution function $f_z(z)$ of the parameter $z{\equiv}b/a_{opt}$ ($0<z<1$, $z_{min}{=}b_{min}/a_{opt}$).

The distribution function $f_z(z)$ is, most likely, dependent on the technique of nanocomposite producing. This refers equally to the relation between numbers of prolate and oblate granules that is defined by the parameter x_o. In principle, the relevant information may be obtained by means of electron-microscopic investigations of the system in question. But, as calculations show (see below), the qualitative form of the magnetic field dependence of the magnetoresistance is not critical neither to choosing the distribution function $f_z(z)$, nor to values of the parameters $z_{min}{\ll}1$ and x_o. So, as a simple approximation one could consider the system with the uniform distribution function ($f_z(z)$=const) consisting of prolate granules only (x_o=0), that is the system where prolate ellipsoidal granules of any form, from the spherical (z=1) to needle-like (z=0), are equally probable. In calculations, z_{min} =0.1 was accepted.

Magnetic field dependence of the magnetoresistance of such a system calculated with Eq. (5) is presented in Fig. 3 (the solid line 2). It could be seen that within the broad range of magnetic fields (in this case, at $5<h_{opt}<50$), the field dependence of the magnetoresistance is nearly logarithmic one. As calculations show (see Fig. 3) the character of that dependence is qualitatively the same for various functions $f_z(z)$ and x_o-values. What changes, it is the range of magnetic fields where that dependence is quasi-logarithmic one.
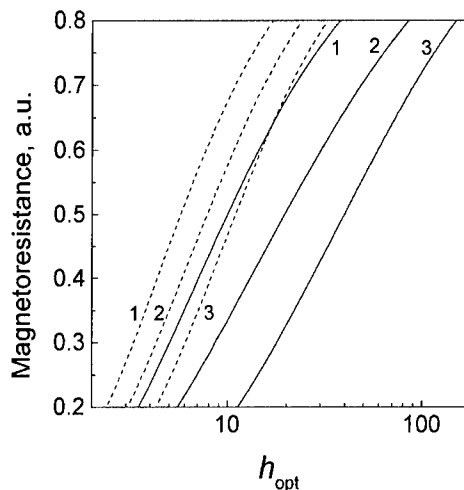
Fig.3. Calculated magnetic field dependencies of the magnetoresistance for the granular ferromagnetic metal with non-spherical granules of prolate (solid lines, $x_o=0$) and oblate (dashed lines, $x_o=1$) form. The distribution function $f_z(z)$: 1 - linearly-increasing, 2 - uniform, 3 - linearly-decreasing.

Characteristic effective field for the magnetic field range, where quasi-logarithmic dependence of the magnetoresistance should be observed, is of about $h_{opt}\sim20$ (cf. Fig. 3, the solid line 2 for the uniform distribution function $f_z(z)$). Comparing this value with the value of $B/T\sim3\cdot10^{-2}$ T/K, corresponding to the experimentally determined ranges of the magnetoresistance logarithmic dependence at temperatures $T\sim100\text{-}250$ K (cf. Fig. 2), the diameter of the optimal granules $2a_{opt}\sim20$ nm could be derived (in doing so, the saturation magnetization of Fe-granules was considered as being equal to that for the bulk iron, $I_s\approx0.2$ T). It is in a reasonable agreement with the data of electron-microscopic analysis of the investigated nanocomposite.

Let us discuss now the magnetoresistance temperature dependence in the range of its logarithmic magnetic field dependence. In the framework of the considered model, there is the only reason for such a dependence - the variation of the larger granule size a_{opt} of the optimal cluster with temperature. That dependence occurs to be the same as Eq.(1), $a_{opt}(T) \propto T^{-5/9}$. It means that the magnetoresistance depends only on that parameters' combination which defines the value of $h_{opt} \propto BV_{opt}/T \propto B/T^{8/3}$. Therefore, in the framework of our model there is a parametric magnetoresistance dependence which has the following form $MR=MR(B/T^{8/3})$. In other words, every value of the reduced magnetization $\Delta R/R$ as a function of the parameter $B/T^{8/3}$ has to fall on a single master curve. Experimental data presented in the respective form (cf. Fig. 4) support that theoretical prediction. Thus, the considered model provides qualitatively correct description of the experimental results concerning the magnetoresistance of the granular ferromagnetic metal $Fe_x(SiO_2)_{1-x}$ under high magnetic fields.

In conclusion, we have shown that the model of the nanocomposite with granules of various non-spherical forms leads to the quasi-logarithmic magnetic field dependence the magnetoresistance of such a system under high enough fields. This is, obviously, associated

---

[2] According to Eq. (1), $a_{opt}(T)\propto T^{-1/2}$ and, hence, the calculated optimal granule size at $T=4.2$ K equals $2a_{opt}(4.2$ K$) \sim 100$ nm. However, there are no such big granules in the real system and, hence, it is incorrect to employ the considered model at so low temperatures.

with the great volume scattering of granules constituting the optimal cluster. The magnetoresistance saturates together with the magnetization of this cluster, but with
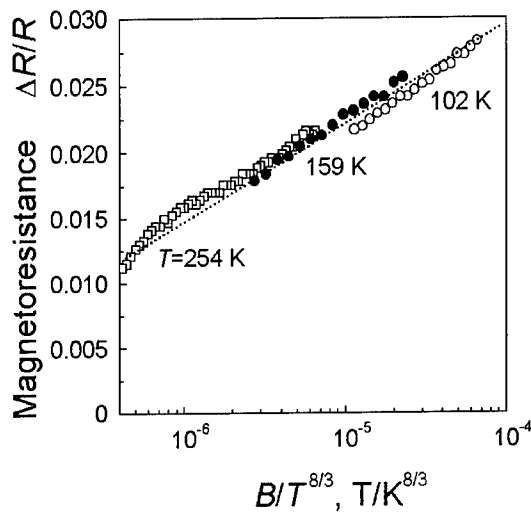
Fig. 4. Parametric dependencies of $Fe_x(SiO_2)_{1-x}$ – nanocomposite magnetoresistance ($x \approx 0.6$) in the high field region. The dotted master line is the guide for eye.

increasing field more and more small granules become contribute to the magnetization. It is this "extended" contribution that results in quite slow (quasi-logarithmic, as has been shown) saturation of the magnetization and, hence, of the magnetoresistance, as well.

REFERENCES

1. J.S. Helman, and B. Abeles, Phys. Rev. Lett., **37**, 1429 (1976).
2. J. Inoue, and S. Mackawa, Phys. Rev. B, **53**, R11927 (1996).
3. E. Z Meilikhov., JETP, .**88**, 819 (1999).
4. E. Z Mcilikhov., JETP Letters, **69**, 623 (1999).
5. E. Z Mcilikhov., JETP, **89**, 1184 (1999).
6. E. Lifshits, L. Pitaevskii, L. Landau, *Electrodynamics of continuum media* (Elsevier, 1985).

ACKNOWLEDGMENTS

Hybrid High-Temperature Nanostructured Magnets

David J. Sellmyer, J. Zhou, H. Tang, and R. Skomski
Behlen Laboratory of Physics and
Center for Materials Research and Analysis
University of Nebraska
Lincoln, NE 68588-0113, USA

ABSTRACT

The hysteretic behavior of two-phase permanent magnets for high-temperature applications is examined. A variety of systems have been synthesized and investigated, including Sm-Co-Cu-Ti bulk magnets, $SmCo_5$:Cu-Ti thin-film materials, and mechanically milled Sm-Co-Zr magnets. The hybrid character of the material leads to very high room-temperature coercivities, between 30.2 and 43.6 kOe, and to the survival of a comparatively large part of the coercivity at high temperatures (12.3 kOe at 500 °C for $SmCo_{6.5}Cu_{0.8}Ti_{0.3}$). The coercivity reflects the structure and chemical composition of the material. When ferromagnetic grains are separated by a ferromagnetic boundary phase, the boundary phase acts as a pinning center, but when the grain-boundary phase has a comparatively low Curie temperature, the high-temperature magnetism of the system is that of a weakly interacting ensemble of magnetic particles. In spite of some residual paramagnetic exchange coupling, which is discussed in this work, this mechanism enhances the coercivity.

INTRODUCTION

Recently there has been a resurgence of interest in Sm-Co-based permanent-magnet alloys. The reasons for this are twofold. First, Sm_2Co_{17} and phases based on this composition have the highest known Curie temperature (T_c) and thus have the best chance of creating a practical magnet for use at high temperatures such as 500 °C. Second, $SmCo_5$ has the highest-known uniaxial anisotropy constant which leads generally to maximum values of coercivity. $SmCo_5$ also is a relatively high-temperature magnet. In the quest for new nanocomposite magnets based on the exchange coupling of hard and soft phases with nanoscale dimensions, the use of $SmCo_5$ as the hard phase has the major benefits of being both extremely hard and a high-temperature magnet. The clear challenge for workers in the design of high-temperature and high-energy product nanoscale magnets is to synthesize hybrid systems that exploit the properties of at least two phases to create magnets with much improved figures of merit including operating temperature and coercivity.

In this paper we present results of recent work in our laboratories based on controlling the nanostructure and phase mixtures of hybrid or composite magnets based on $SmCo_5$ (1:5), Sm_2Co_{17} (2:17), $SmCo_7$ (1:7) and related compounds. First, we discuss a series of Sm-Co-Cu-Ti alloys containing 2:17 and 1:5 phases. This system has a cellular structure and has produced the highest known coercivity (H_c) at 500 °C (12.3 kOe). Second, we outline results on $SmCo_5$:Cu-Ti nanocomposite magnets prepared in thin-film form with sputtering methods. These magnets have led to H_c values above 40 kOe at 295 K. Third, the technique of mechanical milling has been used to prepare two-phase magnets containing $SmCo_5$. These systems also have large H_c

values (> 30 kOe) at room temperature. Finally, in an outlook section, we discuss the magnetic behavior of conceivable two-phase magnets where the grain-boundary phase is paramagnetic.

Sm-Co-Cu-Ti HYBRID BULK MAGNETS

Renewed impetus for better high-temperature magnet materials has come from demands for aircraft engine components functioning at temperatures to about 500 °C. Conventional $Sm_2(Co,Fe,Cu,Zr)_{17}$ permanent magnets have large energy products and coercivities at room temperature. In the last couple of years efforts have been made to improve the properties of this class of material by adjusting the composition and H_c values up to 10 kOe have been obtained at 500 °C [1]. Recently we have discovered a relatively simple Sm-Co-Cu-Ti alloy that consists of two phases, 2:17 and 1:5, and which has a positive dH_c/dT and H_c values above 10 kOe at 500 °C [2,3]. We discuss here our most recent improvements in this material and our understanding of its behavior.

Alloys of the form $SmCo_{7.05-x-y}Cu_xTi_y$, where $0.4 \leq x \leq 0.9$ and $y = 0.25$ or 0.3, were prepared by arc melting under flowing argon. The samples generally were heat treated by annealing in argon at 1165 °C for 3 hrs., cooled to 825 °C and annealed for 8 hrs., followed by slow cooling to 550 °C at the rate of 1 °C/min. Characterization methods include x-ray diffraction (XRD), transmission electron microscopy (TEM), and magnetization with SQUID or VSM to 600 °C. XRD results show that the arc melted samples had the disordered 1:5 structure (the so-called 1:7 structure). After the heat treatment the structure reverts into two phases: 2:17 and 1:5. This is shown clearly by the thermomagnetic data of Figure 1, where the T_c values of Sm_2Co_{17} (~920 °C) and a doped $SmCo_5$ phase (~700 °C) are seen. TEM micrographs show a cellular nanostructure reminiscent of the conventional 2:17 magnets. The 2:17 cells have dimensions of order 70 nm and the 1:5 boundary phase has a thickness of order 10 nm.
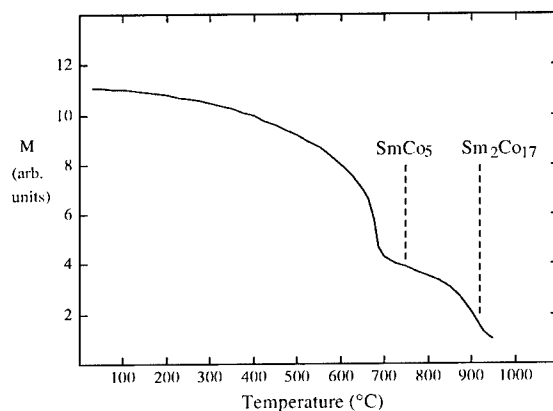
Figure 1. Thermomagnetic analysis of $SmCo_{6.1}Cu_{0.6}Ti_{0.3}$ magnet. The dashed lines show the Curie temperatures of the pure Sm_2Co_{17} and $SmCo_5$ phases.

Figures 2 and 3 show examples of hysteresis loops at room temperature and elevated temperatures, respectively. The dependence of H_c on Cu content at 500°C and on temperature for three Cu concentrations is shown in Figures 4 and 5, respectively. Notable features of the data include a pinning controlled initial magnetization behavior and a high H_c value at 295K (Figure 2), and a positive contribution of Cu to the coercivity (Figure 4). To our knowledge, the H_c values of 13.8 kOe at 450 °C and 12.3 kOe at 500 °C are the largest ones reported at these temperatures. The sensitivity of the temperature dependence of H_c on Cu content is seen in Figure 5.
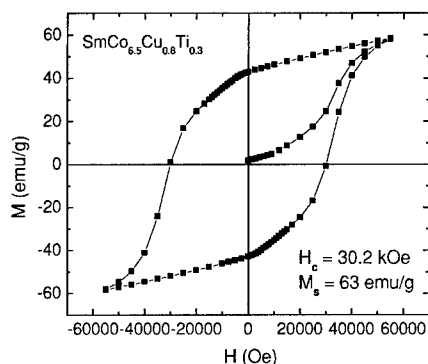
Figure 2. Hysteresis loop of $SmCo_{6.5}Cu_{0.8}Ti_{0.3}$ sample at room temperature.
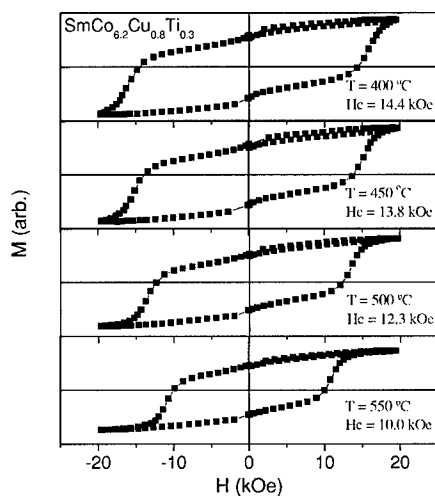
Figure 3. Hysteresis loops of $SmCo_{6.2}Cu_{0.8}Ti_{0.3}$ magnet at various temperatures.
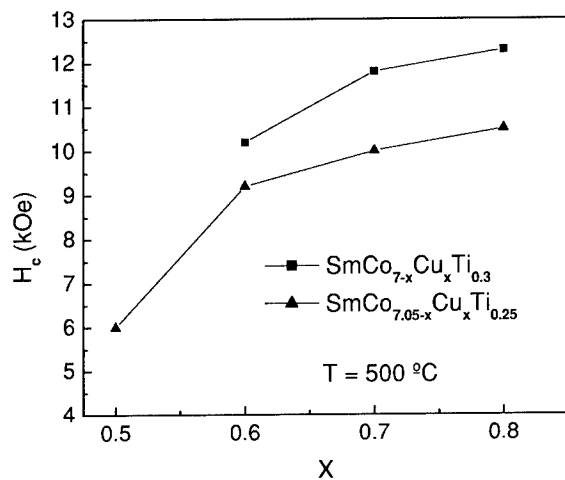
Figure 4. Influence of Cu concentrations on coercivity at 500 °C.
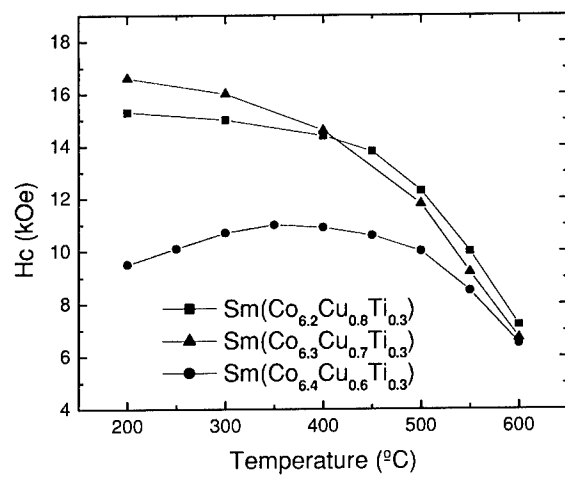
Figure 5. Temperature dependence of coercivity of $SmCo_{7-x}Cu_xTi_{0.3}$.

The temperature coefficient of the coercivity (TCC) can be explained in the following way. These magnets are of the pinning type in which the interaction of the domain wall with the grain boundary controls the behavior [4,5]. A detailed calculation gives

$$H_c = H_0 \left(\frac{\pi}{3\sqrt{3}} \cdot \frac{b}{\delta} \cdot \frac{|\Delta K|}{K_h} \right) \tag{1}$$

where H_0 is the anisotropy field of the main (2:17) phase, K_h is the anisotropy constant of same phase, b is the thickness of the boundary (1:5) phase, δ is the domain-wall thickness, and $\Delta K = K_h - K_s$ where K_s is the anisotropy of the softer boundary phase [3]. By considering the expected temperature dependence of K_h and K_s and the expected dependence of K_s on Cu content, it is possible to rationalize the temperature dependence of $H_c(T)$ shown in Figure 5, including the maximum in $H_c(T)$ seen for the sample with x = 0.6.

A more thorough understanding of the magnetic behavior of these alloys, which we are now pursuing, will require quantitative estimates of the anisotropy of the boundary phase, $SmCo_{5-x}Cu_x$. In addition, these magnets do not contain Zr as do the conventional 2:17 magnets. Preliminary TEM results have not detected a Ti lamellar phase analogous to the Zr one in the conventional magnets. Thus further work is expected to lead to a better understanding of the nanostructure-properties relationship in these materials and, ideally, to further improvements in high-temperature properties.

$SmCo_5$:Cu-Ti NANOCOMPOSITE MAGNETS

We have seen in the above paragraphs that Sm-Co-based compounds, when suitably nanostructured, can produce interesting hard magnetic properties. In addition, earlier work in our laboratories has shown that multilayer sputtering can lead to hard:soft nanocomposite films with near record energy products at room temperature. Specifically, multilayered Fe/Pt films after annealing have been shown to produce $FePt:Fe_{1-x}Pt_x$ nanocomposites with the hard phase being $L1_0$-structure FePt and a soft Fe-rich $Fe_{1-x}Pt_x$ alloy interspersed in 5-10 nm grains in larger FePt grains [6]. The composite was shown to have an energy product, $(BH)_{max}$, of about 53 MGOe, close to the record of about 55 MGOe for $Nd_2Fe_{14}B$.

In the present studies we have made multilayers of the form

$$Si / Cr(90nm) / [SmCo_5 / X]_n / Cr(18nm). \tag{2}$$

where Si is a single-crystal (001) silicon substrate. Cr is used as an underlayer and coating layer for protection against oxidation during annealing, typically in the range 475-550 °C. The magnetic layer consists of 200 nm of $SmCo_5$, $SmCo_5$/Cu, $SmCo_5$/Ti or $SmCo_5$/CuTi. n is the number of layers ranging from n = 1 (single layer) to n = 42. The sputtering techniques and annealing procedures have been described in earlier papers [7].

Preliminary results obtained on these systems include the following. $SmCo_5$ single layer and $SmCo_5$/Cu multilayers do not show any significant coercivity (H_c < 0.1 kOe) before and after annealing. $SmCo_5$/Ti multilayers exhibit H_c values of less than 10 kOe after annealing.

Figure 6 shows an XRD scan of a film with the initial structure Cr 90 nm/[(SmCo$_5$) 4.5nm/ (Cu-Ti) 0.3 nm]$_{42}$/Cr 18 nm. The data are consistent with a nanostructure consisting of 1:5 grains with mostly random orientations. These films show large H_c values after annealing. Hysteresis loops at room temperature for SmCo$_5$(Cu$_{0.9}$Ti$_{0.1}$)$_{0.6}$ are shown in Figure 7 which shows the effect of annealing temperature. There is a slight inflection point near H = 0, suggesting a second magnetic phase that is more strongly exchange coupled to the main hard phase for the higher annealing temperature (525 °C).
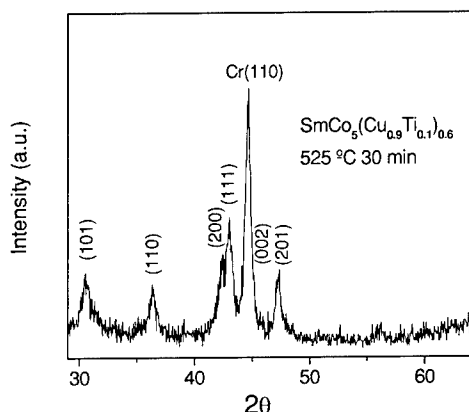
Figure 6. X-ray diffraction for thin films with the initial structure Cr 90 nm [(SmCo$_5$)4.5 nm/ (CuTi)0.3 nm] x 42/Cr 18 nm.

The coercivity is large (43.6 kOe) and decreasing the Cu-Ti fraction by a factor of 2/3 leads to H_c = 41.0 kOe and slightly more evidence for an exchange decoupled second phase.

Electron microscopy studies clearly are needed to determine the nanostructure of these films, and are underway. If these films contain a weakly magnetic intergranular phase that pins domain walls, it may be possible through study of such systems to understand and create bulk magnets with similar structures and enhanced room- and high-temperature properties.

Sm-Co-Zr MECHANICALLY MILLED MAGNETS

The technique of mechanical milling and/or alloying is a well known method to create the nanostructure required for magnetic hardening [8-13]. Often, this approach amounts to creating such small grains (~ 10-20 nm) that the magnet to zero order can be regarded as an ensemble of uniaxial nanoparticles that approach a single random-anisotropy magnet with more or less exchange coupling between the nanograins [10,11]. If the composition of the original alloy, plus the nature of the heat treatment, permits or requires that there be more than a single phase present, then there is the possibility for either exchange decoupling or pinning of "interaction domain walls" by nonmagnetic or weakly magnetic intergranular phases. Alternatively, if the interface coupling between the granular and intergranular phases is favorable, there can be a

magnetization and energy-product enhancement, of course with a concomitant decrease in coercivity [11].
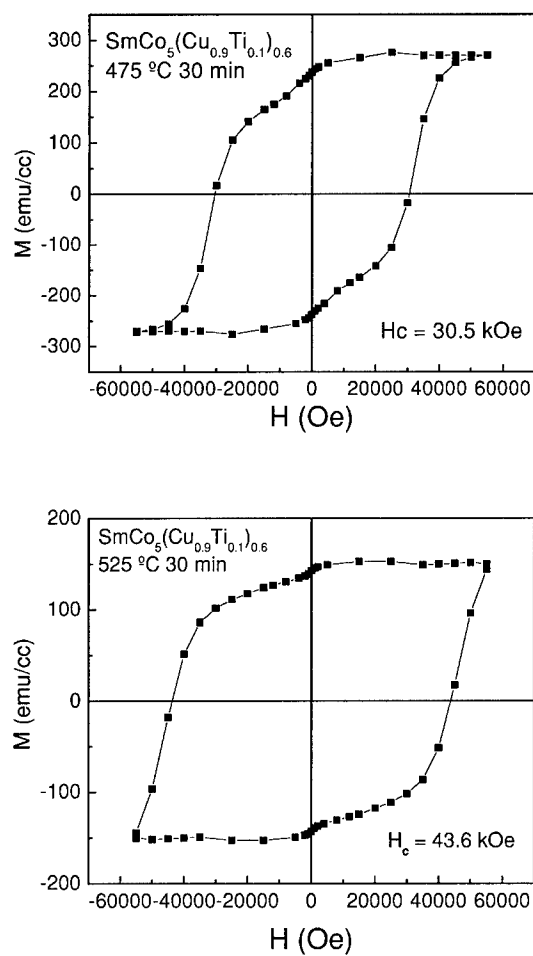
Figure 7. Hysteresis loops of SmCo$_5$Cu-Ti films with different annealing temperatures. The field is in the film plane.

The experiments to be described below involved mechanical milling of Sm(Co,Zr)$_{5.5}$ alloys. The idea was to examine the prospects for producing a hybrid magnet containing 1:5 and other Co-based phases with different anisotropies.

Nanostructured $Sm_{15.4}Co_{84.6-x}Zr_x$ (x = 0-5) magnet powders were synthesized by mechanical milling the as-cast alloys and appropriate annealing. The synthesis and handling of powders were performed under the protection of argon gas with high purity. The powders were milled for 10 hr, and annealed under high-purity argon gas atmosphere at temperature of 700 °C for 20 min. The phase configuration and structure were characterized for the as-cast alloys, milled powders and annealed powders with x-ray diffraction (XRD) with Cu K_α radiation.

Figure 8 shows the hysteresis loops measured at room temperature for the $Sm_{15.4}Co_{84.6-x}Zr_x$ (x = 0, 4) powders subjected to milling for 10 hr and annealing at 700 °C for 20 min. It is clear that high coercivity values can be obtained in these alloys. Comparing the two loops, the case with x = 0 shows a demagnetization behavior with less squareness while the x = 4 case indicates larger coercivity and good squareness. However, the remanent magnetization (M_r) is decreased in the powders with x = 4. Coercivity values up to 32 kOe were obtained in the powders with x = 4.
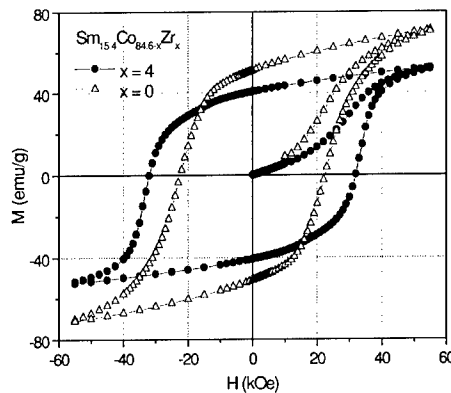
Figure 8. Magnetic hysteresis loops (at 295 K) for $Sm_{15.4}Co_{84.6-x}Zr_x$ (x = 0, 4) magnet powders.

Hard magnetic materials parameters (H_c and M_r) derived from the corresponding magnetic hysteresis loops are presented in Figure 9 for the $Sm_{15.4}Co_{84.6-x}Zr_x$ (x = 0-5) magnet powders. The coercivity value for the $Sm_{15.4}Co_{84.6-x}Zr_x$ (x = 0-5) magnet powders increases from 22.4 kOe for powders with x = 0 to about 32 kOe for powders with x = 4. However, the remanent magnetization decreases from about 51 emu/g for x = 0 to 37.6 emu/g for x = 5, that is, with increasing Zr content.
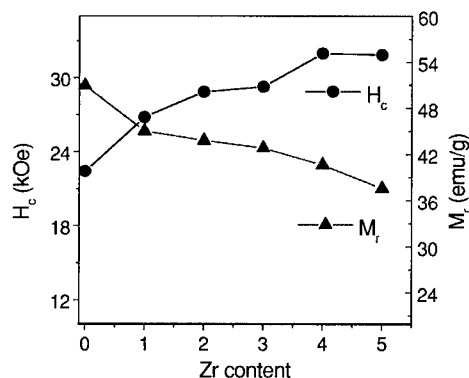
Figure 9. Dependence of room-temperature values of H_c and M_r upon Zr content in $Sm_{15.4}Co_{84.6-x}Zr_x$ ($x = 0$-5) magnet powders subjected to milling for 10 hr and annealing at 700 °C for 20 min.
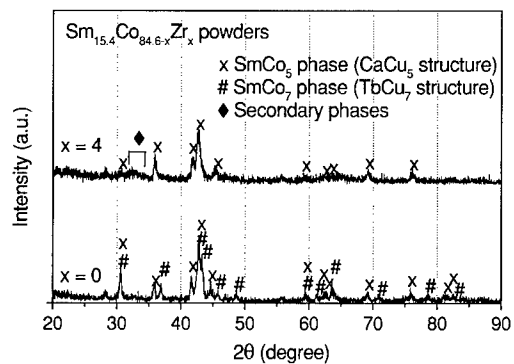
Figure 10. XRD patterns for $Sm_{15.4}Co_{84.6-x}Zr_x$ ($x = 0$ and 4) alloys powders subjected to milling for 10 hr and annealing at 700 °C for 20 min.

Figure 10 shows XRD data for $x = 0$ and 4 samples. For the undoped alloys the structure consists mainly of 1:5 and disordered 1:5 (that is, 1:7) grains. Upon alloying with Zr ($x = 4$), the lines can be indexed mostly with 1:5 structure lines, with evidence for a small admixture of secondary phases that are seen around 32-34 degrees. Sm-Co phases with x-ray lines in this region include Sm_2Co_7, and $SmCo_3$ which also have lines that overlap those of the 1:5 phase.

The grain size of the hard $SmCo_5$ phase evaluated by the Sherrer formula is about 16 nm for the x = 4 powders.

The magnetic hardening seen in Figure 8 as Zr is added to Sm-Co is difficult to understand without further understanding of the nanostructure, especially through TEM studies. The small sizes of the 1:5 grains and the presence of a small amount of secondary phases is consistent with a picture of pinning of interaction domain walls [11,14] as mentioned above. The magnetic characterization of the intergranular phase is needed to assess the possibilities for exchange coupling between the grains as well as the details of the magnetization reversal mechanism. Such characterization studies are underway.

HIGH-TEMPERATURE PERMANENT MAGNETS WITH PARAMAGNETIC BOUNDARY PHASES

One effect of additives such as Cu is to reduce the comparatively large Curie temperature of the cobalt-rich rare-earth intermetallics. In 2:17-1:5 Sm-Co hybrids, the Cu prefers to go into the grain-boundary phase, where it yields a pronounced reduction of the Curie temperature. Indirectly, this is exploited in commercial Sm-Co magnets and in some of the materials discussed in the previous sections: the Curie-temperature reduction in the grain-boundary phase leads to a reduced grain-boundary anisotropy, which enhances ΔK and improves, according to Eq. (1), the coercivity.

It is, however, conceivable to access the region where the grain-boundary phase is paramagnetic. This completely eliminates the harmful effect of domain walls jumping from one grain to the next grain and establishes a kind of Stoner-Wohlfarth behavior. Figure 11 illustrates the idea. Figure 11(a) shows the trapping of a domain wall between two ferromagnetic grains, whereas in Fig. 11(b) the grains are magnetically isolated. As shown in [15], two-phase magnets consisting of phases having different Curie temperatures exhibit a single well-defined and quite high Curie temperature, but at temperatures between the Curie temperatures of the phases the coupling between the 'ferromagnetic' regions is quite small when the thickness of the 'paramagnetic' grain-boundary phase is larger than a very few interatomic distances. This is the case for Sm-Co hybrid magnets, where the grain-boundary thickness is of the order of 5 nm, and where the Curie temperature of the Cu-rich grain boundary phase is significantly lower than the Curie temperature of the main phase.

As a consequence, the magnets can be treated as a weakly interacting array of small particles. The corresponding exchange field between neighboring grains is

$$H_{ex} = c\,k_B T_c\,\frac{\exp(-t_B/\lambda)}{a^2 M_s R} \tag{3}$$

Here λ is a decay length of the order of 0.3 nm, t_B is the thickness of the boundary region, R is the grain size, a is the lattice constant, T_c is the Curie temperature of the main phase, and c is a geometry and lattice-structure dependent constant of the order of one.

The magnetization reversal in these magnets is of the nucleation type [16]. In conventional Sm-Co hybrids, the regime described by Eq. (3) is realized above the Curie temperature of the grain boundary phase, which is quite high (about 650 °C in Fig. 1). However, by specific substitutions, such as adding very large amounts of Cu or other elements, it may be possible to yield a further suppression of the Curie temperature. This would cost a little bit of magnetization

but have a very positive effect on the coercivity, which is the most critical issue in high-temperature permanent magnetism.

(a)　　　　　　　　　　　　　　　(b)
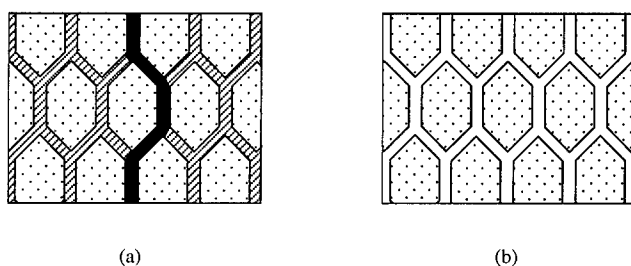
Figure 11. Magnetic structure of a cellular hybrid (a) below and (b) above the Curie temperature of the boundary phase. Magnetization reversal due to domain-wall motion is possible at low temperatures only.

CONCLUSIONS

We have discussed results of several methods for producing hard magnetic nanostructures containing two or more magnetic phases. Clearly there is a need for detailed nanostructure information to understand the secondary phases and their effect on the magnetization reversal mechanism. Theoretical mechanisms involving pinning and paramagnetic grain boundary phases have been discussed and applied to certain of the nanostructured magnets studied experimentally. Further research combining experimental and theoretical work on hybrid magnets of the type discussed here may well lead to new hard magnets with excellent high-temperature properties.

ACKNOWLEDGMENTS

REFERENCES

[1]　J. F. Liu, Y. Zhang, D. Dimitrov, and G. C. Hadjipanayis, *J. Appl. Phys.* **85**, 2800 (1999).
[2]　J. Zhou, R. Skomski, C. Chen, G.C. Hadjipanayis, and D.J. Sellmyer, *Appl. Phys. Lett.* **77**, 1514 (2000).
[3]　J. Zhou, R. Skomski, and D.J. Sellmyer, *IEEE Trans. Magn.* **37** (2001) (in press).
[4]　J. Fidler, *J. Magn. Magn. Mater.* **30**, 58 (1982).
[5]　R. Skomski, *J. Appl. Phys.* **83**, 6724 (1998).
[6]　J.P.Liu, C.P.Luo, Y.Liu, and D. J.Sellmyer, *Appl. Phys. Lett.* **72**, 483(1998).
[7]　J.P.Liu, Y.Liu, R.Skomski, and D.J.Sellmyer, *IEEE Trans. Mag.* **35**, 3241 (1999).

[8] Z.M. Chen, X. Meng-Burany, H. Okumura, and G.C. Hadjipanayis, *J. Appl. Phys.* **87**, 3409 (2000).

[9] H. Tang, Y. Liu, and D.J. Sellmyer, to be published.

[10] P.G. McCormick, *Handbook on the Physics and Chemistry of Rare Earths*, Vol. **24**, ed. by K.A. Gschneidner, Jr. and L. Eyring. (Elsevier Science B.V., 1997), and citations therein.

[11] G.C. Hadjipanayis, *J. Magn. Magn. Mater.* **200**, 373 (1999), and citations therein.

[12] J. Ding, P.G. McCormick and R. Street, *J. of Alloys and Compounds* **191**, 197 (1993).

[13] J. Ding, Y. Liu, P.G. McCormick and R. Street, *J. Magn. Magn. Mater.* **123**, L239 (1993).

[14] K.J. Strnat, in: *Ferromagnetic Materials*, Vol. **4**, edited by E.P. Wohlfarth and K.H.J. Buschow, (Elsevier Science Publishers B.V., 1988), p. 131, and citations therein.

[15] R. Skomski and D.J. Sellmyer, *J. Appl. Phys.* **87**, 4756 (2000).

[16] Localized nucleation rather than coherent rotation or curling; the critical single-domain size is irrelevant in this context (see e.g. R. Skomski and J. M. D. Coey, "Permanent Magnetism", Institute of Physics, Bristol and Philadelphia 1999).

Magnetostriction

SPONTANEOUS AC FIELD INDUCED MECHANICAL ROTATION IN MAGNETOSTRICTIVE FeSiB-BASED WIRES SUBJECTED TO THERMAL TREATMENTS

V.Raposo[1,2], A.Mitra[1,3] and M.Vázquez[1]

[1] Instituto de Ciencia de Materiales de Madrid, CSIC, 28049 Cantoblanco, Madrid, Spain
[2] Dpto. Física Aplicada, Universidad de Salamanca, 37008 Salamanca, Spain
[3] National Metallurgical Laboratory, Jamshedpur, India

ABSTRACT

An astonishing new phenomenon has been recently observed in magnetic wires. It consists of the spontaneous rotation of the wires when submitted to an exciting AC axial field with frequency of the order of kHz and amplitude above some threshold. The rotation is believed to appear due to interaction between generated magnetoelastic standing waves and induced eddy currents. In the present work rotational characteristics of $Fe_{77.5}Si_{7.5}B_{15}$ and $Fe_{73.5}Si_{13.5}B_9Cu_1Nb_3$ wires in their as-cast amorphous state and after heat treatments leading to devitrification has been investigated. It is proved that this rotational phenomenon is only observed in samples with large enough magnetostriction irrespective of their structural character. Moreover, changes in rotational characteristics are ascribed to the structural modifications accompanying the devitrification process.

INTRODUCTION

The mechanical rotation of Fe base amorphous wires with bistable magnetic behavior when subjected to an alternating AC field of several kHz has been recently reported [1-3]. Rotational wire frequencies oscillate around tens of Hz. Wire rotation frequency depends on magnetostriction constant, and it has been observed for both positive and negative values as shown in [2]. The influence of the length of the wire in the excitation frequency that causes a rotation and the appearance of rotation at higher harmonics of some fundamental frequencies reveals the existence of a resonant magnetoelastic standing wave in intimate correlation with the origin of the rotation. This phenomenon has been proved to have potential applications in different fields such as in micro-motors or viscosimetry [4,5].

Although a quantitative theory is not currently available, our results show that this is a general property of materials with high magnetostriction constant, no matter their crystalline structure, since it is present in amorphous but also in polycrystalline wires, as recently reported [6]. Consequently, the rotational behavior is nowadays expected to be determined neither by the alloy composition, nor by the structural nature of the material, nor by the domain structure, but seemingly by the magnetostrictive character of the sample.

The aim of this work has been to study the AC field induced rotation of $Fe_{77.5}Si_{7.5}B_{15}$ and $Fe_{73.5}Si_{13.5}B_9Cu_1Nb_3$ amorphous wires exhibiting large magnetostriction in their as-cast state and after annealing that finally results in the devitrification of the samples [7]. In fact, in the case of $Fe_{73.5}Si_{13.5}B_9Cu_1Nb_3$ wires, annealing leads to homogeneous and stable partial crystallization with noticeable reduction of magnetostriction and disappearance of that phenomenon.
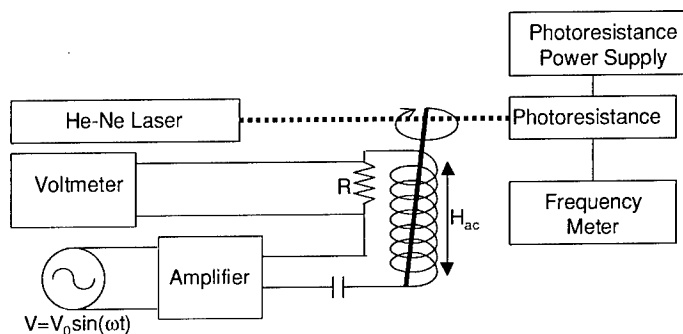
Figure 1. Schematic block diagram of the measuring set-up

EXPERIMENTAL TECHNIQUES

$Fe_{77.5}Si_{7.5}B_{15}$ and $Fe_{73.5}Si_{13.5}B_9Cu_1Nb_3$ amorphous wires have been prepared at the laboratory by in-rotating-water quenching-technique. The diameter of the wires was $120\mu m$ and pieces about 50 mm in length were taken for the AC field induced rotation experiments. The experimental set-up for measuring the rotation frequency of the wire is shown schematically in Figure 1. The wire was placed inside a 40 mm long solenoid generating an axial magnetic field (constant of $125Am^{-1}/A$). The solenoid was fed by a current to produce axial AC magnetic field by a function generator (model HM 8030-5) coupled with an amplifier. A thin glass tube of 4 mm in diameter was placed inside the coil and its bottom was sealed with a flat glass piece. Thus, the wire rotates freely leaning on its bottom end in a vertical position. The frequency of the applied axial AC magnetic field ranged from 1 kHz to 35 kHz. The rotational speed of the wires was measured by the interception of a laser beam, which was directed towards a detector (photoresistance) connected to a frequency meter. The measured frequency actually showed double value of the real frequency of rotation since the interception with the laser beam was twice that of a complete rotation of the wire.

Magnetic hysteresis loops of the samples used for rotational experiments were measured using a conventional low-frequency induction technique.

Isochronal (30 min.) thermal treatments were performed in a conventional Joule heated furnace under argon atmosphere for a range of annealing temperatures up to 650°C.

DISCUSSION OF RESULTS

Hysteresis loops of the as-cast and annealed wires of $Fe_{77.5}Si_{7.5}B_{15}$ and $Fe_{73.5}Si_{13.5}B_9Cu_1Nb_3$ are presented in Figures 2 and 3, respectively. As it can be seen, as-cast wires of both compositions do not present the usual bistable squared loops due to their short length (50 mm), smaller than the closure domain structures formed at the ends of the wires to reduce the magnetostratic energy [8]. As annealing temperature is increased the samples loose completely the large Barkhausen jumps due to the relaxation of internal stresses. After annealing at 540°C the $Fe_{77.5}Si_{7.5}B_{15}$ sample looses the amorphous structure (Fe_3Si and Fe_2B grains segregate) and its soft magnetic properties (coercive field increases up to 65 Oe).
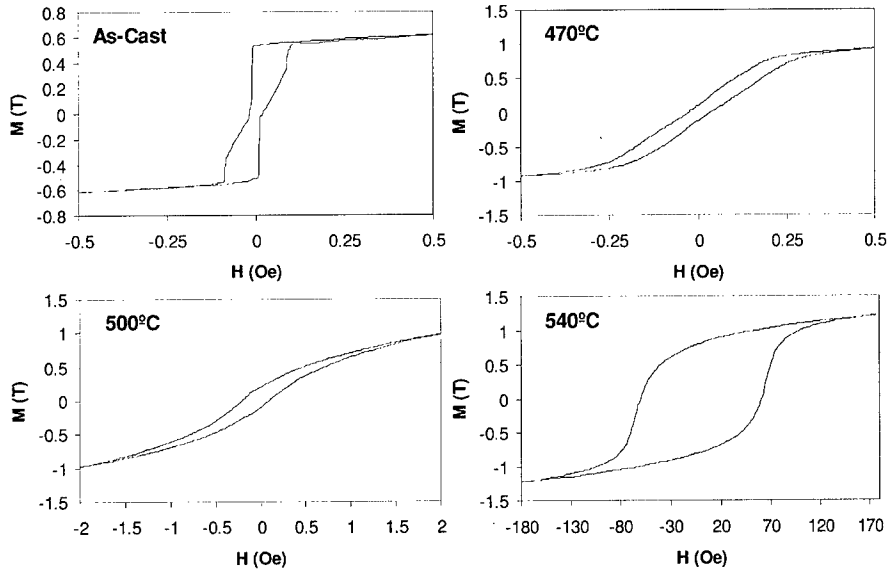
Figure 2. *Hysteresis loops for the As-Cast and annealed $Fe_{77.5}Si_{7.5}B_{15}$ wires.*

In the case of $Fe_{73.5}Si_{13.5}B_9Cu_1Nb_3$ wires, α-FeSi nanograins (around 10 nm average grain size) segregate after treatment at 540°C. The devitrification process goes further with increasing the annealing temperature resulting in grain size increase and appearance of new phases (i.e. Fe_2B). In particular, after annealing at 650°C a magnetic hardening is observed similar to that obtained annealing at 540°C for the $Fe_{77.5}Si_{7.5}B_{15}$ wire.

Figure 4 shows the $Fe_{77.5}Si_{7.5}B_{15}$ wire rotation frequency as a function of the exciting field frequency for a constant AC field amplitude of 90 Oe for as-cast and annealed wires. Rotation of the as-cast wire is found at certain characteristic frequencies of the applied field and at their higher harmonics. Figure 5 shows the corresponding spectra for the $Fe_{73.5}Si_{13.5}B_9Cu_1Nb_3$ wires at the same AC field amplitude.

To determine the characteristic fundamental frequencies at which rotation takes place, the experimental data have been fitted to a superposition of Gaussian distributions, $y(t)$, around the characteristic frequencies as:

$$y(f) = \sum_{i=1}^{N}\sum_{j=1}^{4} A_{ij}(f)\exp\left[-\sigma\left(f - jF_i\right)^2\right] \tag{1}$$

where F_i are the characteristic frequencies, σ is related to the width of the Gaussian distribution N is the number of fundamental frequencies and $A_{ij}(f)$ is an amplitude parameter that depends on the field amplitude. The index j denotes the corresponding harmonic number. For the $Fe_{77.5}Si_{7.5}B_{15}$ wires there are two fundamental frequencies, but for the $Fe_{73.5}Si_{13.5}B_9Cu_1Nb_3$ wires up to four frequencies are needed to characterize the spectra. As shown in Figures 4 and 5 the rotation is observed not only at one frequency, but also in a narrow frequency range around these fundamental ones with a Gaussian-like shape.
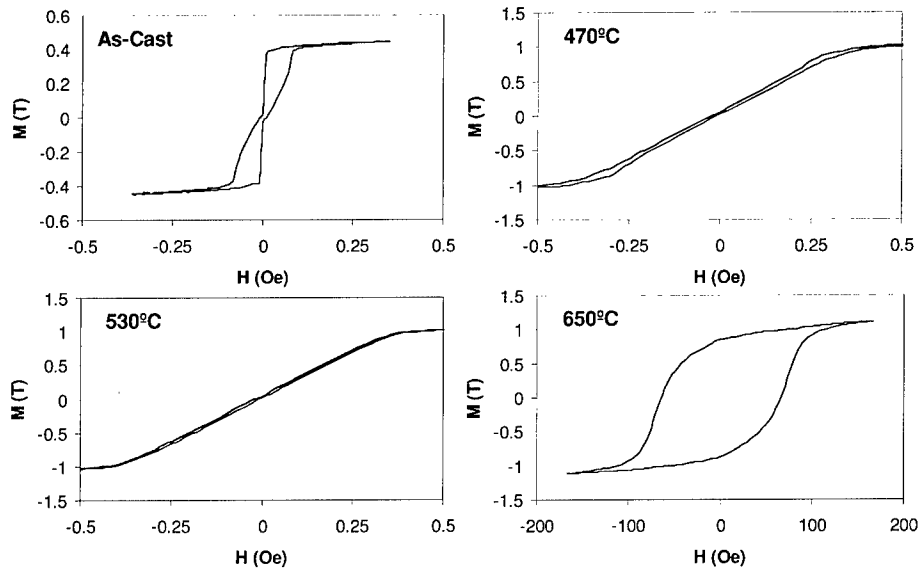
Figure 3. *Hysteresis loops for the As-Cast and annealed $Fe_{73.5}Si_{13.5}B_9Cu_1Nb_3$ wires.*

In spite of the complex spectra (see Figure 4), the higher harmonics of a set of fundamental frequencies can be extracted. The number N of fundamental frequencies found for $Fe_{77.5}Si_{7.5}B_{15}$ and $Fe_{73.5}Si_{13.5}B_9Cu_1Nb_3$ samples is 2 and 4, respectively. In the $Fe_{77.5}Si_{7.5}B_{15}$ wire for all the annealing temperatures there are two fundamental modes around 5 and 8 kHz, being the one at 5 kHz quite wide. Only the devitrified sample has a very different spectra with reduced number of modes and frequencies of rotation. Also, an increase of the wire rotation frequency with exciting frequency can be observed. This result supports the idea that the rotation is caused by the coupling of the eddy currents induced in the wire when there is a magnetolastic resonance. As frequency is increased so are the induced currents, and accordingly the Lorentz force. This force is not canceled due to the lack of perfect symmetry in the system, as the wire is standing in a non-uniform alternating magnetic field. In $Fe_{77.5}Si_{7.5}B_{15}$ samples, the changes in magnetostriction constant are negligible during structural relaxation [9]. This fact explains the quite similar spectra of wire rotation frequency for all the samples. The differences in the 540°C annealed sample can be explained by the crystallization and the induced magnetic hardening.

This is in contrast with the results obtained for the $Fe_{73.5}Si_{13.5}B_9Cu_1Nb_3$ wires. In these wires, annealing results in intermediate devitrification and quite large change in the magnetostriction constant [10]. This change modifies the rotational spectra of the wires as shown in Figure 5. Fundamental frequencies found in the as-cast state (4.7, 7.5, 10.8 and 12.5 kHz) shift with annealing and eventually, after treatment at 550°C rotation disappears. This temperature corresponds to the optimum soft magnetic properties when the lowest magnetostriction value is achieved. Rotation is observed again upon a new increase of magnetostriction with further crystallization (e.g. aneealing at 650°C).
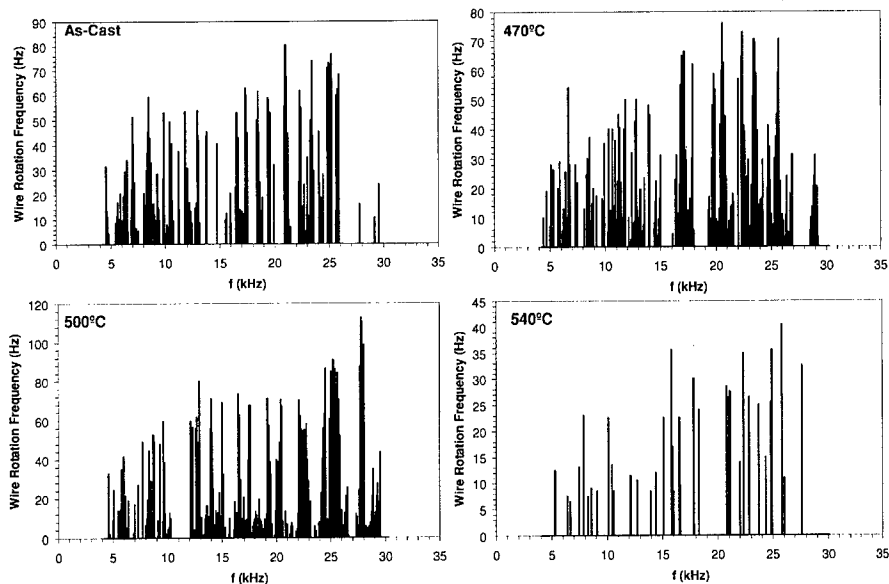
Figure 4. Rotational spectrum (wire frequency vs exciting field frequency) for the as-cast $Fe_{77.5}Si_{7.5}B_{15}$ wire and after annealing at different temperatures as indicated.

All these results show that AC field induced rotation has its physical origin in the magnetoelastic resonance, which is more important as magnetostriction constant is increased. This parameter can be tailored in some compositions as the $Fe_{73.5}Si_{13.5}B_9Cu_1Nb_3$.

CONCLUSSIONS

A new effect consisting of the AC field induced mechanical rotation has been studied in $Fe_{77.5}Si_{7.5}B_{15}$ and $Fe_{73.5}Si_{13.5}B_9Cu_1Nb_3$ wires subjected to thermal treatments that modify their structural nature. In the case of the $Fe_{77.5}Si_{7.5}B_{15}$ wire, rotational characteristics are almost unchanged by annealing, at least until crystallization is achieved, which is ascribed to the fact that the magnetostriction constant does not change significantly. In contrast, $Fe_{73.5}Si_{13.5}B_9Cu_1Nb_3$ wires undergo noticeable changes of magnetostriction before full crystallization. Rotational characteristics are determined most importantly by magnetostriction but are also modified by the structural nature and the degree of magnetic softness. The influence of exciting AC frequency also supports the assumption that the rotation is caused by the coupling of the induced eddy currents with the non-uniform magnetic field that exist in the coil. In short, for this phenomenon to be observed, magnetically soft materials are required but exhibiting large enough magnetostriction.
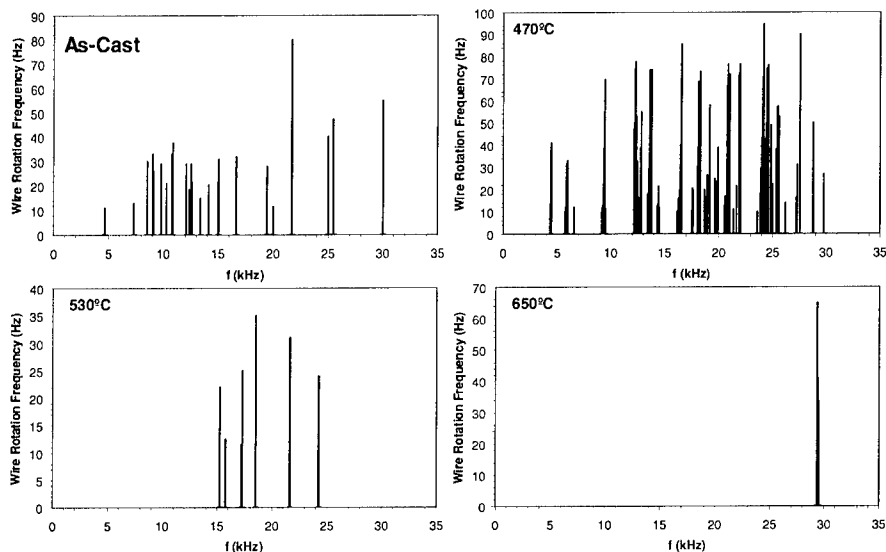
Figure 5. *Rotational spectrum (wire frequency vs exciting field frequency) for the as-cast $Fe_{73.5}Si_{13.5}B_9Cu_1Nb_3$ wire and after annealing at different temperatures as indicated.*

ACKNOWLEDGEMENTS

REFERENCES
1. H. Chiriac, C.S. Marinescu, and T.-A. Ovári, IEEE Trans. Magn. 33 (1997) 3349.
2. F.J. Castaño, M. Vázquez, D.-X. Chen, M.Tena, C. Prados, E. Pina, A. Hernando, and G. Rivero, Appl. Phys. Lett. 75 (1999) 2117.
3. H. Chiriac, T.-A. Ovári and C.S. Marinescu, J. Magn. Magn. Mat. 215-216 (2000) 413.
4. F.J. Castaño, M. Vázquez, T.-A. Óvári, D.-X. Chen, and A. Hernando, IEEE Trans. Magn. 36 (2000) 2791.
5. M. Vázquez, F. J. Castaño, T.-A. Óvári, V. Raposo, and A. Hernando, Sensors and Actuators A. 2934 (2001) (in press)
6. V. Raposo, T.A. Óvári and M. Vázquez , IEEE Trans. Magn. (in press, issue July 2001)
7. P. Marín, M. Vázquez, A.O. Olofinjana and H.A. Davies, Nanotructured Materials 10 (1998) 299.
8. M. Vázquez and D.-X. Chen, IEEE Trans. Magn. 31 (1995) 1229.
9. A. Hernando and M. Vázquez, in "Rapidly solidified alloys" (ed. H.H. Liebermann), Marcel Dekker, Inc. New York, 1993 p. 553-590.
10. G. Herzer, "Nanocrystalline Soft Magnetic Alloys", Handbook of Magnetic Materials, Vol.10 (ed. K.H.J Buschow), Elsevier Science B.V. 1997, p 417-461.

Observation of Patterns by Magnetic Force Microcopy in Fe-alloys with Shape Memory Effect

M. I.N. da Silva, J. C. González and M. S. Andrade[1]
North Carolina State University, Analytical Instrumentation Facility,
Raleigh, NC, 27695-7531, U.S.A.
[1]Laboratório de Nanoscopia, Setor de Tecnologia Metalúrgica – CETEC, Av. José Cândido da Silveira, 2000, Belo Horizonte-MG, 31170-000, Brazil.

ABSTRACT

In this study, we investigated the magnetic domains of a FeMnSiNiCr stainless steel sample using Magnetic Force Microscope (MFM). We compared the magnetic patterns obtained by scanning the sample with three coated probes with different magnetic properties: Medium magnetic moment (MM), low magnetic moment (LM), and low coercivity (LC). The probe-surface separation was varied between 25 to 300 nm in order to quantify the magnetic microstructure of the sample. A simple model for the probe-sample interaction was used to interpret the contrast change as a function of the probe-surface separation. The experiment showed that the average maximum frequency decreases with the probe-surface separation and the intensity of the frequency is the strongest for the MM probe. X ray diffraction experiments were used to identify the different phases present in the sample. The X-ray diffraction experiments together with the MFM showed that α-phase islands surrounded by a γ-phase matrix are responsible for the magnetic properties of the sample.

INTRODUCTION

Fe-based alloys with Shape Memory Effect (SME) [1] have great technological importance. The SME effect correspond to a martensitic transformation in the material and may be defined as the property of recovering its original shape during a thermal cycle after a material has been apparently deformed in a permanent way. In order to maximize the SME, it is important to eliminate or reduce at minimum other phase present in the material that not contribute to the SME. In our case the ferromagnetic phase α play an important role reducing the SME efficiency, being important the study and characterization of the magnetic microstructure of the sample. Magnetic force microscopy (MFM) has proven to be a useful tool for imaging the magnetic microstructures in a variety of magnetic materials [2]. This technique has characteristics such as high spatial resolution and minimum sample preparation. MFM is based on the interaction between a magnetic sample and a magnetic coated Atomic Force Microscopy (AFM) probe or tip. The AFM tip can be coated with a variety of materials with different magnetic properties. The contrast observed in this kind of microscopy depends strongly of the magnetic interaction between the sample and the AFM tip as well as the modifications that the magnetic AFM tip can induce on the magnetic microstructure of the sample. The choice of magnetic coating for the AFM tip can reveal fine microstructure in the magnetic domains of the sample or simply modify the microstructure itself leading to an erroneous characterization of the

sample. In this work, the magnetic domains of a FeMnSiNiCr stainless steel sample, with strong SME, were studied using the MFM technique. We compared the magnetic patterns obtained by scanning the sample with three coated probes with different magnetic properties: Medium magnetic moment (MM), low magnetic moment (LM), and low coercivity (LC). The tip-surface separation was varied from 25 to 300 nm in order to quantify the magnetic microstructure of the sample. A simple model for the magnetic tip-sample interaction was used to interpret the contrast change as a function of the tip-surface separation, for all the three AFM tips. X ray diffraction experiments were used to identify the different phases present in the sample.

EXPERIMENTAL DETAILS

A Digital Instruments Dimension 3000 Scanning Probe Microscope (SPM) was used in Tapping/Lift^{TM} mode. In this mode the tip oscillates close to its mechanical resonance frequency. These measurements are based on a two-pass technique for each scanline. In the first pass, the topographical data from the surface of the sample is acquired. The tip is then raised up and a second pass is done keeping a constant separation between the tip and the surface of the sample (lift height). During the second pass, the shift in the resonant frequency induced by the interaction of the dipolar field of the sample with the magnetic moment of the tip is acquired at each point of the scanline. The lift mode virtually eliminates the cross link with the topography of the sample during the MFM measurements.

The AFM tips used in this work were Silicon cantilevers with pyramidal tips from the Digital Instruments MESP series. The first tip used in this work was a standard MESP tip (MM) coated with 50 nm of CoCr alloy. This tip is considered to have a medium coercivity with a value of approximately 400 Oe, as well as a medium magnetic moment of approximately 10^{-13} emu. The second tip used was a MESP-LM tip (LM) coated with 15 nm of CoCr alloy. This tip has a coercivity of approximately 400 Oe, and a magnetic moment three times lower than the MM tip, both of which are considered low. The third tip was a MESP-LC tip (LC) coated with a NiFe alloy. With a coercivity value less than 1 Oe and a magnetic moment similar to the MM tip, the coercivity and the magnetic moment values of this tip are considered low.

The FeMnSiNiCr stainless steel used in this work has the following composition (weight %): 66Fe-14Mn-6Si-9Cr-5Ni. An ingot was prepared by induction melting of purity materials under an argon atmosphere. A square sample of 1×1 cm^2 of area and 2 mm thick was cut from the ingot, embedded in epoxy, and polished with a diamond past of 1 μm grain size in order to obtain a flat surface. Following this process the sample was rinsed with DI water, dried with Ar, and mounted in the SPM to be imaged.

The X-ray experiment was carried out in a Rigaku Geigerflex 2037 diffractometer. Monochromatic CuKα radiation was used. The data was collected in the 2θ mode.

RESULTS AND DISCUSSION

Figure 1 shows an X-ray diffractogram of the sample at room temperature. X ray results showed the presence of three phases in the sample: a paramagnetic γ–phase, a ferromagnetic α–phase, and a tetragonal crystal structure σ-phase. Based on these results, we expected the MFM measurements to reveal small magnetic areas surrounded by a large paramagnetic matrix. Due to the fact that the γ-phase and σ-phase are both of paramagnetic nature, it was not possible to
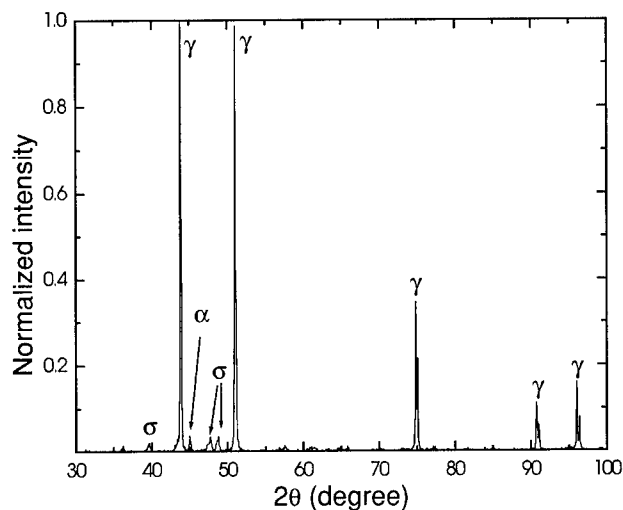
Figure 1. X-ray diffractogram obtained at room temperature.

differentiate the two phases in the MFM measurements. Only the magnetic areas of the α-phase can clearly be distinguish from the rest of the matrix.

Figure 2 presents the MFM measurements obtained with the three different tips. A topographic image of the surface of the sample is shown in Figure 2(a) with z scale of 15 nm. The sample is relatively flat and only small scratches from polishing are visible. Figures 2(b) through (d) are MFM images obtained with the MM, LC, and LM tips, respectively, from the same region of the sample as shown in 2(a). Figures 2(b) through (d) present an interesting magnetic microstructure not observed in the Figure 2(a). Z scale is 12 Hz for figure 2(b) and 2 Hz for figure 2(c) and 2(d). In these images, two distinct patterns are easily identified: a lighter region, which is paramagnetic in nature as well as a larger ferromagnetic region with characteristic dark and light stripes.

Images 2(c) and (d) have an apparent larger lateral resolution than 2(b). This "loss" of resolution in Figure 2(b) is caused by the remagnetization effect [3] that the high coercivity and medium moment tip induces into the low coercivity sample. A reverse in contrast of the images shown in 2(b) and (d) is observed in Figure 2(c). This change in contrast is caused by the realignment of the magnetic moment of tip [4]. In this case, the dipolar field from the sample is high enough to rotate the moment of the low coercivity tip, which leads to the misinterpretation of the direction of the dipolar field of the sample. In the case of Figure 2(d), the high coercivity and low moment tip reads the true magnetic microstructure of the sample without inducing a remagnetization of the domains in the sample with the resulting lost of resolution, as observed in the case of the MM tip. In addition, there is no realignment of its own moment that can cause a misinterpretation of the direction of the dipolar field of the sample, as in the case of the LC tip. As can be seen from the results, the choice of coating material, and as a consequence the magnetic properties, of the tip are extremely important to evaluate the real magnetic
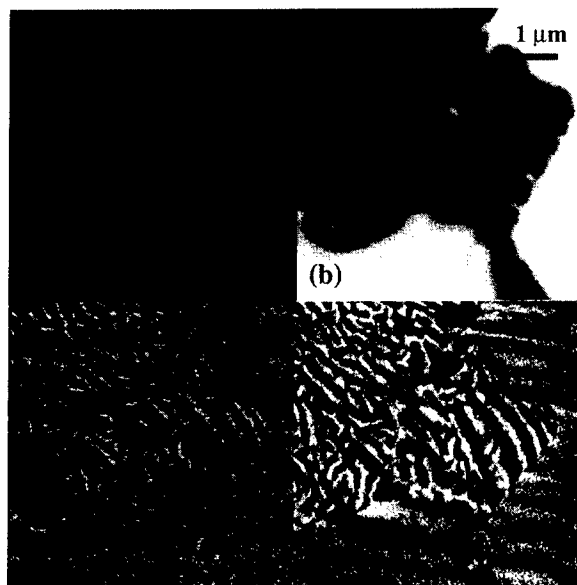
Figure 2. Images of the sample. Topographic image (a), MFM image using MM tip (b), MFM image using LC tip (c), and MFM image using LM tip (d).

microstructure of the sample. We think the best option is to choose a tip with a magnetic moment low enough to produce a magnetic field lower than the coercivity field of the sample, but with coercivity field larger than the dipolar field produce by the sample. However, the magnetic moment of the tip has to be relatively large in order to maximize the interaction with the sample.Figure 3 shows MFM images of the sample, taken with the MM tip at different lift heights. Figure 3(a) is the topographic image of the surface of the sample. Figures 3(b) through (h), are MFM images of the same region with a tip-surface separation of: 25, 50, 100, 150, 200, 250, and 300 nm, respectively. The z scale is 30 nm for image (a) and 80 Hz for images (b) through (h). In these images the magnetic α-phase appears as an island in the center of the images surrounded by the paramagnetic phase. As the tip-surface distance increases, the frequency shift of the cantilever decreases indicating a weakness of the magnetic signal from the sample. The frequency shifts as a function of the tip-surface separation for the MM tip and LC tip are shown in Figures 4(a) and 4(b).
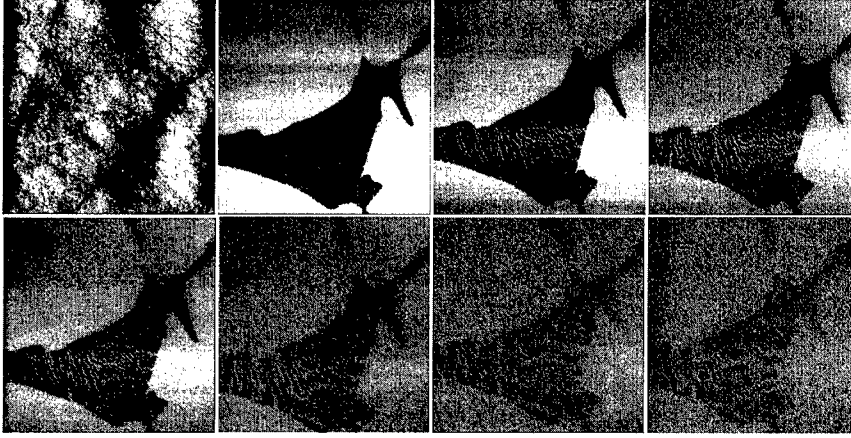
Figure 3. Topographic image (a) of a 50 µm x 50 µm field of the sample, (b) through (h) are MFM images with a tip-surface separation of 25, 50, 100, 150, 200, 250, and 300 nm, respectively.

In order to understand the decrease in the frequency shift with the lift height, a very simple model [5] for the tip-sample interaction was developed. This model considers the interaction between a magnetic probe of magnetic dipole m along the z direction with the stray magnetic field H_z from the sample. In order to calculate the stray field H_z from the sample a very simple approximation is made: considering the magnetic domains can be represented by disks of radius b and magnetization M along the z direction at a distance h from the surface of the sample. The magnetic force gradient Δf_0 in the direction z can be expressed as following equation:

$$\Delta f_0 = \frac{\omega_0}{2k} m \frac{\partial^2 H_z}{\partial z^2} = \frac{3\pi b^2 \omega_0 M\, m}{k} \frac{z+h}{\left[(z+h)^2 + b^2\right]^{5/2}} \tag{1}$$

where z is the tip-surface separation, k is the spring constant, and ω_0 is the natural frequency of the cantilever.

The best least squares solid lines in Figure 4 shows fit of expression (1) to the experimental data and the values of the parameters are summarized in Table I.

The fairly good fit to the experimental data shown in Figure 4 corroborates the validity of the model used. Note that the size and depth of the domains found by the MM tip are almost two (1.78) times larger than the respective values found by the LC tip, confirming the remagnetization effect induced by the MM tip in the structure domain of the low coercivity sample. However, the two tips sense the magnetic domains at approximately the same depth.
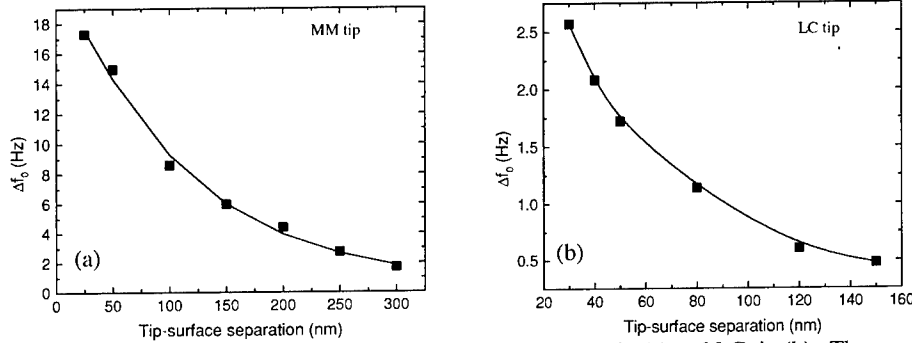
Figure 4. Frequency shift versus tip-surface separation for MM tip (a) and LC tip (b). The squares are experimental data and the lines are the fit using expression (1).

Table I. Parameters for the two tips, HM and LC, obtained by fitting experimental points with expression (1).

Tip	ω_0 (kHz)	b (nm)	h (nm)	Mm' (nm^2)
MM	55.35	187	156	6.39
LC	77.98	105	130	5.00

CONCLUSION

The MFM technique has been shown to be a powerful tool to identify ferrite phases in Fe-alloys with shape memory effect. Different magnetic patterns were observed when MM, LC, and LM tips were employed. A broadening of the magnetic domains due to the remagnetization effect induced by the MM tip in the sample was observed. A contrast inversion was observed in the MFM images produced by the LC tip. This contrast inversion was related to the rotation of the magnetic moment of the low coercivity tip induced by the relatively strong dipole field of the sample. A high coercivity and low magnetic moment tip proved to be ideal for the study of magnetic microstructure of this kind without inducing misinterpretation of size and orientation of the magnetic domains in the sample. A simple model was used to understand and quantify the tip-sample interaction and the magnetic microstructure of the sample.

ACKNOWLEDGEMENTS

REFERENCES

[1] M. I. N. da Silva et al, Mat. Res. Soc. Symp. Proc. **604**, 227 (2000).
[2] H. K. Wickramasinghe, Acta Mater. **48**, 347 (2000).
[3] L. Folks, R. C. Woodward, J. Magn. Magn. Mater. **190**, 28 (1998).
[4] D. L. Bradbury, L. Folks, and R. Street, J. Magn. Magn. Mater. **177-781**, 980 (1998).
[5] B. R. A. Neves and M. S. Andrade, Applied Physics Letters, **74**, 2090 (1999).

Tailoring of Magnetic Properties of Glass coated Microwires

A.P. Zhukov[1,2], J. González[3] V. Zhukova[3] and J.M. Blanco[4]

[1] Donostia International Physics Centre, P. M. de Lardizabal 4, 20018 San Sebastián, Spain
[2] "TAMag" S.L., C/ José Abascal 53, Madrid, Spain
[3] Dept. Material Physics, Chemistry Faculty, P.O. Box 1072, 20080 San Sebastián, Spain
[4] Dept. Appl. Phys. I, EUITI, UPV/EHU, Avda Felipe IV 1B, 20011, San Sebastián (Spain).

ABSTRACT

The magnetic behaviour of the glass-covered metallic microwires with a wide compositional range of composition with soft and hard magnetic character is presented. The effect of conventional furnace and *dc* current annealing under *dc* axial magnetic field or without it as well as of a chemical etching on the magnetic properties of Co and Fe-based glass coated microwires has been studied. Such treatments modify the magnetic parameters. In particular, annealing under applied magnetic field (field annealing) can improve significantly such magnetic parameters as permeability. Such phenomenology can be interpreted considering the noticeable magnetic anisotropy induced by the combined effects of the magnetic field and strong internal stresses arising from the coating. Giant magnetoimpedance (GMI) effect was observed in nearly-zero magnetostrictive amorphous microwires. Upon careful heat treatment, FeCuNbSiB amorphous microwires devitrificate into nanocrystalline structure with large variety of magnetic parameters. Hard magnetic materials with coercivity up to 800 Oe were obtained as a result of decomposition of metastable phases in Co-Ni-Cu microwires as well as after crystallization process of FeCuNbSiB amorphous microwires.

1. INTRODUCTION

Studies of ferromagnetic amorphous wires obtained by in-rotating-water quenching technique with a typical diameter of around 120 μm has become a classic topic of applied magnetism owing to their very particular magnetization properties. Large Barkhausen jump between two stable remanent states (so-called magnetic bistability, MB) and Giant Magneto-Impedance (GMI) effect have been observed and intensively studied in the last few years [1].

An alternative technology, the Taylor-Ulitovsky method, was recently employed to produce continuous microwire (0.4 Km/min) with a metallic nucleus (typically from about 1 μm to 20 μm in diameter) covered by insulating Pyrex-type glass coating sheath (with the thickness of 1- 10 μm). A number of outstanding magnetic properties, such as magnetic bistability, enhanced magnetic softness and GMI effect (up to 130%) have been found recently in such microwires [2-5]. The magnetic properties of microwires are correlated with their microstructure, composition and internal stresses originated from the difference of thermal expansion coefficients of the metal and the glass. Consequently, the magnetic properties could be improved by adequate treatment: heat treatment or chemical etching of the glass coating or by the selection of adequate chemical composition of the metallic nucleus.

The aim of this paper is to present novel results on compositional dependence and processing of glass-coated microwires in order to design their magnetic properties.

2. EXPERIMENTAL DETAILS

Microwires of different Fe-and Co-rich composition were obtained by the Taylor-Ulitovsky technique.

Varying the fabrication parameters, the microwires were fabricated with a different ratios, ρ, of the glass coating thickness, t, to the total radius, R, of the wire. The axial M_z - H_z hysteresis loop of the samples was obtained by conventional induction method at 50 Hz. Chemical etching of the external glass coating was produced in diluted (10% or 20%) solution of hydrofluoric acid (HF). The evolution of the structure after the annealing was observed using X-ray diffraction with CuK_α radiation. Furnace and current annealing treatments were used. Such treatments were carried out under the presence of a magnetic field (FA) and without field (CA).

The electrical impedance of the microwire was evaluated by means of the four-point technique. The magnetoimpedance ratio, $\Delta Z/Z$, has been defined as:

$$\Delta Z/Z = [Z(H) - Z(H_{max})]/Z(H_{max}) \qquad (1)$$

A maximum direct current longitudinal magnetic field, H_{max}, up to 2400 A/m was applied by a long solenoid.

3. EXPERIMENTAL RESULTS AND DISCUSSION
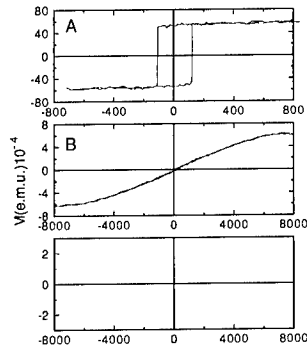
Figure 1. Hysteresis loops of $Fe_{70}B_{15}Si_{10}C_5$ (λ_S >0), $Co_{75}Si_{10}B_{15}$ (λ_S<0) and $Co_{68}Mn_7Si_{10}B_{15}$ (λ_S ≈0) microwires.

Hysteresis loops of three of studied microwires: Fe-rich (positive magnetostriction constant, λ_s), Co-rich (negative λ_s) and Co-Mn (nearly-zero λ_s) are shown in figures 1 (a-c) respectively. As can be seen, the shape of the hysteresis loops as well as main magnetic properties (coercivity, H_c, magnetic anisotropy field, magnetic permeability) depend on the composition of the sample. The conventional annealing (CA) in the range of 100 - 200 °C produces mainly small changes in the coercive field, ascribed to the relaxation of internal stresses. Nevertheless, if the thermal treatment was carried out under the presence of an axial magnetic field (field annealing, FA), significant changes of the hysteresis loop were detected (figure 2). This change produces an increase of the initial permeability, μ_i, coercivity, H_c, remanent magnetization, μ_0M_r, and a decrease of the anisotropy field, H_K (see figure 3). The changes of the shape of the hysteresis loop with FA should be connected to the induction of magnetic anisotropy with an easy axis along the longitudinal direction of the microwire. The field of induced anisotropy, ΔH_k has been calculated as the difference between the

Figure 2. Effect of magnetic field annealing (FA) on hysteresis loops of $(Co_{0.92}Mn_{0.8})_{75}Si_{10}B_{15}$ microwire at different annealing temperatures.
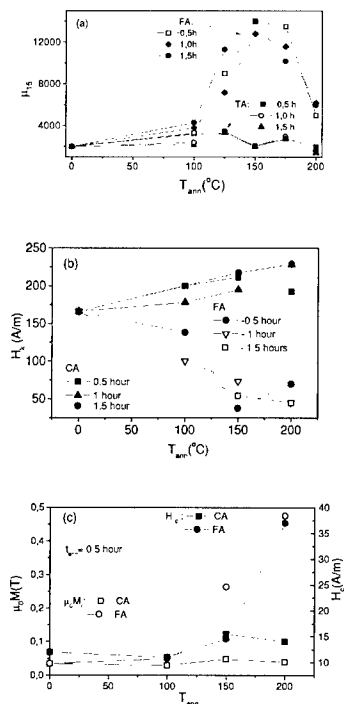
Figure 3. Effect of annealing on magnetic properties of $Co_{69}Mn_6Si_{10}B_{15}$ microwires: initial magnetic permeability, μ_{15} (a), anisotropy field, H_k (b), coercivity and remanent magnetization (c)

In the case of the sample $Fe_{70}B_{15}Si_{10}C_5$, both treatments (CA, FA) at 30 mA ($j=227\ A/mm^2$) caused a decrease of H_c with the t_{ann}. In the case of FA such decrease of coercivity is more significant.

In contrast, in the case of $Co_{56.5}Fe_{6.5}Ni_{10}B_{16}Si_{11}$ samples, both treatments result with opposite effects. CA treatment gives rise to roughly monotonic decrease of the coercivity, while FA results in an increase of H_c, with a broad maximum at $t_{ann}\approx10$ min. Similarly with $Fe_{70}B_{15}Si_{10}C_5$ samples, a monotonic decrease of H_c has been observed for $Co_{68}Mn_7Si_{10}B_{15}$ sample after both CA and FA treatments. Besides, as in the case of the $Co_{56.5}Fe_{6.5}Ni_{10}B_{16}Si_{11}$ sample, the FA treatment results in higher H_c, as comparing with the CA treatment.

anisotropy field before and after treatments. In case of FA treatment ΔH_k is of around 120 A/m. It must be noted that the moderate values of the annealing temperature cannot assume the pair ordering mechanism. We believe that this anisotropy is developed by the combine effect of the high internal stress and the magnetic field applied during the treatment [5].

Dependencies of the coercivity on the annealing time, t_{ann}, for current annealing CA and FA with current density 227 for three microwires is shown in Figure 4.
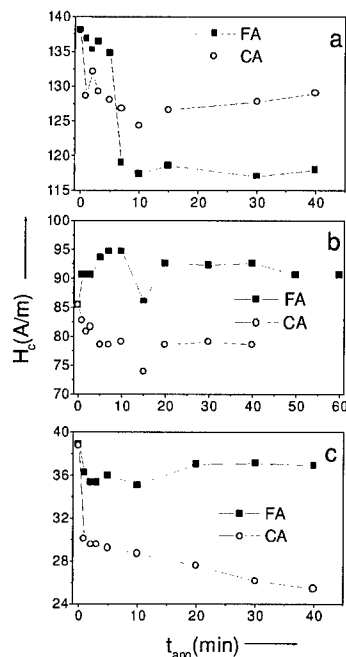
Figure 4. Comparative evolution of H_c with annealing time for CA and FA of $Fe_{70}B_{15}Si_{10}C_5$ (a), $Co_{56.5}Fe_{6.5}Ni_{10}B_{16}Si_{11}$ and $Co_{68}Mn_7Si_{10}B_{15}$ (c) microwires annealed at $j\approx227\ A/mm^2$ with the annealing time, t_{ann}, as a parameter.

Like in the case of conventional annealing (figures 3 and 4) we can explain the observed difference between the CA and FA as the effect of the stress+longitudinal field induced magnetic anisotropy in the last case, where the strong internal stresses contribute as the reinforcing factor.

A chemical etching treatment can also significantly change the magnetic properties. The effect of the chemical etching time, t, on coercivity, H_c, and remanence, $\mu_0 M_r$; is presented in figure 5. These observed experimental dependencies could be understood taking into account additional magnetoelastic energy arising from the glass coating. Strong internal stresses (up to 10^3 MPa) can even modify value and sign of the magnetostriction constant, especially if the magnetostriction constant is quite low. Consequently, removing of the glass coating gives rise to the stress relaxation.
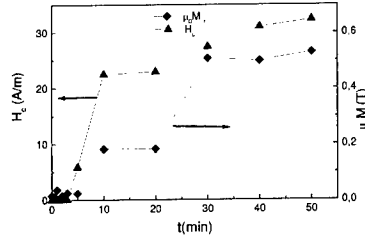
The very soft magnetic behaviour found in $Co_{68.5}Mn_{6.5}Si_{10}B_{15}$ microwires with small negative magnetostriction constant makes them very attractive to investigate the magnetoimpedance effect. A really high GMI has been observed in $Co_{68.5}Mn_{6.5}Si_{10}B_{15}$ microwire annealed at 100 °C for 1 hour (see figure 6). A maximum maximum, H_m, increase with frequency of driving current, f (see figure 6). This GMI effect is extremely sensitive to the application of external tensile stresses (figure 6b). The origin of this dependence is related with the magnetoelastic anisotropy induced by the tensile stress. It is remarkable to mention that the position of the DC axial field that corresponds to the maximum GMI ratio, H_m, should be attributed to the static circular anisotropy field, H_k. This allows us to estimate the magnetostriction constant using the well-known expression for the stress dependence of anisotropy field:

$$\lambda_s = (\mu_0 M_s/3)(dH_k/d\sigma) \qquad (2)$$

The $H_m(\sigma)$ dependence is roughly linear with a slope of around 0.7 A/(m×MPa), that gives $\lambda_{s,0} \approx -2\times10^{-7}$, which is reasonable in comparison with the recently reported values estimated for the similar composition ($\lambda_{s,0} \approx -3\times10^{-7}$) [6]

Annealing temperature, T_{ann}, dependence of the coercivity, H_c, for the $Fe_{71.8}Cu_{1.0}Nb_{3.1}Si_{15.0}B_{9.1}$ alloy with the geometric characteristics as parameter is shown in the figure 7. Generally a decrease of H_c has been observed at T_{ann} below 400 °C. Weak local minimum of H_c has been observed at about 400-450 °C with the temperature of that minimum depending on both alloy composition and geometry. Such decrease of H_c could be ascribed to the structural relaxation of the material remaining the amorphous character such as has been widely reported in metallic glass alloys. A small relative hardening (increase of coercivity) can be observed after annealing around 450-500 °C, which could be ascribed to the very beginning of first stage of devitrification. It is interesting to note the effect of the sample's geometry on this increase of the coercivity. A deeper softening (optimum softness) with rather low value of H_c is obtained in the samples treated at $T_{ann} = 500$-600 °C. Finally, abrupt increase of H_c is shown by the samples treated at T_{ann} above 600 °C, indicating the

Figure 5. Effect of chemical etching on the magnetic parameters of the $Co_{68}Mn_7Si_{10}B_{15}$ amorphous microwire.

GMI ratio, $(\Delta Z/Z)_m$, as well as a field of

Figure 6. Effect of the frequency, f, (a) and applied stresses (b) on $\Delta Z/Z$ ratio of $Co_{68.5}Mn_{6.5}Si_{10}B_{15}$ amorphous microwire
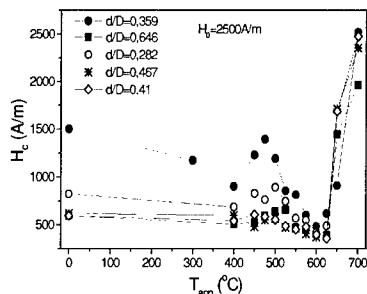
Figure7. Dependence of coercivity on the annealing temperature, T_{ann}, for $Fe_{71.8}Cu_1Nb_{3.1}Si_{15}B_{9.1}$ with the ratio d/D ranging from 0,282 to 0.646
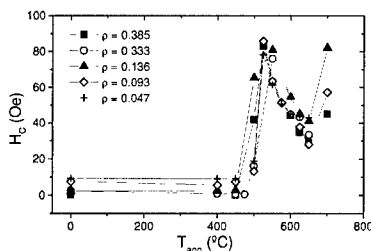
Figure 8. Dependence of the coercivity on the annealing temperature, T_{ann}, of the $Fe_{72.3}Cu_1Nb_{3.1}Si_{14.5}B_{9.1}$ microwires with the ratio d/D as the parameter.

beginning of the precipitation of iron borides (with grain size larger than 50 nm). Such beginning of the increase of H_c varies depending mainly on sample composition as well as on geometry. It must be noted that for the thickest glass coating the increase of H_c 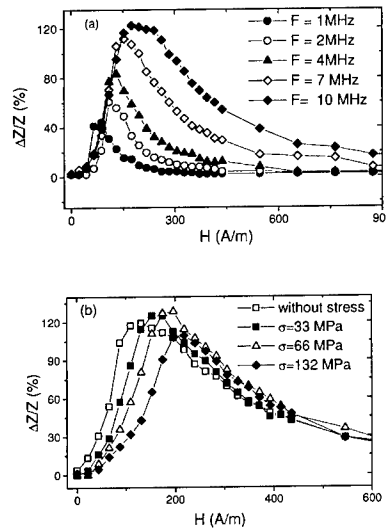appears at lower temperature, which could be related with the fact that the internal stresses induce some ordering to hinder the crystallization.

Slight change of the chemical composition results in drastic change of $H_c(T_{ann})$ dependence. Effect of the annealing temperature on the coercivity, H_c, of the $Fe_{72.3}Cu_1Nb_{3.1}Si_{14.5}B_{9.1}$ alloy with the ratio ρ as parameter is shown in the figure 8. A sharp magnetic hardening (significant increase of the coercivity) can be observed after annealing (500 – 550 ºC during 1 hour).

It should be indicated that the maximum of H_c takes place at the same range of annealing temperature as first small increase of coercivity in $Fe_{71.8}Cu_{1.0}Nb_{3.1}Si_{15.0}B_{9.1}$ related with the first re-crystallization process (see figure 7).

X-ray analysis of as-prepared $Fe_{72.3}Cu_1Nb_{3.1}Si_{14.5}B_{9.1}$ microwire does not detect a presence of crystalline phases after annealing at 550 ºC. Nevertheless, TEM diagram allowed to detect a small amount of fine grains of α-Fe, γ-Fe and α-Fe(Si) with the average grain size of such crystallites around 20-70 nm in annealed sample at 550 ºC.

The difference in magnetic behaviour with respect to the conventional *finemet*-type microwires can be attributed to different composition as well as to high internal stresses. It is well known that the best magnetic softness is achieved when the nanocrystalline structure consists of small α-Fe(Si) grains embedded in a residual amorphous matrix with vanishing magnetostriction constant. Probably, a small change in the composition of the metallic nucleus does not permit to achieve the vanishing magnetostriction constant. In addition, strong internal stresses dye to the glass coating can result in a change of structure of the precipitates (it is well known that internal strains of different nature can be as the origin of a martensitic-type transformation in Fe alloys). Probably, the strong internal stresses in the metallic nucleus could induce a precipitation of γ-Fe fine grains during the first stage of the crystallization process. Particularly, the presence of γ-Fe crystallites could be attributed the magnetic hardening observed in this microwire. To clarify this point new studies actually are in progress.

Figure 9 shows the $H_c(T_{ann})$ behaviour for the crystalline $Co_{29}Ni_{25}Cu_{45}Mn$ microwires. The as-prepared sample shows a relatively low coercivity (50 —100 Oe). Rising the annealing temperature until 973 K a strong increase in H_c is obtained,

Figure 9. $H_c(T_{ann})$ dependence in $Co_{29}Ni_{25}Mn_1Cu_{45}$ microwire

reaching the maximum value of around 800 Oe. A further increase of the annealing temperature results in a decrease of the coercivity such as can be observed in figure 9. The largest reduced remanence ratio $M_r/M_s = 0.5$ is also found after annealing at 973 K and the estimated saturation magnetization is of about 3.6 KG.

In the as-prepared microwire, quenched from a high temperature, only a single phase, with a lattice parameter $a = 0.3573$ nm was found (figure 10a). When the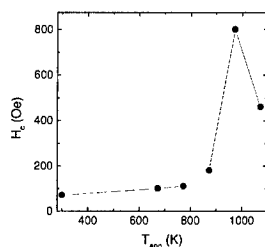 sample was heated at high temperatures, this metastable phase started to decompose. This can be seen in the sample treated at 973 K, where the segregation is not yet complete (figure 10b). After annealing at 1073 K, the sample shows the equilibrium phases, consisting of a copper matrix ($a = 0.3591$ nm) with Cu-rich particles ($a = 0.3545$ nm) (figure 10c).

These results are in agreement with the magnetic hardening in bulk Co-Ni-Cu permanent magnet alloys, and the maximum value of coercivity obtained after annealing at 973 K during 1 hour agrees with that previously reported by Bozorth [7].
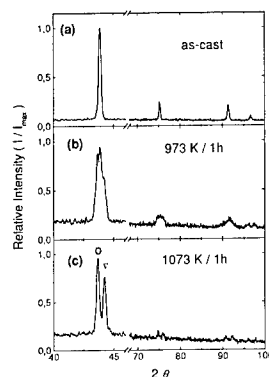
Figure 10. Effect of annealing on X-ray patterns of $Co_{29}Ni_{25}Mn_1Cu_{45}$ microwire

4. CONCLUSIONS

Magnetization process of glass-coated microwires determines by the magnetoelastic and shape anisotropy. Sign and value of the magnetostriction constant affect strongly the magnetization process. Significant changes of soft magnetic properties have been observed in Fe- and Co-rich microwires after different treatments (conventional and current annealing with or without axial magnetic field as well as chemical etching). The observed experimental results on the soft magnetic properties in Fe- and Co-rich microwires submitted to conventional and current annealing (with or without field) can be explained as a consequence of the induced magnetic anisotropy arising from the counterbalance between internal quenched-in stresses owing to the difference in thermal expansion coefficients of the metal and the glass. This induced anisotropy should be understood as originating from the simultaneous action of the large internal stresses and the axial applied magnetic field. Enhanced magnetic softness and GMI effect (up to 130%) has been observed after adequate thermal treatment. Significant stress dependence of this GMI effect has been found. The magnetostriction constant ($\lambda_{s,0} \approx -2\times10^{-7}$) is estimated from stress dependence of the GMI ratio.

It must be noted that the coercivity obtained by annealing Co-Ni-Cu-(Mn) microwire with a metastable single phase in the as-prepared state is enhanced up to 800 Oe by decomposition of the metastable phase. In the case of Fe-based (*finemet*-type) microwire, the strong magnetic hardening at low annealing temperature (around 550 °C) could be ascribed to the role of the internal stresses induced by the glass coating on the metallic nucleus.

References
[1] M. Vázquez, M. Knobel, M.L. Sánchez, R. Valenzuela and A. Zhukov, Sensors and Actuators A **59** 20 (1997)
[2] M. Vázquez and A.P. Zhukov, *J.Magn.Magn.Mat.*, **160** 223 (1996).
[3] H. Chiriac and T.A. Ovari, *Progress Mater.Sci.*, **40** 333 (1997).
[4] A.P. Zhukov, M. Vázquez, J. Velázquez, A. Hernando and V. Larin, **170** 323 (1997)
[5] A. Zhukov, J.González, J.M. Blanco, M. Vázquez and V. Larin, *J.Mat.Res* **15** 2107 (2000)
[6] A.F.Cobeño, A. Zhukov, A.R. de Arellano-López, F. Elías, J.M. Blanco, V. Larin and J.González, *J. Mat. Res.* 14 (1999) 3775
[7] R.M. Bozorth in *"Ferromagnism"* (Van Nostrand, New York, 1951) 402.

Domain Structure of 'Thick' Amorphous Microwires with Nearly Zero Magnetostriction

Horia Chiriac, Tibor-Adrian Óvári, Minoru Takajo[1], Jiro Yamasaki[2], and Arcady Zhukov[3]
National Institute of R&D for Technical Physics, 47 Mangeron Boulevard,
6600 Iaşi, Romania
[1]Nishinippon Institute of Technology, Department of Electrical Engineering,
Kanda, Fukuoka 800-0394, Japan
[2]Kyushu Institute of Technology, Department of Electrical Engineering,
Tobata, Fukuoka 804-0015, Japan
[3]Universidad del Pais Vasco, Departamento de Fisica de Materiales, P.O. Box 1072,
20080 San Sebastian, Spain

ABSTRACT

Nearly zero magnetostrictive glass-coated amorphous microwires are suitable materials for sensor applications. Samples with metallic core diameters below 20 μm exhibit almost nonhysteretic BH loop, related to the existence of a domain structure with azimuthal easy axis. The magnetic behavior of these microwires is changing drastically when the metallic core diameter increases over 25 μm, i.e. they display a bistable magnetic behavior at low fields, that is a one step magnetization reversal at a certain value of the applied field, called switching field. Results on the direct domain observation in nearly zero magnetostrictive $Co_{68.25}Fe_{4.5}Si_{12.25}B_{15}$ glass-coated amorphous microwires by means of Kerr microscopy are reported for the first time. The effect of glass removal on the domain structure has been also studied. AC hysteresis loop measurements have been employed to establish a correlation between domain structure and magnetic behavior.

Glass-coated microwires exhibit a single domain configuration with the magnetization pointing mostly to the wire axis. The domain structure does not change qualitatively after glass removal, but the parameters of the squared hysteresis loops are modified. The remanence to saturation ratio increases after glass removal, while the switching field decreases.

The obtained results are of interest for sensor applications, and show that the metallic core diameter is a dimensional factor that contributes to important changes in the domain structure and magnetization process of such microwires.

INTRODUCTION

Ferromagnetic amorphous glass-coated wires, also called microwires, represent a new class of materials, very suitable for sensors applications [1, 2]. Such microwires are usually prepared from three ferromagnetic alloy categories: (i) Fe-based with large and positive magnetostriction (e.g., $Fe_{77.5}Si_{7.5}B_{15}$ with $\lambda_S = 25 \times 10^{-6}$), (ii) Co-based with negative magnetostriction (e.g., $Co_{80}Si_{10}B_{10}$ with $\lambda_S = -4 \times 10^{-6}$), and (iii) Co-based with small amounts of Fe or Mn with nearly zero magnetostriction (e.g., $Co_{68.25}Fe_{4.5}Si_{12.25}B_{15}$ with $\lambda_S = -1 \times 10^{-7}$). Nearly zero

magnetostrictive microwires are mostly employed as sensing elements for magnetic sensors based on the giant magneto-impedance effect [3], due to their high azimuthal permeability and favorable domain structure.

CoFeSiB microwires with typical dimensions - diameters of the metallic core below 20 µm and glass coating thickness up to 15 µm - exhibit a domain structure with azimuthal easy axis of magnetization that results in an almost nonhysteretic axial BH loop [4].

The aim of this paper is to report for the first time results on the magnetic behavior of CoFeSiB amorphous microwires with the metallic core diameter over 25 µm and large total diameter (over 60 µm). In order to make a difference between such samples and microwires with typical dimensions, we called them 'thick' amorphous microwires.

EXPERIMENT

CoFeSiB amorphous microwires cut to 7 cm long samples have been investigated. Axial hysteresis loops were determined by an inductive method, using an AC axial field with a frequency of 60 Hz and a maximum amplitude of 4 Oe. Direct domain observations were performed based on longitudinal Kerr effect optical microscopy using an image processor.

Two sets of samples were studied: sample A with a total diameter of 101 µm, the metallic core diameter being 34 µm, and sample B with a total diameter of 63 µm, the metallic core diameter being 27 µm. Both sample A and B were measured before and after glass removal by chemical etching. The samples after glass removal were denominated as sample A1 and B1, respectively.

Figure 1 shows the low and high field axial hysteresis loops for sample A. The low field loop corresponds to a maximum applied field of 0.08 Oe, while the high field one is obtained for a maximum applied field of 4 Oe. One observes that the sample displays a bistable axial magnetization process, i.e. a single and large Barkhausen jump that occurs at a switching field value, H*, of 31.5 mOe.
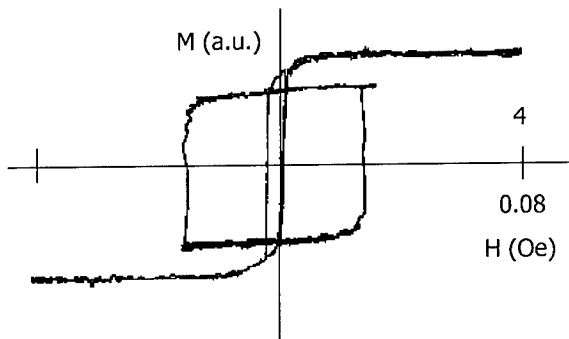
Figure 1. Low and high field axial hysteresis loops for a glass-coated CoFeSiB amorphous microwire with the metallic core diameter of 34 µm and a total diameter of 101 µm (sample A).

This magnetic behavior is different from that of microwires with the same composition, but with typical dimensions. Thus, the axial direction is a hard axis for typical microwires with this composition, while in this case it is an easy axis of magnetization. The explanation for this fact is related to the dominant energy terms from the expression of the total free energy, whose minimization decides the formation of domain structure.

In the case of typical microwires with nearly zero magnetostriction, it has been shown that the magnetoelastic energy minimization is responsible for the formation of a domain structure with transverse easy axis of magnetization, i.e. azimuthal in cylindrical coordinates, which are the most appropriate for the geometry of such materials [5]. In this way, the coupling between negative magnetostriction and large axial tensile stresses in the wire's inner region, and large compressive azimuthal ones at the surface, results in both cases in an easy axis of magnetization perpendicular to the axial direction. However, in the case of 'thick' microwires, it seems that the magnetoelastic energy is no longer the term whose minimization mainly decides the domain structure formation, but rather the magnetostatic energy plays this role. This hypothesis is supported by internal stress calculations. For example, the maximum value of the axial tensile stress within the microwire's inner region is about 1.5 GPa, and the maximum value of the compressive azimuthal stress at its surface is about -2.8 GPa for a microwire with a metallic core diameter of 7 μm and a glass coating thickness of 5 μm (total diameter 17 μm), while for the microwire with the metallic core diameter of 34 μm and the glass coating thickness of 33.5 μm (sample A) these values decrease to 450 MPa and -1.75 GPa respectively. Thus, it is expected to have a less important role of the magnetoelastic term in 'thick' microwires. The magnetoelastic term should count mostly near the surface of the metallic core, were the azimuthal compressive stresses are still large. Consequently, the magnetostatic energy minimization would result in an axial easy axis of magnetization, mainly due to the sample's shape.

Figure 2 shows the domain structure of sample A, before and after magnetization reversal. One observes a single domain configuration, that explains the measured hysteresis loops and sustains the above hypothesis.

Wire axis
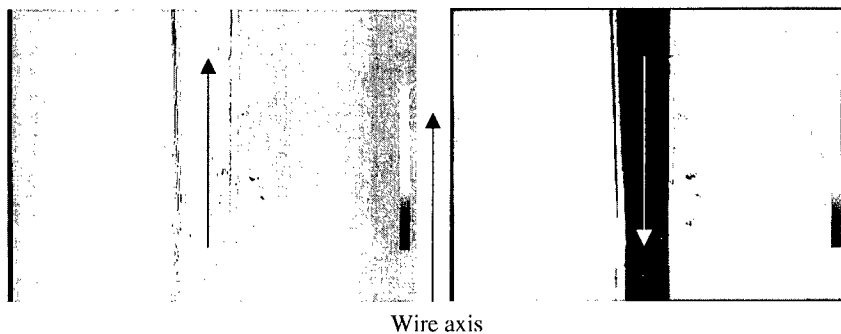
Figure 2. Kerr microscopy image showing the domain pattern of a glass-coated CoFeSiB amorphous microwire with the metallic core diameter of 34 μm and a total diameter of 101 μm (sample A).

Figure 3. Low and high field axial hysteresis loops for a CoFeSiB amorphous microwire with the glass coating removed, having the metallic core diameter of 34 μm (sample A1).

By analyzing the domain structure and the value of M_r/M_s (0.68), correlated with the quite large values of the azimuthal stresses towards the surface of the metallic core, one can state that 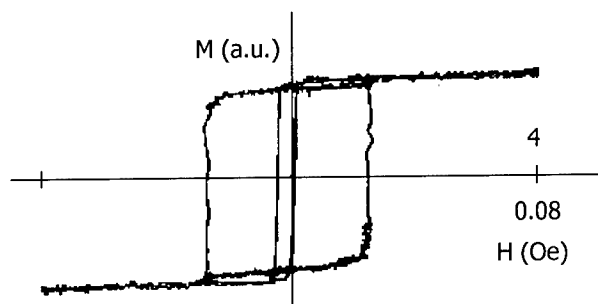near the surface the easy axis of magnetization has some inclination with respect to the axial direction as a result of the local importance of the magnetoelastic term.

Figure 3 shows the axial hysteresis loop for sample A1 (sample A after glass removal). One observes that the magnetic bistability is maintained (the large Barkhausen jump occurs at a somewhat lower value of H^*: 27.7 mOe). On the other hand, the remanence to saturation ratio increases after glass removal, being 0.88.

These changes in the magnetic behavior are in agreement with the transformations suffered by typical microwires with the same composition at glass removal [5]. Hence, typical microwires become bistable after glass removal, mainly due to stress relief that accompanies glass removal. In the case of 'thick' microwires after glass removal, stress relief improves bistability, i.e. the switching field decreases while the remanence to saturation ratio increases. Thus, stress relief is expected to reduce the influence of the magnetoelastic term even near the surface of the metallic core, and consequently the inclination of the easy axis in this region, and the microwire becomes magnetically softer on the axial direction.

Results of direct domain observation by Kerr microscopy, illustrated in figure 4, for the case of sample A1 show that the single domain configuration with the magnetization pointing to the wire axis is maintained.

Similar magnetic behavior and domain configurations have been observed for samples B and B1. For sample B, H^* is 66.8 mOe and M_r/M_s is 0.82, while after glass removal H^* decreases to 46.3 mOe and M_r/M_s increases slightly to 0.88. In this case, the maximum value of axial tensile stress reaches to 750 MPa, while the maximum azimuthal compressive one is -1.5 GPa. The larger value of H^* for sample B, with respect to the value obtained for sample A, is related to the differences in the shape anisotropy and other contributions like smaller demagnetization. The larger value of M_r/M_s originates in the even weaker contribution of magnetoelastic energy near the surface of the metallic core as compared to the case of sample A, which is perfectly explainable if we refer to the ratio between glass thickness and metallic radius. Thus, it has been previously shown that the magnetoelastic term's contribution is larger in

Wire axis
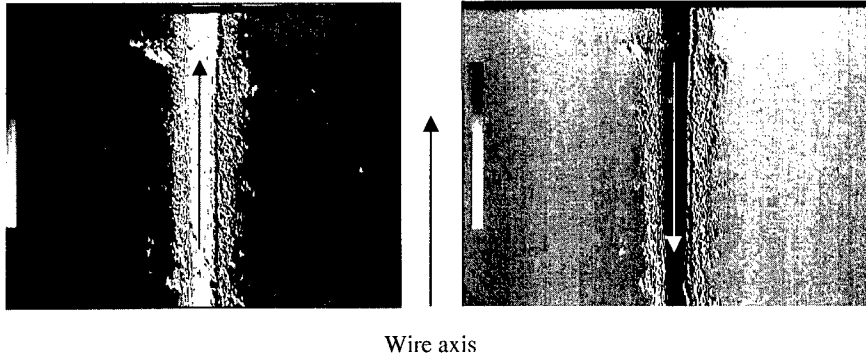
Figure 4. Kerr microscopy image illustrating the domain configuration of a CoFeSiB amorphous microwire with the glass coating removed; the metallic core diameter is 34 μm (sample A1).

microwires with larger ratios between glass coating thickness and metallic core radius [6]. In the case of sample A, this ratio is 1.97, while in the case of sample B it is 1.33.

Glass removal induces similar changes in the characteristics of the magnetic behavior of sample B as in the case of sample A. The fact that M_r/M_s reaches to the same value (0.88), indicates some kind of 'saturation' of the remanence to saturation ratio, that should originate in the local action of the magnetoelastic term that is always important near the surface of the metallic core. Results of direct domain observation by Kerr microscopy show for both samples B and B1 the single domain configuration with axial magnetization. The domain configuration for sample B is illustrated in figure 5.

Wire axis
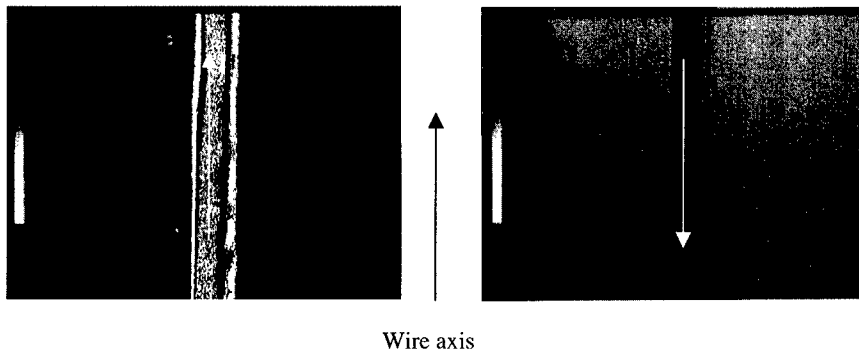
Figure 5. Kerr microscopy image of the domain configuration of a glass-coated CoFeSiB amorphous microwire with a metallic core diameter of 27 μm and a total diameter of 63 μm (sample B).

CONCLUSIONS

Results on the magnetic behavior and domain structure of 'thick' amorphous microwires with nearly zero magnetostriction were presented for the first time.

We observed that such samples display single domain configuration with the magnetization direction pointing mostly to the wire axis. In addition, the low field axial magnetization process of the investigated samples is achieved by a single and large Barkhausen jump that occurs at a certain value of the axially applied magnetic field. The domain configuration and magnetization process do not change after glass removal, but an enhancement of the soft magnetic properties on the axial direction was observed.

The obtained results show that the microwire dimensions are a critical parameter that can determine abrupt changes in the magnetic behavior of microwires with the same composition, i.e. changes in the mechanism of magnetization.

REFERENCES

1. H. Chiriac and T.-A. Óvári, *Prog. Mater. Sci.* **40**, 333 (1996).
2. M. Vázquez and A. Zhukov, *J. Magn. Magn. Mater.* **160**, 223 (1996).
3. H. Chiriac, T.-A. Óvári, and C.S. Marinescu, *IEEE Trans. Magn.* **33**, 3352 (1997).
4. A.F. Cobeño, A. Zhukov, A.R. de Arellano-Lopez, F. Elias, J.M. Blanco, V. Larin, and J. González, *J. Mater. Res.* **14**, 3775 (1999).
5. H. Chiriac, Gh. Pop, T.-A. Óvári, and F. Barariu, *IEEE Trans. Magn.* **32**, 4872 (1996).
6. H. Chiriac, T.-A. Óvári, Gh. Pop, and F. Barariu, *IEEE Trans. Magn.* **33**, 782 (1997).

X-ray Magnetic Linear Dichroism of Fe-Ni Alloys on Cu(111)

T.F. Johnson,[1] S. Chiang,[1] Y. Sato,[1] D.A. Arena,[2] S.A. Morton,[3] M. Hochstrasser,[2] J.G. Tobin,[2] J.D. Shine,[1] J.A. Giacomo,[1] G.E. Thayer,[1] D.P. Land,[4] X.D. Zhu[1]

[1]Dept. of Physics, University of California, Davis
[2]Lawrence Livermore National Laboratory, Livermore
[3]University of Missouri, Rolla
[4]Dept. of Chemistry, University of California, Davis

ABSTRACT

We have prepared Fe_xNi_{1-x} multilayers on Cu(111) in order to learn how to control the structure and magnetism of these thin alloy films, which are relevant to the giant magnetoresistance (GMR) effect used in magnetic disk drive heads. Using the Spectromicroscopy Facility (7.0.1.2) on Undulator Beamline 7.0 at the Advanced Light Source, we have measured X-ray magnetic linear dichroism (XMLD) signals from both Fe and Ni 3p lines for fourteen different thin Ni-Fe alloy films on Cu(111), with Fe concentration ranging from 9% to 84% and for a variety of film thicknesses. The Curie temperature for all of these samples was in the range 200K to 500K. For many of these films, the Curie temperature was considerably lower than was previously seen for similar films deposited on Cu(100). For a particular Fe concentration x, the Curie temperature increases with alloy film thickness. For a specific film thickness, the Curie temperature has a maximum near $x \approx 0.4$.

INTRODUCTION

The ability to control growth at the atomic level has led to renewed interest in the study of magnetism and magnetic materials. This control allows for the study of the relationship between magnetic and structural properties for optimization of magnetic devices based on thin film technologies, as well as testing the theoretical predictions for such systems.[1] We are studying layer-by-layer synthesis of ultrathin metal films by controlling the composition and structure of these films at the monolayer level, including the interfacial region. We have prepared Fe_xNi_{1-x} multilayers using simultaneous evaporation of pure Ni and Fe on Cu(111) in order to better understand the GMR effect in NiFe/Cu systems that are relevant to magnetic disk drive heads.

Using core-level photoelectron spectroscopies on magnetized samples allows for exploitation of the fact that symmetry is broken due to the presence of magnetization. The effect is due to spin-orbit interaction in the presence of exchange interaction. X-ray magnetic linear dichroism (XMLD) is one such technique that clearly exhibits asymmetry due to magnetization. XMLD can be observed in angle resolved, spin-integrated photoemission experiments for p-polarized light under oblique incidence.[2] The first example of this effect was shown on a thin Fe(001) film, for which the Fe 3p core level peak position and line shape changed when the magnetization of the sample was reversed.[2] Because of its dependence on photoemission from a core level, the effect can be used for surface sensitive, element-specific magnetometry. In this study, we have observed this effect for 14 samples of different thicknesses with Fe concentration from 9% to 84%. This paper discusses the temperature dependence of the dichroism signal.

EXPERIMENT

The sample used in the experiment was a copper (111) single crystal, 1 cm in diameter and ~3 mm thick. This crystal was polished mechanically and electrochemically. Laue X-ray diffraction was used to determine that the miscut was within 1°. The sample was mounted in the Spectromicroscopy Facility[3] on Beamline 7 at the Advanced Light Source (ALS), Berkeley, for sample preparation and dichroism experiments. Sample cleaning consisted of cycles of argon ion sputtering (3kV, 20μA) and annealing to 550-600°C. Alloy samples were formed by simultaneous electron beam evaporation of Fe and Ni. Actual composition and thickness of the films were determined *in-situ* by X-ray photoelectron spectroscopy (XPS) with 1250eV photons. Figure 1 is a full range XPS survey scan measured on a $Fe_{0.64}Ni_{0.36}$ alloy sample with thickness of ~5ML. This scan clearly demonstrates the chemical purity of this sample, as there is no evidence of carbon or oxygen contamination. The Cu, Ni, and Fe 2p peaks are clearly observed, as are the Cu and Fe 3p lines. The elemental composition and thickness of such a thin film sample is determined quantitatively from the 2p peak heights in such a scan.

Soft x-ray radiation from Undulator Beamline 7.0 was used to perform XMLD experiments using the SpectroMicroscopy Facility (7.0.1.2). We utilized 190eV p-polarized photons to measure photoemission of Fe and Ni 3p core levels in normal emission with 2° angular resolution. The photon beam was incident at 60° to the surface normal. The magnetization direction was along the [1, -1,0] direction in the plane of the Cu(111) sample and also perpendicular to the plane determined by the electron emission and the propagation direction of the light for maximum contrast upon magnetization reversal.[4] Elementally specific magnetometry of the Ni-Fe alloys on Cu(111) was performed as a function of composition, thickness, and temperature. The dependence of the XMLD signal on temperature was used to obtain an approximate Curie temperature for the samples, as a function of Fe concentration.
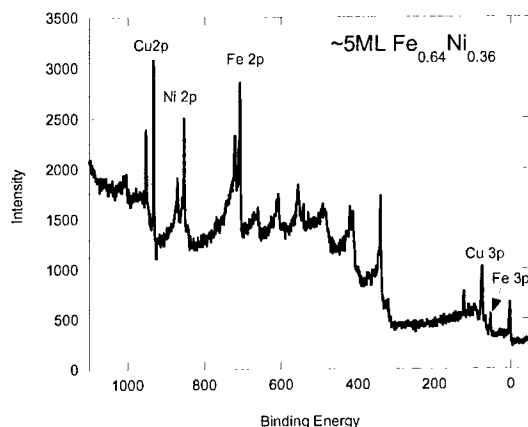
Figure 1. Wide scan survey of a $Fe_{0.64}Ni_{0.36}$/Cu(111) sample using plane polarized soft x-ray radiation at 1250eV. Sample concentrations are determined by normalized peak ratios with corrections for the cross sections and mean free paths.

RESULTS AND DISCUSSION

Figure 2 shows the XMLD effect for Fe concentration of 0.55 and thickness of 10 ML. The Ni and Fe 3p lines were measured with photon energy of 190eV. The upper panel clearly shows that the XPS data are different depending on the orientation of the applied field relative to the sample. The Fe 3p and Ni 3p lines were measured for magnetization up and down, and the difference is the XMLD signal. The lower panel shows the difference between the two spectra in the upper panel and thus exhibits the dichroism effect. We have examined the size of the dichroism signal as a function of both composition and film thickness, and those data will be published separately.[5] We have also measured the dichroism signal from both the Fe and the Ni peaks. The asymmetry, $\dfrac{\mathrm{MagUp} - \mathrm{MagDown}}{\mathrm{MagUp} + \mathrm{MagDown}}$, as measured from the XMLD signal, is proportional to the total magnetization of the sample.
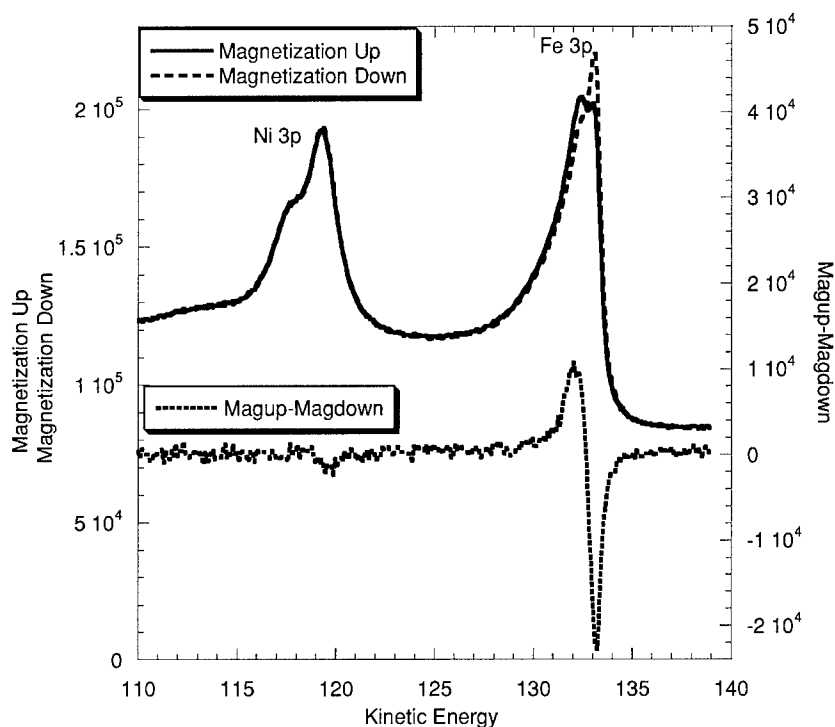
Figure 2. XMLD data from $Fe_{0.64}Ni_{0.36}$ film, 10 ML thick, on Cu(111). Top of figure shows the Ni 3p and Fe 3p XPS lines, measured with photon energy of 190eV, for magnetization up and down. Bottom of figure shows difference spectrum, which is proportional to the dichroism.

Our XMLD spectra clearly indicate that samples of specific thicknesses and Fe concentrations are ferromagnetic. Furthermore, our recent studies using the photoelectron emission microscope (PEEM2) instrument on Beamline 7.3 at the ALS indicate that both Fe and Ni are magnetic and well mixed in these thin alloy films.[6]

Figure 3 shows the asymmetry (in %) as a function of temperature for films with three different Fe concentrations, all ~5ML thick. The manual feedback system resulted in temperature variations of less than $\pm 5^\circ$C during the measurement of a dichroism spectrum. Although the data appear to fit the predictions from mean field theory, detailed fits to the theory are still in progress.

An approximate Curie temperature (T_c) for the ferromagnetic samples was extracted by extrapolating asymmetry data as a function of temperature, such as those in Figure 3, to find the temperature at which the magnetic asymmetry disappears. Figure 4 illustrates the change in Curie temperature T_c for varying thickness and concentration. As could be seen in the data in Figure 3, for a particular film thickness, as the Fe concentration x increases, T_c increases until $x \approx 0.4$ and then decreases. For all of our samples, T_c was in the range from 200K to 500K. Note that for even for film thicknesses larger than 5ML, T_c was below room temperature for low Fe
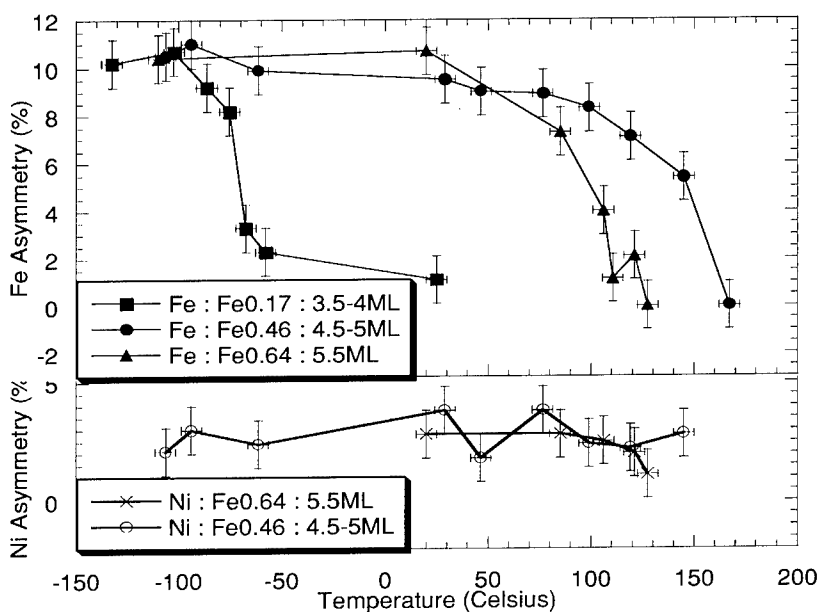
Figure 3. Fe and Ni asymmetry, in percent, as a function of temperature, for three samples, with varying Fe concentration. All thicknesses are about 5ML. The lines are drawn as a guide to the eye.
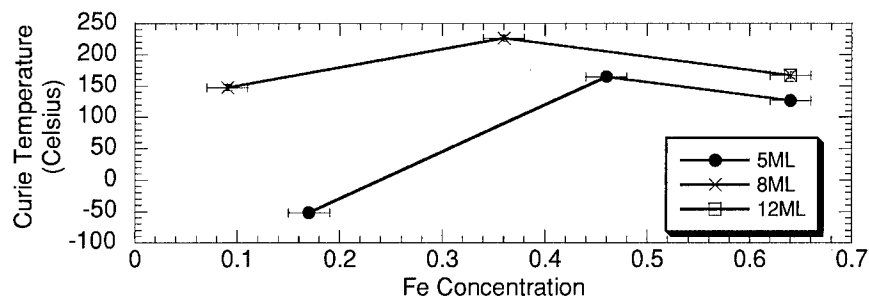
Figure 4. Approximate Curie temperature of $Fe_xNi_{1-x}/Cu(111)$ samples as a function of Fe concentration, for three different film thicknesses. Note the maximum in the Curie temperature occurs near x=0.4.

concentration. In contrast, an earlier XMLD study of Fe_xNi_{1-x} films on $Cu(100)$ found that T_c was above 250K for film thicknesses larger than ~2ML.[7] For a specific Fe concentration, Figure 4 also shows that the Curie temperature increases for higher film thickness.

CONCLUSIONS

This paper has presented dichroism data on thin layers of Fe_xNi_{1-x} on $Cu(111)$. Data on the temperature dependence of the dichroism was shown and discussed. The trends in the Curie temperature as a function of film thickness and concentration were also reviewed. In addition, an ultrahigh vacuum surface magneto-optical Kerr effect (SMOKE) apparatus is under development in our laboratory. This apparatus will make it much easier to measure the Curie temperature of additional thin alloy samples, making it possible to obtain further data as a function of alloy composition and thickness in our own laboratory. Further studies are in progress in our group to study the structure of the Fe_xNi_{1-x} alloy films on $Cu(111)$ in more detail using several other techniques, such as low energy electron microscopy (LEEM), scanning tunneling microscopy (STM), and PEEM, in order to correlate the observed structure of the films with their magnetic behavior.

ACKNOWLEDGMENTS

REFERENCES

[1] R. Schellenberg, E. Kisker, M. Faust, A. Fanela, Phys. Rev. B, **58**, 81 (1998).
[2] C. Roth, F. U. Hillebrecht, H. B. Rose, E. Kisker, Phys. Rev. Lett., **70**, 3479 (1993).
[3] J. G. Tobin, K. W. Goodman, G. J. Mankeya, R. F. Willis, J. D. Denlinger, E. Rotenberg, A. Warwick, J. Appl. Phys. **79**, 5626 (1996).
[4] J. G. Tobin, F. O. Schumann, Surf. Sci. **478**, 211 (2001).
[5] T.F. Johnson, S. Chiang, Y. Sato, D.A. Arena, S.A. Morton, M. Hochstrasser, J.G. Tobin, J.D. Shine, J.A. Giacomo, G.E. Thayer, D.P. Land, X.D. Zhu, to be published.
[6] Y. Sato, S. Chiang, T. F. Johnson, A. Scholl, F. Nolting, D. P. Land, X. D. Zhu, to be published.
[7] F. O. Schumann, R. F. Willis, K. G. Goodman, J. G. Tobin, Phys. Rev. Lett. **79**, 5166 (1997).

A LANDAU-GINZBURG DESCRIPTION OF Sb OVERLAYERS

R. SKOMSKI,[1] T. KOMESU,[1] H.-K. JEONG,[1] C. N. BORCA,[1] P. A. DOWBEN,[1] D. RISTOIU[2] and J. P. NOZIERES[2]

[1]Department of Physics and Astronomy and Center for Materials Research and Analysis, University of Nebraska, Lincoln, NE 68508.
[2]CNRS, Laboratoire Louis Néel, Avenue des Martyrs BP 166, 38042 Grenoble, CEDEX 09, France.

ABSTRACT

The spin polarization of Sb overlayers on the semi-Heusler alloy NiMnSb is investigated in terms of the Landau-Ginzburg approach. The half-metallic semi-Heusler alloy NiMnSb acts as a ferromagnetic perturbation and induces a spin polarization in the semimetallic Sb overlayer. Using a Gaussian approximation, the propagation of the spin perturbation in the overlayer is calculated. The results are compared with spin-polarized inverse photoemission spectroscopy (SPIPES) results and with recent spin-dependent envelope-function approximation (SDEFA) predictions. The Landau-Ginzburg parameters are both band-structure and temperature dependent, and it is argued that thermal spin excitations lead to an injection depth decreasing as $1/\sqrt{T}$ law at high temperatures.

INTRODUCTION

The spin structure at interfaces is key to understanding spin electronics. Of particular interest are interfaces between different classes of materials, such as interfaces between magnetically ordered and semiconducting materials. Here we focus on the interface between a halfmetallic high-polarization ferromagnet and a semimetal. Halfmetallic materials are ferromagnets characterized by a ↓ subband which is completely filled, whereas the ↑ electrons provide metallic conductivity. Semimetals are reminiscent of ordinary paramagnetic semiconductors, except that they exhibit a negative 'energy gap'.

This work deals with NiMnSb layers covered by Sb overlayers. NiMnSb is a halfmetallic semi-Heusler alloy crystallizing in the cubic $C1_b$ structure. It may be considered as a derivate of the parent Heusler alloy Ni_2MnSb and has a ↓ band gap of less than about 0.5 eV [1]. Antimony is a semimetal characterized by a very small negative energy gap [2]; the overlap and Fermi energies are about 180 meV and 90 meV, respectively, and the electron and hole carrier densities are of comparable magnitude (about 5×10^{-19} cm^{-3}) [2]. The preparation and characterization of the sputtered NiMnSb films considered in this work has been described elsewhere [3-5]. The Sb grows epitaxially on NiMnSb, with a <100> orientation, a cubic structure, a 3.1 Å lattice constant [6].

The magnetism of the Sb overlayer films was investigated by a combination of X-ray absorption spectroscopy (XAS) and spin-polarized inverse photoemission spectroscopy (SPIPES) experiments [4,6]. Our approach yields a layer-specific analysis of the spin polarization, in contrast to methods such as that used in [7], where spin injection is probed indirectly, by considering the exchange coupling through a semiconducting medium.

The measured spin asymmetry exhibits an oscillatory behavior and extends quite well into the Sb layer (up to about 1 nm). In the spin-dependent envelope-function approximation (SDEFA) used in [8], the unusual range of the spin polarization is explained by taking into account that there are no spin-down states available at the NiMnSb Fermi level. The $\uparrow$ electrons are able to move from the Sb overlayer into the NiMnSb, whereas the $\downarrow$ electrons are reflected at the NiMnSb/Sb interface. The latter boundary condition means that the wave functions $\psi_{k\downarrow}(\mathbf{r})$ are equal to zero at $x = 0$. Using the solution of the spin-independent scattering at an infinite potential barrier [9] one obtains the $\downarrow$ electron density

$$n(x) = \frac{k_F^3}{3\pi^2} \left(1 + 3\frac{\cos(2k_F x)}{(2k_F x)^2} - 3\frac{\sin(2k_F x)}{(2k_F x)^3} \right)$$

(1)

which yields an oscilatory spin polarization $m = (n_\uparrow - n_\downarrow)/(n_\uparrow + n_\downarrow)$ of the carrier electrons [8]. In other words, the comparatively long range of equilibrium spin injection from the half-metal NiMnSb into the Sb is explained by the semimetallic character of the Sb overlayer.

Here we start from a slightly different point of view. The NiMnSb/Sb interface is considered as a perturbation which creates a spin polarization in the Sb overlayer, and this perturbation is described in terms of a Landau-Ginzburg theory. This approach was originally designed to discuss strongly paramagnetic and weakly ferromagnetic dilute alloys [10], but it can also be used to describe thin-film problems [11, 12]. In this paper, we discuss the electronic origin and the temperature dependence of the Landau-Ginzburg parameters and investigate the influence of boundary conditions.

CALCULATION AND RESULTS

Gaussian Approximation

Neglecting nonlinear contributions and restricting ourselves to long-wavelength terms (up to $\nabla^2 \sim k^2$) which we will discuss below, the energy functional can be written without considering higher-than-quadratic terms in k-space. The problem reduces to a Landau-Ginzburg equation:

$$E = \int \left(\frac{C}{2}(\nabla m)^2 + \frac{A}{2}m^2 - h(\mathbf{r})\,m \right) d\mathbf{r}$$

(2)

In this equation, m($\mathbf{r}$) is the local magnetization, C can be interpreted as a kind of exchange stiffness, A indicates the tendency towards ferromagnetism, and h($\mathbf{r}$) is an 'external' exchange field. In the present context, h($\mathbf{r}$) is the exchange-field created by the NiMnSb; in the Sb layer, h = 0.

Exploiting that the Gaussian approximation is exact for quadratic energy expressions we obtain the free energy:

$$F = \frac{1}{V_e} \int \left(\frac{C}{2} (\nabla m)^2 + \frac{A + k_B T}{2} m^2 - h(\mathbf{r}) \, m \right) d\mathbf{r} \tag{3}$$

where V_e is the volume per electron. For A < 0, this equation provides a very crude description of ferromagnetism below $T_c = |A|/k_B$ [13], whereas for paramagnets it yields a finite susceptibility at all temperatures.

Minimization of the free energy Eq. (3) yields

$$- C \nabla^2 m + (A + k_B T) \, m = h(\mathbf{r}) \tag{4}$$

In the present case, h is the exchange field acting on the Sb spins at the interface. Since the three-dimensional character of the Sb electron gas is incorporated in the parameters A and C, the resulting problem is one-dimensional, and the solutions of Eq. (4) are of the type $\exp(\pm qx)$, where $q = (A+k_B T)^{1/2}/C^{1/2}$. In the simplest case, the spin polarization decays with an exponential decay length R = 1/q.

Electronic origin of the Landau-Ginzburg terms

Due to the small overlap of the conduction and valence bands the band-structure of the antimony conduction electrons can be treated as free-electron like. (True free-electron behavior is restricted to the Γ point). The corresponding free-electron Fermi wave vector is of the order of 0.1/Å, but due to the quite eccentric ellipsoidal shape of the Fermi-surface pockets [2] this value is only semiquantitative.

The free-electron response to a weakly varying magnetic inhomogenity is described by $C = 1/12 D(E_F) k_F^2$, $A = 1/D(E_F)$, and $h = \mu_o \mu_B H(\mathbf{r})$ [14]. In a homogeneous field, where the C-term is unimportant, Eq. (4) reproduces the Pauli susceptibility $\chi_p = \mu_o \mu_B M_s D(E_F)$. Coulomb interactions modify the the free-electron behavior, and for $A = 1/D(E_F) - I < 0$, where I is the Stoner interaction parameter, Eq. (4) predicts ferromagnetism [14,15]. However, in antimony the density of states is very low, so that the spin susceptibility is very weak cannot compete against the diamagnetic contribution.

The free-electron parameters yield the zero-temperature decay length $(12)^{-1/2}/k_F$. The involvement of large wave vectors, caused by the sharp interface and seen as Friedel (or RKKY) oscillations, leads to somewhat larger effective decay lengths. Figure 1 compares the experimental data with theoretical predictions. Figure 1(a) shows the spin asymmetry at E_F as a function of the Sb layer thickness. Only the Sb top layer is probed by this method, and the measured spin asymmetry characterizes, in crude way, the magnetic polarization of that layer. The lengths in Fig. 1(a) are given in arbitrary units, because it was not possible to obtain an exact value for the total coverlayer thickness

(roughly, the range shown correspond to 1 nm). Figure 1(b) shows a SDEFA prediction (solid line) with a corresponding Landau-Ginzburg decay (dashed line, R = 0.941/k_F).

(a)   (b)
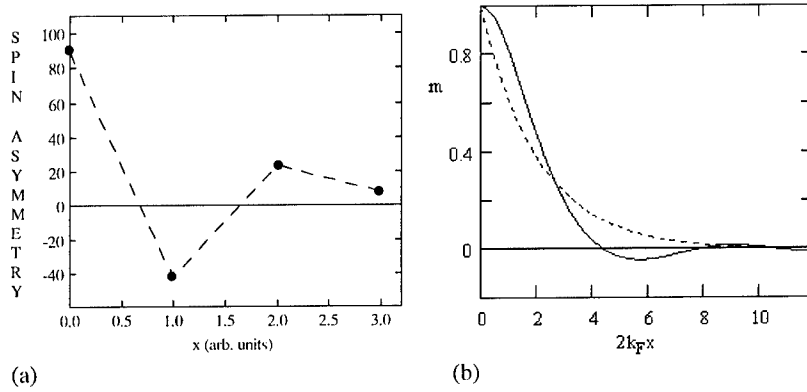
Fig. 1. Spin polarization in an NiMnSb: (a) spin-polarized inverse photoemission data at E_F (the spin asymmetry is measured in %) and (b) SDEFA and Landau-Ginzburg predictions.

Temperature dependence

Thermal activation leads to the involvement of excited electron states with small wavelengths. This effect tends to reduce the decay length. Neglecting the small exchange enhancement (Stoner parameter), we obtain

$$R = \sqrt{\frac{C}{A + k_B T}} \qquad (5)$$

In the high-temperature limit, this amounts to a $1/\sqrt{T}$ law. On the other, k_F and $D(E_F)$ exhibit an intrinsic temperature dependence, associated for example with the thermal expansion of the lattice and the corresponding change of the overlap, so that A and C are temperature dependent quantities. This contribution is not necessarily much smaller than the explicit dependence shown in Eq. (5). Note that R can be interpreted as an equilibrium spin-penetration depth or equilibrium spin-injection length; it is not related to ballistic effects.

Boundary conditions

For planar geometries, Eq. (4) yields solutions of the type exp($\pm$qx). The admixture of exp(qx) character depends on the boundary conditions. For semi-infinte Sb,

$$m = m_o \exp(-qx) \qquad (6)$$

whereas for a thin film of thickness t
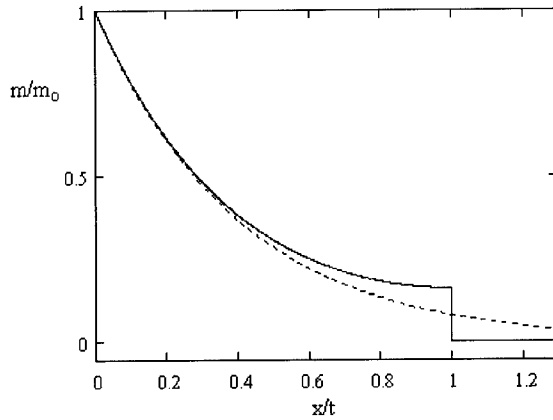
Fig. 2. Spin polarization in NiMnSb/Sb: Sb film of thickness t (solid line) and seminfinite Sb (dashed line).

$$m = m_o \frac{\cosh(qt - qx)}{\cosh(qt)} \tag{7}$$

Figure 2 shows the difference between the two boundary conditions.

DISCUSSION AND CONCLUSIONS

The main difference between the SDEFA and Landau-Ginzburg approximations is the involvement of the Fermi surface. The SDEFA result (solid line in Fig. 1(b)) is of the RKKY type and exhibits oscillations arising from the sharp Fermi surface. As in the original RKKY theory [14], the oscillations mean that the electrons' finite wave vectors make it impossible to match perturbations on a local scale. However, our geometry differs from that of the original RKKY theory: we consider a planar geometry rather than the interaction between two localized moments. Note, furthermore, that our approach is reminiscent of the description of quantum confinement in thin-film semiconductors and loosely related to the approach by Hunziker and Landolt [7], where spin effects in semiconductors are discussed by considering the Heisenberg exchange between two hydrogen-like orbitals characterized by a small effective mass m*. (The effective mass is very low in semiconductors and semimetals.)

In the RKKY and SDEFA theories, the smearing of the Fermi surface due to thermal excitations suppresses the oscillatory character of the response and reduces the

penetration length (decay length). Simply speaking, excited electron states have shorter wavelengths and their integral response to surfaces and impurities exhibits a higher resolution. By contrast, the Landau-Ginzburg theory is insensitive to details of the Fermi surface. The reason is that the Landau-Ginzburg energy is restricted to terms quadratic in k: there is no sharp wave-vector cutoff, and k_F enters the energy only indirectly, by determining the parameters A and C.

In conclusion, we have investigated the problem of equilibrium spin injection from the half-metal NiMnSb into the semi-metal Sb. The comparatively long range of the Sb spin polarization is explained by the semimetallic character of the Sb overlayer, which leads to small Fermi wave vectors (wave-vector differences) k_F and fairly large decay lengths. The decay is described in terms of a Landau-Ginzburg approach whose parameters are both electronic-structure and temperature dependent.

ACKNOWLEDGMENT

REFERENCES

[1]   R. A. de Groot and K. H. J. Buschow, J. Magn. Magn. Mater. **54-57** (1986) 1377.
[2]   Y. Liu and R. E. Allen, Phys. Rev. B **52** (1995) 1566.
[3]   C. N. Borca, T. Komesu, H.-K. Jeong, P. A. Dowben, D. Ristoiu, Ch. Hordequin, J. Pierre, and J. P. Nozières, Appl. Phys. Lett. **77** (2000) 88.
[4]   D. Ristoiu, J. P. Nozières, C. N. Borca, B. Borca, P. A. Dowben, Appl. Phys. Lett. **76** (2000) 2349.
[5]   D. Ristoiu, J. P. Nozieres, C. N. Borca, T. Komesu, H.-K. Jeong, and P. A. Dowben, Europhys. Lett. **43** (2000) 624.
[6]   T. Komesu, C. N. Borca, H.-K. Jeong, P. A. Dowben, D. Ristoiu, J. P. Nozières, Sh. Stadler, Y. U. Idzerda, Phys. Lett. A **273** (2000) 245.
[7]   M. Hunziker and M. Landolt, Phys. Rev. Lett. **84** (2000) 4713.
[8]   R. Skomski, T. Komesu, C. N. Borca, H.-K. Jeong, P. A. Dowben, D. Ristoiu, and J. P. Nozières, J. Appl. Phys. (2001) in press.
[9]   García-Moliner and F. Flores, "Introduction to the Theory of Solid Surfaces", University Press, Cambridge 1979.
[10]   D. M. Edwards, J. Mathon, and E. P. Wohlfarth, J. Phys. F **5** (1975) 1619.
[11]   J. Mathon, J. Phys. F **16** (1986) L217.
[12]   P. A. Dowben, W. Hürsch, and M. Landolt, J. Magn. Magn. Mater. **125** (1993) 120-124.
[13]   Q.-N. Qi, R. Skomski, and J. M. D. Coey, J. Phys. CM **6** (1994) 3245.
[14]   W. Jones and N. H. March, "Theoretical Solid State Physics I", Wiley, London 1973.
[15]   R. Skomski and J. M. D. Coey, "Permanent Magnetism", Institute of Physics, Bristol 1999.

SYMPOSIUM V

**Phase Change Recording
Materials and Mechanisms**

Progress of the Phase-change Optical Disk Memory

Takeo Ohta, Noboru Yamada, Hiroaki Yamamoto, Tsuneo Mitsuyu[1], Takashi Kozaki[2],
Jianrong Qiu[3], Kazuyuki Hirao[3]

Optical disk systems development center
Matsushita Electric Industrial Co., Ltd.
Kadoma, Kadoma City, 571-8501 Osaka, Japan

[1] The Nakao Laboratory
[2] Matsushita Techno-Research
Matsushita Electric Industrial Co., Ltd
Yagumo Naka-machi, Moriguchi City, 570-8501 Osaka, Japan

[3] Photon Craft Project, ICORP, JST
Keihanna-plaza,
Hikaridai, Seika-cho, 619-0237 Kyoto, Japan

1. Introduction

Optical memory has two recording modes: the photon-mode as a silver halide photograph and the heat-mode as a laser optical disk. Though laser heat-mode recording has the advantage of environmental stability, it has limitations due to thermal diffusion phenomena, which will be discussed in this paper.

Optical disk memory has the unique feature of read-only media performance, which is also compatible with the rewritable function and is different from HDD (hard disk drive) technology.

Rewritable optical disk technology progressed with the race between the magneto-optical (MO) disks and the phase-change rewritable (PCR) optical disks. With the increasing use of multimedia, phase-change rewritable optical disks are becoming more popular due to their CD (compact disk) and DVD (digital versatile disk) compatibility.

In 1968, S. R. Ovshinsky discovered a new memory phenomenon in chalcogenide film materials. This order-disorder phase-change memory effect came to be called the "Ovonic Memory"[1]. In developing this storage medium, the main issues have been the stability of the film materials, the stability of the reversible cycle characteristics and the recording sensitivity. The author and his colleagues were the first to achieve a breakthrough in these areas, which led to the commercialization of phase-change optical disk products. The first version of the phase-change optical disk product was shipped in 1990 from Matsushita/Panasonic. The PD(phase-change dual) and CD-RW(rewitable) followed, and now a rewritable DVD with 4.7 GB capacity and 3.4 Gbit/in^2 density is being produced.

Blue laser technology, large numerical aperture lens, volumetric recording and multi-level recording technologies are candidates for the future of high-density phase-change recording technology.

This paper describes the phase-change optical disk memory progress of high-density recording, phase-change optical disks with a density of approximately 100 Gbits/in^2 and more, and discusses the basic effect of the ultra-short laser pulse of the femto second laser pulse response on phase-change media.

2. Principle of the phase-change overwrite memory

2.1 Overwritable phase-change material

The rewritable optical memory phenomenon has been observed in $Te_{81}Ge_{15}Sb_2S_2$ composition material[2]. This material was modified from a $Te_{85}Ge_{15}$ eutectic composition by adding Sb and S elements. Figure 1 shows the phase diagram of the Ge-Te system. At the eutectic composition, the melting temperature decreases to 375℃. In the early stage of the investigation of phase-change materials, it was important to obtain simple amorphizing compounds, and therefore the eutectic compound composition was chosen. For the eutectic composition, the melting temperature is at a minimum and viscosity is expected to increase. It is thus easy to freeze the bonding structure in the liquid phase through the cooling

process. In the next stage, applicable materials that have rather high-speed crystallization characteristics were used.

Phase-change materials for over-writing using one laser spot need to have high-speed crystallizing characteristics. Thus, high-speed crystallizing materials such as the In-Se system were discovered[3]. Then Ge-Sb-Te system was proposed[4, 5] and in the GeTe-Sb$_2$Te$_3$-Sb system shown in Fig. 2, the material shows nucleation dominant crystallizing characteristics[6]. Recently, at the ODS (optical data storage conference, Whistler, May 14-17, 2000) crystallizing growth-dominant compositions in the eutectic composition system, such as Sb$_{69}$Te$_{31}$, were proposed for high density and high data-rate recording[7].

2.2 Model of the phase-change memory

The phase-change processes of the Ge-Sb-Te amorphous material were examined by DSC (differential scanning calorimeter) measurement. Figure 3 shows that there are two exothermal peaks and one endothermal peak. The first exothermal peak corresponds to the crystallization phase-change and the second to the fcc-to-hexagonal crystalline structure change.
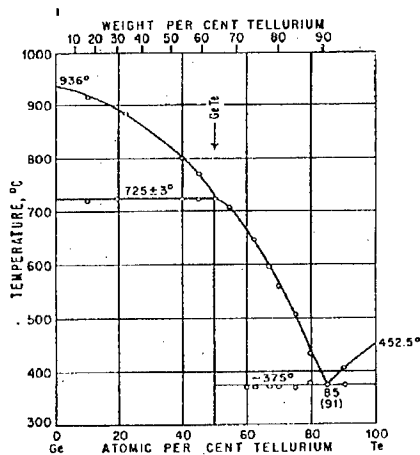
Fig.1. Phase diagram of Ge-Te system.
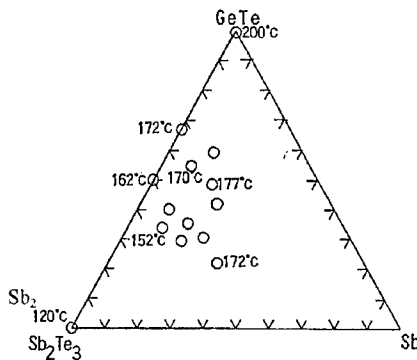
Fig. 2. Crystallizing temperatures of the GeTe-Te$_3$-Sb alloy system.
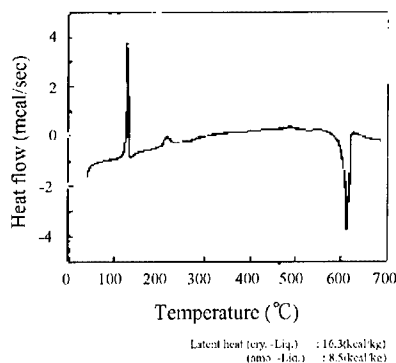
Fig. 3. DSC (differential scanning calorimeter) analysis of Ge-Sb-Te film at a heating rate of 10 °C/min.

The third peak, the endothermal peak, corresponds to the melt-phase transition[8]. The latent heats of crystalline to liquid (16.3 kcal/kg) and amorphous to liquid (8.5kcal/kg) were obtained from this measurement, the later was calculated as the subtraction value of the exothermic heat from the former value. Figure 4 shows the model of the phase-change memory. The enthalpy of the amorphous state and the crystalline state is different. The complex refractive index N = n + ik of the film is different for the two phases. When the cooling rate is above the critical cooling rate (3.4 K/ns) of amorphizing, the portion of the film at "f" enters the amorphous phase[9].

3. Key technologies of the phase-change optical disk media
3.1. Thermally-stable new dielectric protection layer

In the early phases of its development, the most important subject of the phase-change optical disk was cycle degradation. Figure 5 shows a high resolution TEM (transmission electron microscope) image of ZnS and the new ZnS-SiO$_2$ mixture protection films. The grain size of the ZnS-SiO$_2$ film is very small, at around 2 nm[10]. The new ZnS-SiO$_2$ dielectric layer is thermally stable and does not show grain growth, even after annealing at 700℃ (5 min). Grain growth in the ZnS layer was one reason the phase-change optical disks degraded after many rewrites. The first version of the phase-change optical disk product with a 4-layer structure produced a greater than 100,000 overwrite cycle performance.
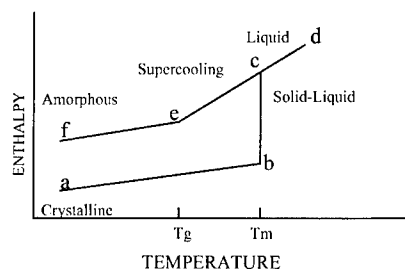
Fig. 4 Model of the phase-change memory

(a)   (b)
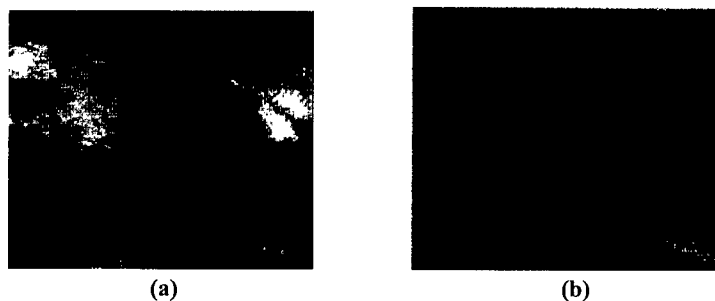
Fig. 5. High resolution TEM (Transmission electron microscope observation of ZnS (a) and new ZnS-SiO$_2$ mixture (b) dielectric films. layers.

3.2 Basic 4-layer disk structure and an additional SiO$_2$ layer

Figure 6 shows a cross-sectional TEM image of the basic 4-layer structure of a phase-change optical disk of PD. The layers comprise a protection layer, a bottom dielectric layer of ZnS-SiO$_2$ (155 nm), an active layer of GeTe-Sb$_2$Te$_3$-Sb (24 nm), an upper dielectric layer of ZnS-SiO$_2$ (45 nm) and a reflection layer of Al-alloy (100 nm). All the layers are sputter deposited on a polycarbonate disk substrate.

These layers work as a multi-layer optical interference structure, controlling disk reflectivity, which is the difference of the reflectivity between the amorphous mark and the crystalline erased state.

The other cycle degradation model is that the sub-nanometer level space deformation of the disk layers, which works as the motive force of the sub-nanometer displacement of the active layer components. The deformation occurs by thermal expansion of the layers along the thermal diffusion process. Table 1 shows the optical, thermal and mechanical properties of the disk layers.

Figure 7 shows the thermal simulation results of the temperature distribution in the cross-sectional view of the first version phase-change optical disk. The temperature distribution is calculated after the 30 ns laser-spot irradiation on the rotational disk. The linear velocity is V = 8 m/s, the laser wavelength of is 830 nm and the lens numerical aperture is 0.53. It shows that the temperature rising area is wider than the spot size of 0.76 μm (FWHM)(full width half maximum) caused by the thermal diffusion in 30 ns. The temperature distribution profile is asymmetrical between the forward area and the backward area because of the thermal diffusion process.
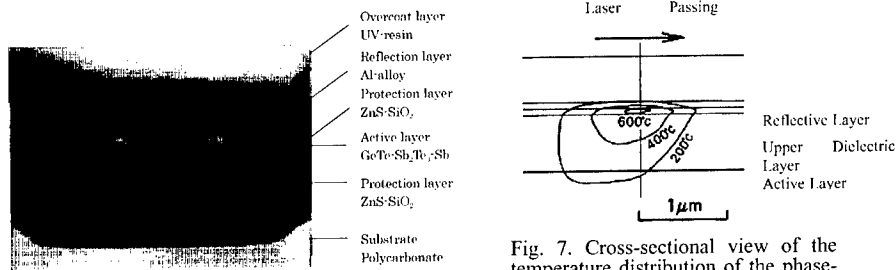
Fig. 6. Cross-sectional TEM observation of the basic 4-layer phase-change optical disk.

Fig. 7. Cross-sectional view of the temperature distribution of the phase-change optical disk at 30ns laser spot scan.

Table 1   Optical, Mechanical and thermal Properties of Materials

Material	Reflactive Index λ -830nm	Density (kg/m^3)	Young's Modulus (N/m^2)	Poisson's Ratio	Specific Heat (J/(kg·K))	Thermal Conductivity W/(m·K)	Coefficient of Linear Expansion
GeTe-Sb$_2$Te$_3$-Sb (Amorphous)	4.9+1.4i	6150	5.49x10^{10}	0.33	0.209x10^3	0.581	1.1x10^{-5}
GeTe-Sb$_2$Te$_3$-Sb (Crystal)	5.7+3.4i	6150	5.49x10^{10}	0.33	0.209x10^3	0.581	1.1x10^{-5}
2 : 1 : 0.5 (mol ratio) ZnS-SiO$_2$	2.0	3650	7.81x10^{10}	0.2	0.563x10^3	0.657	7.4x10^{-6}
4 : 1 (mol ratio) SiO$_2$	1.46	2202	7.81x10^{10}	0.2	0.753x10^3	1.313	5.5x10^{-7}
Al Alloy	2.2+7.5i	2750	7.03x10^{10}	0.345	0.892x10^3	0.215x10^3	2.2x10^{-5}
Polycarbonate	1.58	1200	2.26x10^9	0.3	0.126x10^2	0.223	7.0x10^{-5}

Latent Heat (Crystal⇔Liquid)   0.682x10^6 (J/kg)

(Amorphous⇔Liquid)   0.356x10^6 (J/kg)

Thermal expansion coefficients of the dielectric materials of SiO_2 and ZnS-SiO_2 are 5.5×10^{-7} and 6.1×10^{-6}, respectively. We compared the thermal deformations of the first version disk structure and new disk structure. Figure 8(a), (b) shows the simulation results of the thickness change of the layers by thermal expansion as the temperature distribution simulation.. All layers show that the thermal expansion and thickness changes are several sub-nm. These deformations are considered the motivating force of the micro-displacement of the active layer components. Figure 8(a) shows the thickness change of the first version disk structure. Figure 8(b) shows the thickness change of the new disk layer structure. When the SiO_2 layer for the ZnS-SiO_2 layer is introduced to the upper dielectric layer, the thickness change of the upper dielectric layer becomes negligible small, compared the value of ZnS-SiO_2 of $0.04nm$[11]. The new disk structure, which has a SiO_2 upper dielectric layer, produces more than 1,000,000 overwrite cycles. Figure 9 shows the results of one million overwrite cycle test of the disk of SiO_2 upper dielectric layer. The Error bit counts, C/N ratio, Erase ratio and Jitter (window % for 10^{-4}bit error rate) are almost stable through the test.

A conventional laser recording using rather long pulse widths of 10 ns to 60 ns (10^{-9}s) shows large thermal diffusion phenomena in the disk. The pulse means that the irradiation time of a laser spot at a certain point on the rotational disk, and is the time the laser spot takes to go through the point. A short pulse width, such as a femto second (10^{-15}s), will be expected to suppress the thermal diffusion phenomena extremely. The interaction effect of the femto second laser pulse on phase-change films will be discussed later in this paper.

(a) 1st version disk   (b) New structure disk
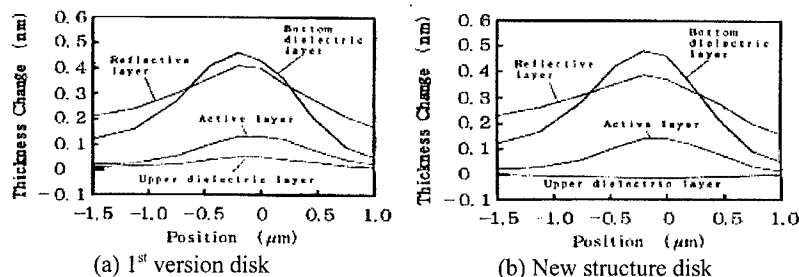
Fig. 8. Distribution of the thickness changes of the disk layers by thermal expansion.
1st version disk (a) : substrate / DL, 160nm / AL, 20nm / DL, 35nm / RL, 130nm
DL : ZnS-SiO_2, AL : $GeTe$-Sb_2Te_3-Sb, RL : Al-alloy
New disk (b) : upper DL is replaced by SiO_2 (35nm)
Horizontal axis : laser passing direction,   Zero position : center of the laser spot
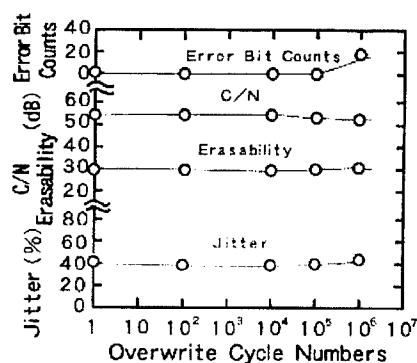
Fig. 9. One million overwrite characteristics of a phase-change optical disk with SiO_2 upper dielectric layer.
Linear velocity: 11m/sec

3.3 Nitrogen doped GeTe-Sb$_2$Te$_3$-Sb active layer

In the phase-change optical disk media development procedure of 1990, we found curious phenomena in the phase-change sample disks. Almost periodically, special disks were sputtered that showed a number of overwrite cycle characteristics almost 10 times larger than the other disks. Our investigation found that these special disks were formed right after the sputtering chamber was cleaned. This means that some adsorbed components in the chamber during the chamber cleaning improved the cycle.

Air is comprised of nitrogen, oxygen, some H$_2$O, and so on. For the chemical stability of the media, we choose nitrogen as a doping component in the active layer. We control the quantity of nitrogen doping by a gas flow ratio of N$_2$/Ar into the sputtering chamber. The active layer of doped nitrogen shows an N$_2$ doping dependency of the optical constant (n, k), an increasing N$_2$ component, and a decreasing refractive index n and extinction coefficient k. This means that nitrogen forms nitride material of M-N in the active layer. Usually, nitride materials show a high melting temperature, which is believed to indicate suppression of the micro-displacement of the active layer components through the overwriting cycle measurement[12].

Figure 10 shows the XPS (x-ray photoelectron spectroscopy) measurement results of the N2-doped phase-change film. The spectral data shows a large peak at the binding energy of 397.2 eV, which corresponds to Ge-N bonding.

After overcoming the cycle issue by key technologies, the phase-change optical disk became a reliable data-recording disk, and its advantage of ROM (read-only memory) disk compatibility it becomes to be multimedia optical disks such as PD, CD-RW and rewritable DVD. We developed a high-density 90 mm diameter phase-change optical disk for an ISO (International Organization for Standardization) standardization proposal in 1995[13]. This disk featured top-level technologies such as a red light laser diode, a large NA(numerical aperture) (NA=0.6) lens and a thin disk substrate (0.6 mm)[14),15]. A thin disk substrate is effective for resolving the disk tilt problem during high-density recording. A thin disk substrate of 0.6 mm thickness has lower cross-talk characteristics. These technologies were adapted in the 4.7GB DVD in 1995.
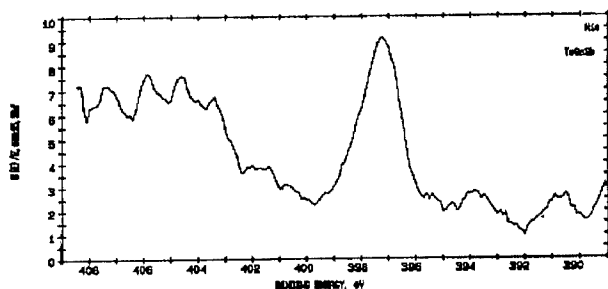
Fig. 10. XPS analysis of GeTe-Sb$_2$Te$_3$-Sb film sputtered in N$_2$/Ar atmosphere.
Binding energy of Ge-N : 397.2eV.

4. High density recording technologies of phase-change optical disks

4.1 Density competition between MO disk and Phase-change optical disk

Magneto-optical disks have recently been demonstrated to show the unique capability of MSR (magnetic induced super-resolution)[16], and now feature MAMMOS (magnetic amplifying magneto-optical system) [17] and DWDD (domain wall displacement detection) [18] for high-density recording using both an optical pick-up and a magnetic head. These features provide small-mark detection, high signal output and ISI (inter-symbol interference) free high-density reading methods, respectively. They have a recording density of around 11 Gbit/in^2 using a conventional optical system (laser wavelength = 650 nm, lens numerical aperture NA = 0.6[19]. However they have certain drawbacks, such as a complex disk structure composed of both a recording magnetic layer and a reading magnetic layer, as well as a sensitivity variation caused by ambient temperature during both recording and reading.

The phase-change recording layer has the advantages of a high-signal output and response to a wide wavelength spectrum. Table 2 shows the wavelength dependency of the complex refractive index of the phase-change material film in the amorphous and crystalline state, which shows that the phase-change film has a wide wavelength response.

Three main approaches have been proposed to increase the recording density of phase-change optical disks. The first is to combine a short wavelength laser with a large NA lens, recently DVR technology is proposed, which is applying larger numerical aperture lens of NA=0.85 and the new disk structure of thin cover-layer[20], the thickness is 0.1mm for 0.6mm disk substrate. The other are SIL(solid immerosion lens) and Near-Field technology, which is effective for surface recording. The recording density increases to double that of a conventional DVD and the blue laser increases the capacity to 23 GB [20].

The second is dual layer recording, creating volumetric rather than two-dimensional surface recording. The dual-layer phase-change optical disk has a density of 6.4 Gbit/in^2 using a conventional optical system (laser wavelength = 650 nm, lens numerical aperture NA = 0.6)[21]. This technology features enhanced density and compatibility with DVD pick-up. The third is the possibility of multi-level recording on phase-change optical disks.

4.2 Blue laser Dual-layer phase-change optical disk

Dual-layer recording is another form of volumetric technology. The first such commercial product was a dual-layer DVD for a DVD 8.5 GB ROM disk for a cinema title.

Rewritable 8.5 GB phase-change dual-layer experimental results were announced in 1998[19]. Figure 11 shows the blue laser 27 GB basic dual-layer disk structure[22].

Table 2 Wavelength dependency of complex refractive index (N= n+ixk) of phase-change material GeTe-Sb$_2$Te$_3$-Sb film.

Wavelength	Refractive index	
	Amorphous	Crystal
830nm	4.61+1.05i	5.67+3.01i
780nm	4.47+1.40i	5.07+3.42i
650nm	4.21+1.89i	4.56+4.23i
430nm	3.08+2.51i	2.21+3.77i
405nm	2.90+2.51i	2.03+3.58i
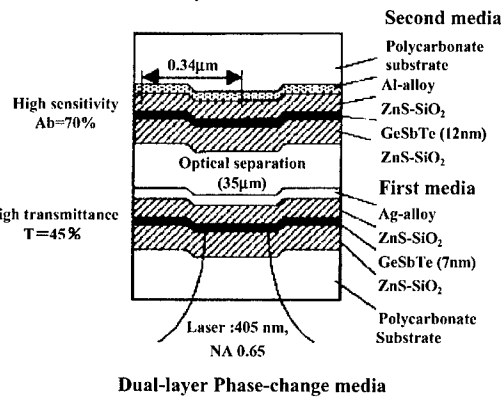
Fig. 11. Cross-sectional view of the Blue laser Dual-layer rewritable Phase-change optical disk.

The first medium has a high transmission characteristic of 45% in the crystalline state with a recording reflectivity difference of 7%. The second medium has a high reflectivity-difference signal output of 24% combined with a high sensitivity characteristic. As a result, the signal output of the second medium becomes 24 x 0.5 x 0.5 = 6 % by the absorption of the first medium, which closely matches the value of the first medium. The blue laser, DVD compatible optical pick-up, NA = 0.6 and 0.6 mm substrate method increases the capacity to 27 GB.

4.3 MRWM (mark radial width modulation) concept of multi-level recording

Multi-level recording was first announced in a phase-change electrical switching memory (Ovonic memory) device in 1997 that had 16 switching levels [23].

The phase-change optical recording layer has a large reflection-difference characteristic between the crystalline state (around R_{cry} = 30%) and the amorphous state (around R = 7%) of the same order as in the CD-ROM pit signal output. M. P. O'Neill demonstrated an 8-level phase-change recording technology at ODS2000 and 2 GB of CD-RW capacity capability [24].

We propose to subdivide this large signal output into multi-level (ML) signals on a phase-change optical disk using the MRWM (mark radial width modulation) method [25].

Figure 12 shows the TEM observation of MRWM recording marks on a phase-change optical disk. The mark radial widths are 200 nm, 400 nm and 600 nm for level 1, level 2 and level 3, respectively. The idea of MRWM recording is to assign a specific laser pulse width and power level to a specific mark level. The assigned laser pulse widths are 114 ns, 84 ns and 46 ns, and the assigned laser power is 6 mW for Level 1, 7 mW for Level 2 and 11 mW for Level 3. Figure 13 shows the C/N (carrier-to-noise) and amplitude of the MRWM recording method with various pulse widths and power conditions. The C/N value is 50.1 dB, 57.5 dB and 61.5 dB for the Level 1, Level 2 and Level 3 marks, respectively. The minimum mark length is defined by the beam factor of the optical path and is controlled by the assigned power level and the pulse width.

5. Combination technology of high-density recording

The density of one side of the 4.7 GB version rewritable DVD holds 3.4 Gbit/in². A dual-layer phase-change rewritable disk whose capacity is 8.5 GB has an effective density on one side of 6.4 Gbit/in², increasing the density 1.9 times. By introducing the magnification factor of the multi-level recording of M = 4 (x1.76) to M = 8, the recording density will further increase approximately 2 to 3 times.
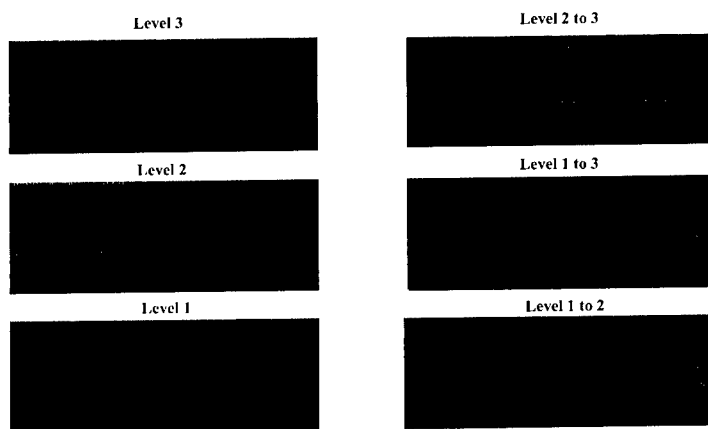
Fig. 12. TEM observation of MRWM recording marks (Track widh: 600nm)
Each marks, Level 1, 2, 3 and the set recording marks (1 to 2), (1 to 3), (2 to 3)

Another density increasing strategy is to apply a large numerical aperture lens of NA = 0.85 and a 0.1 mm-thin overcoat layer for 0.6mm substrate. The recording density will increase to double that of an equivalent DVD due to the factor of 0.85/ 0.60. The blue-violet laser wavelength of 405 nm will increase the density to approximately 2.6 times that of the 650 nm laser system. The recording density is predicted to be 63.2 Gbit/in^2 and the capacity will rise to 87GB/120mm/side. By magnifying the multi-level recording from M = 4 to M = 8, the density is expected to increase to more than 100 Gbit/ in^2.

J. Tominaga has announced a phase-change Super-RENS(super-resolution near-field structure) recording technology, which achieves 13 Gbit/in^2 using the conventional optical system (laser wavelength = 640 nm, lens numerical aperture NA = 0.6[26]. The Super-RENS effect can be combined with the above technologies, resulting in a potential density increase of approximately four times to achieve 250 Gbit/in^2 in the future.

Near-Field recording technology is now actively developing, applying SIL technology on phase-change optical disks with GaN blue laser. K. Kishima demonstrated a 40 Gbit/in2 recording density at ODS2000 [27]. Figure 14 shows the area recording density expansion of the phase-change optical disk with the combination of high density recording technologies.

There are two strategies for next generation high density phase-change optical disk, the one is DVD compatible strategy which keeps the lens numerical aperture (NA=0.6) optical pick-up and the thin substrate (t=0.6mm) DVD disk structure and combines dual-layer technology and multi-level technologies so on. The other is new disk strategy different from DVD and is introducing larger numerical aperture (NA=0.85) optical pick-up and thin cover-layer (t=0.1mm) disk structure which is not compatible with DVD but can be introduced the technologies, such as dual-layer or multi level recording.
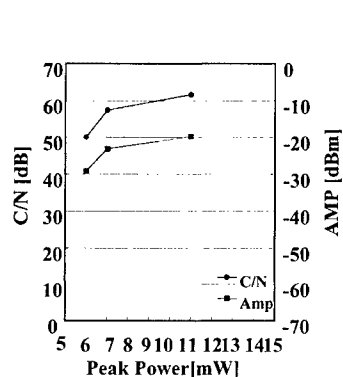
Fig. 13. Pulse width and Power assigned MRWM recording characteristics of Phase-change optical disk.
Level 1(113.3ns, 6mW)
Level 2 (83.1ns, 7mW)
Leel 3 (45.3ns, 11mW)
Signal: f=6.6MHz, v=8.2m/s

$$(650/\lambda)^2 \; x(NA/0.6)^2$$
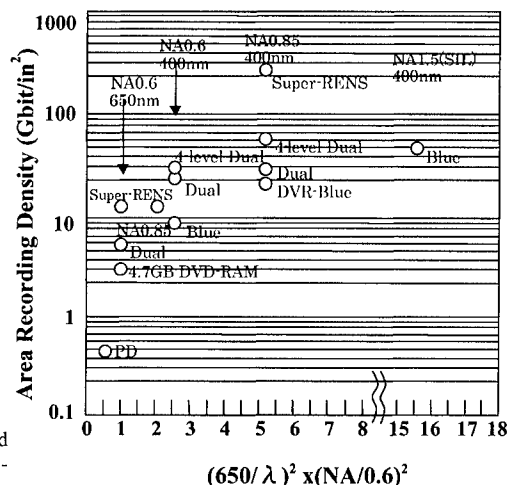
Fig. 14. Areal recording density growth of Phase-change optical disk.
PD (λ =780nm, NA=0.5), 4.7GB DVD-RAM
(λ =650nm, NA=0.6), 8.5GB Dual-layer disk,
Blue wavelength 27GB Dual –layer disk, DVR,
SIL (NA=1.5)
Multi-level recording

6. Femto second laser response on phase-change thin film

6.1 Why femto second laser recording on phase-change media should be challenged

Recently, short pulse width lasers such as the femto to pico second pulse laser have become popular. In high-speed fiber communication, the high-resolution laser processing field and ultra-high-speed time-resolution measurement technology, these femto lasers have achieved ultra high-speed chemical reactions and bio-molecular dynamics. A 120 fs laser pulse of laser wavelength 800 nm in silicate glass demonstrated a photo-induced refractive index change which is considered by multi-photon absorption process [28]. The threshold recording power density was 120 nJ/ μ m^2. The dynamics of the magnetization of the MO films were monitored by the femto second laser[29].

Laser spot recording is usually a heat-mode recording; the recording layer absorbs the laser light energy and the temperature increases beyond the threshold temperature. For example, the threshold temperatures are the melting temperature for phase-change material (Tm=600°C), the Curie temperature of the Magneto-Optical media (Tc = 200°C), the decomposing temperature of the recordable Dye media (Td=350°C), and so on.

Conventional optical disk recording is performed by laser spot irradiation on the rotational disk. In this case, the laser irradiation time on the portion of the disk is around 10 ns to 100 ns, a rather long time compared with the femto second laser spot irradiation. At the conventional laser spot recording on the disk, the heating time on the disk is rather long and the recording process includes the heat diffusion in the layers. The temperature increasing area is wider than the laser spot size, which means that the mark size and the position of the mark are determined by not only the beam factor (λ/NA), but also the disk thermal characteristics and the pulse duration. Heat diffusion of the conventional laser recording limits the performance of future high-density optical disks.

Recently, high-density recording technologies applying a large numerical aperture lens, the SIL, the blue laser short wavelength, and so on, have been introduced. These technologies display the following characteristics: the mark size becomes around 100 nm; the high density and high data rate for example, 40Mbps. The width of the area out of the spot size (FWHM) that is heated up by heat diffusion is the so-called dead space, and the mark position variation influences Jitter performance more strongly.

6.2 Experimental setup and the sample structure of the phase change media

For this experiment, the response of the femto second laser pulse on the phase-change thin film media was examined first to obtain the features of the ultra-short pulse laser recording. Figure 15 shows the schematic of the femto second laser exposure setup for the sample. A mode-locked Ti:sapphire laser is amplified and the femto second laser pulse is formed and stabilized by a pulse compressor. The laser pulse is introduced to the optical microscope, which has a CCD (charge-coupled device) monitor and an X-Y-Z stage.

For the femto laser irradiation experiment, the wavelength was λ= 800 nm and the pulse width was 120fs. The laser pulse was introduced to the optical microscope. The sample was put on the X-Y stage, the lens numerical aperture was NA = 0.95, and the laser exposure was on the layer side.
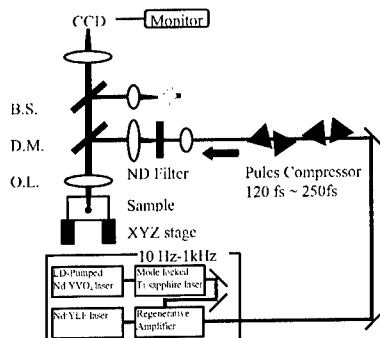
Fig. 15. Femto second laser measurement system.
Wavelength : 800nm
Pulse width : 120fs ~ 250fs

The phase-change media sample structure is a polycarbonate substrate/ZnS-SiO$_2$ 155nm/GeSbTe 24nm/ZnS-SiO$_2$ 45nm/Air without a reflection layer, making it easy to observe the mark formations with the optical microscope. The structure of the conventional laser recording media has a reflection layer on the above sample and the recording is from the substrate side.

6.3 Femto second laser recording mark and discussions

Figure 16 (a) shows the TEM observation of the mark of the conventional several-tens nanosecond long pulse-width laser exposure (50 ns) on the rotational disk and (b) shows the mark formed by the femto second laser exposure (120 fs). The lens numerical aperture was NA = 0.5, the laser wavelength was λ= 780 nm, and the recording power was 11 mW. The marks are amorphous and surrounded by a large crystalline band edge.

The most significant difference between the mark formed by the femto second pulse laser and the marks formed by the conventional several-tens nanosecond pulse laser is the mark edge figure. The conventional pulse forms intermediate space between the amorphous mark and the crystalline background dead space of 160 nm. The femto second pulse forms an amorphous mark without the crystalline edge band. The intermediate space is a large-grain size crystalline state that is formed by the recording laser spot when melted and re-crystallized in the cooling step. The recording energy density of the femto second mark of the phase-change media was 1nJ/μm^2, and the conventional disk recording energy density was approximately 2nJ/μm^2.

The conventional laser disk recording process has three stages. The first is a laser spot exposure, the second is heat diffusion outside of the laser spot, and the third is cooling after the laser spot passes away from the portion. The laser exposure time is from 10 ns to 100 ns, depending on the laser spot diameter and the disk rotational speed. The conventional laser recording method appears in the second and third process, and comes from the thermal diffusion process. The mark dead space out of the laser spot and the variation of the mark position are caused by the thermal diffusion from a rather long pulse-laser irradiation.

The femto second laser pulse irradiation is quite different from the conventional laser recording because the thermal diffusion is limited in the fs to ps order, the mark is accurately formed in the laser spot, and the variation of the mark position is negligible without thermal diffusion variation. The short pulse width of 120 fs recording on the phase-change media indicates a high-recording data rate capability of more than 1 Tbit/s.

Overwrite process needs ultra high speed crystallizing characteristics and now investigations start for this new material area.

re-crystallization   no re-crystallization

(a) 60ns mark   (b) 120fs mark
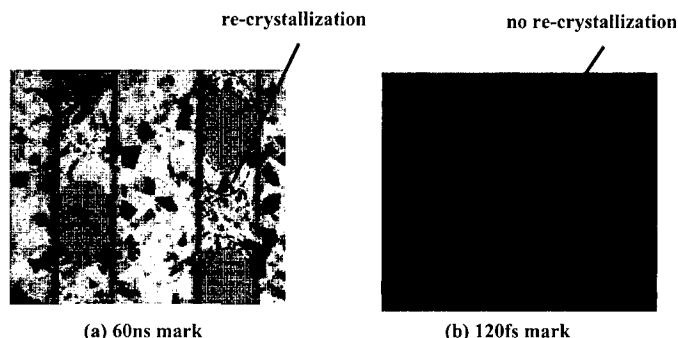
Fig. 16. TEM observation of the amorphous marks on phase-change optical disk.
(a) Conventional laser recording : λ =780nm, NA=0.5, t=60ns, (with a reflection layer)
(b) Femto second pulse laser recording : λ =800nm, NA=0.95, t=120fs, (without a reflection layer)

7. Conclusion

Key technologies obtained by materials research and disk structure development have achieved multimedia rewritable 4.7 GB DVD products. The application of blue laser light and volumetric (dual layer) recording have the potential to increase the recording density to

20 Gbit/in^2 with an NA = 0.6 lens. The phase-change optical disk has multi-level high-density recording capability. A multi-l evel recording method and an NA of 0.85 in combination with other technologies indicates the potential for the recording density of the phase-change optical disk to exceed 100 Gbits/in^2 .

Ultra-short pulse femto second laser recording on phase-change media is one candidate for a breakthrough of the laser thermal recording limit.

Reference

1) S. R. Ovshinsky, Phys. Rev. Lett., 21(1968)p.1450.
2) J. Feinleib, J. de Neufville, S.C. Moss, S. R. Ovshinsky: Appl. Phys. Lett., 18(1971)p.122.
3) M. Terao, N. Nishida, Y. Miyauchi, S. Horigome, T. Kaku, N. Ohta: Proc. SPIE 695, (1986)p.105.
4) N. Yamada, E. Ohno, N. Akahira, K. Nishiuchi, K. Nagata and M. Takao,: Proc. Int. Symp. on Optical Memory, (1987)p. 61.
5) M. Suzuki, I. Doi, K. Nishimura, I. Morimoto, K. Mori: Proc. Optical Memory Symposiup'88(1988)p. 41.
6) T. Ohta, M. Uchida, K. Yoshioka, K. Inoue, T. Akiyama, S. Furukawa, : K. Kotera, S. Nakamura, Proc. SPIE, Vol. 1078(1989)p. 27.
7) G. F. Zhou, H. J. Borg, J.C.N. Rijpers, M. Lankhorst: ODS. Tech. Digest (2000) TuB4, p.74.
8) N. Yamada, E. Ohno, K. Nishiuchi, N. Akahira: J. Appl. Phys., Vol. 69, No. 5 (1991) p.2849.
9) T. Ohta, K. Inoue, S. Furukawa, T. Akiyama, M. Uchida, S.Nakamura: Electro. & Comun.Technical Research Meeting Rep. CPM89-84(1989)p. 41.
10) T. Ohta, K. Inoue, S. Furukawa, K. Yoshioka, M. Uchida, S.Nakamura: Electro. & Comun.Technical Research Meeting Rep. CPM90-35(1990)p. 43.
11) K. Inoue, S. Furukawa, K. Yoshioka, K. Kawahara, T. Ohta: Proc. ASME, Vol.2, (1992)p.593.
12) T. Ohta: ODS(1991), Tech. Digest, (1991)p.84.
13) 1.3GB 90mm Phase-change optical disk, ISO/IEC JTC: Project 1.23.14760(1995).
14) T. Ohta, K. Inoue, T. Ishida, Y. Gotoh and I. Satoh, : Jpn. J. Appl. Phys. Vol. 32(1993)p. 5214.
15) T. Sugaya, T. Taguchi, K. Shimura, K. Taiara, Y. Honguh,,H. Satoh, : Jpn. J. Appl. Phys., Vol. 32(1993)p.5402.
16) K. Aratani, A. Fukumoto, M. Ohta, M. Kaneko, K. Watanabe: Proc. SPIE1499, Optical Data Storage Topical Meeting(1991) p.209.
17) H. Awano, A. Yamaguchi, H. Shirai, S. Sumi, S. Ohnuki, K. Tazawa, N. Ohta: Appl. Phys. Lett., (1996) p.4257.
18) T. Shiratori, E. Fujii, Y. Miyaoka, Y. Hozumi: J. Magn. Soc. Jpn. Vol. 22, Supplement No. S2, (1998) p.47.
19) S. Kai, A. Fukumoto, K. Aratani, S. Yoshimura, K. Tsutsui, M. Arai, Y. Takeshita: Technical Digest, ISOM/ODS'99, TuA4(1999)p. 75.
20) K. Kurokawa, M. Nito, K. Yasuda, T. Kashiwagi, O. Kawakubo: Technical Digest, ISOM/ODS'99, (1999)p. 197.
21) K. Nagata, K. Nishiuchi, S. Furukawa, N. Yamada, N. Akahira:Jpn. J. Appl. Phys. Vol. 38(1999)p.1679.
22) T. Akiyama, M. Uno, H. Kitaura, K. Narumi, K. Nishiuchi, N. Yamada,: We-C-01, Tech. Digest ISOM2000, (2000) p.16.
23) S. R. Ovshinsky: Proc. The 9th Symp. on Phase Change Recording(1997)p. 44.
24) M. P. O'Neill, T. L. Wong: ODS. Tech. Digest (2000) WB2, p.170.
25) T. Ohta, K. Nishiuchi, K. Narumi, Y. Kitaoka, H. Ishibashi, N. Yamada, T. Kozaki: Jpn. J. Appl. Phys. Vol. 39(2000)p. 770.
26) H. Fuji, J. Tominaga, T. Nakao, N. Atohda, H. Katayama: Technical Digest, ISOM/ODS'99, TuD29(1999).
27) K. Kishima, I. Ichihara, K. Yamamoto, K. Osato, Y. Kuroda, A. Iida, K. Saito: Technical Digest, ODS2000, (2000), MC2, p.33.
28) K. Miura, J. Qie, H. Inoue, T. Mitsuyu, K. Hirao: Appl. Phys. Lett. 71 (1997)p.3329.
29) J. Hohlfeld, Th. Gerrits, M. Bilderbeek, H. Awano, N. Ohta, Th. Rasing: J. Magn. Soc. Japan, Vol. 25, No.3-2,(2001) p.202.

Phase-Change Media for High-Density Optical Recording

Herman Borg, Martijn Lankhorst, Erwin Meinders and Wouter Leibbrandt
Philips Research Laboratories,
Prof. Holstlaan 4, 5656 AA Eindhoven, The Netherlands

ABSTRACT

Rewritable optical-storage systems are quickly gaining market share in audio, video and data-storage applications. The development of new rewritable optical-storage formats with higher capacity and data rate critically depends on innovations made to the recording media incorporating so-called phase-change materials. These materials allow reversible switching between a low and high reflective state induced by laser heating. In this paper, we highlight phase-change media aspects as optical and thermal design, sputter-deposition, materials optimization, and the development of new recording strategies. Focus is on the speed race in optical recording.

INTRODUCTION

Over the past few years, the field of optical recording has evolved rapidly. Read-only disc standards (such as CD-Audio and CD-ROM) have been extended with recordable (CD-R) and rewritable (CD-RW) systems, allowing the user to create personal CDs. Simultaneously, higher-capacity systems for digital video and data applications have been developed by using shorter-wavelength lasers and stronger objective lenses. The market introduction of DVD players is proceeding even faster than the introduction of the CD some 20 years ago, and is currently being followed by rewritable versions. With the introduction of the blue-laser diode [1] and the development of high-numerical-aperture (NA) objective lenses [2], optical-storage research is currently focussing on the development of a third-generation high-capacity recording system for video and data applications. Last year, Sony and Philips presented the rewritable Digital Video Recorder (DVR) format with a user data capacity of 22.5 GB on a 120 mm disc [3], by using a blue laser (?=405 nm) and an NA=0.85 objective lens.

The technology used for these rewritable optical-storage systems is phase-change recording. The recording mechanism is based on the reversible phase transition between a crystalline and amorphous state of the recording material, induced by heating with a focussed laser beam. (Sub)micron-sized amorphous marks are written in a crystalline thin-film by using a short laser pulse to locally melt the recording layer. After switching off the laser the molten state cools down rapidly and becomes frozen in the amorphous state. Erasure of recorded marks proceeds via re-crystallization, by heating the recording material to a moderate temperature by applying an erase power level for a longer period of time.

The readout mechanism of a phase-change optical disc is similar to that of a read-only disc, as the recorded marks have a lower reflection than their crystalline surrounding. The digital information is contained in the length of the amorphous marks and the crystalline spaces in-between them. By using a recording strategy, consisting of alternating write-pulse trains with
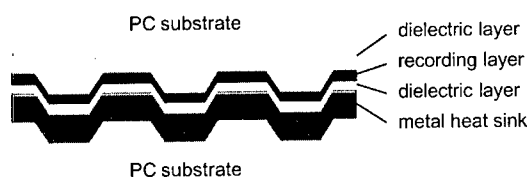
Figure 1. Typical structure of a rewritable phase-change disc, consisting of a recording stack sputter-deposited onto a pre-grooved plastic substrate.
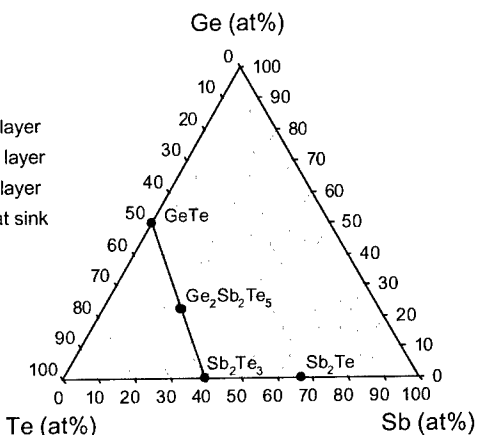
Figure 2. The Ge-Sb-Te ternary diagram. Indicated are the two classes of commonly used phase-change recording materials, $i.e.$ stoichiometric compositions on the GeTe-Sb_2Te_3 tic-line and compositions near the eutectic Sb_2Te.

constant erase-power levels, it is possible to vary the length of marks and spaces and to record new data directly over previously recorded data.

In this paper, we discuss a major challenge in phase-change recording research, $i.e.$ the increase of the recording speed. The maximum recording speed that can be achieved in phase-change recording is determined by the re-crystallization time of recorded amorphous marks. For high-speed recording, faster crystallizing materials as well as new write strategies to handle the increased crystallization rate have to be developed.

PHASE-CHANGE RECORDING MATERIALS

Phase-change optical-recording media generally consist of a recording stack which is sputter-deposited onto a pre-grooved polycarbonate substrate. The groove structure acts as a grating for the reflected beam, and is used for radial tracking. Address information can be included in a number of ways in the molded substrate, by superimposing a phase- or frequency-modulated sinc-shaped wobble onto the groove structure, or by including read-only information in the shape of pits (headers) along the spiral-shaped tracks.

Current recording stacks comprise at least four layers. The actual recording or phase-change layer is sandwiched between dielectrics; behind this tri-layer a metal layer is present which acts as a reflector and heat sink (Figure 1). The dielectrics have various functions: They isolate the phase-change layer from the environment to prevent oxidation and segregation, they prevent the phase-change material from fluidization or evaporation during the write process, and their thickness can be used to optimize the optical contrast between the crystalline and amorphous state. Additionally, the thermal properties of the stack are strongly influenced by the dielectrics:

The thin dielectric layer between the phase-change layer and the metal mirror acts as a heat resistor, and its thickness and heat conductivity must be chosen such to combine a high cooling rate of the recording material with sufficient write-power sensitivity of the disc.

The search and development of proper recording materials is an important aspect of phase-change recording research. The suitability of the material is related to the following properties:

1. The amorphous and crystalline state have sufficient optical contrast at the recording wavelength;
2. The melting point of these materials is sufficiently low (500-1000°C), so that the material can be molten with the available laser power;
3. The crystallization of the amorphous state is sufficiently rapid. In direct-overwrite applications, the amorphous marks should be erased (re-crystallized) completely within the thermal dwell time of the laser spot, *i.e.* within a period of less than 100 ns. At the same time, for sufficient archival life of the media the amorphous phase must be stable against spontaneous crystallization at ambient and storage temperatures up to approximately 60°C. This means that the glass-transition temperature (typically 50-70% of T_{melt}) must be well above 100°C;
4. The crystalline-to-amorphous and amorphous-to-crystalline phase transitions are reversible many times (> 1000) under recording conditions.

Currently used phase-change recording materials belong to the group of semiconductor chalcogenides. The specific compositions that are being used can be divided in two classes: stoichiometric compositions on the GeTe-Sb_2Te_3 tie-line and compositions close to the eutectic Sb_2Te (Figure 2). Looking closer at the crystallization behavior of these materials, some marked differences can be observed. Figure 3 shows transmission electron microscopy (TEM) images of amorphous marks recorded in the stoichiometric $Ge_2Sb_2Te_5$ material (left panel) and a doped eutectic Sb_2Te alloy (right panel). The background of the pictures shows the crystalline state of the material obtained after initialization, i.e., after heating the as-deposited amorphous state of the material with a focussed broad array laser while rotating the disc. The crystallite size and morphology of both materials is rather different. In the stoichiometric material small spherical grains are present, whereas in the eutectic larger crystals with irregular shape can be seen. These differences can be understood by looking closer at the crystallization mechanism. In general,
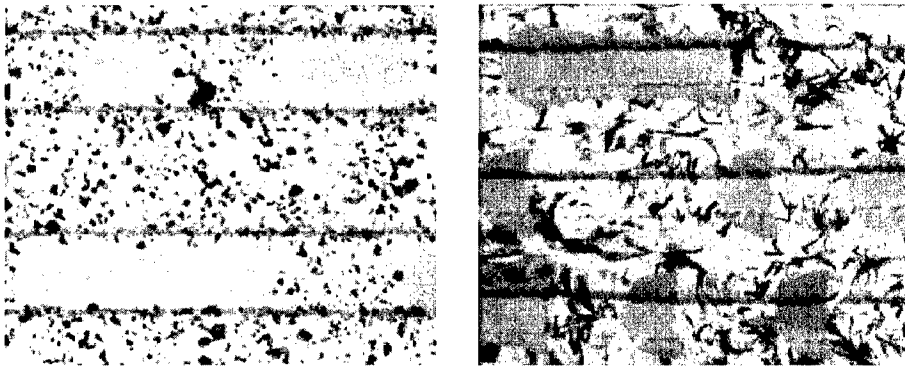
Figure 3. Transmission electron microscopy images of recorded phase-change optical discs. The left panel shows a typical image for marks recorded in the nucleation-determined stoichiometric $Ge_2Sb_2Te_5$ material, the right panel shows marks recorded in a doped eutectic Sb_2Te material.
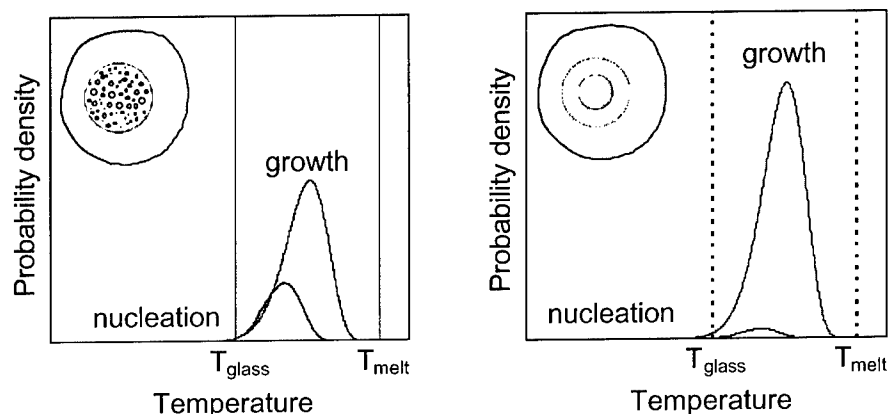
Figure 4. Schematic representation of the temperature-dependent nucleation probability and growth velocity for stoichiometric $Ge_2Sb_2Te_5$ and doped eutectic Sb_2Te compositions. In the top left corners, the resulting mechanism of mark erasure is depicted.

crystallization of the sputter-deposited amorphous state entails two processes, nucleation and growth. In the stoichiometric materials the nucleation probability is high and the growth speed is moderate. Therefore, during heating the amorphous material nuclei will be formed abundantly and grow until they coalesce. In the eutectic compositions the nucleation probability is very low while the growth speed is high. In this case, the few nuclei that are being formed during heating will grow at a faster speed, resulting in larger crystallites. Because the growth speed is relatively high, these crystallites will be irregularly shaped and contain a lot of defects.

The relative probabilities of nucleation and growth also determine the way amorphous marks are being erased (re-crystallized) under recording conditions (Figure 4). For the $Ge_2Sb_2Te_5$ and other materials with a high nucleation probability, the amorphous marks will be erased by abundant nucleation followed by moderate growth, very much like the crystallization of the sputter-deposited state ('nucleation-determined erasure'). For the doped eutectic Sb_2Te and other material with a very high growth rate, the amorphous marks will be erased by growth of the crystallites at the mark edge towards the center of the mark ('growth-determined erasure'). The nucleation probability for these materials is so low that nucleation will statistically almost never occur during the short heating cycle during recording.

HIGH-SPEED PHASE-CHANGE RECORDING

Since the introduction of CD-RW, the write speed of this system has already doubled several times, and for future higher-density rewritable-disc systems a similar speed race may be anticipated. Essential ingredients in high-speed phase-change recording are materials optimization and the development of new recording strategies. Control of the crystallization kinetics of the recording material is of crucial importance. The reduced dwell time of the spot at higher disc velocities urges for faster-crystallizing materials, while at the same time the thermal

stability of the amorphous state should not be sacrificed. At current disc velocities the time for re-crystallization is typically 100 ns or less, while the amorphous marks should be stable against spontaneous crystallization for at least 30 years at room temperature. In practice, these requirements appear often contradictory, because the methods used to increase the crystallization speed of the material are often at the expense of its thermal stability.

As discussed in the previous section, two main classes of phase-change materials are currently being used for phase-change recording, nucleation-determined $Ge_2Sb_2Te_5$ and fast-growth doped-eutectic Sb_2Te. The data rates that are currently being used in rewritable DVD systems based on both types of media are similar, ranging from 11-33 Mbit/s (DVD 1X-3X speed). However, the different mark-erasure mechanism of these two types of materials has important consequences for the data rates that can be realized in phase-change recording systems with a higher bit density. The maximum write speed in direct-overwrite recording is determined by the ability to erase (re-crystallize) previously recorded amorphous marks in a single pass of the laser spot. For nucleation-determined re-crystallization, a fixed period of time is required to erase an amorphous mark. When the size of the laser spot is reduced at constant linear velocity of the disc, the dwell time of the spot will decrease. This implies that the maximum linear velocity for direct overwriting decreases with decreasing laser-spot size. Because the linear bit density increases with decreasing spot size, both trends will counterbalance. Experiments indicate that for the nucleation-determined $Ge_2Sb_2Te_5$ material the maximum write data rate is indeed essentially independent of the laser-spot size (Figure 5). For a particular growth-determined material, the maximum linear velocity that can be achieved during recording is closely related to the maximum growth speed of the recording and independent of the laser-spot size. As the linear bit density increases with decreasing laser-spot size, the maximum data rate that can be achieved with a growth-determined material increases with decreasing spot size. Experimental data have confirmed this so-called spot-size effect (Figure 5). These results indicate that doped eutectic Sb_2Te materials are becoming increasingly attractive in higher-density storage systems based on short-wavelength lasers and high-numerical-aperture lenses, and therefore these materials form
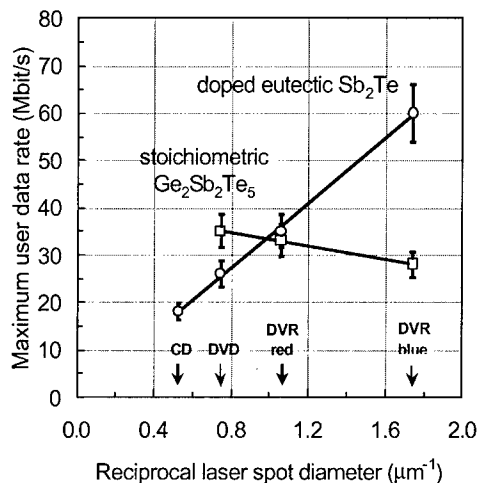
Figure 5. Maximum write data rate of the nucleation-determined $Ge_2Sb_2Te_5$ and a growth-determined doped eutectic Sb_2Te phase-change recording material, as a function of the inverse diameter of a focussed laser beam.

Figure 6. Left panel: Target used for co-sputtering, consisting of Ge, Sb and Sb_2Te_3 segments. Right panel: Magnet configuration of the rotating-magnetron cathode used for co-sputtering.

the basis for the current DVR media [4,5].

The experiments in Figure 5 were performed for the same phase-change composition and stack structure for the different laser spot sizes. In the remainder of this section we will discuss how the crystallization speed of eutectic Sb_2Te alloys can be enhanced by optimizing the composition of the alloy. For fast composition optimization we have developed a new method of co-sputtering. In this technique, a single 200-mm-diameter sputter target composed of segments of different composition is used in combination with a rotating-magnetron cathode (Figure 6) and a rotating disc-holder. While rotating the magnetron, the sputter power of the plasma can be varied from target segment to target segment. In this way, the sputter rate of the individual compounds can be controlled in a rather wide range. To achieve good uniformity of the layer thickness and composition across the entire disc, a (fixed) diaphragm with a radius-dependent aperture is mounted between the sputter target and the rotating disc. In this way, the layer's thickness and composition non-uniformity could be minimized to within 2 percent.

The eutectic Sb_2Te composition was chosen as the starting point for our experiments. The segmented target for co-sputtering consisted of Sb and Sb_2Te_3 segments of equal size, so that the Sb/Te atomic ratio could be varied easily by modulating the sputter power at both segments. Because the crystallization temperature of the eutectic is too low for practical applications, some Ge was added to the layer to improve the archival life stability of the material [6]. To this end, a small Ge-segment was included in the sputter target.

The crystallization speed of the eutectic GeSbTe alloys was studied first by using a static-tester setup [7]. In static-tester experiments, amorphous marks of different size were written by varying the write power at a fixed write-pulse length. The size of the amorphous marks was estimated from the ratio between the write power P_{write} and the power P_{melt} required to just melt the phase-change layer. Subsequently, the marks were erased by systematically changing the erase pulse power and length. In this way, the complete erasure time (CET), *i.e.* the minimum time to erase the amorphous mark, was determined [7]. The experiments were performed on actual discs, consisting of 4-layer recording stacks sputter-deposited onto a polycarbonate substrate. Figure 7 shows the measured CET values as a function of amorphous mark size, for GeSbTe alloys with an increasing Sb/Te atomic ratio and a constant Ge-concentration. For all compositions, the CET increases with the size of the amorphous mark. This is partially due to the larger distance that the mark edge has to grow, but is also caused by the decreasing temperature rise at the mark edge, due to the Airy intensity profile of the laser spot [8]. By increasing the
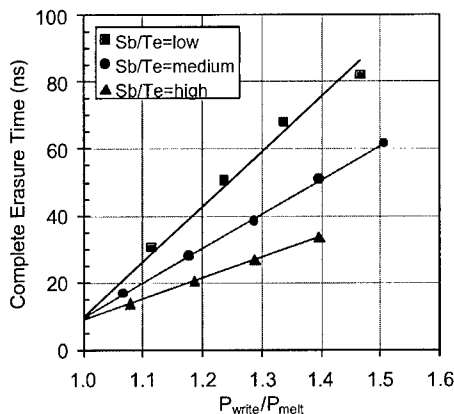
Figure 7. Complete erasure time (CET) for amorphous marks of increasing size, for eutectic GeSbTe alloys with various Sb/Te atomic ratio
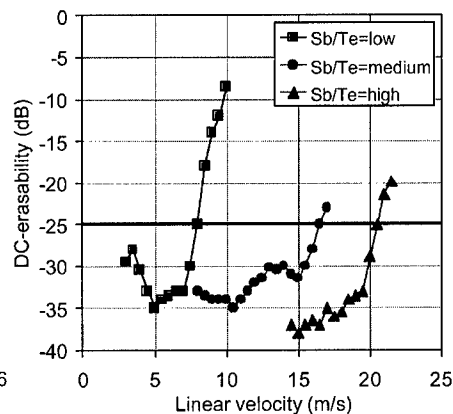
Figure 8. DC-erasability of long marks (11T pattern) as a function of the linear disc velocity, for eutectic GeSbTe with different Sb/Te atomic ratio and constant Ge concentration.

Sb/Te atomic ratio, the CET decreases significantly due to the increased growth speed of the alloy.

The phase-change composition currently used for DVD+RW is approximately equal to the slowest composition in Figure 7, and can be recorded at linear disc velocities up to 8.5 m/s (corresponding to a user-data rate of 26.5 Mbit/s). A good indication of the recording speed that can be achieved with the faster materials is given by the maximum velocity at which amorphous marks can still be erased sufficiently. Figure 8 shows DC-erasability measurements for the compositions given in Figure 7. In these experiments, data of a fixed frequency (11T, with T the channel clock period) were recorded and subsequently erased by operating the laser at DC-power at various linear velocities. The DC-power level was optimized for optimal erasability at each velocity. For proper direct overwriting a DC-erasability of at least –25 dB is required. Figure 8
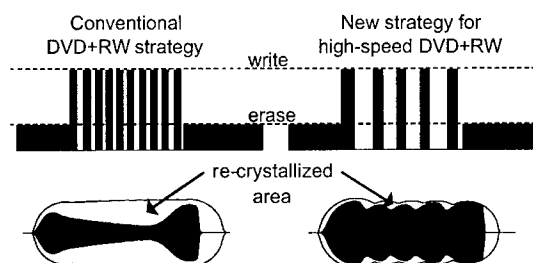
Figure 9. Conventional and new recording strategy for high-speed phase-change recording, and the (simulated) corresponding amorphous mark shapes. By reducing the number of laser pulses for writing an amorphous mark, re-crystallization during the write process can be reduced.
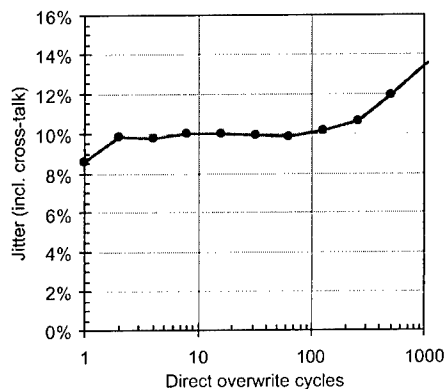
Figure 10. Timing jitter measured during direct overwriting at 53 Mbit/s (DVD 4.8X) under DVD rewritable recording conditions (λ=658nm, NA=0.65)
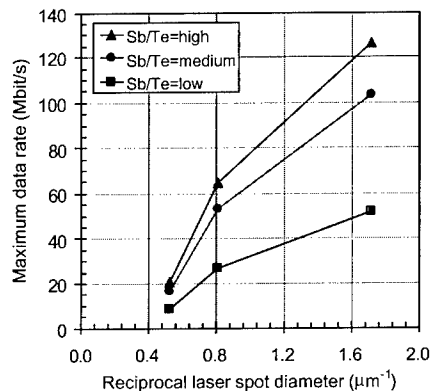
Figure 11. Extrapolation of the maximum data rate of current doped eutectic Sb_2Te alloys to the CD and DVD rewritable formats.

indicates that a linear velocity of more than 20 m/s can be achieved for the fastest GeSbTe alloys.

After optimizing the phase-change alloy composition to obtain a higher growth speed, recording experiments were performed to optimize the write strategy for high-speed recording. In a conventional recording strategy, a mark with a length of N channel bits (the channel-bit length being the shortest repetitive unit during recording) is written by applying N-1 high-power laser pulses. Each pulse results in an amorphous dot, and due to the partial overlap of the dots an amorphous mark of the correct length is recorded. However, when this conventional strategy is used in combination with fast-crystallizing materials, the temperature increase due to the next write pulses results in significant re-crystallization of the just recorded amorphous dots. This effect leads to significant reduction of the amorphous mark width, resulting in a loss of the signal amplitude. The re-crystallization phenomenon is visualized in the left panel of Figure 9, which shows the molten area and the resulting mark shape after cooling down of the disc. The mark shape was simulated by including the melt process and the temperature-dependent growth speed of the phase-change material in a thermal model of the recording process [9].

A solution to reduce the extent of re-crystallization during recording is by reducing the number of laser pulses to write an amorphous mark [10]. The right panel of Figure 9 shows a high-speed recording strategy in which the number of write pulses is only half that of a conventional strategy. Because the distance between consecutive laser pulses has doubled, the temperature increase due to consecutive pulses will be significantly reduced, reducing the extent of re-crystallization.

By increasing the Sb/Te ratio of doped eutectic Sb_2Te alloys and using high-speed recording strategies as depicted above, a significant increase of the recording speed could be realized. Figure 10 shows the jitter measured during direct overwriting under DVD rewritable conditions at a linear velocity of 16.8 m/s, corresponding to a bit rate of 53 Mbit/s (DVD 4.8X). The jitter

level is close to the 9% criterion used for DVD+RW. The static tester and DC-erasability experiments indicate that materials with even higher growth speeds are still available, so that higher data rates may be realized in the near future.

It is interesting to extrapolate the data rates obtained under DVD recording conditions (λ=658 nm, NA=0.65) to the CD-RW system (λ=780 nm, NA=0.50) and the high-density DVR system (λ=405 nm, NA=0.85). As discussed before, the maximum *linear* velocity that can be achieved is more or less independent of the laser spot size for growth-determined re-crystallization. This means that the data rates that can be achieved under CD-RW and DVR conditions can be estimated by correcting for the linear bit density and the efficiency of these formats relative to the DVD+RW format. Figure 11 shows such an extrapolation for the materials discussed previously. The data rates for the CD-RW system are much lower than would be expected on the basis of the laser-spot size, due to the relatively low linear density and efficiency of this format. For the DVR system data rates of over 100 Mbit/s are predicted for these doped Sb_2Te alloys. In this context, it is interesting to note that we have already reported a data rate of 80 Mbit/s under DVR-blue recording conditions [5].

CONCLUSIONS

The field of optical recording is evolving rapidly, showing an increasing market share for rewritable disc systems based on phase-change recording. The recording mechanism is based on writing (sub)micron-sized amorphous marks in a crystalline recording layer by heating with the focussed laser beam. The recorded marks can be erased by re-crystallization. The recorded data can be read from the reflectivity difference between both states, similarly as in read-only discs. The popularity of phase-change technology can therefore partially be explained by the playback compatibility of the rewritable media on read-only drives.

Current phase-change media are generally based on either of two material classes: stoichiometric compositions on the GeTe-Sb_2Te_3 tie-line, in particular $Ge_2Sb_2Te_5$, or compositions close to the eutectic Sb_2Te. An important difference between both materials is the erase mechanism of recorded marks: In the stoichiometric compositions re-crystallization is dominated by nucleation, whereas in the doped eutectic Sb_2Te re-crystallization is determined by growth of the mark edge.

The maximum write data rate in phase-change recording is determined by the time required to erase previously written amorphous marks. For nucleation-determined erasure, the data rate that can be achieved is independent of the laser-spot size. For growth-determined erasure, a significant increase of the write speed can be realized by using a smaller laser spot. This implies that materials with growth-determined crystallization such as doped Sb_2Te become increasingly attractive at higher recording densities.

By using a new method of co-sputtering, the composition of the eutectic Sb_2Te was varied to investigate its feasibility for recording at higher write speeds. By increasing the Sb/Te atomic ratio of the alloy, the growth speed could be increased significantly, whereas the addition of some Ge improved the thermal stability of the amorphous state. The higher growth speed leads to increased re-crystallization during the write process. To reduce this effect, a new recording strategy with a reduced number of write pulses has been developed. In this way, data transfer rates of up to 53 Mbit/s have been achieved for rewritable DVD+RW media. Scaling this value

to the higher density of the rewritable DVR system, data rates of higher than 100 Mbit/s will be realized by using a blue-laser diode and a higher-numerical aperture lens.

ACKNOWLEDGEMENTS

REFERENCES

1) S. Nakamura and S. Fasol: *The Blue Diode Laser* (Springer-Verlag, Berlin, 1997).
2) K. Yamamoto, K. Osato, I. Ichimura, F. Maeda and T. Watanabe, *Jpn. J. Appl. Phys.* **36**, 456 (1997).
3) K. Schep, B. Stek, R. van Woudenberg, M. Blüm, S. Kobayashi, T. Narahara, T. Yamagami and H. Ogawa, to be published in *Jpn. J. Appl. Phys.* **40** (2001).
4) H.J. Borg. P.W.M. Blom, B.A.J. Jacobs, B. Tieke, A.E. Wilson, I.P.D. Ubbens and G.F. Zhou, Optical Data Storage/International Symposium on Optical Memories 1999, *Proceedings SPIE* **3864**, 191 (1999).
5) H.J. Borg, M. van Schijndel, J.C.N. Rijpers, M.H.R. Lankhorst, G.F. Zhou, M.J. Dekker I.P.D. Ubbens and M. Kuijper, *Jpn. J. Appl. Phys.* **40**, 1592 (2001).
6) M.H.R. Lankhorst and H.J. Borg, this symposium, to be published in MRS Proceedings.
7) J.H. Coombs, A.P.J.M. Jongenelis, W. van Es-Spiekman and B.A.J. Jacobs, *J. Appl. Phys.* **78**, 4906 (1995).
8) G.F. Zhou, H.J. Borg, J.C.N. Rijpers, M.H.R. Lankhorst and J.J.L. Horikx, Optical Data Storage 2000, *Proceedings SPIE*, **4090**, 108 (2000).
9) E. R. Meinders, H.J. Borg, M.H.R. Lankhorst, J. Hellmig and A.V. Mijiritskii, Optical Data Storage 2001, to be published in *Proceedings SPIE*.
10) M. Horie, N. Nobukuni, K. Kiyono and T. Ohno, Optical Data Storage 2000, *Proceedings SPIE* **4090**, 135 (2000).

Exploring the limits of fast phase change materials

Han-Willem Wöltgens, Ralf Detemple, Inés Friedrich, Walter K. Njoroge, Ingo Thomas, Volker Weidenhof, Stefan Ziegler, Matthias Wuttig
I. Physikalisches Institut der RWTH-Aachen, D-52056 Aachen, Germany

Abstract

In the last decade a number of chalcogenide alloys, including ternary alloys of GeSbTe and quaternary alloys of InAgSbTe, have been identified which enable fast phase change recording. In the quest for materials with improved phase change kinetics we present two different approaches. By comparing alloys with well-defined stoichiometries the mechanisms which govern the transformation kinetics are determined. Optical and electrical measurements determine the activation energy for crystallization to 2.24 ± 0.11 eV for $Ge_2Sb_2Te_5$ and to 3.71 ± 0.07 eV for $Ge_4Sb_1Te_5$, respectively. It is shown that for GeSbTe-alloys with different composition the activation energy increases linearly with increasing Ge content. Power-time-reflectivity change diagrams recorded with a static tester reveal that $Ge_2Sb_2Te_5$, in agreement with previous data, recrystallizes by the growth of sub critical nuclei, while $Ge_4Sb_1Te_5$ grows from the crystalline rim surrounding the bit.

To speed up the search for faster materials we employ concepts of combinatorial material synthesis by producing films with a stoichiometry gradient. Then laterally resolved secondary neutral mass spectroscopy (SNMS) combined with the static tester are used to identify the composition with superior properties for phase change applications.

INTRODUCTION

Materials at the pseudo-binary line $(GeTe)_x(Sb_2Te_3)_{1-x}$ are known to have good properties for fast phase change applications [1,2]. Nevertheless we need to characterize and understand the transformation kinetics of these materials if we want to develop a microscopic understanding of phase change dynamics. Hence, we have investigated the phase transformation on a microscopic and macroscopic scale for two compounds along the pseudo-binary line.

From the understanding of the transformation kinetics for these compounds we try to obtain insight into the behaviour expected for an arbitrary compound like $A_\alpha B_\beta C_\gamma Te$. Then combinatorial concepts in conjunction with efficient strategies to measure transformation kinetics are applied to further improve our understanding of the kinetics and the properties of phase change materials.

EXPERIMENTAL DETAILS

The GeSbTe-compounds used for microscopic and macroscopic studies were deposited on glass or silicon substrates at room temperature by dc magnetron sputtering [3]. A static tester as described in [4] is used to measure the reflectance change upon short laser pulse irradiation. The sheet resistance was measured with a four-point probe setup following the procedure proposed by van der Pauw [5]. Further experimental details are already described elsewhere [6]. x-ray refractometry (XRR) measurements were performed to determine the thickness, roughness and the density while x-ray diffractometry (XRD) measurements were used to determine the film structure at room temperature.

The Sb_xTe_{1-x} sample was evaporated onto glass in an molecular beam epitaxy (MBE) system designed for combinatorial synthesis. The background pressure of the evaporation system is $3 \times$

10^{-10} mbar. Up to five evaporation sources can be assembled into the system to prepare multi element thin films with any desired stoichiometry. Up to four evaporators can be aligned under 45 degrees with respect to the sample normal. Basic emission laws show that the film thickness distribution then will be inhomogeneous [7]. A fifth source can be inserted perpendicular to the sample. Superposing the thickness distributions of the different elements will lead to lateral stoichiometry gradients. In this situation, the exact composition of the samples can then be controlled by adjusting the evaporation rate of the different sources. The stoichiometry gradient is then determined by in situ secondary neutral mass spectrometry (SNMS), so that we know the exact composition of the sample for different positions. Finally, a static tester is used to characterize the behaviour of these samples.

RESULTS AND DISCUSSION

In the following we will first discuss macroscopic measurements to characterize the crystallization behaviour. Subsequently, microscopic measurements are employed to determine the crystallization mechanism. Finally first results from samples prepared by combinatorial methods are presented.

Temperature dependent measurements of the electrical resistance are very sensitive to the phase transition since the resistance is changing over several orders of magnitude at the critical temperature T_C. This enables a precise determination of the transition temperature. From the change in T_C as a function of heating rate the effective activation energy for exothermal crystallization for the specific phase transition can be determined using Kissinger plots [8]. Figure 1 shows the temperature dependence of the sheet resistance (R_S) of 80 nm thin $Ge_2Sb_2Te_5$ and $Ge_4Sb_1Te_5$ films.
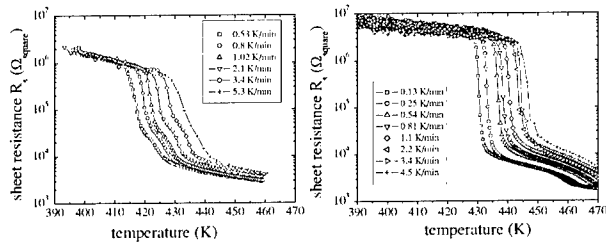
Figure 1. Temperature dependence of the sheet resistance R_S of 80 nm $Ge_2Sb_2Te_5$ (left) and 80 nm $Ge_4Sb_1Te_5$ (right) with different heating rates leading to a change in the critical temperature T_C.

From the analysis of the variation of T_C with the heating rate an activation energy of 2.24 ± 0.11 eV is observed for $Ge_2Sb_2Te_5$ [6] and 3.72 eV ± 0.07 eV for $Ge_4Sb_1Te_5$, respectively.
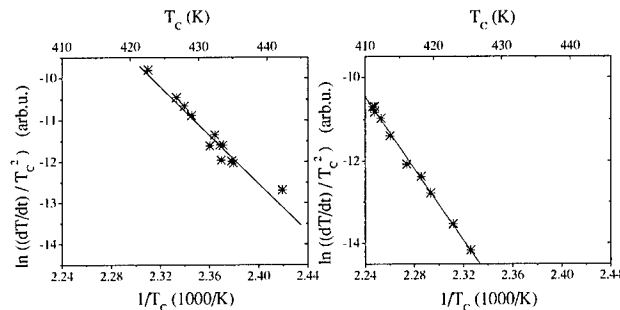
Figure 2. The activation energy E_A of the amorphous to crystalline transition at T_C is determined from Kissinger plots: (left) The slope of the linear fit determines the activation energy to 2.24 ± 0.11 eV for $Ge_2Sb_2Te_5$ films [6].

The activation energy for the $Ge_4Sb_1Te_5$ films is determined to 3.72 eV ± 0.07 eV. To determine the nature of the transformation XRD scans of 200 nm thin $Ge_2Sb_2Te_5$ and $Ge_4Sb_1Te_5$ films were performed after different isothermal annealing steps (figure 3). After deposition the films are amorphous. Crystallization into the rock salt cubic phase is observed at 415 K for $Ge_2Sb_2Te_5$ and at 430 K for $Ge_4Sb_1Te_5$. For $Ge_2Sb_2Te_5$ a second phase is formed after annealing at 573 K. These peaks are characteristic for the formation of an hexagonal structure. This second phase transition for $Ge_2Sb_2Te_5$ has an activation energy of 3.64 ± 0.19 eV [6]. For $Ge_4Sb_1Te_5$ no hexagonal phase could be found for the annealing temperatures accessible.
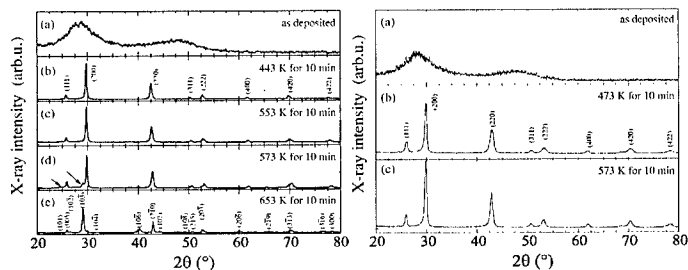
Figure 3. X-ray diffraction scans of 200 nm thin $Ge_2Sb_2Te_5$ (left) and $Ge_4Sb_1Te_5$ (right) films on Si substrates after different annealing procedures. Both annealing temperature and time are denoted. Left: diffraction pattern of (a) an amorphous $Ge_2Sb_2Te_5$ film, (b)-(d) rock salt structure and (e) hexagonal structure. The arrows in (d) indicate the changes due to beginning transition from the rock salt to the hexagonal structure. Right: diffraction pattern of (a) an amorphous $Ge_4Sb_1Te_5$ film, (b) and (c) of rock salt structure. For $Ge_4Sb_1Te_5$ no hexagonal structure could be found.

Interesting insight into the crystallization mechanism is obtained by plotting the activation energies for crystallization of several compounds along the pseudo-binary line against the number of Ge-Te bonds. In figure 4 data obtained from our measurements as well as literature data [2] are shown. It is noteworthy that there is a clear correlation between the activation energy for crystallization and the amount of Ge-Te bonds. This indicates that the kinetics of crystallization are controlled by the energetics of the Ge-Te bond. In addition, this result is in good agreement with several structural studies which show a very strong preference for Ge and

Te atoms to occupy different lattice sites, i.e. A and B sites in the rock salt lattice [2,9]. This is evidence for a strong Ge-Te bond, which is apparently also related to the activation energy for crystallization. Hence, this activation energy can be varied just by varying the amount of Ge-Te-bonds.

Even though this figure already suggests how activation energies for crystallization can be tailored through the film stoichiometry, it does not yet provide any detailed understanding of the microscopic mechanism of crystallization.
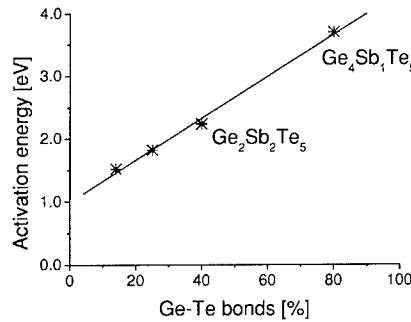
Figure 4. A summary of activation energies of several phase change materials as function of Ge-Te bonds in the material. The values are obtained from our electrical resistance measurements and literature data [2]. There is a strong correlation between activation energy and the number of Ge-Te bonds in the phase change material.

For a microscopic understanding power-time-effect diagrams for amorphous 85 nm films $Ge_2Sb_2Te_5$ and $Ge_4Sb_1Te_5$ were recorded with the static tester. These diagrams, displayed in figure 5, show the reflectance change at 830 nm upon variable laser irradiation.
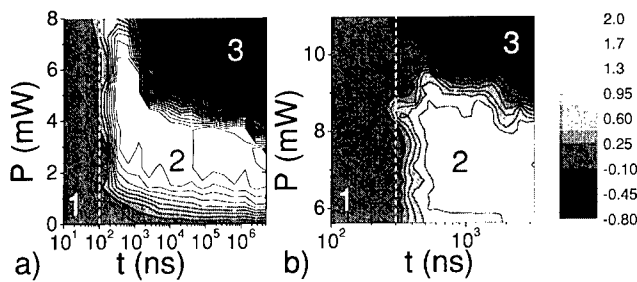
Figure 5. Power time effect diagrams of a) 85 nm thin amorphous of $Ge_2Sb_2Te_5$ films on glass and b) 85 nm thin amorphous films of $Ge_4Sb_1Te_5$ on glass. The diagrams show the relative reflectance change (%) upon absorbed power P (mW) as function of the pulse duration t (ns). A reflectance increase is assigned to crystallization, a decrease of reflectance to ablation. A missing reflectance change shows that no crystallization has taken place. A minimum time of 100 ns for $Ge_2Sb_2Te_5$ and 300 ns for $Ge_4Sb_1Te_5$, respectively, is needed to crystallize the materials.

Both diagrams show 3 regions. In region 1 the reflectance change is zero and thus the pulse is to weak to crystallize. In region 2, the material crystallizes and in region 3 the pulse is strong enough to ablate the irradiated area. Furthermore, both materials need a minimum time until crystallization starts. For $Ge_2Sb_2Te_5$ a minimum time of 100 ns is needed and for $Ge_4Sb_1Te_5$ 300 ns are required, respectively.
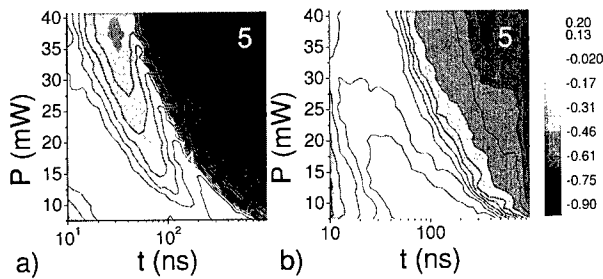
Figure 6. Power-Time-Effect diagram of a) 80 nm cubic crystalline $Ge_2Sb_2Te_5$ on glass and b) 80 nm cubic crystalline $Ge_4Sb_1Te_5$ on glass. The diagrams show the relative reflectance change (%) upon absorbed power P (mW) as function of the pulse duration t (ns) after a an amorphous bit has been written. A reflectance increase is assigned to recrystallization, a decrease of reflectance to amorphization. In region 1 no recrystallization takes place. In region 2 recrystallization takes place and in region 3 amorphization is observed. In region 4, which only occurs for the $Ge_2Sb_2Te_5$ material melt crystallization occurs and finally in region 5 the film ablates.

Since recrystallization is the more important transformation power-time-effect diagrams were recorded for 80 nm thick crystalline films of $Ge_2Sb_2Te_5$ and $Ge_4Sb_1Te_5$ with NaCl structure. The corresponding diagrams are shown in figure 6. Again, several regions can be distinguished. In region 1 the pulses are to weak to recrystallize while in region 2 recrystallization takes place. In region 3 the pulse melts the material but due to the short pulse duration the material can not relax into the crystalline state and remains amorphous. Then $Ge_2Sb_2Te_5$ shows melt crystallization in region 4. In region 5 the irradiated material is ablated. The minimum pulse durations needed for recrystallization is below 10 ns for $Ge_2Sb_2Te_5$ and about 16 ns for $Ge_4Sb_1Te_5$. Thus, recrystallization proceeds much faster than crystallization and the material with the lower macroscopic activation barrier also recrystallizes faster. We have shown that $Ge_2Sb_2Te_5$, in agreement with previous data [9,10], recrystallizes by the growth of sub critical nuclei, while $Ge_4Sb_1Te_5$ grows from the bit rim [11].

The fact that recrystallization can proceed by two different mechanisms opens different strategies to boost performance. For growth dominated recrystallization increasing the temperature upon recrystallization is a straight forward approach to enhance diffusion. For nucleation dominated growth on the contrary the influence of surrounding dielectric layers could be exploited.

To obtain a larger database to extract similar correlations combinatorial concepts can be applied. Hence a Sb_xTe_{1-x} sample has been prepared for which x varies over the sample. The areas investigated with the static tester had the compositions of $Sb_{25}Te_{75}$, $Sb_{29}Te_{71}$ and $Sb_{32}Te_{68}$. The power-time-effect diagrams are shown in figure 7.
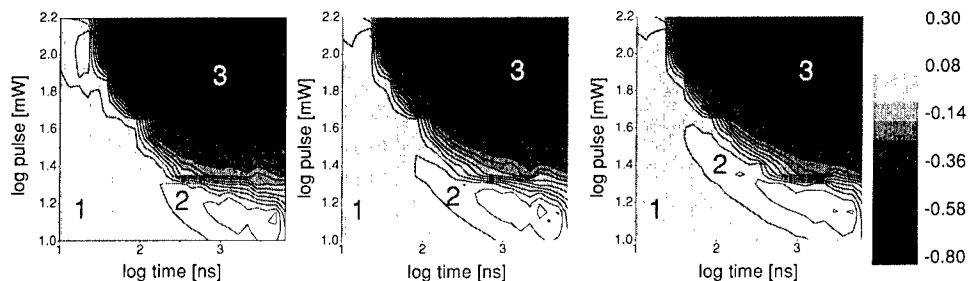
Figure 7. Power time effect diagrams of 60 nm of amorphous Sb_xTe_{1-x} on glass. The diagrams show the relative reflectance change (%) upon absorbed power P (mW) as function of pulse duration t (ns). The stoichiometries measured with SNMS are changing from $Sb_{27}Te_{75}$, to $Sb_{29}Te_{71}$ and $Sb_{32}Te_{68}$. Region 2 shifts to shorter minimum crystallization times with decreasing Sb amount.

The shift of region 2 to the left means that the minimum times needed for crystallization decreases with Sb amount. This, still somewhat preliminary result already indicates that the use of combinatorial concepts will enable a faster determination of crucial factors which control the kinetics. Hence this can be exploited to push the materials to the achievable limits needed for ultra fast phase change recording.

ACKNOWLEDGEMENTS

REFERENCES

1. J. Gonzales-Hernadez, B.S. Chao, D. Strand, S.R. Ovshinsky, D. Pawlik and P. Gasiorowski, Appl. Phys. Commun. **11** (1992) 557
2. N. Yamada, MRS Bulletin **21** (9),48-50 (1996)
3. V. Weidenhof et al., J. Appl. Phys. **86** (10), 5879 (1999)
4. V. Weidenhof et al., J. Appl. Phys. **88** (2), 657 (2000)
5. L.J. van der Pauw, Philips Res. Rep. **13**, 1 (1958)
6. I. Friedrich et al., J. Appl. Phys. **87** (9), 4130 (2000)
7. R. Glang, in *Handbook of Thin Film Technology*, edited by L.I. Maissel and R. Glang (McGraw-Hill Book company, New York) chap. 1
8. H. E. Kissinger, Anal. Chem. **29**, 1702 (1959)
9. J. H. Coombs et al. J. Appl. Phys. **78** (1995), 4918
10. J. Park et al., Jpn. J. Appl. Phys. **38** (1999) 4775
11. St. Ziegler et al., (private communication).

Materials Issues in the Development of High Data-Transfer-Rate Phase-Change Compounds

Martijn H.R. Lankhorst and Herman J. Borg
Philips Research Laboratories,
Prof. Holstlaan 4, 5656AA, Eindhoven, The Netherlands, (Martijn.Lankhorst@philips.com)

ABSTRACT

A model is presented to calculate glass-transition temperatures. This model in combination with experimental data is used to evaluate archival-life stability of common phase change materials $Ge_2Sb_2Te_5$ and doped eutectic Sb_2Te compositions.

On the basis of this model, novel high-data-rate phase change compositions have been identified near and on the pseudo-binary line InSb-GaSb in the ternary system Ga-In-Sb.

INTRODUCTION

Phase-change optical recording has evolved to a mature technology that is applied in re-writable data-storage systems such as CD-RW, DVD+RW and DVD-RAM. In these systems, the recording of information is based on writing and erasing amorphous marks in a crystalline layer of a phase-change material. Besides sufficient optical contrast between the crystalline and amorphous state and a sufficiently low melting point attainable with moderate lasers powers, the crystallisation behaviour at various temperatures is one of the most important aspects in developing phase-change materials. At elevated temperatures the crystallisation time of amorphous marks should be short to enable high data-rate (<100ns). This is because the maximum rate at which previous data can be overwritten with new data (within a single pass of the laser spot) is limited by the rate at which amorphous marks of the previous data can be crystallised. On the other hand, at room temperature the crystallisation rate has to be virtually zero in order to ensure that recorded amorphous marks are stable against spontaneous re-crystallisation for 30-50 years (archival-life stability). These two conflicting requirements complicate the development of new phase-change materials for high-speed rewritable discs.

In the first part of the paper, the archival-life stability of phase-change discs is addressed. A model is presented that can be applied to select and improve promising phase-change materials compositions with respect to their amorphous-mark stability. Isothermal crystallisation experiments on recorded amorphous marks have been performed to support the model and to determine the archival life of phase-change discs.

Based on the model, novel compositions of Ga-In-Sb phase-change materials were investigated as possible candidates for high data-rate rewritable optical recording. Dependence of stability and high speed crystallisation of amorphous marks on composition is discussed.

AMORPHOUS MARK STABILITY

The archival life of a phase-change disc is generally determined by the thermal stability of recorded amorphous marks. When the disc is stored at elevated temperatures, the marks may spontaneously re-crystallise, resulting in progressive deterioration of the data. To accelerate

optimisation of phase-change materials a model has been developed [1] that can be used to calculate glass-transition temperatures for phase-change materials of various compositions. These glass-transition temperatures are used to estimate the amorphous-mark stability and the corresponding archival life. The glass-transition temperature represents the temperature above which an amorphous matrix can attain various structural configurations and below which the matrix is frozen into a structure which cannot easily change to another structure. Thus, crystallisation below the glass-transition temperature is extremely slow and a strong correlation between glass-transition temperature and thermal stability of recorded marks is expected.

It is reasonable to assume that the glass-transition temperature must be related to the magnitude of the cohesion forces within the amorphous network since these forces must be overcome to allow atomic movement. Therefore, a promising approach to determine glass-transition temperatures is to find a correlation with atomisation energies of the amorphous network. These energies can be calculated by summing all individual bond energies, taking into account the number of bonds per atom and the energy per bond. The number of bonds per atom is determined by the number of valence electrons of the corresponding atom. For instance, Te has 6 valence electrons and forms 2 bonds, while Ge has 4 valence electrons and forms 4 bonds. In a covalent matrix, metallic-like elements form 4 covalent bonds, but donate additional bonds to their neighbouring chalcogenide atoms (Te, Sb etc.) by transfer of valence electrons. Bond energies can be obtained from the known atomisation energies of stoichiometric compounds [1]. In table I, bond energies and number of bonds are listed for a selected set of elements.

In the literature many glass-transition temperatures are reported for covalent amorphous materials of various compositions. With the method described above we can calculate the atomisation energy for each composition and relate them to the reported glass transition temperatures. The overall empirical relation found between the glass-transition temperature T_g (in Kelvin) and atomisation energy, E_a, (in kJ/mol) is [1]

$$T_g = 3.44E_a - 480$$

Using the above model, glass-transition temperatures were calculated for the ternary system Ge-Sb-Te. This system contains the well-known stoichiometric phase-change compounds along the GeTe-Sb_2Te_3 tie-line, i.e. GeTe, $Ge_2Sb_2Te_5$ and $Ge_1Sb_2Te_4$. The Ge-Sb-Te system also includes the compound Sb_2Te. This compound forms the basis for the so-called fast-growth materials (FGM) currently applied in media CD-RW and DVD+RW discs. These phase-change materials can be viewed upon as Sb_2Te doped with Sb, In, Ag and/or Ge.

Table I. Bond energies (in kJ/mol) for combinations of selected elements. The number of bonds formed by each element is indicated between brackets.

	Te (2)	Sb (3)	Ge (4)	Ga (4+1)	In (4+1)	Ag (4+3)
Te (2)	197	186	192	152	133	76
Sb (3)	186	175	181	138	120	64
Ge (4)	192	181	186	142	123	69
Ga (4+1)	152	138	142	90	70	21
In (4+1)	133	120	123	70	50	2
Ag (4+3)	76	64	69	21	2	-50
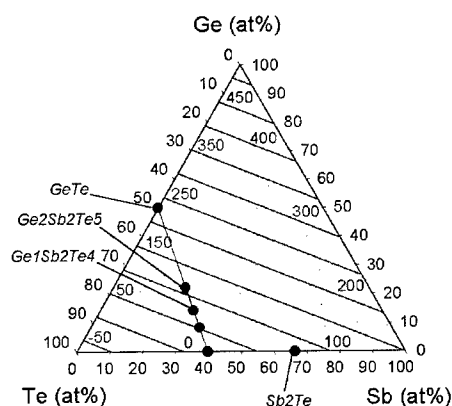
Figure 1. Calculated glass-transition temperatures (in °C) for the system Ge-Sb_2Te. Stoichiometric phase-change compositions on the pseudo-binary line GeTe-Sb_2Te_3 are shown in the plot. The binary compound Sb_2Te is also shown, since current CD-RW and DVD+RW materials are based on doping Sb_2Te with Sb, Ag, In and/or Ge.

Figure 1 shows calculated lines of constant glass-transition temperature for the ternary system Ge-Sb-Te. It is seen that increasing the Ge content is very effective for increasing the glass-transition temperature. This is due to the fact that Ge forms 4 bonds with relatively high bond energy. Also a high Sb/(Sb+Te) ratio is beneficial for a high glass-transition temperature. Assuming that a minimal glass-transition temperature of 100°C is required for sufficient amorphous-mark stability, one sees that the compounds GeTe and $Ge_2Sb_2Te_5$ fulfil this requirement, while the compounds $Ge_1Sb_2Te_4$ and Sb_2Te do not. It has been found that phase-change discs based on $Ge_1Sb_2Te_4$ indeed have insufficient archival-life. The model shows that the amorphous mark stability of Sb_2Te can be increased by alloying. Calculations for $(Sb_2Te)_{0.93}Y_{0.07}$ with Y = Ge, Ag or In yields glass-transition temperatures of 106, 83 and 71°C, respectively, which have to be compared with the value of 76°C for Sb_2Te. Addition of Ge is thus expected to be more effective for increasing the amorphous-mark stability than addition of In and Ag.

A first indication for the archival-life stability of phase-change materials is generally obtained by measuring the crystallisation temperature of the sputter-deposited amorphous state. A more accurate prediction can be obtained by measuring the (low temperature) activation energy for crystallisation of recorded amorphous marks, and by using this value to extrapolate the lifetime of recorded marks at ambient temperatures. Such experiments have been performed for $Ge_2Sb_2Te_5$ and for eutectic Sb_2Te doped with In or Ge.

Figure 2 shows transmission electron microscope (TEM) images which visualise what happens when amorphous marks recorded in doped eutectic Sb_2Te are heated in a furnace. These materials are characterised in that crystallisation proceeds by growth of the crystalline edge towards the mark centre [2], as is clearly seen in the figure. The crystallisation mechanism for stoichiometric $Ge_2Sb_2Te_5$ is completely different. For this material, crystallisation takes place by nucleation of many crystallites in the interior of the mark until the mark is completely filled [2].
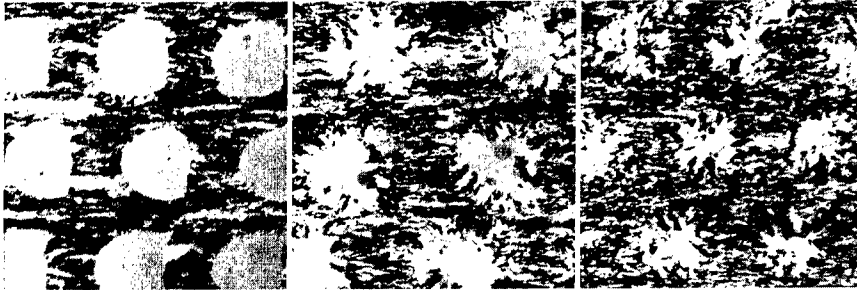
Figure 2. TEM-images of amorphous marks (400nm) recorded under DVD-conditions in a phase change disc based on Ge-doped eutectic Sb_2Te, after recording (left panel), after annealing for 1 hr at 165°C (central panel), and after annealing for 1 hr at 175°C (right panel).

Figure 3 shows the extrapolated archival life as a function of temperature for $Ge_2Sb_2Te_5$ and for the doped eutectic Sb_2Te compositions. The archival life was estimated as 10% of the measured isothermal crystallisation time since partly re-crystallised marks already will deteriorate the read-out significantly. The eutectic materials appear to be more stable than $Ge_2Sb_2Te_5$ at ambient temperature, which is mainly due to the higher activation energy involved. In accordance with the calculated glass transition temperatures, addition of Ge is much more effective than addition of In to increase the amorphous stability of doped eutectic Sb_2Te.
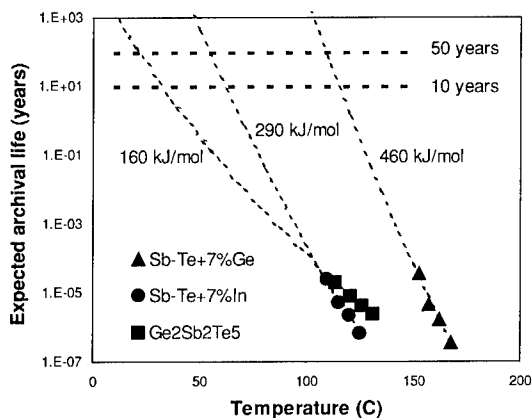
Figure 3. Expected archival life of recorded amorphous marks (DVD conditions). Activation energies are shown in the plot. The activation energy of $Ge_2Sb_2Te_5$ is remarkably lower than that of the doped Sb-Te materials. This might be related to the different type of crystallisation process involved.

PROPERTIES OF NOVEL PHASE CHANGE MATERIAL: GaInSb

More than 15 years ago, InSb and GaSb were discovered to show extremely fast crystallisation upon laser heating of the amorphous state [3]. At that time, they were basically regarded as write-once materials instead of rewritable materials, because their high crystallisation speed would make it impossible to write amorphous marks in a crystalline layer. Since then, cooling rates of phase-change stacks have improved and also laser drivers have been developed allowing

laser pulses of only nanosecond duration. This has led us to re-investigate these compounds and mixtures thereof for application in high data-rate rewritable recording.

First, we calculated glass-transition temperatures using the model described in this paper. The results are plotted in Figure 4. It is seen that InSb-rich compositions and compositions to the right of the InSb-GaSb tie-line have low glass transition temperatures. The latter compositions only have sufficiently high glass-transition temperature at high Ga/In-ratio.

Static tester experiments [4] were performed to measure the complete erasure time (CET) of written amorphous marks. Five compositions on the InSb-GaSb tie-line were measured. Measured CET-values are plotted in Figure 4. The CET-values were independent of the amorphous mark-size, which is typical for nucleation dominated crystallisation. Short crystallisation times below 25 ns were observed for InSb-GaSb mixtures with more than 25% GaSb. Ultra-short crystallisation times close to 10 ns were observed for GaSb rich compositions. Additional measurements showed that crystallisation times could be decreased even further by using nucleation-promoting cap-layers, or by increasing the thickness of the phase change layer.

In Figure 5 are plotted the expected archival life of InSb, $In_{38}Ga_{12}Sb_{50}$ and $In_{25}Ga_{25}Sb_{50}$ as determined experimentally with the procedure described in the previous section. The expected archival life of the respective compositions at 25°C is 2 days, 1 year and 3000 years. GaSb-rich compositions combine a high crystallisation rate with a high amorphous mark stability. These compositions, however, have 2 drawbacks. First, the laser power required for writing marks is relatively high, due to the gradual increase in melting temperature when going from InSb to GaSb. Second, the optical contrast between amorphous and crystalline state gradually decreases when going from InSb to GaSb.

Recorder experiments under DVD+RW conditions were performed for some compositions. Data could be written and erased at high speed with sufficient modulation using stacks with low crystalline reflection and high amorphous reflection. Important media parameters such as the number of direct overwrite cycles and erasability need to be further optimised.
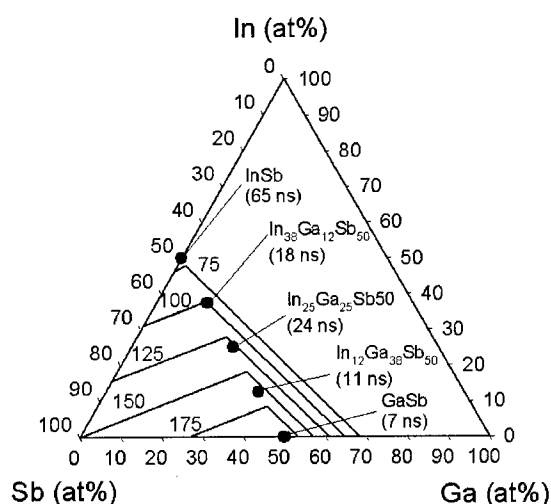
Figure 4. Calculated glass transition temperatures (in °C) for the system Ga-In-Sb. Compositions for which complete erasure times of written amorphous marks have been measured (under DVD conditions) are shown also in the plot together with the corresponding values. Stack design: substrate/ZnS-SiO₂/ GaInSb (25 nm)/ ZnS-SiO₂/Al.
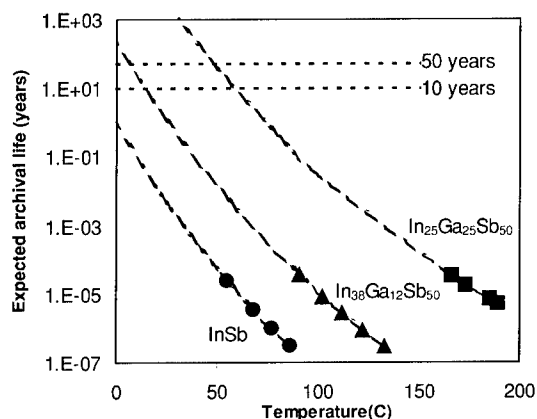
Figure 5. Expected archival life of recorded amorphous marks (DVD conditions) for 3 Ga-In-Sb compositions: InSb, $In_{12}Ga_{38}Sb_{50}$ and $In_{25}Ga_{25}Sb_{50}$. Data was measured using the procedure described in the text. The activation energy is approximately 140kJ/mol, which value is close to that determined for $Ge_2Sb_2Te_5$, for which the crystallisation is also nucleation dominated.

CONCLUSIONS

Phase-change discs based on Ge-doped eutectic Sb_2Te have excellent archival life. As predicted by model calculations, the archival life of In-doped eutectic Sb_2Te is much less. Its value is, however, still sufficient (more than 100 year at 25°C). The estimated archival life of $Ge_2Sb_2Te_5$ is 10-50 years at room temperature. In the ternary system Ga-In-Sb, novel phase change compositions have been identified which combine short crystallisation time (<25ns) with sufficient stability of recorded amorphous marks (more then 50 year at 25°C).

ACKNOWLEDGEMENT

REFERENCES
[1] M.H.R. Lankhorst, 'Modeling of glass transition temperatures of phase-change materials for optical recording', submitted to J. Non-Cryst .Solids, (2001)

[2] G.F. Zhou, H.J. Borg, J.C.N. Rijpers, M.H.R. Lankhorst and J.J.L. Horikx, *Proceedings of SPIE*, 'Optical Data Storage 2000', **4090**, 108-115 (2000)

[3] D.J. Gravesteijn, *Applied Optics,* **27**, 736, (1988)

[4] J.H. Coombs, A.P.J.M, Jongenelis, W. van Es-Spiekman, and B.A.J. Jacobs, *J. Appl. Phys.,* **78**, 4906, (1995)

Analysis of Multipulse Strategies for High Data Rate Phase Change Optical Recording

Aparna C. Sheila, T.E. Schlesinger,
DSSC, ECE Department, Carnegie Mellon University
Pittsburgh, PA 15213, U.S.A

ABSTRACT

Multipulse strategies for two disk rotation velocities of the same phase change optical disk, were analyzed using simulations, at red and blue wavelengths. Results showed that at either wavelength, lower pulse duty cycles are needed at lower velocities to reduce recrystallization and higher duty cycles are needed at higher velocities. Optimal erase powers and cooling width for minimal overwrite jitter were also found.

INTRODUCTION

To achieve higher data rates in phase change (PC) optical recording, there are two options: one is to write smaller bits by decreasing the laser wavelength and/ or increasing the numerical aperture (NA) of the objective lens while the other option is to increase the disk rotation velocity for a given wavelength and NA. Using higher linear velocities is advantageous from the reliability and removability of the disk perspective, since the distance between the PC media and the lens has to be decreased when a high NA lens is used. In this paper, we look at some issues in achieving high data rates by increasing the disk rotation velocity. The maximum data rate achievable in a phase change recording material is limited by the time taken to crystallize or erase an amorphous mark. When constant angular velocity mode is used, different locations on the PC disk will be subjected to different linear velocities. The maximum velocities that give reasonable erasability depends on wavelength. We consider two velocities each, at red (640nm) and blue (430nm) wavelength and investigate how the multipulse parameters such as the pulse duty cycle, erase power and cooling width should be modified to give comparable performance at the two velocities.

SIMULATION

The time spent by any point on the disk under laser irradiation is referred to as the effective heating duration [1] $t_h = d/v$, where d is the laser spot diameter and v is the linear velocity. GeSbTe (GST) alloys crystallize through nucleation followed by grain growth. The minimum time for crystallization is therefore limited by nucleation time. It was shown that using the GST alloys, velocities upto 50m/s, with an effective heating duration of 17.5 ns would give reasonable erasability of 30 dB [1]. We assume that with crystallization enhancement layers on either side of the phase change layer, t_h can be 15ns. This gives for red (640nm) and 0.85 NA, a maximum velocity of 50m/s and for blue (430nm) with 0.85 NA, 33.5m/s.

We numerically solved the thermal diffusion equation and the crystallization kinetics of nucleation and growth alternately in each time interval, taking into account the phase

changes that occur. The time interval between nucleation events was modeled as a random variable with an exponential density function. We assume two-dimensional nucleation and growth. The details of the simulation are given in Ref.2. The intensity of a read back beam was convolved with the reflectivity of the disk to generate read back signals. We consider 10m/s and 50m/s at 640nm and 10m/s and 30m/s at 430nm.

While overwriting, the difference in absorption between the two phases results in different sized marks depending on the previous state of the medium. To compensate for this, absorption controlled disks [4] were designed and are shown in Fig.1. A Si layer is added for absorption control at 640nm and at 430nm, a tri layer dielectric structure is used. Thin layers of SiC and SiN are used in the red and blue respectively for promoting crystallization. Our model assumes homogenous nucleation, but to take into account the heterogeneous nucleation from the interfaces, we use a lower value of activation energy.

RESULTS AND DISCUSSION

Fig.1 shows a typical multipulse that is used in the simulations. The effect of pulse duty cycle on the signal modulation is shown in Fig.2. Duty cycle is the ratio of the pulse width (time spent in write power level, P_{wr}, within T (Fig.1)), to the pulse period, T. By modulation, we mean the difference between the maximum and minimum of the read back signal. At 10m/s, both at 640nm and at 430nm, we see that the signal modulation level first increases with duty cycle, reaches saturation and then starts decreasing. At the higher velocity of 50m/s and 30m/s for the red and blue respectively, it may be seen that at high duty cycles, the modulation level increases. This may be explained as follows. When the pulse duty is increased, there are two mutually opposing effects: one is the increase in mark size due to the larger molten area, and the second is the increase in recrystallization due to a decrease in cooling rate. If the extent of recrystallization overcomes the increase in mark size due to increase in pulse duty, the modulation will decrease compared to the value at lower duty cycles. This is what happens at the lower velocity since there is more time for recrystallization than at the higher velocity (see fig.3). At the higher velocity, the increase in mark size overcomes the recrystallization effect and so the modulation increases. However, the mark also tends to become tear drop shaped at high duty cycles and this is undesirable.

Al Alloy (200nm)
Si (20nm)
ZnS-SiO$_2$ (30nm)
SiC(5nm)
GST(10nm)
SiC(5nm)
ZnS-SiO$_2$ (50nm)
Substrate

Al Alloy (200nm)
ZnS-SiO$_2$ (25nm)
SiN(5nm)
GST(10nm)
SiN(5nm)
ZnS-SiO$_2$ (42nm)
SiO$_2$(50nm)
ZnS-SiO$_2$ (40nm)
Substrate
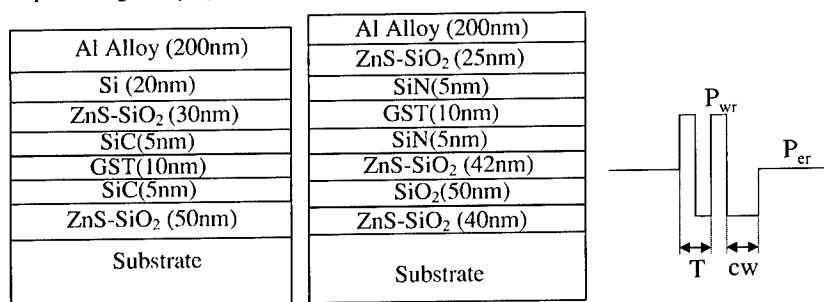
Fig.1. Disk structures used for the red wavelength (left) and for the blue wavelength. Also shown is the multipulse waveform for a 3T pulse (nT pulse has (n-1) pulses)

The minimum duty cycle that gives close to saturation modulation was chosen as the optimal duty cycle. At 10m/s, we chose 20% duty in the red and 25% duty in the blue. At 50m/s, red and at 30m/s, blue, 40% duty is chosen. At the higher velocity, the duty cycle is higher, as expected, to give the same performance
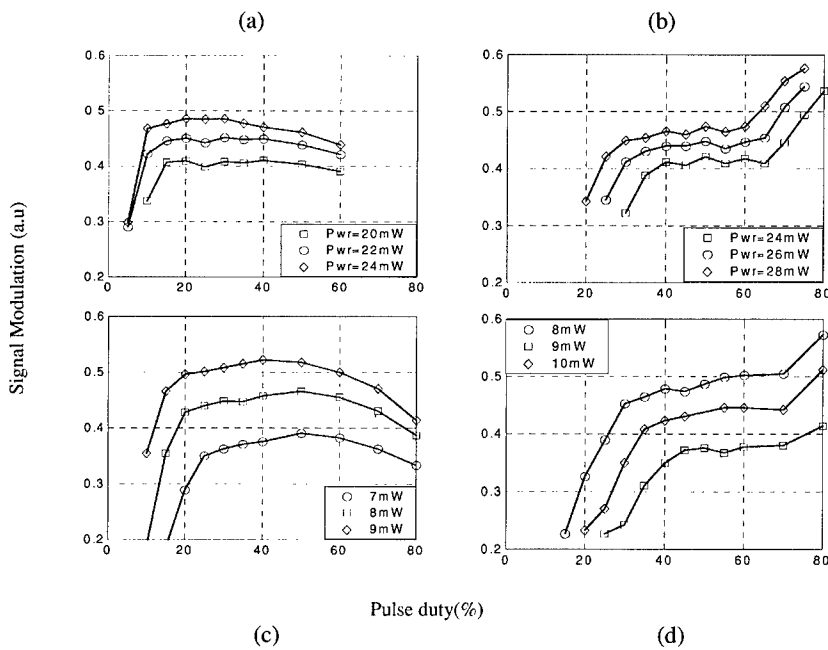
Fig.2. Plots of modulation as a function of the pulse duty cycle. 2.a and 2.b are for red wavelength and 2.c and 2.d are for the blue wavelength. 2.a and 2.c are at 10m/s linear velocity while 2.b and 2.d are at 50m/s for red and 30m/s for blue respectively.
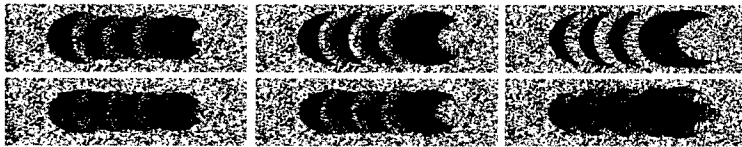
Fig.3. Images of simulated 5T marks at red wavelength. Top (L-R) 20%, 40% and 70% duty, all at 10m/s and bottom (L-R) 40%, 60% and 70% duty at 50m/s.

Fig.4 shows modulation as a function of write power using the optimal duty cycles. The modulation increases with write power and saturates. It may be noted that the power required in the blue is much less due to the smaller spot sizes and higher power densities. Also, the maximum modulation obtained with the blue is higher than red. This is due to

the absence of the Si layer in the blue disk which makes it a more rapidly cooling disk as compared to the red disk, resulting in less recrystallization upon writing a mark.
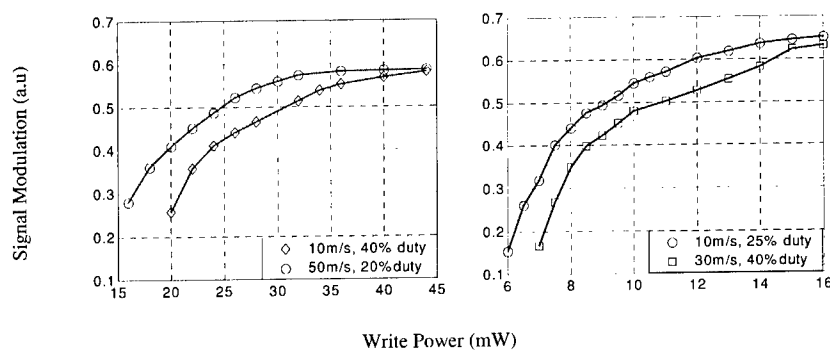
Write Power (mW)

Fig.4. Signal modulation as a function of write power at red (left) and blue wavelength

Overwrite jitter is a major concern at high velocities and arises from the difference in absorption between the two phases. At low velocities, as the laser beam moves forward, it crystallizes areas ahead of it, so regardless of the previous state, the new mark is always written on a crystalline area. At high velocities however, there is insufficient time for this crystallization and so the new mark sizes depend on the previous state and overwrite jitter increases. We simulated overwrite jitter as follows. A 6T mark was first written and a 3T mark was overwritten on the 6T mark at different delays. The full width at half maximum (FWHM) of the 3T mark varies depending upon where it is overwritten. The standard deviation of FWHM gives the overwrite jitter.

First the effect of the erase power on overwrite jitter was simulated. The plots are shown in Fig.5. There is an optimal value of the erase power at which the overwrite jitter is minimum. At low erase powers, there is insufficient erasure of the old marks as may be seen from Fig.6a. This gives rise to high values of jitter. At high erase powers, the temperature goes above the melting point at the erase locations and this again leads to high jitter (Fig.6c). It may be seen from Fig.5, that the jitter at the blue wavelength is lower than that at the red and this we think is due to the fact that the disk structure for blue is of the rapid cooling type. Also, the range of usable erase power is narrower compared to red.

Another important parameter that controls overwrite jitter is the cooling width (cw, see Fig.1). Cooling width is the time duration immediately following the last write pulse in the multipulse, during which power is maintained at a low bias level. Cooling width controls the extent of recrystallization at the trailing edge and is therefore is one of the critical parameters to take care of, to minimize jitter. The effect of cw on jitter was investigated for the two wavelengths and is plotted in Fig.7. In DVD's cw is usually taken to be 1T, however, we find that at the higher velocities used here, the cooling width has to be much lower for minimum jitter. At 10m/s, for instance, the minimum is at 0.35T for blue and 0.4T for red and at the higher velocity, the value reduces further to 0.1T for blue and 0.3T for red. At cw values lower than optimal, there is insufficient time for cooling and the molten area spreads leading to higher jitter (see Fig.8c). At higher

cooling widths, the previous mark will be incompletely erased since the erase power following the write power is farther away (Fig.8a). The effect at high *cw* is much more pronounced at the blue than at the red. This is due to the faster heat diffusion which gives less chance for return erase in the blue disk compared to the red, thereby resulting in high jitter. The same effect can again be seen at the higher velocity.
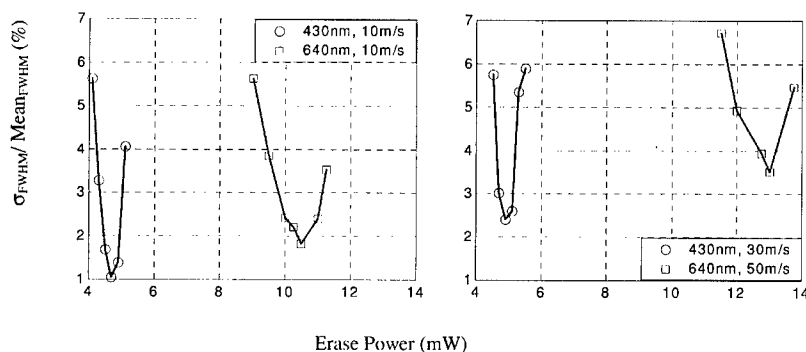
Erase Power (mW)

Fig.5. Effect of erase power on overwrite jitter

(a)   (b)   (c)
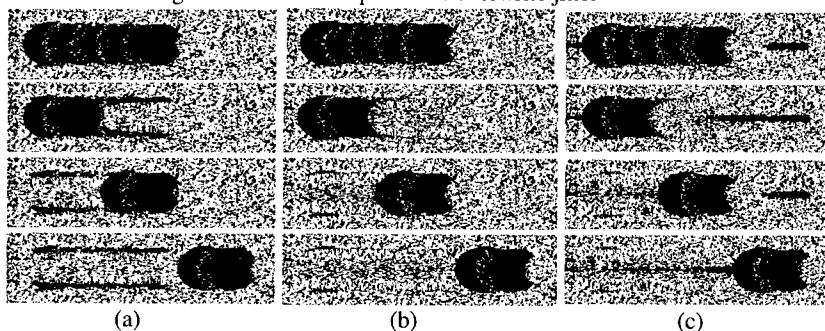
Fig. 6. Images showing the effect of erase power on overwrite. These are images at red wavelength at 50m/s. (a), (b) and (c) are at P_{er} of 11.5mW, 12.75mW and 13.25mW. Top row shows 6T marks and the next three rows are 3T marks written at delays of 0T, 2T and 6T (T-B). Each frame is 2.6μm x 0.8μm.

CONCLUSIONS

In this paper, we showed how some of the multipulse parameters should be varied at two different velocities for the same disk, to give comparable performance. The study was done at both red and the blue wavelength. The maximum velocity achievable at the two wavelengths differ due to the difference in the laser spot size. It was seen at either wavelength, the pulse duty cycle should be lower at lower velocity (20% and 25% duty at
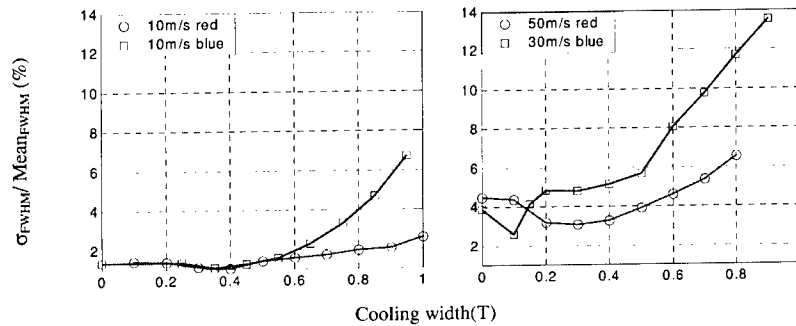
Fig.7. Effect of cooling width on overwrite jitter

(a) (b) (c)
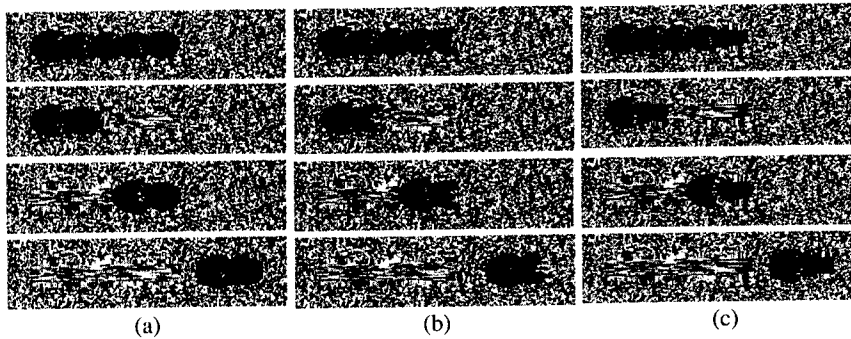
Fig.8. Images of marks written with blue laser at 30m/s showing effect of cooling width on overwrite. (a), (b) and (c) are at cooling widths of 0.85T, 0.1T and 0.0T. Frame size and delays are same as Fig.6.

10m/s in red and blue) and higher (40%) at higher velocities (30m/s, blue and 50m/s, red) to give maximum signal modulation. To reduce overwrite jitter, cooling width is seen to be a critical factor and the cooling widths required at higher velocities are lower (0.1T, 0.3T at blue and red) than what is needed for minimal jitter at the lower velocities(0.3T, 0.4T at blue and red). Also, significantly lower powers are needed in the blue compared to red and the maximum modulation obtainable with the blue is higher than at red. Finally, the minimum overwrite jitter at blue is also less than at red.

REFERENCES

1. N. Yamada, ODS Digest, p 98, 1997.
2. Aparna Sheila, D.N.Lambeth, T.E. Schlesinger, SPIE **4090**, 116, 2000
3. S. Ohkubo, M. Okada, M. Murahata, T.Ide, T.Iwanaga, Jpn. J. Appl. Phys., **32**, 5230, '93.
4. Y. Kasami, Y. Kuroda, K. Seo, et al., Jpn. J. Appl. Phys. **39**, 756, Part 1, No. 2B, 2000

A Novel Approach to Obtain GeSbTe-Based High Speed Crystallizing Materials for Phase Change Optical Recording

Tae-Yon Lee[1], Byung-ki Cheong, Taek Sung Lee, Sung Jin Park, Won Mok Kim, Kyung Seok Lee, Ki-Bum Kim[1], and Soon Gwang Kim
[1]School of Materials Science and Engineering, Seoul National University,
Shilim-dong, Kwanak-gu, Seoul 151-742, Korea.
Materials Design Laboratory, Korea Institute of Science and Technology,
Hawolgok-dong, Sungbuk-ku, Seoul 136-791, Korea.

ABSTRACT

A new approach is proposed to obtain fast crystallizing materials based on a conventional GeSbTe alloy for rewritable phase change optical data storage. By means of co-sputtering, $Ge_1Sb_2Te_4$ alloy was mixed with $Sn_1Bi_2Te_4$ alloy so as to form pseudo-binary alloys $(Ge_1Sb_2Te_4)_{1-x}(Sn_1Bi_2Te_4)_x$ (x is a mole fraction). From structural and optical analyses of the co-sputtered and annealed alloy films, the formation of stable crystalline single phases was observed along with a Vegard's law behavior, suggesting a homogeneous mixing of the two alloys. By use of a 4 layered disk with $(Ge_1Sb_2Te_4)_{0.85}(Sn_1Bi_2Te_4)_{0.15}$ recording layer, a preliminary test of writing and erasing was carried out and the results were compared with the case of the disk with $Ge_1Sb_2Te_4$ recording layer. The $(Ge_1Sb_2Te_4)_{0.85}(Sn_1Bi_2Te_4)_{0.15}$ recording layer was found to yield markedly higher erasibility, especially with increasing disk linear velocity.

INTRODUCTION

With a rapid progress of information and communication technology, there has been growing need for higher density and higher speed information storage. As for phase change optical data storage, boost in recording density and data transfer rate has been achieved primarily by ways of reduction in beam spot size and/or increase in disk linear velocity. Beam dwell time, expressible in terms of beam spot size divided by linear velocity, has diminished accordingly. This has led to a sustaining demand for faster crystallizing recording materials. In the cases of the GeSbTe alloys, enhanced crystallization kinetics has been attained by modification of alloy composition through addition of single elements such as Au, Pb[1,2], N[3], Sn[4], Bi[5] and/or by use of

crystallization promoting layers such as SiC, GeN[6,7]. In this report, we propose a novel approach that may be utilized to promote the crystallization kinetics of the GeSbTe alloys. In doing so, we address specifically the case of the stoichiometric $Ge_1Sb_2Te_4$ alloy that is presently in wide use besides $Ge_2Sb_2Te_5$ alloy.

PROPOSED APPROACH AND EXPERIMENTAL ALLOY SYSTEM

The present approach hinges on a well-known fact that a stoichiometric compound alloy tends to have faster kinetics of amorphous to crystalline transformation since only short range atomic reconfiguration would attend the transformation. An interesting question arises; suppose a stoichiometric alloy is mixed with another alloy that has the same stoichiometry but with a stronger tendency for crystallization, would the resulting alloy have an enhanced crystallization kinetics ?

Herein, we mix $Ge_1Sb_2Te_4$ alloy with an isomorphous ternary alloy $Sn_1Bi_2Te_4$ of the same stoichiometry. $Sn_1Bi_2Te_4$ alloy is selected on the following bases. Firstly, Sn and Bi belong to the same family as Ge and Sb, but the bond energies of Sn-Sn, Bi-Bi, Sn-Te and Bi-Te are less than those of Ge-Ge, Sb-Sb, Ge-Te and Sb-Te, respectively[8]. We consider that the reduced bond energies would lead to the enhanced nucleation kinetics during amorphous to crystalline transformation of the mixed alloy. Secondly, the equilibrium crystalline phase of $Sn_1Bi_2Te_4$ alloy has the same space group symmetry as that of $Ge_1Sb_2Te_4$ alloy, with only a slight difference in lattice parameters (a=0.421 nm, c=4.06nm for $Ge_1Sb_2Te_4$ and a=0.441 nm, c=4.1511 nm for $Sn_1Bi_2Te_4$)[9,10]. These, together with similar melting temperatures of the two alloys[11](615 °C for $Ge_1Sb_2Te_4$ and 596 °C for $Sn_1Bi_2Te_4$), suggest that the two alloys may have a strong tendency to form a homogeneous single phase solid solution over a wide range of mixing.

EXPERIMENTS

Targets of $Ge_1Sb_2Te_4$ and $Sn_1Bi_2Te_4$ alloys were co-sputtered in a RF magnetron sputter system. In order to produce thin films of varying composition $(Ge_1Sb_2Te_4)_{1-x}(Sn_1Bi_2Te_4)_x$, sputtering power for a $Ge_1Sb_2Te_4$ alloy target was varied with the power for $Sn_1Bi_2Te_4$ target constant. From RBS (Rutherford Backscattering Spectrometry) spectra of the sputtered films, elemental compositions of Ge and Bi, yielding clearly separable RBS peaks from the rest, were determined and in turn overall compositions were estimated in terms of the mole fraction x assuming the respective stoichiometry of $Ge_1Sb_2Te_4$ and $Sn_1Bi_2Te_4$ is preserved during sputtering. For crystallization, co-sputtered films were annealed either at 150 °C or at 300 °C for 30 minute

in a vacuum furnace with Ar flow. Structural analyses of films were made with XRD(X-ray Diffractometer, M18XHF-SRA). Refractive indices (n) and extinction coefficients (k) of films were determined from the simulation of phase difference(Δ) and azimuth angle(Ψ) measured with variable angle spectroscopic ellipsometer (VASE) using the Lorentz-Drude oscillation model. Disk samples with recording layers of selected compositions were tested with a laboratory-built disk dynamic tester equipped with a laser diode of λ=650 nm and an objective lens of N.A.=0.6.

RESULTS AND DISCUSSIONS

Shown in figure 1 are the X-ray diffraction spectra of the co-sputtered films of various compositions (x = 0, 0.125, 0.1837, 0.2244, 0.3152, 0.4818, 1) annealed at 150 °C. It is found that diffraction spectra for each composition can be indexed as a crystalline FCC single phase except for the $Sn_1Bi_2Te_4$ case (x=1). A sputtered film of the $Sn_1Bi_2Te_4$ alloy was found to exist as an FCC phase in the as-deposited state and as a two phase mixture of an FCC and an HCP in the annealed state. From figure 1, one should notice a telling feature with increasing mole fraction x. Each peak, for instance 220 peak, undergoes a positional shift toward a smaller 2θ angle with a concomitant gradual peak broadening. Without homogeneous mixing of $Sn_1Bi_2Te_4$ and $Ge_1Sb_2Te_4$ on an atomic scale, each FCC peak would appear two split peaks with relative intensity ratio continuously changing with mole fraction x. Quite possibly, the peak broadening is then considered to result from lattice distortion due to accommodation of atoms
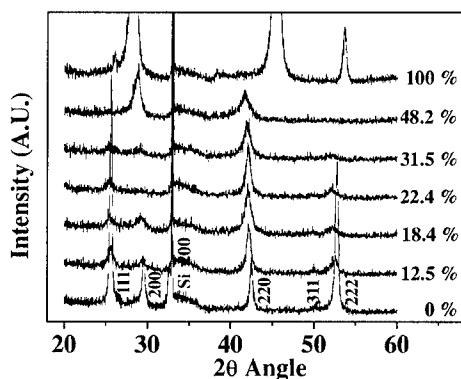
Figure 1. X-Ray diffraction spectra of the co-sputtered $(Ge_1Sb_2Te_4)_{1-x}(Sn_1Bi_2Te_4)_x$ films annealed at 150 °C. Peaks can be indexed as an
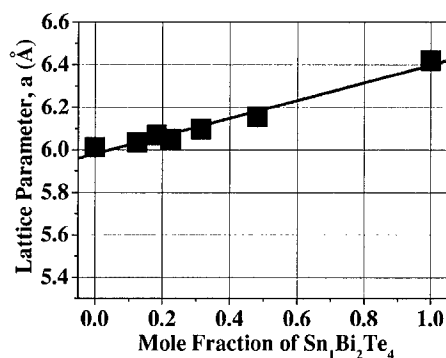
Figure 2. Variation of lattice parameter with the mole fraction (x) of $Sn_1Bi_2Te_4$, as measured from co-sputtered $(Ge_1Sb_2Te_4)_{1-x}(Sn_1Bi_2Te_4)_x$ films annealed at 150 °C.

with different sizes. The dependence of FCC lattice parameter on the mole fraction x, as suggested by the shift of the peak position, was determined from diffraction spectra as shown in figure 2. One can clearly see a nearly linear relationship representing a Vegard's law behavior as expected for a homogeneous solid solution. A similar relationship were also observed from the co-sputtered films annealed at 300 °C where an HCP phase is the prevailing crystalline state for the entire range of mole fraction.

Optical constants of the as-deposited films as well as the annealed films have been determined, from which optical band gap energies were derived. The results are summarized in figure 3, depicting the dependence of optical band gap energy on $Sn_1Bi_2Te_4$ content in the co-sputtered alloys of various structural states. As for both annealed films, optical band gap energy has a very weak compositional dependence with increasing $Sn_1Bi_2Te_4$ content. As for as-deposited films, the trend runs similar up to around x=0.15 where band gap energy undergoes a steep decrease in conjunction with the appearance of the crystalline as-deposited state.

In order to find out whether the present approach can be applied to high speed phase change optical storage, dynamic tests of the disks were carried out using disk samples of 4 layer stacks consisting of AlCr(100 nm) / ZnS-SiO$_2$(20 nm) / Active layer(20 nm) / ZnS-SiO$_2$ (270 nm) on 1.2 mm polycarbonate substrate. As for active layers, $(Ge_1Sb_2Te_4)_{0.85}$ $(Sn_1Bi_2Te_4)_{0.15}$ alloy was selected along with $Ge_1Sb_2Te_4$ alloy for comparison (for brevity, a disk with the $(Ge_1Sb_2Te_4)_{0.85}(Sn_1Bi_2Te_4)_{0.15}$ recording layer is denoted hereafter as disk A and the one with the $Ge_1Sb_2Te_4$ as disk B). Reflectivity values of the as-deposited amorphous (R_a) and initialized crystalline (R_x) states, as measured with λ=650 nm and N.A.=0.6 optics of the disk tester, were respectively 3 % and 11 % for disk A and 3.5 % and 10 % for disk B.
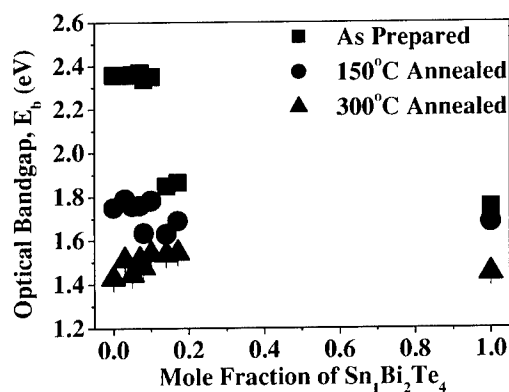
Fig 3. Dependence of optical band gap energy on the mole fraction of $Sn_1Bi_2Te_4$, as measured from co-sputtered $(Ge_1Sb_2Te_4)_{1-x}(Sn_1Bi_2Te_4)_x$ films of various structural states.
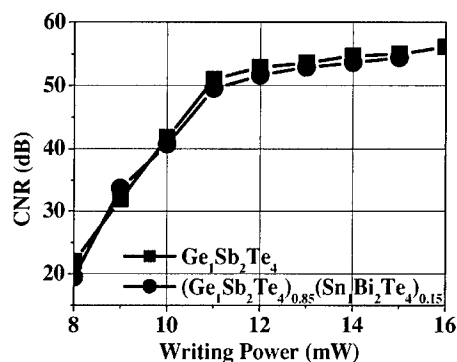
Fig 4. Comparison of writing power dependence of CNR between disks of the two different recording layer materials
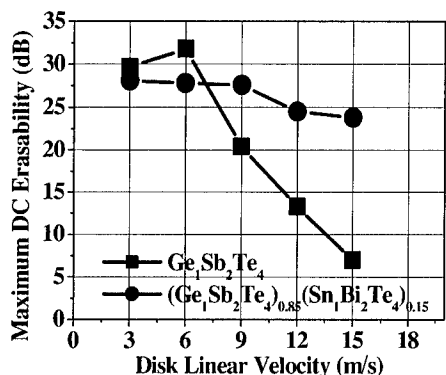
Fig 5. Comparison of the dependence of maximum DC erasibility on the disk linear velocity, between disks of the two different recording layer materials

Writing of amorphous marks was performed at the linear velocity of 9 m/s by use of a writing pulse consisting of a writing power level of $3T_w$ (T_w=23.3 nsec) duration followed by a readout power level (1 mW) of $7T_w$ duration. In figure 4, CNR values are shown as a function of writing power, measured at the readout frequency of 4.29 MHz. Between the two disks, CNR values appear remarkably similar with only 1 to 2 dB difference regardless of a writing power. Since contrast ratio $(R_x-R_a)/(R_x+R_a)$ difference between the two disks (0.48 for disk A and 0.57 for disk B) accounts for 1.5 dB CNR difference, it follows that sizes of amorphous marks may be comparable between the two disks and thermal constants of the recording layers as well.

In contrast to writing, a striking difference was observed between the two disks during erasing. For this experiment, amorphous marks were formed with 15mW writing power under the same writing conditions specified above and subsequently DC-erased while varying disk linear velocity. In figure 5, maximum DC erasibility due to a respective optimum erasing power is shown as a function of linear velocity. As for disk A, erasibility decreases very rapidly with disk linear velocity, reaching below 20 dB near 9 m/s. On the contrary, disk B displays no appreciable decrease with increasing disk linear velocity but maintains a high erasibility around 25 dB even at the velocity of 15 m/s.

CONCLUSION

An approach is proposed to obtain fast crystallizing materials for rewritable phase change optical storage. The approach makes a purposeful use of a homogeneous mixing of a conventional stoichiometric GeSbTe alloy with an isomorphous alloy of the same stoichiometry but with a stronger tendency for crystallization. By means of co-sputtering, $Ge_1Sb_2Te_4$ alloy was mixed with $Sn_1Bi_2Te_4$ alloy and preliminary analyses of the co-sputtered films were carried out. Evidences of a homogeneous mixing as well as of a promoted crystallization were attained. We suppose that faster crystallization of the co-sputtered alloys may result from the reduced pairwise bond energies particularly of Sn-Te and Bi-Te relative to Ge-Te and Sb-Te by way of promotion of nucleation kinetics.

ACKNOWLEDGMENT

REFERENCES

1. E. Ohno, N. Yamada, T. Kurumizawa, K. Kimura, and M. Takao, *Jpn. J. Appl. Phys.* **28** (7), 1235 (1989)
2. F. Jiang, M. Jiang, L. Hou, F. Gan, and M. Okuda, *Proceedings of International Sympositum on Optical Memory*, **28**(Suppl. 28-3), 293 (1989)
3. C. Trappe, B. Bechevet, B. Hyot, O. Winkler, S. Facsko and H. Kurz, *Jpn. J. Appl. Phys.* **39** (2B), 766 (2000)
4. R. Kojima and N. Yamada, *Proceedings of the 12th Symposium on Phase Change Optical Information Storage*, Shizuoka, Japan, p36 (2000)
5. C.M. Lee, T.S. Chin, and E.Y. Huang, *J. Appl. Phys.* **89** (6), 3290 (2001)
6. N. Yamada, M. Otoba, K. Kawahara, N. Miyagawa, H. Ohta, N. Akahira, and T. Matsunaga, *Jpn. J. Appl. Phys.* **37** (4B), 2104 (1998)
7. G.F. Zhou and B.A.J. Jacobs, *Jpn. J. Appl. Phys.* **38** (3B), 1625 (1999)
8. D. R. Lide (ed.) *Handbook of Chemistry and Physics, 81st ed.*, The Chemical Rubber Company, Florida, 9-52 (2000)
9. K.A. Agaev and A.G. Talybov, *Kristallografiya*, **11** (3), 400 (1966)
10. T.B. Zhukova and A.I. Zaslavskii, *Kristallografiya*, **16** (5), 796 (1971)
11. P. Villars, A. Prince, and Okamoto (eds.) *Handbook of Ternary Alloy Phase Diagrams*, ASM International, Ohio (1997)

Microscopic studies of fast
phase transformations in GeSbTe films

Ralf Detemple, Inés Friedrich, Walter Njoroge,
Ingo Thomas, Volker Weidenhof,
Han-Willem Wöltgens, Stefan Ziegler, Matthias Wuttig
I. Physikalisches Institut der RWTH-Aachen, 52056 Aachen, Germany

ABSTRACT

Vital requirements for the future success of phase change media are high data transfer rates, i.e. fast processes to read, write and erase bits of information. The understanding and optimization of fast transformations is a considerable challenge since the processes only occur on a submicrometer length scale in actual bits. Hence both high temporal and spatial resolution is needed to unravel the essential details of the phase transformation. We employ a combination of fast optical measurements with microscopic analyses using atomic force microscopy (AFM) and transmission electron microscopy (TEM). The AFM measurements exploit the fact that the phase transformation from amorphous to crystalline is accompanied by a 6% volume reduction. This enables a measurement of the vertical and lateral speed of the phase transformation. Several examples will be presented showing the information gained by this combination of techniques.

INTRODUCTION

Rewritable optical data storage plays a key role for multimedia applications and could also be an interesting alternative for the mass storage of data. Phase change recording is a promising technique for the field of optical data storage since it is conceptionally compatible with present CD technologies. The principle behind phase change recording is the reversible transformation of small bits of the active layer between the stable crystalline and the metastable amorphous phase. Writing of bits corresponds to the formation of small amorphous marks in a crystalline matrix whereas the recrystallization of the amorphous areas leads to the erasure of the bit. Amorphization is achieved by locally melting the film using a focused laser beam. With rates between 10^9 and 10^{10} K/s the melt cools down and is trapped in the amorphous phase (called "quenching"). Heating the bits to a temperature between the glass transition and the melting temperature leads to its fast recrystallization. The amorphous phase can be distinguished from the crystalline phase by their optical properties. Therefore data can be read with a low power laser beam monitoring the local changes in reflectance.

One of the most important factors, which limits the applications for phase change-media like $Ge_2Sb_2Te_5$ [1], is a better understanding of the underlying microscopic processes, which occur during the phase transformation from amorphous to crystalline or vice versa. To unravel the processes occurring during the phase transformation, a high lateral and depth resolution is needed. We have established a combination of two techniques, atomic force microscopy and experiments with a static tester, which were used to investigate the amorphous and crystalline phases of written bits.

EXPERIMENTAL PROCEDURES

GeSbTe-alloys were deposited on glass or silicon substrates at room temperature by dc magnetron sputtering. The background pressure of the sputter system is 2×10^{-7} mbar. An argon pressure of 7.5×10^{-3} mbar and a power of 100 W was used to deposit the films. The resulting growth rate was determined to 0.5 nm/s.

X-ray reflectometry (XRR) measurements were performed to determine the thickness, roughness and the density while X-ray diffraction (XRD) measurements were used to determine the structure of the films. These measurements were carried out using a Philips X'pert MRD system. All measurements were performed at room temperature.

The bits were written with a static tester. A GaAlAs-laser diode with a wavelength of 830 nm driven by a pulse generator serves as a light source. The light is coupled into an objective with a numerical aperture of 0.9 and is focused onto the phase change material deposited onto glass. After the laser-induced modification of a certain region the sample can be moved with a piezo scan stage with nanometer precision. This allows us to write bit arrays in a region of 60×60 μm^2. The light reflected from the phase change material is monitored by a photo detector.

AFM measurements were performed with a Dimension 3100, which reveals the surface topography of the bits. The lateral resolution is limited by the curvature of the tip, which is around 10 nm.

RESULTS

AMORPHIZATION

XRR measurements were carried out to determine the change in density with annealing temperature. The density of the analysed sample was derived from the position of the total reflection edge Θ_c according to the formula

$$\rho = \left(\frac{\Theta_c}{\lambda}\right)^2 \frac{A\pi}{N_a r_0 (f_0 + f')} \qquad (1)$$

, where N_A is Avogadro's constant, r_0 is the Bohr radius, λ is the wavelength of x-rays, A is the atomic mass and (f_0+f') are the atomic form factors [2].
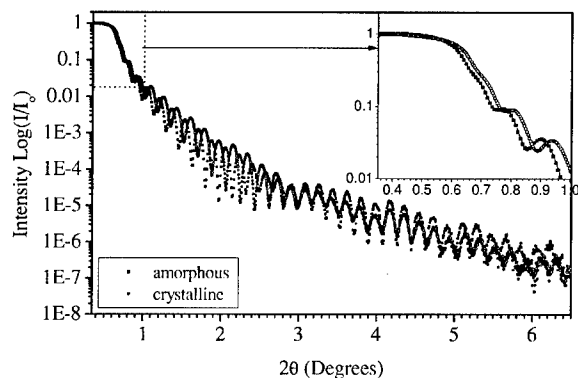
Figure 1: XRR spectra of an 80 nm thick Ge$_2$Sb$_2$Te$_5$ layer before (solid squares) and after (open circles) crystallization. The inset shows the shift of the total reflectivity edge, which was used to determine the density.
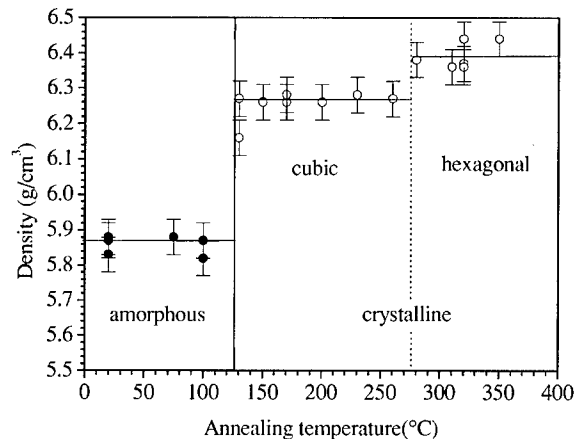
Figure 2: Density of Ge$_2$Sb$_2$Te$_5$ as a function of annealing temperature. The samples were annealed in an oven for 10 minutes. Above 130° C the rock salt structure (cubic phase) appears, at even higher temperature of 275° C the hexagonal phase is found.

The thickness of the as deposited amorphous and the crystalline sample was determined from simulations of the experimental spectra [3]. Typical spectra are shown in figure 1, where two measurements for the as deposited and crystalline cubic phase are compared. The calculated density is plotted in figure 2, which shows clearly three regimes of increasing density. The density of the amorphous phase is constant up to 130° C. Above this temperature, the rock salt

structure is formed. This phase transformation is accompanied by a density change of 6.8 %. The transformation to the hexagonal phase occurs if the temperature rises to values above 275° C, where a density change of 8.9 % with respect to the amorphous phase is found.

XRR measurements are, as mentioned above, performed on macroscopic samples annealed for 10 minutes in an oven. Nevertheless we can make use of the information displayed in figure 2 to understand the change in local topography created by a focussed laser pulse (figure 3). Amorphization in a crystalline matrix with cubic structure should lead to 6.8 % increase in thickness. For a film with a thickness of 80 nm this corresponds to a height change of about 5 nm. This is indeed what is observed by AFM. This height change enables us to track the lateral and depth growth. The density-difference between both phases and the measured height change (denoted as Δz in figure 4) was used to calculate the amorphous fraction of the bit. For this analysis we have subtracted the height change caused by delamination which is clearly visible in the outer halo. The remaining height change is attributed to the density change upon amorphization. Using a linear interpolation between a completely crystalline (thickness d) and an amorphous one (thickness $d \times \rho_c / \rho_a$) results in a relationship for the amorphous fraction χ:

$$\chi = \frac{\Delta z}{d\left(\dfrac{\rho_c}{\rho_a} - 1\right)} \qquad (2)$$
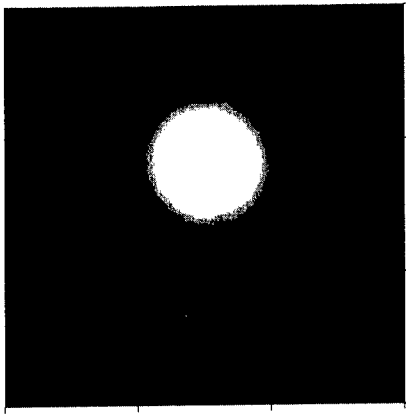
Figure 3: An AFM image of an amorphous bit in a crystalline environment. Only the inner white region consists of amorphous material, whereas the outer halo contains crystalline material. The halo is caused by a local stress relief which leads to a film delamination.
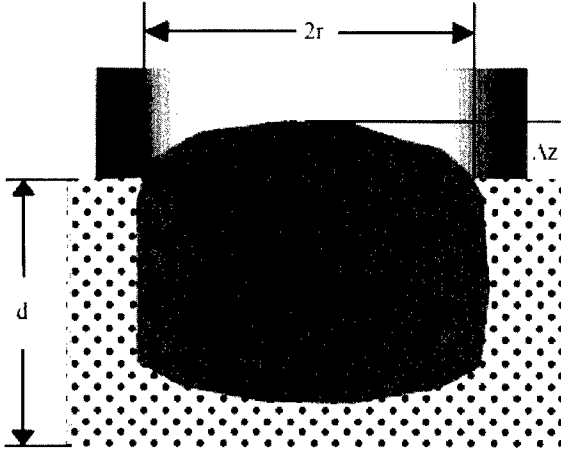
Figure 4: Schematic drawing of an amorphous bit. The total reflected power constitutes of an amorphous inner part and a crystalline surrounding area. Due to the gaussian form of the beam, both parts have to be weighted accordingly. The inner part is weighted with the factor f, which leads to an effective reflectivity $f \cdot R\chi$. The surrounding surface has an effective reflectivity of (1-f) $\cdot R_c$ due to the crystalline phase. This method is used to calculate the optical reflectivity from AFM data. See text for details.

The simplest model, which can be used, describes the relation between reflectance and amorphous fraction is a linear relationship. More sophisticated models, including a depth dependent degree of amorphisation, will not lead to a better fit to the data. Defining the reflectivity as a linear function of the amorphous fraction, the reflectivity of the amorphized surface can be calculated:

$$R_\chi = R_c + \chi(R_a - R_c) \qquad (3)$$

Until now, only the reflection of the amorphous bit has been taken into account. The crystalline surrounding also contributes to the total reflected intensity. Furthermore, the gaussian form of the beam is taken into account by weighting both contributions. The fraction of the laser beam, which illuminates the inner region, is denoted as f.

$$f = 1 - \exp\left(-2(r/r_0)^2\right) \qquad (4)$$

where r is the bit radius and r_0 is the gaussian radius. Compiling all informations gives the total reflectivity:

$$R = f \cdot R_\chi + (1 - f) \cdot R_c \qquad (5)$$

These theoretical reflectivities are compared with experimental data measured by the static tester in figure 5 [4]. A general agreement between the calculated values using AFM data and the reflectivity measured by the static tester has been found, which shows that from the AFM data we can determine the essentials of the process. Nevertheless the experimental data points still show a deviation from the theoretical values, which has two reasons. The curvature radius of the AFM tip is about 10 nm. In the worst case, this leads to an error of about 6% in the determination of the lateral size of the bit. The second source for deviations is the error in density, which was used to calculate the amorphous fraction χ. A third possible source for deviations, that can not be quantified, is the optical difference between the as deposited and the quenched amorphous phase.. The optical constants and the density used for the calculations were measured using as deposited samples. Since we have not observed any density change upon annealing up to the crystallization temperature, we believe that the density of the amorphous phase is almost identical for the as deposited and the laser quenched phase. The agreement shown in figure 5 proves, however, that AFM and static tester experiments give consistent results, despite the shortcomings mentioned above.

To identify the processes, which limit the speed of amorphization, the growth of amorphous bits has been decomposed into the lateral and vertical dimensions. Assuming a sharp boundary between the crystalline and amorphous phase, the vertical growth is given by the depth of the boundary:

$$d_{int} = \chi \cdot d_{cr} = \frac{\Delta z}{\left(\dfrac{\rho_c}{\rho_a}\right) - 1} \qquad (6)$$
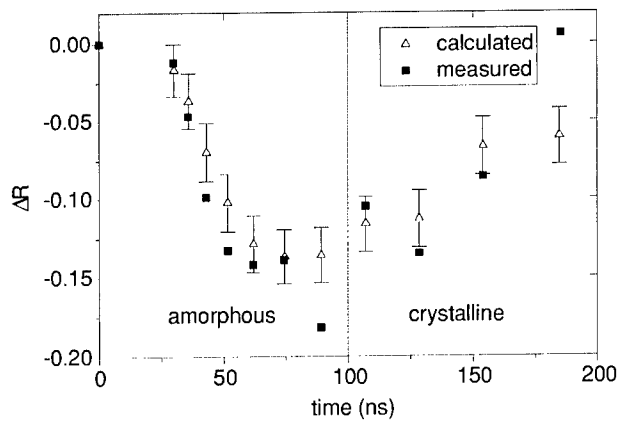

Figure 5: Comparison of experimental and theoretical reflectivity. For pulses shorter than 100 ns amorphization takes place. When the pulse length increases above this limit, melt-crystallization occurs.

Figure 6a shows the evolution of reflectivity measured by the static tester. The lateral size and the depth of the boundary in vertical direction are depicted in 6b and 6c as a function of pulse duration. The derivatives with respect to time show a strong correlation between the optical signal and the vertical growth speed. The process of amorphization is therefore mainly limited by the vertical growth speed, which reaches values up to 1 m/s. This can be explained by the gaussian beam profile, because the inner amorphous mark contributes the main fraction to the optical signal. The lateral growth of the bit has only a small impact on the readout signal, since the outer regions are only illuminated by a small fraction of the total laser intensity [5].

From the discussion presented above we can conclude that amorphization should be faster for thinner films. Therefore films with a thickness of 5 and 80 nm were compared. To determine the shortest time for successful amorphization, the power necessary to write an amorphous bit was varied and is visualized in figure 7. The reflectivity change as a function of pulse length (x-axis) and pulse power (y-axis) is color coded. If the laser power is low and the pulse duration too short, no phase change will be induced and the corresponding reflectivity change is close to zero (region I). With a laser power of about 5 mW, amorphization starts. In this region II, the illuminated area is molten and afterwards quenches into the amorphous phase. For a successful amorphization, a high temperature gradient is required to cool down the molten phase ($10^9 - 10^{10}$ K/s). When the volume around the molten bit gets warmer due to longer pulses (region III), the temperature gradient is too small and melt-crystallization takes place. For longer pulses and higher laser powers, ablation and loss of material occurs (region IV). The result of this experiment proves a faster amorphization for a 5 nm thin film. For example, when the 5 nm thick film needs 10 ns to amorphize at 20 mW, the 80 nm film needs 30 ns.
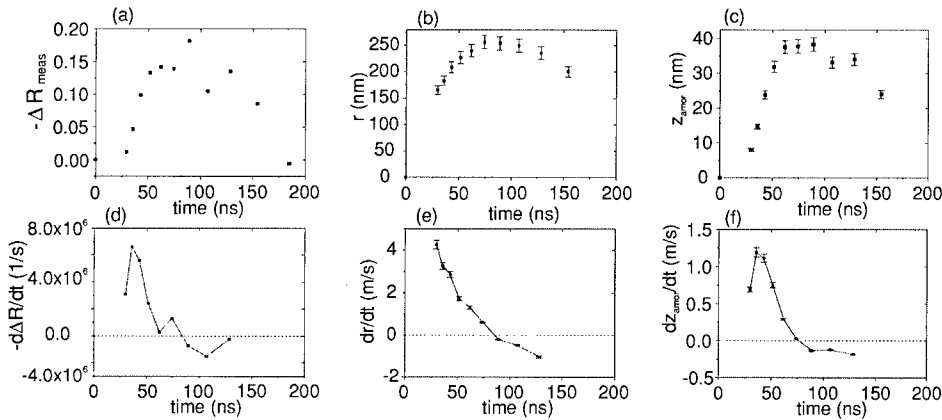
Figure 6: The upper row shows the evolution of the reflectivity change and the bit topography upon pulse length. The time derivatives of these data were calculated and presented in the bottom row. The change of reflectivity measured with the static tester is shown in the left column, while the lateral bit growth and the height change can be found on the right hand side. The change in reflectivity (6d) is dominated by the vertical growth (6f). The vertical growth speed (right bottom diagram) of about 1 m/s limits the maximum speed of amorphization.
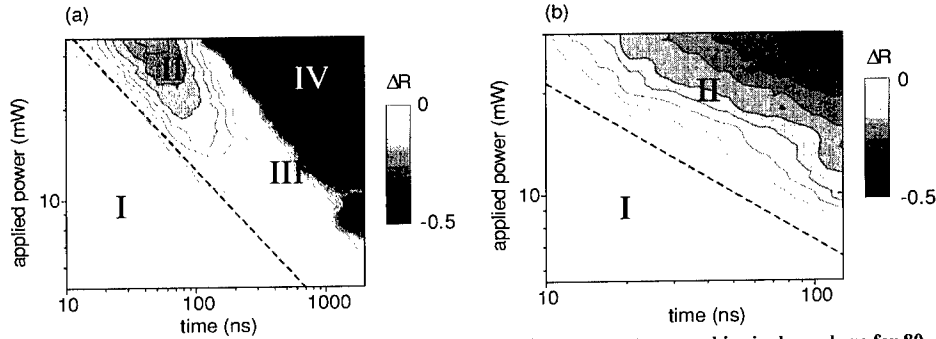
Figure 7: The influence of film thickness upon the pulse length necessary to amorphize is shown here for 80 nm (left) and 5 nm (right) films. Amorphization in 10 ns for thick samples can be achieved, if the laser power will be increased above 40 mW. Lower laser powers are sufficient for the thin sample (right picture), where a successful amorphization takes place for 20 mW in 10 ns.

CRYSTALLIZATION

To erase the written bits, they must be crystallized. Figure 8 shows the influence of the phase of the material surrounding the crystallized bit upon the pulse duration and pulse power necessary to crystallize.

In the left diagram of figure 8, an amorphous environment for the crystallization was chosen. The corresponding power-time-effect diagram shows a minimum time for crystallization of around 100 ns, which limits the crystallization process under these circumstances. This time of 100 ns is identified as the incubation time [6,7], which is needed to reach an equilibrium distribution of subcritical nuclei.

The minimum time to crystallize can be reduced by one order of magnitude if a crystalline environment is chosen, which is demonstrated in figure 8, right diagram. In contrast to prior shown PTE-diagrams, two pulses were used for every data point: First a pulse with fixed parameters to write a bit (amorphize the illuminated region), followed by a pulse with varying pulse power and duration. The respective change in reflectivity from the state before the first pulse and after the second one was measured. Region II marks the parameters for successful recrystallization, which starts at 10 ns. A second amorphization is also possible, as seen in region III. The physics related to a further increase in time is similar to amorphization, where melt-crystallization is observed.

This fast recrystallization is attributed to one of the two different mechanisms of recrystallization: Either small crystalline nuclei which are incorporated inside the amorphous material can start the recrystallization or it is started from the surrounding rim [10]. A differentiation can be made by measuring the recrystallized fraction ε after the second pulse as a function of the diameter of the initial, amorphous bit where ε is defined as

$$\varepsilon = 1 - \frac{R_{rec} - R_i}{R_i - R_a} \qquad (7)$$

R_i is the initial reflectivity, R_a the reflectivity after the amorphization pulse and R_{rec} the reflectivity after recrystallization pulse. R_{rec} is the weighted sum of the reflectivity of the recrystallized area and the remaining amorphous part. In the presence of small nuclei the recrystallization starts homogenously distributed throughout the amorphous part. Hence there is

no correlation between ε and the bit diameter. On the contrary, if the recrystallization starts from the rim, the recrystallization efficiency depends on the bit diameter. Regarding equation (7) we then expect a decrease in ε with bit diameter. This experiment was carried out with two different materials, $Ge_2Sb_2Te_5$ and $Ge_4Sb_1Te_5$ (figure 9). In the case of $Ge_2Sb_2Te_5$ there is no dependency between ε and bit diameter and thus small crystalline nuclei have to be present in the amorphous phase. However, in the case of $Ge_4Sb_1Te_5$ ε decreases with bit diameter and thus recrystallization has to start from the crystalline rim.
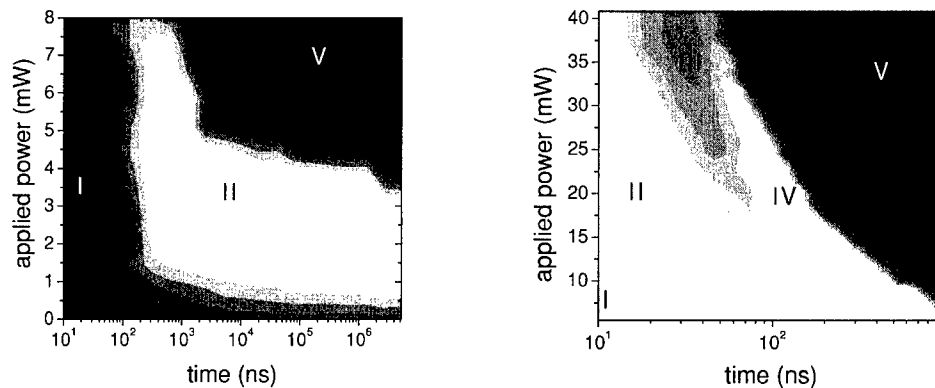
Figure 8: The influence of the environment surrounding the bits can be seen from these two power-time-effect diagrams. The diagram on the left hand side shows the effect of crystallization in an amorphous environment. Important is the minimum time for crystallization of 100 ns (region II). Using a crystalline environment considerably reduces this time limit, a successful crystallization (region II) is possible for pulse lengths of about 10 ns. Here two pulses were used: first one for amorphization (writing the bit) with constant parameters. The second pulse was varied in power and duration. If the second laser pulse is short and intense, amorphization can take place (region III). Like in figure 7, melt-crystallization can be observed for longer pulses, denoted as region IV.
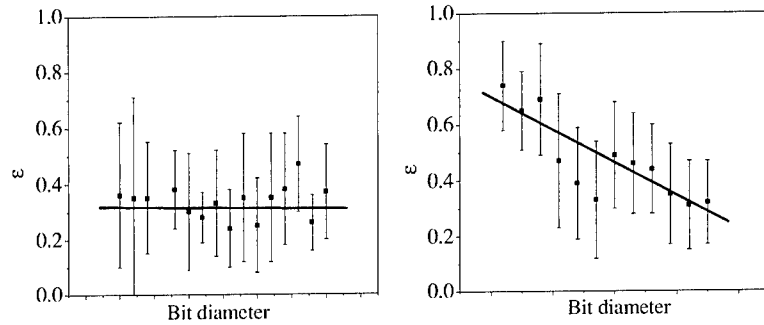
Figure 9: Recrystallized fraction of recrystallized bits as function of bit diameter. The left diagram corresponds to the material $Ge_2Sb_2Te_5$, which starts to recrystallize from small nuclei inside the amorphous material. The material $Ge_4Sb_1Te_5$ is shown on the right hand side. A shrinking remaining fraction indicates a crystallization, that starts from the rim.
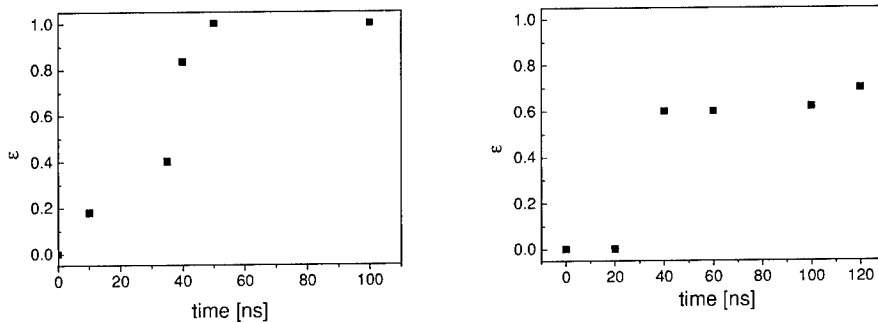
Figure 10: Erasure of amorphous bits in different crystallographic environments. Left: a cubic structure of the rim leads to a perfect erasure, which is identified by an epsilon of one. This state of the bit is reached after 50 ns. If a hexagonal structure is present, epsilon will not reach one, even after 120 ns. This is due to the phase transformation of the amorphous bit into the rock salt structure, which has a different reflectivity than the surrounding hexagonal phase.

We conclude, that the recrystallization starts for $Ge_2Sb_2Te_5$ at small crystallites. Until now it is not clear, what the structure of these nuclei is. To determine this microstructure, experiments with different macroscopically crystallized samples were carried out: a) cubic rock salt structure and b) hexagonal phase. The crystallized fraction ε as function of pulse duration of the recrystallization pulse is shown in figure 10. The erased bits, grown in an environment with cubic phase, were completely erased. This is indicated by the saturation level of epsilon = 1 for times longer than 50 ns. If the environment consists of the hexagonal crystal structure, also a saturation is reached, but now at a level of 0.6. This can be explained by the different optical properties of

both crystalline phases: The recrystallized volume will always consist of the cubic phase, so no difference between the initial and the final phase occurs ($\varepsilon=1$). In case b), the initial phase and final phase are different in respect to their crystal structure and also their optical properties ($\varepsilon=0.6$). The formation of the cubic phase for these nuclei can be explained by the shorter diffusion path needed to create the cubic in contrary to the more complex hexagonal phase. This is in good agreement to macroscopic experiments [11].

INFLUENCE OF A DIELECTRIC LAYER UPON AMORPHIZATION

In data storage applications, the active layer is sandwiched by dielectric layers. Hence, phase change materials on glass were covered with a 30 nm thick protective layer of $ZnS:SiO_2$ to study the effect of capping layers on the power-time-effect diagrams. For long pulses and high powers the formation of large bubbles of considerable height was observed, which were detected by AFM (figure 11) [9]. Such 125 nm high bubbles could be a major problem for near-field recording techniques. Argon which is incorporated during magnetron sputtering process is the most probable candidate responsible for these bubble formations. With Rutherford Backscattering it was shown that up to 0.8 atomic % argon is incorporated into the film during deposition. While the amorphization takes place, the temperature is larger than the melting temperature of the phase change material. In this liquid phase the argon gas will thermally expand and thus exert a pressure on the dielectric layer causing dome formation. Applying the equation of ideal gases at the melting temperature of the phase change material should give rise to a pressure of 5-7 MPa inside the bubbles. However, from surface curvature and surface energy we obtained a pressure
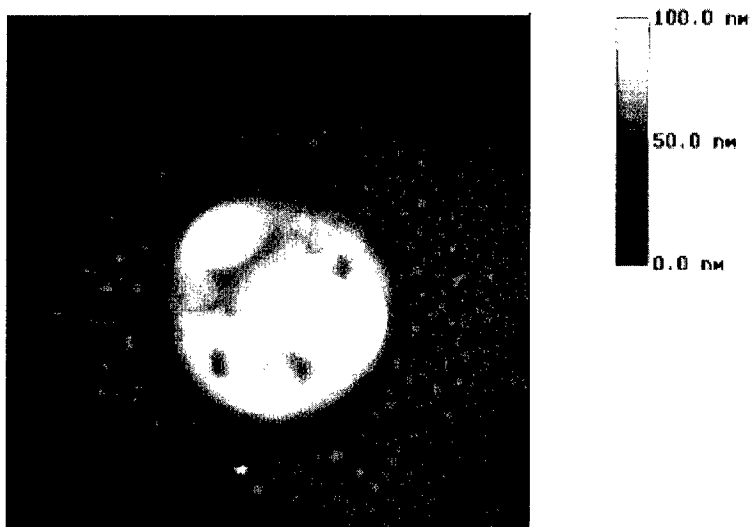

FIGURE 11: Amorphisation of $Ge_2Sb_2Te_5$ covered with 30 nm thin $ZnS:SiO_2$ with high laser powers leads to the formation of bubbles. These bubbles can grow up to 300 nm. The origin is the thermal expansion of the incorporated argon, deposited by the magnetron sputtering process.

of 12 MPa, which is from the same order as the value mentioned before. Combining these values with geometry a Young's Modulus of 35 – 50 MPa for the dielectric cover layer is calculated. This value is in good agreement to literature data [8], and hence proves that the incorporated argon is acting as the origin for the bubbles. Other sources for the volume change such as the expansion of the phase change material can be neglected. While Ar leads to a 40% volume expansion, the changes in volume due to the phase transformation is at most 9% (assuming a hexagonal reference phase).

CONCLUSIONS

We have examined the process of amorphization and crystallization in $Ge_2Sb_2Te_5$ to unravel the microscopic transformation mechanisms. The result of a maximum growth speed of 1 m/s leads to a thickness dependent minimum amorphization time. No kinetic superheating for times longer than 10 ns was observed. Fast erasure of amorphized bits within 10 ns is only possible in a crystalline environment, where two types of recrystallization, i.e. starting from small subcritical nuclei or from the rim, were identified for different stoichiometries of the alloys. The recrystallized bits always have the cubic structure, independent of the surrounding environment. A capping layer on top of the phase change material was lifted by thermal expansion of incorporated argon.

ACKNOWLEDGEMENTS

REFERENCES

1. M. Libera and M. Chen, MRS Bull. **15**, 40 (1990)
2. D.K.G. de Boer, Glancing-Incidence X-ray Fluorescence of layered materials, Phys. Rev. B 44 (1991) 498.
3. W. K. Njoroge, (unpublished)
4. V. Weidenhof et al., J. Appl. Phys. **88** (2), 657 (2000)
5. V. Weidenhof et al., J. Appl. Phys. **86** (10), 5879 (1999)
6. J. W. Christian, The Theory of Transformations in Metals and Alloys, Pergamon, New York (1965)
7. S. Nagpal and P.K. Bhatnagar, Phys. Stat. Sol. **161**, 59 (1997)
8. H. Ebert, Physikalisches Taschenbuch, Vieweg. Seite 260.
9. I. Thomas, Charakterisierung und Optimierung der Phasenumwandlungskinetik in GeSbTe-Legierungen, Diploma thesis, RWTH Aachen (2000)
10. J. H. Coombs et al. J. Appl. Phys. **78** (1995), 4918
11. I. Friedrich et al., J. Appl. Phys. **87** (9), 4130 (2000).

**Magneto-Optic and Holographic
Recording: Materials, Mechanisms
and New Concepts**

Super-Resolution Readout for Magneto-Optical Disk
by Optimizing the Deposition Condition of Non-Magnetic Mask Layer

Takayuki Shima, Johoo Kim, Hiroshi Fuji[1], Nobufumi Atoda and Junji Tominaga
Laboratory for Advanced Optical Technology (LAOTEC), National Institute of Advanced Industrial Science and Technology (AIST),
Tsukuba Central 4, 1-1-1 Higashi, Tsukuba, Ibaraki 305-8562, Japan
[1]Advanced Technology Research Laboratories, Sharp Corporation,
2613-1 Ichinomoto-cho, Tenri, Nara 632-8567, Japan

ABSTRACT

Super-resolution near-field structure (Super-RENS) was prepared by a heliconwave-plasma sputtering method to improve the disk property that is combined with a magneto-optical (MO) recording disk. Antimony and silver-oxide mask layers were prepared by the method and refractive indices were measured. Recording and retrieving of signals beyond the resolution limit (<370 nm) were achieved for both mask cases. Attempts to optimize the disk structure were also made using a conventional sputtering method. The smallest mark size was around 200 nm and the highest carrier-to-noise ratio (CNR) was 30 dB for 300-nm mark and 22 dB for 250-nm, when using a laser wavelength of 780 nm and a numerical aperture of 0.53. We have found that there is a competing super-resolutional mechanism besides Super-RENS that appears when high readout laser power is applied. This mechanism played rather an important role at least in the mark-size range of 200-370 nm.

INTRODUCTION

Tominaga et al. have proposed a technique called Super-RENS (super-resolutional near-field structure) and described that it is one of the promising for high-density optical recording and readout [1]. Super-RENS consists of a mask layer sandwiched by dielectric layers. Antimony (Sb) [1] and silver oxide (AgOx) [2] have been used for the mask layer and are expected to work as an optically transparent aperture (TA) and a light scattering center (LSC), respectively, by focusing the laser beam. When Super-RENS and a phase-change (PC) disk is combined and the distance between the mask and recording layer is controlled in shorter than ~50 nm, small marks beyond the optical resolution limit can be successfully recorded and retrieved. Kim et al. have recently combined the technique with magneto-optical (MO) recording layer and obtained super-resolutional readout with LSC-type [3]. However, the smallest mark size was around 200 nm and it is still much larger than 60 nm in PC case [4]. Further attempts to achieve smaller mark readout and also to improve carrier-to-noise ratio (CNR) are necessary in MO case for the moment.

Two approaches are made to improve the disk property of MO that combines with Super-RENS. One is to make high-quality Super-RENS by using heliconwave-plasma (HWP) sputtering method. HWP sputtering method has the potential to make smooth and dense film, and is used to prepare multi-layer X-ray mirrors and optical devices [5]. In this proceeding, preparation of Super-RENS by the method and an attempt to combine it with MO are described. Another is to optimize the structure mainly by controlling the thickness of each layer. Here just summarizes the results briefly and one should refer to the recent work of Kim et al. in detail [6].

We also discuss on another competing mechanism besides Super-RENS that makes super-resolutional readout possible at least near the optical resolution limit.

EXPERIMENTAL

Both HWP and RF-magnetron sputtering methods were used to prepare films for the disk structure. For HWP sputtering, background pressure of the chamber was kept at the order of 10^{-6} Pa and distances between the substrate and targets were 200 mm. The target RF-power and sputtering pressure were varied in the range of 30-200 W and 0.25-0.8 Pa, respectively. The power for RF-induced coil was fixed at 20 % of the one for the target. For RF-magnetron sputtering, the background pressure of the deposition chamber was at the order of 10^{-4} Pa and the distances were about 40 mm. The sputtering RF-power and pressure were fixed at 200 W and 0.5 Pa, respectively.

Films were deposited on glass substrates for the objectives of film-deposition rate and refractive indices, and on polycarbonate disk substrates to evaluate disk properties. All the films were prepared at room temperature. The film-deposition rate was estimated from the thickness measured by a surface texture measuring system (Sloan Technology, Dektak3) and the sputtering time. Refractive indices were measured by an ellipsometer (Mizojiri Optical Co., DHA-OLX/S4M) at a laser wavelength of 632.8 nm. Raman scattering measurements were performed with a Renishaw Ramanscope using a wavelength of 488 nm, in back-scattering geometry. An X-ray fluorescence spectrometer (Rigaku Corporation, RIX2100) and a vibrating sample magnetometer were used to evaluate on composition ratio and coercivity of the MO layer, respectively. Recording and retrieving of the signals for the prepared disk were carried out using a MO disk drive tester (Nakamichi, OMS-2000) with a wavelength (λ) of 780 nm and a numerical aperture (NA) of 0.53. Details on the disk-evaluation can be found elsewhere [3, 6].

RESULTS

Prior to Super-RENS preparation by HWP sputtering method, Sb and AgOx thin films were directly deposited on glass substrates and their refractive index values were measured. Figure 1 shows the indices change of Sb film as a function of its thickness. Hence, the target RF-power and sputtering pressure were 50 W and 0.4 Pa, respectively. As the thickness increased from 5 to 15 nm, there was a large change on the extinction coefficient k from 3.0 to 5.4. In Raman scattering spectra, a broad peak ($\sim$144 cm^{-1}) was observed for 5-nm film and two sharp peaks (114 and 150 cm^{-1}) for 15-nm film, and they correspond to amorphous [7] and crystalline Sb [8], respectively. Thus the increase of k value observed in Fig. 1 derives from an amorphous-to-crystalline transformation [9]. As the thickness further increased above 15 nm, coefficient k decreased when high sputtering pressure (>0.2 Pa) was used [9]. In Raman scattering spectra, two crystalline peaks were observed and there were no evidences of the film being amorphous. Similar decrease of k value can also be recognized when Sb film was prepared by RF magnetron sputtering method, but at much higher sputtering pressure (>1.0 Pa). We believe that the effect of sputtering pressure is more evident in HWP sputtering since the distances between the substrate and targets are long (200 mm) compared to a conventional sputtering method. Furthermore, index of refraction n decreased monotonically from about 4.1 to 2.8 as the thickness is increased and was less dependent on the sputtering pressure. For TA-type Super-RENS, it is necessary to prepare an opaque crystalline Sb film in as-deposited condition [1]. Therefore, the film-thickness
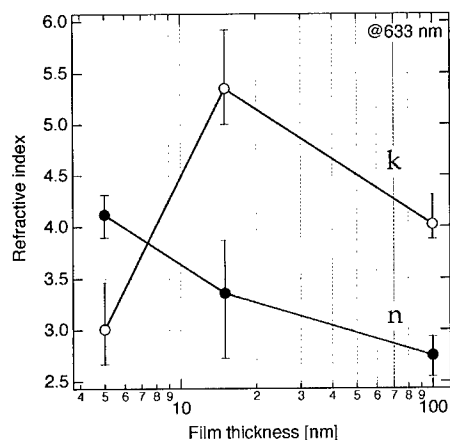
Figure 1. Refractive index of Sb films prepared by the HWP sputtering method as a function of film thickness. Closed circles: index of refraction (n) and open circles: extinction coefficient (k).

should be 15-nm or thick. Also it is preferred to use lower sputtering pressure to avoid any deterioration of the film quality, especially for thick Sb film [9].

Figure 2 shows the indices change of AgOx film as a function of oxygen-gas flow ratio. The target RF-power and sputtering pressure were 100 W and 0.4-0.5 Pa, respectively. As oxygen-ratio is increased, k-value rapidly decreased and became nearly transparent at the ratio higher than 0.25. The result is almost similar to the one made by RF magnetron sputtering [2] and this confirms that AgOx film is successfully made by the HWP sputtering method. Refractive indices
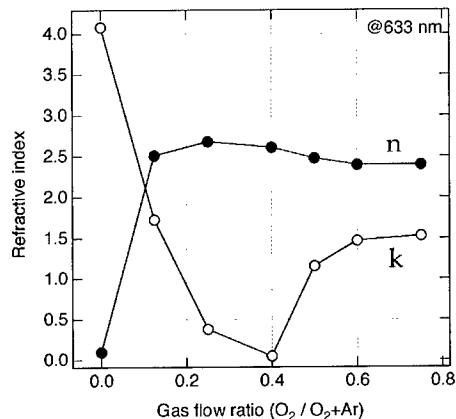

Figure 2. Refractive index of AgOx films prepared by the HWP sputtering method as a function of oxygen gas flow ratio. Closed circles: index of refraction (n) and open circles: extinction coefficient (k).

Reflective layer (Ag, 50 nm)
Dielectric layer (SiN, 25 nm)
MO recording layer (TbFeCo, 25 nm)
Dielectric layer (SiN, 40 nm)
Mask layer (Sb or AgOx, 15 nm)
Dielectric layer (SiN, 130 nm)
Polycarbonate substrate

Figure 3. The disk structure with Super-RENS and MO recording layer.

for AgOx were less dependent on the film thickness, as far as we examined. Previous work on LSC-type Super-RENS showed that AgOx film work as a LSC when the oxygen ratio is higher than 0.4 [2]. This may suggest that LSC-type is not restricted to the sputtering condition and can easily be prepared.

Taking above results into consideration, TA- and LSC-type Super-RENS were tentatively made by the HWP sputtering method. A schematic of the disk structure is shown in Figure 3. On polycarbonate disk substrate, Super-RENS (SiN/Sb/SiN or SiN/AgOx/SiN) was first deposited by the HWP sputtering method. Refractive indices of Sb mask was n=3.3 and k=5.2, and of AgOx mask was n=2.4 and k=1.0. MO recording layer (Tb-Fe-Co) and the rest were then deposited by a conventional RF-magnetron sputtering method. Some attempts were made to deposit Tb-Fe-Co layer by the HWP sputtering method, however the effect of sputtering pressure was quite obvious. Composition ratio, refractive index and magnetic property of the film were difficult to be controlled. We here concentrated on preparing Super-RENS by the HWP
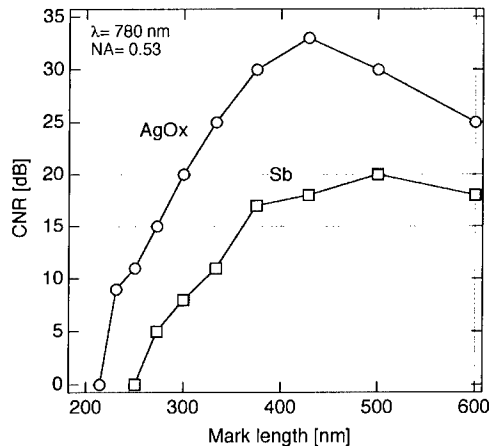
Figure 4. Relationship between mark size and the CNR with different mask layers prepared by the HWP sputtering method. Circles: AgOx and squares: Sb.

sputtering method and MO layer by a well-understood method. Composition ratio of the MO film was Tb 20 at%, Fe 71 at% and Co 9 at%, and the coercivity was about 10 kOe.

Figure 4 shows the relationship between mark size and the CNR of Super-RENS MO disks prepared by HWP and RF magnetron sputtering methods. Resolution limit can be calculated as $\lambda/(4 \times NA)$, and it is about 370 nm. It is clear in the figure that recording and retrieving of the signals are achieved beyond the limit for both Sb and AgOx cases. For Sb, it was for the first time to observe super-resolutional property when Super-RENS is combined with MO recording layer. For AgOx, the result was similar to the one prepared simply by RF-magnetron sputtering [3] and advantages of using HWP method cannot be well recognized at this moment.

Besides, some attempts to retrieve smaller marks and to obtain high CNR were made by optimizing the disk structure using RF magnetron sputtering method alone. Mark-size limit and CNR were dependent on the preparation condition, however the smallest mark size was always at around 200 nm. One of the highest CNR was 30 dB for 300-nm mark and 22 dB for 250-nm, when AgOx thickness was optimized to 60 nm [6].

DISCUSSION

Super-resolutional property itself was highly reproducible in the experiments we carried out. However, attempts to make high quality Super-RENS or to optimize the structure did not bring a drastic improvement on the super-resolutional properties. We therefore performed additional experiments to understand what is going on in our Super-RENS MO disks. First, Fuji et al. have recently observed recorded marks by magnetic force microscope (MFM) and showed that marks smaller than 180 nm can no longer be identified each other [10]. Thus a CNR drop at around 200-nm mark in Fig. 4 can be explained by the limit on recording of small marks. Second, we have prepared a conventional MO disk and found that super-resolutional property can still be observed by optimizing the laser power for readout. Figure 5 shows the relationship between
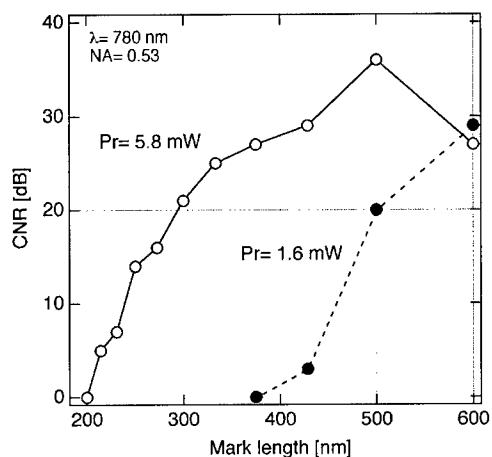
Figure 5. Relationship between mark size and the CNR for a conventional MO disk with different readout power (Pr). Closed circles: 1.6 mW and open circles: 5.8 mW.
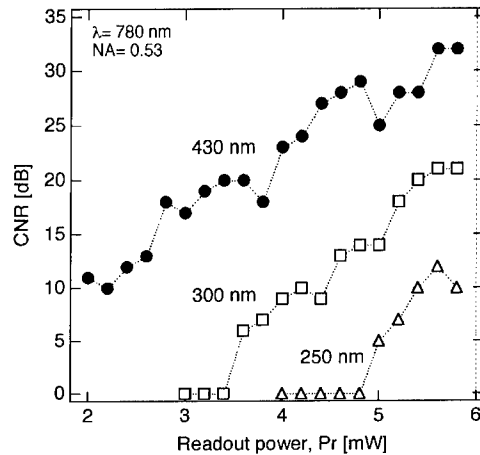
Figure 6. Relationship between readout power (Pr) and the CNR for different mark size.
Triangles: 250 nm, squares: 300 nm and closed circles: 430 nm.

mark size and the CNR with a low (1.6 mW) and a high (5.8 mW) readout power. Disk structure
is almost similar to the one shown in Fig. 3, but no mask layer was prepared between two
dielectric layers. When the readout power is low, CNR became zero at the resolution limit and no
super-resolutional property can be found. When the power is raised high, super-resolutional
readout can be clearly observed in the mark-size range of 200-370 nm. Figure 6 shows the
relationship between readout power and the CNR for different mark sizes of 250, 300 and 430
nm. It was evident that smaller marks appear at higher readout power. The mechanism for this
high-power super-resolutional (HP-SR) readout is under investigation [11]. Above 6.0 mW, a
recording process started to take place and the CNR rapidly dropped to zero.

Super-RENS also requires a high readout power to create silver LSCs in the mask layer. It is
thus difficult to distinguish Super-RENS and HP-SR at this moment when evaluating Super-
RENS MO disks. If one assumes that HP-SR mechanism was rather dominant, then it is
reasonable that the improvement on the disk property was not well achieved by the modification
of Super-RENS. Since CNR property can only be obtained down to 200-nm mark size, our
discussions here concentrated on a short range between it and the resolution limit, i.e., 200-370
nm. Silva et al. have shown that silver cluster (~30 nm) works as a probe to image the contrast
provided by the MO Kerr effect with high-resolution [12]. This suggests that a combination of
LSC-type Super-RENS and MO recording layer is a promising for high-density recording and
readout. When Super-RENS mechanism became a dominant one at a certain small mark-size,
optimization based on attempts examined here should play more important role. HP-SR
mechanism just contributes to improve the CNR at least in the range of 200-370 nm and there is
no need to distinguish or to remove for the practical use. As MFM result indicated, it is first
necessary to record small marks of ~100 nm in MO layer, and this is probably a key to evaluate
the potential of combining Super-RENS and MO recording layer.

CONCLUSIONS

Super-RENS was prepared by HWP sputtering method and combined with MO recording layer. Super-resolutional property can be obtained for both AgOx and Sb mask cases. Improvement on the disk property was not sufficiently achieved here by the use of HWP sputtering and by the attempts to optimize the structure. Smallest mark size stayed at around 200 nm and CNR was 30 dB for 300-nm mark. This was partly explained by the coexistence of different super-resolutional mechanism that appears when high readout laser power is applied, at least in the mark-size range of 200-370 nm. For smaller mark (<200 nm) recording and readout, we found from MFM mark observation that recording property of MO should be first improved and combination with Super-RENS is then expected to play more active part in readout.

ACKNOWLEDGMENTS

REFERENCES

1. J. Tominaga, T. Nakano and N. Atoda, Appl. Phys. Lett. **73**, 2078(1998).
2. H. Fuji, J. Tominaga, L. Men, T. Nakano, H. Katayama and N. Atoda, Jpn. J. Appl. Phys. **39**, 980(2000).
3. J. Kim, Y. Yamakawa, H. Fuji, T. Nakano, D. Büchel, J. Tominaga and N. Atoda, Appl. Phys. Lett. **77**, 1774(2000).
4. J. Tominaga, H. Fuji, A. Sato, T. Nakano and N. Atoda, Jpn. J. Appl. Phys. **39**, 957(2000).
5. e.g., X. Wang, H. Masumoto, Y. Someno and T. Hirai, Thin Solid Films **338**, 105(1999).
6. J. Kim, T. Shima, H. Fuji, T. Nakano, D. Büchel, J. Tominaga and N. Atoda, J. Magn. Soc. Japan 25, 387(2001).
7. J.S. Lannin, Phys. Rev. **B15**, 3863(1977).
8. J.B. Renucci, W. Richter, M. Cardona and E. Schönherr, Phys Status Solidi **b60**, 299(1973).
9. T. Shima, J. Kim, J. Tominaga and N. Atoda, J. Vac. Sci. & Technol. A (in press).
10. H. Fuji, K. Watanabe, M. Hamamoto, J. Sato, K. Kojima, H. Katayama, J. Kim, T. Shima, T. Nakano, D. Büchel, J. Tominaga and N. Atoda, Abstracts of the 8th Joint MMM-intermag Conference, San Antonio, TX, 2001, BE-01.
11. T. Kikukawa, T. Kato, H. Shingai and H. Utsunomiya, Abstracts of the Optical Data Storage Topical Meeting, Santa Fe, NM, 2001, TuD1.
12. T. J. Silva and S. Schultz, SPIE Proceedings **1855**, 180(1993).

Materials Development for Thermally-Assisted Magnetic Recording Media

C.F. Brucker and T.W. McDaniel
Seagate Technology, 47050 Kato Road
Fremont, CA 94538, U.S.A.

ABSTRACT

We have carried out a combined experimental and computer simulation study to specify and identify candidate films to support high areal density, thermally-assisted magnetic recording. The motivation of this work is to utilize the enhanced writability of very high coercivity materials that thermal assistance can provide. Media with high coercivity (and anisotropy K_u) are known to be essential to achieve a sufficiently high ratio of $K_u V/k_B T$ necessary to maintain magnetic stability at temperature T in media switching units (grains; single domains) of volume V. Nominally, we expect $V \propto D^{-3/2}$, where D is the medium bit density per unit area in recording. A micromagnetic recording simulation tool with a capability of representing realistic grain size distributions, temperature-dependent magnetic properties, and spatially-varying imposed temperature distributions was employed to study the interplay of thermal and magnetic field gradients in the recording process. In addition, a simple LLG-based thermomagnetic switching model supplemented the micromagnetics model. We fabricated improved Co/X multilayer media for recording evaluation, and performed standard materials characterization.

RATIONALE FOR HYBRID RECORDING

Data storage technology has been advancing rapidly for several decades, with magnetic recording in particular having accelerated its rate of advancement several times in the past dozen years. With annual compound growth rates of areal density (count of "bits" per unit area on the recording medium's surface) rising above 100% in the last few years, magnetic recording technology in rigid disk drives (RDD's) appears to be approaching fundamental physical limits for the first time in its one hundred year history [1]. This situation has prompted accelerated research and development to modify the course of the technology's evolution, spurring renewed interest in perpendicular recording, and more recently drawing attention to novel approaches of patterned media and hybrid recording [1].

This paper deals with storage media materials development for hybrid recording. We define "hybrid recording" as an alternative approach to conventional magnetic recording in which thermal-assistance of the record and/or playback processes is invoked to improve system performance. Sometimes optical irradiation of media has been used to impart heating, but other means of introducing thermal energy can be envisioned. Nevertheless, the term hybrid recording has most often been understood to mean a merging of aspects of magnetic and optical recording.

The writing process in hybrid recording is essentially thermomagnetic recording very similar to that employed in magneto-optic recording [5]. One uses the temperature-dependence of the recording medium's magnetic properties to advantage for enabling high quality magnetic recording in a situation where the magnetic writing head is incapable of supplying a sufficient magnetic field to the medium to switch its magnetization at the ambient temperature of the storage device. Specifically, elevating the medium's temperature generally lowers its coercivity

so that the magnetization can be switched with a more modest head field. A second, equally important benefit accrues when the medium immediately cools back to the ambient temperature, since the coercivity rises markedly and thereby stabilizes the recorded magnetization against unwanted reversal. Such reversal can occur due to either the influence from sufficiently strong internal or external magnetic fields, or from spontaneous decay under the influence of ambient temperature (or both) over long periods of time [2].

Magnetic recording engineers have become interested in hybrid recording for both of these reasons, although initially it was concern over media thermal decay in conventional longitudinal recording that prompted serious consideration of thermally-assisted recording. The specter of media thermal decay in RDD's arose as the areal density of recorded information continued its relentless exponential rise. Most magnetic recording media (particulate or thin film) is composed of assemblies of (ideally) independent magnetic particles, and a zone of such "particles" representing a recorded bit of binary data should contain of the order of several hundred of them. The medium signal-to-noise (power) ratio (SNR) performance scales proportionally to this number [3]. A rising areal bit density implied that the bit sizes were shrinking, and to hold SNR constant required shrinking the particle sizes proportionally with the bits. The theory of superparamagnetism establishes a minimum magnetic particle volume for stability of the particle's magnetization at temperature T – specifically, the ratio $K_u V/k_B T$ representing the particle's magnetic anisotropy energy relative to its characteristic thermal energy should exceed ~25. When this ratio falls below 25, the particle's magnetization can spontaneously reorient under thermal agitation, and the particle ceases to be a stable ferromagnet – it is "superparamagnetic" with zero time-averaged magnetic moment in any particular direction due to thermal fluctuation. Superparamagnetism is thus a mechanism for spontaneous decay of recorded information if individual magnetic particles comprising the bit undergo magnetic reorientation under the influence of ambient thermal energy.

A natural means of suppressing superparamagnetism is to maintain the energy ratio $K_u V/k_B T$ at sufficiently high levels, in spite of the technological pressure to drive V downward. Since the operating temperature of data storage devices is unlikely to be a parameter that the design engineer has much leverage in changing significantly, one is left with only the option of elevating the media's magnetocrystalline anisotropy K_u. This intrinsic material parameter is intimately connected with the extrinsic media design parameter coercivity, the mean switching magnetic field of the material. Raising K_u has therefore become a primary materials strategy to preserve thermal stability of media [4]. But since coercivity H_c rises more or less in proportion to K_u, eventually a concern develops as to whether the recording medium can be switched with available recording heads at ambient temperature. The output fringe field of writing heads for switching magnetic media is proportional to the saturation magnetization M_s of the head's pole tip material at the gap. There is a strict upper limit on values of M_s for head materials ($4\pi M_s$ ~ 25 kilogauss), largely imposed by the ferromagnetic elements found in the periodic table – Fe, Co, Ni. Engineers today cannot envision writing fields ever exceeding this limit. And yet, one can envision medium coercivity rising toward 100 kilo-oersted using known materials [4]. Thus, a writability crisis in magnetic recording has arisen from the effort to preserve the essential performance requirements of SNR and media stability, and hybrid recording is thus logically established as a candidate method to address this issue.

It has been established in prior work that heating a magnetic medium during readout, particularly using light, can offer some benefits to this phase of the recording process [5]. Optical readout of MO media is a well-developed technology in optical storage, and use of an

MO process to read in RDD's is a possible future benefit of hybrid recording. This is particularly true in view of challenging technological issues surrounding continued extendibility of magnetoresistive readout that has been so prevalent in the past decade. For optical readout to be viable at tomorrow's areal densities necessarily implies that we work beyond the diffraction limit that governs the localization (focusing) of electromagnetic energy in the far-field of the radiation pattern, since bit lateral dimensions will lie in the range of tens of nanometers at areal densities approach 1 Tb/in^2. This means that only near-field optics will be a useful ingredient in hybrid recording.

Previous work in Japan [5] considered another potentially important aspect of future hybrid readout in RDD's, namely manipulation of data track widths using a combination of localized heating imparted to the medium with multilayer interaction between magnet films. More broadly, this could introduce to RDD's a potential strategy of using multiple film layers to attempt to jointly optimize media design for both writing and reading, a technique common in MO recording.
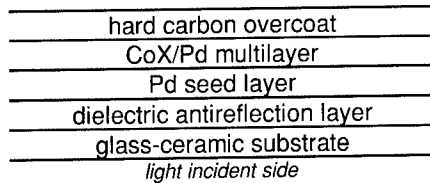
MEDIUM MATERIALS DEVELOPMENT

In this work, we consider means of improving the materials engineering of Co/X multilayer films previously considered for perpendicular recording [6]. If the technology of hybrid recording emerges into products, it is fairly certain that the magnetic medium will exhibit perpendicular anisotropy, since the advantages of vertical recording are reasonably well established for future high areal density recording [7]. Media for hybrid recording presents additional challenges and opportunities beyond conventional perpendicular media. Thermal design of the film and substrate structure will clearly be necessary to set thermal response times and possibly heat flow control (axial and lateral) [8]. If optical means are used to impart heating, then optical reflectance and absorbance of the medium surface must be designed to insure efficient energy transfer from the heating transducer to the disk. On the other hand, hybrid recording may allow the media designer to avoid use of the often onerous "soft underlayer" that appears essential for perpendicular media [7], or if necessary, have it also function as a heat sink. In hybrid recording, most of the writability assistance is provided by heat, and a conventional inductive ring writer may provide vertical fields of adequate quality with heated media.

The ideal recording material for our hybrid recording experiments must satisfy not only certain magnetic performance requirements but also demanding technical requirements for application in high areal density hard disk drives. Key magnetic property requirements are high perpendicular anisotropy, high coercivity, high magnetization, and appropriate temperature dependence of these properties for thermally assisted magnetic recording. Key technical requirements are small and uniform physical grain size, controllable exchange coupling between grains, and environmental stability adequate for drive applications with vanishingly thin (< 50 Å) protective overcoats.

We consider Co/Pt and Co/Pd multilayer media as promising material candidates for thermally assisted recording. In prior hybrid recording experiments [9], we utilized perpendicular Co/Pt multilayer media that was fabricated without special attempts to control intergranular magnetic exchange coupling, or to minimize irreversible physical changes upon thermal cycling of the film structure. Not surprisingly, the playback of recorded patterns

| hard carbon overcoat |
|---|
| CoX/Pd multilayer |
| Pd seed layer |
| dielectric antireflection layer |
| glass-ceramic substrate |

light incident side

Figure 1. Typical structure of the hybrid media fabricated in this study.

exhibited considerable media noise, and recording performance could depend on the thermal history of the media. In the engineering of granular, thin film, longitudinal magnetic media for hard disk drives, materials strategies for producing decoupled grains along with the full suite of other desired (room temperature) properties are well-developed. We adopted similar approaches, by choosing Cr and other Co dopants in the multilayer system CoX/Pd, and by employing substrate temperature during and/or after deposition of the multilayer to induce dopant diffusion to grain boundaries.

Single-sided disk media samples were fabricated in a multiple cathode dc-magnetron sputtering system with 3×10^{-8} torr base pressure, rotating disk holder, and radiant infrared heating of the disk substrate during deposition. Disk temperature was monitored using an infrared pyrometer imaging the uncoated side and calibrated using an identical disk substrate instrumented with a chromel-alumel thermocouple. Film structures as shown in Figure 1 were deposited with no vacuum break on 84 mm diameter glass ceramic disk substrates which had been previously etched in selected regions. An antireflection underlayer (e.g. reactively sputtered Si_3N_4) was utilized to reduce the through-substrate reflectance from about 60% to the $10 - 30\%$ range. A Pd seed layer was used to enhance the coercivity and minimize initial layer disorder in the multilayer. Substrate heating could be applied before, during, and/or after the multilayer deposition. The multilayer was co-deposited from 5.1 cm. diameter Co-alloy and Pd targets at a target-substrate separation of 6.4 cm in Ar or Kr gas. The individual layer thicknesses were controlled by the deposition rate and rotation speed (20 rpm typical) of the substrate. The final vacuum deposited layer was a hard amorphous carbon overcoat, to which conventional liquid lubricant was applied for flying head testing at glide heights as low as 12.5 nm.

Media Film Characterization

The magnetic properties of the multilayers were controlled over a considerable range by adjusting the thickness and processing parameters of the seed layer and the temperature treatment of the multilayer. Coercivity H_c varied up to 11.1 kOe, squareness $S = M_r/M_s$ ranged between 0.8 and 1.0, coercive squareness S^* varied from 0.3 to 0.9, with a remanent moment-thickness product $M_r t$ of typically 0.5 memu/cm^2. For perpendicular media another parameter gaining favor is $\alpha = 4\pi(dM/dH_{appl})|H_c$, i.e. the slope of the hysteresis loop evaluated at the coercive point, which provides an indirect but useful indication of the degree of exchange coupling in the media (S^* also gives a measure of slope, but, unlike α, is a function of H_c). High α (>5) indicates strong exchange, an extreme example of which would be the rectangular hysteresis loops observed for continuously exchange coupled TbFeCo-based magneto-optic films [14]. At the other extreme, a completely exchange decoupled media would exhibit a sheared loop with slope determined by the sheet demagnetizing field, $4\pi M_s$, for which the limiting value of $\alpha = 1$. Multilayer properties can easily be adjusted over a large range of α, examples of which
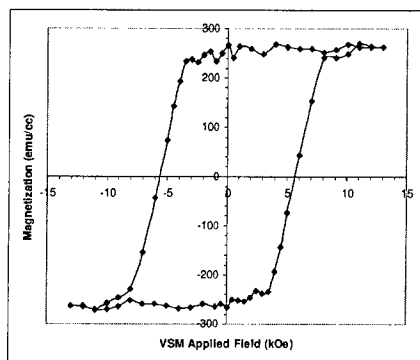
Figure 2. Perpendicular VSM hysteresis loop for a (CoX/Pd:2.6Å/8Å) x 17 multilayer sputtered at ambient temperature, then exposed to room air and annealed in vacuum at 250-300°C for 15 minutes. Slope parameter α = 1.5.
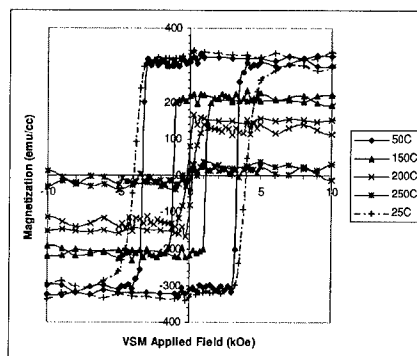
Figure 3. Perpendicular VSM hysteresis loops measured at temperatures from 25°C to 250°C for a (CoX/Pd:2.6Å/8Å) x 17 multilayer sputtered at 300°C substrate temperature. The 25°C loop was the last loop measured in this series. A 25°C loop was also measured at the beginning of the series, but for clarity is not plotted.

are shown in Figures 2 and 3, for which α ranges from 1.5 to over 20. Strong decoupling (low α) can be achieved using processing conditions which likely result in physical separation of grains to break exchange, e.g. ambient temperature deposition and high sputter pressure to reduce surface mobility, and rough seed layers to create incoherent nucleation sites. TEM images of films grown under such conditions typically exhibit a network of voids and rough surface morphology, supporting a picture of physically isolated grains. The multilayer in Figure 2, although sputtered at ambient temperature, was subsequently exposed to room air and then annealed in vacuum at 250-300°C for 15 minutes. Although unconfirmed, it is likely that oxide formation, e.g. at grain boundaries, is also playing a role in the decoupling mechanism for this sample. In contrast, an example of strong coupling is shown in Figure 3 for a multilayer grown at 300°C substrate temperature. The higher M_s for this sample compared with that in Figure 2 can be explained by an increase in film density, consistent with enhanced temperature induced surface mobility of depositing species. A possible explanation for the resultant strong coupling is that film densification dominates over any dopant segregation effects.

A requirement unique to hybrid recording is that the media must also be stable against thermal cycling under the action of the thermal assist heat source. Porous sub-dense films typically suffer irreversible physical change upon heat cycling. It is not unusual to observe a 50% reduction in VSM coercivity upon annealing at 300°C and re-measuring at room temperature. Both films corresponding to Figures 2 and 3 show marked improvement in thermal stability compared to films processed entirely at room temperature. The film in Figure 3 is remarkably stable against annealing at 300°C for 15 minutes in flowing N_2. H_c and M_s are virtually unchanged, and α remains high, as shown in Figure 4. We note that α is extremely sensitive to small changes in coupling for these highly rectangular loops. Similarly, the film of Figure 2 has been re-annealed in vacuum at 300°C with virtually no change in room temperature hysteresis properties, within the precision of the measurement. Thus, films with much improved
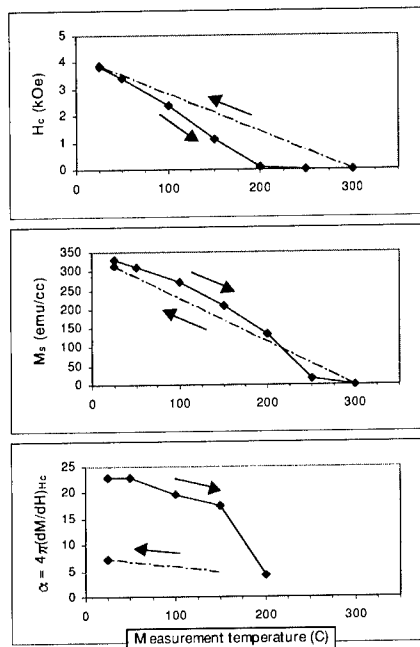
Figure 4. Temperature dependence of H_c, M_s, and $\alpha = 4\pi(dM/dH_{appl})|H_c$, corresponding to the temperature dependent hysteresis loops of Figure 3. After the sequence of measurements up to 300°C (solid lines, right hand arrows), the film was returned to room temperature and a final measurement made (dashed lines, left hand arrows).

thermal stability have been achieved, with resultant α in the range 1.5 - 5, through substrate heating either during or after deposition, and, in the case of Figure 2, an intermediate air exposure.
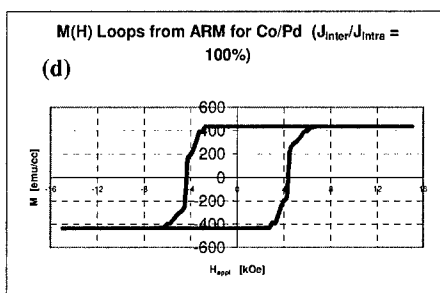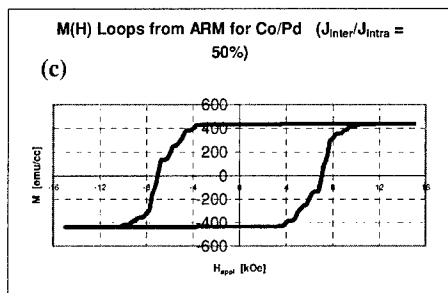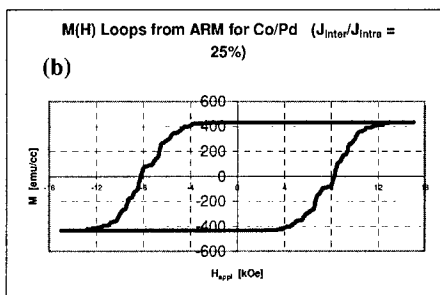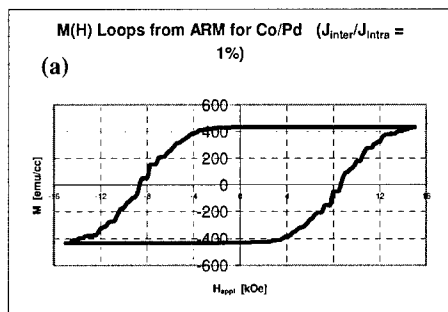
Recording measurements and simulation (see below) indicate that noise is correlated with α, i.e. noise decreases (transition sharpness increases) with decreasing α. The challenge alluded to in Figures 2 and 3 is to engineer a film which at the same time is not only properly decoupled and thermally stable, but also smooth to minimize head-to-media spacing and chemically receptive to the protective overcoat (which argues against surface oxide formation). We continue to explore methods combining physical (with minimal void space and reduced roughness) and chemical (e.g. dopants, oxygen) grain separation for media optimization.

MODELING OF HYBRID RECORDING

Two types of recording simulations were used to explore hybrid media materials design and recording performance. The first was a micromagnetics model structured for recording medium design and recording process assessment [10]. The second was an extension of a much simpler model reported by Ruigrok [11] which considers the magnetization reversal of a single particle on short time scales as described by a modified Landau-Lifshitz-Gilbert (LLG) equation. One of us (tm) added to the Ruigrok model time-dependent heating and incorporation of temperature-dependent magnetic properties to more fully investigate the predictive power of this model for hybrid recording.

Voronoi Grains - Log Normal Distribution

9000 grains
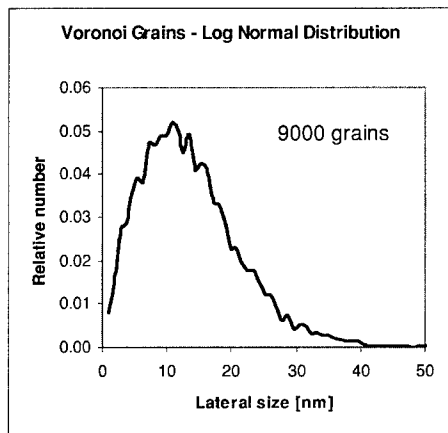
Figure 5. Medium grain size distribution from micromagnetics simulator. Mean size is ~10 nm.

M(H) Loops from ARM for Co/Pd (J_{inter}/J_{intra} = 1%)

(a)

M(H) Loops from ARM for Co/Pd (J_{inter}/J_{intra} = 25%)

(b)

M(H) Loops from ARM for Co/Pd (J_{inter}/J_{intra} = 50%)

(c)

M(H) Loops from ARM for Co/Pd (J_{inter}/J_{intra} = 100%)

(d)

Figure 6. Modeled M(H) hysteresis loops for cases of the ratio of inter- to intra-granular exchange coupling equal to 1, 25, 50, and 100%. Medium grain size distribution for these loops is shown in Figure 5.

Table I. Micromagnetics modeling parameters

Parameter	Units	Mean Value	σ
Saturation magnetization M_s	emu/cm^3	437	10 to 40
Anisotropy field H_k	Oe	10500	200 to 1050
Anisotropy axis perpendicular alignment	degrees	0	0 to 5
Intra-granular exchange coefficient A_x	erg/cm	10^{-7}	0
Inter-granular exchange coefficient A_x	erg/cm	10^{-10} to 10^{-7}	10^{-11} to 10^{-8}
Gilbert damping constant		0.1	0.1
Curie temperature	K	663	
Media grain size	nm	10 to 28	2 to 8
Ring head pole width	nm	1200	
Ring head gap length	nm	300	
Pole head length, width	nm	200, 200	
Head - medium spacing	nm	30	

Table II. M(H) hysteresis parameters for modeled loops such as those shown in Figure 6.

J_{inter}/J_{intra}	Hc [kOe]	Mr [emu/cc]	S*	α
0.001	8.83	434.00	0.583	1.48
0.01	8.63	434.00	0.651	1.81
0.05	8.81	434.01	0.667	1.86
0.25	8.22	434.05	0.789	3.14
0.5	7.04	434.08	0.855	5.34
1	4.35	435.50	0.92	15.73

In the first use of the micromagnetic model, we set up a hypothetical medium with film properties approximating those of our film samples. This model can construct a granular medium with Voronoi grains that match log normal size distributions such as those measured experimentally using transmission electron microscopy (TEM). Table I shows a set of film properties incorporated in the modeled medium in the micromagnetic model. Figure 5 depicts a typical grain size distribution in the model, while Figure 6 presents modeled M-H hysteresis loops (with demagnetization shearing present) for the perpendicular medium represented in Table I. The shape of the loop gives information concerning the degree of grain decoupling [12], which is a controllable parameter in this model. Inter-granular exchange was varied as a percentage of the intra-granular value, and the resultant effect on loop shape is evident in Figures 6(a)-6(d). Table II summarizes the hysteresis loop characterization.

The micromagnetic model provides for simulation of a thermomagnetic recording process by incorporating steady-state medium thermal profiles transcribed from a separate medium thermal model (see Ref. [14]), and by imposing writing fields from a specified recording head. The relative positioning of the two fields in the medium can be set to explore potential design issues for an integrated hybrid recording transducer. For the recording simulations that follow, a steady-state thermal profile in the medium is created by a 10 milliwatt laser beam focused to a

spot of 700 nm FWHM. The peak temperature at the thermal field's center was 658K. The coercivity of the magnetic recording layer was simulated with a linear decrease versus temperature to match curves measured experimentally with a VSM. The aim of the recording simulations was to explore the apparent quality of the recorded domains and transitions, given a range of modifications in the magnetic design of the media films.

Recording system parameters incorporated in the model are listed in Table I. Given the perpendicular anisotropy and its dispersion built into the recording medium, we expect that the vertical magnetic field of the head, along with the thermal profile in the medium, are the most significant determinants of the global recorded domain shapes. Additionally, the detailed structure of magnetization transitions in the medium should be governed by the medium grain structure, intergranular exchange, and medium demagnetization effects.

Figure 7 shows simulated, statically recorded patterns using a single pole head on heated media with an SUL. For this combination of head field and medium heating chosen, the writing quality was excellent on this exchange-decoupled medium. Notice that the transition on the trailing (left) edge of the pole head (footprint shown in outline) is smooth and sharp, corresponding to low noise, high signal contrast recording.

Figure 8 illustrates a short sequence of simulated, recorded patterns using a Lindholm inductive ring head writing on moving perpendicular media without an SUL. For the chosen combination of head deep gap field and medium heating, the writing quality was poor on this highly exchange-coupled medium. The transitions are very ragged, with magnetic percolation from grain to grain being evident. We see curvature of reversed domain as observed in our spinstand experiments.
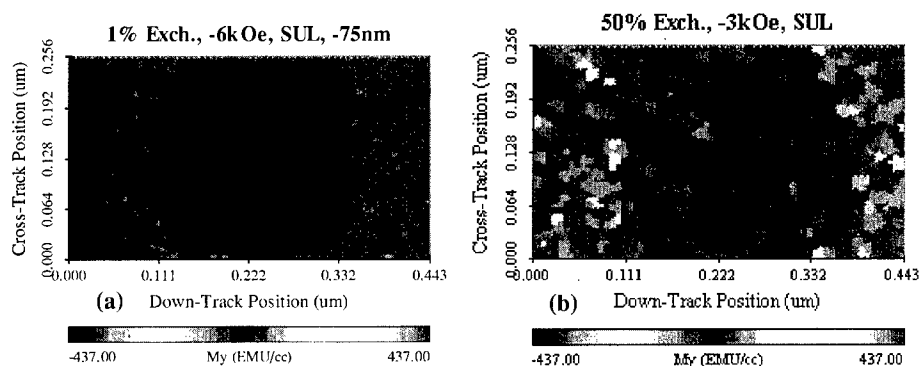

Figure 7. Simulated thermomagnetically written marks on perpendicular media with 10 nm mean grain size on an SUL, using a square footprint pole head of edge length 200 nm. Center of 700 nm FWHM heating spot is 75 nm to right of pole head center, and medium velocity is zero. (a) Medium with inter-granular exchange of 1% of the intra-granular value. Notice that the left edge of the reversed domain is written sharply and smoothly due to high field and temperature gradients. (b) Same situation, except with medium having 50% inter-granular exchange. Note the uncontrollable writing as the grain switching percolates beyond the edge of the pole head, and into the hotter zones toward the right. The transition zone on the left edge is ragged (noisy).

50% Exchange
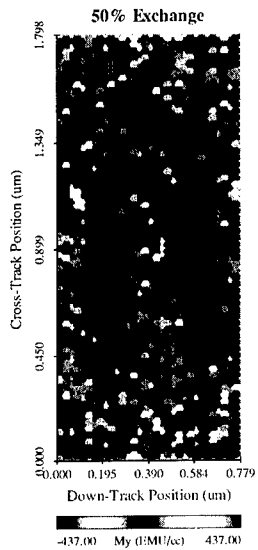
Figure 8. Simulated thermomagnetically written marks on perpendicular media with a rather large 28 nm mean grain size, using the Lindholm ring head in Table I. Center of 700 nm FWHM heating spot is in the gap center, and medium velocity is 10 m/s from right to left. The medium had inter-granular exchange of 50% of the intra-granular value. The writing quality is fairly poor since the head field strength was set very low (4kOe). Granular percolation is evident, and transition zone is ragged (noisy).

A single particle thermomagnetic model [11] was constructed to further investigate the interplay of temperature and head magnetic field, along with magnetization reversal dynamics. A modified form of the Landau-Lifshitz-Gilbert (LLG) with an added term to reflect finite temperature effects of the medium thermal bath was employed [15]. Magnetic parameters of the switching particle were allowed to be temperature-dependent, and the history of the thermal and writing (magnetic) fields at the site of the particle moving under a hybrid recording head were tracked. We simulated an assumed future high-density recording configuration in which a heating, near-field, Gaussian optical beam of 50 nm FWHM was used in conjunction with a magnetic head capable of producing field gradients on a similar length scale.

Figure 9(a) shows the thermal history of the particle as the heating beam moves over it, along with some assumed temperature-dependent magnetic parameters of the particle. We found in thermal modeling that the depicted temperature rise was achievable with an integrated optical
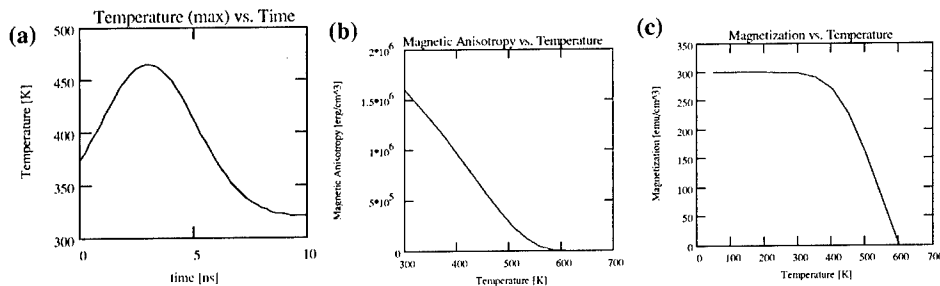
Figure 9. (a) Thermal history of a magnetic particle moving at 10 m/s below a 50 nm Gaussian heating beam on a well heat sunk medium. Ambient temperature is 320K. (b), (c) Assumed temperature dependence of the particle's magnetic anisotropy K_u and saturation magnetization M_s.
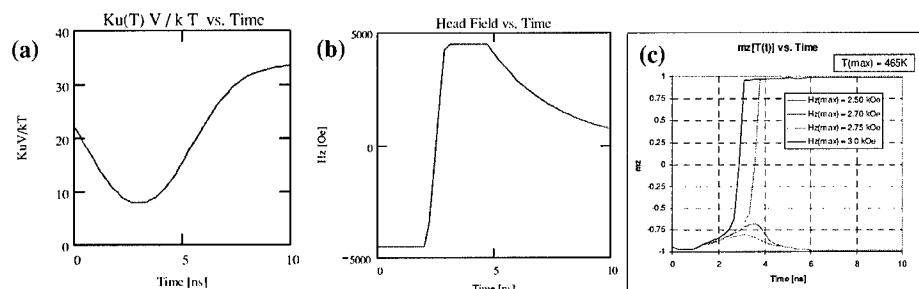
Figure 10. (a) Temperature dependence of magnetic particle's thermal stability parameter $K_u V/k_B T$. (b) An example of the head field experienced by the particle in the moving medium. (c) An example of the sensitivity of the particle's magnetization reversal to applied head field according to the LLG equation for a peak temperature of 465K during the switching sequence.

power of 1-2 mW in the 50 nm beam. Figures 9(b) and 9(c) show the assumed temperature dependence of the particle's magnetic anisotropy and magnetization.

Figure 10(a) gives the particle's thermal stability energy ratio $K_u V/k_B T$ versus time for the thermal history of Figure 9(a), using $K_u(T)$ of Figure 9(b). An example vertical head field history in Figure 10(b) will induce particle switch when combined with a suitable magnetic "softening" due to particle heating. Finally, in Figure 10(c) we see an example of the onset of particle magnetization reversal as the applied head field becomes sufficiently strong at a peak medium temperature of 465K. With this model, one can study the tradeoffs of head field strength versus medium temperature for fast particle switch. Additionally, with the thermal decay term in the modified LLG equation, the impact of excess or prolonged heating on particle thermal stability during and immediately after writing is accessible.

SPINSTAND RECORDING TESTING

Previous hybrid recording experiments in a spinstand environment were reported [9,13]. Successful thermomagnetic recording on both longitudinal and perpendicular media was shown. The Co-alloy longitudinal media tested was well-engineered for product application, and showed excellent SNR performance due to its refined crystalline structure with low inter-granular exchange coupling. The Co/Pt multilayer perpendicular media evaluated consisted of laboratory samples which were fabricated to have relatively high coercivity, but which had not undergone extensive materials engineering to establish exchange decoupling among the crystalline grains. Consequently, this media was useful for demonstrating the principle of thermally-assisted writing, but it did not exhibit remarkable SNR performance due to the relatively large inter-granular exchange.

We anticipate future recording testing work on the materials reported in this paper, which is expected to yield improved SNR performance in hybrid recording. This prediction is supported by the recording simulations reported above.

SUMMARY AND CONCLUSIONS

We have undertaken experimental materials development of Co/Pd multiplayer samples for use in hybrid magnetic recording. We prepared coupon samples that met design targets for reduction of inter-granular coupling and improvement of magnetic stability in thermal cycling. Disk samples with these coatings were prepared to have mechanical and magnetic properties suitable for spinstand testing. Computer simulations of the Co/Pd material's magnetic hysteresis and thermomagnetic recording performance helped guide our materials development work. The recording simulations showed that reduction of inter-granular exchange coupling should result in excellent media SNR performance, since recorded transitions will be smooth and free of large, irregular magnetic clusters due to unwanted coupling. Modeling was helpful in illustrating the recording performance improvement enabled by reducing the breadth of the distributions of key media material magnetic and structural parameters, such as magnetic anisotropy strength, anisotropy axis alignment, and grain size. The simulations also clarified the importance of proper setting and co-location of the thermal and magnetic field gradients in the hybrid recording process.

ACKNOWLEDGEMENTS

REFERENCES

[1] Dieter Weller and Andreas Moser, *IEEE Trans. Magn.* **35**, 4423 (1999).
[2] S.H. Charap, Pu-Ling Lu, and Yanjun He, *IEEE Trans. Magn.* **33**, 978 (1997).
[3] Roger Wood, *IEEE Trans. Magn.* **36**, 36 (2000).
[4] D. Weller, *et al*, *IEEE Trans. Magn.* **36**, 10 (2000).
[5] H. Saga, *et al*, Proc. MORIS 1999, *J. Magn. Soc. Jpn.* **23**, Suppl. S1, 225 (1999); H. Nemoto *et al*, *ibid*, p.229; H. Katayama, *et al*, *ibid*, p.233 (1999); H. Katayama, *et al*, *IEEE Trans. Magn.* **36**, 195 (2000).
[6] Wenbin Peng, *et al*, Intermag Conference 2000, to be published in *IEEE Trans. Magn.*
[7] H.N. Bertram and M. Williams, *IEEE Trans. Magn.* **36**, 4 (2000).
[8] T.W. McDaniel, *J. Magn. Soc. Jpn.* **23**, Suppl. No. S1, 251 (1999).
[9] M. Alex, A. Tselikov, T. McDaniel, N. Deeman, T. Valet, and D. Chen, Intermag Conference 2001 paper HC-01, to be published in *IEEE Trans. Magn.*
[10] Euxine Technologies, *Advanced Recording Model* (ARM), Broomfield, CO 80020 USA
[11] Jaap J.M. Ruigrok, Proc. MORIS / APDSC 2000, Nagoya, Japan; to be published in *J. Magn. Soc. Japan.*
[12] Kazuhiro Ouchi and Naoki Honda, *IEEE Trans. Magn.* **36**, 16 (2000).
[13] M. Alex, T. Valet, T. McDaniel, and C. Brucker, MORIS / APDSC 2000, Nagoya, Japan; to be published in *J. Magn. Soc. Jpn.*
[14] C. Brucker, "Magneto-Optical Thin Film Recording Materials in Practice," *Handbook of Magneto-Optical Data Recording*, ed. T.W. McDaniel and R.H. Victora, (Noyes, 1997) pp. 279-361.
[15] K.B. Klaassen and J.C.L. van Peppen, Intermag Conference 2001 paper EA-06, to be published in *IEEE Trans. Magn.*

Integrated Surface Emitting Laser Arrays with Flat-Tip Microprobes for the Near-Field Optical Data Storage

Young-Joo Kim*, Shu-Ying Ye, Kazuhiro Suzuki and Kenya Goto
Dept. Information & Communication Technology, Tokai University
317 Nishino, Numazu, Shizuoka, 410-0395, Japan
*E-mail: yjkim@goto.fc.u-tokai.ac.jp

ABSTRACT

Current optical data storage is challenging to increase its memory capacity and data transfer rate for realizing high-quality image and rapid service in the coming digital, multimedia and network era. To actualize more effective and simple data storage, a novel parallel near-field optical system has been proposed using vertical cavity surface emitting laser (VCSEL) microprobe arrays. The new parallel optical system is based a multibeam recording head consisting of a VCSEL array with apertures of nanometer size as a near-field wave exit. We have developed some candidates for the parallel recording head, including the direct aperture formation on the VCSEL emitting surface and the preparation of microprobe arrays with flat-tip structure. The new flat-tip microprobe array has advantages for improving the optical efficiency and stabilizing the contact head system with optical media since it is prepared from semiconductor materials of high refractive index. Silicon nano-aperture probe array has been prepared successfully with the aperture size of 150 to 500nm using micro-fabrication techniques. We have also investigated the integrated microprobe array by the direct fabrication of flat-tip probes on the substrate of bottom emitting VCSEL arrays. Finally the reading mechanism has been studied theoretically using a finite difference time domain (FDTD) simulation and an optical feedback effect of semiconductor lasers for the integrated microprobe VCSEL array. We believe this nano-aperture VCSEL probe array is sufficiently effective to be applied to the parallel recording head for the near-field optical data storage of a high data capacity and fast transfer rate.

INTRODUCTION

Both a high data capacity and fast transfer rate are required in the fields of magnetic and optical data storage. In the last ten years, several near-field optical data storages have been developed to increase a data capacity using evanescent waves. However, these still have a limitation to speed up a data transfer rate to follow the ability of magnetic hard disk system. In order to overcome this speed barrier of optical data technology, some approaches such as 2-D parallel near-field recording and 3-D holographic system have been proposed and studied [1]. Since two dimensional array system which was proposed by our research group is based on a multibeam recording with the small spot size using the microprobe and VCSEL array, it has advantages for realizing both a fast data transfer rate and high memory capacity [2,3]. As shown in figure 1, the VCSEL array will be inclined at a specific angle (for example, 0.57° for 100x100 array head) to the track direction to align all light sources on separate data tracks. In this array head, all lasers will be manipulated simultaneously to record the data on and read them from

multi- tracks, resulting in a huge increase of the data transfer rate. The realization of small laser beam with sufficient power is another requirement for increasing the memory capacity in this parallel optical system. Thus, the fabrication of nano-aperture microprobes having high optical efficiency will be a key process to expose a strong near-field wave on the optical media. In order to realize this two-dimensional optical data storage, we have developed some array head systems, including the direct aperture formation on the VCSEL emitting surface and the preparation of microprobe arrays with the flat-tip structure. New microprobes of flat-tip structure are prepared from semiconductor materials having high refractive index so they have advantages for improving the optical efficiency and stabilizing the contact head system with the optical media. The concept and fabrication process for new array heads are discussed with their optical properties and microstructures in this paper. In order to apply theses new types of array heads to the actual near-field optical head, we have also been developing the integrated microprobe array by preparing flat-tip microprobes directly on the substrate of bottom emitting VCSEL arrays. The structural design of the integrated VCSEL microprobe array will be discussed with simulation results for the reading mechanism from the phase change media using a finite difference time domain (FDTD) analysis and an optical feedback effect on the semiconductor laser.
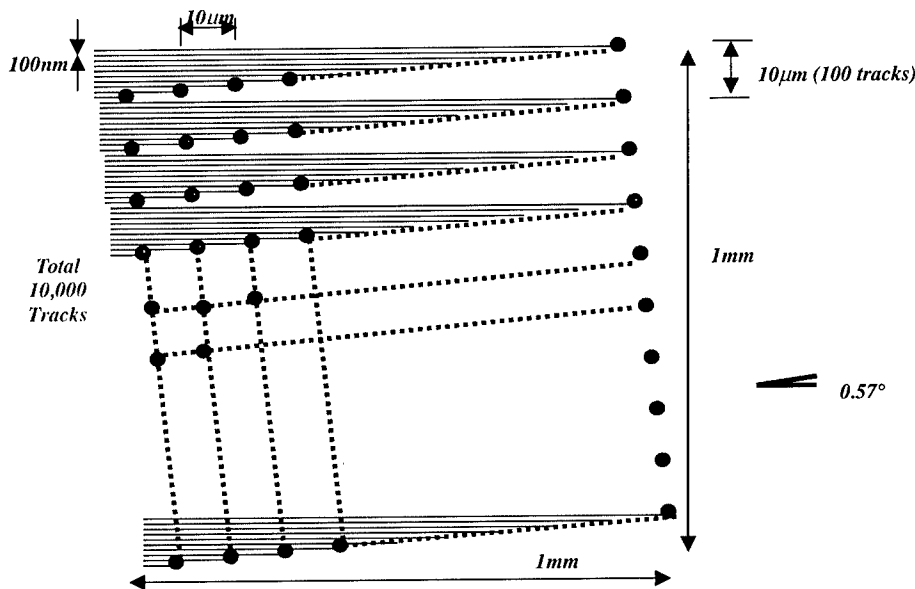
Figure 1. Schematic diagram of the two-dimensional array system to realize a high data transfer rate. VCSEL array is inclined at a specific angle (for example, 0.57° for 100x100 array head) to the track direction to align all light sources on separate data tracks.

NANO-APERTURE VCSEL ARRAY

Since our parallel recording system must include a VCSEL array as light sources, it is a good idea to use a VCSEL array for the exit of near-field waves without any other components. Thus, we have studied the fabrication of simple head structure using a nano-aperture VCSEL array, where a tiny aperture is formed directly on the emitting surface of VCSEL using the focus ion beam (FIB) method as shown in figure 2(a). In order to realize the best optical efficiency, a phase matching layer of Si_3N_4 film was first deposited on the VCSEL surface with a specific thickness of 107.3 nm, and the metal deposition of thin Cr adhesion layer (5 nm) and Au reflective layer (50-200 nm) was followed. Then, a small nano-aperture was formed on the VCSEL emitting surface through metal layers using the FIB equipment. We could control the FIB etching conditions and thus, fabricate very small apertures of around 50 nm size successfully. AFM image of the VCSEL emitting surface after the aperture formation is shown in figure 2(b). An aperture of around 100-nm-diameter is formed on the surface through metal layers where the metal surface also shows a good property with the surface roughness below 10 nm (p-v).

(a)   (b)
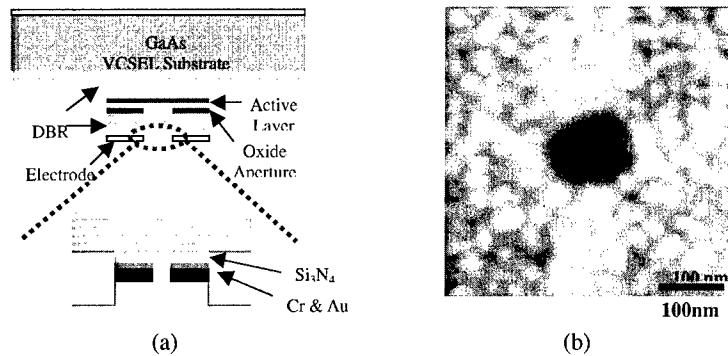
Figure 2. (a) The preparation procedure for the nano-aperture VCSEL array with a dielectric layer of Si_3N_4 and metal reflective layers of Cr and Au. (b) AFM image of the100-nm-diameter aperture prepared on the emitting surface of VCSEL.

The optical output of nano-aperture VCSEL was measured with a photodetector in the far-field range using a collecting lens before and after the aperture formation, and the result is summarized in figure 3. The VCSEL used in this measurement has the optical output of 4.1mW at the 16mA current before the deposition of dielectric and metal layers (see figure 3(a)). With the deposition of dielectric and 50-nm-thick metal layers, the output power of VCSEL drops to 0.054mW at the same current as shown in figure 3(b). This small power comes from the leakage light through the reflective metal layer since it is not sufficiently thick to block the laser light entirely. If we increase the thickness of the metal reflective layer, the leakage light will disappear, however, it is also difficult to penetrate the near-field light through a long hole after the nano-aperture formation. Thus, we have fixed the thickness of the reflective metal layer as 50 nm in this research.
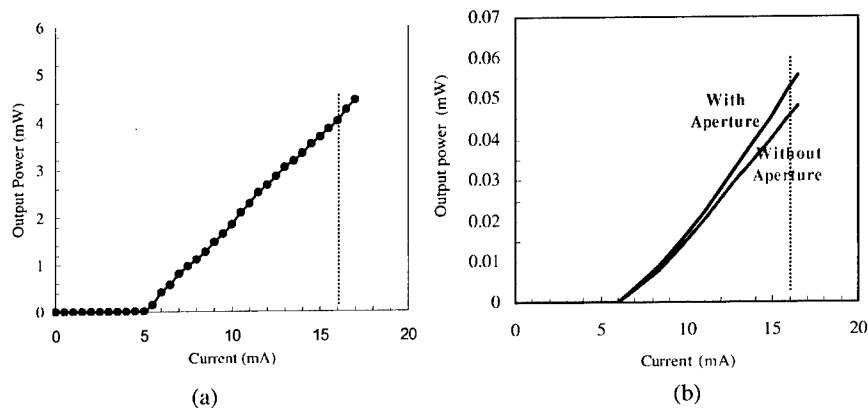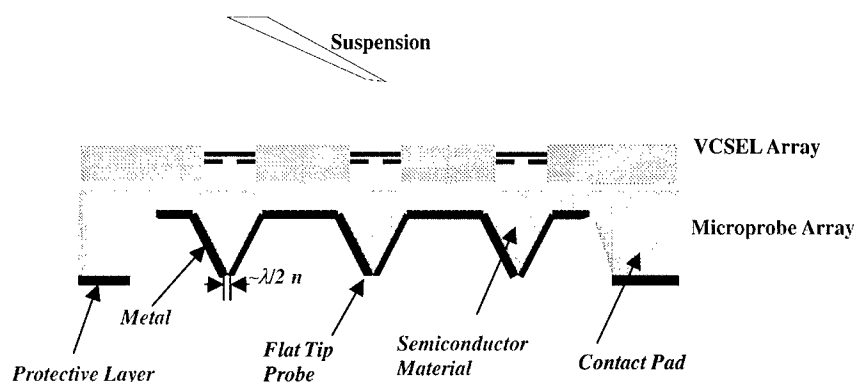
Figure 3. I-V characteristics of VCSEL; (a) before the metal deposition and (b) after the metal deposition and the aperture formation. A tiny aperture of 100-nm-diameter was formed on the VCSEL emitting surface, which results in a little increment of the output with around 7 μW.

The VCSEL output power shows a little increment of around 7 μW after the formation of 100-nm-size aperture (see figure 4(b)). Even though we need more data for the beam size and power distribution in the near-field range, this result indicates the possibility to apply the nano-aperture VCSEL head to the recording application. However, this output increment is not sufficient for the actual optical recording system since the optical media usually requires more power to be recorded. Therefore it is strongly required to increase the optical output while keeping the small aperture size for the light exit. There are some possible approaches to increase the optical power with a tiny aperture, including the surface plasmon enhancement [4] and the introduction of microprobe arrays. Thus, we have developed new type of flat-tip microprobe arrays to realize higher optical throughput and better structure design for the contact head required in our parallel optical system [5]. This flat-tip microprobe array will be combined with a VCSEL array to realize the parallel near-field recording head.

FLAT-TIP MICROPROBE ARRAY

The optical power and efficiency of new flat-tip probe arrays strongly depend on the shape and aperture size of microprobes. Since the fundamental propagation wave in metal-coated microprobes decays rapidly below the cutoff diameter that is defined theoretically as $\lambda/2n$, it is possible to obtain small spot size without a huge power loss if semiconductor materials having high refractive index are used for the microprobe array. Thus, we have developed better recording array structure using the flat-tip microprobe, as shown in figure 4. This microprobe structure has another advantage in its uniformity of probe height, which is very important for our contact head system. Since contact pads are in touch with the disk via a very thin lubricant layer, the recording gap can be controlled by the small height difference between the contact pads and

probe tips. In our probes, both surfaces of the flat-tips and contact pads have the same height after the etching process because both are prepared from the same wafer plane. After depositing a very thin protective layer of 10 nm thickness only on the contact pads, we can keep the distance between the probe tips and disk surface at around 10 nm.

Suspension

VCSEL Array

Microprobe Array

~$\lambda/2\, n$

Metal

Flat Tip
Probe

Semiconductor
Material

Contact Pad

Protective Layer

Figure 4. Schematic diagram of the parallel near-field optical memory including a VCSEL array and flat-tip microprobe array. The gap between the flat-tip surface and media surface is controlled by the thickness of the protective layer deposited only on the contact pads.

Semiconductor single crystals are the best candidate material for the flat-tip microprobe array since they have a high refractive index and are manipulated easily with a stable micro-fabrication process. We have selected three different wafers for the flat-tip probe array, gallium phosphide for the 650 nm, silicon for 850 nm and gallium arsenide for 980 nm wavelength applications. They have a high refractive index and negligible extinction coefficient at their specific wavelengths except silicon. Silicon has an extinction coefficient of 0.004 at an 850 nm wavelength so it may not be suitable for the optical application. However, if we use very thin silicon wafer, the light can penetrate through it at that wavelength. For example, a laser beam of 850 nm wavelength can penetrate with 43.7% transmittance theoretically through the 14-μm-thick silicon wafer, as calculated using Lambert's law defined as $T=I/I_o=\exp(-4\pi kt/\lambda)$ [7]. Figure 5 shows the experimental data of transmittance for the thin silicon substrate of 14 μm thickness. With an anti-reflection (AR) coating of Si_3N_4 layer, the thin Si substrate results in the transmittance of 40% at 850 nm that shows a good agreement with the theoretical calculation. Although we lose around half of optical power with the 14-μm-thick wafer, silicon is still attractive for the microprobe array due to its high refractive index and well-developed microfabrication process.

We used the microfabrication technique to prepare flat-tip microprobe arrays with nanometer size apertures using the silicon-on-insulator (SOI) wafer, consisting of the 14-μm-thick silicon layer, 0.5-μm-thick silicon oxide layer and 400-μm-thick silicon substrate. Figure 6 shows SEM photomicrographs for the flat-tip microprobe array and the nano-aperture prepared on the microprobe tip. The array consists of 625 microprobes and three contact pads even though SEM photomicrograph includes only some part of microprobes, where each microprobe has 17 μm edge and 12 μm height with the 20 μm pitch (see figure 6(a)). The microprobe has a 70 deg

angle between two side planes; however, it shows the flat area on the probe tip as a result of careful control for the silicon etching process. Top surface of microprobes has a square shape with the edge length of 150 to 500 nm even though some probes of rectangular surface are included in the array. Though they have a little variation in size, all microprobes in the array have the same height because top plane was prepared from the same surface of Si wafer. The smooth surface of microprobes also enables the optical wave to propagate into the microprobe without any scattering loss and, thus, it will be another important advantage of the flat-tip microprobe. In order to apply the microprobe array to an actual recording head, the outside of microprobe must be coated with the reflective metal layer and followed by the formation of tiny aperture on the probe tip for the exit of laser beam. In this research, we have developed new mask process for making an aperture on the flat-tip microprobe that is suitable for the array system and mass production. In this method, the SiO_2 mask layer on the tip (it is used originally for the probe fabrication) was re-sized from 12 μm to 1.3 μm with the careful control of isotropic etching rate. After depositing metal layers from both the top and side directions, we etched out the remaining SiO_2 mask, resulting in the tiny aperture on the microprobe tip, as shown in figure 6(b). More detailed process and microstructural evaluation for this flat-tip microprobe array has been discussed in the previous paper [5].
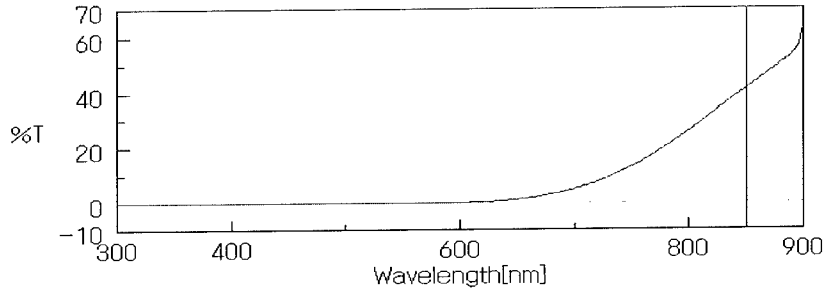
Figure 5. Experimental data for the optical transmittance of the 14-μm-thick silicon having an anti-reflection (AR) coating. It shows around 40% transmittance at an 850 nm wavelength.

(a)   (b)

Figure 6. SEM photomicrographs of (a) the flat-tip microprobe array and (b) the nano-aperture prepared on the probe tip. The microprobe array consists of 625 probes and three contact pads.

INTEGRATED VCSEL MICROPROBE ARRAY AND READING SIMULATION

Integrated VCSEL microprobe array

Although we have proposed new concept of flat-tip microprobes for the high optical throughput and realized the microprobe array with silicon and GaP [5,6], it still requires further improvement to complete the near-field optical system, including the alignment and bonding of the microprobe array to VCSEL array. Thus, we have studied the integrated VCSEL array head using a bottom emitting VCSEL array. As shown in figure 7, the light travels downwards through the substrate in this type of VCSEL, thus it is more suitable for the integration because there is no electrode at the bottom side. Since 650 nm and 850 nm lasers cannot penetrate through GaAs substrate, the original substrate must be removed and replaced with other transparent substrate such as gallium phosphide or thin silicon wafers for the light traveling to the bottom side. Then, we can fabricate a flat-tip microprobe array directly on the new substrate. After attaching a VCSEL array to the glass holder, the GaAs substrate of VCSEL was grinded mechanically to around 40 µm thickness and followed by the chemical etching with NH_4OH/H_2O_2 to remove the remaining substrate. It is possible to etch out just the remaining GaAs substrate by the chemical etching process since the VCSEL array includes an etch stop layer. After attaching a SOI wafer to this VCSEL array, we pressed them under constant stress and loaded them in the furnace at 250°C for 2 h for the direct bonding. The integrated VCSEL microprobe array can be realized by fabricating the microprobe array having small apertures on the SOI wafer using the techniques explained above. We believe this integrated nano-aperture VCSEL microprobe array is sufficiently effective to be fabricated and applied to the parallel recording head, though further research is still required to confirm the optical usefulness of this new VCSEL microprobe array. Currently we are attempting to evaluate the optical properties of flat-tip microprobe arrays and improve the head structure to complete the parallel near-field optical recording system using the integrated VCSEL microprobe array.

Figure 7. Schematic diagram of the layer structure of near-field phase change media and the integrated VCSEL microprobe array prepared using a bottom emitting VCSEL. (Contact pads of this array are not shown in this figure.)

Simulation results for the reading mechanism using optical feedback in VCSEL

Both types of conventional optical media, the magneto-optical (MO) and phase change (PC) disks, are considered to be applied to our two-dimensional optical system. In case of the MO media, the system requires extra reading array head of giant magnetic resistance (GMR) element to get magnetic signals from the media. However, we can use the same recording array head to detect the reflective difference from the crystalline and amorphous phase for the PC media without any other reading head or optical elements. The basic concept of this reading mechanism was developed using a stripe laser diode before, including our research work for the lensless optical floppy disk [8,9]. The change of output power in the semiconductor laser is induced by the optical feedback from the external surface of different reflectivity using an external oscillation, which can be detected by measuring the voltage change between two electrodes of laser diode [9,10]. In this study, the VCSEL characteristic of voltage change in the integrated VCSEL microprobe system was analyzed theoretically as a function of the amount of returning light from the media that depends on the reflectivity of media. A FDTD simulation was applied to analyze the amount of returning light in this system, including the VCSEL, microprobe and phase change media, as explained in figure 8(a). In the calculation, we assume that the inside material and outside area consist of GaP and vacuum, respectively. The microprobe has a pyramidal shape with a 55 deg angle between the two side planes because it is supposed to be prepared from (100) GaP wafer by the chemical etching. The optical beam of an 850 nm wavelength VCSEL propagates from the base plane to the microprobe, where the oscillation modes of electric and magnetic fields are parallel to the x and y axis, respectively. The PC media consists of 20-nm-thick dielectric layer (ZnS-SiO$_2$), 20-nm-thick Ge$_2$Sb$_2$Te$_5$ layer, 20-nm-thick dielectric layer (ZnS-SiO$_2$), and 100-nm-thick reflective Al layer. The observation plane for the reflectivity difference is assumed at the location 0.1μm below the VCSEL emitting surface.

(a)   (b)
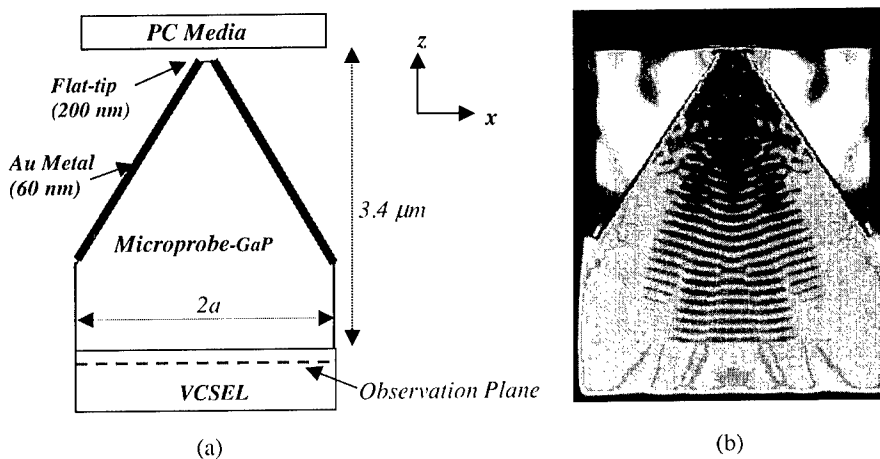
Figure 8. (a) Analysis model for an optical feedback effect in the integrated VCSEL microprobe array and (b) the electric field distribution for the crystalline phase of the PC media. The observation plane is assumed at the location 0.1μm below the VCSEL emitting surface.

Figure 8(b) shows the electric field distribution of the integrated VCSEL microprobe for the crystalline phase of the PC media. As expected, the light is reflected both by the Au metal layer of the microprobe surface and the crystalline phase of the media. From the field distribution for the crystalline and amorphous phase, we can calculate the relative reflectivity of two different phases by dividing them to the initial VCSEL field separately. The difference of relative reflectivity is shown in figure 9(a) as a function of the location in the x direction at the observation plane. It shows roughly 3% reflectivity difference even though there is a little variation with the location. From this reflectivity difference, we can calculate the carrier density in VCSEL using the continuity equation [11] and finally get the theoretical value for the voltage change using the equation:

$$\Delta V = \frac{2kT}{q}\frac{\Delta N}{N_0}$$

where N is the intrinsic carrier density, k is Boltzmann's constant, q is the electron charge and T is the temperature. The voltage change across two electrodes in the VCSEL is summarized as a function of the reflectivity difference in figure 9(b). The voltage change due to the optical feedback increases linearly with the reflectivity difference and shows higher value for the VCSEL having smaller emitting surface. For the 3% difference in the integrated VCSEL microprobe, the voltage change results in around 0.8mV for the 8 μm diameter emitting VCSEL. Though this value is a little low to be applied to the actual reading head, it still has a possibility to detect the signals from the phase change media. From the simulation results, we can conclude that the voltage change will increase with the shorter distance from the VCSEL to media (for example, smaller size of microprobe), smaller diameter of the VCSEL emitting surface and higher reflectivity difference in the phase change media through the improvement of disk structure.

(a)

(b)
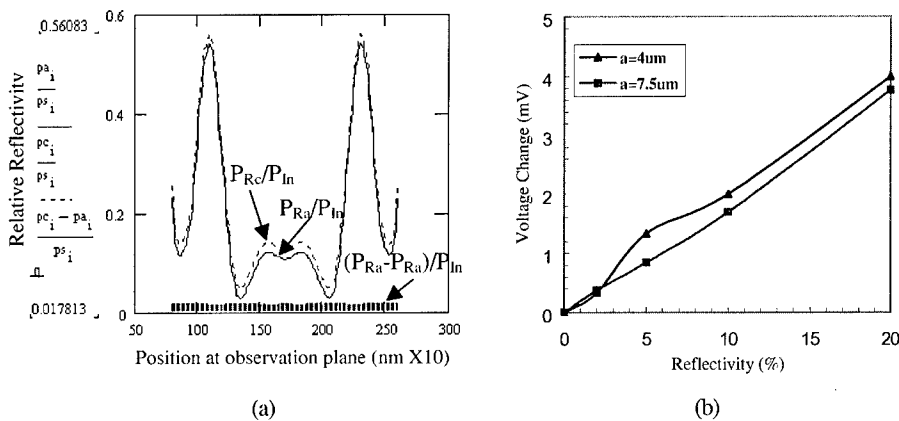
Figure 9. (a) The difference of relative reflectivity as a function of the location in the x direction at the observation plane (P_{In}=initial electric field, P_{Rc} and P_{Rc}=reflected field from the crystalline and amorphous phase) and (b) the voltage change across two electrodes in VCSEL. The voltage change results in 0.8mV for the 8μm diameter emitting VCSEL with a 3% reflectivity difference.

SUMMARY

To actualize more effective and simple data storage of a high data capacity and fast data transfer rate, two-dimensional near-field optical system has been studied using a vertical cavity surface emitting laser (VCSEL) microprobe array. We have developed some candidates for the parallel recording head, including the direct aperture formation on the VCSEL emitting surface and the preparation of microprobe arrays with the flat-tip structure. Apertures with a minimum size of around 50 nm have been prepared using a FIB method after depositing the phase matching layer of Si_3N_4 and reflective layers of Cr and Au on the emitting surface. For the VCSEL having a 50-nm-thick metal layer, the optical output increases 7 μW after the aperture formation of 100-nm-diameter. In order to increase the optical output through a tiny aperture, we also developed new flat-tip microprobe array that has advantages for improving the optical efficiency and stabilizing the contact head system with the optical media. Silicon and GaP nano-aperture microprobe arrays have been prepared successfully with the aperture size below 200 nm using micro-fabrication techniques. We have also studied the integrated VCSEL microprobe array by the direct fabrication of flat-tip microprobes on the substrate of bottom emitting VCSEL. The reading mechanism has been investigated theoretically using a FDTD simulation and an optical feedback effect from the phase change media for the integrated microprobe VCSEL array. The voltage change due to an external reflection can increase with the smaller emitting surface in VCSEL and shorter distance from the VCSEL to media, which leads a guideline for the signal detection in the external reflection mode. We believe this nano-aperture VCSEL microprobe array is sufficiently effective to be applied to the parallel recording head for the near-field optical data storage with a high data capacity and fast transfer rate.

REFERENCES

1. E. J. Lerner: Laser Focus World. **35** No.8, 171 (1999).
2. K. Goto: Jpn. J. Appl. Phys. **37**, 2274-2278 (1998).
3. Y.-J. Kim, K. Kurihara, K. Suzuki, M. Nomura, S. Mitsugi, M. Chiba and K. Goto, Jpn. J. Appl. Phys. **39**, 937-941 (2000).
4. H. F. Ghaemi, T. Thio, T.W. Ebbesen and H.J. Lezec, Phys. Rev. B **58**, 6779 (1998).
5. Y.-J. Kim, K. Suzuki and K. Goto, Jpn. J. Appl. Phys. **40** (2001) (in press).
6. K. Kurihara, Y.-J. Kim and K. Goto, ODS 2001, Tech. Dig. (Santa Fe, USA) (2001).
7. E. D. Palik: *Handbook of Optical Constants of Solid* (Academic Press, Inc., New York, 1985).
8. Y-J. Kim, Y. Hasegawa and K. Goto, Jpn. J. Appl. Phys., **39**, 929-932 (2000).
9. L. N. Langley and K. A. Shore, IEEE Proc. Optoelectron., **144**, 34-38 (1997).
10. K-P. Ho, J. D. Walker and J. M. Kahn, IEEE Photo. Technol. Lett., **5**, 892-895 (1993).
11. R. Juskaitis, N. P. Rea and T. Wilson, Appl. Opt., **33**, 578-584 (1994).

Optical absorption spectroscopy in the metastable state SI of $Na_2[Fe(CN)_5NO]\cdot2H_2O$

Dominik Schaniel[1], Jürg Schefer[1], Bernard Delley[2], Mirco Imlau[3], Theo Woike[4]
[1]Laboratory for Neutron Scattering, ETH Zürich & PSI, 5232 Villigen PSI, Switzerland
[2]Condensed Matter Theory, FUN Department, PSI, CH-5232 Villigen PSI, Switzerland
[3]Fachbereich Physik, University of Osnabrück, D-49069 Osnabrück, Germany
[4]Institute of Mineralogy and Geochemistry, University at Cologne, D-50674 Köln, Germany

ABSTRACT

The metastable state SI in single crystals of orthorhombic $Na_2[Fe(CN)_5NO]\cdot2H_2O$ (sodiumnitroprusside, SNP) was investigated by absorption spectroscopy. The development of the spectra with increasing population of SI was monitored and a new band in the red spectral range was assigned to SI. By comparing with density functional theory (DFT) calculations we were able to assign the band to the electronic transition $2b_2 \rightarrow 7e$. In addition we found that very strong holographic light scattering influences the absorption spectra measured with light polarization along the a- or b-axis of the crystals.

INTRODUCTION

The metastable electronic states in single crystals of nitrosyl-compounds like $Na_2[Fe(CN)_5NO]\cdot2H_2O$ (sodiumnitroprussside, SNP) are of fundamental interest because of their extremely long lifetime of $\tau > 10^8$s below characteristic decay temperatures and the reversibility of the excitation process [1]. They can be used for optical information storage with extremely high capacity by volume holography. The modulation of the refractive index is $\Delta n \geq 4\cdot10^{-2}$, which exceeds those of the well known photorefractive materials like doped $LiNbO_3$, $BaTiO_3$, $LiTaO_3$, $Sr_xBa_{1-x}Nb_2O_6$, etc. by at least two orders of magnitude.

In SNP two metastable states SI and SII can be excited by irradiation with light below characteristic decay temperatures of 198K and 147K, respectively. About 50% of the $[Fe(CN)_5NO]^{2-}$ anions can be transferred into SI with a light polarization perpendicular to the quasi four-fold axis N-C-Fe-N-O using a wavelength of 440-470nm. De-excitation into the ground state (GS) takes place by irradiation with light in the spectral range of 600-1200nm or by thermal heating over the decay temperatures, whereby illumination with light in the region of 900-1200nm transfers about 32% of the anions in SII and the rest into the ground state. In this article we will concentrate on the metastable state SI which we investigated systematically by absorption spectroscopy.

EXPERIMENT

Single crystals of orthorhombic sodiumnitroprusside, space group Pnnm [2] with four molecules per unit cell were grown from aqueous solution and cut perpendicular to the crystallographic axes. Specimens of dimension $20\times10mm^2$ were ground to thickness between 0.3 and 0.05mm using a mixture of Al_2O_3 and propanol and finally etched with a mixture of water and propanol. They were mounted on a sample holder diving into a nitrogen-filled quartz-dewar.

The temperature was kept constant at 95K. The expanded beam of an Ar+ Laser (λ=476.5nm) strikes the sample perpendicular to the entrance face with an intensity of I_L=80mW/cm^2. In order to obtain the maximum population of 50% of SI a total exposure of Q=I_Lt=2500Ws/cm^2 has to be reached, the laser beam being polarized parallel to the crystallographic c-axis. The absorption spectra were measured with a two-beam spectrophotometer (Perkin-Elmer) equipped with a Glan-Thompson polarizer and a quartz-dewar. The wavelength resolution was about 4nm over the whole spectral range of 300-1200nm. Deconvolution of the spectra was done by fitting a sum of Gaussian curves to the corresponding electronic transitions together with a horizontal baseline because we have not made any corrections of the transmission by the reflection given through the refractive indices. Irradiation with a wavelength of λ=476.5nm produces simultaneously about 2% of SII and 45% of SI. By heating the crystal to T=150K the metastable state SII can be completely depopulated so that only absorption caused by the ground state and SI is measured.

RESULTS

Figure 1 shows the absorption spectra of the ground state in a b-cut of SNP at room temperature and at 95K for two different polarization directions of the probing light: E∥c-axis, E∥a-axis. Also indicated in Figure 1 is the deconvolution of the spectra with four Gaussian curves and a horizontal baseline. The fit parameters: position v_{max}, area A and FWHM Γ of the Gaussian bands are summarized in Table I. Parallel to the crystallographic c-axis we can clearly see three transitions whereas along the a-axis the third band is visible only as a shoulder in the steep slope of the very strong fourth absorption band, over which we could not measure. We know from absorption spectra of solutions of SNP in H_2O at room temperature that there is a fourth band lying around 37000cm^{-1}. This transition was therefore constrained to values v_{max} around 37000cm^{-1} in the fit varying only the width Γ and the area of the Gaussian. The width Γ stays within reasonable values around 4000cm^{-1} and therefore we can estimate its influence on the third transition with good accuracy. The third transition is considerably narrower than the others and shows strong temperature dependence in position and size. There exist several theoretical approaches to calculate the orbitals of the $[Fe(CN)_5NO]^{2-}$ anion: calculations based on an idealized ligand-field model [3], the MSXα-method [4] and density functional theory (DFT) [5], all of them using 4m (C_{4v}) symmetry. According to these calculations we made an assignment (notation after [3,5]) for the observed transitions as indicated in Figure 1 and Table I. The two transitions around 20000cm^{-1} and 25800cm^{-1} are allowed whereas the third transition

Table I. Electronic transitions of the ground state in SNP. Values v_{max} [cm^{-1}] from theory for comparison.* $2b_2 \rightarrow 5a_1$ from [5] as in DFT calculations the $5a_1$ and $3b_1$ appear in inversed order compared to [3] and [4].

E∥c	v_{max} [cm^{-1}]	A [cm^{-2}]	Γ [cm^{-1}]	v_{max} [3]	v_{max} [4]	v_{max} [5]
$2b_2 \rightarrow 7e$	20190	0.32×10^6	3750	20540	21170	18490
$6e \rightarrow 7e$	25770	1.12×10^6	5420	25110	23360	22840
$2b_2 \rightarrow 3b_1$	31630	1.56×10^6	3330	33570	33230	36250*
E∥a	v_{max} [cm^{-1}]	A [cm^{-2}]	Γ [cm^{-1}]			
$2b_2 \rightarrow 7e$	19790	0.16×10^6	3750			
$6e \rightarrow 7e$	25960	1.30×10^6	5060			
$2b_2 \rightarrow 3b_1$	31720	1.13×10^6	3360			
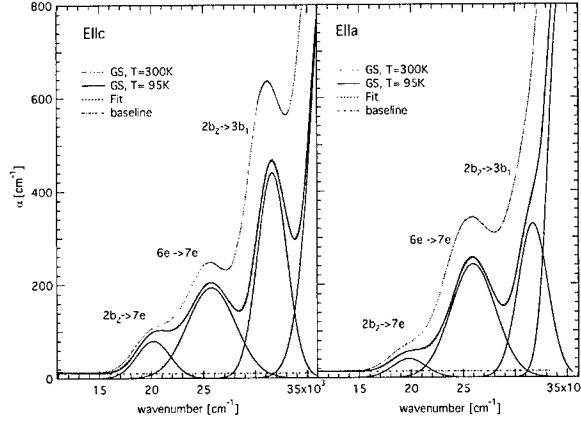
Figure 1. Polarized absorption spectra of SNP in the ground state at room temperature (dotted line) and at T=95K (full line) for polarization of the measuring light along c-axis (left) and a-axis (right) of the crystal. The fit to the 95K data (dashed line) consists of four Gaussians and a baseline (dash-dotted line). Results are given in Table I.

around 31700cm^{-1} is forbidden in 4m-symmetry. The selection rules for electronic transitions in the solid state can be overcome by coupling to phonons. The observed temperature dependence of the third transition can therefore be explained by the freezing of the phonons with decreasing temperature.

By irradiating the single crystals with laser light anions are transferred from the ground state into the metastable states, i.e. the absorption caused by the ground state decreases whereas new absorption bands from the new states appear. Figure 2 shows this process during the population of SI. We measured the absorption spectrum for several different total exposures Q. For the measurement with E∥c we find two isosbestic points at 17800 cm^{-1} and 26700 cm^{-1}, i.e. at these wavenumbers the absorption coefficient α is independent of Q. Inside this interval only the ground state decreases whereas at lower and higher wavenumbers the new bands of SI appear. If only two states (the ground state and SI) are present this gives us the possibility to determine the population P_{SI} of the metastable state SI as a function of exposure Q because the decrease of the ground state must be transferred into the new state SI:

$$P_{SI}(Q) = \frac{n_{SI}}{n_{tot}} = \frac{n_{tot} - n_{GS}}{n_{tot}} = \frac{n_{GS}(Q=0) - n_{GS}(Q)}{n_{GS}(Q=0)} = \frac{\alpha_{GS}(Q=0) - \alpha_{GS}(Q)}{\alpha_{GS}(Q=0)} \tag{1}$$

where n_{SI} and n_{GS} denote the number density of anions in the state SI and the ground state, respectively, and the relation $\alpha_{GS}=n_{GS}\cdot\sigma(\lambda)$ was used with $\sigma(\lambda)$ being the wavelength-dependent cross-section in the ground state. For the polarization of the probing light along the a-axis of the crystal we cannot detect any isosbestic points. Instead we observe an increase of the baseline over the whole spectral range and a very narrow band around 20000 cm^{-1}, which increases in size and changes its position with increasing exposure. Therefore from the absorption spectrum

measured along the a-axis we cannot determine the population of SI, which we have to know to perform the deconvolution of the spectrum with Gaussian curves. This problem can be solved by first measuring along the c-axis and then after turning the polarizer by 90° measuring along the a-axis at the same population. Figure 3 shows the two spectra and their deconvolution for a population P_{SI} of SI of about 41%. We observed one new band in the red spectral range around 13200 cm^{-1}. The fitted parameters of this transition of SI are given in Table II.
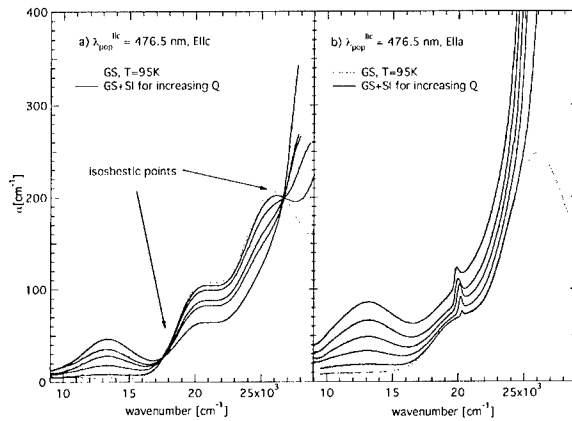
Figure 2. Absorption spectra for different populations of SI showing the two characteristic isosbestic points at 17800 cm^{-1} and 26700 cm^{-1} for E∥c (a) and the increase of the baseline and the very narrow band at 20000cm^{-1} for E∥a (b).
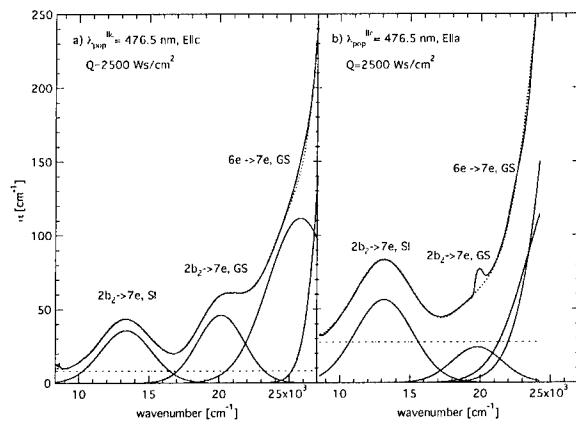
Figure 3. Spectra of a crystal populated to saturation showing the new band of SI in the red spectral range with E∥c-axis (a) and E∥ a-axis (b). The population of SI was determined from equation (1) to about 41%.

Table II. Electronic transitions of the metastable state SI in SNP for 41% population.

E$\parallel$c	ν_{max} [cm^{-1}]	A [cm^{-2}]	Γ [cm^{-1}]	ν_{max} [8]
2b$_2$→7e	13430	0.11×10^6	4200	10160
E$\parallel$a	ν_{max} [cm^{-1}]	A [cm^{-2}]	Γ [cm^{-1}]	
2b$_2$→7e	13180	0.28×10^6	4790	

In the literature the metastable state SI is explained by an elongation of the N-O-bond distances [6] or an inversion of the N-O-bond [7]. In the inversion model the ground state configuration Fe-N-O is inverted by 180° to Fe-O-N in SI. This model is also supported by DFT calculations [5], whereby the 4m-symmetry of the [Fe(CN)$_5$NO]$^{2-}$ anion is conserved. Since the symmetry of SI is the same as in the ground state we can use the same assignments for the transitions. We tentatively assign the absorption band to the 2b$_2$ → 7e transition, assuming that the transition is shifted to the red compared to the ground state, i.e. the 7e orbital is lowered in energy as proposed by DFT [8].

We consider now the origin of the increasing baseline and the narrow extinction band in the spectra measured along the a-axis of the crystals. By illuminating single crystals of SNP with laser light, one writes parasitic holographic gratings into the crystals [10]. The probing light is diffracted at these gratings. Due to the distance between sample and detector the cone of the diffracted light is wider than the area of the detector. Therefore parts of the diffracted light miss the detector, which appears in the spectra as a further extinction. This leads to the increase of the baseline over the whole spectral range with increasing population of SI. The narrow band even shows dynamic behavior. It changes its position as a function of exposure until a saturation value is reached (see Figure 4). We can fit this behavior with the following function, which is typical for the population dynamics of the metastable states:

$$v(Q) = v_0 + B(1 - e^{-\frac{Q}{Q_0}})\qquad(2)$$
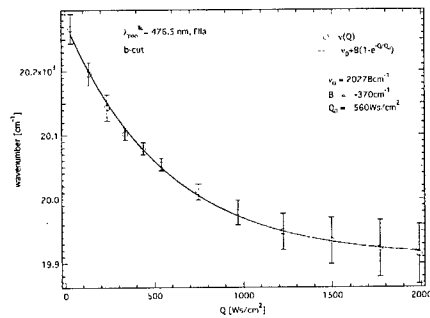
Figure 4. Position of the narrow band in the absorption spectra measured parallel to a-axis of crystal as a function of the exposure. The full line is the fit using equation (2) and yielding the indicated parameters.

The fit yields $\nu_0=20278cm^{-1}$, $B=-370cm^{-1}$, $Q_0=560Ws/cm^2$ and with $I_L=80mW/cm^2$ we get $\tau=7000s$. These values are in reasonable agreement with measurements of Q_0 by differential scanning calorimetry [10].

CONCLUSION

We found four electronic transitions in the ground state and one transition of the metastable state SI using polarized absorption spectroscopy on single crystals of SNP. We assigned them to the corresponding orbitals by using group theoretical arguments and by comparing them with DFT calculations. During population of the metastable state SI we observed two isosbestic points. They appear only for the measurement along the c-axis of the crystals and allow us to determine the population of SI directly from the absorption measurement. These isosbestic points indicate also the spectral range where the population of the metastable states is possible as no absorption bands of SI appear between them. Therefore the absorption measurements allow finding the optimal wavelength for populating the metastable states. The measurements with the electric field vector of the probing light along the a-axis revealed an increase of the baseline over the whole spectral range and a narrow extinction band connected with the population of SI. The same band has first been observed by Morioka [11] in a crystallographic c-cut, and is explained by optical activity of SNP in the metastable state SI. Contrary to this explanation we attribute this extinction to the diffraction of the probing light on written parasitic holographic gratings (optical damage). As the refractive index changes with increasing population of SI, the wavelength fulfilling the Bragg-condition for readout of these gratings changes correspondingly, leading to the observed shift of the narrow extinction band. A detailed description of this phenomenon will be given in a forthcoming paper [12].

ACKNOWLEDGEMENTS

REFERENCES

1. H. Zöllner, Th. Woike, W. Krasser, S. Haussühl, Z. *Krist.* **188**, 139 (1989)
2. F. Bottomley, P.S. White, *Acta. Cryst. B* **35**, 2193 (1979)
3. P.T. Manoharan, H.B. Gray, *J. Am. Phys. Soc.* **87**, 334 (1965)
4. M. Braga, A.C. Pavao, J.R. Leite, *Phys. Rev. B* **23**, 4328 (1981)
5. B. Delley, J. Schefer, Th. Woike, *J. Chem. Phys.* **107**, 23 (1997)
6. M. Rüdlinger, J. Schefer, G. Chevrier, N. Furer, H.U. Güdel, S. Haussühl, G. Heger, P. Schweiss, T. Vogt, Th. Woike, H. Zöllner, *Z. Phys. B* **83**, 125 (1991)
7. M.D. Carducci, M.R. Pressprich, P. Coppens, *J. Am. Soc.* **119**, 2669 (1997)
8. B. Delley, private communication
9. M. Imlau, Th. Woike, R. Schieder, R.A. Rupp, *Phys. Rev. Lett.* **82**, 2860 (1999)
10. Th. Woike, W. Krasser, H. Zöllner, W. Kirchner, S. Haussühl, *Z. Phys. D* **25**, 351 (1993)
11. Y. Morioka, *Solid State Commun.* **82**, 505 (1992)
12. M. Imlau, Th. Woike, D. Schaniel, J. Schefer, M. Fally, R.A. Rupp, to be published

Effect of scattering noise on the data fidelity of holograms recorded in photorefractive crystals

Mingyan Qin, Shiquan Tao, Guoqing Liu, Xiaohong Ding, and Dayong Wang
College of Applied Sciences, Beijing Polytechnic Univ., Beijing 100022, China

ABSTRACT

In this paper a method is proposed to investigate how the scattering noise of photorefractive crystals influences the quality of an input data page in holographic storage. By illuminating the crystal under investigation with an intense coherent light beam, and measuring the signal-to-noise ratio (SNR) of an image formed through the crystal before and after the exposure, the loss of SNR provides a good assessment for the suitability of the crystal for data storage. A variety of doped lithium niobate crystals were investigated. The results show that the intensity of fanning light increases with increase of the doping concentration, but there is no strict correlation between the fanning strength and the fidelity degradation. Owing to the low noise and high data fidelity, iron-and- zinc co-doped lithium niobate crystal is a potential material for high-density holographic data storage.

INTRODUCTION

Holographic data storage is a topic of widespread research interest [1-3]. The ability to store multiple holograms within a small volume of thick materials, such as photorefractive crystals, and to retrieve data pages with thousands of bits in parallel provides an attractive combination of density and speed. However, the various noises, such as the constant noise floor, cross talk between multiplexed holograms and the scattering noise, existing in the holographic systems reduce the capacity far from the ideal value determined by the diffraction limitation. So this is a major obstruction to the practice of volume holographic storage. In order to achieve the high capacity of holographic storage, data retrieved from holograms with high signal-to-noise ratio (SNR), and hence, low bit-error-rate is essential. It is demonstrated that the noise arising from holographic multiplexing can be far less significant than the system noise including the scattering noise arising from the recording medium. [4, 5] In this paper, we investigate the influence of scattering noise on image fidelity, with special attention paid to the influence of the scattering noise in photorefractive lithium niobate crystals on the quality of input data pages before the hologram formation.

THEORY

Photorefractive light-induced scattering noise is usually called "beam fanning", in which a collimated beam of light is scattered into a broad fan as it propagates through a high-gain

crystal. [6] It is proposed that the fan originates from the scattering of defects in the crystal, which then become amplified by the two-beam coupling process. In doped or co-doped LiNbO₃ crystals, the source of the fanning noise comes from the scattering on imperfections in the crystal, and the scattered light interferes with the initial beam, creating a phase grating in the crystal. Both the initial beam and the scattered beam are automatically Bragg matched to this grating, and self-diffraction occurs. Beam fanning can be a strong effect, removing almost all of the light from the incident beam in the worst case.

The mechanism of fanning effect has been widely studied (see, for example, Ref. [7]). The phenomenon is somewhat complicated, and the strength of the effect depends on various factors such as the crystal orientation, size and intensity of the incident light, and material parameters, etc. The following quantities can be used for measuring the fanning effect: (1) the power of scattered light, P_f, which forms a pattern in the observation screen separated from the initial light spot; (2) the scattering ratio R of the total fanning noise intensity to the total incident light intensity, [8] given as

$$R = \frac{I_0 - I_f}{I_0} \qquad (1)$$

where I_0 is the initial intensity of the incident light, and I_f is the final intensity of the incident light after the scattering being saturated. The larger P_f and/or R are, the more serious the scattering is.

The noise grating formed in the crystal through beam fanning can be read out by any beam that is partially Bragg-matched to this noise grating, resulting in some noise in the output beam. In the case of hologram multiplexing, a large number of holographic recordings causes the fanning process to a given hologram, that is, the scattering noise deteriorates the input signal (image), and hence, the quality of the retrieved image.

The fidelity of a holographic data page (image) is normally specified by the signal-to-noise ratio (SNR) that is defined as

$$SNR = \frac{I_1 - I_0}{\sigma_1 - \sigma_0} \qquad (2)$$

where I_1 and I_0 is the average value of bright and dark pixels, respectively, σ_1 and σ_0 is the corresponding standard variation. In this paper we use the loss of signal-to-noise ratio (LSNR) for characterizing the degradation of image fidelity due to the scattering noise,

$$LSNR = 10 \times \log\left(\frac{SNR_0}{SNR_f}\right), \qquad (3)$$

where SNR_0 is the SNR of the original image that was obtained through a "clean" crystal (all gratings previously recorded in the crystal are thermally erased) inserted in a noisy optical imaging system, whereas SNR_f is the SNR of the same image obtained through the same system after the scattering in the crystal reaches saturation. The lower the LSNR of a material, the better the image fidelity it may provide.

EXPERIMENT

We conducted experiments to investigate the effect of scattering noise on the data fidelity of holograms recorded in photorefractive crystals using a traditional Fourier transform holography system. An intense coherent beam with a diameter of 3 mm (total power 38mW for transmission geometry and 80mW otherwise), which acts as the reference beam in holographic recording, illuminated the crystal until the scattering reached saturation. The illumination time T_f depends on the crystal samples. The power of the scattered light P_f and/or the scattering ratio R was measured. For measuring P_f the full aperture of the detector (with an area of about 1 cm^2) was used, while for measuring R the detector was 3-mm apertured. The SNR_0 and SNR_f of an image, formed directly through the crystal inserted near the spectrum plane, were also measured before and after the illumination of the crystal by the reference beam. A relation between $LSNR$ and P_f (or R) was expected to reveal the influence of scattering noise on the image fidelity. By using this method, we tested a variety of lithium niobate crystals doped or co-doped with different dopants and doping concentrations, and with different treatment after crystal growth. The recording configurations under investigation included transmission, reflection, and 90-degree geometry.

RESULTS

The influence of scattering on the image fidelity is highly dependent on the crystal orientation. For a given sample and configuration, we made measurements for two crystal orientations anti-parallel to each other. Shown in Table 1-3 are results for the worse case. The values of scattered power were measured only for reflection geometry.

Table I: Influence of fanning noise on the image fidelity for Fe: LiNbO3 crystals with different doping concentration and treatment. Recording geometry: reflection

Doping Concentration and Treatment	Crystal ID	T_f(min)	P_f (μW)	R	$LSNR$ (dB)
Fe: 0.10%, As grown	A2	20	560	0.76	0.09
Fe: 0.01%, As grown	A	14	116	0.94	0.60
Fe: 0.004%, As grown	D	12	0	NA	0.04
Fe: 0.06%, Oxidized for 4 hours	6#	14	322	0.9	0.18
Fe: 0.06%, Oxidized for 24 hours	7#	20	180	0.9	1.43

Table II: Influence of fanning noise on the image fidelity for different recording geometry

Recording Geometry	Crystal ID	Dopant	T_f(min)	P_f (μW)	R	$LSNR$ (dB)
Reflection	8#	Fe: 0.08%	16	220	0.93	0.13
Transmission	9#	Fe: 0.08%	0.6	NA	0.94	3.47
90-degree	S4	Fe: 0.03%	10	NA	0.95	0.09
	S3	Fe: 0.03%, Ce: 0.1%	13	NA	0.96	0.36

Table III: Influence of fanning noise on the image fidelity for samples with different dopants

Dopant	Crystal ID	Recording Geometry	T_f(min)	P_f (μW)	R	LSNR (dB)
Fe: 0.08%, Mn: 0.05%	2B		29	199	NA	0.81
Fe: 0.03%, Ce: 0.05%	Ce2	Reflection	28	1	0.84	0.36
Fe: 0.08%	8#		16	220	0.93	0.13
Fe: 0.03%, Zn: 6mol%	2#	Transmission	50	NA	0.67	0.03

DISCUSSION

It is obvious from Table 1 that heavy doping of iron in $LiNbO_3$ causes serious fanning which degrades the image quality. This is because the dopants act as additional scattering centers. Strong oxidation makes situation even worse. Since the oxidization process increases the concentration of Fe^{3+}, this suggests that Fe^{3+} irons contribute more to the scattering than Fe^{2+}. Shown in Fig. 1(a) is the image formed through the crystal 9# before it was exposed to the intense reference beam. The image quality is fairly good. In contrast, the image formed through the same crystal after coherent illumination for only 36 seconds was entirely destroyed as shown in Fig. 1(b). From Table 2 one can see that the 90° geometry is least subject to the influence of scattering noise, while the transmission geometry is most. Table 3 shows clearly that an additional dopant of Mn or Ce co-doped with Fe in $LiNbO_3$ crystals causes normally more serious scattering. However, when the additional dopant is Zn, the situation reversed. Doping of a certain amount of Zn as an anti-photorefraction dopand in $LiNbO_3$ effectively reduced the scattering noise effect.

(a)   (b)

Fig. 1 Image formed through crystal 9# (a) before and (b) after the crystal being exposed to an intense coherent beam for 36 seconds (*LSNR*=3.47).

<div align="center">(a)   (b)</div>
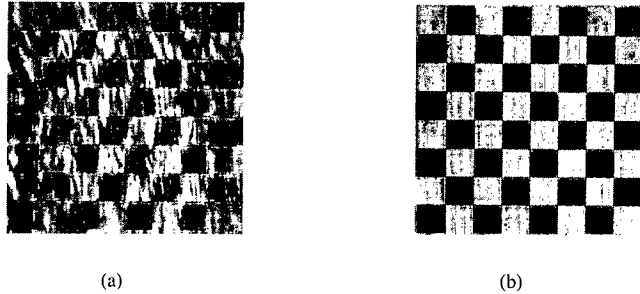
Fig.2 Image retrieved from a hologram stored in (a) crystal 9# with 7 minutes of coherent illumination before storage, and (b) crystal 2# with 50 minutes of coherent illumination before storage.

Comparing the far-right 3 columns in Table 1 through Table 3, we can see that there is no strict correlation between the decrease of SNR of an image and the fanning effect measured as P_f or R. Thus, we cannot determine if a crystal is suitable for holographic storage according only to the amount of measured scattering. On the other hand, the decrease of SNR, $LSNR$, does describe the image fidelity of a hologram. Figure 2 illustrates that holograms of data pages stored in crystal sample 2#, chosen by using the above method, reached satisfactory data fidelity.

CONCLUSIONS

This research investigated how the scattering noise influences the quality of an input data page in holographic storage. The experimental results show that among the three recording configurations, 90° geometry is least subjected to light-induced image-fidelity degradation. The intensity of fanning light increases with increase of the doping concentration, but there is no strict correlation between the fanning strength and the fidelity degradation. Therefore, one should not determine whether or not a crystal is suitable for high-fidelity holographic storage only according to its fanning power. The loss of SNR introduced in our work provides a better assessment for the suitability of the crystal for data storage. Owing to the low noise and high data fidelity, iron-and- zinc co-doped lithium niobate crystals are potential materials for high-density holographic storage.

ACKNOWLEDGEMENTS

REFERENCES

1. D. Psaltis and F. Mok, *Scientific Amer.* **273**, 553 (1972).
2. F. Mok, *Opt. Lett.* **18**, 915 (1993).
3. Geoffrey W. Burr, C. Michael Jefferson, Hans Coufal, Mark Jurich, John A. Hoffnagle, Roger M. Macfarlane, Robert M. Shelby, *Opt Lett.* **26**, 444 (2001).
4. Xianmin Yi, Pochi Yeh, "Cross-talk in Volume Holographic Memory," Proceedings of the IEEE, Vol. 87, No.11, Nov. 1999.
5. Shiquan Tao, Bin Tang, Yan Zhou and Lansun Shen, *Appl. Opt.* **38**, 3767 (1999).
6. J. Feinberg, *J. Opt. Soc. Am.* **72**, 46 (1982).
7. Liu Simin, Guo Ru, Lin Zhenfang, *"Photorefractive Non-linear Optics"*, (China Standardization Press, 1987) pp135-170 (in Chinese)
8. Nouel Kamber, *"Light intensity effect in photorefraction of doped lithium niobate (LiNbO₃) crystal and the improvement of its photorefractive properties with different dopants,"* Ph.D. Dissertation, Nankai University, China (2000)

**Optical Data Storage:
Materials and Mechanisms**

Human Brain Like Memory Behavior in the Magnetic Domain Expansion Type Magneto-Optical Disk

Norio Ota, Hiroyuki Awano, Manabu Tani and Susumu Imai
R&D Division, Hitachi Maxell Ltd.
6-20-1 Kinunodai, Yawaramura, Ibaraki 300-2496 Japan

ABSTRACT

Magnetic Amplifying Magneto-Optical System (MAMMOS) shows human brain like memory behavior. Magnetic field and laser power have threshold to recover the stored memory like the human response of remembering. MAMMOS also has a feature to amplify very small recorded signals like our recovery of memory, e.g. fifty years ago episode.

By adding the meaningful information on the magnetic field pattern, we can get some correlation between our memory and external stimulation. Such scheme is named as "the Active readout MAMMOS" which is analogues to the human process of remembering the memory.

If the applied field pattern and timing phase just coincide with stored information, there occurs the coherent amplification of MAMMOS signal. We can utilize such phenomena as the trigger of "Memory Association".

INTRODUCTION

Human brain long term memory is so mysterious comparing the current man made disk storage like magnetic disks and optical disks. During our life, we may store so huge memory contents inside our brain. In our usual daily life, we never aware of such terribly giant memories, almost seems that we had forgotten almost 99.9% or more. However, once we are stimulated by specific scenes or sounds, we can clearly remember the old episode.

Recent study on brain's long term memory [1] shows very interesting hypothesis, that is, memory perception (writing) and memory retrieval (readout) are bi-directional signaling between temporal cortex (TE) and peripheral cortex (PRh). By the visual pair-association task tested in monkey brain, long term memory stored in PRh are retrieved TE neurons.

Magnetic amplifying magneto-optical system (MAMMOS) gives very huge capacity rewritable disk by using a domain expansion phenomenon in a readout layer overlayered on a recording layer [2,3]. In the area of Magneto-Optical disk storage, the analogy of PRh to the recording layer and TE to the readout layer is useful to create the new type of human made memories. In the very high density area overcoming the optical resolution limit, MAMMOS shows very high signal to noise ratio [3]. For readout, we used mono tone-single frequency external magnetic field to expand and collapse the magnetic domain. In this scheme, external magnetic field only plays giving the excitation energy to readout very faithfully a series of chained stored information.

However, once we changed such scheme, that is, if we intentionally give the some meaningful information on the external magnetic field on behalf of mono-tone field repetition, we can expect human brain like memory behavior in MAMMOS as a new type of association memory, which retrieves long term memory stored in the recording layer. Here, we firstly show such experiments under the name of "Active readout MAMMOS".

PRINCIPLE OF BASIC MAMMOS AND EXPERIMENTS

MAMMOS disk has two magnetic layers as shown in figure 1, one is a recording layer which stores very high density magnetic domains recorded by magnetic field modulation method [4]. Material is TbFeCo amorphous film with 40nm thickness. Another one is 20nm thick readout layer (expansion layer in the figure) made by GdFeCo with a low Coersive force Hc. This readout layer is magneto-statically coupled with TbFeCo recording layer.

By applying a focused laser beam on such coupled films to elevate the temperature to about 120 C, one recorded domain is easily copied to a readout layer. Just at the same timing, the external magnetic field of about 200 Oe is applied upwards. This field causes the expansion of the copied domain in the readout layer, which brings a very large signal enhancement.

Recent results show very remarkable results [5], that is, only 20nm length recorded mark is expanded to 1200nm wide size giving full amplitude saturation level signals. Amplification ratio is 60 (6000%).
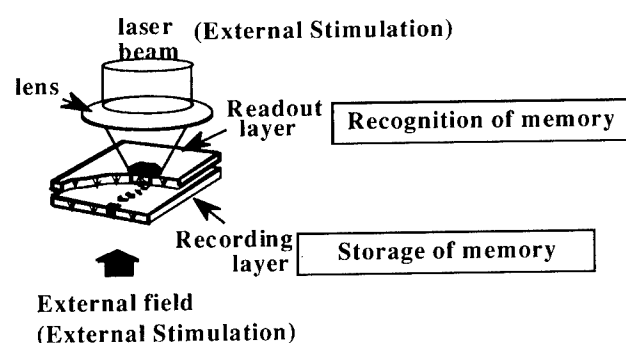
Figure 1. Principle of Magnetic AMplifying Magneto-Optical System (MAMMOS). A recording layer stores very tiny high density magnetic domains. By elevating a temperature by a focused laser beam, a domain is copied to a readout layer, and expanded by an upward direction external field.

Figure 2 shows a typical basic MAMMOS experiment. Wavelength of the laser is 680nm while lens numerical aperture is 0.55. For writing, laser power is 10mW at a linear velocity of 2.5m/s, applied magnetic field is 200 Oe. While for MAMMOS readout experiment, laser power is 2.8mW. Applied field has mono-tone single frequency (6.25MHz) with amplitude of +/- 200 Oe.

The shortest mark/space is 400nm with 160 nsec time period. Figure 2,C is an example of recorded magnetic field pattern equal to stored bit pattern like /100110100010......./. Figure 2, B shows a serial mono-tone external field excitation which causes a MAMMOS readout signal resulting in figure2, A. Full swing large signals are recognized showing very precise recorded pattern.

On the analogy of human brain memory, such basic MAMMOS has two distinct features as like,

1) There is a certain threshold in laser power and magnetic field to remember the memorized contents deeply stored inside of the disk (recording layer). Laser power and magnetic field are regarded as the external stimulation like light beams and/or sounds surrounding us (human beings). Less laser power, less magnetic field brings nothing memory recovery as like our mind are almost calm against so many past memories. It is likely that our inside storage capacity looks so small in usual.

2) The amplification of memory elements is remarkable phenomena in MAMMOS. Our old memory (sometimes 50 years ago episode) may be stored in our brain as some elements with very small signal. However, once we are stimulated by an exceptional happenings, for example when we accidentally met a lost lover on the street, we can clearly remember the fifty years ago scene, sounds, details of conversation and so on.
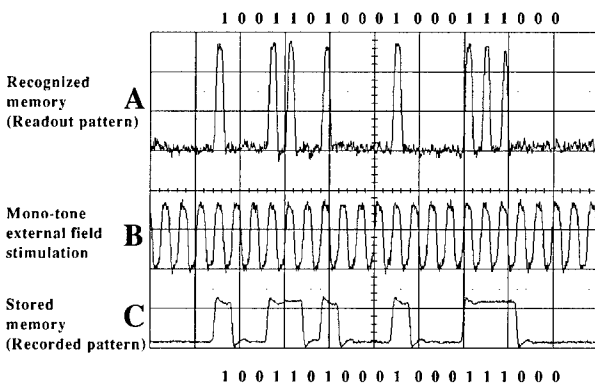
Figure 2. Basic MAMMOS experiments. Mono-tone single frequency modulated magnetic field amplifies recorded signals stored in a recording layer by a domain expansion mechanism in readout layer.

ACTIVE READOUT MAMMOS

Resemblance between Human brain memory and basic MAMMOS, we can consider new schemes of memory recovery, named the Active readout MAMMOS, in which we apply magnetic field pattern having meaningful digital information. One example is shown in figure 3. Applied external field pattern is illustrated in B, which has a series of digits /100110100010.../. Originally stored domains in a recording layer are in C. Only the positions coincided both applied field and recorded domains are amplified as big signals as shown in A.

Applied field pattern is a model of specific external stimulation like a beautiful scenery, comfortable sounds. If this new experience is not matched with old memorized one, we cannot remember it as a similar experience. Coincidence between B and A is not so good.
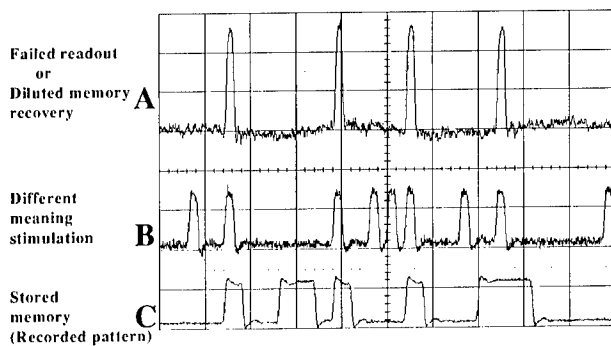
Figure 3. Active readout MAMMOS, applied field has a meaningful digital information (B). Only the matching portions with original recorded patterns (C) are amplified as MAMMOS readout patterns illustrated in A.

IN-PHASE ACTIVE READOUT MAMMOS

If the phase and digital patterns of external field just coincide with original recorded patterns as shown in figure 4,B and C, we can recognize the amplified read out pattern in A as like just exactly the same pattern with B. Comparing with in-put magnetic field pattern B and out put signal pattern A, we can notice that the original recorded pattern is also the same which means we already experienced the similar thing in the past.

This means some kind of Memory Association, or the starting trigger of the memory association. When we notice such nice coincidence between A and B, we may have psychological satisfaction or pleasure in brain. This satisfaction brings a trigger of reading out the succeeding memory contents stored in the next paragraph or sometimes linking to other disks having the similar coincide facts. In our daily expression, it is so called "Memory Association".
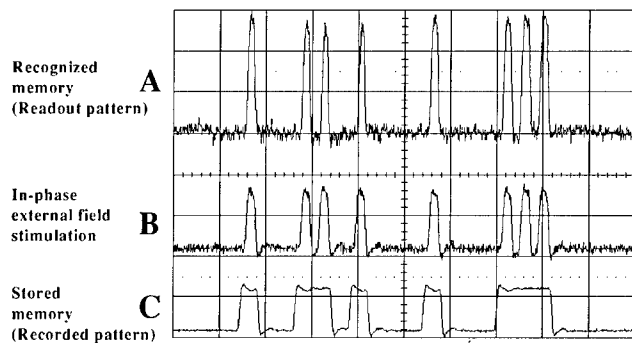
Figure 4. Memory recognition scheme by In-phase Active readout MAMMOS. When the magnetic field pattern and timing phase (B) just coincide with memorized contents (C), recognized pattern (A) shows the best matching with in put pattern. This may suggest the scheme of Memory Association device.

OUT- OF- PHASE ACTIVE READOUT MAMMOS

In active readout MAMMOS, if the timing phase of magnetic field had some shift as shown in figure 5,B and C, there occurs a failure of memory recovery (see figure 5,A). This suggest that we may see in our eyes, hear by ears physically what we already experienced, but never notice the fact until we get some phase matching. In Japan, there is a very famous proverb, "Looking but not seeing".
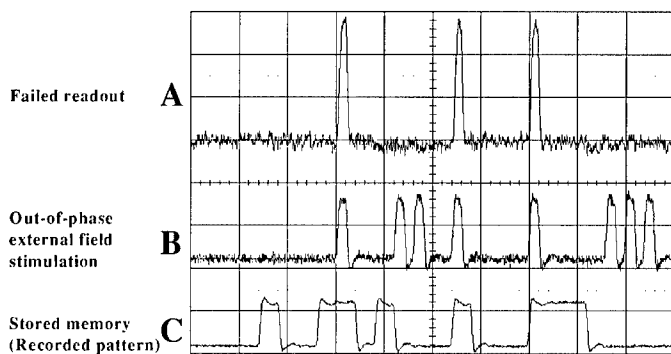
Figure 5. Failure of memory recovery by a out-of-phase external field excitation in Active readout MAMMOS

CONCLUSIONS

Using the phenomena of Magnetic AMplifying Magneto-Optical system (MAMMOS), we proposed a new memory scheme showing human brain like memory behavior, named Active readout MAMMOS.
1) Basic MAMMOS has two features analogues to human memory behavior, one is threshold strength of magnetic field and laser power(external stimulation) to recovery the old memory . Another is an amplification of very small recorded signal like man remembering the 50 years ago episode.
2) By applying the magnetic field corresponding to the previously determined information, the MAMMOS readout signal shows logical "AND" states between the stored memory and field patterns. This active readout MAMMOS is similar to the psychological interaction between our memory and external stimulation.
3) If magnetic field pattern and timing phase just coincide with memory contents, there occurs coherent excitation of MAMMOS signal. We can utilize such status as the trigger of Memory Association.

REFERENCES

1. Y. Naya, M. Yoshida and Y. Miyashita, Science, **291(5504)**, 661 (2001)
2. H.Awano,S.Ohnuki,H.Shirai,N.Ohta,A.Yamaguchi,S.Sumi,and K.Torazawa, Appl.Phys.Letters, **69**, 4257 (1996)
3. H.Awano and N.Ohta, IEEE J.Selected Topics in Quantum Electronics, **4**, 815 (1998)
4. H.Miyamoto,T.Niihara,H.Sukeda,M.Takahashi,T.Nakao,M.Ojima and N.Ohta, J.Appl.Phys., **66**, 6138 (1989)
5. H.Awano,M.Sekine,M.Tani,N.Kasajima,N.Ohta,K.Mitani,N.Takagi and S.Sumi, Jpn.J.Appl.Phys., **39**, 725 (2000)

Investigations of Sputtered Silver Oxide Deposits for the SUPER–RENS High Density Optical Data Storage Application

Dorothea Büchel, Christophe Mihalcea, Toshio Fukaya, Nobufumi Atoda and Junji Tominaga
National Institute of Advanced Industrial Science and Technology (AIST),
Laboratory for Advanced Optical Technology (LAOTEC),
Tsukuba Central Research Site 4,
1-1-1 Higashi, Tsukuba-city, Ibaraki 305-8562, Japan

ABSTRACT

Thin silver oxide films used as mask layers in super-Resolution Nearfield Structure (super-RENS) disks for high density optical data storage were reactively sputter-deposited and their composition was determined by spectroscopic means. We found that the stoichiometry of the films changed with the oxygen content in the sputtering gas atmosphere. With a stepwise increase in the percentage of O_2 from 0 - 100%, the corresponding layers consist of Ag, mixtures of Ag and Ag_2O, Ag_2O, mixtures of Ag_2O and AgO and AgO. Laser activation of such oxidic phase containing deposits results in the decomposition of the material and excitation of strong local plasmons in the remaining silver clusters. This was confirmed by acquiring surface enhanced Raman spectra (SERS) of benzoic acid (BA), copper phthalocyanine (CP) and internal carbon impurities on silver oxide substrates. From this data, we conclude that the sub-wavelength resolution obtained in super-RENS disks is mediated by local surface plasmons on small silver particles forming in the mask layer.

INTRODUCTION

Super-RENS is a promising technique to achieve high density optical data storage. The light scattering center-(lsc-)super-RENS disk (1), developed in 1999 uses a silver oxide mask layer in close proximity to a phase change storage layer to overcome the diffraction limit in conventional optical data storage applications. Kim et al. (2) recently showed that the application of a silver oxide mask layer in combination with a magneto-optical storage layer also enables the generation of marks with dimensions well below the diffraction limit. Figure 1 displays the general super-RENS layer structure together with a comparison of CNR against mark size for the respective structure and a conventional phase-change disk. The applied readout power as well as the required recording power is generally higher in the super-RENS case to obtain the maximum signal resolution. However, the mechanism of LSC super RENS is still under discussion. Recent studies (3) supported the suggestion that the super resolution effect is mediated by strongly scattering local surface plasmons which are stimulated on Ag particles in the mask layer. These Ag clusters are photothermally generated through the decomposition of silver oxide to silver and oxygen. During the read out process, the impinging laser beam excites the Ag particles and simultaneously produces optical near fields on the marks in the recording layer. The
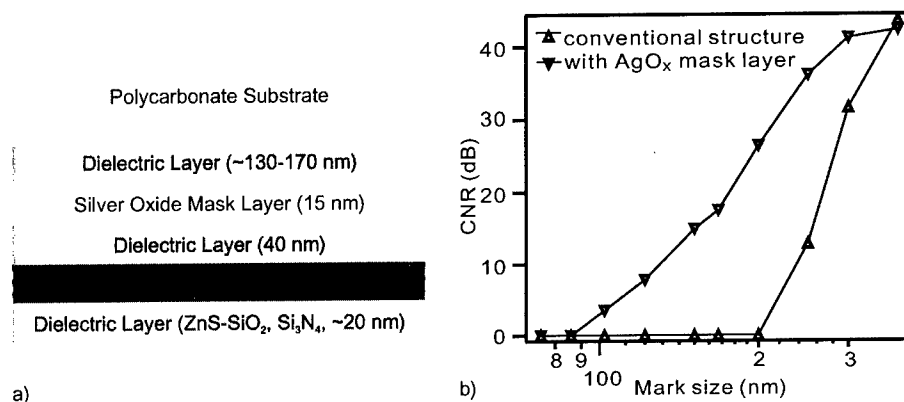
Figure 1. a) Schematic structure of a lsc-super-RENS disk. b) Mark size and correlated CNR for a lsc-super-RENS disk (readout power 3.5 mW) and a conventional optical disk (readout power 1.5 mW). Laser wavelength was 635 nm, NA 0.6 and constant linear velocity was 6 m/sec.

superposition of these laterally confined fields with the local plasmons on the adjacent Ag particles is then thought to give rise to the observed sub-wavelength resolution.

The intention of this work is to gather chemical and optical characteristics of sputtered silver oxide layers for a better understanding of the decomposition pathway and the eventual excitation of local plasmons in emerging silver clusters. It was suggested (3) that local surface plasmons contribute to the enhanced CNR in super-RENS experiments, hence the interaction of such layers with suitable molecules should give rise to surface enhanced Raman scattering (SERS) (4; 5). To prove this, silver oxide layers are produced by reactive sputtering with parameters resembling those of the super-RENS disk fabrication, however, the oxygen concentration in the sputtering gas mixture was varied from 0 to 100% to obtain layers composed of different phases. These layers were probed by Raman spectroscopy and the complex refractive indices were measured.

EXPERIMENTAL

Silver oxide films were deposited by reactive r.f. magnetron sputtering of a 3-inch Ag target (99.999% purity) on either glass slide or polished silicon wafers. Layers of different composition were obtained by changing the gas ratio of O_2 and Ar. Details are given in reference (6). The flow of individual gases was adjusted by mass flow controllers such that a total flow of 20 sccm was maintained. Since the deposition rate changed with varying oxygen content, the sputtering time was always adjusted to obtain films of either 300 nm thickness for the subsequent layer characterization, or of 15 nm thickness to imitate super-RENS conditions during the SERS experiments. The Ag target was pre-sputtered in the respective atmosphere for one minute. The sputtering pressure and applied r.f. power were fixed at 0.5 Pa and 200 W (4.4 W/cm^2) throughout each deposition.
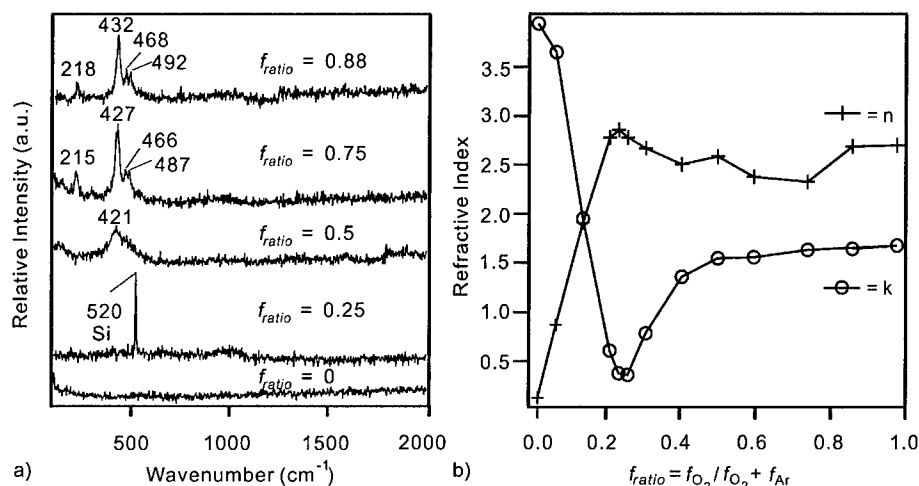
Figure 2. a) Raman spectra of AgO_x layers obtained by sputtering at different f_{ratio}. b) Complex refractive indices of AgO_x layers as a function of oxygen concentration in the sputtering gas mixture.

Micro Raman measurements of the sputtered layers on silicon were carried out with a Renishaw Ramanscope equipped with an argon-ion-laser ($\lambda = 488$ nm) in backscattering geometry. The laser spot size at the sample surface was diffraction limited and estimated to be ≈ 2 μm. The laser power was adjusted to 300 μW and the samples were ice cooled and measured under nitrogen atmosphere to avoid light induced changes in the layers. Detection times of 10 s together with 100 accumulations per run compensated for poor signal to noise ratios. Powder samples of commercially available silver oxides AgO (Fluka, Aldrich) and Ag_2O (Kanto Chemicals), benzoic acid (Kanto Chemicals), copper phthalocyanine (Aldrich) as well as high purity carbon pressings (Kojundo Chemical Laboratory) and 2-propanol (Fluka) were used to confirm reference Raman spectra of the respective compounds.

SER spectra of benzoic acid were acquired by immersing a AgO sample into 10 mL of a 10^{-4} M benzoic acid/2-propanol solution. In the case of copper phthalocyanine, a film several monolayers thick was evaporated directly onto AgO. The resulting intense SER spectra where recorded with an excitation power of 400 μW and 5 s integration time.

Refractive indices of the films were measured with a DHA-OLX/S4M MIZOJIRI ellipsometer at a wavelength of 632.8 nm.

RESULTS

In the following discussion, we describe characteristics of the deposited AgO_x-films obtained at a particular f_{ratio}, whereby f_{ratio} is expressed as ratio of the oxygen flow and the total flow of oxygen and argon in the sputtering gas mixture according to the equation

$$f_{ratio} = f_{O_2}/(f_{Ar} + f_{O_2}).$$

Raman spectroscopy was carried out to determine the layer composition. Spectra of layers with selected f_{ratio} were obtained in nitrogen flow under intensive cooling of the samples and are shown in figure 2 a. It was necessary to apply those precautions, since without them the silver oxide films readily underwent decomposition as a result of interaction with the laser beam. The laser intensity had to be adjusted carefully to compromise between the very low Raman scattering cross section of the silver oxides and their tendency to decompose. Layers obtained at $f_{ratio} = 0$ showed in agreement to bulk Ag no Raman peaks in the region between 110 cm^{-1} and 2000 cm^{-1}. For $f_{ratio} = 0.25$ no specific Raman peaks can be found but the characteristic band of the silicon substrate material at 520 cm^{-1} is clearly visible due to the high transparency of such films (discussed below). Hamilton et al. (7) verified that electrochemically generated Ag$_2$O is not Raman active due to the symmetry of the crystal lattice but assigned bands at about 220 cm^{-1}, 430 cm^{-1}, 470 cm^{-1}, 490 cm^{-1} to AgO. Our layers deposited in the range between $f_{ratio} = 0.5$ and $f_{ratio} = 0.75$ showed the same characteristic bands with increasing intensities for increasing oxygen concentration.

The assignment of specific oxidic phases to distinct f_{ratio} values was substantiated by measurements of complex refractive indices of the layers. Figure 2 b shows values obtained for n and k as a function of the oxygen concentration during the deposition. The graphs show a characteristic run for rising oxygen content in the AgO$_x$ layers. For pure silver, the refractive index was measured to be $n = 0.08 + 3.98i$. For increasing oxygen concentrations up to $f_{ratio} \approx 0.25$, the real part increases to 2.79 whereas the imaginary parts drops to about $0.31i$, indicating the presence of a highly transparent silver (I) oxide (Ag$_2$O) film (10) in accordance to the previously described Raman measurements. Further oxygen addition leads to an immediate rise of the imaginary part to $1.7i$ where it stabilized, while the values for the real part changed only slightly. The results are summarized in table I.

However, when samples were not cooled while Raman spectra acquisition proceeded, they underwent visible changes at the laser position in form of specular spots. Simultaneously, two additional broad and intense peaks at about 1380 cm^{-1} and 1580 cm^{-1} developed and soon dominated the spectrum. These huge peaks have often been observed while performing SERS on suitable silver samples and have been assigned to amorphous carbon (8) or nanocrystalline carbon residues (9) on their surfaces. In our case, carbon traces were incorporated during the deposition process. Figure 3 a shows typical examples of such spectra obtained on different silver oxide substrates. The time dependent development of the SERS intensities in each individual spectrum was different. In case of Ag$_2$O ($f_{ratio} = 0.25$), the surface enhanced peaks were immediately formed whereas layers with higher oxygen content needed a longer activation time. Above a certain threshold

Table **I**. Layer composition as a function of oxygen flow ratio

f_{ratio}	0	0.175	0.25	0.5	0.75
Layer Composition	Ag	Ag + Ag$_2$O	Ag$_2$O	Ag$_2$O + AgO	AgO
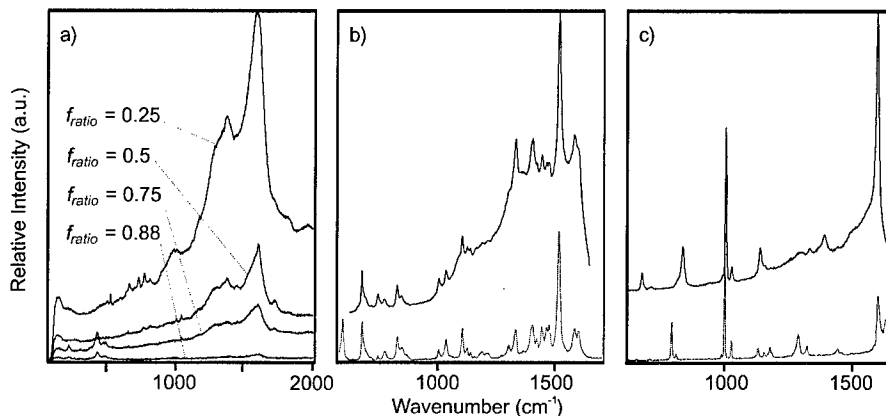
Figure **3.** a) SERS of layer-internal α-carbon impurities and benzoic acid (b)/copper ph-thalocyanine (c) on silver oxide films. The dotted curves are conventional Raman spectra of powder standards shown for comparison.

power, all layers showed comparable activity. Obviously, layers with a smaller oxygen content decompose faster than oxygen rich phases, probably due to silver nucleation sites which are already present in the film. To check for the potential feasibility of the sputtered films to SER spectroscopy, we applied several external chemicals to the layers and recorded the resultant spectra. It turned out that the activated surface is suitable to amplify Raman bands of a variety of low concentrated compounds. Figure 3 b and c shows examples of SER spectra (solid lines) of evaporated copper phthalocyanine and of a 10^{-4} M benzoic acid solution. For comparison, conventional Raman spectra of corresponding powder samples (dotted lines) are also shown. BA and CP were applied to the silver oxide layers in concentrations that are not detectable by conventional Raman spectroscopy but produced a clear and intense SER signal. The observed shifts in specific SERS peak positions and intensities depend on the interaction of the molecules and the silver oxide surface. The bonding of functional groups to the substrate influences the symmetry of the molecule as well as the intermolecular distances and leads to characteristic shifts and/or the appearance of previously forbidden bands in the spectra. A detailed discussion can be found in the SERS review of Moskowits (11).

There is general agreement that a major contribution to SERS effects is achieved by strongly scattering local surface plasmons on specific substrate materials. Our results support the hypothesis that activated silver oxide layers, as applied in super-RENS disks, could provide a mark signal amplification by electromagnetic field enhancement.

Conclusions

Reactively sputtered silver oxide layers were probed by Raman spectroscopy and the complex refractive indices were measured. The results indicated that the main constituents

gradually change from Ag over Ag_2O to AgO with increasing oxygen content in the sputtering gas atmosphere. Raman spectra of cooled thin films provided a characteristic band at 432 cm^{-1} as proof of the presence for AgO. Layers deposited at low oxygen concentration with a refractive index of $n = 2.79 + 0.31i$ were determined to be composed of Ag_2O. Super-RENS mask layers, deposited at a medium oxygen concentration could be identified as a mixture of Ag_2O and AgO. Furthermore, we found that thin oxide layers readily decompose to silver particles and oxygen upon photothermal activation. The silver clusters sustain strong local surface plasmons and change the substrates to effective surface enhanced Raman spectroscopy substrates. This was proofed by the development of characteristic SERS peaks of layer-internal α-carbon trace impurities, diluted benzoic acid/2-propanol solutions and evaporated copper phthalocyanine.

References

[1] H. Fuji, J. Tominaga, L. Men, T. Nakano, H. Katayama, and N. Atoda, *Jpn. J. Appl. Phys.*, **39(I, 2B)**, 980, 2000.

[2] J. H. Kim, D. Büchel, T. Nakano, J. Tominaga, N. Atoda, H. Fuji, and Y. Yamakawa, *Appl. Phys. Lett.*, **77**, 1774, 2000.

[3] J. Tominaga, C. Mihalcea, D. Büchel, H. Fukuda, T. Nakano, N. Atoda, H. Fuji, and T. Kikukawa, *Appl. Phys. Lett.*, **78**, in press, 2001.

[4] M. Fleischmann, J. P. Hendra, and A. J. McQuillan, *Chem. Phys. Lett.*, **26**, 163, 1974.

[5] J. A. Creighton, C. G. Blatchford, and M. G. Albrecht, *J. Chem. Soc. Faraday Trans.*, **2(75)**, 790, 1979.

[6] D. Büchel, J. Tominaga, T. Fukaya, and N. Atoda, *J. Magn. Soc. Japan*, **25(3-2)**, 240, 2001.

[7] J. C. Hamilton, J. C. Farmer, and R. J. Anderson, *J. Electrochem. Soc.*, **133(4)**, 739, 1986.

[8] J. C. Tsang, J. E. Demuth, P. N. Sanda, and J. R. Kirtley, *Chem. Phys. Lett.*, **76(1)**, 54, 1980.

[9] P. J. Moyer, J. Schmidt, L. M. Eng, and A. J. Meixner, *J. Am. Chem. Soc.*, **122**, 5409, 2000.

[10] A. A. Schmidt, J. Offermann, and R. Anton, *Thin Solid Films*, **281-282**, 105, 1996.

[11] M. Moskowits, *Rev. Mod. Phys.*, **57(3-1)**, 783, 1985.

A Study on Batch Method of Thermal Fixing for Multiplexed Holographic Recordings

Zhuqing Jiang, Gang Meng, Guoqing Liu and Shiquan Tao
College of Applied Sciences, Beijing Polytechnic University, Beijing 10002, China

ABSTRACT

We have investigated the batch method of thermal fixing for multiplexed holograms. The batch fixing process is pictured and analyzed, for the first time to our knowledge. The batch procedure of thermal fixing includes optical erasure of electronic gratings by subsequent recordings both in the same batch and in different batches, ionic compensation during thermal fixing in one batch, smoothing of ionic gratings during thermal fixing of subsequent batches, and revealing of ionic gratings. The inter-batch optical erasure time constants of LiNbO3:Fe:Ce crystals are measured in experiment.

INTRODUCTION

Photorefractive crystals are commonly used as a recording medium in volume holographic storage. According to the charge excitation and transport mechanism, the electronic charges constitute holograms in photorefractive crystals to store some desired optical information. However, the above mentioned mechanism similarly causes optical erasure of holograms in further illumination process. Therefore, the recorded holographic gratings, i.e., the electronic gratings, are not permanently maintained in photorefractive crystals. In order to overcome such optical erasure to holograms on readout, thermal-fixing technique has been developed [1-4]. Photorefractive holograms can be stabilized against readout by the thermal fixing process of heating the crystal during or after the writing stage to higher temperature. Most investigations on thermal fixing consist of a single process of heating. Since holographic storage in photorefractive crystals is aimed at achieving high-capacity storage, it is more important to investigate the thermal fixing of multiplex holograms. An et al. recently have performed the thermal fixing of 10000 holograms in Fe:LiNbO$_3$ [5]. However, the procedure of such thermal fixing has not been described well, and the method of thermal fixing for multiplex holograms is still to be further improved for getting higher after-fixing diffraction efficiency.

In this paper, the batch fixing procedure is described in detail by analyzing respective behaviors of both electronic and ionic gratings at every stage. The mechanism of slow optical erasure of electronic gratings by subsequent recordings in different batches and smoothing of ionic gratings during thermal fixing of subsequent batches for batch fixing multiplex holograms is, for the first time to our knowledge, further presented. Moreover, according to the diffraction efficiency measured in every stage of all the batches, the inter-batch optical erasure time constant and the dark decay time constant of electronic gratings at elevated temperature for co-doped lithium niobate crystals have been fitted out.

THEORY

Schemes of single thermal fixing

The procedure of thermal fixing consists of three steps: recording, fixing and revealing. Firstly, electronic gratings, which replicate the exposing light patterns, are recorded in a crystal

via illumination by spatially varying intensity patterns. In a fixing process when ionic conductivity dominates electronic conductivity at elevated temperature, the ions in the crystal move to compensate the light-induced space-charge distribution and form an ionic grating replicating the electronic grating. At room temperature the ionic conductivity is much smaller than the photoconductivity of the electrons. Therefore, in a revealing process at room temperature, the electronic gratings are partially erased by noncoherent uniform light, and then a net space-charge field dominated by the ionic gratings is left. Since the ionic gratings are much more stable against further optical erasure at room temperature than the relevant electronic gratings, the fixed holograms can be preserved for longer time.

At present, there are commonly two kinds of schemes available for thermal fixing of photorefractive holograms, called post-compensation and simultaneous storage and fixing at elevated temperature, respectively. For multiple holograms, the optical erasure time constant of light-induced gratings is a finite value. The diffraction efficiency of each hologram in a large scale of multiplexing holographic storage is commonly very small, since subsequent writing processes can partially erase the existing holograms stored in a photorefractive crystal. The diffraction efficiency of the hologram after fixing is usually much smaller than that of the original hologram. Therefore, if multiple holograms are fixed by using a post-compensation scheme, that is, the crystal is heated only after recording all the desired holograms, their diffraction efficiency will become rather small. If fixed by using a simultaneous-compensation scheme, electronic gratings recorded are almost compensated by ions thermally activated simultaneously, and the effect of ionic pattern's shielding against electronic gratings weakens the optical erasure. Thus, in comparison with a post-compensation scheme, a simultaneous-compensation scheme is of benefit to higher diffraction efficiency after fixing. However, since the recording and revealing processes are carried out at different temperatures respectively, the fixed holograms suffer from distortion caused by thermal contraction and change of the refraction index of the material. Consequently, the variation in the Bragg angles of the fixed holograms, resulting from the above reasons, will bring the difficulty in reconstructing data pages completely for a practical multiplexing storage system. In multiplexed holographic storage, recording and reconstruction of fixed holograms should be performed at the same temperature, commonly at room temperature. Therefore, a batch-scheme of thermal fixing, combining the advantages of both above schemes, will be a good choice.

All the subsequent holograms are broken into several batches. Each batch is recorded at room temperature and then fixed at higher temperature, and finally all the batches are revealed in whole at room temperature. The batch scheme can avoid incomplete Bragg matching caused by thermal effect, because recording and readout both occur at room temperature. With many times heating, the diffraction efficiency of multiple holograms fixed in the batch scheme is able to increase effectively.

Batch scheme of thermal fixing

In the batch scheme of thermal fixing for multiplexed holograms, the multiplexing holograms to be recorded and fixed are divided into several sets, every set of holograms is subsequently recorded at room temperature and fixed at elevated temperature in order, respectively, up to having fixed all the sets of holograms. And then, after cooling down to room temperature, all the holograms of ionic gratings are revealed at the same time by illuminating them with noncoherent or uniform light.

All the N holograms are divided into S sets, each set including an equal number of holograms, $N_h = N/S$. Firstly, the N_h holograms in the first set are subsequently recorded in a

crystal, and then the crystal is heated in an oven so that all the N_h holograms are thermally fixed at the same time. In this process, the ions rapidly migrate at elevated temperature and form ionic gratings of compensating the first set of electronic gratings completely, which makes the net space-charge field become zero. After cooling down to the room temperature, the second set of N_h holograms are recorded in turn, which slowly erases the previous set of electronic gratings and thus partially reveals the respective ionic gratings. Since the migration rate of electrons is larger than that of ions ($\mu_e \gg \mu_i$), the optical erasure of ionic gratings is negligible in this process. Next, after heating the crystal again for the same amount of time, we find that the revealed portion of the first set of ionic gratings has been smoothed out and the second set of electronic gratings compensated with migration of thermal activation ions. The procedure above-mentioned is repeated until all N holograms are recorded and fixed. Thus, in the recording process, each set of electronic gratings except the first set suffer optical erasure by subsequent recordings both in the same batch and in different batches, and then in the fixing process, ionic compensation to the same batch of electronic gratings and smoothing for previous different batches of ionic gratings revealed partially during thermal fixing in every batch are achieved. The electronic grating strength of set m ($m=1,2\ldots\ldots S$) can be expressed by its index modulation Δn_e^m as

$$\Delta n_e^m = \Delta n_0 e^{-\frac{\sum_{i=1}^{S-m} t_{m+i}}{\tau_F}} \tag{1}$$

where t_{m+i} is the total writing time of holograms in the batch $m+i$, τ_F is the optical erasure time constant of electronic gratings by recordings in subsequent batches, and Δn_0 is the index modulation of electronic gratings in the first batch before thermal fixing. Δn_0 can be taken the equal value for all the gratings in the first batch by using proper exposure procedure. In the respective process of optical erasure after ionic compensating, with partially revealing effect of writing beams in subsequent batches on ionic gratings, movable electrons light-excited can drift and diffuse under effect of ionic charge field, and then screen the ionic patterns. The screening effect of trapped electrons on ionic gratings can reduce optical erasing, in that τ_F is larger than the optical erasure time constant τ_E of holograms without fixing. The screening depth considerably depends on the concentration N_a of electrons trapped deeply, space-frequency K of holographic gratings and the strength of photovoltaic effect.

In every process of heating a crystal for fixing holograms of different batches, electrons and ions are thermally activated at elevated temperature, respectively. Electronic diffusion and drifting both occur to decline the grating strength. Meanwhile, since the ionic migration rate is bigger than the electronic one, ions rapidly move to compensate electronic gratings once again. As a result, the strengths of ionic gratings in previous batches further decrease with their respective electronic gratings. Electronic gratings will decay exponentially in dark case. The index modulation Δn_{ed}^m of the set m of electronic gratings, which experience the procedure of optical erasure and dark decay effect during (S-m) times, can be written as

$$\Delta n_{ed}^m = \Delta n_e^m e^{-\frac{(S-m)T}{\tau_r}} \tag{2}$$

where T is the time for heating a crystal to achieve thermal fixing in one batch, τ_T is the dark decay time constant of electronic gratings at elevated temperature, relative to decay of grating strength in the dark case. The ionic grating strength is equal to that of electrons.

After recording and fixing according to the batch procedure, all the fixed holograms are revealed sufficiently. Finally, ionic holograms are obtained in batch fixing. Obviously, the last set of holograms experiences only one thermal fixing procedure of recording - compensation - revealing, but other sets also suffer the procedures of optical erasure and smoothing with different times. The time of optical erasure and smoothing for one batch of holograms depends on the number of batches recorded after it. Therefore, having accomplished the thermal fixing for S batches of holograms, the batch m experiences $(S-m)$ procedures of optical erasure and smoothing and one procedure of thermal fixing with post-compensation.

We refer to a single thermal fixing as the procedure of only including recording, compensation and revealing steps, no matter how many multiplexed holograms to be recorded. In the revealing process of a single thermal fixing, ionic gratings screened in part by trapped electrons are unable to be fully revealed, even though they completely replicate electronic holograms in the fixing process. Therefore, the ionic holograms are partially readout after a sufficient revealing process. For a single thermal fixing, the thermal fixing efficiency η_F for multiplexed holograms is defined as

$$\eta_F = \frac{\eta_i}{\eta_e} \tag{3}$$

where η_i is the diffraction efficiency of revealed ionic gratings, η_e diffraction efficiency of electronic gratings before fixing. Although η_F is a complicated function of both the storage material and optical system [5], it can also be measured experimentally.

Since the index modulation is proportional to the square root of the diffraction efficiency in the small modulation case, according to equations (1)~ (3), we can derive the index modulation Δn_i^m of revealed ionic holograms in the batch m as follow

$$\Delta n_i^m = \sqrt{\eta_F}\,\Delta n_{ed}^m$$

$$= \sqrt{\eta_F}\,\Delta n_0 e^{-\left(\frac{\sum_{i=1}^{S-m} t_{m+i}}{\tau_I} + \frac{(S-m)T}{\tau_I}\right)} \tag{4}$$

The time constants τ_F and τ_T are the complex functions of parameters of photorefractive material. Although time constants τ_T can be calculated according to electronic decay in the dark phase theoretically [3], but it is not practical to calculate τ_F for the respective crystal in theory. On other hands, the time constant τ_F is an important parameter in calculating exposure schedule of multiplexed holograms to equalize their diffraction efficiencies. Therefore, it is necessary to measure time constants τ_F for different crystal samples experimentally.

EXPERIMENT

The holograms were recorded with two ordinarily polarized beams with equal-intensity in reflection geometry. In the experiment, all 25 holographic gratings are divided into 5 batches, each batch including 5 gratings. Firstly, one batch of gratings was recorded at room temperature by use of angular multiplexing. After recording, the writing beams were blocked and the sample with one batch of gratings was heated in the dark to ~150°C to cause fast ionic transport, and soaked for about 20 min. to ensure that these electronic gratings were compensated by ions completely. Next, the sample was cooled to room temperature and the second batch of 5 holographic gratings was recorded in it. Then, the sample stored two batches of holographic gratings are heated to accomplish ionic compensation. Such procedure of recording and heating was repeated for all 5 batches of holographic gratings. Finally, ionic holograms were revealed with a non-coherent erasing beam.

In each recording stage, besides optical erasure inside one batch, recording of the subsequent batch of gratings slowly erased the previous gratings fixed, which results in a little revealing of ionic gratings. The smaller diffraction efficiency generated by the revealed portion of ionic gratings was observed in the experiment. We refer to this kind of optical erasure in different batches as inter-batch optical erasure, which have a longer erasure constant time than one in multiplexed recording without thermal fixing. During each heating process, in addition to compensating the present batch of electronic gratings, fast ionic transport also effaces the revealed portion of ionic gratings in previous batches. Therefore, there was no diffraction to be observed at the end of each heating stage of the experiment. As taken dark decay time constant $\tau_T = 10^{14}$s, the inter-batch optical erasure time constant τ_F of electronic gratings was fitted out according to the diffraction efficiency measured in every stage of all the batches (see figure 1). The inter-batch erasure time constants τ_F of batch thermal fixing for co-doped crystal samples, with different concentrations and treatments, were listed in Table I.
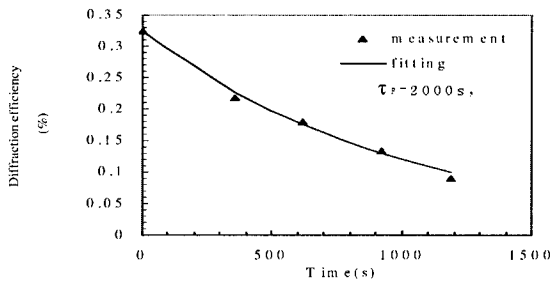
Figure 1. A fitted curve of the inter-batch optical erasure time constant τ_F for a Fe:Ce:LiNbO$_3$ crystal.

Table I. Comparison of ordinary erasure time constant and inter-batch erasure time constant (the wavelength $\lambda=0.633\mu m$, the total intensity $I_0=37$ mw/cm^2, dark decay time constant $\tau_T=10^{14}$s).

No.	Concen-tration (%)	O/R state	ordinary erasure time constant τ_E (s)	Inter-batch erasure time constant τ_F (s)
FC1	Fe:0.03 Ce:0.05	1050°C oxidation, 20 hours	3000	14000
D2B	Fe:0.03 Ce:0.05	As grown	1900	4300
FC2	Fe:0.07 Ce:0.20	1050°C oxidation, 20 hours	1500	4500
D3B	Fe:0.07 Ce:0.20	As grown	455	2000

The experimental results indicate that the inter-batch optical erasure time constant τ_F is indeed much longer than the ordinary erasure time constant τ_E. The result demonstrates that, since the migration of light-induced electrons is hampered by corresponding ionic gratings during inter-batch erasure, the optical erasure becomes much slower in the case of screening effect of ionic gratings on electronic ones.

CONCLUSIONS

The work investigated the batch method of thermal fixing for multiplexed holograms, in which the behavior of both electronic and ionic gratings is discussed in detail. There is a good agreement between the experimental result on inter-batch optical erasure time constant and the theoretical prediction. The result shows that the hampering effect of ionic gratings on trapped electrons reduces optical erasing in batch procedures, and hence, enhances the diffraction efficiency of fixed multiplexed holograms. This optical erasure time constant is required for designing the exposure schedule for large scale multiplexed storage to achieve equal diffraction efficiency holograms.

ACKNOWLEDGMENTS

REFERENCES

1. D. L. Staebler, W. J. Burke, W. Phillips and J. J. Amodei, *Appl. Phys. Lett.*, **26**(4), 182 (1975).
2. M. Carrascosa, and F. Agullo-Lopez, *J. Opt. Soc. Am. B*, **7** (12), 2317 (1990).
3. A. Yariv, S. S. Orlov and G. A. Rakuljic, *J. Opt. Soc. Am. B*, **13** (11), 2513 (1996).
4. J. F. Heanue, M. C. Bashaw, A .J. Daiber, R. Snyder and L. Hesselink, *Opt. Lett.*, **21**(19), 1615(1996).
5. X. An, D. Psaltis and G. W. Burr, *Appl. Opt.*, **38** (2), 386(1999).

Dynamic behavior of azobenzene polyester used for holographic data storage

Árpád Kerekes[a], E. Lőrincz[a], Sz. Sajti[b], P. Várhegyi[b], P. S. Ramanujam[c], S. Hvilsted[d]
[a]Department of Atomic Physics, Budapest University for Technology and Economics
 H-1111 Budapest, Budafoki 8., Hungary
[b]Optilink Hungary Ltd., Graphisoft Park, 1031 Budapest, Hungary
[c]Department of Optics and Fluid Dynamics, Risø National Laboratory,
 DK-4000 Roskilde, Denmark
[d]Danish Polymer Centre, Department of Chemical Engineering,
 Technical University of Denmark, DK-2800 Kgs. Lyngby, Denmark

ABSTRACT

Dynamic behavior of thin photoaddressable polyester films was studied. The saturation process due to Fourier holographic recording was investigated. Model experiments show an optimal intensity ratio of the object and reference beams, where the highest efficiency occurs. This ratio is inversely proportional to the reference intensity. The material has a significantly higher sensitivity at 407 nm than at 532 nm. For 1 µm thick sample an M# of 0.25 was measurable.

INTRODUCTION

Photoaddressable polymers [1] are candidate materials for holographic data storage. Such polymers are being developed at Risø National Laboratory in Denmark [2,3]. High storage density can be achieved by recording Fourier hologram of the binary object. Similar method is used in many applications [4,5]. The presence of high intensity peak at the Fourier plane saturates the recording material therefore a phase mask or shifting from the Fourier plane has to be used [5]. The second solution causes a significant decrease in the storage density. The recording system can be optimized by determining dynamic behavior of the recording material. Experiments with high intensity ratio plane waves were carried out for recording and demonstrating the saturation effect due to recording the Fourier transformed data page. The first section of the paper deals with these experiments.

The storage capacity can be further enhanced by reducing the writing wavelength and by multiplexing. The sensitivity factor of the material has been determined at two different wavelengths (532 and 407 nm). Multiplexing feature of the storage material is usually represented by the M# [6], a property dependent on both writing and erasure dynamics. We carried out several experiments in order to determine it. In the second and third section, we describe the investigation of the wavelength dependent sensitivity and multiplexing ability of the applied material.

SATURATION OF THE POLYMER

In our holographic memory system polarization holography is used [7] and the Fourier transformed data page is recorded by using orthogonal circularly polarized object and reference beams in an appropriate 8f arrangement [4]. A suitable model setup (see figure 1) was built to study the behavior of the material under extreme dynamic circumstances like recording Fourier holograms. Anisotropy gratings were recorded in the storage material using beams with

orthogonal circular polarizations and high intensity ratios. An intensity ratio of 500 has been achieved, which easily occurs when Fourier holograms are recorded.

There were two limiting factors in adjusting proper intensity ratio beams in the experiment. The maximum laser power (frequency doubled Nd:YAG, $\lambda = 532$ nm, $P_{output} = 50$ mW) and the detectability of the recorded holograms determined the upper and lower limits, respectively. These requirements provided the maximum and minimum applied intensities of the recording. We decreased the hologram size by using a lens (f = 140mm) to reach the maximum intensity. Since the hologram radius was small (≤ 0.27 mm) compared to the focal length of the lens, instead of plane waves, beams with nearly planar wavefronts and with negligible radius of curvature were used.
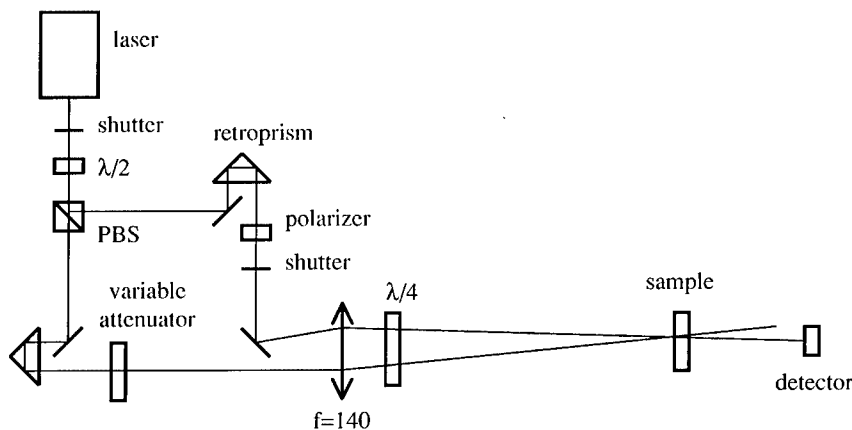
Figure 1. Experimental setup for recording polarization holograms with high intensity ratio beams, i.e. $I_{obj}/I_{ref} \leq 500$.

For the compensation of low coherence length laser (~1-2 mm) two retroprisms were used. The reference and object arms were set for optimum interference condition when maximum modulation of the interference fringes occurs, i.e. when the diffracted intensity has its maximum value.

It is well known that the process of writing polarization holograms in azobenzene polymers is often followed by creating surface grating [3,8] besides anisotropy grating in the bulk material. Since the creation of surface grating is slow [3] at the applied intensities, a suitable short exposure time ($t_{exp} = 0.5$ sec) was used. This exposure time satisfied also the requirement of detectability providing measurable diffracted power. Every hologram was made on the same place of the sample in order to get rid of sample inhomogeneity.

For readout we used the arm equipped with the attenuator in order to maximize the diffracted power. The power of the readout beam was the same for every experiment. Since the readout causes erasure of the hologram, the maximum value of the diffraction efficiency was measured by a detector connected to the computer by means of a fast digitizing card.

The recording material was an amorphous side-chain azobenzene polyester (E1aP) spincoated onto a glass sample. E1aP is prepared through melt transesterification of 3-[4-((4-

cyanophenyl)azo)-phenoxy]-1,2-propanediol and diphenyl phthalate. The thickness of the layer was 2 μm covered with a hard protective SiO_2 layer.

Two sets of measurement were carried out using two different hologram sizes (applied Gaussian beam radii were $w = 0.27$ mm and 0.11 mm). Figure 2 shows measured diffraction efficiency as a function of the intensity ratio of the object and reference beams for the larger hologram size (parameter: reference intensity). There is an optimum intensity ratio for a given reference intensity where the highest diffraction efficiency occurs. This optimum intensity ratio is inversely proportional to the reference intensity.
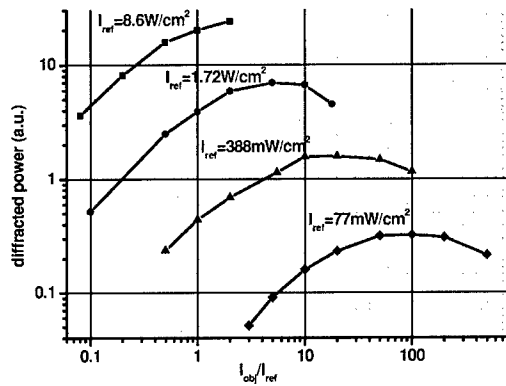
Figure 2. Measured diffracted power as a function of the intensity ratio of the object and reference beams at different reference intensities, radius of beams is 0.27 mm.
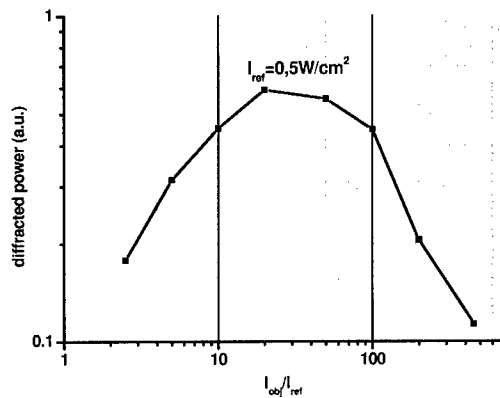
Figure 3. Diffracted power as a function of the intensity ratio of object and reference beams with beam radius of 0.11 mm.

Figure 3 shows results for the smaller hologram size (w = 0.11 mm), here the decreasing part of the diffracted power can is also be seen. The strong decay in the diffracted power for high intensity ratios is due to the saturation of the material.

BLUE SENSITIVITY

There is a strong demand in the optical data storage technology to apply the shortest available wavelength for recording in order to enhance the storage density. In our holographic memory system a frequency doubled Nd:YAG laser was used so far. The appearance of violet laser diode on the photonics market has opened the opportunity of using compact blue laser source for recording. Before the modification of the whole system, determination of the blue response of our polymer has particular importance.

Appropriate polarization holographic setups (similar to the setup in figure 1) were built for comparing blue and green responses of two different polymers (E1aP and E1aP/12) when using transmissive and reflective samples. E1aP12 is a three component polyester that contains both aromatic and aliphatic residues in the main chain.

A Kr^+ laser operating at 407 nm and a frequency doubled Nd:YAG laser at 532 nm were used for writing and we used a He-Ne laser at 633 nm for the readout in order to measure the diffraction efficiency in real time. The polymer has no absorption at this wavelength, so the readout in this region does not cause any erasure.

Time dependent exposures were performed at different intensities in order to compare the sensitivity of the material at different wavelength. Our goal was to determine the thickness independent sensitivity value S defined as usual

$$S = \frac{\sqrt{\eta}}{I \cdot t} \qquad [cm^2/J] \qquad (1)$$

where η is the measured diffraction efficiency at the writing intensity of I when using an exposure time of t. This value is often used in [9] in order to compare different holographic materials. Table I shows calculated sensitivity values of the azobenzene polymer samples when $\eta = 0.5\%$ was taken for comparison.

Table I. Sensitivity values of different transmissive and reflective polymer samples at the two wavelengths (d is the layer thickness).

Sample type and thickness / wavelength [cm²/J]			407 nm	532 nm
Transmissive	E1aP,	d = 0.9 µm	0.182	0.016
	E1aP/12,	d = 1.4 µm	0.245	0.034
Reflective	E1aP,	d = 1 µm	0.142	0.047
	E1aP/12,	d = 1 µm	0.230	0.050

Table I shows increased sensitivity of the azobenzene polymers at 407 nm. The ratio of the sensitivity values at the two wavelengths is between 3 and 11 depending on the polymer type and thickness. The increased sensitivity has a beneficial consequence to the writing speed at 407 nm.

MULTIPLEXING ABILITY: M#

A relevant feature of the holographic recording material is its multiplexing ability represented by the M#. This number characterizes the material and the applied experimental arrangement. There are two ways to determine it [6]. The first method is to make a large number of multiplexing (M) with a proper exposure schedule that results in equal hologram efficiencies. In this case

$$\eta = (M\#/M)^2 \qquad (2)$$

The other method is based on the assumption that each hologram evolves during recording as $A_0[1-\exp(-t/\tau_{rec})]$. This can be approximated at the initial time with A_0*t/τ_{rec} and the hologram decays during erasure as $\exp(-t/\tau_{erase})$. A_0 is the grating strength of the hologram, τ_{rec} and τ_{erase} are the time constants of recording and erasing, respectively. The ratio (A_0/τ_{rec}) and the time constant (τ_{erase}) can be determined by fitting appropriate parts of the experimentally measured $\sqrt{\eta}$ during recording and erasing, respectively. It is important that the writing and erasing intensity must be the same considering the intensity circumstances of multiplexing. The exact expression of the M# number is as follows:

$$M\# = (A_0/\tau_{rec})\,\tau_{erase} \qquad (3)$$

We used the second method for the determination of the M#. Several exposures were made and each of them was followed by erasure. The intensity was equally divided between the writing beams, so the erasing intensity was the half of the writing intensity. In order to be compatible with the theory, we made two holograms on each sample with 1 W/cm^2 and 2 W/cm^2 intensity. When calculating the M#, the evolving (A_0/τ_{rec}) factor was calculated from the measurement at $I = 1$ W/cm^2 writing intensity and the decay (τ_{erase}) factor calculated from the measurement at 2 W/cm^2 writing intensity. The experiments were carried out at both 532 nm and 407 nm either. Table II shows these values and the calculated M# factors.

Table II. M# for different polymer samples.

Transmissive samples		407 nm			532 nm		
		A_0/τ_{rec}	τ_{erase}	M#	A_0/τ_{rec}	τ_{erase}	M#
E1aP	$I = 1$ W/cm^2	0.22	1.6	0.202	0.025	8.04	0.126
$d = 0.9\ \mu$m	$I = 2$ W/cm^2	0.42	0.92		0.032	5.04	
E1aP/12	$I = 1$ W/cm^2	0.22	2.25	0.279	0.038	10.68	0.319
$d = 1.4\ \mu$m	$I = 2$ W/cm^2	0.43	1.27		0.049	8.4	
Reflective samples		407 nm			532 nm		
		A_0/τ_{rec}	τ_{erase}	M#	A_0/τ_{rec}	τ_{erase}	M#
E1aP	$I = 1$ W/cm^2	0.12	4.22	0.214	0.068	3.78	0.205
$d = 1\ \mu$m	$I = 2$ W/cm^2	0.28	1.78		0.090	3.02	
E1aP/12	$I = 1$ W/cm^2	0.22	2.56	0.264	0.055	10.04	0.265
$d = 1\ \mu$m	$I = 2$ W/cm^2	0.35	1.2		0.095	4.82	

M numbers in table II are in the range of 0.25 and there is no difference for the two different wavelengths. However, these values are not small considering the thickness of the layer. Similar values were reported for photoaddressable and photorefractive polymers by [10], but they are still low compared to the M# of thick photorefractive materials [9].

CONCLUSIONS

High storage density can be achieved by recording a Fourier hologram of a binary object. However, the high intensity peak in the Fourier plane saturates the recording material. Model experiments were performed to study saturation behavior of azobenzene polyester material. Results show that the material provides maximum diffraction efficiency when optimum intensity ratio is used for the reference and object beams. The diffraction efficiency strongly decreases when high intensity ratio beams are applied.

Sensitivity factor and multiplexing ability of the materials were studied at two different wavelengths. Results show an increased sensitivity of the materials at 407 nm. For the 1 μm thick samples, the calculated M# values are about 0.25 for the two wavelengths.

REFERENCES

1. J. Eickmans, T. Bieringer, S. Kostromine, H. Berneth, R. Thoma, Photoaddresable Polymers: A new class of materials for optical data storage and holographic memories, *Jpn. J. Appl.* Phys. Vol. 38. p. 1835-1836 (1999).
2. S. Hvilsted, F. Andruzzi, C. Kulinna, H.W. Siesler, P. S. Ramanujam: Novel Side-Chain Liquid Crystalline Polyester Architecture for Reversible Optical Storage, *Macromolecules* Vol.28, p. 2172-2183 (1995).
3. Á. Kerekes, Sz. Sajti, E. Lőrincz, S. Hvilsted, P. S. Ramanujam, Rewritable azobenzene polyester for polarization holographic data storage, in Holography 2000, Tung H. Jeong, Werner K. Sobotka, Editors, *Proc. of SPIE* Vol. 4149, pp. 324-331 (2000).
4. E. Lőrincz, F. Ujhelyi, P. Koppa, A. Sütő, G. Szarvas, G. Erdei, S. Hvilsted, P.S. Ramanujam, P.I. Richter, Rewritable holographic memory card system, in Optical Data Storage 2000, Dougles G. Stinson, Ryuichi Katayama, Editors, *Proc. of SPIE* Vol. 4090, pp. 185-190 (2000).
5. M. P. Bernal, G. W. Burr, H. Coufal, Experimental study of the effects of a six-level phase mask on a digital holographic storage system, *Appl. Opt.* Vol. 37. No. 11. (1998).
6. F. H. Mok, G. W. Burr, D. Psaltis, System metric for holographic memory systems, *Opt. Lett.* Vol. 21. No.12. (1996).
7. T. Todorov, L. Nikolova and N. Tomova, Polarization Holography 2: Polarization holographic gratings in photoanisotropic materials with and without intrinsic birefringence, *Appl. Opt.* Vol.23, No.24, p. 4588-4591 (1984).
8. N. C. R. Holme, L. Nikolova and P.S. Ramanujam, S. Hvilsted, An analysis of the anisotropic and topographic gratings in side-chain liquid crystalline azobenzene polyester, *Appl. Phys. Lett.* 70 (12), p. 1518-1520 (1997).
9. H. J. Coufal, D. Psaltis, G. T. Sincerbox (Eds.), *Holographic Data Storage*, Springer (2000).
10. G. J. Steckman, R. Bittner, K. Meerholz, D. Psaltis, Holographic multiplexing in photorefractive polymers, *Opt. Comm.* 185, p. 13-17 (2000).

Chiroptical Molecular Memory of Amorphous Azopolymer using Light Handedness

Mi Jeong Kim and Dong-Yu Kim
Department of Materials Science and Engineering,
Kwang-Ju Institute of Science and Technology, Kwangju, 500-712, KOREA.

ABSTRACT

For chirooptic molecular memory system, induced chirality on an azobenzene-containing amorphous polymer film was investigated using circularly polarized Ar+ laser with various ellipticity. High intense CD spectrum proved that optical-induced chirality on the amorphous film. Additionally, elliptically polarized light induced much higher chirality than circularly polarized light.

INTRODUCTION

Molecular optical switches, which can interchange between two distinct states by exposing it to light with different wavelengths or polarization, are expected to play an important role in various novel organic optical devices. Many researchers have investigated photochemical compounds, which can interchange between two conformational isomers by selective isomerization reaction upon irradiation at two different wavelengths. Azobenzenes, diarylethenes, flugides, spiropyrans are a few examples [1]. However, most of these photochromic compounds suffer from poor temporal stability and fatigue resistance due to different energy states of two isomers. Another advantage of chirooptical switching is possible non-destructive readout capability by reading the signal outside of absorption band.

Chiral materials are good candidates for these purposes due to two distinct bistable structures with the same energy and non-centrosymmertic properties in both molecular and macroscopic levels. Only difference of stereoisomers is optical rotation in opposite direction. In order to realizing reversible optical data storage systems, proper chiral structures must be designed to exhibit *switchable chirality*, which means two enatiomers are reversibly interchangeable by optical means. Recently, helical shaped molecules were focused for chirooptic molecular memory systems because their two enatiomers with opposite direction helicity can be interchanged by exposing it to circularly polarized light [1].

Azobenzene containing polymers are widely known photochromic materials due to alignment tendency to perpendicular direction of incident light polarization through trans-cis-trans photoisomerization cycles. Photo-induced chirality using circularly polarized light has been reported in azobenzene liquid crystalline polymers [2, 3]. However, for azobenzene-containing amorphous polymers, chirality induction and switching capability using circularly polarized light is not clear at present. The object of this research is to investigate chirooptical induction and memory of azobenzene-containing amorphous polymers without chiral carbon center when its solid film is exposed to various states of circularly polarized light.

EXPERIMENTAL

Epoxy based azobenzene amorphous polymer without chiral carbon center (PDO3) was synthesized as previously reported [4] and the chemical structure is shown in Figure 1. Glass transition temperature (T_g) and thermal stability of PDO3 were measured using differential scanning calorimeter and thermogravimetric analysis (TA Instrument). Substrate for the solid film was glass slide, which was cleaned by sonication in surfactant solution, acetone and water. Optically transparent films were prepared by spin casting process using 10wt% cyclohexanone solution and were baked at 160°C during overnight. The film thickness was 0.48 μm measured by α-step instrument.
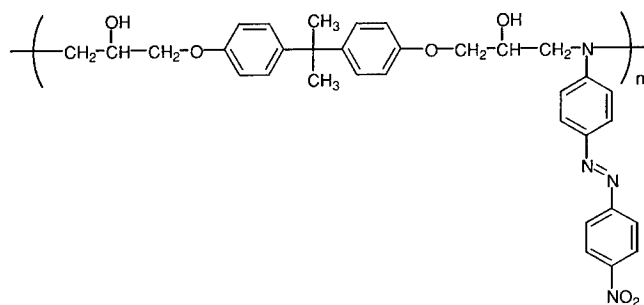
Figure 1. The chemical structure of epoxy based azobenzene amorphous polymer PDO3.

An Ar^+ ion laser beam (Coherent INNOVA skylight 305C) at a wavelength of 488 nm was used as a light source for chirality induction. The intensity of the expanded beam was 160 mW/cm². Ellipticity and handedness of circular polarization were controlled using a λ/4 waveplate and the beam profiles were measured using a linear polarizer before and after irradiation on the azobenzene polymer film. All exposure time was fixed to 10 min. Circular dichroism (CD) spectra of irradiated films as a function of ellipticity of incident light were measured using JASCO 720 instrument.
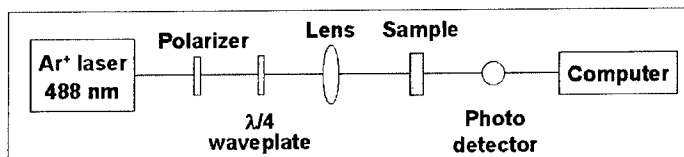
Figure 2. Optical set-up for chirality induction on the polymer film

RESULTS AND DISCUSSION

In order to investigate photo-induction of chirality on azobenzene containing amorphous polymer solid film, we synthesized PDO3 as shown in Figure 1. PDO3 polymer exhibited glass transition at 110°C and were thermally stable up to 266°C with 5% weight loss. The solid film obtained by spin coating was highly transparent due to amorphous properties of the material. The absorption maximum was at 456 nm measured by UV spectroscopy. The polymer films did not show any circular dichroism before irradiation. This was expected from the fact that the polymer structure is achiral.

Figure 3 shows CD spectra results of PDO3 polymer films after irradiation. When the PDO3 films were exposed to circularly polarized light (R-CLP or L-CPL), induced circular dichroism was negligible. However, in the case of elliptically polarized light, much larger CD on the film was induced. The CD spectra of the PDO3 films exposed to right and left-handed elliptically polarized light showed almost symmetric mirror images, which means that two different enatiomeric structures were produced by irradiation with opposite handedness.
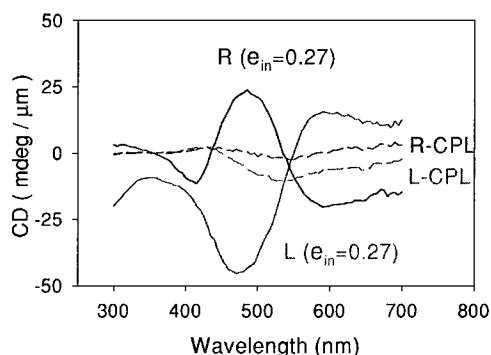
Figure 3. CD spectra of PDO3 films after exposed to circularly right and left polarized light (R-CLP and L-CPL), and elliptically polarized light ($e_{in} = 0.27$) during 10 min. e_{in} designate the ellipticity of incident radiation.

Figure 4 shows that the induced CD signal is strongly dependant on the ellipticity of the incident light, which is varying from linear polarization to circular polarization. Irradiation of the laser beam with linear polarization ($e_{in} = 0$) was not efficient to induce chirality on the azobenzene amorphous polymer PDO3 film. In the case of polarized light with small ellipticity ($e_{in} = 0.05$), the intensity of induced CD was −190 mdeg/μm at 415 nm. As the ellipticity of the beam increased further, the induced CD became smaller, and when the beam profile approached to circularly polarization state, the CD signal became negligible again. Even though dependence of ellipticity on optical rotation was reported [5], this kind of strong dependence of ellipticity on induced circular dichroism has never been reported before. We are currently investigating the detailed mechanism of this process and the nature of the induced CD.

Induced CD signal remained after several days with slightly reduction of the intensity. Therefore, the photo-induced chirality on the amorphous solid film of azobenzene polymer was believed to be due to permanent change of molecular conformation not due to temporary cis isomer population.
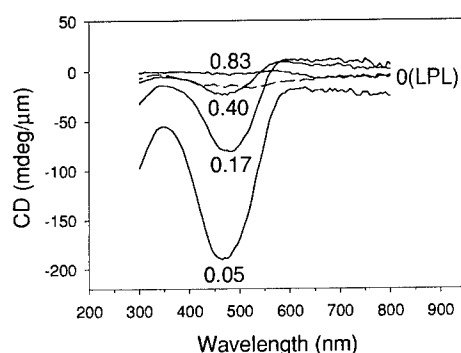
Figure 4. CD spectra of PDO3 films after exposed to left-handed circularly polarized light with different ellipticity during 10 min. The numbers represent the ellipticity of incident radiation in each case.

CONCLUSIONS

In this report, we have clearly shown that chirality can be optically induced in amorphous azobenzene-containing polymer film from measurement of CD spectrum. Elliptically polarized light induced higher circular dichroism on the film than circularly polarized light. It has been argued that highly organized structures such as LC phases may be responsible for this process. However, we have shown, from our experiments, liquid crystalline phase is not necessary to observe optically induced circular dichroism in azo-polymers. Further exploration of this process may open up a novel approach for the bistable chirooptical data storage applications.

ACKNOWLEDGMENTS

REFERENCES

1. B. L. Feringa, R. A. van Delden, N. Koumura and E. M. Geertsema, *Chem. Rev.* **100**, 1789 (2000).
2. L. Nikolova, T. Todorov, M. Ivanov, F. Andruzzi, S. Hvilsted and P. S. Ramanujam, *Optical Materials* **8**, 255 (1997).
3. G. Iftime, F. L. Labarthet, A. Natansohn and P. Rochon, *J. Am. Chem. Soc.* **122**, 12646 (2000).
4. D. Y. Kim, L. Li, X. L. Jiang, V. Shivshanker, J. Kumar, S. K. Tripathy, *Macromolecules* **28**, 8835 (1995).
5. L. Nikolova, L. Nedelchev, T. Todorov, Tz. Petrova, N. Tomova, V. Dragostinova, P. S. Ramanujam and S. Hvilsted, *Appl. Phys. Lett.* **77**, 657 (2000).

AUTHOR INDEX

SUBJECT INDEX